UNIVERSITY OF CALIFORNIA

Santa Barbara

Differential Self-Assembly of Novel Redox Crown Ethers

A dissertation submitted in partial satisfaction of the

requirements for the degree Doctor of Philosophy

in Chemistry

by

Andrew William Merithew

Committee in charge:

Professor Craig Hawker, Committee Chair

Professor Javier Read De Alaniz

Professor Steve Buratto, Department Chair

September 2014

The dissertation of Andrew William Merithew is approved.

_____

Steve Buratto

_____

Javier Read de Alaniz

_____

Craig Hawker, Committee Chair

September 2014

ACKNOWLEDGEMENTS

I would first and foremost like to personally thank my parents, sister and my grandmother Eleanor Curran whom which stood behind me throughout this endeavor. My graduate committee, for their support, guidance and understanding they gave me in preperation of this manuscript.

I gained much knowledge during my time here at UCSB, preparing myself for my my life. I owe a special thanks to Dr. Zenhua Gu, during my time in Dr. Zakarian's organic synthesis group, I will never forget the character you always brought with you to lab. Being humble and offering a few words of advice whether they be half in Chinese, I will always be grateful of the knowledge you gave me, if not about chemistry, about life and working toward your goals. Dr. Ilardi, what can I say except I owe you for making my first year here survivable, I enjoyed sharing lab space with you and the interesting conversations you brought with you to lab each day. The trio of my cohort especially my partner in crime, Dr. Michael Isaacman, E-5 tank soldier and good friend Sean Greenan of the U.S. Army, Katelynn Vargas for all of her help as my undergraduate assistant for years and editing contributions.

Finally I would like to thank my makeshift editing crew especially to a particular individual Javier Rubio-Velazquez of Geography who dedicated much time in helping me derive Chapter 2 along with Dr. Todd Squires (Chem Engineering). Won Hussayaya (Chem), Mira Lazaro (Chem/English), Tom Tran (Geo).

VITA OF ANDREW WILLIAM MERITHEW
September 2014

EDUCATION

Bachelor of Science, Chemistry, California State University, Channel Islands, May 2008 (*cum laude*)

Bachelor of Science, Biology, California State University, Channel Islands, May 2008 (*cum laude*)

Doctor of Philosophy, Chemistry, University of California, Santa Barbara, September 2014

PROFESSIONAL EMPLOYMENT

2008-2010: Teaching Assistant, Department of Chemistry and Biochemistry, University of California, Santa Barbara

Summer 2010: Graduate Student Researcher, INSET Mentor,

2010- May 2013: Graduate Student Researcher, University of California, Santa Barbara

2013- Teaching Assistant, Department of Chemistry and Biochemistry

PUBLICATIONS

Synthesis and Characterization of an Anion-dependent 2:1 and 1:1 Self Assembling 1,2-anthraquinone[benzo]-18-Crown-6 Ether Utilizing 1D and 2D NMR

180 Degrees: Facile Thermal Rearrangement of Monoallylated Di-hydroxyanthraquinones in the Melt (In preparation)

AWARDS

Alzheimer's Institute Inaugural Scholarship, California State University, Channel Islands, Spring, 2007

FIELDS OF STUDY

Major Fields: Organic Synthesis, Materials Chemistry, Nanoscience, Computational Chemistry, Chemical Engineering, Structure-activity Relationships

Studies in Total Synthesis: Scale-up of the reactions in the Synthesis of Pinnatoxin A "The Spiroimine fragment" with Professor Armen Zakarian

Studies in Chemical Engineering Modeling Advanced Transport Properties of Ions with Todd Squires

Differential Self Assembly of Novel Redox Crown Ethers

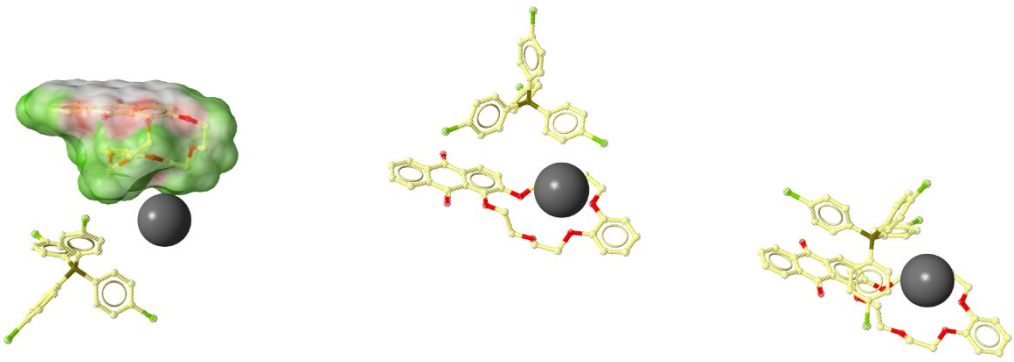

by

Andrew William Merithew

Abstract

Differential Self Assembly of Novel Redox Crown Ethers

By

Andrew William Merithew

Retinal prosthesis relies on the stimulation of living nerve tissue behind the rods and cones of the eye. The current state of the art relies on electrodes controlled by cameras which directly stimulate the nerve tissue to elicit a response to an image. These types of retinal implants have allowed for short-term crude vision in patients but have had limited long term success due to external battery packs and electroplating of the implanted electrodes.

Ionic stimulation is one of the principle mechanisms that sensory neurons utilize in the generation of an action potential. In a complex transduction pathway, ionic gradients are constantly altered inside the neuron by voltage sensors or mechanically controlled gates embedded in the neuronal cell membrane; responsible for the open and close state of these ion channels.

It has been demonstrated that local concentration increases of K^+ by direct injection proximal to the nerve can elicit nerve firing at a concentration of 15-20 mM (3-4X normal concentration) increase in K^+ concentration. As part of a larger concept of integrating biotechnology with nanofabrication, the materials for the development of potassium selective sequestration/storage and delivery were developed in the form of a redox-gated K^+ selective crown ether.

The structure of the anthraquinone-based crown was deduced by computational simulation and stoichiometry of the complex confirmed by mass spec. along with 2D diffusion NMR techniques. In this instance, the stoichiometry could be controlled by the addition of different salts to give a 1:1 complex with large, aromatic anions and a 2:1 complex with smaller anions such as triflate. The synthesis of the molecule was optimized by computational modeling and simulations of transport through an artificial membrane. The selectivity of the architecture developed was specific for K+ over Na+, the other major ionic species present in the blood. The mechanism influencing the self-assembly of this class of compounds has much to do with the breakage of intramolecular π-stacking interactions and the formation of stronger intermolecular π-stacking interactions.

Finally, the transport of K^+ through nanoporous membranes and single nanopores with novel PEG-type polymeric dispersions is demonstrated. This thesis concludes with future work toward developing more advanced transporters and proposes novel uses for anthraquinone-appended polymers as proton exchange membranes and DNA-base pair interchelators.

Table of Contents

Chapter I – Development of Retinal Prosthesis Utilizing Nanobiotechnology

Objective

- Develop an understanding of the visual transduction pathway a nerve physiology
- Introduce the current state-of-the-art in retinal prosthesis
- Examine how selectivity is achieved among different membrane proteins to pass specific ions through the plasma membrane
- Explain the concept behind molecular control by utilizing redox-active organic molecules

Integration of silicon based systems with existing neural architecture has recently become an area of widespread interest in neural prosthesis (Al-Ibrahim, 2004). Fortunately, organosilicon chemistries have been developed to integrate natural enzymes (Yang, 2014), aptamers (Lai, 2007), small molecules and Ionophoric compounds (Wienk, 1990) to interface with the inorganic silicon. These devices have been successfully implanted in several patients, albeit with low to moderate success and there is indeed much room for improvement (Weiland, 2005).

Current approaches utilize inorganic diodes or inorganically coated Indium Tin Oxide (ITO) electrodes to generate the current used to power their device and stimulate the nerve (Privett, 2010), (Park, 2011). The central problem revolves

around the electrochemistry of the nerve and the electrolytic environment surrounding. Most of the current from either of the aforementioned stimulation processes shunts the current through the electrolyte solution instead of through the nerve. Since the desired current isn't reaching the nerve fiber directly, the threshold current for perceiving phosphenes, or packets of light transduction becomes higher from the device standpoint, requiring patients to wear bulky external power sources while raising the amount of current output the device puts out. This raises concerns over overheating (Piyathaisere, 2003) the surrounding tissues and causes electroplating of the electrodes which would then need to be replaced and implanted once again.

An introduction to vision and current state of the art of retinal prosthesis and finish with this thesis' vision for an effective, ionic-based system to stimulate an action potential that circumvents current leakage problems.

The field of ocular prosthetics was pioneered by Foerster who was the first to realize that stimulating certain parts of the brain could elicit the generation of percepts or phosphenes (Foerster, 1929). A phosphene is a perceived light image without light actually ever entering the eye. The current state of the art revolves around placing electrodes coated with different materials proximal to the neuron and passing a current through the extracellular fluid to the nerve. This system works for stimulation of the neural tissue albeit with very low efficacy. This is because most of the current driven by the electrodes gets shunted around the nerve through the highly electrolytic, conductive extracellular fluid.

As the aging population grows, diseases of age such as macular degeneration will become more prevalent. This spurs the need for the research and development of non-traditional remedies for treatments of motor impairments with prosthetic devices. Prosthetics have been implemented in debilitating diseases for decades and more intricate prosthetics are being developed continuously; some improvements on past innovations, some completely novel in nature and function.

The current state of the art rely on two methodologies to alleviate the degenerative modes and these include:

1. **Sub-retinal implants** – an array of micro diodes on the outer surface of the retina flanked by a photoreceptor layer and the retinal pigment epithelium. This type of implant relies on the normal signal processing of the retina and the intactness of the middle and lower layers. Sub-retinal implants work by a grid of micro diodes that respond to light, stimulating the native nerve tissue. The drawbacks are the need for additional power, concerns over heat from the device damaging the retina (Piyathaisere, 2003). The need for an intact lower and middle nerve cell layer is required, which may exclude some patients with advanced degeneration modes.

2. **Epiretinal implants -** sit on the inner surface of the retina and stimulate the ganglion cells directly, bypassing the signal processing needed by other layers of the retina, an advantageous method for those whose disease extends

beyond the photoreceptor layer. The implants are actually tiny silicon-platinum microarrays stabilize by using micro tacks along with the slight pressure created by the vitreous humor. The implant requires the use of an external video camera and an external transmitter for a constant power source. The camera receives the image, processes it and communicates the information to the implant wirelessly (Liu, 2000). The main disadvantage is the need to wear an external apparatus, which can be cumbersome for those whom which do not see already. In clinical studies, 6/6 patients had perception of phosphenes, albeit to varied levels (Klauke, 2011). Another study showed patients could hardly perceive any percepts or phosphenes at all, leaving the area open for further research and development (Rizzo, 2003).

Today, only a handful of people currently have either type of prosthetic implanted in their eye. The main concern thus far has been the failure of more than half of the devices that have been implanted along with unforeseen compatibility issues such as underlying damage of the optic nerve. Success stories with patients whom which have long-term microelectronics surgically implanted to the eye have been demonstrated by (Humayun, 2003) As the number of microelectrodes per grid is relatively small, an estimated 600-1000 electrodes will be needed in order for patient to make out higher order structures such as facial recognition and reading text (Weiland, 2005).

The approach this thesis takes toward retinal implants is similar but instead of electrical energy as the source of stimulation, the aim is to use ionic gradients. The focus is to integrate the very mature field of complementary metal–oxide–semiconductor (CMOS) processing technology for sensing electronics, with a versatile single-molecule detector, the nanopore. By employing a unique combination of digital and analog circuit techniques, feedback and close physical coupling afforded by nanofabrication, this platform will enable a new class of sensory receptors. This unique sensor architecture exhibits low-noise, high-sensitivity, lower heat and will hopefully increase sensitivity and resolution over the current-leaking devices mentioned earlier.

Furthermore, by functionalization of these nanoscale detectors with molecular recognition units (such as redox crown ethers and non-specific redox active DNA interchelators), a new class of biosensors can be designed. In the chapters to follow, we address integration of novel organic compounds with the challenges of building ultrathin nanopore arrays that are crucial to the assembly of an electronically coupled K^+ ion pump. We will further assess the role of K^+ in generating an action potential in the neurophysiology section.

Traditionally biosensors concentrate mainly on the detection platform and not on signal processing. This decoupling can lead to inferior sensors and is exacerbated in nanoscale devices, where device noise is large and large dynamic range is required. Herein, we outline a novel platform that integrates the Nano, micro and macro scales in a closely coupled manner that mitigates many of these problems. Specifically,

integration of molecular recognition elements of crown ethers with the nanopore detector to design a new class of biosensors in a CMOS compatible platform. The formation of multi-stimuli responsive NAND logic gates has been demonstrated by chemical recognition elements occupying multiple energy states and having multiple equilibria (Dagnelie, 2007). The functionalized nanopore detector is designed to allow for unambiguous interpretation of scientific data, rather than ease of experimentation, thanks in large part to the versatility of the unique CMOS platform proposed.

Since nanopore detectors measure changes in pore resistance due to the presence or absence of the target, sensitivity is a function of nanopore thickness. The unique integration of electrodes and electronics afforded by the CMOS platform allows for the pore resistance to be dominant rather than the access resistance as in conventional approaches. Superior sensing and bandwidth is achieved by using a novel bit-stream based computational approach rather than traditional sensor electronics. The digital feedback technique has the potential to greatly enhance the measured data, augmenting and controlling front-end electronics without sacrificing bandwidth. This offers the potential to discover new phenomena, which are beyond the reach of conventional measurement schemes. Additionally, unique integration of the multiple physical scales involved enable the design of cheap, disposable and robust biosensors. Sensors are evaluated on a broad range of criteria such as sensitivity, selectivity, response time and dynamic range with appropriate controls to verify each criterion.

Despite the limited success these prosthetic prototypes and working devices mentioned have had, they will undoubtedly have limited lifetimes because they utilize electrodes to stimulate the nerve tissue. The approach this thesis takes is an avenue of stimulation that alters the electrochemical gradient and generates the same type of action potential by using ions instead of current that are endogenous to the human body.

Conversion of light to chemical energy has been investigated before with gene mutations that incorporate a light-oxygen-voltage mutation which was shown to capture light energy and convert the signal to an active chemical signal in neurons (Yarkoni, 2012).

Figure 1.1 – The plan to couple electrical circuits with electro active organic materials.

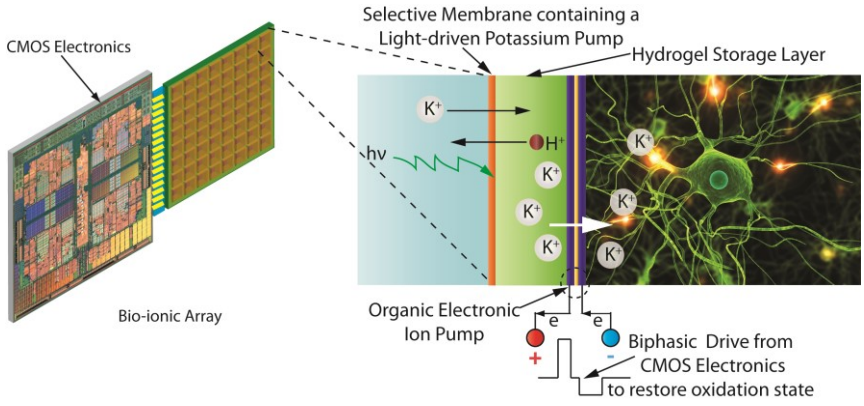

Ion Channels

Ion channels have two basic characteristics; recognition of a substance and the ability to initiate a response. Ion channels effectively meet the definition of a

receptor, they bind ions selectively and initiate an open or close response. An ion channel is a transmembrane pore comprised of three elements; a *pore* responsible for the transit of the ion, one or more *gates* that open and close in response to specific stimuli that are received by the *sensors*.

The gates can be defined in one of two broad categories, conformationally gated and chemically gated. In the latter, a conformation change induces a shift in the position or structure of some cofactor we will deem as X. An effector molecule bound at one site allows the transition to the active, catalytic state of the gate and opens the gate for the ligand to pass through the receptor or pore.

An example of this is with heme-type proteins and more specifically Hemoglobin A itself. This molecule has a hemeprotien which binds diatomic oxygen, oxidizing Fe^{II} to Fe^{III} resulting in a shift from the in-plane conformation to a centralized pyramidal structure within the porphyrin ring (Breslow, 1986). In turn, this causes an increase in affinity and exhibits positive co-opertivity due to the stepwise out-of-plane bending of the histidine residues in the tetrameric alpha and beta subunits of the enzyme and sequential step-down energetic effects in terms of redox potentials of the iron species. Positive coopertivity means that the first bound molecule increases the affinity for binding a second molecule of the same type.

Neurophysiology and Sensory Perception

Specific channels transport certain ions against their gradients by active transport. Ions in the context of nerve cells contain dense junctions of channels that help regulate what is called a nerve action potential. These ions can act on

mechanoselective neurotransmitter receptors, polarizing the membrane leading to an induced conformational shift, opening the gate allowing for a rapid influx of K^+.

The Visual Transduction Pathway

The pathway of visual transduction of an object visualized by the eye starts with a light stimulus which depending on the absorption wavelength of the light. The retina which contains rods and cones contains 11-*cis*-retinal, a form of vitamin A that is bound to the proteins "opsin" to form rhodopsin in the rods and iodopsin in the cones.

Figure 1.2 - Cyclic diagram showing the specific interplay of light transduction by combination of ionic and electrochemical gradients interpretation

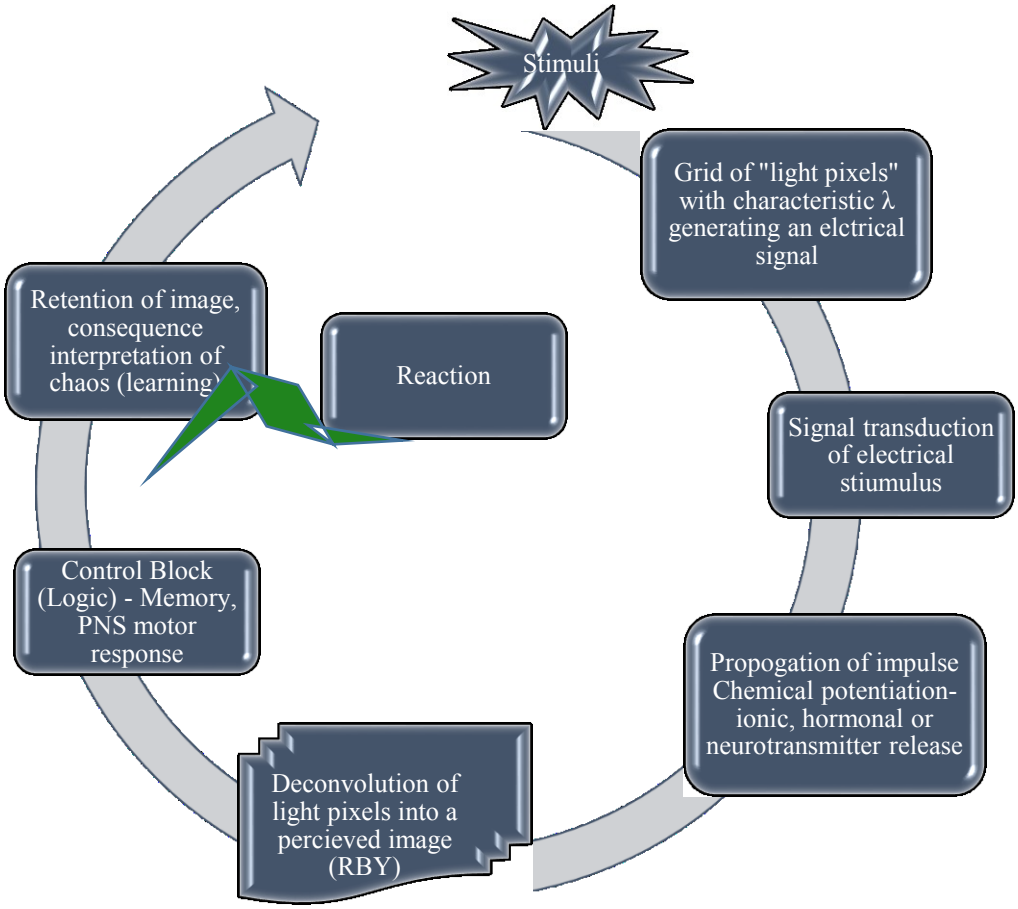

As light enters the eye, the 11-*cis*-retinal is isomerized to the all "trans" form. The all "trans" retinal dissociates from the opsin in a series of steps called photo-bleaching. This isomerization induces a nervous signal along the optic nerve to the visual center of the brain. An action potential is generated, converting potential energy into chemical energy. The retina then stimulates the dendrites (neuron) which is carried by the optic nerve to a junction that deciphers binocular vision from both

eyes responsible for our sense of depth perception. The signal is then carried to the geniculate nuclei which are located on either side of the cerebrum so the brain receives signals from both eyes; and finally terminates at the visual cortex on both sides of the cerebrum.

After the disassociation from opsin, the all *trans*-retinal is recycled and converted back to the 11-*cis*-retinal form by a series of enzymatic reactions. In addition, some of the all-*trans* retinal may be converted to the all *trans*-retinol form and then transported with an interphotoreceptor retinol-binding protein (IRBP) to the pigment epithelial cells. Further esterification into *trans*-retinyl esters allow for storage of *trans*-retinol within the pigment epithelial cells to be reused when needed. The final stage is conversion of 11-*cis*-retinal combining or associating with opsin to reform rhodopsin (visual purple) in the retina. Rhodopsin is needed to see in low light (contrast) as well as for night vision. Deficiencies in retinol (Vitamin A) have proven to show neurotoxic effect in brain development and functioning, suggesting that this intracellular trafficking is vital to this pathway (Spencer, 2012).

Ionic Gradient and Cellular Communication

Elaborate transport of ions across membranes is achieved primarily to maintain the osmotic gradient of electrolytes across the typical cell membrane which on average spans a short distance of 30 nM. The cellular membrane composition is comprised of 50% lipids, which include sterols, cholesterol and unsaturated fatty acids with amphiphilic head groups exposed to the extracellular fluid and fatty acid chains aligned inward, buried due to the hydrophobic nature of these all carbon-

containing chains. The other half consists of proteins such as raft proteins, receptors, antibodies and G-protein coupled receptors that are constantly undergoing reorganization, inserting and diffusing away from the membrane. This is why the cellular membrane is most often referred to as a "fluid mosaic", as it is amenable to various environmental factors and reorganization to achieve cell-specific functionality.

The cell membrane in Eukaryotic cells is responsible for hosting many processes, primarily transport of necessary solutes into the cell and excretion of waste metabolites out of the cell. Cofactors, amino acids, hormones, vitamins and many other soluble and sometimes insoluble solutes endogenous to the body are transported at rates often reaching the limit of diffusion through the membrane.

In the special case of sensory nerve cells, ions play a more crucial role in the transduction of stimuli by using gradients of ions under tight regulation of intracellular and extracellular K^+, Na^+ and Cl^- ion concentrations using ultrafast biphasic ion channel gating on the timescale of picoseconds (10^{-12}). Crucial to the spatial-temporal perception of images by the human eye; ionic gradients along with neurotransmitters are used by the nerve cells (wires) to generate an action potential.

This action potential begins at the dendrites and disseminates through the nerve, away from the cell body, terminating at the axon. The axons are the major conductor or mediator of thousands of inputs from stimulatory neurons. The axon has a highly electrically insulating structure, consisting of the protein Myelin. Myelin is highly

insulating in nature and microns in thickness increasing the membrane resistance and reducing current loss over long distances.

If the location of the stimuli is at the periphery or distant from an axon, the action potential continues on to the next synapse via a combination of neurotransmitters (GABA, acetylcholine, etc.) and ionic signaling at junctions termed synapses, where the impulse is propagated in series during a process termed electrophotonic coupling to the next neuron until it finally terminates at an axon. Photonic coupling concludes with the generation of phosphenes, or the perception of light. The light impulses are gathered by the chief transducer, the optic nerve which carries the gathered inputs into the glia of the brain where an image is perceived.

Figure 1.3- 3D coordinate map that defines all spatial coordinates in the X,Y and Z directions

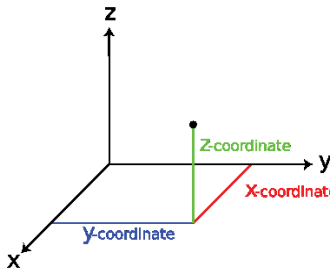

The specificity and spacial-temporal (figure **1.3**) coordinate map that defines the position where the initial nerve impulse is generated regulates the resulting resolution and quality of the image reconstructed by the brain, comparable to "pixels" on a LCD screen. Very high pixilation results in increased resolution of the resulting image by generating a more intricate electrochemical impulse that

propagates down the wire to the main cable, the axon. The action potential ultimately terminates away from the body of the cell and the electrical current is converted back to a chemical signal, resulting once more in the release of neurotransmitters. These neurotransmitters contain the information needed by the cell to decode the light stimulus converting chemical information into "pixels" generated by a specific wavelength of light.

These pixels code for the original light input captured by the rods and cones of the retina. Observables such as brightness, color and shadow are at once processed into a perceivable image.

There are 120 million rods (low-light vision) and 6 to 7 million cones (color sensitivity) in the average human eye. The rods are concentrated toward the periphery and have high specificity for stimuli which involve moving objects, depth perception and low-light vision. Photoreceptor and rods have cones containing hundreds of conjugated molecules and the main component, *(Z)* or *(E)*-retinal, which act as light-induced molecular machines, isomerizing to all *(E)* in the dark and *(Z)* during periods of light.

Figure 1.4 - Single chain of the tetrameric protein Rhodopsin with the isomeric retinal shown buried between the insulating alpha helices and beta-sheets, allowing for efficient long-range electron transfer.

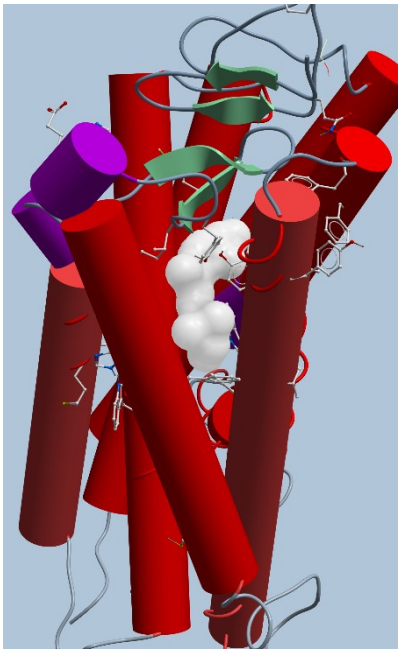

As we age, different diseases states arise due to loss or damage to the rods and cones, leading to macular degeneration. Many approaches to date have addressed this issue such as polymeric-encapsulated neurogenic drugs, which have showed dramatic increase in the recovery of a crushed sciatic nerve animal model (Allen, 2000). Redox approaches in bio-signaling using polyoxalate metal clusters (POMS) have shown to self-assemble, aggregate and compartmentalize reactions in inorganic cells (Cooper, 2011). $Ca2^{+}$ has been used as an effector molecule for ionic stimulation of live tissue (Song, 2011).

Role of Ions and Channels in Action Potential

From the science, theory and recent elucidation of membrane protein function at atomic resolution, we have come a long way in understanding the processes that govern selectivity in natural and synthetic systems by mutagenesis of enzymatic proteins, and by analyzing the solution and solid-state properties of ligand-interactions that mimic what occurs in nature.

Figure 1.5 - As modeled below, the leucine transporter LueT undergoes a favorable allosteric shift once sodium ions (purple) first bind to the molecule (left), allowing luecine to come in a bind to the active site (center) and finally the symporter expels both the amino acid and sodium ions inside, ending the neurotransmitter cascade outside of the cell (right)

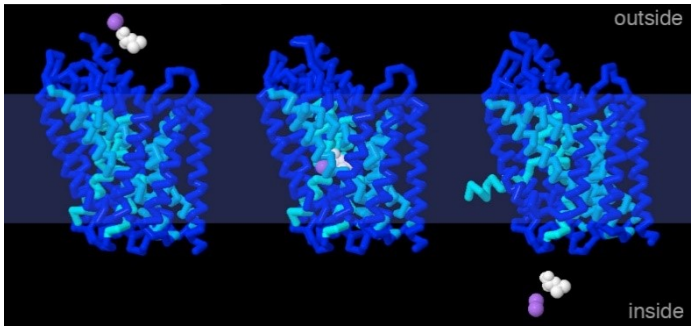

Membrane proteins are highly dynamic in nature and constantly undergoing fluctuating thermal motions that until recently, hindered crystallization by standard methods. When crystals were obtained, membrane biologists could not obtain interpretable X-ray diffraction patterns to reconstruct the electron density maps to visualize a model. While many membrane proteins have proven quite difficult to

crystallize in order to obtain quality diffraction data, bacterial homologues of these types of transporters have been solved and numerous deposits of crystallographic information has been deposited across the Protein Data Bank (PDB). These structures have allowed progression of the study of ion translocation, an example shown in figure **1.5.**

Before the elucidation of the structure of K^+ channels were available at atomic resolution, scientists in the field of structural biology could at best hypothesize which amino acids were critical to the selectivity of the voltage-gated K^+ channels by site directed mutagenesis. Although these experiments provided key information as to which amino acids were essential for selectivity, the method did not compensate for any type of co-opertivity or multi-amino acid induced selectivity.

This was indeed a major setback in gaining further insight as to the function of ion channel selectivity until the late 1990's, when new techniques in stabilization of the protein crystal, with high molecular weight polyethylene glycol molecules (PEG) and collection of diffraction data at ultra-low cryogenic temperatures, allowed for an interpretable diffraction pattern.

Inspirations from biology: Examining a structural motif to mimic

Selectivity in Potassium Transport

The basic structure of potassium channels consists of a four subunits that form the active tetramer comprising the ion channel. Several studies (Long, 2007) over the past decades have proposed an initial snug-fit mechanism for initial complexation of

K^+ from the extracellular fluid coupled with a rapid ion-ion repulsion within the channel enhancing the overall diffusive flux of K^+.

Figure 1.6 – A tetramer of KscA in closed pore (left) with α-helices pointed inward and homologue MTh (right) in its open confirmation with a flatter structure. Copyright Nature Publishing Group.

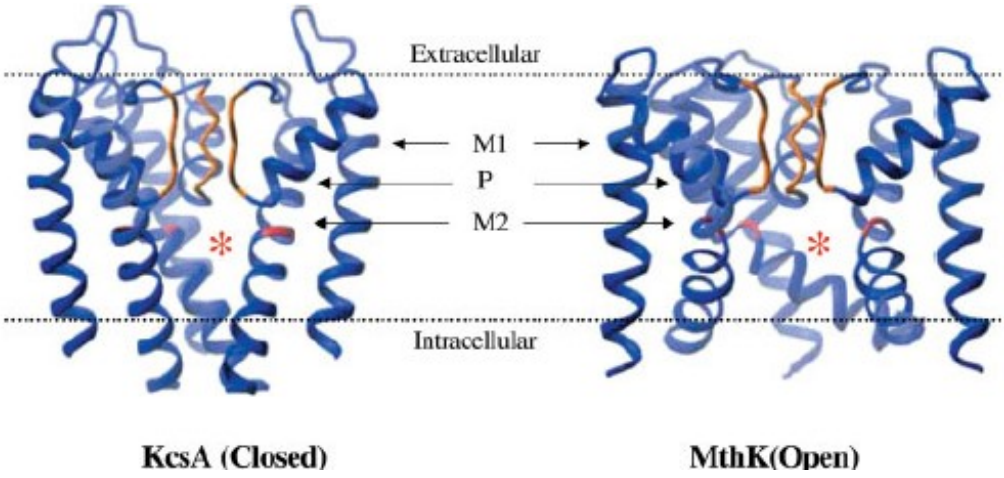

The phenomena is shown figure **1.6**, where the potassium ions are being guided in a head to toe fashion toward the intracellular cytoplasm. The carbonyls of the backbone lie relatively close to the pore channels which provide a host for the molecules as they traverse through the membrane. This elaborate transport phenomena is guided by "gates" or electric field-effects that help modulate the intracellular polarization (Ai, 2010).

Figure 1.7 – Single subunit trimmed away from PDB entry 3LDC KscA channel in the "open" state. Structure was crystallized in 100 mM KCl.

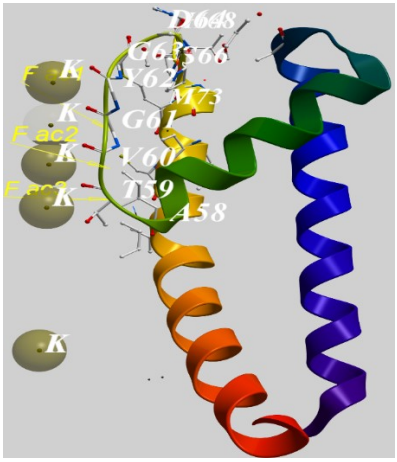

Gates effectively couple all of the gradients (Ai, 2010) of fluid flow, ionic concentrations and electric field by the Poisson-Nernst-Planck equation **1.1**:

$$-\varepsilon f \nabla^2 \phi = F(c_1 z_1 + c_2 z_2) \qquad \textbf{1.1}$$

$$\nabla \cdot N_i \equiv \nabla \cdot (\mathrm{uc_i} - \mathrm{D_i} \nabla c_i - \mathrm{z_i} \frac{D_i}{RT} F c_i \nabla \phi) = 0, i = 1,2 \qquad \textbf{1.2}$$

where ϕ is the electric potential within the fluid; F is the Faraday constant; c_1 and c_2 are, respectively, the molar concentrations of the cations (K^+) and anions (Cl^-) in the electrolyte solution; z_1 and z_2 are, respectively, the valences of cations ($z_1 = 1$ for K^+) and anions ($z_2 = -1$ for Cl^-); N_i is the ionic flux density of the $_i$th ionic species; u is the fluid velocity; D_i is the diffusivity of the ith ionic species; R is the universal gas

constant; and T is the absolute temperature of the electrolyte solution. The thickness of the electric double layer formed is characterized by the Debye length given by **1.3**

$$\lambda_D = \kappa^{-1} = (\varepsilon_f RT / \Sigma_{i=1}^{2} F^2 z_i^2 C_0)^{1/2} \quad \textbf{1.3}$$

K^+ selective passive transport channels (leak channels) are present in the membrane and result in a potential offset of about +18 mV from -88 mV to -70 mV. This makes neurons at rest more permeable to K^+ than Na^+, which has very few leak channels. The selectivity filter in K+ channels is conserved among species with an eight amino acid sequence termed the "signature sequence" TMTTVGYG (Heginbotham, 1994) where initial binding occurs. The sequence confers selectivity as site-directed mutagenesis revealed that replacement of one of these residues results in complete loss of selectivity (Heginbotham, 1994). To aid in defining where this specificity elicits from, computational simulations with different cations traversing the pore have suggested that Na^+ does not bind the signature sequence, more than likely due to its hydrodynamic radius being far smaller than that of K^+ (Bernèche, 2005), (Garofoli, 2003).

The snug-fit is complemented by other triggers such as an allosteric shift (conformational change of enzyme subunits upon ion binding events) where in this case, a phenylalanine π-cation interaction is hypothesized to mediate electronic coupling of the K^+ ion gradient to the pore gating mechanism (Long, 2007). The rim of the pore is also lined with four negatively charged amino acids, which exclude any anions from entering. Other molecules such as tetraethylamine which has a diameter of about 8 Å, (similar to that of K^+ with its hydration shell intact) and can

enter and effectively block the pore but cannot traverse through it, lending more evidence toward complete dehydration of the ion as a selectivity requirement (Shrivastava, 2000).

Since biology uses both ions and neurotransmitters for neural signaling, it must be possible, at least in principle, to design a neural prosthesis that interfaces to the natural neural system using neurotransmitters. Some attempts have been made to design retinal prosthesis using a neurotransmitter based approach. However, none of these have been developed into clinically viable therapies due to the principal issue of having to supply spent neurotransmitter, either via a reservoir or sequestration. A reservoir of neurotransmitter poses significant risk since any rupture of the reservoir would result in catastrophic damage of the surrounding neural tissue. Sequestration of neurotransmitters is not easily possible since the neurotransmitters, such as GABA and glutamate, are taken up by glia and broken down.

One approach to mitigate this is to use an alternative chemical stimulation method, namely ionic stimulation. Ionic stimulation could circumvent the above issue by actively sequestering ions from the extracellular fluid. Another approach that has been explored is the use of ionic modulation to lower the electrical threshold for neural stimulation. In this approach, a calcium sensitive ionophore is used to locally sequester the calcium around the nerve using electrical control. Though, this is a viable approach, it requires large induction times (~1 min), which would prevent it for being used in sensory perception types of devices. Alternative approaches using direct Ca^{2+} stimulation has also been demonstrated (Isaksson, 2007).

The approach taken in this thesis is quite different approach of direct neural stimulation via K^+ ions. It is well know that neurons can be stimulated by elevated extracellular concentrations of K^+ (Weiss, 1986). Neurons are most permeable to potassium in the resting state, making them the most viable ionic stimulation species. Another advantage of the K^+ based approach that active sequestration can be performed using synthetic ionophores. If a potential could be applied across a membrane selective for pumping K^+, one could envision a mechanism to pump K^+ against its concentration gradient. This is turn will elicit a neuronal response creating an electrical signal by the production of phosphenes, or packets of visual perception. The underlying nerve cell fibers orient themselves as model parallel-plate capacitors [+/--/+] with large potential for conduction, it could in fact be possible to utilize a biphasic prosthetic device to trigger an action potential by selective ionic stimulation. The therapy is then in the hands of the patient as they learn to interpret these signals.

Figure 1.8 – Simplified design of the generation I K^+ ion pump.

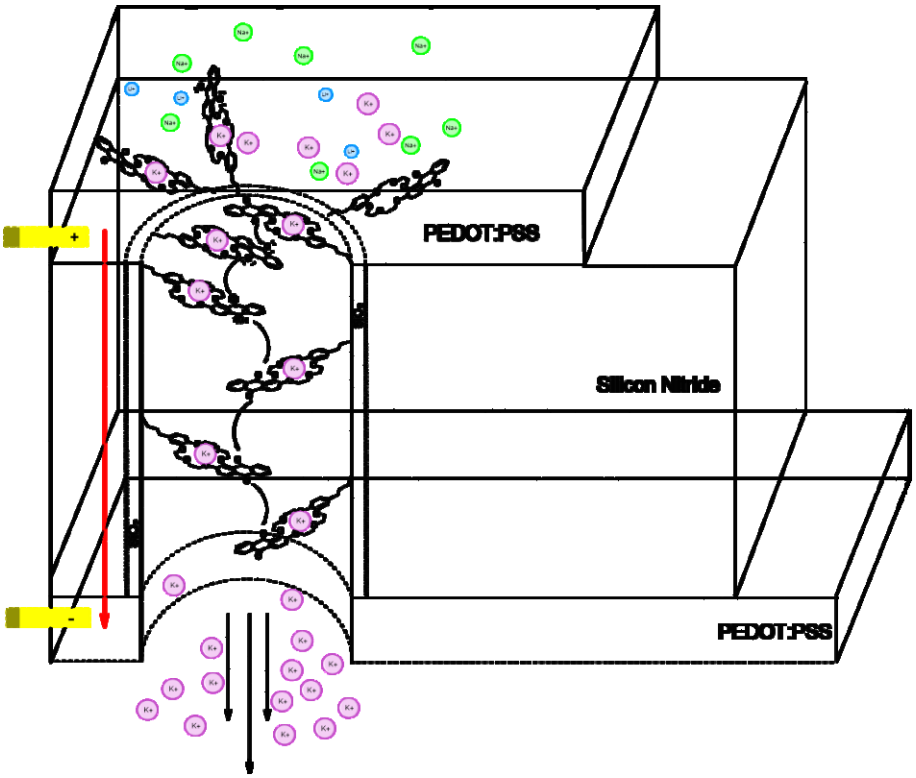

Finding the materials suitable to mimic the receptor functionality while remaining biocompatible, our attention turned to ion selective field-effect transistors (ISFET's). ISFET work by producing an electrical response once a target analyte or ion in this case is bound to the receptor. Small changes in current are sensed by the proximal induced electric field and the length of the organic-inorganic spacer which should be rather short in order to produce a maximum in the sensitivity and response elements of the ISFET. The device would rely on generating an ionically-induced stimulatory response by the selective release of K^+ ions.

From the science, theory and recent elucidation of membrane protein function at atomic resolution we have come a long way in understanding the processes that govern selectivity in natural and synthetic systems by mutagenesis in the context of enzymes and by analyzing the solution and solid-state properties of potential ligand-interactions that mimic what occurs in nature. Developments in host-guest chemistry have become so sophisticated, we can even manipulate single crystal to single crystal transitions upon cooperative guest translocation through non-porous lattices to achieve transport (Atwood, 2002).

In this thesis, we present our first effort towards the rational design of a supramolecular ionophore that is selective to K^+ ions under redox-gated control. At the heart of our Supramolecular assembly is the anthraquinone motif, enabling both a preorganization of the crown ether ring (see Chapter V), and redox activation.

The supramolecular bio-inspired structures synthesized would function by active sequestration of K^+ ions and storage of the ions in a pre-selective, much thicker "hydrogel" layer, while loading into the gel occurs by electro-diffusion. The delivery of the ion to the neuron (figure **1.8**) can be effected by using a variant of an organic ion pump. The electrochemical ion pump is an electron to ion transducer based on a conducting polymer, namely Poly (3,4-ethylenedioxythiophene) doped with polystyrene (sulfonate) (PEDOT:PSS). By introducing a selective blocking layer that prevents electron transport through the polymer film, either by over oxidation or design, ion transport can be effected. When a negative potential is applied to the PEDOT:PSS layer, current flows by the oxidation of $PEDOT^0$ (eq. **1.3)**. If this layer

is exposed to an electrolytic solution then a cation (M^+) from the electrolyte will be incorporated into the film to maintain charge neutrality (eq. **1.4**). Alternatively, a film that is in its reduced state can be made to give up its cation (M^+) if a positive potential is applied to it (Eq. **1.5**). The half-cell reactions at the anode (+) and cathode (-) are given by:

$$PEDOT^0 + PSS^- : M^+ \rightarrow PEDOT^+ : PSS^- + M^+ + e^- \text{ (anode)} \qquad \mathbf{1.3}$$

$$PEDOT^+ + PSS^- : M^+ + e^- \rightarrow PEDOT^0 : PSS^- : M^+ \text{ (cathode)} \qquad \mathbf{1.4}$$

By applying the right polarity of the potential, cations can be made to travel from one electrode to another where they can then diffuse into the electrolyte if the concentration is lower.

Though we are using a current drive to eject the potassium ions the current is confined to the PEDOT:PSS layer and does not travel through the electrolyte and hence does not interfere with the recording electrode if one is present, thereby enabling simultaneous stimulation and recording of neural signals.

Biological transport systems operate mainly in the diffusion-limited domain. The nanoscale dimension makes this domain favorable since the length scale and the time that it takes to diffuse through it are connected through an inverse square relationship. Bio membranes are a fundamental component in enabling this operation. Bio membranes provide a structural framework via their amphiphilic nature and a functional framework by incorporation of channels, receptors and pumps.

Self-assembly is a key property that nature relies on in generating these membranes. By exploiting the hydrophobic-hydrophilic interactions these membranes assemble into nanometer thick bilayers as well as other structures. If the goal is to mimic the principle of natural Nano-architectures; self-assembly is essential as a key component. Unfortunately, natural bio-membranes are very fragile and cannot be directly incorporated into an engineered Nano system.

Designing an artificial membrane

Much attention to the development of crown ethers specific for their cations inherent size was initially developed by Gokel, Voyer and Pederson in the 1970's and has since lost interest in the scientific community. Crown ethers based on the reversible Fc/Fc^{+} couple have been used as both calcium divalent cation (Isaksson, 2007) and chloride anion sensors (Evans, 2011), (Langton, 2014). Triggered release by [Diaza 18-C-6] cobalt and copper complexes by addition of HCl protonates the amine of the crown ether, releasing the colored substrates into the aqueous phase (Dergunov, 2011).

As these novel compounds found increasing functionality in their uses, entire conferences were devoted to exploring and discussing the ideas of crown ether structure and selectivity. These derivatives included branched, linear, basket-type (Kou, 1993), calixarenes (Mathews, 2002), (Casnati, 1996), (Gargiulli, 2009), rosette (Hoebin, 2005), molecular clefts (Pliska, 2001) and crown ether lariats (Zhang, 2010) as single cation binders as well as the former bound to polymers (Marsella,

2003), (Sakai, 2010), some with peptide-like backbones (Ouelett, 2010) exploited the popularity of the field at the time but has since fallen off the charts (Breslow, 1986).

Crown Ether Current State of the Art

Today, it has since been five decades since Pedersen began his initial quest to develop a complexing agent for divalent cations (Pederson, 1967). Heteromacrocycle chemistry has gone through several phases during the ensuing years. At the start of the discovery of crown ethers, the main focus was on structural diversity so that a general template could be realized. The second and third phases of the crown era involved studying the physical properties of the crowns both in the solid and liquid state. As some would agree, these fundamental studies paved the way for modern day supramolecular chemistry.

Once the structural and physical chemistry was understood, outside fields such as biology and the sciences alike began to utilize crown ethers for solid state chromatographic separations, anion/cation exchange chromatography, chiral separation of amines (Reed, 1991) as well as both D- and L- amino acids (Ariga, 2014). As more and more novel scaffolds unfold in the form of polymeric, dendrimeric, sol-gel and solid state matrices along with other assemblies yet to be discovered; applications of these novel compounds show no obvious bounds and will continue to have their niche in chemistry (Stang, 2012).

Approaching the Molecular Dimension

Single nanopores along with arrays of multiple nanopores are a new and emerging technology that has contributed to furthering the science of single molecule detection including single molecules of dangerous bio warfare agents such as Ricin (Ding, 2009). Other applications in DNA sequencing (Ai, 2010), (Furnkies, 2010) single nucleic acid detection, peptide sensing (Niedzwiecki, 2010) and control of molecular transport (Ding, 2009). Nanopores are very versatile in their functionalization with amenable groups and varied chemistries such as thiol-ene click chemistry (Killops, 2008), (Bertin, 2009)

Other approaches to functionalization involve hetero or homogenous molecular functionalization (Vasile, 2013); where in the homogenous case, the molecule is synthesized with the reactive silane and one-step functionalization. In the heterogeneous method, the synthesis relies on functionalizing with a smaller reactive electrophile such as isocyanopropyltriethoxysilane (PICTES) or a good nucleophile such as aminopropyltriethoxysilane (APTES) followed by secondary reaction with the same functional molecule appended with the appropriate reactive group. The latter method returned a slightly higher count (CPS) in the x-ray photoelectron spectra (XPS) for carbon, suggesting this method may effectively graft more functionality due to the lower steric hindrances of the smaller precursor (Tagliazucchi, 2010). Non-covalent grafting of Host molecules is another method if the organic functionality is stable to E- beam deposition (Thontasen, 2010), which very few are.

Functionalized Nanochannels

Biologically, it has been shown that HEK neuronal cells have grown successfully on alumina nanoporous substrates, (Wolfrum, 2006). Wu Et al examined the effects of Nano confinement on mesoporous TEOS-functionalized alumina nanowires and found that remarkable helices and doughnut shaped domains were found to spontaneously self-assemble, with more spherical structures developing as the pore diameter decreased to <10 nm (Wu, 2004). In contrast, Mühlstein Et al studied Brij-56 which tends to favor cyclic mesoporous structures and found predominantly lamellar phases formed and were able to successfully characterize the presence of the surfactant by ^{13}C NMR in the solid state (Mühlstein, 2009). Yamaguchi Et al studied mesoporous silica "nanochannels" and found that nanoscale size-exclusion of molecules could be precisely controlled for one biological substance over another based on size alone (Yamaguchi, 2004). A. Yamaguchi found that the diffusion constants of a 2,2-Ru-bipyridyl macromolecule increased by a factor of 2 when C-10 alkyl chains were functionalized to alumina pore walls but decreased drastically when any groups possessing hydrogen bond donors and acceptors was introduced. Their reasoning was attributed the combination of hydrogen-bonding with the silanol substrates as a major factor slowing the diffusion of the bipyridine-metal complex, while the C-10 alkyl effectively blocked these interactions and lowered the interfacial surface tension (Yamaguchi, A, 2006). Mutalib Md Jani examined a novel approach to the anodization of alumina, etching the aluminum down to an intermediate depth, functionalizing with a silane and anodizing once more to

functionalize with a different silane which would react with a fluorophore (Mutalib Md Jani, 2009). The findings showed only the bottom anodized layer to be functionalized with the fluorophore showing proof of concept of their serial anodization/silanization process (Mutalib Md Jani, 2009). Yajima Et al further examined 15-crown-5 derivatives functionalized to either mesoporous silica or encapsulated within a sol-gel matrix in the Nano domain. The findings showed inversion of selectivity as the bis-15-crown-5 structure transported K^+ instead of the expected Na^+. The 15-C-5 had 2:1 stoichiometry with K^+ and formed 1:1 structures with Na^+ showing that the inherint selectivity of these crowns could exhibit differential behaviors depending on their environments and matrix material used in the nanopores (Yajima, 2010).

Figure 1.9 – Circular diagram of a transporter possessing the three most important characteristics – Selectivity, diffusivity and release.

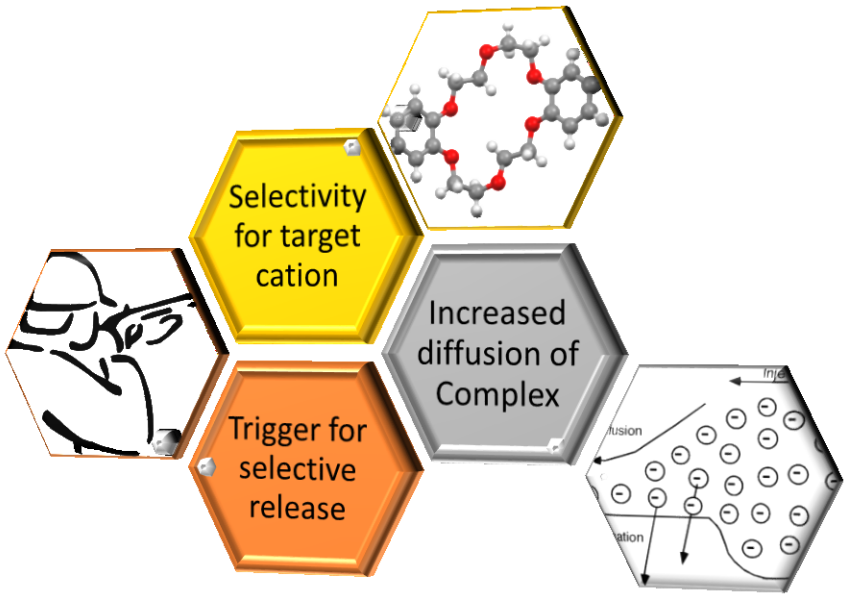

Trigger for release and selectivity

In designing an effective transporter, many different redox-active materials were considered, their synthesis being discussed in Chapter **III**. These molecules allow for reversible one and two electron transfers and act as electron shuttles in the electron transport chain in the mitochondria as shown in figure **1.10** below (Duveau, 2010).

Figure 1.10 – The reversible 2 electron, 2 proton transfer between the hydroquinone and benzoquinone is a native biological system for redox transfer reactions in the body.

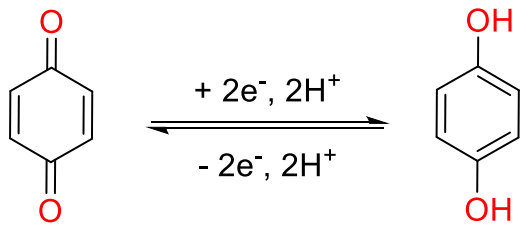

The electrons can flow from a reduced molecule or cofactor to an oxidized molecule, as long as their standard reduction potential E˚ is lower than the molecule to be reduced. I.E. electrons always flow from the species with the lower reduction potential to an entity with a higher reduction potential. With the exception of some underwater sidephores which utilize heme –containing channels, there are not many species in existence that utilize redox properties in the regulation of their ion channels. Recently Liu Et al. showed selective "gating" of a structure that interconverts between carcerand to hemicarcerand (Liu, 2014). The group discovered

this phenomena computationally when they noticed the side chains of the carcerand underwent multiple allosteric transitions, allowing for guest capture and escape.

Figure 1.11 - The four standard crown ethers and their cation counterparts (anions excluded for clarity)

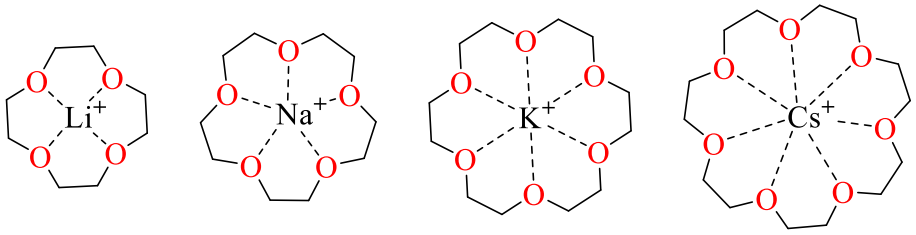

Utilizing redox species built into the traditional crown ether structure (figure **1.11**) has become a widespread strategy in materials as a switch for intramolecular coupling, closing acyclic pseudo-crowns to heavy metal sensors for cadmium (Privett, 2010). The equilibrium constant however, may change in favor of one ion over another leading to an increase in selectivity if the reduction or oxidation changes the conformation of the crown to a more preferential binding mode. This is the intended functional outcome of what is desired in a redox switchable pump.

Once bound in the membrane in the reduced state, the K_D should be high and k_{off} rate constant low to prevent unwanted leakage of the complexed potassium ions. To deliver the potassium stimulus, a fast reversal of the potential to a positive $\Delta E°$ and subsequent oxidation of the transporter should increase the k_{off} rate constant causing a local charge repulsion (all (-) species are now absent) leaving (+) charges

in the form of H_3O^+ ions along with K^+ ions that are rapidly expelled through charge-charge repulsion as the potential is lowered to a slightly negative potential, driving the positive charge toward the intracellular side of the membrane which in turn generates the action potential. Radical processes and supporting observations has been studied by specially designed IR cells (Bu, 2000) and extensively by EPR (Delgado, 1988), (Song, 2006).

Diffusion-controlled Reactions and Mobile e- carriers

Diffusion is best described as the random path a solute takes in some medium per unit time, which we call the diffusion coefficient of that solute. Different macromolecules have different sizes and shapes and effectively displace a path through the medium, displacing solvent molecules with viscosity η. The diffusion coefficient depends mostly on the relative size of the molecule and is best modeled by the Stokes-Einstein equation given below

$$D = \frac{k_B T}{6\pi\eta r} \quad \textbf{Stokes-Einstein equation} \qquad \textbf{1.5}$$

with terms including the hydrodynamic radius, r, Boltzmann Constant, k_B, temperature, T and 6π for distance dependence of the electric field around a spherical object. This simplistic form of the very well accepted Stokes equation is not always acceptable as a descriptor once a medium is rendered heterogeneous such as diffusion through ordered block copolymers domains. Effects seen in block copolymer domains have unpredictable properties that which sometimes can be explained through experiment and theory as in this thesis.

Formation and resulting stability of nanostructures, such as lamellar and cylindrical block copolymer phases, often depend on surface energy along with net charge which can shift the apparent diffusion coefficient. Liquids have very high diffusion coefficients allow diffusion to occur with ease (solutes dissolved in liquids) or can be infinitesimally slow (salt diffusing into solid concrete). We must also take into account the movement of charged particles in terms of their specific chemical potential given by the electrical mobility equation **1.6**:

$$D = \frac{\mu_q k_B T}{q} \qquad \textbf{1.6}$$

We see that the diffusion coefficient in this case can be influenced by $\boldsymbol{\mu_q}$, the electrical mobility of the particle, which is dependent on the drift velocity $\mathbf{v_d}$, a charged particle reaches under the influence of an electric field

$$v_d = \mu E \qquad \textbf{1.7}$$

Where **μ** is the electric mobility and **E** is the magnitude of the applied electric field. The resulting relation for electrical mobility is the ratio of the drift velocity to the magnitude of the electric field.

$$\mu = \frac{v_d}{E} \qquad \textbf{1.8}$$

Each substance and solute in a system has a diffusion coefficient, a measure of how random molecules disperse in a finite medium. If the system is comprised of many solutes, then binary, ternary or higher order mean diffusion coefficient which describes the body of solutes diffusing globally through the system is attained. Often times in the literature, anomalous behavior occurs with diffusion coefficients with

varied salt concentrations. That is because the solute-solvent interaction is a function of more than one than just one physical parameter. Changes in salt concentrations in D_2O for instance have led to anomalous behavior of decreasing and then increasing apparent D values. The authors attribute this to the salt itself; being that the salt effectively makes the solvent more hydrophobic because its hydration properties are organizing themselves around the ions themselves (Gomaa, 2012). This effectively leads to an apparently faster diffusion coefficient due to the apparent increase in ion hydrodynamic radius while there is less interaction with water coordination of the complexed cation.

The diffusion coefficient can be influenced by temperature, viscosity and net charge. Temperature is perhaps the most variable property that governs any change in the diffusion of a substance. Changes in temperature change the viscosity of the solution as well. According to Stokes Law there can thus be little information on the temperature effect of the diffusion coefficient due to the inverse relationship between viscosity and temperature (As T increases, v decreases and vice versa) in the case of solutions. If the medium contains a mixture of components and the interest is in isolating one diffusion coefficient for a particular solute, the coefficient must be separated by at least one order of magnitude to obtain reliable diffusion data (Sandor, 2011).

Diffusion constants can be found by various other methods by conducting electrochemical experiments, using bulk diffusion cells and more recently, by nuclear resonance spectroscopy. Much of the work in the field of nuclear magnetic

resonance (NMR) to correlate the chemical shift of a particular substance with its diffusion coefficient for both solids and mainly liquids has been performed (Chemlka, 2005), (Evan-Salem, 2007), (Feliz, 2006). Major pharmaceutical companies look to diffusion NMR to separate out bulk components of biological samples to see how drugs are metabolized and what metabolites are being formed (Chapman, 2007), (Alvarado, 2011). The method is relatively simple and straightforward, assuming the right processing steps and the parameters used to collect the data are pertinent to the sample (Fielding, 2000). Thermal noise generation in the probe and the first-stage receiver electronics dominates noise in NMR experiments (Cohen, 2005).

Investigation of host/guest complexes and interactions with the use of two dimensional diffusion-ordered spectroscopy, or DOSY as we will refer to it from here on has been performed for various neutral (Ouellet, 2010), (Guerrero-Martínez, 2006), (Guo, 2010) and charged complexes (Tominaga, 2009). DOSY studies on crown ethers with anions with observable nuclei for both the host and guest can be monitored spectroscopically if the assumption that the guest does not increase the hydrodynamic radius is valid. If a 1:1 stoichiometric complex is formed, both the host/guest will return the same trace along the 2D coordinate axes because they diffuse as one and possess one binary diffusion coefficient. Neglecting the fact of self-diffusion within the complexes themselves, much can be learned about the type of complex formed and if the stoichiometry is 2:1, 1:2 or 1:1 by integration of the 2D

plane (Botana, 2011). This can be complementary to other methods such as Job's method of continuous variation.

Other variables can be examined as well and new characteristics of complexes can be examined such as ion-pair separation as anions have much higher diffusion coefficients in solution (aq.) than their counterparts, cations (Cohen, 2004). More insight as to whether the anion diffuses as part of the complex or freely in the NMR solvent can then be answered.

We will now describe the reduction potential in terms of a gate. One may think of this as effectively a fence with a finite height E_m, which a baseball must be thrown over (or an electron in our case).

$$\delta G_o = -nF\delta E_m \quad \textbf{1.9}$$

There are a variety of factors that can have an effect on the oxidation midpoint (Em) the most prominent effectors of the oxidation midpoint (Em) include proximity of metal centers, Van der Waals constraints, distance restraints, hydrogen bonding, electrostatics, hydrophobicity and whether or not the system is in an aqueous or hydrophobic environment.

The "gating" effect of an electrochemically gated pore is in effect a slow reaction that involves the buildup of charge (Uysal, 2011). After an activation threshold is reached - the pore may change conformation, allowing a rapid increase in kinetics arising from favorable pore coordination and intra-charge repulsion between cations as they collide with one another along a "single file" axis that spans the pore (Song, 2006).

Supramolecular assemblies must have regularly spaced redox sites which serve as relays in the intramolecular electron exchange process. The redox-active species must be in close proximity and possess a favorable charge-transfer environment for high rates of electron transfer reactions (Marcus, 2012). Charge neutrality and the buildup of charge in one direction also must be accounted for by the electrolyte solution. For every charge into the system, there must be an equal but opposite charge such as the K^+/H^+ antiport mechanism to compensate for the charge buildup or eventually transport of charge in one direction will cease; the one exception being active transport, which uses ATP to actively pump ions against the gradient. In most cases, for every cation pumped in, a proton must be pumped out to maintain the osmotic balance of the cell. Alternatively, the cation and proton in a ditopic receptor with two binding sites can function as a symporter, carrying both charges to one side of the membrane which builds a chemical potential and polarizes one side of the membrane.

To summarize, natural systems of ionic stimulation use precise gradients of ions and the regulatory "gates" are the preceding steps controlling ion transport.

Facilitated Diffusion

Facilitated Diffusion is the assistance that drives transport that otherwise would be too energetically unfavorable to occur independently. Facilitated diffusion by mobile membrane carriers enhances both the selectivity and the rate of interfacial flux through bulk liquid membranes as a result of increased solubility of the charged ion-carrier complex in the membrane phase. Facilitated diffusion accelerates the rate

at which a transport processes occur; effectively coupling transport to one or more processes such as a favorable electrochemical gradient (Weiss, 1996), solvation of otherwise insoluble salts in lipid membranes or favorable H-bonding interaction which can be further controlled by both pH gradient (protonation of amines, deprotonation of carboxylic acids and phenols to form carboxylates and phenoxides which can all drastically increase the magnitude of the interaction (either repulsive or attractive).

In the case of facilitated diffusion via ionophores, the case is slightly more simplistic the first step is collision, absorption and the stripping an ion of its hydration shell (desolvation energy of a hydrated ion). Since the Boltzmann distribution term for thermal molecular collisions, (*kT)* is completely random, selectivity is imparted into the system by how well oriented the substrate is when colliding or diffusing around the ionophore molecule.

Figure 1.12- Thin-Film Models for 1:1 and 1:2 stoichiometric complexes with red discs representing reduced species and blue representing oxidized species. Step 1 – collision and stripping of hydration shell 2 – complexation by a second carrier (H_2) 3 – Pre-equilibrium complex 4 – Formation of the capsular complex and transport across the membrane 5 – oxidation of the crown to neutral state, decomplexation (k_D decreases).

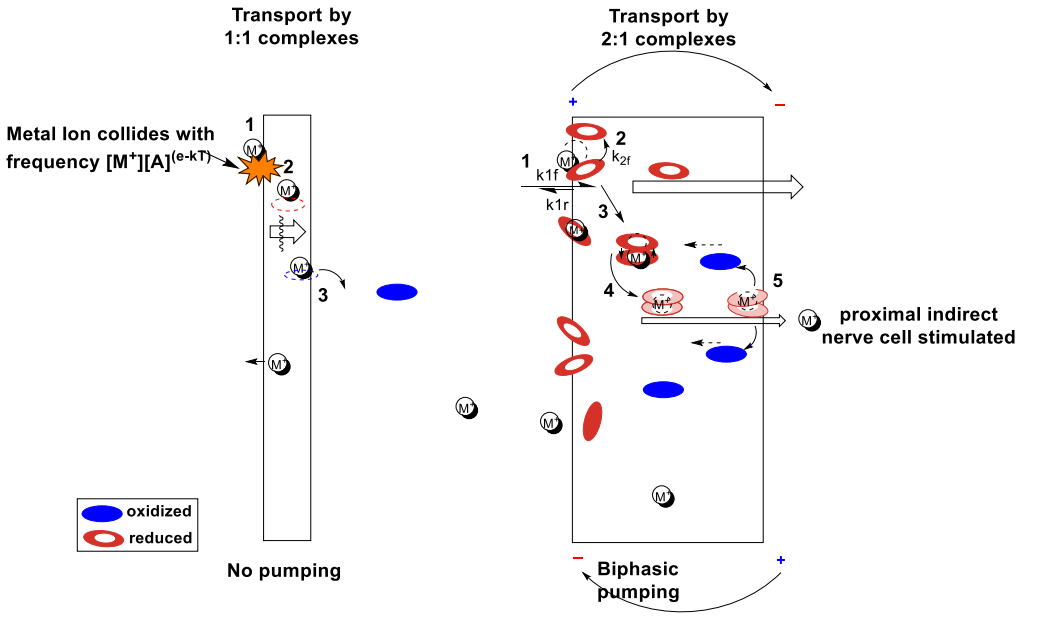

From reaction rate theory it is well known that enzymes often have higher turnover numbers and that rates such as in the case of ion transfer approach the limit of diffusion. The overall affinity of the receptor is proportional to the rate at which it binds to the lower-energy transition state or intermediate (ΔG‡). This contribution is overall geometric constraint coupled with contributions from electrostatics of the ion as well as its charge.

$$\Delta G_{ET} = E_{ox} - E_{red} - \frac{e2}{\varepsilon r} - E_{00} \qquad \textbf{1.10}$$

Reaction Rate Theory and Implications for binding

To understand the physics that should approximate phenomena on the nanoscale and deriving an expression for our theoretical device we first turn our attention to the thin film model and assume that the reservoirs on either side of the pump d_{res} >>> d_{mem} which validates the steady state concentration for bulk diffusion. Also in consideration is the fact that changing the potential energy of the electrons given by eq. **1.10** by 1 eV effectively changes the forward rate constant by a factor of e^{20} (Squires, 2013)!

Understanding the kinetics and association of molecular complexes can be quite challenging especially in the case of mixed stoichiometry where two or more guests may bind to one host or more than one host bind co-operatively to one guest molecule (Conners, 1987). Differential salt concentrations can also manifest problems in interpreting complex reaction kinetics and one must carefully analyze the data to make a sensible interpretation of the mechanism of action of such complexes. We must first define the equilibrium disassociation constant, k_D, with units of M^{-1} and clarify that this is not the association constant k_{on}, with units of M^{-1} min^{-1} and finally the disassociation constant, k_{off} with units of min^{-1}. The equilibrium constant is a powerful value that a system maintains despite the concentration of guest, the host binds the same value or quantity of guest regardless of the concentration of either H or G.

$$H+ G \rightarrow H_{(n)}G \qquad k_D = [HG]/[H][G] \qquad \textbf{1.11}$$

Furthermore, from reaction rate theory and enzyme kinetics we know enzymes often have higher turnover numbers and that rates such as in the case of ion transfer is in fact diffusion limited. The overall affinity of the receptor is proportional to the rate at which it binds to the lower-energy transition state or intermediate (ΔG‡). This contribution is overall geometric constraint with some contributions from electrostatics of the ion and its charge density. Perhaps the most complicated and unpredictable property is the fact that the host molecule may undergo an allosteric shift (a change in geometry altering the binding site geometry) resulting in sometimes favorable or unfavorable consequences for binding.

Figure 1.13 – Different conformers of the same molecule with different complexation properties

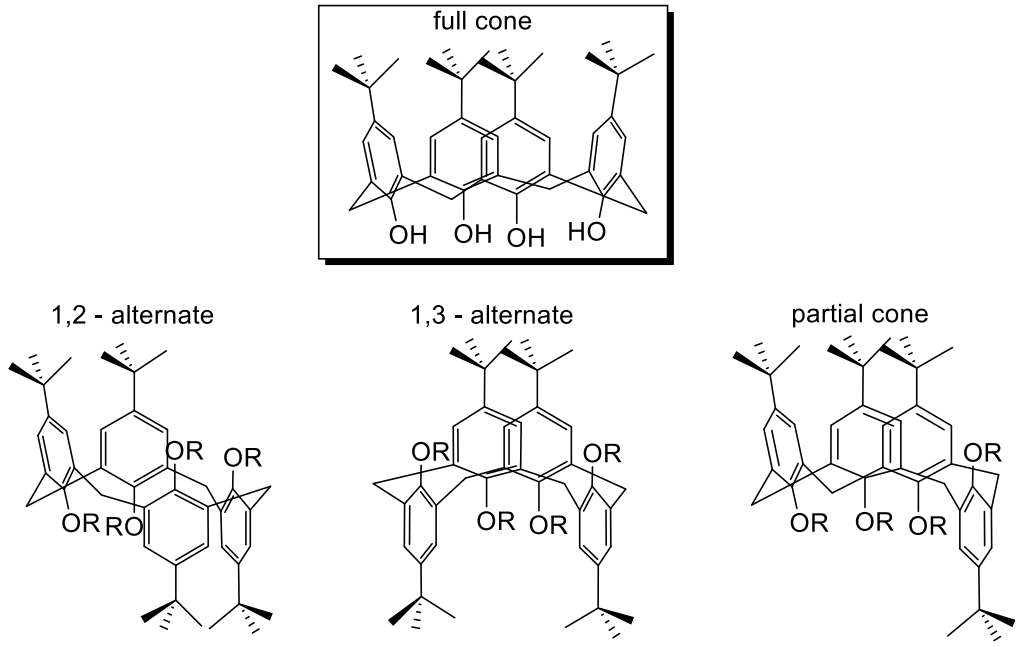

In the case of facilitated diffusion ionic transporters often occur a slow step in their uptake due to the requirement of first stripping the ion of its hydration shell. Once this process has occurred the ion is bound via ion-dipole forces to the ether oxygen, pending favorable geometric constraints, (ionic radius ≈ crown ether radius). The latter dictates the magnitude of the equilibrium k_D disassociation constant whereas the kinetics are proportional to how well oriented the substrate is to undergo this multistep binding process (co-operative effects).

Figure 1.14 – K^+ bound to the ionophore Valinomycin

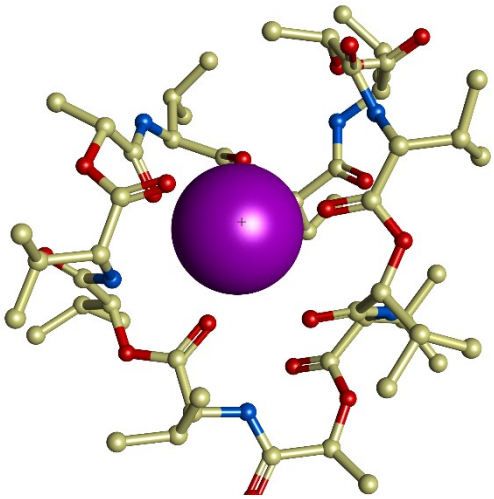

Cyclophanes, rosettes', cyrptands as well as natural ionophores such as Valinomycin (figure **1.14**) and Nonactin form weak to strong intramolecular forces with guest molecules and even with themselves such as in the case of the rosette shown in figure **1.16**. Although one may think of a hydrogen bond being between species with Lewis basic or acidic hydrogen or lone pair, one can see that much weaker hydrogen bonds are formed to hold the guest benzene ring in the plane of a network of six hydrogen bond donor and acceptor molecules. It is this network which holds DNA together and is so predictable by computational simulations that groups such as Dr. Luc Jaeger have pioneered these effects into what is termed "DNA origami" (Grabow, 2011).

Figure 1.15– The crystal structure adopted by cyclophane urea complex by both Strong and weak forces. **Figure 1.16–** cyclic rosette crystal structure adopted by weak Hydrogen bond network coupled with favorable geometric constraints while in Benzene solvent.

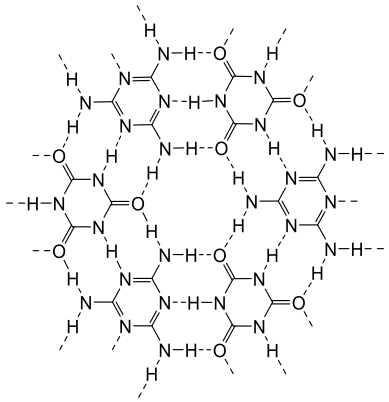

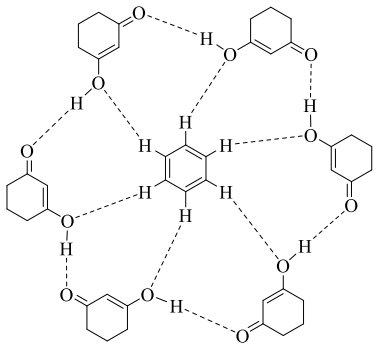

To find the synthetic organic material targets to achieve the desired transport properties as outlined in this chapter; it was necessary to familiarize ourselves with the characterization techniques by using a previously synthesized receptor (Sun, 1995). Crown ethers are an attractive avenue due to the relative ease of synthetic complexity and the inherently large binding constants and selectivity. These properties are unveiled after the characterization of the synthesized complex is complete and are usually complemented by more than just one piece of spectral data to confirm the identity of the complex. Over the last decade, science has focused much effort in to the understanding of intermolecular forces that govern secondary structure assembly.

Physical Considerations

To start, we examined each of the crown ethers in figure **1.11** are depicted with the selected cation because the affinity for that cation is highest. These crown ethers form a complex in solution with the highest apparent equilibrium constant K_{eq}. This constant is valid for ideal, dilute solutions and is rarely measured under conditions that define the provisos; with the limiting factor including instrument sensitivity, low solubility, changes in solubility (upon complex formation) and purity of the resultant complex that remains in solution. Often times these are ignored in the literature with such reported values (log scale) ranging from $K = 10^1\ M^{-1}$ to values up to $K = 10^9\ M^{-1}$ (Frensdorff, 1971), (Gokel, 2004), (Fielding, 2000).

For ligands binding to receptors with more than one binding site, the equilibrium number of bound molecules can exceed the actual amount of receptor in solution (Thordarson, 2011). There can also exist ditopic receptors which effectively complex a cation and anion in an ion-pair separated supramolecular assembly (Gargiulli, 2009), (Tochtrop, 2002). Recently published articals exemplify this phenomena by postulating that two [porphyrin-(4) 18-C-5] dimerize to encapsulate 4 K^+ cations to form a 2:1 receptor-ligand complex (Lu, 2010), (Giribabu, 2006).

To summarize, neuronal prosthetics are an important part of the future if society wishes to have the luxury of sight as we grow as a population grow older and older and diseases of age become more prominent. Many collaborative research efforts between materials scientist, neurologist, biologist and electrical and computer engineering must be utilized to render this endeavor a success. Vision is perhaps one

of the most complicated situations in designing a functional prosthetic for any part of the human body. Our device hinges on the resting potential of the neuron and its permeability to K^+ cations in eliciting an excitatory stimulus on demand. To achieve this endeavor, it is determined that an artificial cation pump must be synthesized that is specific for K^+ only. Upon successful achievement of this endeavor, fabrication and process engineers will assemble the device for testing as a prototype for a new prosthetic.

Before tackling the synthesis of such a complicated macromolecular assembly, in the next chapter we will first examine the mathematical underlying of transport properties through thin films as a model to help us define the boundaries of reaction and diffusion parameters coupled together. This was done to familiarize the author's understanding of the transport process involved and be able to qualitatively describe the flux through a nanoscale membrane.

Chapter II: A look at the Thin Film Model of Reactive Flux of Ion Transfer by Ionophoric Macromolecules.

Objective:

The goal of this Chapter is to introduce a theoretical problem that pertains to the simplified case of facilitated diffusion with reaction through a 2D slab or film. The aim is to define the reaction parameters γ, α and β and use these parameters to define cases where the reaction of a mobile carrier [B] is the limiting step; or when diffusion of the mobile ion, A, carrier is the limiting step. We will then derive the overall flux through the membrane with a single expression.

We will examine the effects of speed of complexation and diffusion of reactants and their overall implication on the reaction rate. Four cases will be presented where the ion concentration [A] is:

1. So high that the carrier concentration [B] becomes depleted and limiting on the source side under high ionic concentration.
2. The same condition but with no limits on the carrier concentration [B],
3. The converse condition, where the ionic concentration [A] is low but reaction fast.
4. The condition where we have both low ionic concentration and slow reaction.

These are all the possible transport phenomena that account for the disassociation constant of the crown and the diffusion of the solute through ultrathin membranes. These derivations should help us to qualitatively and quantitatively understand the results of our transport experiments later on.

A chemical Engineering perspective

Our system was modeled to represent a process used by biology and industry for separation of different molecules of solute by mobile redox-active electron carriers. The following demonstrates limiting cases in terms of the scale and dimensionality of our nanoporous membrane. Shown below in figure **2.1** is the representative scheme for our facilitated diffusion model (Squires, 2013). The solute (K^+, Na^+, $Ca2^+$) is in an aqueous solution with concentration [A_o], which is insoluble in an organic liquid film of thickness 2*d*, located between $-d < z < d$. The crown ether with concentration [B_o] is contained in the liquid organic layer and is immiscible in water. The carrier B is designed to specifically complex and solubilize K^+ by forming a solvent-separated ion pair. The carrier specifically functions through the mechanism of facilitating diffusion through the organic membrane, allowing for ion specific transport.

Deriving an expression for our theoretical device, we first turn our attention to the thin film model and assume that the reservoirs on either side of the pump $d_{extra} >>> d_{intra}$ which validates the Steady State concentration for bulk diffusion. We are interested in the extremes of these cases and where diffusion plays a role within our device. Since our device is essentially an ion-exchange membrane specific for K^+

ions under electrochemical control, many electrodes must be strategically placed so that an even charge distribution can be achieved across the membrane. Since the membrane is non-conducting to electrons and ion-conducting in nature, effects such as diffusion take on a significant role in the overall flux equation. For example, an applied voltage of just 1 Ev speeds up the electro migration of ions by an astounding e^{20} (Squires, 2013). This is an astounding increase in flux.

Figure 2.1 - Illustration of facilitated diffusion, (left) where solute A is soluble in aqueous solution on either side of a hydrophobic organic liquid film but immiscible with the organic film itself. Our crown ether transporter, B is solute in the film only. B and A can react at the membrane interface (right) to form a complex, which can now freely diffuse across the film which is shown in the definition sketch.

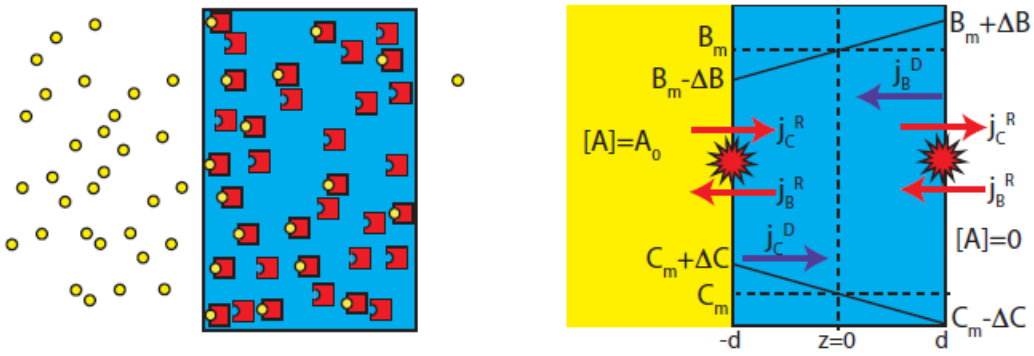

In the derivations to follow, we will examine this system in a theoretical context detailing the implications of diffusion as the molecular dimension is reached. To solve this problem we solve for the Steady State flux of A across the film. The

diffusivities of B and C are D_b and D_c, respectively, and the concentration of each can be defined as:

$$\mathrm{B}(z) = B_m - \Delta B \frac{z}{d} \quad \textbf{2.1}$$

$$\mathrm{C}(z) = C_m - \Delta C \frac{z}{d} \quad \textbf{2.2}$$

2.2

$$B_m + C_m = B_o \quad \textbf{2.3}$$

These equations have (unknown) mean values B_m and C_m and gradients – $\Delta C/d$ and $\Delta B/d$. All four unknowns *(Bm, Cm,* ΔB and ΔC) are all positive as defined. We can assume the concentrations of A on either side of the film to be held fixed,

$$A(z = -d) = A_o \quad \textbf{2.4}$$

$$A(z = +d) = 0 \quad \textbf{2.5}$$

And the reactive diffusion flux, j_R at each boundary to be given by

$$j_R = k_{on}\mathrm{AB} - k_{off}\mathrm{C} \quad \textbf{2.6}$$

With dissociation constant

$$\mathrm{k_D} = \frac{k_{off}}{k_{on}} \quad \textbf{2.7}$$

There exists four unknowns but since we are assuming Steady State concentrations we know that the Steady State flux of the three species must be equal. Some of the fluxes are redundant; the reactive flux of B is (-1) times the reactive flux of C at each boundary.

To reiterate, there are three independent fluxes (reactive at left and right, and diffusive through the middle). The fourth condition is on the sum of B and C

concentrations ($B_m + C_m$). Since C is a complex containing B, the following condition must be enforced

$$B_m + C_m = B_o \qquad \textbf{2.8}$$

i.)We will first relate the diffusive fluxes of B and C to arrive at **2.9**

$$\Delta C = \gamma \Delta B \qquad \textbf{2.9}$$

Where we will identify γ and its significance

At Steady State, net flux = 0

$$J_R^B + J_D^{B+} J_R^C + J_D^C = 0 \qquad \textbf{2.10}$$

$$J_R^B = -J_R^C \rightarrow J_R^B + J_R^C = 0 \qquad \textbf{2.11}$$

$$J_D^B + J_D^C = 0 \Rightarrow J_D^B = -J_D^C \qquad \textbf{2.12}$$

$$-D_B \frac{\delta B}{\delta z} = -D_C \frac{\delta C}{\delta z} \qquad \textbf{2.13}$$

$$+D_B \frac{\Delta B}{d} = +D_C \frac{\Delta C}{d} \qquad \textbf{2.14}$$

$$\Delta C = \frac{D_B}{D_C} \Delta B \Rightarrow \Delta C = \gamma \Delta B \qquad \textbf{2.15}$$

$$with\ \gamma = \frac{D_B}{D_C} \qquad \textbf{2.16}$$

ii.) We will now derive an expression that relates the diffusive flux of carrier C to the reactive flux at z = d to give eq. **2.24**. We will define the reaction parameter α.

$$j_R^c \rangle z = -d = -j_R^c \rangle z = d \qquad \textbf{2.17}$$

$$k_{on} AB - k_{off} C \Big|_{z=d} = -Dc \frac{\partial c}{\partial z} \Big|_{z=d} \qquad \textbf{2.18}$$

$$k_{on}(0)(B_m + \Delta B) - k_{off}(C_m - \Delta C) = -Dc\frac{\Delta C}{d} \quad \textbf{2.19}$$

$$k_{off}Cm - k_{off}\Delta C = D_c\frac{\Delta C}{d} \quad \textbf{2.20}$$

$$k_{off}C_m = \left(k_{off} + \frac{D_c}{d}\right)\Delta C \quad \textbf{2.21}$$

$$Cm = \frac{\left(k_{off} + \frac{D_c}{d}\right)}{k_{off}}\Delta C \quad \textbf{2.22}$$

$$Cm = \frac{\left(\frac{dk_{off}}{D_c} + 1\right)}{\frac{dk_{off}}{D_c}}\Delta C \quad \textbf{2.23}$$

$$Cm = \left(\frac{1+\alpha}{\alpha}\right)\Delta C \quad \textbf{2.24}$$

$$\alpha = \frac{dkoff}{Dc} \quad \textbf{2.25}$$

Where α is defined as the Damkohler number, which represents the ratio of reaction rate to the diffusion rate of the reactant complexes.

We arrive at our new equation for concentration in the membrane:

$$Cm = \left(\frac{1+\alpha}{\alpha}\right)\gamma\Delta B \quad \textbf{2.26}$$

iii) We can calculate the reactive fluxes of C at $\pm d$ and arrive at equation **2.28**:

$$\Delta B\left(1 + \beta\left(\frac{1+\alpha}{\alpha}\right)\gamma\right) = \mathrm{B_m} \qquad \textbf{2.27}$$

$$j_R^c\big|_{z=-d}\; j_R^c\big|_{z=d} \qquad \textbf{2.28}$$

$$[k_{on}AB - k_{off}C]|_{z=-d} = [-k_{on}AB + k_{off}C]|_{z=d} \qquad \textbf{2.29}$$

$$k_{on}A_o(B_m - \Delta B) - k_{off}(C_m + \Delta C) = -k_{on}(0) + k_{off}(C_m - \Delta C) \qquad \textbf{2.30}$$

$$k_{on}A_0B_m - k_{on}A_0\Delta B = k_{off}C_m + \cancel{k_{off}\Delta C} + k_{off}C_m - \cancel{k_{off}\Delta C} \qquad \textbf{2.31}$$

$$k_{on}A_oB_m = k_{on}A_o\Delta B + 2k_{off}C_m \qquad \textbf{2.32}$$

$$k_{on}A_oB_m = k_{on}A_o\Delta B + 2k_{off}\left(\frac{1+\alpha}{\alpha}\right)\gamma\Delta B \qquad \textbf{2.33}$$

$$k_{on}A_oB_m = \left[k_{on}A_o + 2k_{off}\left(\frac{1+\alpha}{\alpha}\right)\gamma\right]\Delta B \qquad \textbf{2.34}$$

$$B_m = \left[1 + \frac{2k_{off}}{k_{on}A_o}\left(\frac{1+\alpha}{\alpha}\right)\gamma\right]\Delta B \qquad \textbf{2.35}$$

$$B_m = \left[1 + \frac{2k_D}{A_o}\left(\frac{1+\alpha}{\alpha}\right)\gamma\right]\Delta B \qquad \textbf{2.36}$$

$$B_m = \left[1 + \beta\left(\frac{1+\alpha}{\alpha}\right)\gamma\right]\Delta B \qquad \textbf{2.37}$$

$$\text{where } \beta = \frac{2k_D}{A_o} \qquad \textbf{2.38}$$

Now k_D = equilibrium disassociation constant, i.e.

$$k_D = \frac{A_oB}{C} \Rightarrow \frac{2k_D}{A_o} = \beta = \frac{B}{C} \qquad \textbf{2.39}$$

β is the ratio of B and C at equilibrium, gives us insight to the relative populations of B and C (like a partition coefficient)

$$\Delta B = \frac{B_o}{1+\left(\frac{1+\alpha}{\alpha}\right)\gamma(1+\beta)} \quad \textbf{2.40}$$

Relating the diffusive flux, C to reactive flux of solute $C_{z=d}$, gives eqn. **2.42**

$$B(z) = B_m + \Delta B\frac{z}{d}, \quad C(z) = C_m - \Delta C\frac{z}{d} \quad \textbf{2.41}$$

$$with\ \gamma = \frac{D_B}{D_C} \quad \textbf{2.42}$$

iv) We will now use the conservation equation **2.43** to get a second equation relating Bm and ΔB, this time to B_o

$$B_m + C_m = B_o \quad \textbf{2.43}$$

$$B_m + \left(\frac{1+\alpha}{\alpha}\right)\gamma\Delta B = B_o \quad \textbf{2.44}$$

$$\left[1+\beta\left(\frac{1+\alpha}{\alpha}\right)\gamma+\gamma\right] = B_o \quad \textbf{2.45}$$

$$i.e.\ k_D = \frac{A_o B}{C} \rightarrow \frac{2k_D}{Ao} = \beta = \frac{B}{C} \quad \textbf{2.46}$$

$$\Delta B = \frac{Bo}{1+\beta\frac{(1+\alpha)}{\alpha}\gamma+\gamma} \quad \textbf{2.47}$$

$$\Delta B = \frac{Bo}{1+\left(\frac{1+\alpha}{\alpha}\right)\gamma(1+\beta)} \quad \textbf{2.48}$$

$$j_A = j_{C^D} = -D\frac{\partial c}{\partial z} = \frac{D_c \Delta C}{d} = \frac{D_c}{d}\gamma \Delta B \qquad \textbf{2.49}$$

$$\boxed{j_A = \frac{D_c \gamma B_o}{d\left[1+\left(\frac{1+\alpha}{\alpha}\right)\gamma(1+\beta)\right]}} \qquad \textbf{2.50}$$

Considering the situation where A_o is so high that essentially all of B is depleted at the left (B(-*d*) = 0), A_o is not limiting in any way. Also considering the reaction at right to be so rapid that C(*d*) = 0. There are now two unknowns, B(*d*) and C(-*d*); they are related to the total concentration B_o and equality of diffusive fluxes. We will figure out which diffusive flux limits the mass transport. To solve for the limiting diffusivity, we will write out γ in terms of D_B and D_C and consider the case where $D_B >> D_C$ and vice versa to figure out the limiting form of the flux. The dimensionless variables α, β, γ will be identified in terms of which variable expresses the relative size of Ao, along with the size of Ao that validates the limit. Also, we will define which variable expresses the speed of the reaction and the value of k_{off} that validates this limit. Finally, we find the solution from the latter derivation along with the limits of α, β, γ (usually 0, infinity or undetermined) to get the limiting form of the flux and determine whether it agrees with our simple estimate.

$$B\big|_{z=-d} = 0, \quad C\big|_{z=+d} = 0 \qquad \textbf{2.51, 2.52}$$

$$B_m - \Delta B = 0, \quad C_m - \Delta C = 0 \qquad \textbf{2.53, 2.54}$$

$$B_m = \Delta B \ , \quad C_m = \Delta C \qquad \textbf{2.55, 2.56}$$

Now, $B_m + C_m = B_o$ **2.57**

$$\Delta B + \gamma \Delta B = B_o \quad \textbf{2.58}$$

$$\Delta B = \frac{B_o}{(1+\gamma)}, \quad \Delta C = \frac{\gamma B_o}{(1+\gamma)} \quad \textbf{2.59, 2.60}$$

$$j_A = D_c \frac{\Delta C}{d} = \frac{D_c \gamma B_o}{(1+\gamma)d} \text{ , Where } \gamma = \frac{D_B}{D_C} \quad \textbf{2.61, 2.62}$$

$$\boxed{j_A = \frac{D_C}{1} \frac{D_B}{D_C} \frac{B_o}{\left(1 + \frac{D_B}{D_C}\right)d}} \quad \textbf{2.63}$$

$$j_A = \left[\frac{Db}{\left(1 + \frac{Db}{Dc}\right)} \right] \frac{B_o}{d} \quad \textbf{2.64}$$

Now when, $D_B >> D_C$, $j_A \approx \frac{D_B}{D_B} \frac{D_C}{,} \frac{B_o}{d} \approx \frac{D_C}{} \frac{B_o}{d}$ **2.65**

The diffusive flux is limited by mass transport of C

-When $D_B << D_C$, limited by the mass transport of B

Full Solution:

$$\boxed{j_A = \frac{D_c \gamma B_o}{d\left[1 + \left(\frac{1+\alpha}{\alpha}\right)\gamma(1+\beta)\right]}} \quad \textbf{2.66}$$

$$\gamma = \frac{D_B}{D_C}, \alpha = \frac{dk_{off}}{D_C}, \beta = \frac{2k_D}{A_o} \quad \textbf{2.67}$$

β Represents the relative size of A_o, for this limit to be valid

$$A_o >> 2k_D \Rightarrow \beta \to 0 \qquad \textbf{2.68}$$

α Represents the relative speed of reaction, for this limit to hold, $\alpha >> 1$

$$\Rightarrow k_{off} >> D_C/d \qquad \textbf{2.69}$$

If $\alpha >> 1 \Rightarrow \left(\frac{1}{\alpha}\right) + 1 \approx 1$, therefore as $\beta \to 0 \Rightarrow 1 + \beta \approx 1$ **2.70**

$$j_A = \frac{D_C \gamma B_o}{d\left[1+\gamma\right]} = \left[\frac{D_B}{1+\frac{D_B}{D_C}}\right]\frac{B_o}{d} = \underline{\text{same result as}}\ \underline{\text{before}} \qquad \textbf{2.71}$$

Considering the case where A_o so high that essentially all B is depleted at the left ($B(-d) = 0$) we will assume the reactions are very slow. The implications on $C(-d)$ and $C(+d)$ will be deciphered along with $B(+d)$, arriving at the flux for this case and deduce whether or not it agrees with the relevant limits

$$A_o >> 1 \ (\beta \to 0)$$

In the case $A_o >> 1 \ (\beta \to 0)$, the case of slow reaction is dominant i.e. $\alpha << 1$

$$B\big|_{z=-d} = 0 \Rightarrow B_m - \Delta B = 0 \Rightarrow B_m = \Delta B \qquad \textbf{2.72}$$

$$j_B{}^C = -D_c\frac{\partial c}{\partial z} = D_c\frac{\Delta c}{d} \qquad \textbf{2.73}$$

$$j_R{}^C\big|_{z=d} = j_D{}^C\big|_{z=d} \Rightarrow C_m = \left(\frac{1+\alpha}{\alpha}\right)\Delta C \qquad \textbf{2.74}$$

$$\Delta C = \left(\frac{\alpha}{1+\alpha}\right)C_m \qquad \textbf{2.75}$$

$$\alpha << 1 \Rightarrow \Delta C \to 0 \qquad \textbf{2.76}$$

Now, $$B_m + C_m = B_o \qquad \textbf{2.77}$$

$$\Delta B + C_m = B_o \qquad \textbf{2.78}$$

$$\frac{\Delta C}{\gamma} + C_m = B_o \qquad \textbf{2.79}$$

$$C_m \approx B_o \qquad \textbf{2.80}$$

Flux $$j_A \approx k_{off} C_m \qquad \textbf{2.81}$$

$$j_A \approx k_{off} B_o \qquad \textbf{2.82}$$

From our full solution

$$\beta \to 0, \quad 1+\beta \approx 1, \quad \alpha << 1, \quad 1+\alpha \approx 1 \qquad \textbf{2.83}$$

$$j_A = \frac{D_c \gamma B_o}{\left[1+\left(\frac{1+\alpha}{\alpha}\right)\gamma(1)\right]d} \qquad \textbf{2.84}$$

$$j_A = \frac{D_c \gamma B_o}{\frac{1}{\alpha}\gamma d}, \qquad \left(\frac{1}{\alpha} >> 1\right) \qquad \textbf{2.85}$$

$$j_A \approx \alpha \frac{D_c}{d} B_o = k_{off} \frac{d}{D_c} \frac{D_c}{d} B_o \qquad \textbf{2.86}$$

$$j_A \approx k_{off} B_o \quad = \text{same result as before} \qquad \textbf{2.87}$$

We now consider a case where A_o is very small, such that little B reacts. Considering very fast reactions, such that C(d) = 0, an expression is derived for the total flux in the appropriate limit of the full solution.

$$A_o << 1 \Rightarrow \beta >> 1 \qquad \textbf{2.88}$$

Very fast reactions $\alpha >> 1$ **2.89**

$C\big|_{z=d} = 0$ Very little B reacts $\Rightarrow \Delta B \approx 0 \Rightarrow B_m - \Delta B \approx B_m$ **2.90**

$$C_m - \Delta C = 0 \Rightarrow C_m = \Delta C \quad \textbf{2.91}$$

$$B_m + C_m = B_o \quad \textbf{2.92}$$

$$B_m + \Delta C = B_o \Rightarrow B_m = B_o - \Delta C \quad \textbf{2.93}$$

Also, $$j_{R^C}|_{z=-d} = -j_{R^C}|_{z=d} \quad \textbf{2.94}$$

$$k_{on}A_o(B_m - \Delta B) - k_{off}(C_m + \Delta C) = -k_{on}(0) + k_{off}(C_m - \Delta C) \quad \textbf{2.95}$$

$$\therefore k_{on}A_oB_m - k_{off}(2\Delta C) = 0 \quad \textbf{2.96}$$

$$\therefore B_m = \frac{2k_{off}\Delta C}{k_{on}A_0} = \beta\Delta C \quad \textbf{2.97}$$

$$\Delta C = B_o - B_m \text{ , } \Delta C = B_o - \beta\Delta C \Rightarrow \Delta C = \frac{B_o}{1+\beta} \quad \textbf{2.98}$$

$$j_A = -D_C\frac{\partial C}{\partial z} = \frac{D_C\Delta C}{d} = \frac{D_CB_o}{d(1+\beta)} \quad \textbf{2.99}$$

$$\beta >> 1 \text{ since } A_o << 1 \therefore 1 + \beta \approx \beta \quad \textbf{2.100}$$

$$j_A = \frac{D_cB_o}{d\beta} = \frac{k_{on}A_oB_oD_c}{2dk_{off}} \quad \textbf{2.101}$$

From full solution:

$$j_A = \frac{D_c\gamma B_o}{d\left[1 + \left(\frac{1}{\alpha} + 1\right)\gamma(1+\beta)\right]} \quad \textbf{2.102}$$

$$\alpha >> 1 \Rightarrow \frac{1}{\alpha} << 1 \therefore \frac{1}{\alpha} + 1 \approx 1 \qquad \textbf{2.103}$$

$$\beta >> 1 \Rightarrow 1 + \beta \approx \beta \qquad \textbf{2.104}$$

$$j_A = \frac{D_c \gamma B_o}{d\left[1 + \gamma\beta\right]} \qquad \textbf{2.105}$$

$$Now \Delta B \to 0 \therefore \text{very little B reacts}$$

$$\Delta B = \frac{1}{\gamma}\Delta C \Rightarrow \frac{1}{\gamma} \to 0 \Rightarrow \gamma >> 1 \quad (\text{for} \quad \Delta B \to 0)$$

2.106

$$1 + \beta\gamma \approx \beta\gamma \qquad \textbf{2.107}$$

$$j_A = \frac{D_c \gamma B_o}{d\gamma\beta} \qquad \textbf{2.108}$$

$$j_A = \frac{k_{on} A_o B_o D_c}{2 d k_{off}} \Rightarrow \text{ same as before} \qquad \textbf{2.109}$$

iv). For the final case we assume Ao is very small, such that little B reacts but now with very slow reactions. We will derive the flux under these conditions and verify it's consistency with the full solution in the appropriate limit.

From full solution: $A_o << 1 \Rightarrow \beta >> 1$ **2.110**

$$\text{Slow reactions} \Rightarrow \alpha << 1$$

$$\text{Very little B reacts} \Rightarrow B_m - \Delta B \square \qquad \text{i.e. } \Delta B \to 0$$

$$\Delta C \to 0 \text{ thus } C_m - \Delta C \square \qquad \textbf{2.111}$$

$$j_R{}^C \Big|_{z=-d} = -j_R{}^C \Big|_{z=d} \qquad \textbf{2.112}$$

$$k_{on} A_o (B_m - \Delta B) - k_{off} (C_m + \Delta C) = -k_{on}(0) + k_{off} (C_m - \Delta C) \qquad \textbf{2.113}$$

$$k_{on}A_oB_m - k_{off}C_m = k_{off}C_m \quad \textbf{2.114}$$

$$k_{on}A_oB_m = 2k_{off}C_m \quad \textbf{2.115}$$

$$\therefore B_m = \frac{2k_{off}}{k_{on}A_o}C_m \Rightarrow B_m = \beta C_m \quad \textbf{2.116}$$

$$B_m + C_m = B_o \quad \textbf{2.117}$$

$$\beta C_m + C_m = B_o \Rightarrow C_m = \frac{B_o}{1+\beta} \quad \textbf{2.118}$$

Flux $$j_A = k_{off}C_m = k_{off}\frac{B_o}{1+\beta} \quad \textbf{2.119}$$

$$\beta >> 1 \Rightarrow 1 + \beta \approx \beta \quad \textbf{2.120}$$

$$j_A = k_{off}\frac{B_o}{\beta} \quad \textbf{2.121}$$

$$j_A = \frac{k_{off}B_o k_{on}A_o}{2k_{off}} \quad \textbf{2.122}$$

$$j_A = \frac{k_{on}}{2}A_oB_o \quad \textbf{2.123}$$

From full solution: $$j_A = \frac{D_C\gamma B_o}{d\left[1+\left(\frac{1}{\alpha}+1\right)\gamma(1+\beta)\right]} \quad \textbf{2.124}$$

$$\alpha << 1 \Rightarrow \frac{1}{\alpha} >> 1 \Rightarrow \frac{1}{\alpha} + 1 \approx \frac{1}{\alpha} \quad \textbf{2.125}$$

$$\beta >> 1 \Rightarrow 1 + \beta \approx \beta \quad \textbf{2.126}$$

$$j_A = \frac{D_C\gamma B_o}{d\left[1+\frac{\gamma\beta}{\alpha}\right]} \quad \textbf{2.127}$$

$$\beta >> 1, \frac{1}{\alpha} >> 1 \;\; \therefore \;\; \frac{\gamma\beta}{\alpha} >> 1 \Rightarrow 1 + \frac{\gamma\beta}{\alpha} \approx \frac{\gamma\beta}{\alpha} \qquad \textbf{2.128}$$

$$j_A = \frac{D_c \gamma B_o}{d\gamma\beta}\alpha \qquad \textbf{2.129}$$

$$j_A = \frac{D_c}{d}\frac{B_o}{2k_{off}}\frac{A_o}{}\frac{k_{on}}{}\cdot\frac{dk_{off}}{D_c} \qquad \textbf{2.130}$$

$$j_A = \frac{k_{on}}{2} A_o B_o \qquad \textbf{2.131}$$

Same as before

Summary

First, we solved the problem for the Steady State flux of **A** across the film, defining all variables, parameters, and assumptions involved to arrive to a general solution. Second, we analyzed the four boundary cases, which let us quickly define the limiting extremes on permeability of the whole system. Setting these limits or boundaries, let us to define with more confidence the experimental part of our study problem.

The three parameters: **α**, **β**, and **γ** govern the whole process. They interact dynamically. If we move one, we will have a different result. Determining the values of each parameter in the extreme conditions allow us to define the range where the processes take place.

- **α** is the Damkohler number which represents the ratio of reaction rate to the diffusion rate of the reactant complexes: $\alpha = \frac{dk_{off}}{D_C}$

- **β** is the ratio of B and C at equilibrium, gives us insight to the relative populations of B and C (like a partition coefficient). $\beta = \frac{2k_D}{A_o}$, where

$$k_D = \frac{A_o B}{C} \Rightarrow \frac{2k_D}{A_o} = \beta = \frac{B}{C}$$

- **γ** is the ratio between de Diffusivity of B over the Diffusivity of C. $\gamma = \frac{D_B}{D_C}$

Chapter III – Device Design, Synthesis and Fabrication

Objective

An engineered approach toward on-chip transistor-based molecular devices is perhaps the most efficacious method of synthesizing "smart" materials in today's world. This chapter reviews the implications of our design, including the planning and resulting streamlined synthesis of effective transporters.

What makes a device fabrication a success or failure? The answer is simple: Good planning. It should suffice to say that one would never build a house without first consulting an architect and structural engineer first. This is because they know what is and what is not possible when it comes to building structures which is analogous to building molecular structures.

The theory presented in the previous chapter along with molecular descriptors helped aid in synthesizing a transporter suitable to perform the intended device function. The device is comprised of both recognition unit and functional molecular machine that relies upon redox enhancement to bind and deliver K^+ cations. To synthesize the device we must first:

- Derive the redox-enhanced rate expressions to theoretically quantify the extent of binding enhancement under redox conditions
- Examine device responsiveness/noise at the nanoscale as a function of sensor tether length and proximity to the surface

- The effects of the geometry and asperities that may be present in our nanoporous membranes

Second, we examine a route pursued in this work for some time that would lead to a self-powered cation pump by the use of a molecular triad and discuss some of pitfalls along the way.

We then demonstrate the synthesis taken on by many groups of a 1,4-benzoquinone-18-C-5 (BQ-18-C-5)/ 1,4-hydroquinone-18-C-5 (HQ-18-C-5); Exploring both the published and novel route developed in this thesis that ultimately led to improved cyclization yields.

We then first modeled and screen prospective synthetic targets computationally that ultimately lead to a concise K^+ selective crown synthesis in just three convergent steps starting from catechol and alizarin. Higher order derivatives are then synthesized in order to refine the cyclization yield and increase functionality (discussed in Chapter 6, Future Work in more detail)

Lastly, the auxiliary material synthesis of anodized aluminum nanoporous membranes, thin films and hydrogel matrices is presented.

Design Considerations

Field effect transistors

Field effect transistors (FET) are semiconducting devices which promote electron hoping based on a threshold voltage through a semiconducting material. The intermediate layer of the FET contains the semiconducting charge transport layer

that will govern the electrical properties of the device. The transistor in this case is more precisely an ionic-field effect transistor (ISFET); with the electron hoping being promoted by a favorable electrochemical potential applied across the lattice framework and the vacancies inherently present in semiconducting materials. When the threshold voltage for the electron transfer is reached the ISFET functions via electron-cation pair hoping.

Biological sensors and switches have been fabricated from field-effect transistors (FETs), ISFETs and organic field effect transistors (OSFETS). This class of semiconducting materials has been widely employed in the detection of biological agents, toxic ions, enzymes and single-nucleotide sensing.

To fabricate a hybrid inorganic/organic FET, a device which couples redox potential to ion flow under favorable electrochemical potential was proposed as the framework for our mission.

It is imperative the process be reversible such that the direction of the E_{field} can be reversed to reoxidize spent redox carriers and transduce the signal in reverse, maintaining the feedback logic loop of the device in terms of the patients' perception and response.

Redox Processes

In the scheme shown in figure **3.1** below some examples of the fate of electrochemically generated radicals are shown. The diagram depicts a 1,4-benzoquinone molecule undergoing a series of different reactions, all reversible, to

arrive at protonated and deprotonated forms of semiquinone, quinol and hydroquinol intermediate species. The interrelated forms of the quinone depends on the solvent, presence of oxygen and temperature. The 1,4-benzoquinone/hydroquinone couple is ubiquitous throughout nature and is the main energy carrier involved in the electron transport chain.

Figure 3.1 - Possible fates of generated radicals and e^- species for the 1,4-quinone redox system

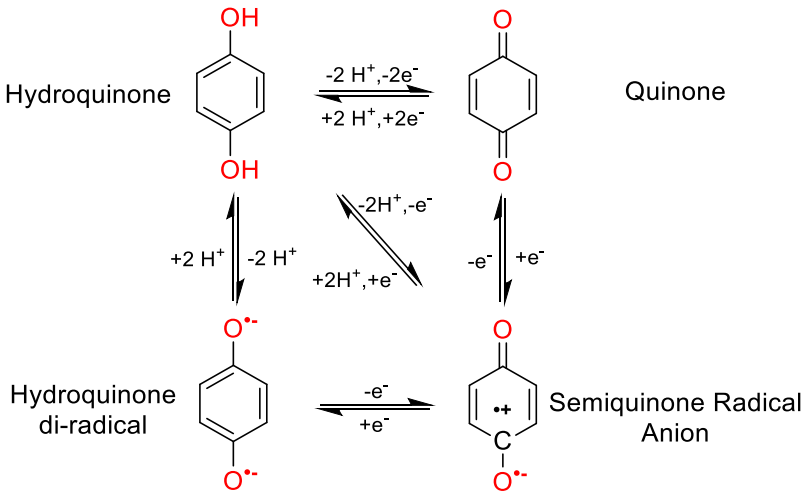

The Crown Ether and Its Role in Rate of Cation Complexation

Crown ethers have been around since Pederson discovered the first of these remarkable structures in 1967 (Pederson, 1967). Pederson observed that dicyclohexyl-18-crown-6 could effectively solvate potassium cations in a solution of benzene. The physical phenomenon driving this force is the breaking of the ionic bond to form a stable, neutral complex in which anions may play a significant role. Ionic disassociation between two molecules proceeds in one of two ways;

1. Breaking of the ionic bond (polar solvents) (eq. **3.1**) and formation of an encounter complex; or

2. Formation of strong electrostatic interaction to mediate ionic separation (apolar solvents such as THF, Et_2O, hexanes) (figure **3.2**, eq. **3.2**).

Polar solvents are those containing H-bonding groups and have rather short or no alkyl chains at all. Examples of very polar solvents such as water, which disassociate completely to form ions H_3O^+ and OH^-, serve as the host medium for cations and anions and a stabilizing medium for dissociation. This is why salts are very soluble in aqueous and very polar solvents and not soluble in nonpolar solvents.

Figure 3.2 - The radical forms generated by reduction of anthraquinones

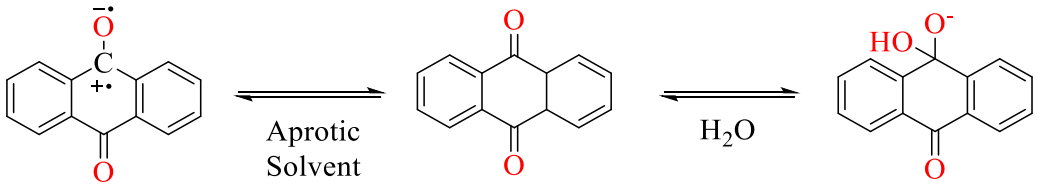

Polar Solvents

$$CA \underset{}{\overset{kdis}{\rightleftharpoons}} C^+ + A^- \overset{kchem}{\rightleftharpoons} A^- + C^+ + Crown \overset{kD}{\rightleftharpoons} [C^+ \quad \cdot A^- \qquad \textbf{3.1}$$

Apolar Solvents

$$A^- \cdot C^+ \overset{kchem}{\rightleftharpoons} [A^- \cdot C^+ \cdots Crown] \overset{kD}{\rightleftharpoons} [C^+ \quad \cdot A^- \qquad \textbf{3.2}$$

Rate Constants: Diffusion coupled with electrochemical processes

The rate constant given by diffusion of the reacting species is given by

$$k_d = 4\pi(D_A + D_B)(R_A + R_B) \quad \textbf{3.3}$$

Which can be rearranged to give

$$= k_d = \frac{2kT}{3\eta}\frac{(R_A + R_B)^2}{R_A R_B} \quad \textbf{3.4}$$

If the case is that A and B are the same or very similar, the following holds

$$k_d = \frac{8kT}{3\eta} \quad \textbf{3.5}$$

We can see now that the rate constant for diffusion depends only on the viscosity (η) of the medium and on the temperature. The overall rate constant in terms of the diffusivity of reactants is defined as

$$k_r = \frac{k_{chem}}{1 + \frac{k_{chem}}{k_d}} \quad \textbf{3.6}$$

The following equation has two limiting cases. When $k_{chem} >> k_d$, the overall rate constant equals k_d, the reaction being controlled solely by diffusion. This is often seen in dense liquids and gases at very high pressures. The other end of the extremes is $k_{chem} << k_d$ in which case there is no effect of the medium on reaction rate.

Liquids on the macroscopic scale show no particular order but show regular order on the microscopic level considering interactions amongst neighbors. This is

due in part by the interaction potential between the particles. Two particles interacting in a liquid leads to eq. **3.7**

$$k_{liq} = k_{gas} \int d^3 r p(r) e^{-W(r)/kT} \qquad \textbf{3.7}$$

Where p(r) is the radial distribution function (the probability that the two particles are at a distance r) in the solution and W(r) is their interaction potential.

The cost to separate the charges in the medium is given by the electrostatic interaction equation

$$E_{\text{int}} = \frac{q_1 q_2}{\varepsilon r_{12}} \qquad \textbf{3.8}$$

Here, the larger dielectric constant ε, the less the energy cost of separation. The dielectric is a measure of how well a solvent is able to solvate charges q_1 and q_2, with the distance between ions represented as r_{12}.

Ions dissolved in a medium will attract ions of opposite charge, contributing to short range order. In some cases this order may be so strong that liquid crystals form in the solution (Sczech, 2008). In the gas phase, ions of opposite charge exists bound tightly together because there exists no medium to stabilize the separate charges. Debye-Huckel theory supports that the concentration of the counterion decreases exponentially with distance, with the screening constant given by 1/κ (**eq. 3.9**), with

$$\kappa^2 = \frac{e^2}{\varepsilon T} \sum_{\alpha} Z^2 \frac{N_\alpha}{V} \qquad \textbf{3.9}$$

And the resulting interaction potential

$$V(r) = \frac{Z_e e^{-\kappa R}}{4\pi\varepsilon R} \qquad \textbf{3.10}$$

Where Z is the valance state of the ion. In polar mediums with high dielectric constants, κ^{-1} becomes very large and the positive and negative ions can be considered to move independently.

The practical application of these redox-based crowns was first pioneered by (Saji, 1986) where ferrocene crown-aza quinones effectively formed metal ion-pairs and served as the donor in the process. Gokel then studied the reversibility of the ferrocene-crown adduct and discovered that the redox process was fully reversible (Gokel, 1992). Redox active crown-aza cryptands which formed bis-complexes with Rb^+ and Cs^+ have also been previously studied (Hall, 1980). With the almost endless possibility of different supramolecular architectures, the field became a large area of focus, appearing frequently in the literature (Gokel, 2004).

Electrochemical enhancement

Quinones are reduced to corresponding quinol in the presence of 2 $H^+/2e^-$ in aqueous solution as shown for the anthraquinone species in figure **3.3** on the following page. Both single and multiple quinones have been incorporated into calix[4]semitube diquinone (Webber, 2003), benzo-crown ethers (Sun, 1995), (Delgado, 1992). Anthraquinone acyclic crown ethers were also developed early on from 1,8-dihydroxyanthraquinone adducts (Maruyama, 1985).

Predicting the enhancement of the overall rate by coupling both diffusion and electrochemical reduction with multiple electron species present in different forms is a challenge. The best approximation that could be devises as it pertains to this work are given in eq's **3.11** to **3.18**.

Figure 3.3 – Possible electrochemical transfer and reduction pathways of PEDOT:PSS membranes doped with crown ether 1

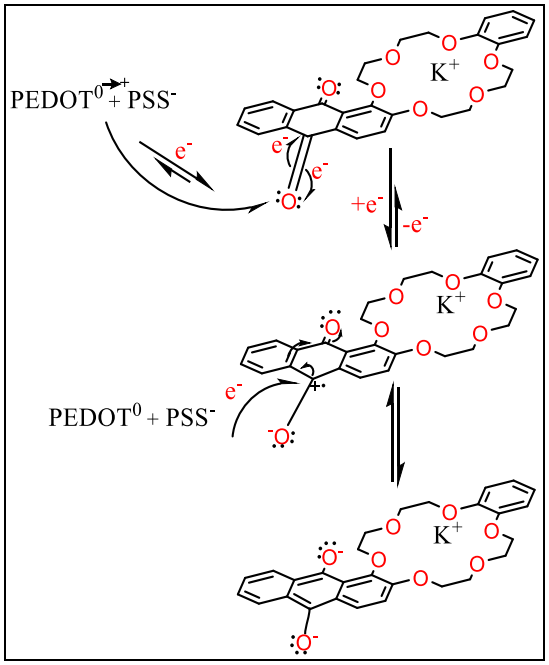

The rate limiting step which governs k_{obs} is the rate of ion capture due to much slower processes such as desolvation of the ion hydration shell and allosteric shifts in the host molecule. Complete reversal of selectivity has been shown with a 15-C-5 embedded in a sol-gel semi-solid to favor transport of K^+. In that particular case, the matrix in which the crown was embedded was the primary effector material that governed selectivity (Yajima, 2010).

In the equations **3.11-3.18** that follow, we derive the overall rate constant due to favorable ion-radical pairing events and factor in the number of radical-recombination events that lead to no observed enhancement.

$$-\frac{d[radicalionpairs]}{dt} = (k_{recomb} + k_{radicalion}) \cdot [radicalionppairs] \quad \textbf{3.11}$$

$$\frac{d[freeions]}{dt} = (k_{recomb}) \cdot [radicalionppairs] \quad \textbf{3.12}$$

$$\frac{d[radicalion]}{dt} = (k_{radicalion}) \cdot [ionppairs] \quad \textbf{3.13}$$

$$[ionpairs] = [ionpairs]_0 \cdot e^{-(k_{radicalion} - k_{recomb}) \cdot t}$$

3.14

$$[freeions] = [ionpairs]_0 \cdot \frac{kradicalion}{krecomb \cdot kradicalion} \cdot [1 - e^{-(k_{radicalion} - k_{recomb}) \cdot t}] \quad \textbf{3.15}$$

$$[recombinedpairs] = [ionpairs]_0 \frac{krecomb}{kradicalion \times krecomb} \cdot [1 - e^{-(k_{radicalion} - k_{recomb}) \cdot t}]$$

3.16

$$[freeions] \cdot [radicalion] = [radicalions]_0 - [recombinepairs] = \quad \textbf{3.17}$$

$$[radicalions]_0 \times \frac{k_{recomb}}{(k_{radicalion} + k_{recomb})} \cdot e^{-(k_{radicalion} - k_{recomb}) \cdot t}$$

$$+[radicalions]_0 \times \frac{k_{recomb}}{(k_{radicalion} + k_{recomb})}$$

Comparing eq. **3.17** with the single exponential decay function $C(t) = C_0 \cdot e^{-k_{obs} \cdot t} + C$ shows that the experimentally observed rate constant enhancement imparted by electrochemical reduction is the sum of $k_{radicalion}$ and k_{recomb}.

$$k_{obs} = k_{radicalion} + k_{recomb} \quad \textbf{3.18}$$

Another consideration is if a radical ion was to be generated near the plane of the crown ether, there exists the possibility of the host crown forming a hydration shell in solution. This imparts an even lower rate constant, as the ion now has to penetrate the crown ether hydration shell, displacing water in the process, along with shedding its own hydration shell before binding electrostatically.

As explained by Marcus Theory, electron mobility is a function of the relative permittivity of the medium and the distance the electron must travel from one molecule to the next (Marcus, 2012). Thus, a crucial design aspect was to have an adjustable redox potential at the pinch-off threshold hold of the organic transistor. This can be mediated by incorporating electron deficient redox subunits such as 9,10-anthraquinones (figure **3.3**), appended to a polymer backbone to create a step-down potential where intermediate species lower the threshold for the amount of applied voltage needed to reduce the species than if no mediator was present.

Materials required for fabrication

The necessary organic materials required included formulations of different thin film dispersions of ionically conductive PEDOT^0 doped with PSS$^-$ (figure **3.4**) for use as our organic electrodes, a hydrogel storage/filler layer of ion-conductive matrices of PEO or POLYUREA and a potassium selective reversible crown ether -See figure **3.5**.

Figure 3.4 – Chemical structure of the ion-conductive polymer, $PEDOT^{0}$:PSS^{-}

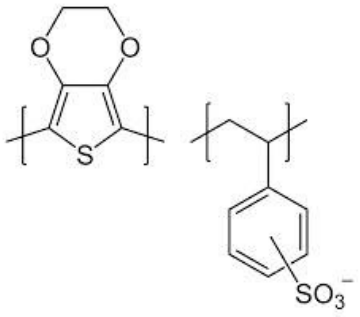

To fabricate the proposed device as depicted in figure **3.5**, both organic and inorganic components would need to be integrated in a precise fashion.

A secondary requirement which will be discussed in detail later in the chapter are monofunctional silane derivatives that covalently attach directly to the substrate to prevent leaching or the reorganization of the materials once encapsulated in the device.

Necessary inorganic materials include:

1. The nanoporous alumina (or other semiconductor) arrays for multi-channel functionalization with the monofunctional silanes.

2. Single pores drilled by electron beam (E-beam lithography) to study the effect of functionalized single and arrayed pores and the selectivity imparted by each.

Considering the minute quantities of ionic species to be delivered peripherally to excite the nerve, the nanopore device must elicit a very fast, uniform response with low levels of noise. To eliminate this unwanted noise, cylindrical pores with regular nanoscale dimensions and avoidance of any defects such as pitting or runaway

anodization must be avoided; resulting possibly in etching parallel to the plane rather than perpendicular.

Figure 3.5 - Schematic of the revised potassium-selective redox ion pump utilizing nanoporous Al_2O_3 to form arrays of nanopores that would be readily available for further functionalization.

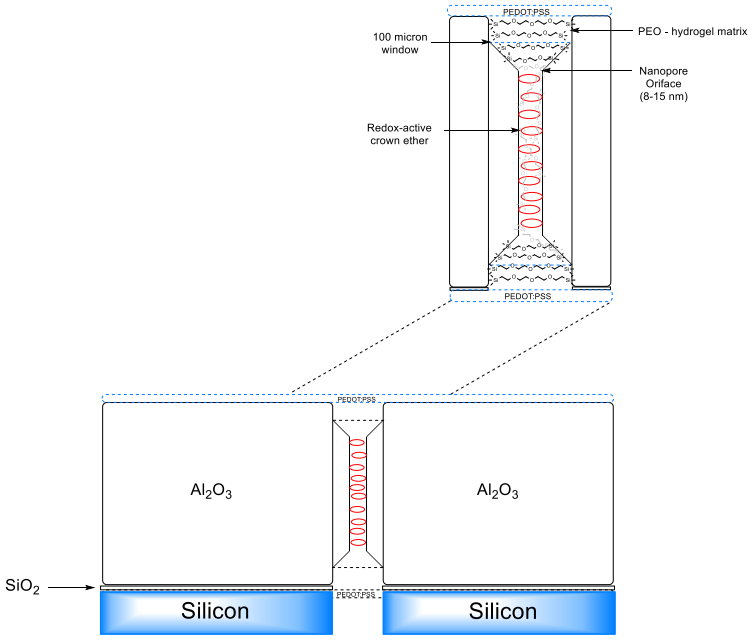

The anodization of aluminum can produce amorphous nanopores that have a gyroidal-type architecture depending on the temperature, time, voltage and electrolyte used during the anodization process (see end of this chapter). Several papers have explored these phenomena leading our processes in the right direction by pointing out all of the potential pitfalls one could encounter. Multi-level iterative functionalization has been achieved has been achieved by anodizing to an intermediate level of aluminum, functionalization, and another anodization step to

expose more aluminum to be functionalized into a multi-tiered functional stack (Mutalib Md Jani, 2009). This process suggests organic functionality installed in the latter step stays intact throughout an applied potential of 40 V during the anodization process. Yamaguchi Et al. discovered the self-assembly properties of mesoporous silica into ordered domains (Yamaguchi, 2004). Models for these new membranes have been examined computationally to gain new insights into their behavior (Peter, 2005).

Organic Materials – Initial Route – A molecular triad

Initially, we wanted a device that would ideally power itself upon light stimuli, since vision in the dark was not the goal of this endeavor. This would undoubtedly involve some type of charge-transfer complex that had both an n-type and p-type semiconductor - along with an electron source, in this case, from a metal center.

The key principle to our redox active "pump" is the ability to drive metal ions, in this case K^+ ions against their concentration gradient in the cell. To achieve this, many strategies mimicking natural photosynthesis have been attempted, albeit with little success to date. Voyer Et al. showed that transport could be effected by 18-C-5 ethers spaced 6 Å apart along a short polypeptide backbone (Voyer, 2010). The vesicles formed by the peptide polymer at 30% crown grafted to the side chain were able to selectively translocate K^+ by Brownian motion and physical diffusion.

Utilizing a crown ferrocene ether, active transport of Ca^{2+} against its concentration gradient was achieved by Saji Et al. in an electrochemical transduction cascade across a liquid membrane comprised of methylene chloride in a typical U-

tube experiment (Saji, 1986). The same approach with anions was used in the sensing of Cl^- anions by a ferrocene complex (Evans, 2011). Multi-redox 1,4-benzoquinone crown ethers joined by oxidative intramolecular coupling have also proven to show electrochemical enhancement upon reduction (Maruyama, 1985), (Webber, 2003).

Figure 3.6 – Methanolysis of the propionic acid fragment to give all *E*-retinol to form our p-type junction acceptor.

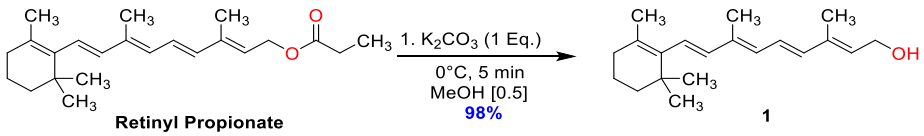

Approaching the System from a Biological Perspective

We examined several biomimetic approaches including the use of copper phthalocyanin (figure **3.8**) as a photoactive redox-center with two different e-/hole relays to form a molecular triad (Benniston, 2010). The electron would be accepted by our crown ether and the hole traveling down the conjugated naturally-derived molecule *E*-retinol, derived from methanolysis of Retinyl propionate (figure **3.6**) in the presence of one equivalent potassium carbonate at 0 °C. This novel reaction was realized and resulted from the work of (Platonov, 2002) who discovered that a small amount of methoxide anion exists in equilibrium in a basic solutions of methanol. Extrapolating this to the delicate methanolysis of Retinyl propionate, the theory of methoxide-induced attack of the ester carbonyl proceeded as predicted by the mechanism shown in figure **3.7** where a methoxide ion attacks the carbonyl carbon

and liberates methyl propionate, leaving the resonance stabilized alcohol form of the molecule cleanly intact with excellent yields and fast reaction times (<5 m.) (Platonov, 2002).

Figure 3.7 – Reaction mechanism of the facile cleavage of the unsaturated Retinyl propionate chain by methoxide to give all *E*-retinol.

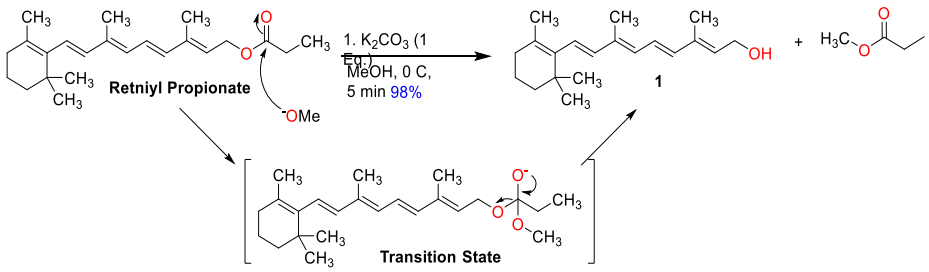

The anthraquinone-based crown ether (presented later in this chapter) acceptor and retinol hole acceptor had thus far been assembled.

The problem arose when the author took the approach of utilizing a metalized porphyrin of low purity. Copper Pthalocyanine has three acid groups which were all subjected to EDC coupling, Dean-Staark esterification, and conversion to the tri-acid chloride. Although some products could be identified by ^{1}H NMR, the Cu^{2+} center caused the NMR signal to noise ratio to drop drastically due to the interconversion of $Cu^{(I\text{-}II)}$ forms and the influence of spin-orbit coupling between aromatic protons on the porphyrin ring in the square-planar conformation.

Solubility also posed a significant problem in that the porphyrin itself was only soluble in concentrated H_2SO_4, DMF and slight solubility in hot $CHCl_3$, CH_2Cl_2 solutions.

Figure 3.8 – Chemical structure of the Chlorophyllin A porphyrin with possible functional group interconversion sites.

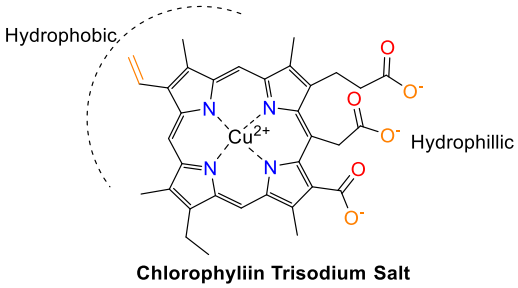

We envisioned installing the retinol by EDC, DCC coupling or conversion of the trisodium salt as mentioned (figure **3.8**), to the tri-acid chloride in a solution of CH_2Cl_2 with catalytic DMF using oxalyl chloride.

Problems were encountered during the purification of the delicate crude material. As mentioned previously the chlorophyllin compound itself was only slightly soluble in organic solvents DMF and $CHCl_3$ and all resulting compounds from ester, amide forming coupling reactions seemed to behave the same way. This lead to very dilute, high molecular weight samples to characterize by NMR, which often times was not even feasible despite the high-field NMR spectrophotometers used.

Chemistry of Anthraquinones

Figure 3.9 – The synthesis of substituted anthraquinones via Diels-Alder condensation

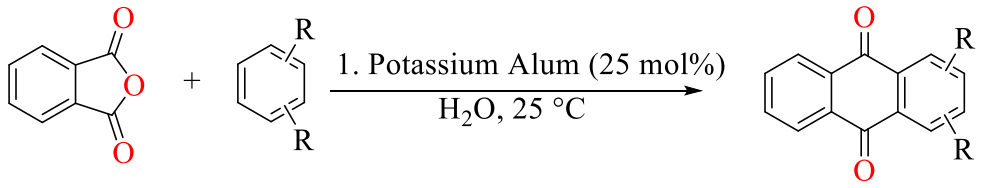

The chemistry of the anthraquinones is vast in nature but the construction of the skeletal fragments by Diels-alder cycloaddition (figure **3.9**) reactions from the corresponding di-phenol and acetic anhydride (Dhananjeyan, 2005) is the most straightforward route to substituted anthraquinones. Anthraquinones are frequently encountered and used in the textile industry as pigments or dyes for clothing due to their rich color spectrum and resistance to photo bleaching effects (Cysewski, 2012). Anthraquinone derivatives are also showing promise as anti-tumorigenic compounds along with DNA interrelation ability due to its rich tricyclic ring system coupled with its ability to hydrogen bond (Surkau, 2010).

Anthraquinones were ultimately chosen as the organic redox subunit to head this study due to the reasonable voltage it undergoes its first reduction potential (-0.57 V), a trait we wanted to exploit by biasing the potential; holding the anthraquinone in the semiquinone form and effectively "gating" K^+ in our nanoporous channels. We envisaged this would assist in speeding redox-triggered diffusion by hopping field effects and complementary interactions between [e^- - $^+$ion] pair as they traverse the channel.

The scheme below was worked out to create a variety of derivatives with nearly the same properties. Since Erk Et al. reported the synthesis of anthraquinone 18-C-6

ether, the novel addition of the benzo group separates this ether from other ethers already reported in the literature.

In figure **3.10**, all of our synthons described in theory were envisioned to be developed into a molecular triad that could induce charge separation while keeping the source and acceptor molecules in close proximity to each other.

Figure 3.10 – Original synthons for creating the molecular triad for renewable, self-powered ionic stimulation of nerve tissue

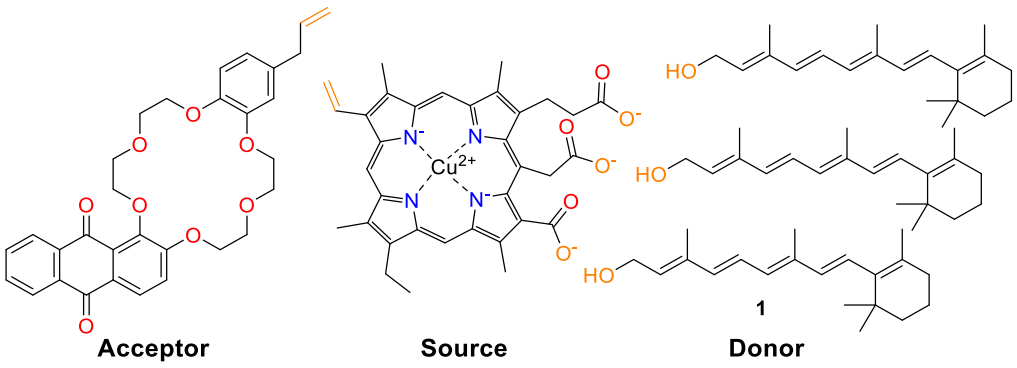

The one step synthesis of retinol from retinyl propionate was indeed a success but each effort to couple donor and source molecules was hampered by ether the presence of the tightly chelated Cu^{2+} square planar center or steric hindrances of the acid functionality.

Computationally, these were modeled to be above and below the plane in an alternating fashion but even esterification coupling conditions using 1-ethyl-3- 3-dimethylaminopropyl carbodiimide hydrochloride (EDC), N,N'-Dicyclohexylcarbodiimide (DCC) with Hydroxybenzotriazole (HOBt), dimethylaminopyridine (DMAP) and imidazole (ImH).

Since this was the key step to turn an amphiphilic porphyrin to a very polar, rigid scaffold, it was decided to abandon the synthesis of such a large macromolecular assembly (fig **3.11**) and instead fabricate two organic electrodes to supply the reduction potential to reduce our quinone.

Figure 3.11 – The molecular triad consisting of derivatives from retinol propionate, Chlorophyllin A trisodium salt and the novel anthraquinone redox macrocycle was ultimately abandoned in route to our molecular device.

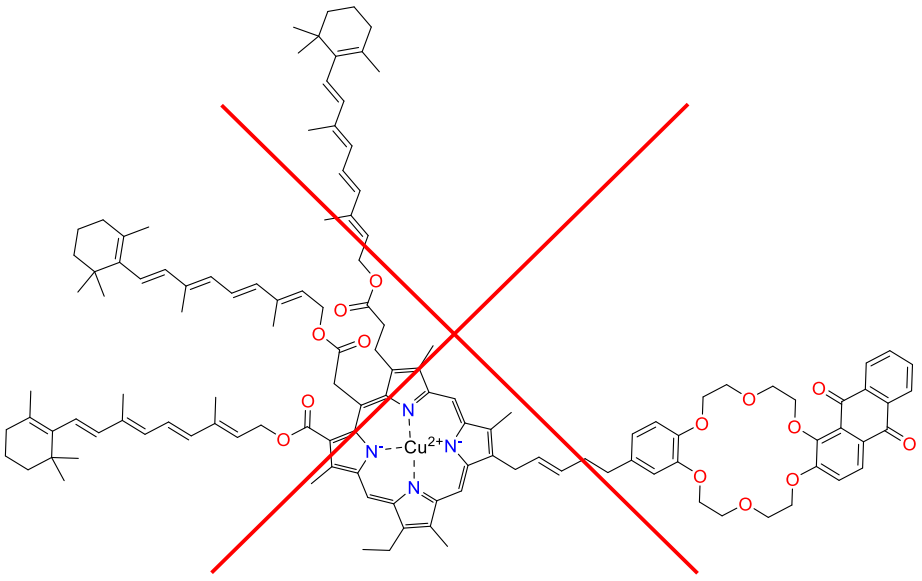

Alternative Route I

Electro-migration by ions

Redox processes effectively charge otherwise neutral molecules containing redox-active functional groups in their structure or are linked to a material (the "Fe" in ferrocene) making them good hosts for the formation of radical anions or cations giving them a formal (-) or (+) charge. In this case, we want to put an electron into the system to form a radical anion – cation pair at a given potential.

The material must be robust, reversibly oxidative/reductive, and stable enough to hold a fixed charge for a finite amount of time to capture and maintain potassium stores and must contain enough redox-containing hosts to allow for intermolecular electron hopping to redox sites on adjacent molecules. In this manner, the binding constant, K, changes in both magnitude and number because we are inputting electrochemical work into the system, altering the geometry and chemical potential of the system.

The kinetics also are affected as now a field of negative charge is proximal to the redox center, biasing the cation to drift toward the negative charge. When the molecule is oxidized back to its neutral state and conformation, electrostatic repulsion kicks the cation out of the ring and the ion-metal pairing interaction is lost. The cations then drift toward the negatively biased electrode, hopping in the direction of the E-field between binding events.

To trigger the release of potassium; it would make sense to exploit the chemical potential and reversibility of the reduction of quinones (fig **3.12**), making them the renewable source for ion sequestration and delivery.

Figure 3.12 - Oxidized (left) and reduced (right) forms of the macrocycle **1** synthesized as the first model redox crown ether in or study.

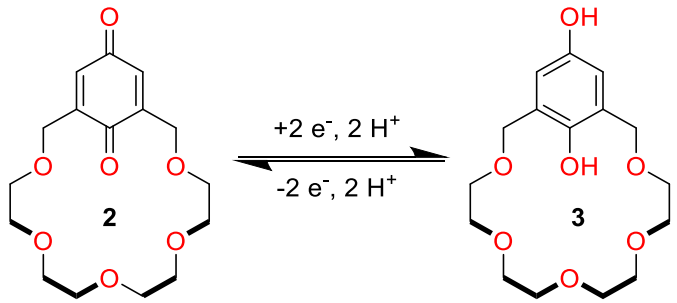

Material Synthesis

Figure 3.13 - Synthesis of Crown Ether nucleophiles and electrophiles for Model Study

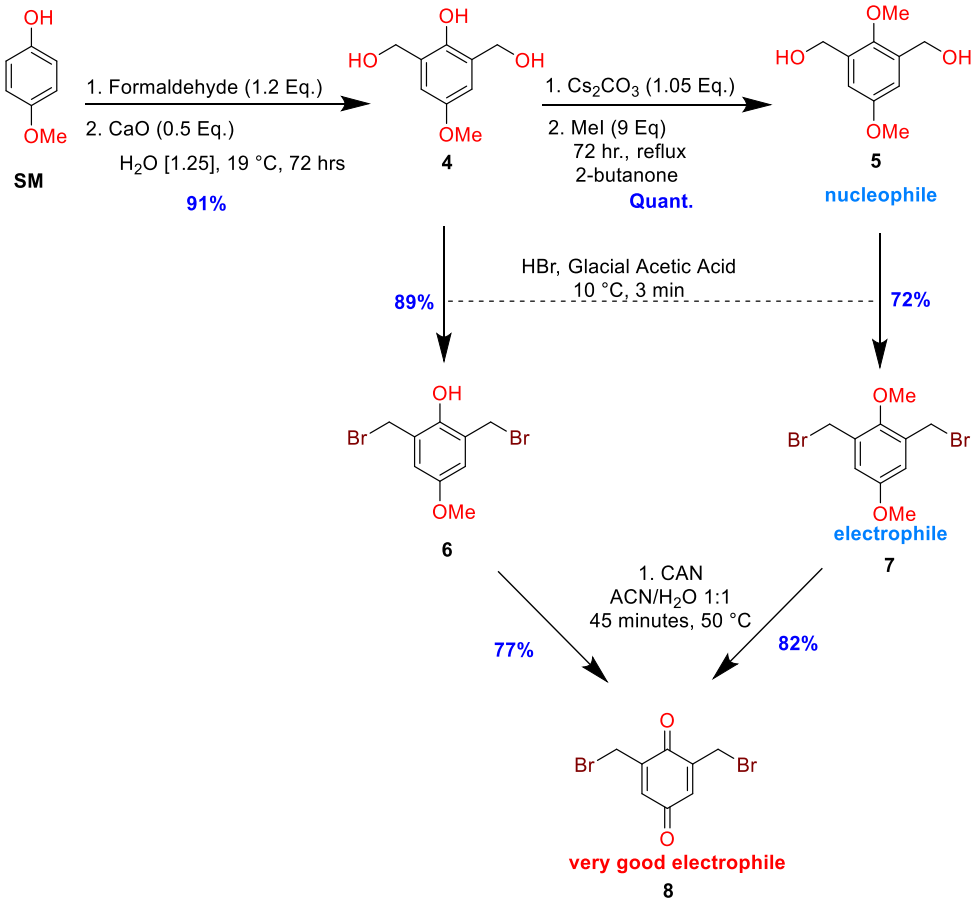

HQ-18-C-5 Synthesis

To synthesize our first crown ether to familiarize ourselves with the characterization techniques involved in host-guest chemistry, we completed a synthesis of a well-known ionophore by Sun Et al. with a few minor modifications and improvements. The hydroxymethylation (figure **3.13**) to form **4** from 4-hydroxyanisole proceeded in very good yields of 91% using formaldehyde with aqueous calcium oxide as the base (Moran, 1952). The second step required some modifications from the original procedure to effect complete conversion to the bismethoxy derivative **5** by switching the base and solvent from NaOH in ethanol to Cs_2CO_3 in 2-butanone (Kellogg, 2006). Using this method led to complete conversion to the 1,4-dimethoxy derivative. The cyclization to give the pseudo 1,4-dimethoxyanisole-18-C-6 **13**, with yields around 50%, similarly reported by the authors (Sun, 1995), (Sugihara, 1981).

Alternatively, the same macrocycle was obtained in optimal yields utilizing a novel cyclization strategy. With the successful methylation of **4** to give **5**, we took the approach of converting the electron rich nucleophilic benzyl alcohols to electrophilic benzyl bromides by reaction with anhydrous hydrobromic acid in a solution of glacial acetic acid at 10-15˚C. This reaction proceeded remarkably fast, taking only 3 m. to complete at 10˚C for the conversion of **4** to **6** (89%) as well as **5** to **7** (72%) to give the dibromides in good to fair yields. The dimethoxydibenzylalcohol, **5** had much less solubility in acetic acid than that of **4**, explaining the lower yields. In a similar manner, tetraethyleneglycol was converted to the ditosylate **12** in 96% yield in a biphasic mixture of aqueous sodium hydroxide/tetrahyrofuran using a slight excess of tosyl chloride.

Figure 3.14 – Synthesis of protected dibromonated hydroquinol species from 2,6-dimethyl-1,4-dihydroquinone and appropriate protecting group

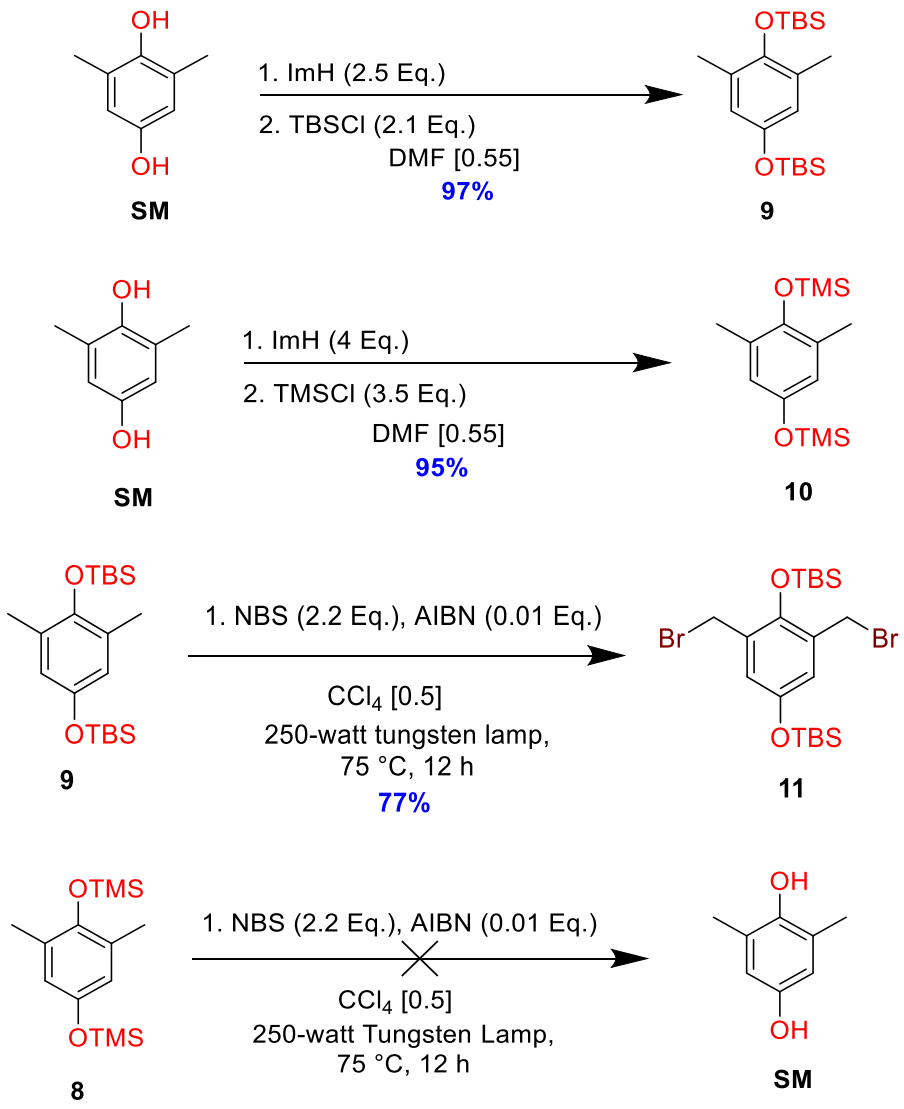

Working from 2,6 dimethylhydroquinonone (fig **3.14**) as a starting material, protection of the OH phenols went as planned as both the tert-butyl dimethylsilyl (TBS) (**9**) and trimethylsilane (TMS) silyl-protected ethers (**10**) were formed in anhydrous DMF at 60°C after overnight stirring. Corresponding free-radical induced benzylic bromonation of the TBS derivative, **9** proceeded in good yield giving almost exclusively the disubstituted

bromide **11** in 77% yield utilizing AIBN as a radical initiator and N-bromosuccinamide as the brominating agent.

Figure 3.15 – (Top two schemes) Traditional synthesis utilizing OTs-TEG-OTs (**12**) as the electrophile in the macrocycliztion to form **13**. Bottom two schemes (TEG) is used as the nucleophile to react with the benyl bromides of the 1,4-dimethoxy and 1-4-benzoquinone electrophiles

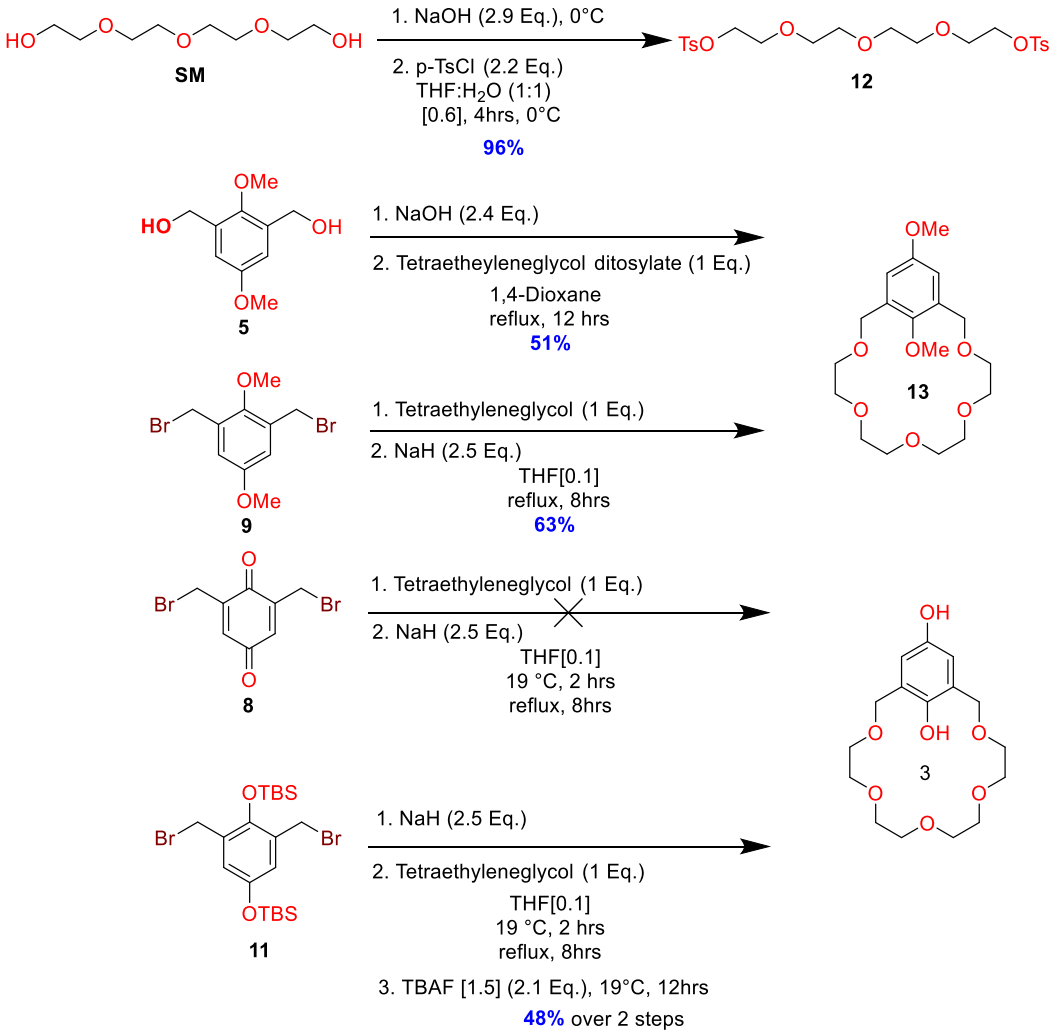

The TMS protected derivative, however could not hold up against the harsh reaction conditions, undergoing desilytion from compound **8** back to the starting material. Likewise,

electrophilic dibromide did not cyclize to the expected di-silyl protected crown which is mostly likely explained by the use of sodium hydride and possible enolization of the quinone. The more stable TBS-derivative protected intermediate (fig **3.15**) crown was immediately desilylated without isolation by utilizing a slight excess of tetrabutyl ammoniumfluoride (TBAF) in THF to give an overall yield of 48% over two steps. Altogether, the reaction of the dimethoxydibenzylbromide proved to give the best yield of **13** (63%) of all routes discussed.

Figure 3.16 – Oxidative demethylation by cerium ammonium nitrate (CAN) to give the crown quinone **16,** followed by reduction with sodium dithionate yielding the reduced form, **17.**

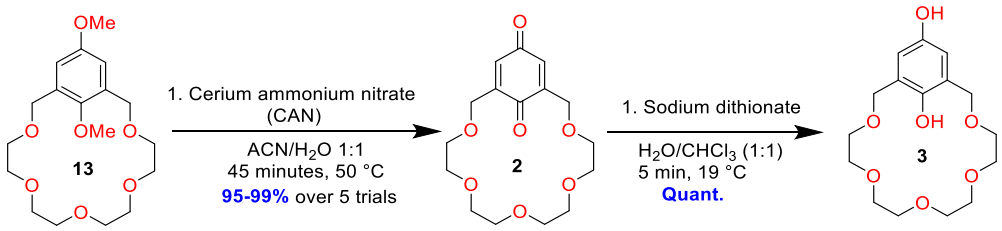

Oxidative demethylation (fig **3.16**) of **13** using CAN in a 50/50 solution of acetonitrile/diH_2O at 50°C for 45 minutes gave **2** followed by reduction in a separatory funnel between equal amounts of $CHCl_3$ and a solution of sodium dithionate yielded **3**. Alternatively, **3** could be obtained by the route in figure **3.17** by direct BBr_3 demethylation in excellent yield by holding the solution at controlled temperatures for at least 1 h. at -40°C in anhydrous dichloromethane, as holding the solution for only 10 m. at -50 °C with gradual

warming to room temperature led to quantitative cleavage of the phenethoxy ethers of the crown ring to give the starting material 2,6-dimethylhydroquinone.

Figure 3.17 – Direct double demethylation of aryl methyl ethers to the 1,4 hydroquinol form of the crown ether.

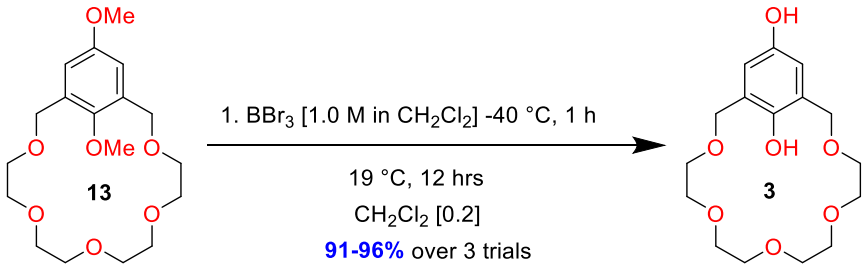

The next step in our functionalization of benzoquinone crown ether **3** was to proceed by one of two routes. The first would rely on selective allylation of the distal phenol on the periphery of the ring by using a cation to block the intra-annular phenol from being alkylated. The second method would hinge itself on $Bi(OTf)_3$ catalyzed reductive allylation of quinones or other type of soft nucleophilic conjugate addition. We proceeded with a model reaction as shown in figure **3.18** in a promising 89% yield with a model substrate very similar to the architecture the target molecule.

Figure 3.18 – Model reaction of allyltrimethylsilane using 5 mol% $Bi(OTf)_3$ gave the intended allylated product of 2,5-dimethylbenzoquinone, synthesized prior from Jones reagent in sulfuric acid. 1, 2 conjugate additions of amines, allyltrimethylsilanes failed to elicit the same reaction in the case of **16**, despite the successful model reaction with 2,6-dimethylbenzoquinone (Carrion, 1984).

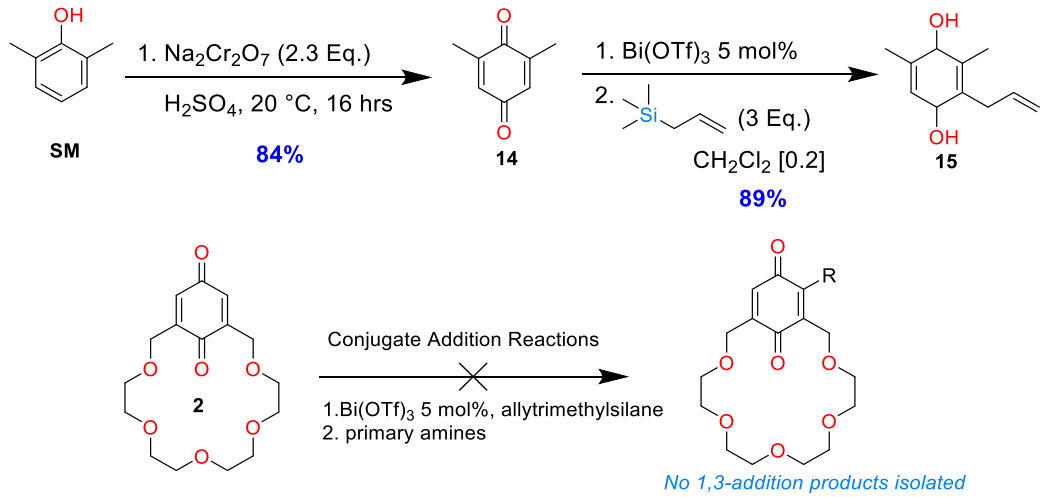

The same process was repeated with varied amounts of Bi(OTf) on substrate **2**, but the macrocyclic embedded quinone did not undergo the analogous conversion to the reduced hydroquinone.

This led us to explore our second option, regioselective allylation followed by Claisen Rearrangement. Unfortunately, after many attempts at selective allylation with almost every Group I carbonate salt, a mixture of intra-annular, distill and di-allylated products were generated (figure **3.19**). The ratio of observed products ranged to favor only one of the two isomers giving ratios of (1.3:1.0) at best and could easily be analyzed by the vinyl proton signal falling much more downfield than normal for the intra-annular allylated phenol

isomer. Since only one equivalent of base was used, the mixture did however consist of mostly mono-allylated products. In effect, this ended our search for a functionalization scheme for the above class of compound. The ^{1}H NMR titration of the crown ether with Na^{+} and K^{+} triflate salts along with cold-temp NMR of the 1:1 complex is presented in the next chapter.

Figure 3.19 – Regioselective allylation selective substitution strategy: Exploit phenoxide salt formation/ pKa differences of phenolic compounds

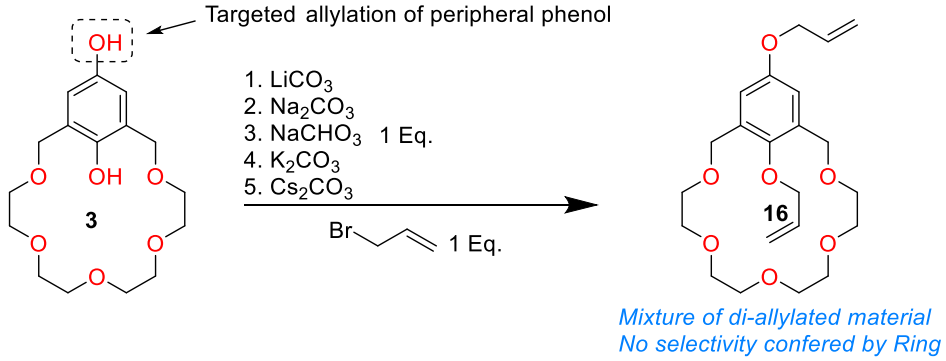

Allylated crown ethers for pore functionalization control studies/use as ionic pre-concentrators in the hydrogel layer.

As a pre-selective layer, four versions of the crown were prepared in order to test the selectivity through the cross-linked hydrogel network.

These extended crowns were meant to serve two purposes:

1. Serve as monomeric baseline controls, providing resulting C/V trace data that could be assessed as a baseline for efficacy of the film as they would be functionalized to the nanopore walls o.

2. Attempt to elicit incorporation by radical polymerization with acrylates in the hydrogel pre-concentration layer with PEG-based acrylates to form a selective pre-concentration layer atop the PEDOT:PSS$^-$.

Figure 3.20– 18-crown-6 and 15-crown-5 allyl and pentenyl substituted crown ethers prepared by reaction with sodium hydride and the appropriate halide in THF.

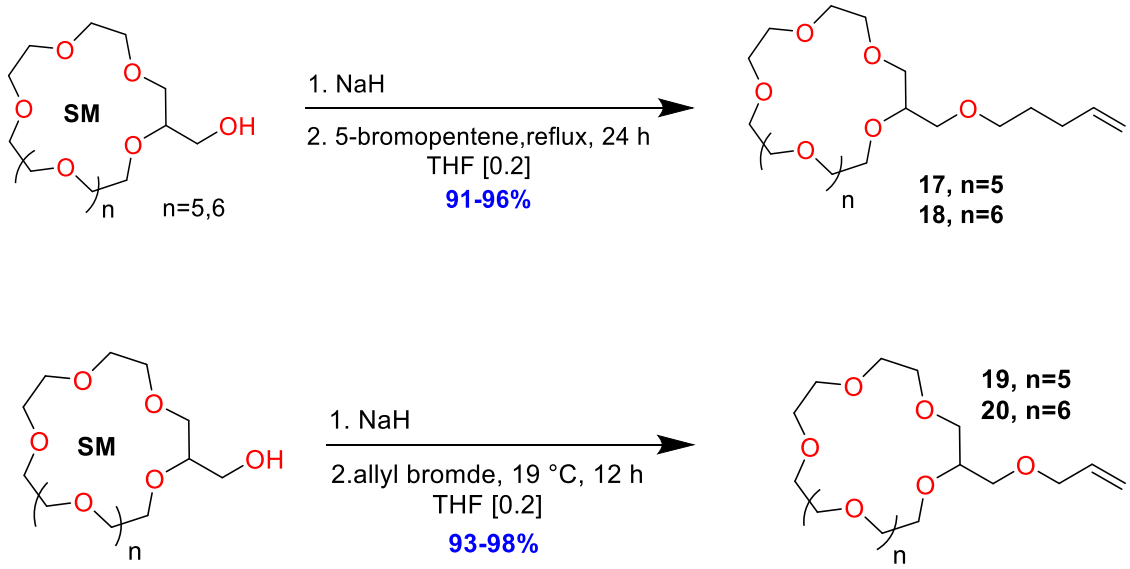

The traditional five and six membered crown ethers shown in figure **3.20** above were prepared by the Williamson ether synthesis from the corresponding 2-hydroxymethyl substituted crown ether by treatment of the alcohols with NaH in anhydrous THF. The allylation of the crown with allyl bromide to form **19** and **20** went to completion at 19 ˚C while the unconjugated 5-bromopentene crowns **17** and **18** required heating to reflux for 24 hours to reach completion.

Anthraquinone Crown Ethers: Generation II

The next synthetic target was inspired by examining the properties of a whole new class of crown ether that hinged off the anthraquinone subunit as the active redox quinone embedded in the structure that we had mentioned earlier. Analysis of the pertinent literature on the synthesis and properties of these new class of crowns (shown in figure **3.21, 3.22**) revealed that very little selectivity was imparted by these stiff tricyclic bisanthraquinone, anthraquinone and acyclic anthraquinones. There was something common to the structure of the first generation crown synthesis earlier and these anthraquinone crowns; retention of the intraannular carbonyl of the quinone subunit. While possibly envisioned as the sight of first reduction, the intra-annular carbonyl is the last carbonyl to be reduced due to the increased electron density from the ortho positions of the ethoxy crown ring. The peripheral carbonyl is meta-directing and further enhances delocalization at the intra-annular carbonyl. After careful review, it was concluded that including the carbonyl in the plane of the ring would not benefit our synthesis as far as electrochemical enhancement, ultimately due to steric factors.

Figure 3.21 – Crown ethers (A-C) synthesized by Nakatsuji Et al (Nakatsuji, 1983) showed poor selectivity toward K^+ cation due to steric effects. The macrocycle D, by Rahmen Et al showed selectivity for $NH4^+$ cation and not K^+ (Rahmen, 2004).

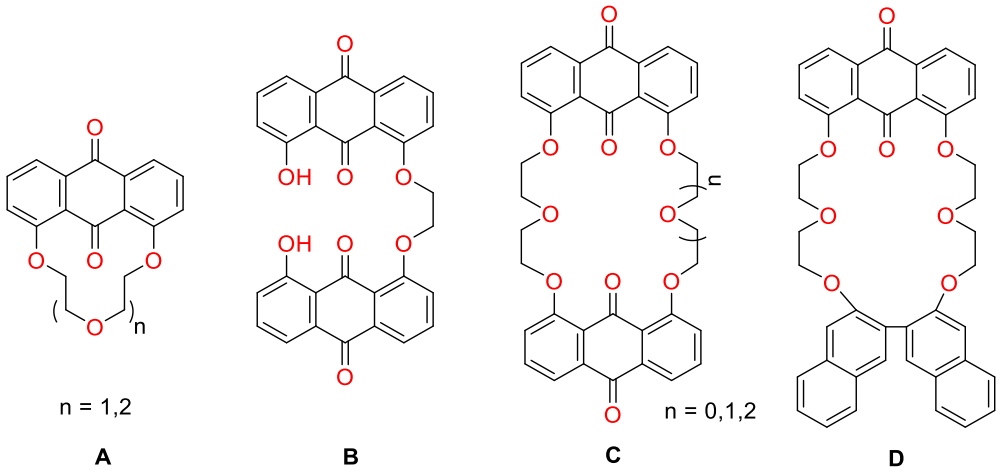

Figure 3.22 – Acyclic crown methylethers developed by Delgado Et al (Delgado, 1988). The first synthesis from 1,2-dihydroxyanthraquinone (Alizarin) by Peter and Vogtle (Peter, 1981) showed promising selectivity which later was also pointed out by Erk Et al in two independent publications (Erk, 2000 p3582, Erk, 2000 p229).

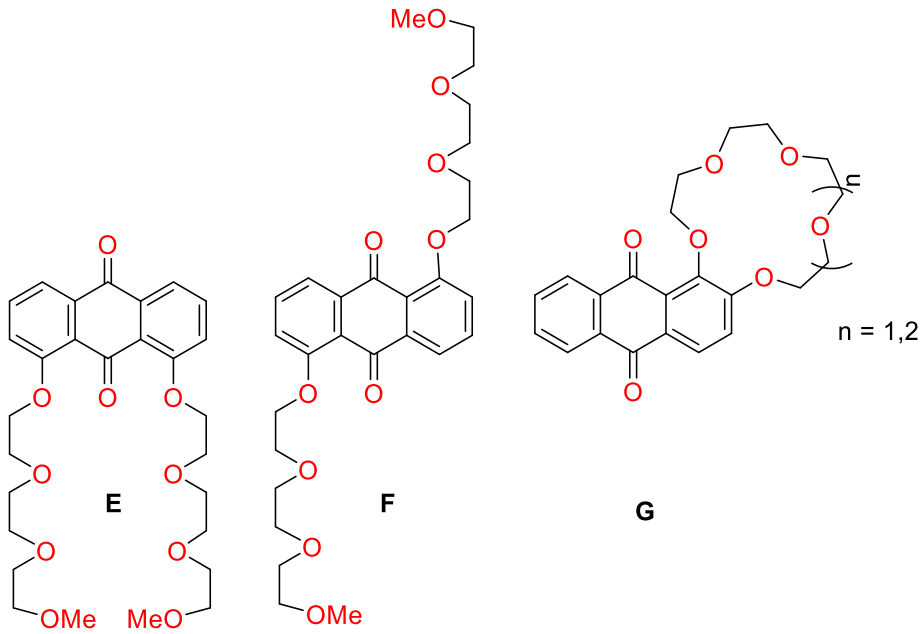

The Taft equation (eq. **3.18**) was used in computational simulations where $\log(k_s/k_{carbonyl})$ is the ratio of the rate of the substituted(or unsubstituted in this case) reaction to the reference rate, E_s is the steric substituent constant, ρ^* is the sensitivity factor to polar effects and δ is the sensitivity factor of the reaction to steric effects (Taft, 1953).

$$\log\left(\frac{k_s}{k_{carbonyl}}\right) = \rho^* o^* + \delta E_s \qquad \textbf{3.18}$$

This equation effectively encompasses a qualitative structure-activity relationship (QSAR) for the complexation reaction. In essence, it is very similar to the Hammet equation but in addition, accounts for the steric effect of substiuents on the reaction rate in addition to field, inductive and resonance effects the Hammet equation asseses.

Utilizing this equation in conjunction with the program Molsoft ICM Browser Pro (ICM), a negative correlation of -0.42 R^2 between the increased steric bulk of the carbonyl and binding of K^+ to the central cavity of the crown. With this analyses, structures such as those shown in figure **3.21, 3.22** were excluded as targets for synthesis. Instead, a synthesis was devised where the anthraquinone is retained but the carbonyl group excluded from the plane of the ring by switching the starting material from 1,8-dihydroxyanthraquinone to the 1,2-diydroxy derivative, common name Alizarin.

The Ultimate Crown Ether

While synthetic methods to construct the macromolecule were ongoing along with its subsequent characterization, the inorganic membrane was to be constructed in parallel in a convergent manner as the anodization procedures were developed.

The glycolytic leaving groups chosen for crown ether synthesis was intended to provide structural diversity in cyclization coupling partners. The kinetics of cyclization and yield were of principle interest in which fragments would cyclize best in a 2+1 or 1+1 type cyclization to form the macrocyclic crown ether ring.

After synthesis of the appropriate glycol ether from a substituted catechol in acetonitrile or DMF using anhydrous potassium carbonate; distillation of the crude diol by kugelrohr or fractional distillation vacuum distillation yielded clear, viscous oils. This step yielded between 90% to near quantitative yields (on large scales). The crude diol was then converted to tosylate, iodide or mesylate or protected with the THP protecting group for other manipulation. Treatment of either of the later substrates (OTs or OMs) with anhydrous ammonium iodide yielded the bisdiiodide in quantitative yield. The bis-tosylation of the diol along with mesylation always proceeded in high yield and were cost-effective to produce on large scales. Attempts to convert the diol directly to the dihalide with triphenylphosphine/I_2 failed to yield a product that could be worked up in a facile manner.

Figure 3.23 - Synthesis of glycols and leaving groups used in stage 1 of this synthesis

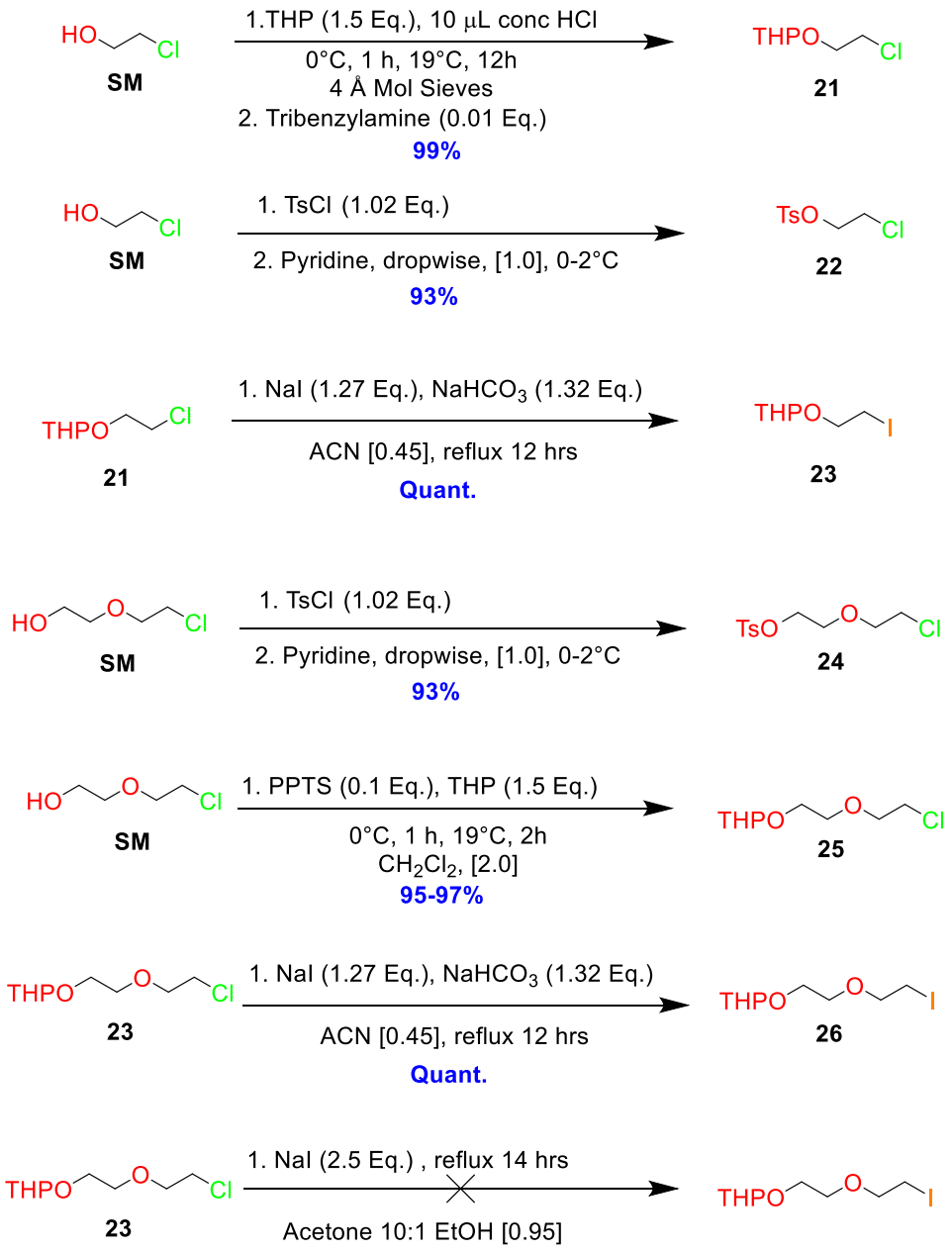

In the reverse method; Banerjee Et al synthesized a Ru^{II}-polypyridyl-crown-anthra-quinone complex in 54% yield after 5 days of reaction at 90 °C in DMF utilizing a catechol derivative as the nucleophile and extended Alizarin terminated with tosylate leaving groups as the coupling partners. The problem we envisioned with Banerjee's route was the 10 day

alkylation reaction with 2-(2-chloroethoxy)ethanol, which proceeded in a mere 40% yield after column chromatography to yield the extended diol.

Our synthesis also shifted directions as we decided to extended out the alizarin molecule with the glycols, but getting the reaction to go to completion with these polar opposite compounds took 10 days at 80°C in DMF utilizing cesium carbonate as the base in slight excess. The switching of the halide from chloride (fig **3.23**) to iodide drastically reduced the reaction time and temperature from 10 to 3 days for complete conversion and at a much milder temperature of 60 °C.

During alkylation of catechol with extended halogenated THP-protected glycols, the reaction was much more homogenous and proceeded much quicker than when R=OH, presumably due to the stabilization of the transition state by hydrogen bonding of the glycols whereas with the THP ether, no hydrogen bonding is present to stabilize the transition state. For the deprotection of the bis-THP protected alcohol, 10% methanolic HCl was utilized in a solution of MeOH for 1 h. at 0 °C to afford the diol in nearly quantitative yield. (Patel, 2006)

The crown ether AQ-18-C-6 was devised computationally (see chapter **V** for more detailed procedure) to give a favorable twisted boat conformation when paired with anions the approximate size of the triflate hydrodynamic radius, per previous experiments.

The glycol derivatives were prepared in a straightforward manner but some unexpected had to be overcome in converting the chloride to iodide in a typical Finkelstein reaction with THP-protected chloro derivative **23** (figure **3.23,** bottom). When using the procedure by (Patel, 2006), the only thing that was yielded was the original unchanged starting material as the chloride. The odd combination of 9:1 acetone to ethanol solvent was something not usually observed to be used in the former. Changing the solvent from acetone/ethanol to the

aprotic acetonitrile, while adding some mild base to maintain the reaction at neutral from to prevent any dehydrohalogention, a quantitative yield was obtained upon the first trial of the reaction and no further optimization was required.

Figure 3.24 – Synthesis of intermediate molecules for alternative synthetic strategies toward increasing the macrocyclic ring yield

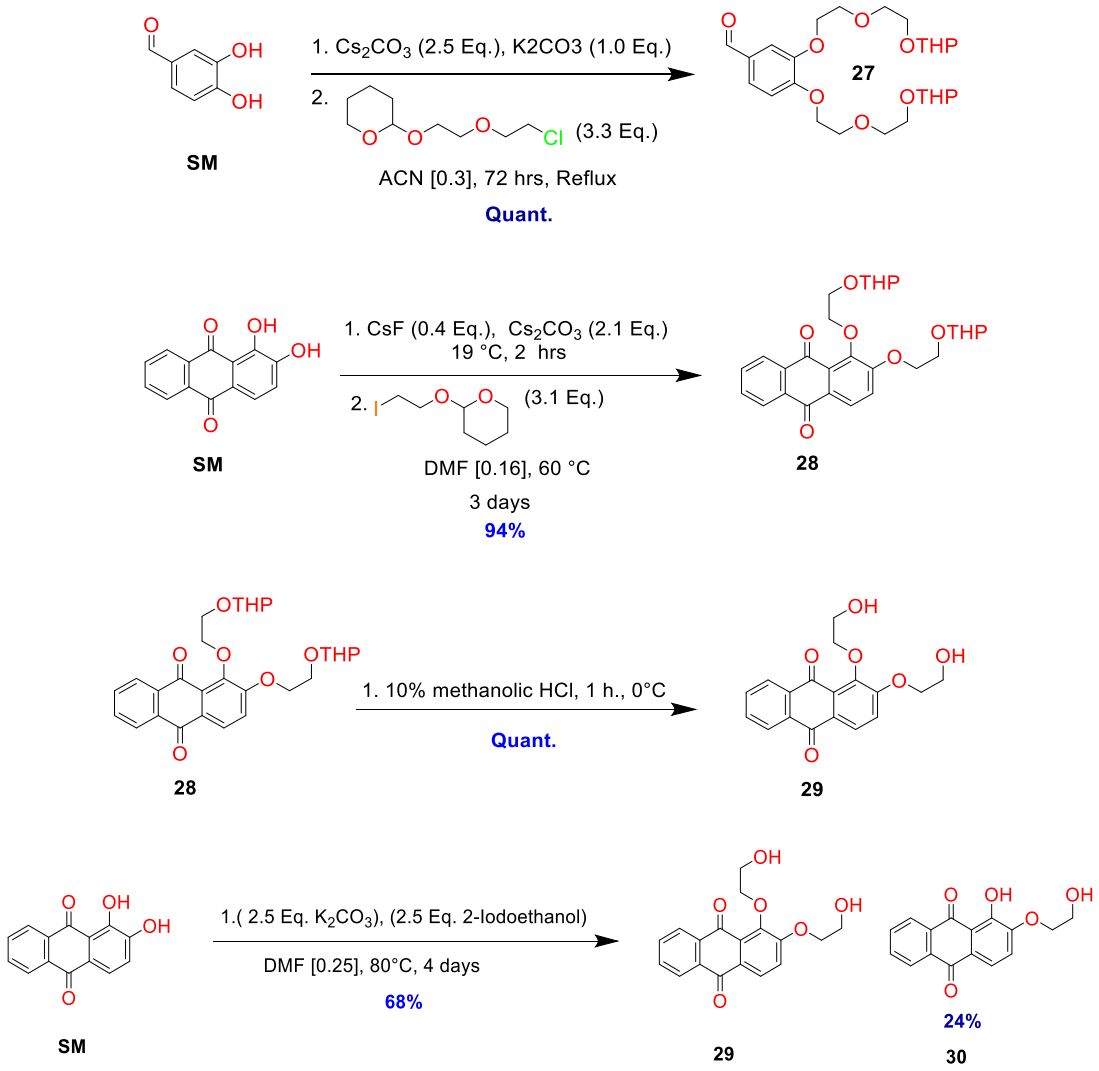

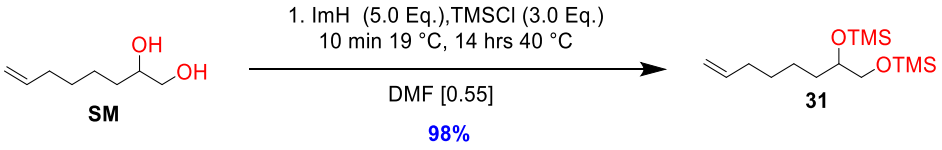
1. ImH (5.0 Eq.),TMSCl (3.0 Eq.)
10 min 19 °C, 14 hrs 40 °C
DMF [0.55]
98%
OH
OH
SM
OTMS
OTMS
31

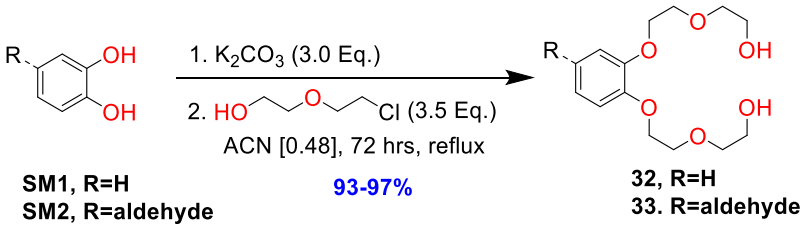
R
OH
OH
1. K2CO3 (3.0 Eq.)
2. HO
Cl (3.5 Eq.)
ACN [0.48], 72 hrs, reflux
93-97%
SM1, R=H
SM2, R=aldehyde
32, R=H
33. R=aldehyde

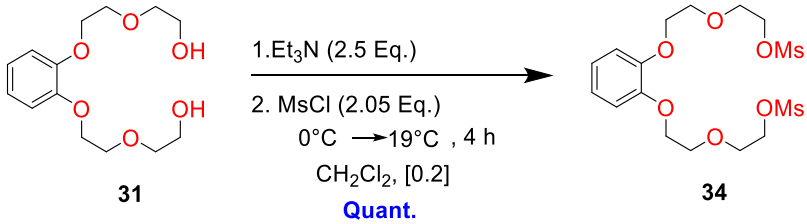
OH
OH
1.Et3N (2.5 Eq.)
2. MsCl (2.05 Eq.)
0°C 19°C , 4 h
CH2Cl2, [0.2]
Quant.
OMs
OMs
31
34

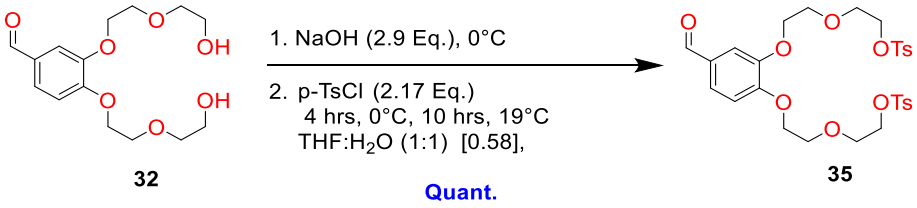
O
OH
OH
1. NaOH (2.9 Eq.), 0°C
2. p-TsCl (2.17 Eq.)
4 hrs, 0°C, 10 hrs, 19°C
THF:H2O (1:1) [0.58],
Quant.
OTs
OTs
32
35

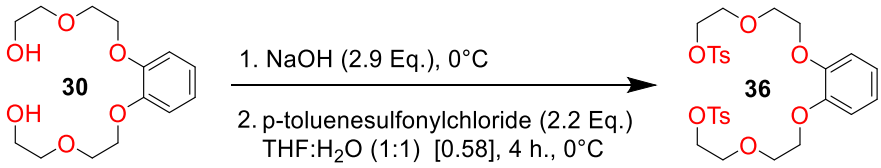
OH
OH
30
1. NaOH (2.9 Eq.), 0°C
2. p-toluenesulfonylchloride (2.2 Eq.)
THF:H2O (1:1) [0.58], 4 h., 0°C
98%
OTs
OTs
36

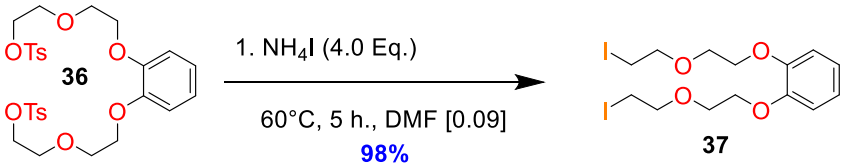
OTs
OTs
36
1. NH4I (4.0 Eq.)
60°C, 5 h., DMF [0.09]
98%
I
I
37

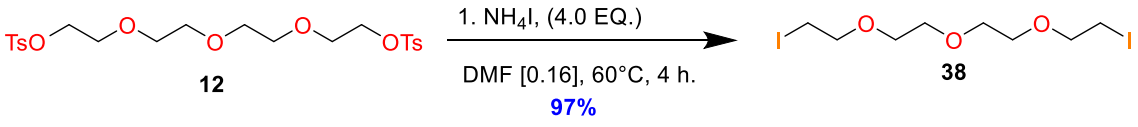
TsO
OTs
12
1. NH4I, (4.0 EQ.)
DMF [0.16], 60°C, 4 h.
97%
I
I
38

In figure **3.24**, the overall strategy was to first convert the prepared diols into their respective tosylated glycols, followed by conversion to the iodide as iodide is known to be a better leaving group in SN2 reactions we would be conducting. In addition, extension of the anthraquinone 1 and 2 positions eliminated the weak, resonance stabilized phenoxide at the 1 position due to electron withdrawing effects.

Figure 3.25 – Two different synthetic routes to access the extended diol **41**.

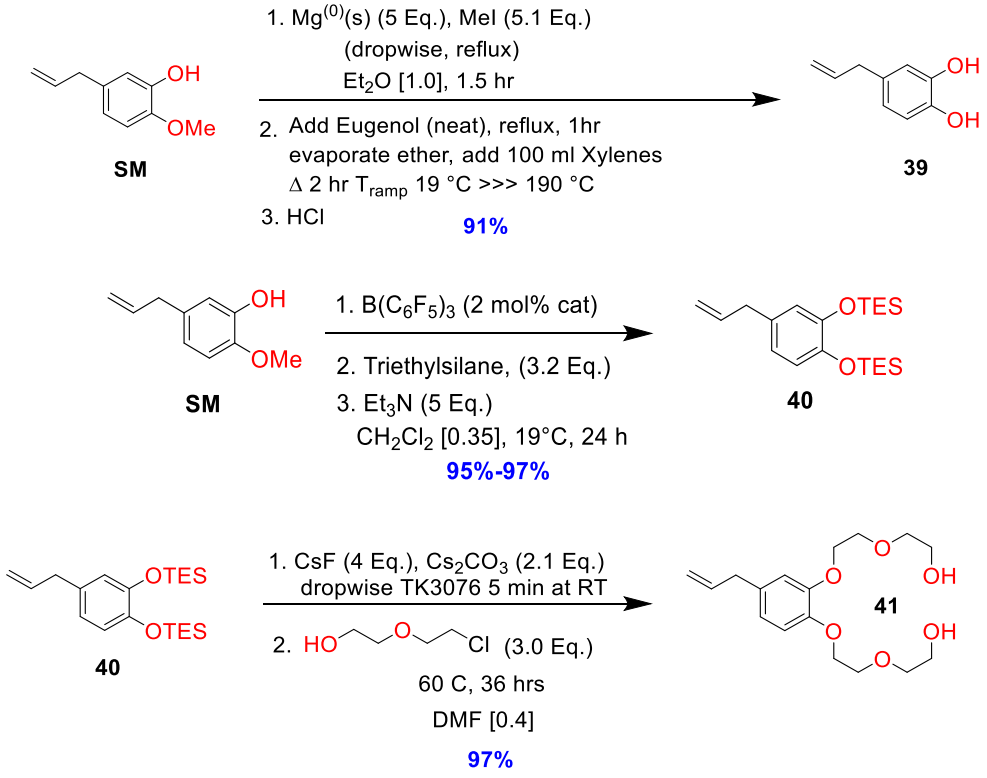

After a successful but overly complicated reaction to elicit demethylation of the methoxy-group (fig **3.25**) of the molecule Eugenol to yield a clear oil, the compound quickly turned black and much of the material (about 40 % by NMR) degraded under Ar (g), even when caution was taken, with the compound being stored in a dark -20 °C freezer. Taking this into account with the complexity and safety of a neat MeMgI demethylation at elevated

temperatures, the bis-TES-protected form of Eugenol, which was derived from catalytic demethylation/hydrosilyation using $B(C_6F_5)_3$ in dichloromethane using the methods in the table shown in figure 3.26 below

Figure 3.26 - Table of strategies employed in the one-step double deprotection/alkylation of TES ether of Eugenol provided by Taigon Kang, Hawker Group.

Substrate	Deprotection Reagent/catalyst	Base	Time (hr.)	Temperature (°C)	Yield (%)
TK3076 100 mg	KF(2.2 Eq.) 18-C-6 (2.2 Eq.)	N/A	72 h	60	N/A
TK3076 100 mg	TBAF (2.2 Eq.)	N/A	44 h	19, 14 hr. 60, 24 hr.	N/A
TK3076 100 mg	KF on Alumina 5.5 mmoL F-/g (2.2 Eq.)	N/A	42	60	75/25 ratio of dialkylated to monoalkylated, **50%** isolated
TK3076 100 mg	CsF (5.0 Eq.)	N/A	28	80	N/A
TK3076 100 mg	CsF (8.0 Eq.)	N/A	48	80	N/A
TK3076 100 mg	CsF (4.0 Eq.)	Cs2CO3 (2.1 Eq.)	36 h	60	**91%**
TK3076 5.0g scale	CsF (4.0 Eq.)	Cs2CO3 (2.1 Eq/)	36 hr	60	**97%**

***For each run, the alkylating agent was freshly distilled 2-(2-chloroethoxy)ethanol (from Drierite/3 A mol sieves). The number of equivalents were held constant at (3.0 Eq.)/run.**

Figure 3.27 - Synthesis of AQ-18-C-6 from 1,2-dihydroxyanthraquinone and catechol-extended

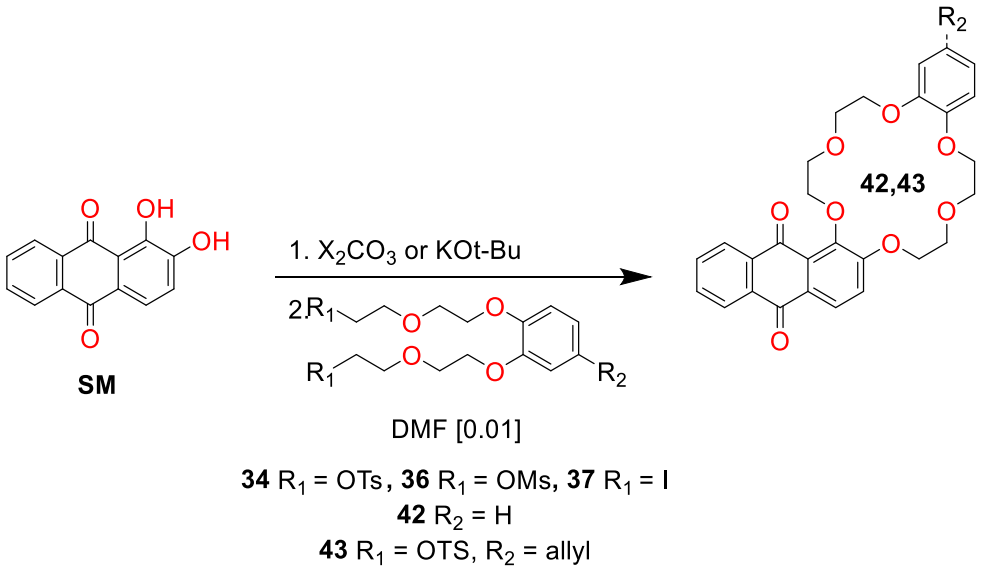

Figure 3.28 – Table of the yields obtained by cyclization using different leaving groups while varying the base used and the templateting cation.

Substrate	***R Group R2 group***	***Base***	***Time (hr.)***	***Temperature (°C)***	***Yield (%)***
Alizarin(1,2-dihydroxy-9,10-anthracene dione)	R= OTs R2=H	KOt-Bu	72	120, 72 h	11
Alizarin	R = OTs R2=H	Cs2CO3	72	40, 24 h 80, 48 h	2.1
Alizarin	R = OMs R2 = H	Cs2CO3	72	80, 72 h	3.0
Alizarin	R = I (small scale) R2 = H	Cs2CO3	72	80, 72 h	33
Alizarin	R = I R2 = H	Cs2CO3	48	80, 48 h	46
Alizarin	R = OTS R2 = allyl	K2CO3	36 hr.	40, 24 hr 60, 12 hr	72

Figure 3.29 – 2-step homogenous synthesis of the mono-ethoxy silanes from intermediate acid chloride

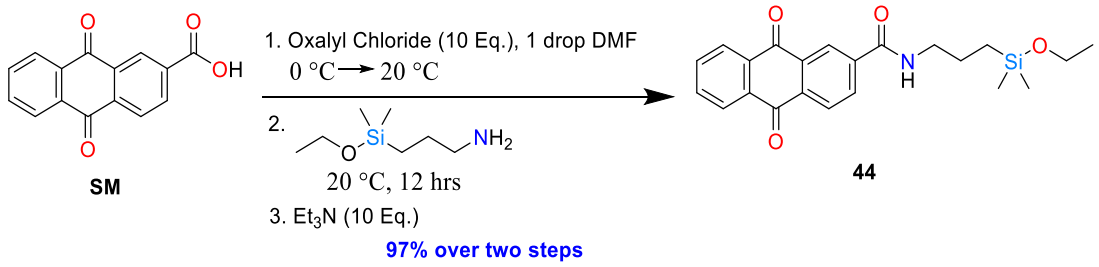

Figure 3.30 - Synthetic scheme for regio and chemo-selective alkylation of diphenolic anthraquinones followed by novel Claisen Rearrangement to form the 2 and 3 substituted allylated quinones. The scheme with yield highlighted in red is currently the only published method for rearrangements of these types of molecules.

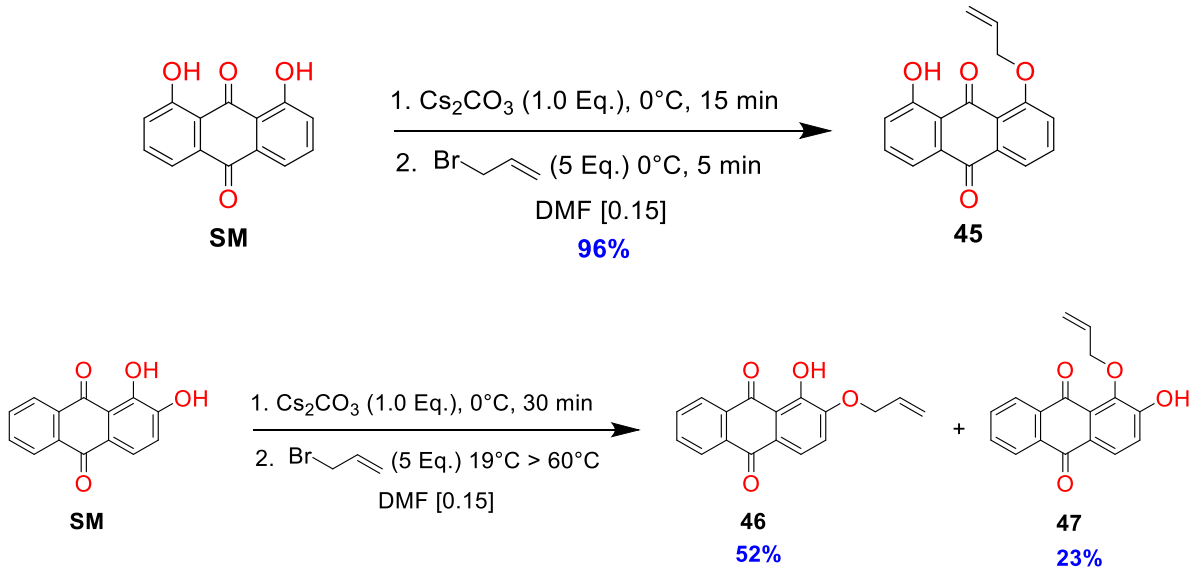

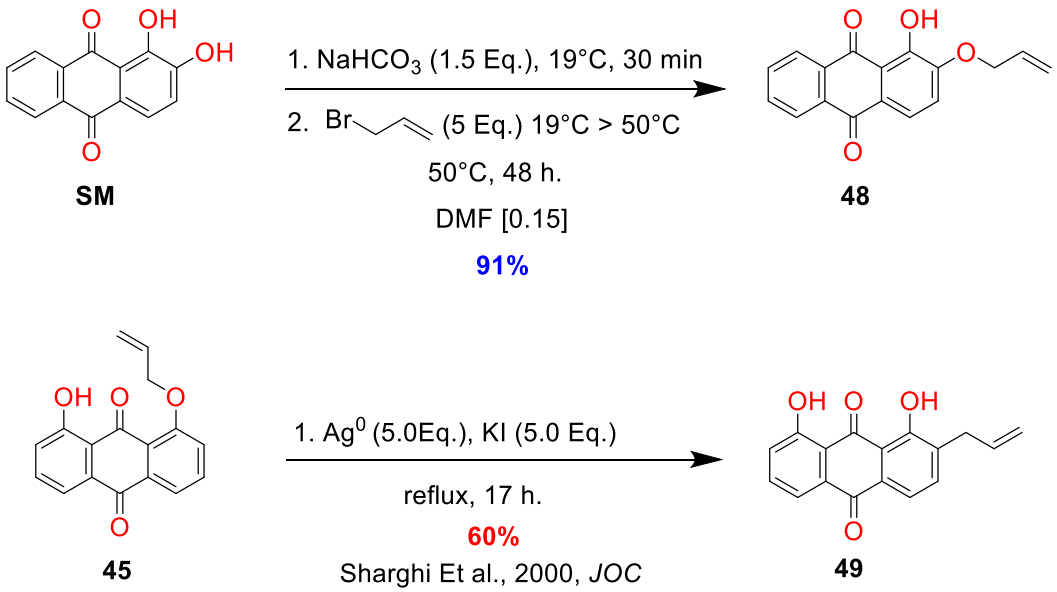

Figure 3.31 – Claisen Rearrangement of the 1-allyloxy-8-hydroxyanthraquinone and **Figure 3.32**– Claisen of the corresponding 3-allyoxy-1-hydroxyanthraquinone.

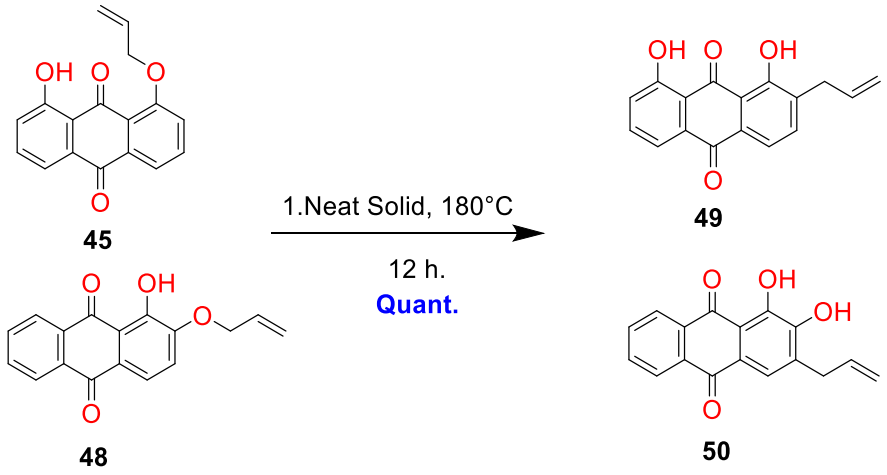

Figure 3.32 – Synthesis of quinone monomers from p-methoxyphenol for hydrosilyation studies with sTO-PDHMS/PDMS-OTs end-blocker

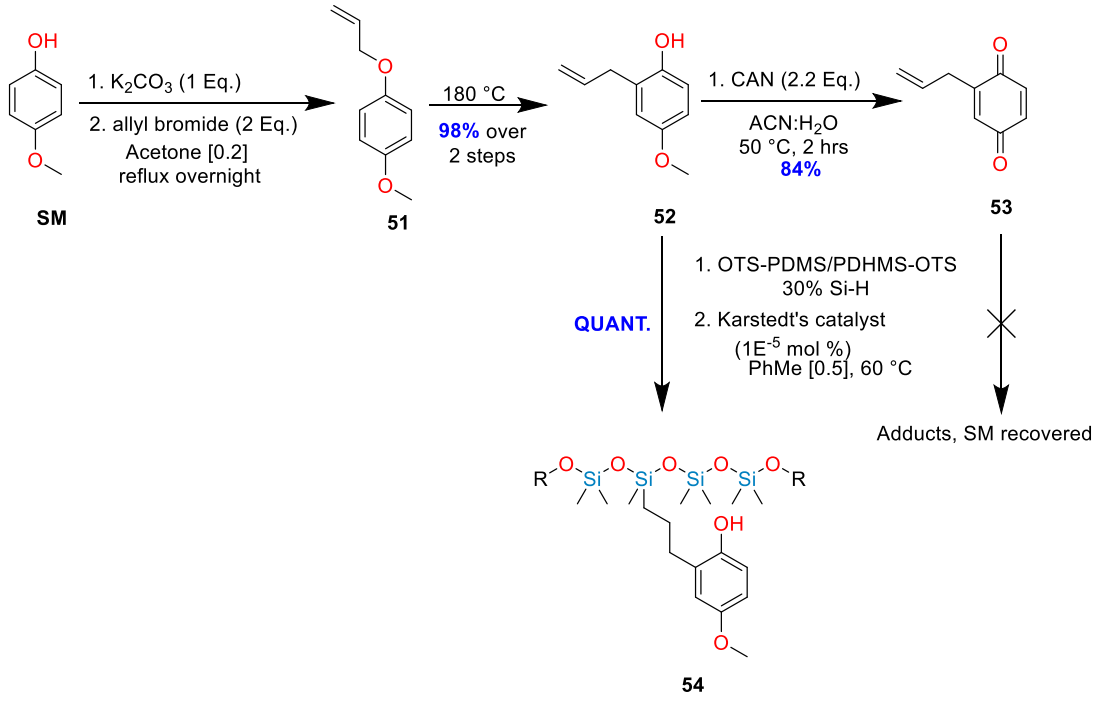

Claisen Rearrangement

The Claisen rearrangement is a convenient method for the introduction of terminal alkenyl subunits for further functionalization including epoxidation, cleavage by $OsO_4/NaIO_4$ to the aldehyde and hydrosilylation as well as many coupling reactions such as the Heck, Grubbs. Most often the Claisen rearrangement of allyloxy-phenolic ethers is carried out under Lewis acidic catalysis with a AcOH/Ag+ and in the case of liquid compounds the rearrangement is carried out thermally under solvent-free conditions. To the best of our knowledge, quantitative, regioselective Claisen rearrangements of high M.P. anthraquinone derivatives has yet to be reported. We herein report the facile rearrangement

of solid allyoxyanthraquinones in the melt in sealed vials to give the ortho-directed propenel group in excellent to quantitative yield as a new solid derivative.

A variety of mono and dihydroxy anthraquinones underwent smooth regioselective allylation presumably due to their phenolic pKa differences and chelation-effect of the carbonyl-oxygen. The resulting mono-allylated derivatives underwent a smooth rearrangement to form the corresponding ortho-substituted dihydroxyanthraquinone derivatives.

Upon heating in the melt under an inert atmosphere, solid allyloxyanthraquione derivatives underwent a facile, quantitative and regioselective thermally induced 1-3,-ClaisenRearrangement yielding terminal substituted alkenel functional handles that has proven can further be carried on to derivatives such as phenaldehydes, phenol acetic-acids and precursors to doxorubicin-type drugs. This two-step green process flow hinges on the selective monoalkylations of di-phenolic anthracenediones utilizing group I alkali metal carbonates to give what is usually always a bright orange, low melting point solid. The second stage takes place with no reactants at all, just the solid monoallylether in the case of the anthraquinones, and neat oils in the case of the allyloxy-substituted benzenes.

Figure 3.33 – Synthesis of higher-order architectures using a protection strategy

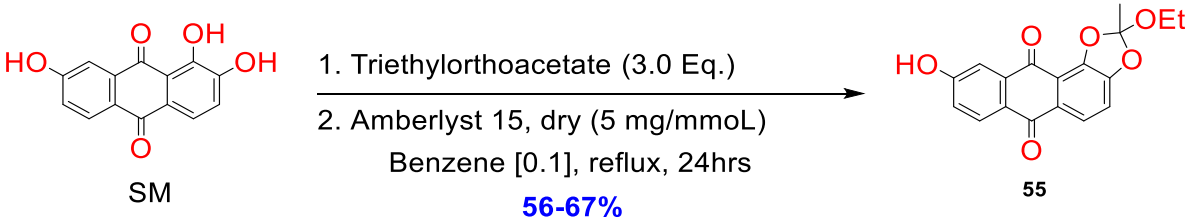

Figure 3.34 – Synthesis of macrocyclic ester **60** from the starting diol by alkylation, reduction and conversion to the acid chloride followed by reaction of the 1, 2-ethoxyethanol extended alizarin with bis-acid chloride **59**.

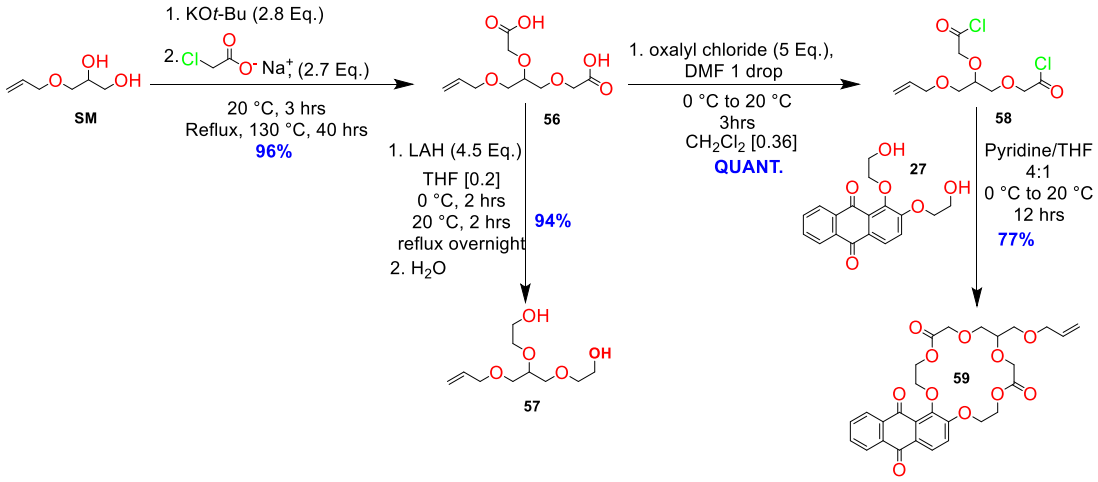

Alumina/ silicon dioxide/ silicon nitride functionalization

There are two general methods for covalent attachment of organic functionality to inorganic substrates:

1. Heterogeneous – Molecules of different reactivity (electrophilic or nucleophilic) are first deposited covalently to the substrate, followed by secondary reaction with the appropriate polar opposite coupling partner. This method takes two separate functionalization reactions to complete but often yields a higher density of functionality due to increase in surface precursor groups.

2. Homogenous- The molecule is first synthesized entirely with the attachment functionality in place then attached to the inorganic functionality. These molecules are often sterically cumbersome and attachment efficiency is adversely affected (Park, 2011).

In the approach this author took, both methods were used, in line for a reductive amination by a primary amine on the benzaldehyde of the glycol derivative. In this manner, the nanopore would first be functionalized with short-chain amino groups that have high mobility in the molecular vapor deposition process (MVD), ensuring complete coating per nm^2. These functionalized pores are then reacted with aldehyde to form the Schiff base and finally reduced with sodium borohydride in methanol to form the secondary amines.

In the second scheme shown in figure **3.36**, the entire molecule is synthesized such as the dimethyl ethoxy silane derivative from hydrosilyation of an olefin as shown in figure **3.35** and then reacted in just one step with a suggested lower grafting density versus the latter method due to steric crowding (Bronson, 2005).

Figure 3.35 – Generally accepted mechanism of trichloro and trimethoxy silanes in wet organic solvents/H_2O. First, hydrolysis by H_2O affords the silanols followed by condensation/in-plane reticulation with the inorganic silanols with accompanying loss of H_2O.

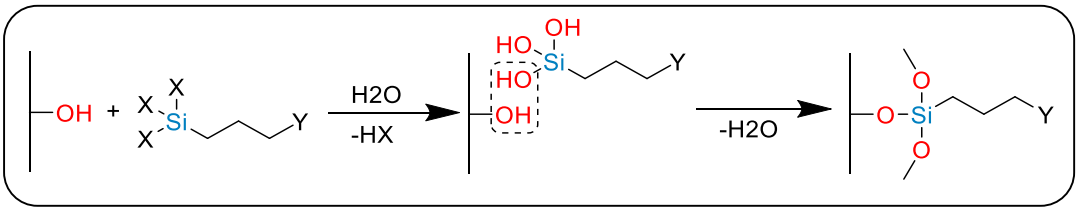

Figures 3.36 – SN2-type reaction with liberation of EtOH (g) in refluxing Toluene

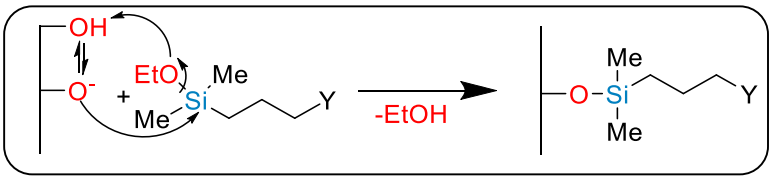

As first pointed out by Brzoska Et al. the accepted mechanism is shown in figure **3.35** above whereas the author proposes an SN2-type mechanism figure (**3.36**) for the attachment of mono-functional ethoxy silanes at elevated temperatures (Brzoska, 1994). The proposed mechanism is based on the relative pKa of the silanol group in aqueous solution of 13.6 for triethylsilanol versus 19 for tert-butyl alcohol (Lickess, 1995).

Monofunctional silanes have become more prominent in industry and academia (Bronson, 2005) due to their favorable tendencies to form monolayers of high grafting density exclusively. Replacement of two oxo-groups or two halides with hydrophobic methyl groups also prevents hydrolysis of the silane functionality at elevated temperatures and in buffer solutions making them more suitable for use in devices where device failure is not an option.

Figure 3.37 – Polymeric network of nucleophilic primary amines sometimes encountered during varying methods of APDMS deposition

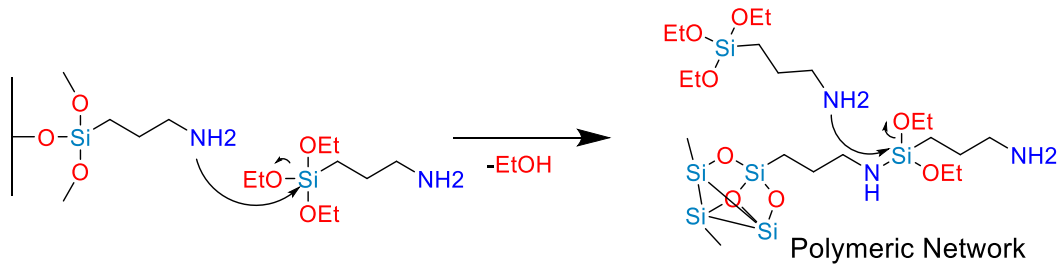

Hydrophilic groups near the inorganic/organic interface have proven susceptible to hydrolysis. (Dekeyser, C M) grafted tri-functional PEG chains of 6-9 ethylene oxide units on SiO_2 and found that complete hydrolysis of the chains in PBS buffer at 37 °C had indeed occurred. In lieu of this, the dimethylethoxysilane series, although much less reactive confers the advantage in that two hydrophilic groups at the interface are replaced with two hydrophobic methyl groups. In effect, this prevents water from penetrating the lattice, preventing unwanted hydrolysis and making for a more durable monolayer coating.

The one disadvantage to using this molecule is the ease of attachment. Monoethoxysilanes are very stable and do not hydrolyze in water. Thus the mechanism proposed by (Brzoska, 1994) may not be operative since hydrolysis of the ethoxy group is unlikely. Several catalysts such as titanium isopropoxide for the attachment are available; however these have the disadvantage of introducing heavy metals during the deposition process which may be difficult to clean or completely abolish prior to the next process step.

Shown in the bottom portion of figure **3.36** is a proposed mechanism by the author where an equilibrium exists between the alkoxysilanes and silanols. The lower pKa of

silanol protons due to inductive electron withdrawing from the electropositive silicon presents a favorable equilibrium for a one step displacement of the ethoxy group with protonation of ethanol occurring via water or neighboring silanol. The methyl groups are not that bulky compared to other silanes such as TIPS or other heavily branched derivatives and thus an attack by an alkoxysilane at high temperatures is plausible.

To ensure we had a reliable, we needed a surface activation method that was a non-destructive technique that would not interfere with other steps in the process. With the knowledge from previous works and the failure to successful record signals with multiple polymerized molecules on the surface forming networks of sensors nanoporous membranes with charge-feedback type impulse responses, much searching and combing of the literature was conducted and one paper by (Han Et al, 2006) proved to give be the most extensively studied and focused on functionalization in the presence of microelectronics.

A paper published by Han Et al in *Thin Solid Films* shows an excellent study comparing the different activation methods out there and the testing and characterization of each for ensuring a clean, non-degraded surface with the least etching and no activation of any other inorganic substrates. The paper concluded a combination of 50:50 concentrated HCl: Methanol solution produced the cleanest surface, resulted in the highest concentration of reactive surface hydroxyl groups and had the lowest RMS deviation with regard to surface roughening when compared to other popular etchant techniques such as Piranha (a concentrated H_2SO_4/H_2O_2 soln., chromium trioxide/nitric acid, KOH/ etc. The mechanism is unknown but probably has to do with protonation of the silanol groups and elimination of water from surface silanol groups leaving reactive alkoxide ions upon neutralization with pH 7 Water. The treatment is usually conducted at room temperature with freshly prepared

etchant solution for 1 hr. prior to further treatments. The next step is to copiously rinse the quartz with Millipore water and ensure a low contact angle has developed. The wafer is then carefully removed with Plasma-cleaned tweezers (previously rinsed with Millipore water) and dried under a stream of Nitrogen. The wafers are then placed in a Plasma Cleaner air bleed (medium Rf power) 10 minutes, quickly removed, and finally placed directly into the waiting solution of Toluene with the appropriate dissolved silanol under Argon gas. The wafer is stirred under a gentle reflux for 24hrs, removed and quickly rinsed with anhydrous Toluene followed by 100% electronic grade isopropyl alcohol and placed in a wafer holder under an evacuated Argon atmosphere over Drierite and stored until further process steps.

Figure 3.38 – Monoethoxysilanes for DNA intercalation functionalization of single nanopores

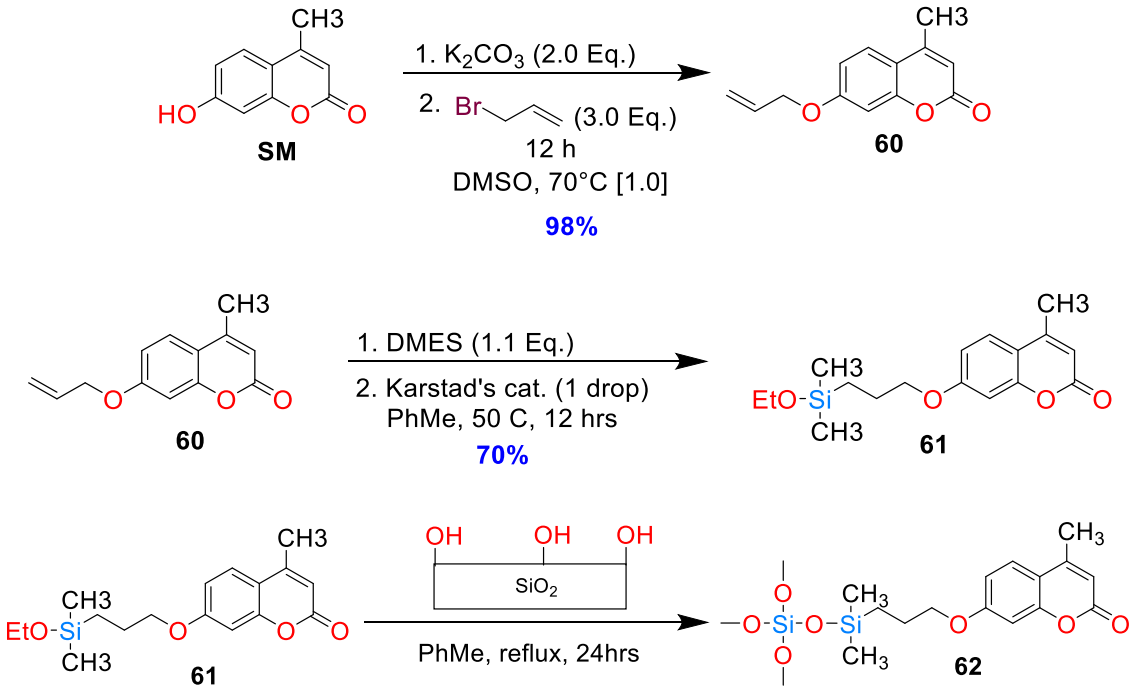

As the XPS clearly shows (Chapter **IV**), the monofunctional silane derivatives are just as the paper reported, giving monolayer results using an activation protocol from one paper and a reaction procedure from another. Since our pores were to be on the order of about 5-10 nanometers in diameter, it was crucial that we design are molecules to stretch that width, or use an ALD back-filling process to shrink the pore size before the functionalization. (The latter results in poor secondary structure of the deposited material and the thickness is less than uniform.) Indeed we had our work cut out for us but were sure of the crown ethers mechanism of action and confident as we explored ways to synthesize tethers long enough to start initial surface-flow experiments with very short tethers such as the propyl spacer of Eugenol derived crown ether **43**.

Surface Functionalization: Practical Considerations

Figure 3.39 – Synthetic scheme to make ion-conductive polymer films out of polyethylene glycol to act as the filler molecule in void space of the nanopores. 2 D case shown below for modeling purposes only.

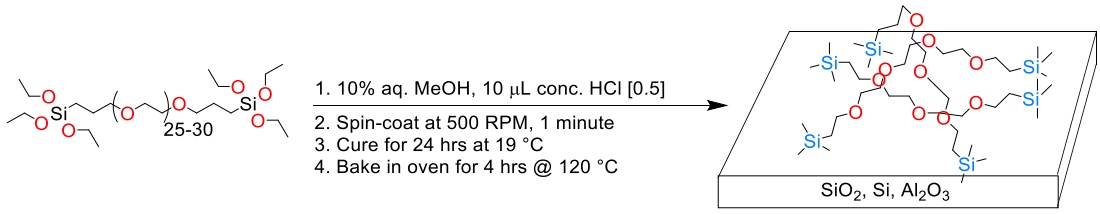

Different functionalization procedures are employed each day to introduce effector molecules to create anti-fouling, microarray, DNA sequencing devices, biosensors and tissue culture (Albert, 2010). One area we are just beginning to understand or perhaps observe is the phenomena of self-assembly and functionalization in the Nano regime of materials

science. Often times in the literature authors claim that functionalization has been carried out successfully due to current differences in nanopores, authors often assume that the substrate has been functionalized and that routine characterization is not needed (Cho, 2008). This is not the case as clogs, unwashed organic functional framework or the possibility of strong electrostatic adhesion are the contributors to the phenomena observed with the particular device.

Asperities in the surface result in reorientation of the electric field lines, guiding them around their normal direction perpendicular to the plane of the plates. This condition poses a few problems; first, the carrier mobility μ, is reduced for single asperities. This effectively means the electron must travel farther, reducing the magnitude of the E_{field} and lowering v_F. Periodic, closely spaced asperities can produce profound problems as well as far as the device life is concerned (figure **3.40**). While the E_{field} lines become regular again around periodically spaced asperities, local field enhancements contrary to the latter are predominant due to the fact that the electron has to travel less distance. This can lead to short circuits and overcurrent that can be damaging or catastrophic to device performance. Nanoscale parallel plate capacitors behave differently due to the fact that electrostatic potentials experienced by electrons are determined by both the number and location of all the electrons that contribute charge effects in the device. The dimensionality and length scale of our particular case make the number of electrons present much smaller with hard to predict equipotential surfaces due to the complex topology of the electrode plates.

Figure 3.40 – Normal Efield lines run perpendicular to the plane of the electrodes with the field traveling from the cathode to anode. (Left) A single roughness defect disturbs the Efield lines whereas (right) multiple, closely spaced defects

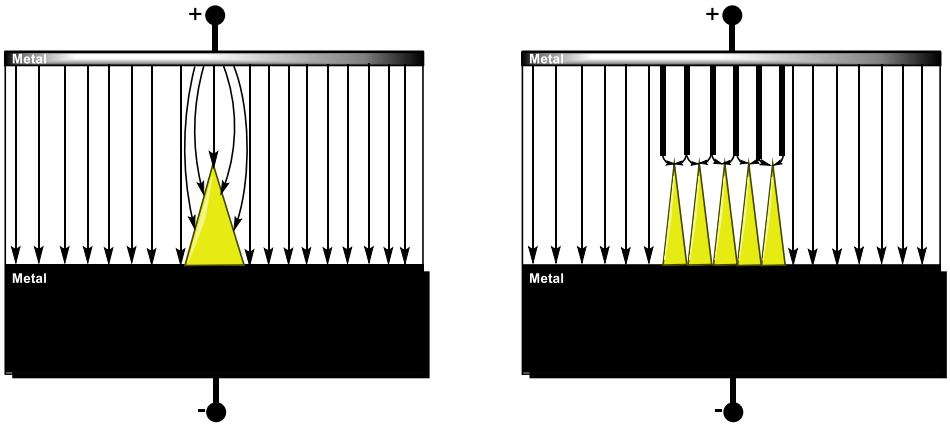

Selection of a linker Group

To effectively couple our synthesized receptors in the preceding schemes to nanopore domains in a monolayer formation it was essential that we choose a monofunctional silane to avoid polymerization of covalently grafted silanes (Han, 1996) (Albert, 2010), in this case dimethylethoxysilane (DMES) was chosen as the reactive linker group (Graf, 2008). Several papers in the literature were examined for activation of the substrate and for all intents and purposes, we choose a combination of HCl/MeOH (50:50 v/v) at room temperature for 1 hour as our surface activation step (Han, 2006), (Davis, 1996), (Walschus, 2005). This would provide the least amount of etching, increase in root mean squared roughness increase, surface loss and leave the native surface activated with the highest density of silanol groups (Trevisiol, 2003). For ease of characterization, the silanization was performed on a 10mmX10mm quartz chip as a model reaction. The substrates would later be

characterized by X-Ray photoelectron spectroscopy (XPS) and analyzed for their atomic composition using Eq. **3.19**:

$$[A]\text{Atomic \%} = \{[IA/Fa]/ \sum(I/F) \text{ X } 100\% \quad \textbf{3.19}$$

The second method of functionalization following the method (Dorvel, 2010) was molecular vapor-phase deposition of a precursor molecules DMPES-Isocyanate(IDMPS)/ DMPES-Amino-propyl (APDMS) silane which are both volatile due to their low molecular weight were functionalized onto the same quartz chips used in the solution deposition. This type of functionalization process was completed based on the assumption that vapor phase deposition effectively enhance diffusion of the feed substrate into the middle of the nanopore due to the molecules increased mobility in the gas phase (Vasille, 2013). Gases have the highest diffusion coefficients of all states of matter due to unrestricted movement through such a low viscosity medium.

To cover each aspect and unanticipated problem a reactive electrophile or nucleophile would have to be incorporated into the synthesis to react with these specific groups, specifically an aldehyde as the electrophile for APDMS and an alcohol for IDMPS. In this manner, better nucleophiles are more likely to react with the non-volatile crown 1 in solution (Dorvel). Since these linker molecules are very short, they do not decrease the circumference of the pore significantly, assuming the formation of a monolayer.

Many catalysts are available today commercially for the hydrosilyation of olefins including many electrophilic boron complexes, platinum and ruthenium complexes

stabilized with different ligand substitution (Chung, 2007), (Evans,2007), (Lewis, 1997), (Stein, 1991).

Auxiliary Materials

Gel Matrices for filler matrix material and Thin Films

Matrices constructed using the sol-gel, hydrogel or block copolymer architectures form the basis of selectivity in some instances by excluding some ionic species by size, shape, hydrophobicity, charge and redox properties (Hu, 2014), (Ghosh, 2005). Complete changes in conventional behavior of neutral 15-C-5 native binder for Na^+ between sol-gel and mesoporous silica's was attributed to the formation of the high-affinity bis-15-C-5 complex with K^+ in the sol-gel preparation due presumably due to aggregation where the crowns are in close proximity (Yajima, 2010).

Figure 3.41- Structures of the covalent network polymers used to make the filler matrices for deposition after crown monomer deposition.

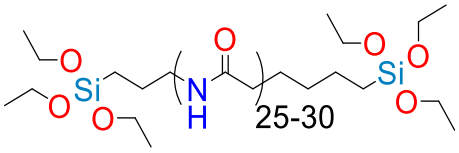

Triethoxysilanepolyamide - Polyamide TES-PEA

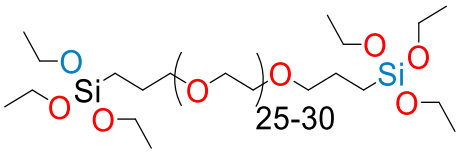

Triethoxysilane polyethylene glycol – TES-PEG

Figure 3.42 – Structures of base material and plasticizer to form novel cross-linked networks by radical polymerization by light or radical generators

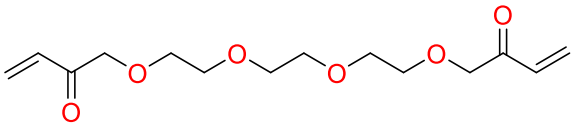

Tetraethyleneglycoldiacrylate (TEGDA) Base

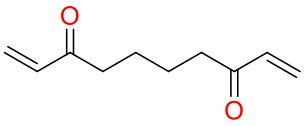

Hexane Diacrylate (HD) Plasticizer

Figure 3.43 – Novel plasticizer synthesis by Fisher esterification/alkylation

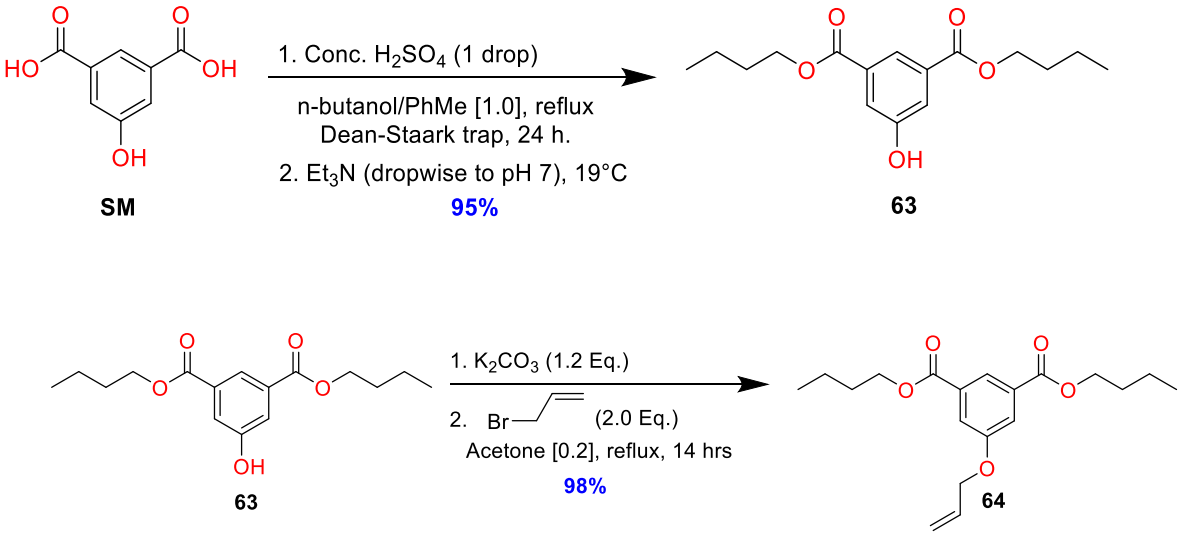

Bis(triethoxypropyl)-polyethylene oxide (25-30 EO units) was used as is from Gel-Est Inc. As the polymer strands are dispersed anywhere between 25 and 30 ethylene oxide units apart, we developed this material hoping to have a favorable result with this material serving as an insulator comprising the gate portion in the nanoporous matrix. The functionalization of crown monomers would be carried out first, followed by deposition and curing of this filler material.

Figure 3.44 – Table of spin-coat results on fabricated alumina membranes

Formulation	Base Material/ Substrate	Plasticizer	Initiator	Resulting cured thickness (Dektak prof)	*Swollen Thickness 1M KCl	Physical Characteristics
A	TES-polyamide @ 5K	None	conc. HCl	450 nm	450 nm	Solid, Rigged Glass
B	TES- PEG @ 5K	None	conc. HCl	150 nm	320 nm	Flexible, foggy glass
C	TEGD -99.5% @ 5K	0%	**BP0.5 %	70 nm	140 nm	Flexible glass
D	TEGD -99.5% @ 3K	0%	BP 0.5%	280-335 nm	720-800nm	Flexible glass
E	TEGD - 70% - @ 5K	29.5%	BP 0.5%	250 nm	350 nm	Gel Matrix-semi-solid
F	TEGD – 60% - @ 5K	39.5%	BP 0.5%	270 nm	340 nm	Unstable gel-like matrix
G	TEGD – 50% - @ 5K	49.5%	BP 0.5%	50-200 nm	≈220 nm	Spotty film with islands
H	TEGD – 50% - @ 3K	49.5%	BP 0.5%	750 nm	1.1 μm	Deformable semi-solid
I	TEGD – 40% 5K	59.5%	BP 0.5%	50-100 nm	***N/T	Discontinuous film with islands
J	TEGD – 40% 3K	59.5%	BP 0.5%	170 nm	220-250 nm	Poorly defined semi solid

***2 h. submersion test in 0.005 M standardized KCl**
**** (BP) benzoyl peroxide**
**** (N/T) not tested**

The prediction was that some of the bi-functional polymer ends would attach covalently to any remaining hydroxyl silanols after the functionalization or cross linking on each other

after undergoing hydrolysis. This would create a rather open network that may be able to incorporate small amounts of water to form water channels that may aid in the transport. To form the filler material, instead of using a strong acid we decided to use a sulfonium photo acid generator which would provide a catalytic amount of H^+ cation to hydrolyze the ethoxy end groups (Babu, 2014). Upon exposure to UV light with 2% photo acid generator, a clear glass like polymer formed which was soft in nature. Upon exposure to water, some swelling was observed (about 2X after 1 hr. submersion test), returning to V_{int} after 3 h. at 19°C but no detachment from the control slide (spotted material on glass slide and cured with UV light) was observed leading us to conclude the formation of a durable, organic network of PEO units that could undergo rapid swelling and de-swelling kinetics and aid in cation hoping and transfer from the monomeric crown ethers spanning the nanopore by the incorporation of water (Song, 2006), (Clavier, 1998).

Organic Siloxane Polymers as neutral pH cation exchange membranes

While originally synthesized for DNA sequencing, PDMS/anthraquinone copolymer derived from the Claisen rearrangement of di-hydroxyanthraquinones, a liquid siloxane B block was hydrosilyated with allylated, solid anthraquinone under $Pt^{(0)}$ catalysis to yield a bright red colored solid gel (**64**) with a gel transition temperature of 40 °C via DSC (data not shown) (Lewis, 1997); (Dae-won, 2007); (Bronson, 2005); (Evans, 2007).

.

Figure 3.45 - PDMS/anthraquinone copolymer terminated with R=Tosyl

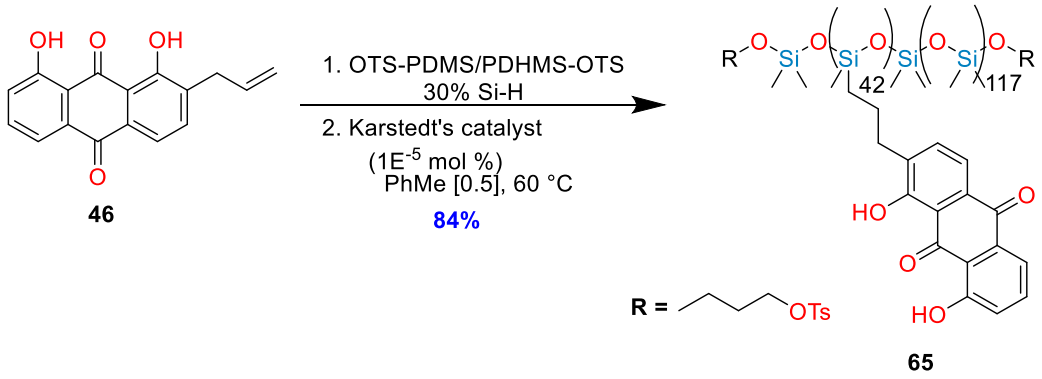

We choose to synthesize this material (fig **3.44**) with the knowledge that one of the two quinone hydrogen's had a pKa of around 7 and would help to maintain charge neutrality in our electrochemical cell, pumping one H^+ out as each K^+ crossed the membrane. Anthraquinones have been reported to be excellent gelators due to their amphiphilic properties (Babu, 2014).

Our original method although not as viable as the former was to spin coat or dip our electrodes to be placed on either side of the nanoporous membrane in an ionically conducting matrix of $PEDOT^0$:PSS^-. As the spin coating method proved to be only somewhat reproducible after many different trials and formulations, we opted for the dip method to encapsulate our electrodes followed by curing in an oven at 120°C for 4 h. to rid of any water. (See experimental for further details)

The only issue we ran into here was the solubility of PEDOT:PSS in water being very high. Each time we began to conduct electrochemical testing on the assembled membrane, we ran into trouble with a constantly diffusing bluish substance (PEDOT:PSS) contaminating the device electrolytes being used in the experiment.

Anodization of Aluminum to form Al_2O_3 nanoporous layer

Production of nanoporous membranes with SiO2 proved to be very time consuming and costly and was effective for producing small quantities of single nanopores that would ultimately be used in the transport studies (described later in Chapter 5), thus the process team (Sam Beach and myself) decided it was best to produce anodized aluminum to form dense arrays of nanopores rather than trying to study transport though a single pore (Wu, 2004, *Nano Lett.)*.

Figure 3.46 – Setup used for the anodization process described below

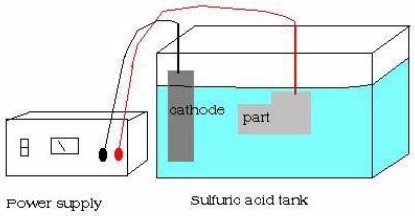

Microfabrication

Microfabrication is crucial to the miniaturization and integration of the proposed concepts. There are two facets, one of which was investigated in this thesis, addressed by microfabrication: 1) the fabrication of the electrochemical synapse. 2) The co-integration of the CMOS electronics with the electrochemical synapse. The electrochemical synapse fabrication begins with the deposition of aluminum metal on Si(s) substrate followed by anodization of aluminum to alumina to form dense arrays of nanopores (Sun, 2002), (Wolfrum, 2002), (Sulka, 2009).

The backside of the anodized pore array are opened to expose a trapezoidal window approximately 100 μm X 100 μm is exposed exposing the pores on the array. The array is then functionalized by solution deposition of custom synthesized (Chapter **III**) crown ether monoethoxysilanes under reduced pressure to make sure all the voids in the membrane contact the reaction solution. After sonication of the dye (Chip) in Toluene followed by Methanol, a single layer of monomeric quinone crown ethers are hypothesized to traverse and adsorb to the pore walls, spanning the entire pore length.

In the case that this method does not produce the intended outcome, MVD will be used instead since the reaction mechanism relies on the number of reactive entities colliding per unit time per surface area otherwise known as random diffusion. If organic substance has a low enough M.W. and is relatively volatile, the MVD technique of deposition will undoubtedly lead to the highest density of grafted silanes with gaseous molecules having the highest diffusion coefficient of all states of matter. After this step is verified by XPS and preliminary electrochemical data, the next step is to add the filler matrix material for the windows and pores in the form of the PEO-hydrogel, cross-linked with cat concentrated HCl. For the formation of a non-corrosive, durable and wear resistant dielectric layer comprising our nanoporous membrane, the method of using 6% H_2SO_4 as our electrolyte, a working voltage of 10 V and a passing current of 100 mA an anodizing down the top 2 nm.

Alumina was deposited layer by E-beam evaporation of aluminum onto SiO_2 oxide gate atop Si lead to the smallest (5-15nm) pores and gave the highest concentration of pores/SA. This method also proved to produce the most brittle porous membranes when back side release was conducted utilizing phosphoric acid to etch away the remaining unreacted alumina and open the pores (Platschek, 2011).

This was quite a successful process but produced pores that were not very ordered and were quite gyroidal in there orientation. To hydrate the alumina to increase the structural integrity of the membrane and provide surface hydroxyl groups to react with our organic functionality, the membranes underwent a sealing process where they were placed in a beaker of gently boiling deionized water for 1 h.

These membranes were produced on a wafer scale for further processing, attachment of organic functionality, synthesizing electrodes form organic ion-conducting matrices.

Specifically, we were looking for any type of asymmetry in the C/V scans as we ran the current biphasically through the solution. We then wanted to examine how this would change when loading what we planned to use as our filler gel material upon crosslinking and hydration under vacuum to limit/abolish any voids in the nanoporous membranes. C/V curves were recorded with three different salts, NaCl, KCl and $CaCl_2$. Potassium always had the highest current through the membrane between the monovalent cations due to the higher diffusion coefficient of K^+ vs. Na^+ in water; and as expected twice the current of potassium was observed for the $Ca2^+$

While the synthesis of the crown ether with the extended allyl functionality had just been finished; one step separated us from step away from being finished, my time at this University had since expired and synthesis of the crown ether for covalent attachment was handed off respectively to a Post-Doc in our group for the final hydrosilyation of the DMES molecule.

Molecular Vapor Deposition of Small Molecule Precursors

The first organic functionality was introduced by vacuum deposition of APTES at an oven and source temperature (Dorvel, 2010) of 100° C at 30 Torr for a duration of 12 hours as per the method of Dorvel. The chips were mounted upright in a Teflon-coated rack specially designed to hold the exact dimension of the chip. The chamber was evacuated followed by opening of a 3-way T-junction with tubing hooked up to a 10 ml vial being held at 100° C up to a vial containing 1 mL neat APTES. Following the silane evaporation, the junction was closed and the substrates exposed to the silane vapor at 100 ° C and 30 Torr for an additional 12 hrs. The setup was cooled to room temperature and the oven was then purged by cycling with dry nitrogen three times. The substrates were removed and sonicated in toluene for 2 min followed by sonication in methanol for two minutes and finally a deionized water rinse followed by drying via N2 stream and storage in a nitrogen-filled desiccator. Functionalization with 3-cyanopropropyltriethoxysilane was carried out in the same manner and the resultant XPS can be found in the supporting information.

Chapter IV: Characterization of Crown Ether Complexes, Nanoporous Membranes and Polymeric Hydrogels

Objective

Characterization of both the 1,4-benzoquinone-18-C-5 (BQ-18-C-5), 1,4-hydroquinone-18-C-5 as well as the novel anthraquinone crown ether (AQ-18-C-6) synthesized in Chapter III will be presented. Characterization includes methods to elucidate secondary structure, kinetics, Ultra-Violet (UV) absorbance, Nuclear Magnetic Resonance (NMR) characteristic shifts/through-space interaction as well as Mass Spectroscopy (MS). The characterization of the anodized alumina pores follows thereafter.

For first past analysis, ^{1}H NMR shifts of all 1:1 complexes of the crown ethers synthesized in Chapter III were taken after 72 hours to examine any shift changes present at all. Finding the right solvent conditions for an observable NMR, the right salt, and the optimal temperature to acquire the spectra was a challenge. The solvents used ranged from highly polar aprotic (ACN, d6-DMSO, acetone) to solvents with extremely low levels of polarity; mainly the halocarbons $CDCl_3$, CD_2Cl_2, the cyclic ether THF, as well as co-solvent mixtures of THF:CDCl3. The salts utilized in all NMR studies were either sodium triflate Na(OTf), potassium triflate K(OTf) or potassium (4-Cl)-tetraphenylborate K(4-Cl)-TPB. These particular salts were chosen due to their corresponding anion size (small or large). The presence of three ^{19}F nuclei or a single ^{10}B nuclei are both observable in the 1D and 2D dimensions.

Titrations such as the titration of the 9,10-anthraquinone crown with K(4-Cl)TPB initially start out as heterogeneous in pure $CDCl_3$. After a period of about 5-10 m. the salt

mixture was completely homogeneous, solubilizing up to 1.2 equivalents of the guest borate per equivalent of crown. Qualitative physical phenomena along with the quantitative NMR data associated with the resultant mixtures provided the most insight into the secondary structure of the molecule and the role of the two anions used in the study for the case of AQ-18-C-6. Utilizing the method of Job's, plots were constructed to preliminarily deduce complex stoichiometry (Conners, 1987).

Diffusion NMR complements the findings through integration of the 2D plane along the diffusion trace, corresponding to 1:1 and 2:1 HG complexes existing in the NMR solution, as well as solvent-separated anions.

Mass Spectroscopy is used to deduce the absolute stoichiometry of a 1:1 mixture of salt and host crown and the resulting selectivity of the complex for K^+ over Na^+ revealed through competitive ion bombardment experiments.

Upon titration with K(4-Cl)TPB, at several different titration points, photo bleaching of the complex occurs and the optical absorption first drops and then recovers past 1 Eq. of K^+. The spectrum is rationalized as to what causes the loss in absorption. Kinetic trials are also carried out holding the amount of crown constant and varying the concentration of salt to deduce the overall reaction rate law.

Results from the anodization process used to prepare the nanoporous membranes will be examined. The chapter will conclude with the proprietary cross-linked hydrogel materials developed, the results from different PEDOT spin curves, and thin films dispersions.

^{1}H NMR Titration

Contrary to the literature data suggesting that tetraphenylborate salts are soluble in 99.9% $CDCl_3$, it was found empirically that the (4-Cl)TPB salt was completely insoluble in pure $CDCl_3$, soluble to about 2 mM in a 3:1 $CDCl_3$:THF mixture and soluble to 6.66 M in well mixed 2:1 (v/v) $CDCl_3$:$THFd_6$. When this particular salt was mixed with AQ-18-C-6, almost immediate solvation of the salt occurred, presumably due to the superior phase-transfer capabilities of the crown in low dielectric mediums.

Characterization was performed using high-field (600 or 800 MHz) NMR ^{1}H, ^{19}F and ^{10}B NMR studies as well as 2D studies such as COSY, NOESY, DOSY, HSQC and HMBC of the complexes synthesized in the previous chapter. Cross-characterization techniques confirm the existence of the hypothesized 2:1 complex, complementing the data from Job's method of titration, ESI-MS, calculation of the equilibrium constant by mass spec and 2D DOSY.

The ^{1}H NMR titration characterization of molecular complexes occurs under fast (non-observable) or slow exchange (observation of individual peaks). Fast exchange occurs when the signals cannot be resolved on the NMR time scale, distinguishing the new complex peaks and the non-complexed peaks due to rapid equilibrium exchange between the bound and unbound states. This effectively causes the shifts to coalesce at a chemical shift that is the weighted average of the two peaks. Slow exchange most often occurs when the k_D is high, k_{on} high and k_{off} low, making it possible to distinguish individual peaks corresponding to the bound and unbound Host. Complexes in the fast exchange regime at ambient temperatures can enter the slow-exchange regime by cooling the NMR acquisition

temperature to the lowest possible value without freezing the sample. This effectively slows down the thermal motion and contributes to a higher degree of order by lowering the free energy of the system. We present results from our cold-temp 600 MHz NMR experiment later in the chapter.

In conducting a proper titration, it is best to titrate between 0.2 and 0.8 mole fraction of the Host under characterization and avoid titrating the "tails" which can give artificially large ppm shifts making the binding isotherm chaotic and uninterpretable (Fielding, 2000), (Thordarson, 2011). The results from Sugihara's extraction experiments suggested a Log K_a of 3.18 L/mol (1514) for K^+ and 2.39 L/mol (245) for Na^+, with the assumption of 1:1 stoichiometry (Sugihara, 1981).

Figure 4.1 – Chemical structure of the Host/Guest titrated with Na (OTf) with numbering scheme for clarity (refer to Figs **4.2** and **4.3**).

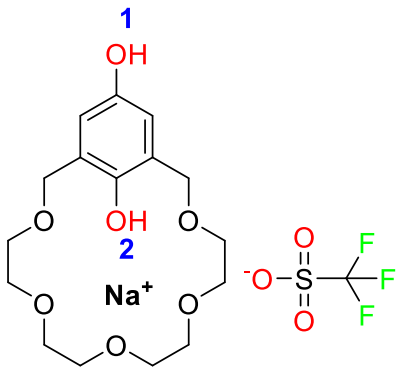

Figures 4.2 (left) -[1]H NMR titration of 1,4-dihydroquinone with Na(OTf) in ACN and

Figure 4.3 (right) – Aromatic phenol proton expansion spectra.

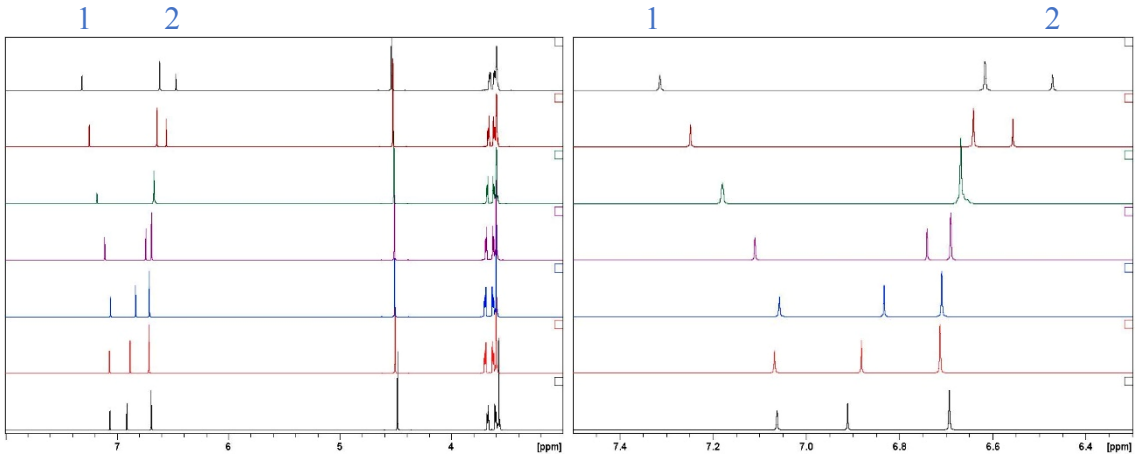

[1]H NMR Titration of HQ-18-C-5

Both the oxidized and reduced forms of the BQ-18-C-5/HQ-18-C-5 were analyzed; first as their 1:1 complexes, with the reduced quinol (HQ-18-C-5) giving the only dynamic response by proton NMR titration. The titration of the HQ-18-C-5 sodium salt of triflic acid is shown in figure **4.1** with the resulting stack plots generated in figure **4.2** and an expanded view of the region of interest in figure **4.3**. Upon first analysis, there is much less of a pronounced chemical shift difference between the aromatic and crown ether protons versus the two phenolic protons. The peripheral phenolic hydroxyl **1** shifts upfield from 7.32 ppm to 7.06 ppm (ΔPPM = -0.26), while the intraannular phenolic proton **2** shows a more pronounced downfield shift from an initial value of 6.48 to 6.92 ppm (ΔPPM +0.44). There is insignificant shift to report of the crown aromatic and ether peaks. (ΔPPM = +0.61).

Figure 4.4 – K^+ (purple sphere) cation sitting above the benzoquinone ring stabilized by its anion; additionally by Π-cation interactions.

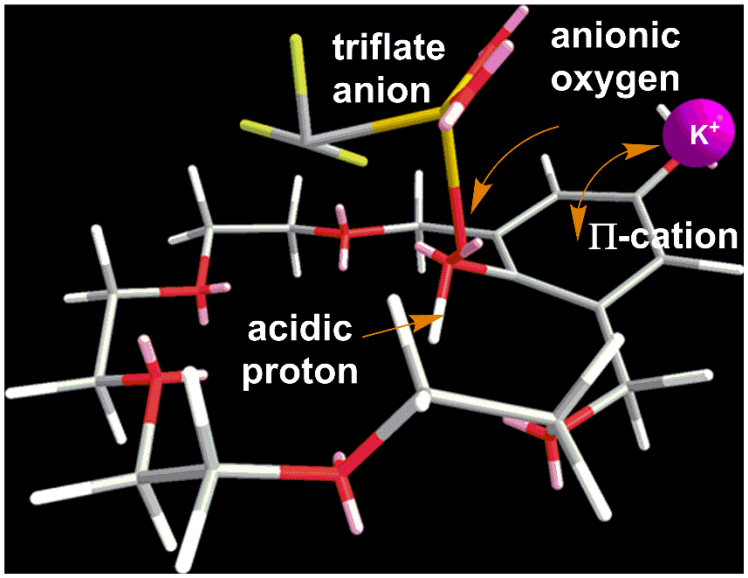

Figure 4.5 – Chemical Strucutre of the Host/Guest complex titrated with K(OTf) with corresponding numbering scheme.

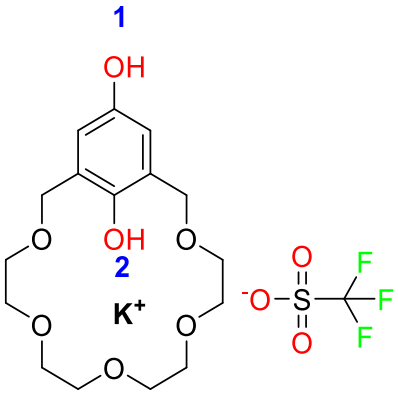

Figures 4.6 -^{1}H NMR titration of 1,4-HQ-18-C-5 with K(OTf) in ACN and **Figure 4.7 –** phenolic proton expansion spectra.

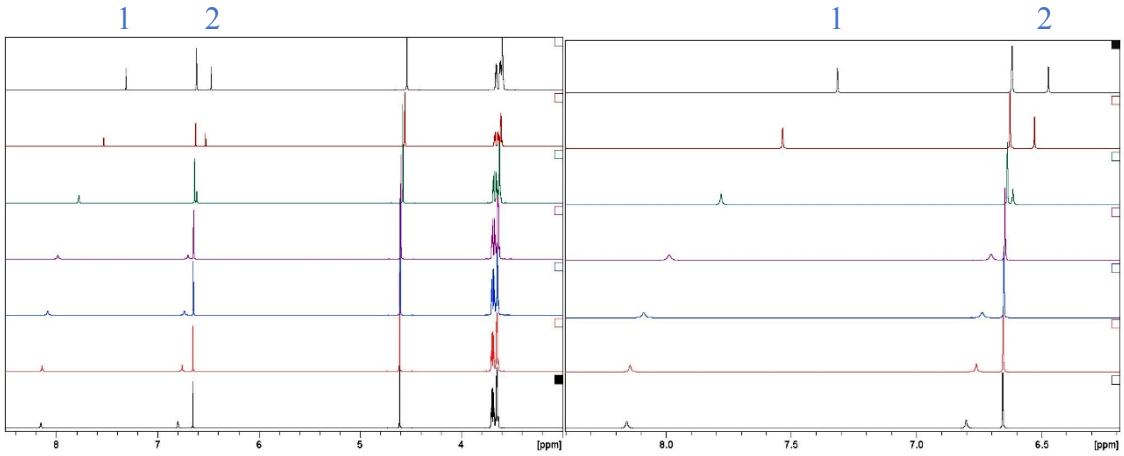

The chemical shifts for K^{+} are opposite in directionality and much larger in magnitude with the peripheral phenol proton shifting strongly downfield from an initial value of 7.32 to 8.16, a shift of (ΔPPM +0.84) and less so for the intraannular phenol, shifting from an initial value of 6.48 to a final chemical shift of 6.80 (ΔPPM +0.32).

Computational simulation results of the complex shown in figure **4.4** agree with this data when the crown ether is in its hydroquinone form, with the intraannular proton causing charge-charge repulsion and resulting exclusion of the cation from the ring. The anion sits proximal to the cation, acting as a very weak Lewis base, pulling more electron density from the already very acidic –OH phenolic proton while the cation sits above the plane of the aromatic ring making a Π-cation interaction.

With the simulation data for K^+ and Na^+ coupled with the NMR titration, the suggested trend is that Π-cation interactions along with delocalization of the triflate ion with the acidic phenol proton mediates a deshielding of both protons in the case of K^+. The effect is less explainable in the case of Na^+, which shows one downfield and one upfield displacement with computational simulations (not shown), adding to the confirmation of ion exclusion from the crown ether ring.

Figure 4.8 - (left) ^{1}H NMR titration curves for phenolic protons of 1,4-benzohydroquinone using Na(OTf) and **Figure 4.9** - (right) ^{1}H NMR curve for the same molecule but with K(OTf).

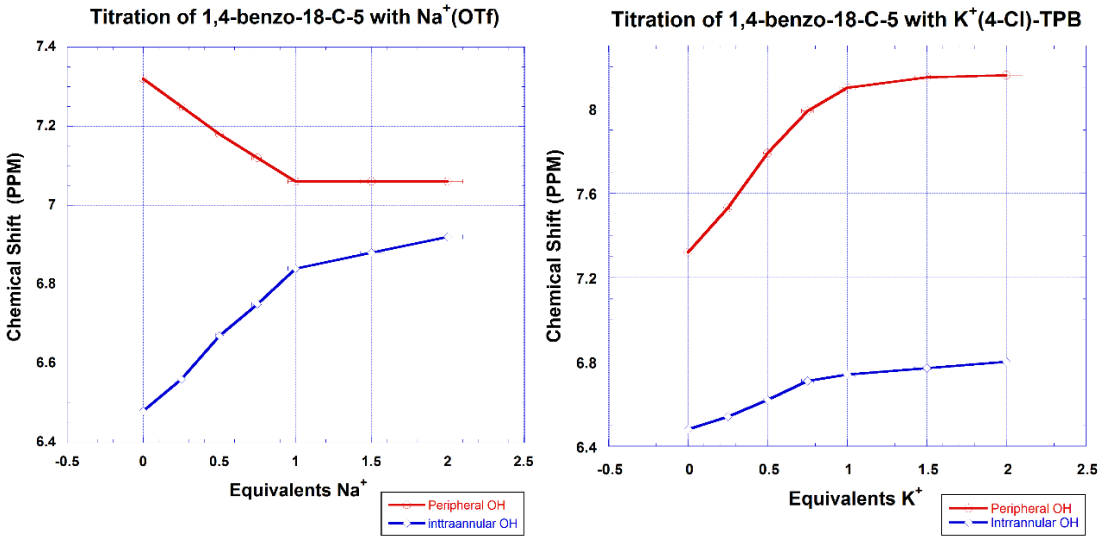

Examining the resultant titration plots in figures **4.8** and **4.9** above, Na^+ shows a distinct preference for the 1:1 stoichiometry but the curves in the case of K^+ suggests that higher order positive co-operative behavior may be playing a role in binding.

Figure 4.10 – Job's continuous variation plot for the titration of 1,4-BQ-18-C-5 using K(OTf)

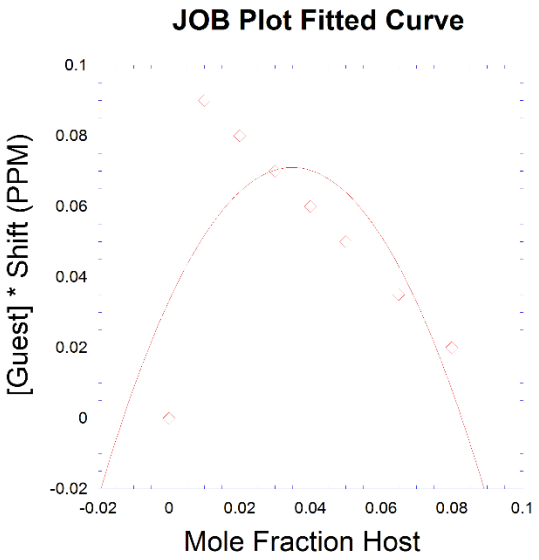

Further data supporting this stoichiometry resulted from the construction of a Job's Plot. The host concentration is then plotted as a function of the product of guest concentration multiplied by the chemical shift for each point. The Job plot can theoretically give three maximums, which correspond to the stoichiometry of the complex under examination. The theoretical, ideal maximums occur at the mole fraction 0.33 [H_2G], 0.5 [HG] and 0.66 [HG_2] (Connors, 1987).

Shown in figure **4.10,** the plot was constructed for the case of K^+, returning a non-ideal value with the maximum lying at an undefined region, most suggestive of a 2:1 complex at X = 0.33 Host.

The collective data drawn from these experimental results suggests the crown ether mediates charge-salt formation more so than serving as a neutral host molecule for the two

ions examined. The multiple configurations and binding processes occurring simultaneously made it impossible to fit the data in figures **4.8** and **4.9** to a least squares regression model.

With such uncertainty in the observations and the mode or mechanism of binding, further synthesis and characterization of this complex was not pursued. Chapter **V** discusses the possible models leading to the observed behavior in greater detail.

^{1}H NMR Characterization of AQ-18-C-6 Ether

The characterization of AQ-18-C-6 scaffold serves as an important focal point for which all other device characterization and observed phenomena rely upon. This next section provides detailed information on solid state and solution properties of the crown ether shown in figure **4.11**.

Figure 4.11 - ^{1}H NMR shift assignments of uncomplexed AQ-18-C-6 in $CDCl_3$.

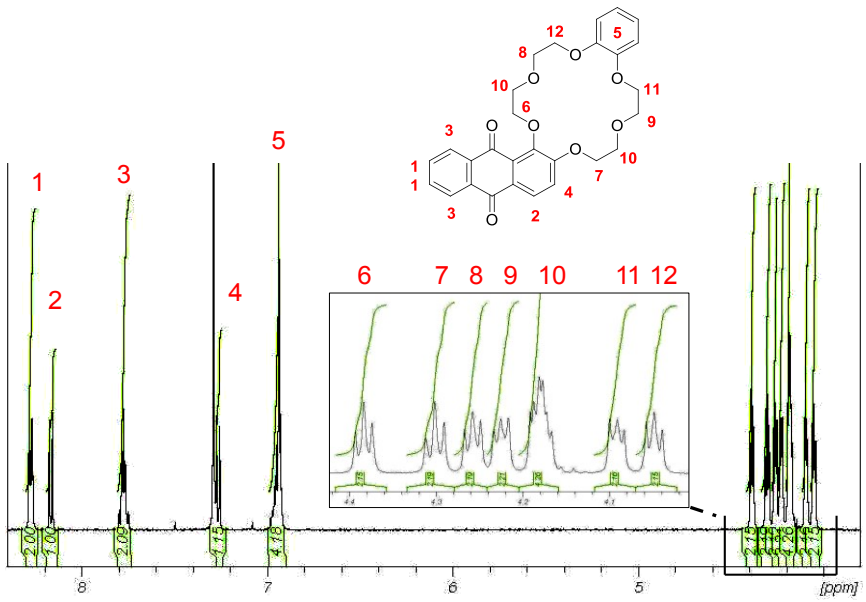

To deduce the assignments in figure **4.11**, required the use of high-field 800 MHz NMR in the acquisition of HSQC and HMBC spectra (see supporting information) to make the proper C-H and C-C assignments. All carbons give their individual peaks and only 2 peaks overlapped (assignment 10) in the proton spectra.

Figure 4.12 (left) - ^{1}H NMR titration of Crown 1 with Na^{+} triflate and **Figure 4.13 (right) -** 1H NMR titration with K^{+} triflate.

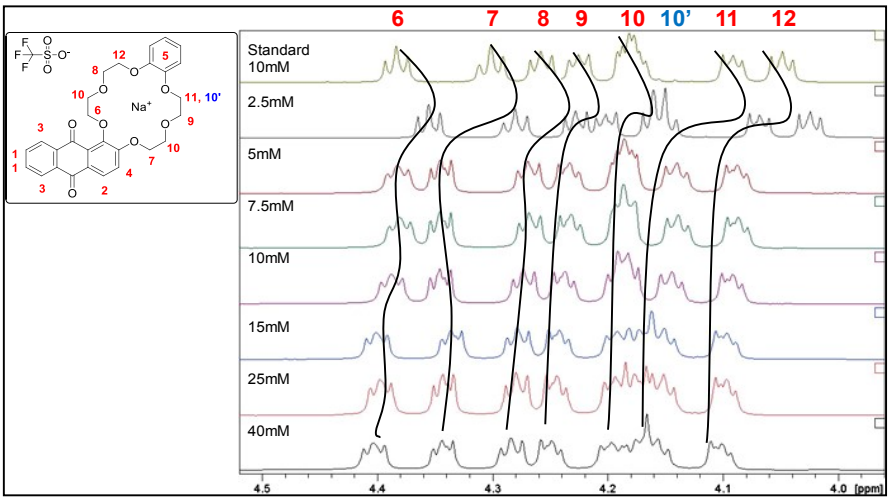

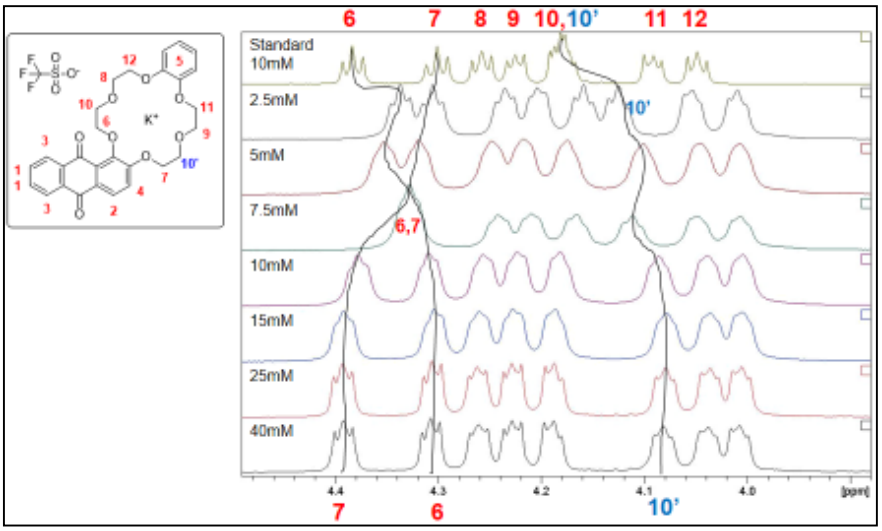

Only after these assignments were made we were able to construct the titration stack plots for both K^+ and Na^+, shown in figures **4.12** and **4.13**.

As can be observed from the stack plots in the above figures, beginning with figure **4.12,** the peaks take a sharp swing upfield at very low concentration of guest and immediately return to the downfield position at a host concentration of 0.5. There are no crossing of peaks and the ovelapping proton 10 never completely seperates into 10 and 10' through the entire concentration range. Peak 11 blends into these two peaks, creating a multiplett integrating for 6 protons from 1.5 to 4.0 equivalents of Na^+ versus the host concentration.

The case for K^+ is markedly different, with peak 10 immediately branching off to form 10 and 10' and 8 individual peaks while retaining spin multiplicity. HSQC/HMBC of the 1:1 sample show unambiguous crossing of peaks 6 and 7, the two oxethylene peaks nearest the anthraquinone subunit. This inversion of chemical shift suggests a marked change in the conformation of the parent stucture.

To deduce the stoichiometry, we returned again to the method of Job's to find a maximum at approximatetly 0.35 for K^+ (2:1 stoichiometry) and 0.57 for Na^+ (data not shown - 1:1 stoichiometry).

Figure 4.14 – Job´s plot for peak 9 in the titration of the anthraquinone parent crown ether with K^+.

The 2:1 binding model suggests a phenomenon known as co-opertivity playing a role in the binding of K^+ by the two hosts. It is known theoretically that when fit correctly to a 2:1 complex the following equation holds true for the value of the equilibrium constant: (Thordarson, 2010), (Connors, 1987)

$$K_2 = 4K_1 \qquad \textbf{4.1}$$

Figure 4.15 – Scatchard Plot of the Job´s plot samples produces a concave up hyperbola.

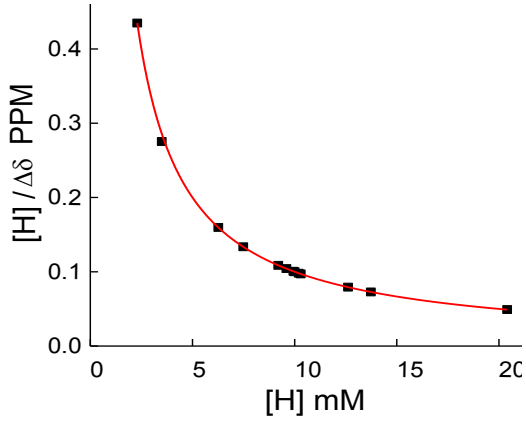

Shown in the figure **4.15** is further evidence of 2:1 complexation mmode as the Scatchard Plot which when plotted with the parametrers [H] vs [H]/Δδ ppm should give a linear relationship. A concave up graph suggests higher order processes are occuring, in this case the upward concavity suggests positive co-opertivity. At low host concentration, a relatively large response is given in terms of NMR shifts.

The reasoning behind this phenomenon is rather complex, but it should suffice to say that if the binding sites are not identical in that they have differing binding affinities, each approach or equilibrium can be attained in 2 ways for K_1 and 2 ways for K_2 giving a possibility of 2 • 2 = 4 ways for binding to occur relative to a single-site receptor. This also introduces another descriptor: the co-opertivity factor α. Suppose each time a binding event K_1 occurs, the affinity of the neighbooring site goes up or down in a defined manner leading to a series of microscopic binding constants for the host. This stepwise binding can accelerate or slow the rate of binding for the additional sites on the molecule. As a result, the co-opertivity factor α, can give an idea whether or not a system is positively co-opertive ($\alpha > 1$) or negatively co-opertive ($\alpha < 1$) or neither ($\alpha = 1$). For a 2:1 system,

Eq. **4.2** is valid:

$$\alpha = \frac{K_2}{4K_1} \qquad \textbf{4.2}$$

The value of the equilibrium constants K_1 and K_2 can be determined by the formula in equation **4.3**

$$\Delta\delta = \frac{\delta_{\Delta HG}[G_0]K_1[H] + 2\delta_{\Delta H_2G}[G_0]K_1K_2[H]^2}{1 + K1[H] + K_1K_2[H]^2} \qquad \textbf{4.3}$$

Our expression for free host concentration follows from eq.'s **4.4-4.7**

$$H^3(A) + H^2(\mathrm{B}) + H((C)) - [\mathrm{H}]_0 = 0 \qquad \textbf{4.4}$$

$$A = (K_1K_2) \qquad \textbf{4.5}$$

$$B = \{K_1(2K_2[\mathrm{G}]_0 - K_2[H]_0 + 1)\} \qquad \textbf{4.6}$$

$$C = \{K_1([\mathrm{G}]_0 - [H]0) + 1\} \qquad \textbf{4.7}$$

The binding isotherms for K^+ in figure **4.14** and Na^+ in figure **4.15** were found using the method of least squares, solving the quadratic for two shift values similtaneouly utilizing multi-model computational software suite Graphpad Prism® according to equations **4.2-4.6** listed above where $\Delta\delta$ represents the shift change due to complexation.

Figure 4.16 – (left) The fitted ^{1}H NMR binding isotherms for peak 9 in the case of K^+ and **Figure 4.17 - (right)** the binding isotherm for Na^+

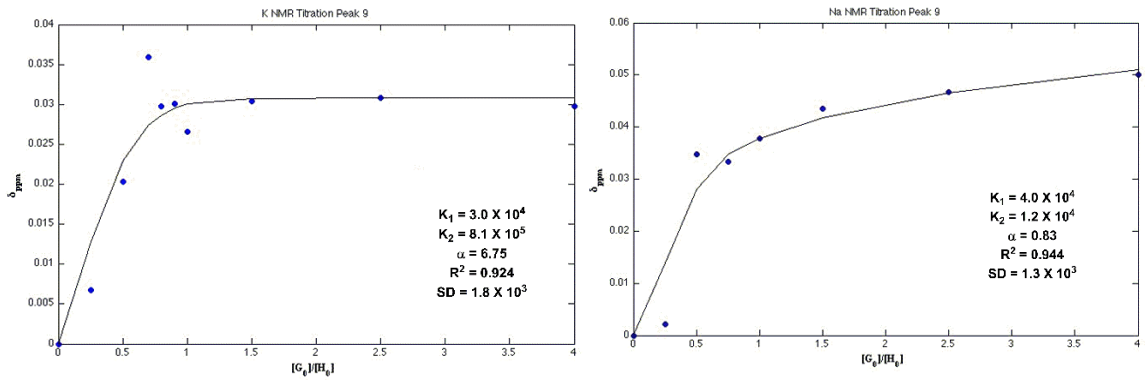

The best fit curves from the least squares method are shown in figures **4.16** and **4.17** above and parameters summarized in figure **4.18** below. In the case of K^+, positive co-opertivity occurs with a calculated $\alpha = 6.75$, suggesting strong binding to form the stable 2:1 Host:Guest complex. Na^+ was also fitted 2:1 for direct comparison and assessment of co-opertive factors. The value for K_2 was appreciable but the much larger value of K_1 in this case gives an $\alpha = 0.62$, suggesting negative co-opertivity effects are playing a role in the binding.

Figure 4.18 – Summary of Stepwise binding constants for the 1H NMR titration of AQ-18-C-6 in $CDCl_3$.

Parameter	**K^+ Titration**	**Na^+ Titration**
K_1	3.0×10^4	4.0×10^4
K_2	8.1×10^5	1.2×10^4
Keq	8.4×10^5	5.2×10^4
α	6.75	0.83
R^2	0.92	0.94
Std Dev	1.8×10^3	1.3×10^3

To complement the titration conducted in the relatively non-polar $CDCl_3$, a second NMR titration was carried out to examine the other extreme in polarity using $_{d6}$DMSO with the initial equimolar stiochiometric complexes screened and resulting spectra stacked in figure **4.19**. K^+ was the only ion that produced any sort of shift in dDMSO, so a full titration

was not carried out, but it is worth noting that the dielectric of the mediums ($CDCl_3$ or DMSO*d6*) as well as their viscosity are quite different leading to different solution-phase ordering. K^+ must then still be able to complex even with the highly solvation competition from DMSO.

Figure 4.19 – Results from initial 1:1 experiments in *d6*DMSO show very little shift at 10 mM concentration in the crown ether region, with the exception of K^+, which differentiates 10 and 10' producing 8 triplets in the ether region.

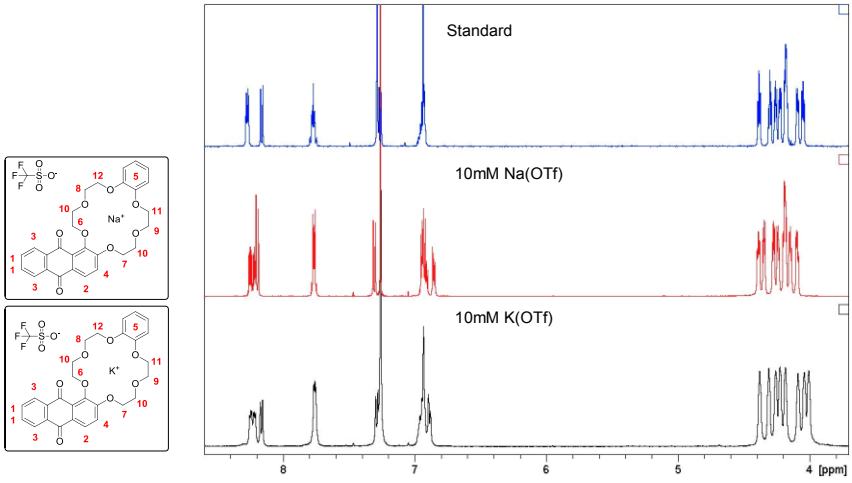

^{13}C NMR of the triflate complexed in $CDCl_3$

The ^{13}C NMR of the resulting 2:1 triflate/crown complex was acquired on a Bruker 800 MHz spectrophotometer at ambient temperature. Note that one can account for all 28 carbons present in the free host with each crown ether having its own characteristic signals between 68.43 and 73.09 ppm. In contrast, the complex spectra loses all but two of these crown ether carbon signals, retaining only the 73.10 and 68.08, signals respectively. Along with the complexed ^{13}C NMR spectra of the crown, there should exist a quartet

corresponding to the triflate anion lone carbon with three fluorine atoms attached due to the spin-spin coupling of the ^{19}F nuclei and its odd multiplicity. No signal attributed to the triflate anion were observed at 800 MHz, indicating the 2:1 complex may exist without a counter-anion in low-polarity solvents. This could be due to the concentration difference as well where the standard ^{13}C NMR for the triflate anion was observed in dDMSO at 10 mM concentration where the 800 MHz spectra of the complex was taken at concentrations as low as 1.2 mM

Figure 4.20 – ^{1}H, ^{1}H COSY enhancements as outlined in the diagram matching the theoretical models K^{+} (purple sphere), Na^{+} (yellow sphere)

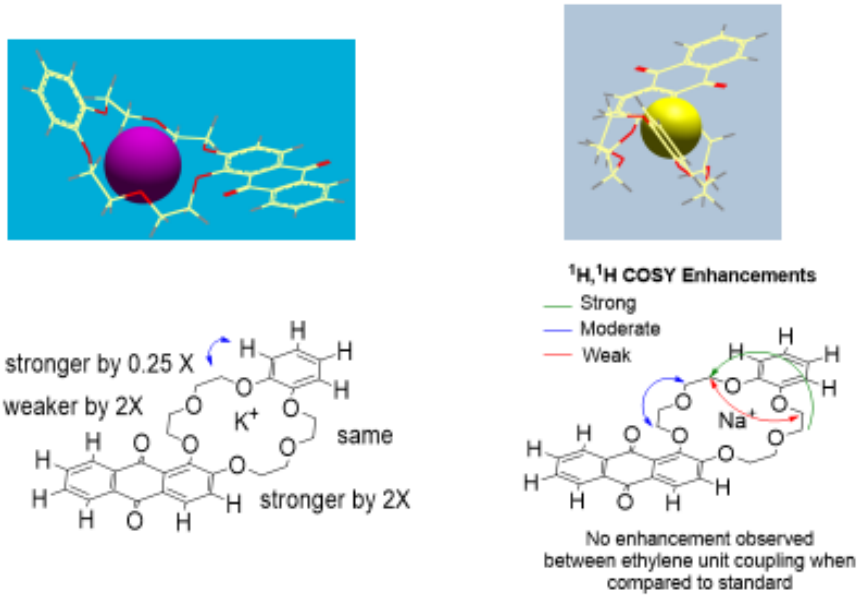

2D NMR Studies

^{1}H, ^{1}H COSY Spectra of Triflate Complexes

The resulting COSY enhancements are summarized in figure **4.20** with trajectories of the prominent interactions ranging from weak to very strong. Also shown in the figure is the

lowest energy conformer minimized by MMF94 force field (assuming no anion present for simplicity) to aid in the visualization of these interactions. In the case of Na^+, cross-coupling of opposite face ethylene protons causes enhancements on opposite faces of the ether ring while the K^+ structure is rather flat, with the catechol ring and ethylene protons lying in the same plane as one another, creating eclipsed conformers in the bound state.

These enhancements suggests a pocket too large for the binding of Na^+, with a contorted structure dynamically trying to adjust to the smaller geometry.

The 1:1 K^+ structure suggests a stiffening of the ring upon binding of the ion, the K^+ lying slightly out of the plane from the crown ether. Nonetheless, almost all of the adjacent protons in the bound structures had some sort of enhancement and a 4X coordination was determined to be the most probabilistic conformer. This 4X coordinated structure is hypothesized to be the driving force behind the formation of the 2:1 complex existing as the most energetically favorable state in order to form the preferred octahedral complex.

A similar anthraquinone derivative prepared by Erk. Et al. (Erk, 2000), without the catechol moiety showed very low affinity for Na^+, supporting the hypothesis of 4x coordination of the oxygen ethers and dimerization as an octahedral array of coordination sites organize.

2D diffusion-ordered Spectroscopy (DOSY) characterization of K^+- Crown Complex

Diffusion-ordered spectroscopy effectively analyzes 1D peaks in the ^1H NMR and correlates the peaks with points in the second dimension by analyzing the rate of exponential decay of a magnetic field pulse gradient. Substances that are diffusing quickly through the

medium respond to the field with very long decays while larger, slowly diffusing solutes decay rapidly.

Transforming the acquired data set into interruptible results, the number of expected components in the mixture is defined and the range of values of predicted diffusion coefficients is entered. The resolution and number of repetitions is entered until one obtains a transform that is well resolved with no overlapping peaks. This procedure is termed the "Bayesian" transformation of the data set where the 1D spectral encoding is transformed and aligned with the Z-dimension through the following relationship:

$$\mathbf{S(f,z) = S_A(f)\ exp^{(-dAz)}} \qquad \mathbf{4.8}$$

Where $\mathbf{S_A(f)}$ is the spectral intensity of component **A** in zero gradient ('normal' spectrum of **A**) and $\mathbf{d_A}$ is its diffusion coefficient. The 1D spectral encoding sequence is aligned with the generated points along the 2D diffusion axis and the diffusion line is integrated quantitatively to give the absolute integration along that particular diffusion trace.

One may check that the 2D integration matches the integral ratio between the ^{1}H NMR integral and calibration with standards that have known diffusion coefficients and are known to not interact with other solutes. A very good standard for this is tetramethylsilane (TMS).

DOSY is not limited to just proton samples as many other elements with high natural abundance such as the ^{19}F nuclei with 100% natural abundance and ^{11}B nuclei, are amenable to the same method. In this manner, more complex mixtures of organic compounds can be analyzed for composition by following a broader range of peaks across a larger spectral width (Gerig, 2001), (Zhang, 2013), (Chapman, 2007), (Mouro, 2002). 2D DOSY can be

complementary to other methods of characterization when separation of compounds is not plausible by other methods.

In the DOSY experiments, the strength of the diffusion-encoding gradient is arrayed and the diffusion coefficients are calculated according to the Stejskal-Tanner formula:

$$S(G_{zi}) = S(0)\exp(-D_i\gamma^2\delta^2(G_{zi})^2(\Delta - \delta/3)) \quad \textbf{4.9}$$

where G_{zi} and $S(0)$ are the signal intensities obtained with gradients strengths of G_{zi} and 0, respectively; D is the diffusion coefficient; γ is the gyromagnetic constant; δ is the gradient pulse duration; and Δ is the diffusion delay.

Convection currents are caused by small temperature gradients in the sample and result in additional signal decay that can be mistaken for faster diffusion. The convection conditions are described by the *Rayleigh-Bénard* equation:

$$Ra = \frac{g\beta R^4}{v\chi}\frac{\partial T}{\partial z} \quad \textbf{4.10}$$

Where g is the gravitational acceleration, v is the viscosity, c the thermal diffusivity, b the expansion coefficient of the liquid, R the internal diameter of the NMR tube, and $\frac{\partial T}{\partial z}$, the temperature gradient along the sample axis. When the critical Rayleigh number (R_a) is exceeded, convection will occur.

Figure 4.21 – Proper gradient attenuation for 2D DOSY experiment collected on Sample F (2.0 Eq. Guest, 1.0 Eq. Host) using K^+(4-Cl)TPB^-. Spectra recorded on a Varian 600 MHz with cryoprobe.

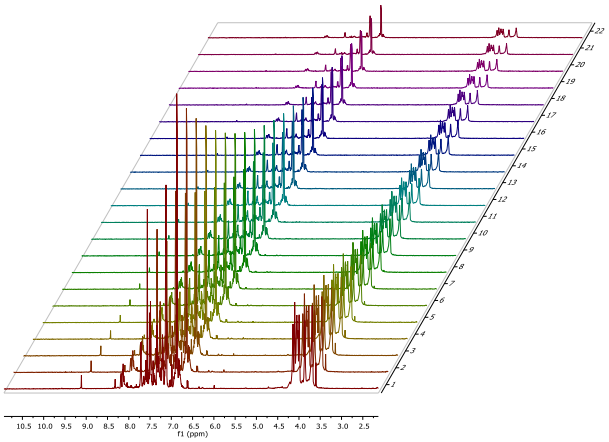

To observe proper signal attenuation, the power of the gradient is adjusted until the highest peak decays down to 10% of its original strength, figure **4.21.** Effectively capturing anything diffusing in the second dimension, as the shorter peaks will naturally decay before the largest signal.

DOSY has not seen widespread use until present day because of the acquisition time and the relatively concentrated samples needed to obtain reliable spectra. If a mixture in which a particular component only made up 1% of a 10 mM sample, the sample will not produce a signal intense enough to generate the appearance of a cross peak. This problem arises because the spectral width is too wide and the probability of the z and x-y components of the vector space matrix is low, which in turn leads to a weak or poorly resolved signal due to the large space being sampled. To circumvent this problem, spectral width is narrowed down and only the peaks corresponding to decays of interest are recorded in a sequence called 2D HADAMARD Encoding (Steinbeck, 2005). In this method, the acquisition time is

roughly cut down 5X making the experiment much more feasible for routine use (Feliz, 2007).

Our studies utilizing the aforementioned method concentrated on deciphering the diffusion coefficients of complexes with the two anions used in this study, the triflate anion ($^{-}$OTf) and the (4-Cl)TPB^{-} anion. The triflate anion was analyzed for the symmetrical ^{19}F spectrum since the carbon spectra produced 4 separate lines due to the odd spin multiplicity of the three ^{19}F nuclei present in the triflate anion.

The protons attached to the 4-ClTPB^{-} anion were directly analyzed and this gave the most consistent result, as we could verify two distinguishing peaks by direct integration. The ^{19}F data for the triflate anion could only be obtained in *d*DMSO, where K^{+} ($^{-}$OTf) is completely soluble and free to diffuse (Gerig, 2001), (Dalvit 2012). The standard spectra (10 mM) gives a shift of -78.51 ppm and the complexed *d*6-DMSO spectra returned a substantial shift value of -74.57 ppm (Supporting Materials). This is a significant shift in terms of averaging over the 3 fluorine nuclei environments.

DOSY NMR Experiments for individual complexes

This next section will present DOSY data for complexes with a stoichiometry of 1.1:1.0 G/H. The counter-anion to K^{+} will be examined in terms of the overall complex diffusion and differential self-assembly of the AQ-18-C-6.

Figure 4.22 – Standard DOSY of the uncomplexed crown ether region of the novel crown quinone showing the ^{1}H NMR as well as the 2D NMR with integrations within +/- 0.03 of their absolute value. A diffusion trace at 0.95 cm^{2} •sec^{-1} was observed as the single constant in $CDCl_3$

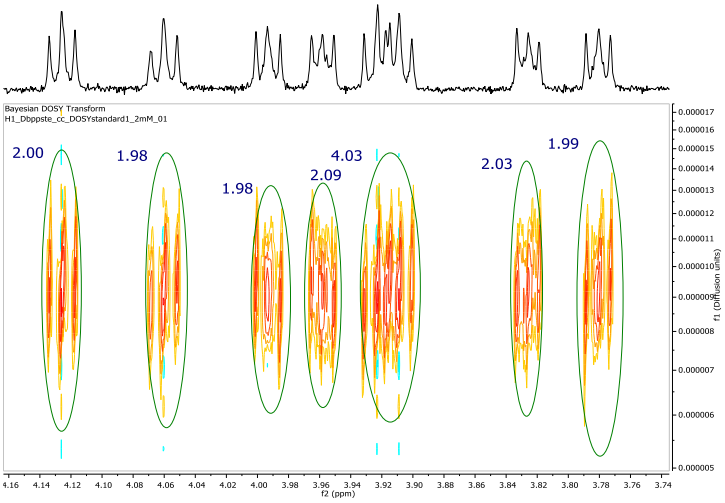

The standard uncomplexed spectrum shown in figure **4.20** above shows all the characteristic data of an ideal DOSY acquisition. With the spectrum highly resolved one can make out:

1. The integration of the 2D plane.
2. The number of diffusing entities.
3. The splitting in the 2D plane as it corresponds to the 1D spectra.

Figure 4.23 – DOSY spectrum of the sample used to construct the JOB's plot (1:1 overall ratio. Note there is an aromatic doublet signal hidden by the CDCl3 peak. The diffusion constant at this stoichiometry is 0.43 X 10^{-5} m^2 • sec^{-1}

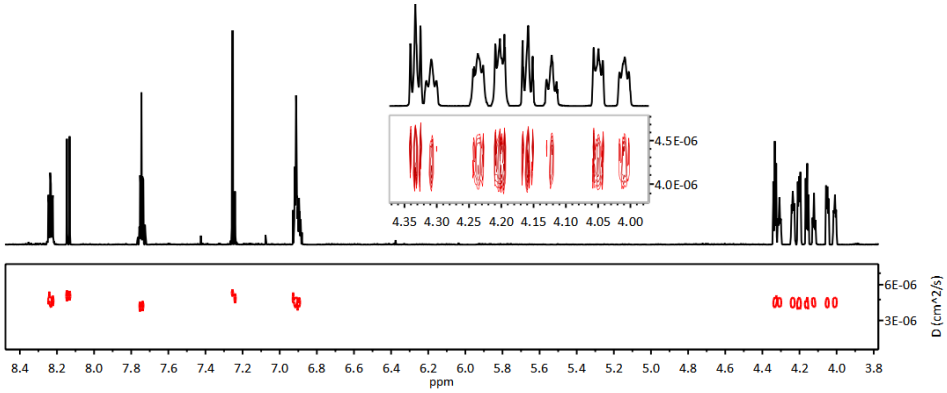

With this, we set out to conduct a few different experiments on different complexes so that we could further

1. Confirm the hypothesized 2:1 stoichiometry of the K^+ triflate complex.
2. Examine the effect of different anions present in organic solvents and the resulting stoichiometry.
3. Deduce Keq by competition experiments utilizing 5 mM Crown, 5 mM guest and 5 mM standard 18-crown-6.
4. Examine the phase transfer capabilities of the Host toward 4-ClTPB salt (insoluble in CDCl3) at t = 3min and t = 72 hrs.

Figure 4.24 – Table of standard diffusion recorded in this work.

Table of Standardized Diffusion Coefficients				
Compound	**Solvent**	**ξr****	**D (X 10-5 cm^2 • sec^{-1})**	**Method**
18-C-6	CDCl3	4.81	2.10	^{1}H NMR
18-C-6	DMSO	47.24	2.07	^{1}H NMR
AQ-18-C-6	CDCl3	-	1.42	^{1}H NMR
AQ-18-C-6	THF	7.52	6.00	^{1}H NMR
AQ-18-C-6	DMSO	-	1.21	^{1}H NMR
Na(OTf)	DMSO	-	3.43	^{19}F NMR
K(OTf)	DMSO	-	3.65	^{19}F NMR
K(4-Cl)TPB	THF	-	1.26	^{11}B NMR
K(4-Cl)TPB	THF	-	1.28	^{1}H NMR
K(4-Cl)TPB	CDCl3	-	0 - N/S	^{1}H NMR
K(4-Cl)TPB	2:1 CDCl3:THF	-	0.85	^{11}B NMR
K(4-Cl)TPB	2:1 CDCl3:THF	-	0.84	^{1}H NMR
K(4-Cl)TPB	3:1 CDCl3:THF	-	0.32	^{11}B NMR
K(4-Cl)TPB	3:1 CDCl3:THF	-	0.31	^{1}H NMR

***ξr = Dielectric Constant**
****CRC Handbook of Chemistry and Physics 2009/2010 edition Ed. 1990 Dacv Ed. 90 David R Lide (Editor in Chief)**

Figure 4.25 – Bar graph of the diffusion coefficient of (4-Cl)TTB as a function of the volume fraction THF added.

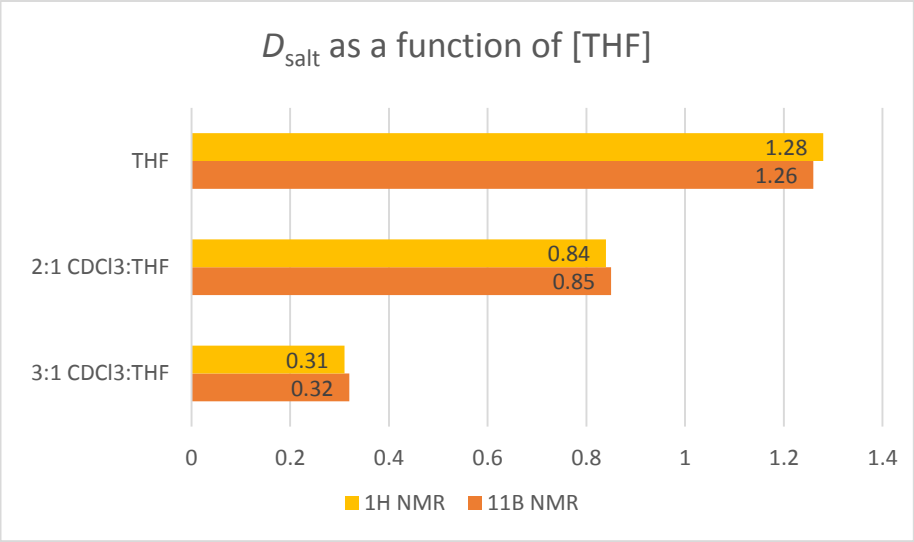

Figure 4.26 – Minimized structure of the (4-Cl) Tetraphenylborate salt showing potassium (purple), the borate (gold) and chlorine structures (green).

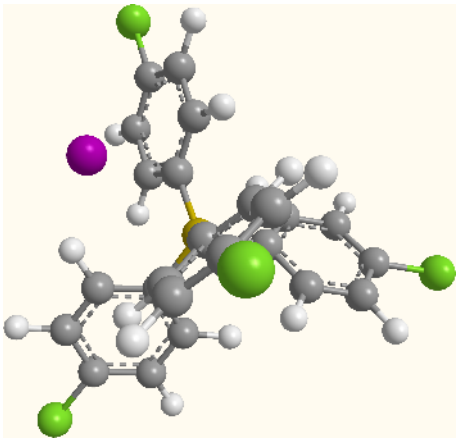

Most often (4-Cl)TPB is used as a neutral cation exchanger in organic phospholipid membranes to aid in the phase transfer of hydrophilic salts through the hydrophobic membrane (Gehrig, 1990). The mechanism of phase-transfer catalysis hinges off the charge

at the central borate atom, which bears a highly delocalized charge calculated to be -0.11 Hartree.The four chlorine atoms *para* to the borate do not have any substantial effect on the delocalized charge when compared to the regular potassium tetraphenylborate (Gehrig, 1990).

For the solubility and resulting diffusion complex measurements the insoluble neutral ion carrier K(4-Cl)-tetraphenylborate was utilized. This salt was chosen due to its M.W. being almost identical (S.D. 2 g/mol) to our parent crown ether. It was hoped that this would make determination of diffusion constant more predictable than using a salt of intermediary weight. Another aspect of the system that was to be examined was the effect of large and small anions on the self-assembly of the [K^+: crown ether] complex. The rich aromatic system was also further reason for us to examine which effect was governing the assembly of structures in solution with this salt.

As pictured in figure **4.27**, we obtained DOSY spectra for heavy metal anion complexes to observe any peculiar behavior of the aromatic system of our crown ether as well for the sake of completeness. In this particular case, a slight excess of K^+ was used and peaks became quite broad when 1.1 Eq. guest to 1.0 Eq. host ratio was sampled in pure $CDCl_3$. Although the peaks became broadened, the integration could be made out quite well, with some peaks merging into others.

Figure 4.27 – 2D DOSY spectra DONESHOT sequence measuring the diffusion of [$K^+Au^-Cl_4$ - Crown Ether] Complex in a 1.1 Guest to 1.0 Host ratio. The diffusion trace returned a coefficient of 1.44 X 10^{-5} cm^2 •sec^{-1}

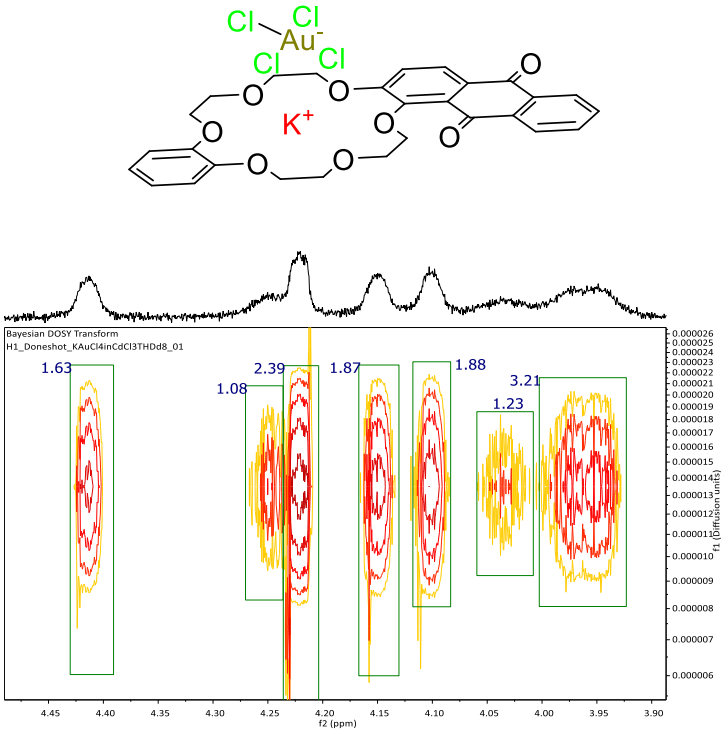

Pre-diffusion Complexes of loose ion pairs

Ion pairs have been studied for quite some time as well as their behavior in solution. From activity coefficients to molarity, molality as well as the many other physical properties of solutions with ions as solutes dissolved in mediums such as water is now well understood and quantified. What has lagged behind is our knowledge of the solution ordering of ionic species in organic mediums. Discussed in earlier chapters was the enthalpic cost to separate an ion from its counterpart in non-aqueous media, a force that many organic solvents cannot

overcome by themselves without the use of ionophores. What forces are predominant in exchanging an ionic bond for what one would consider to be a simple charge-dipole interaction? The answer must be accounted for in the form of some type of energy. This energy must come from the solvent or carrier molecule which must lower the free energy enough to induce ion-pair separation as well as maintain this ion-pair separation as the structure stabilizes itself into its lowest energy conformer.

In the next study, the uptake of the insoluble K(4-Cl)TPB in $CDCl_3$ is studied by diffusion NMR to examine the effects of this ion-pair separation and the implication it may have on the diffusion of the complex, anion or both. Furthermore, of most importance was to study the ion capture process and assess the binary diffusion coefficient of the anion-host-cation complex.

Figure 4.28 – Homogeneous pre-equilibrium Complex with free anion as the K^+(4-ClTTB) is complexed and phase transferred into the $CDCl_3$ solution at t = 3 min post-salt addition.

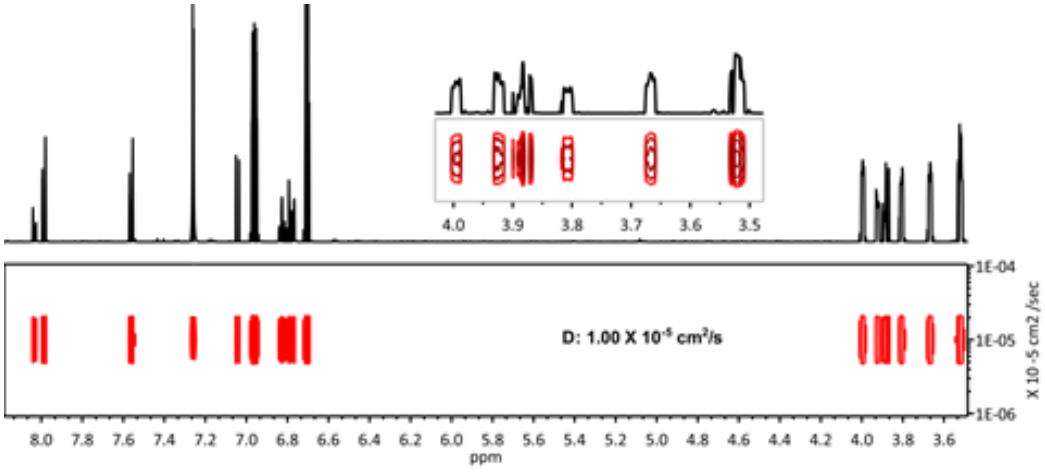

In figure **4.28** above, only one binary diffusion trace exists for the similar M.W. anion (M.W. 496.1) and host (M.W. 490.5). The stoichiometry at the time of addition was **1.0** Eq. Host AQ-18-C-6 to **1.1** Eq. Guest (4-Cl)TPB in pure $CDCl_3$ which formed a heterogeneous mixture. As shown in the spectra, the two peaks corresponding to the TPB anion can be observed at 6.95 and 6.74 along the diffusion trace of 1.00 X 10^{-5} cm^2 • sec^{-1}. Note that there is no residual TPB anion species found in the mixture.

Figure 4.29 – Heterogeneous 2D COSY Spectra attained immediately after the acquisition of DOSY Spectra in Figure 4.23 (approximate t = 45 m. post-addition of K^+)

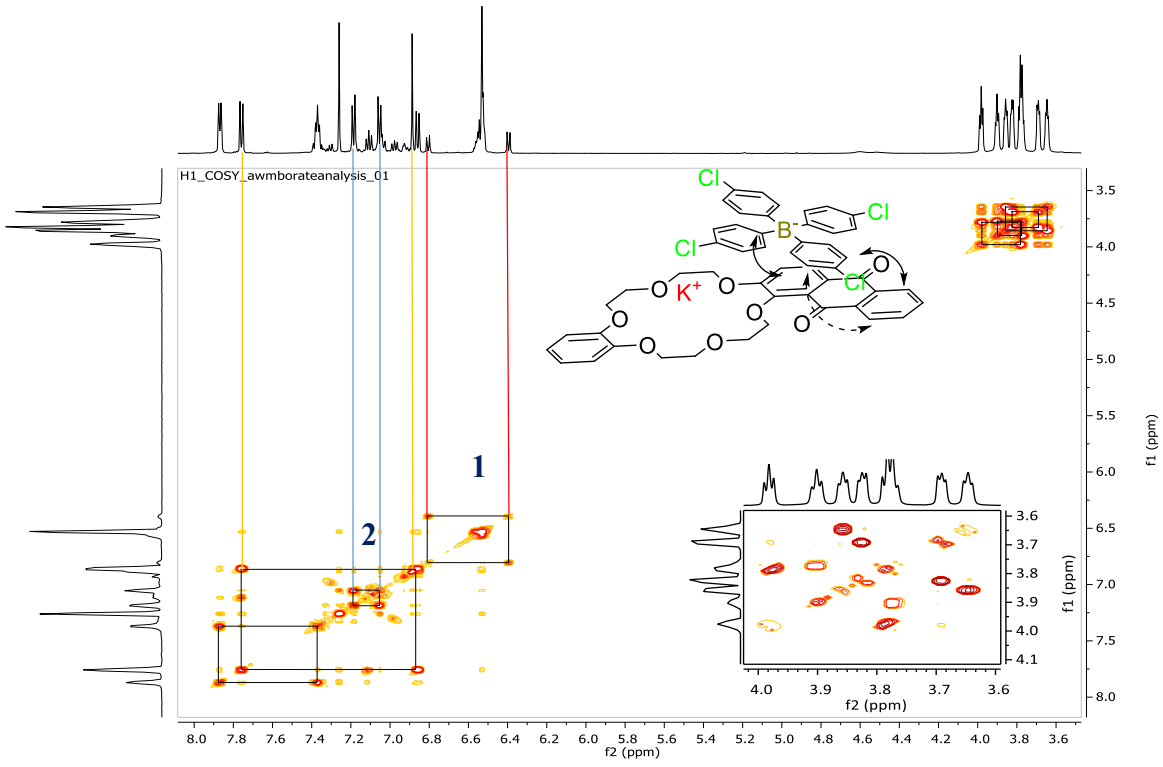

The COSY Spectra of the pre-equilibrium complex between K(4-Cl)TPB and AQ-18-C-6 show strong interaction, the first being the inversion of peaks 6 and 7. There are interactions among 4 crown ether proton sets, but none of these couple with any of the catechol or anthraquinone protons. Self-coupling between the free anion (Box 1, red drop lines) along with coupling of one adjacent TPB anion proton at the 2-position coupling to the 3-position on the anthraquinone subunit (Box 2, blue drop lines). Finally, there exists one interaction between the 3-sites on the TPB anion with either the 5 or 8 position on the TPB anion aromatic ring.

Figure 4.30 – NOESY Spectrum of 1:1 pre-diffusion complex of Crown with K^{+}4-ClTPB^{-} recorded in sequence after completion of a DOSY acquisition (t = 22 m). The most intense cross-peaks occur in the uppermost left-hand corner between the TPB aromatic protons interacting strongly with the crown ether region.

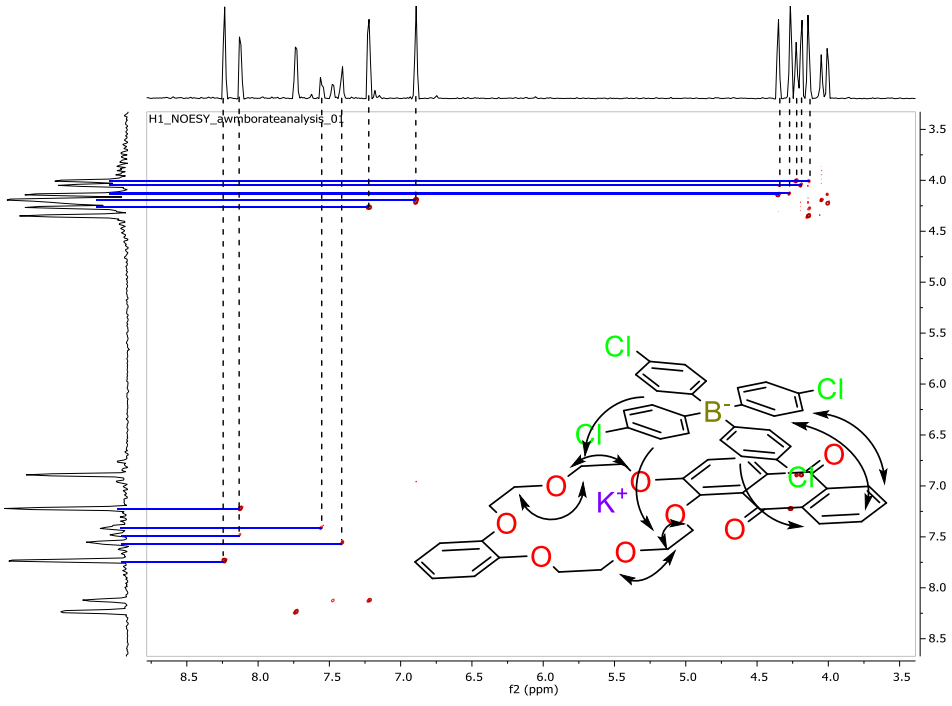

The NOESY spectra along with the interaction map is given in the above figure. It should suffice to say that the main information obtained from this spectrum is the conformation of aromatic-aromatic couplings due to the hypothesized Π-stacking effects of the borate with the anthraquinone subunit. The secondary interactions with the crown ether protons themselves which suggests flattening out effects of the ring skeleton as well as the coupling between planes of the crown ether and TPB anion.

The best analogy to what is happening can be related back to the problem of a pill dissolving into a medium until it is saturated. The concentration of the pill rises exponentially in the liquid phase and decreases exponentially in the solid phase until some equilibrium is reached. Our next set of spectra shows just how much dissolves and diffuses with the carrier present and also shows a unique phenomenon which is a reversal of the common ion effect.

Figure 4.31 – DOSY spectra of the same complex recorded at t = 3 h post-addition of the guest. The integration at t = 3 h matches the theoretical integration of a 1:1 complex 18C6-K+ complex. 16 aromatic protons (Guest) + 6 aromatic host + 16 crown ether protons. A slight residual of the free TPB anion integrates for 5 protons due to the slight excess present in solution. See text for details.

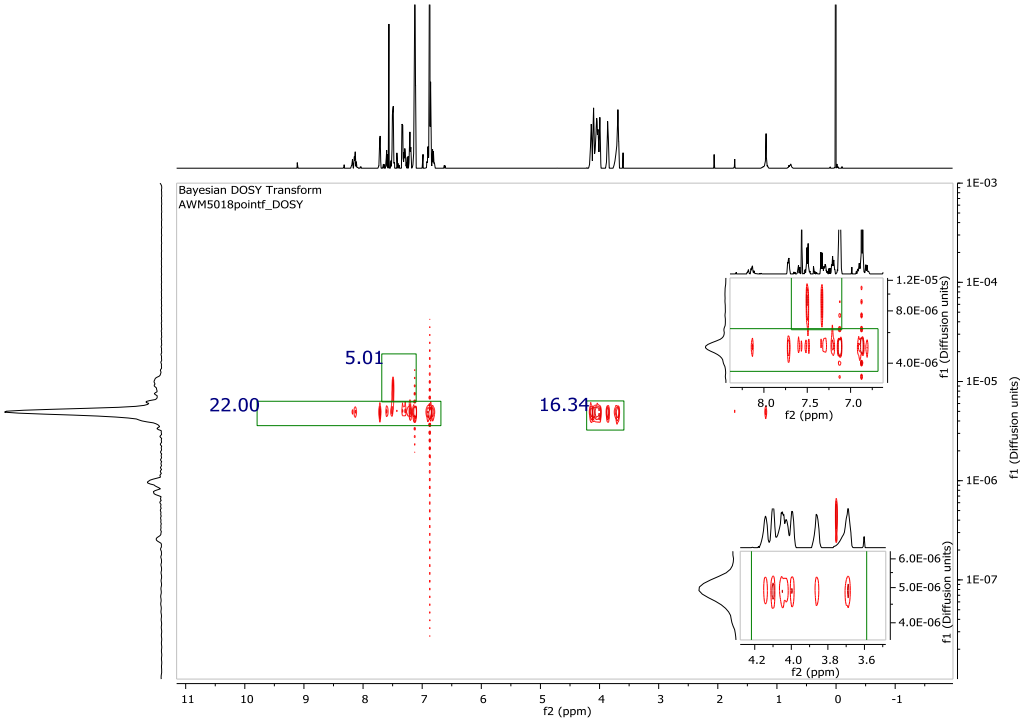

Instead of ions precipitating ions out of solution due to concentration, we noticed a marked increase in the solubility over the first five minutes post-addition of the K^+ source in a qualitative manner. As can be seen in Figure **4.31** above, the integration in the 2D plane leaves what is believed to be the solvent-separated anion co-existing in solution with the bound anion. A signal downfield from the standard (4-Cl)TPB integrates for 5 protons, but is not bound to the crown ether a t = 3 h when the spectra was acquired. There should theoretically be 10 aromatic protons for the crown and sixteen (17 due to the 1.1 Eq. to 1.0 ratio) for the TPB anion for a total of 26 aromatics and 16 crown ether protons which are all

accounted for in the spectra at t = 3 h. This means that there exists 4/5 unbound TPB protons for the crown to bind to, and instead, only 22/26 aromatics are occupied at the 3 h mark. The complex formation thus helps to solubilize the remaining K(4-Cl)TPB as more and more of the binding sites become occupied. There are two possible hypothesis for this occurrence:

- The solution is becoming more ionic in nature, providing "hopping" sites where anions and cations can exist as solubilized ion pairs.
- The Π-character of the TPB anion is promoting solubility by creating a Π-stacked network of organic anions/cations able to solubilize.

Figure 4.32 – Homogeneous equilibrium 1:1 complex diffusing with a single binary coefficient of 1.02 X 10^{-5} cm^2 • sec^{-1} at t = 72 h. HADAMARAND encoding was used to narrow the spectral window and increased the spectral resolution while decreasing acquisition time

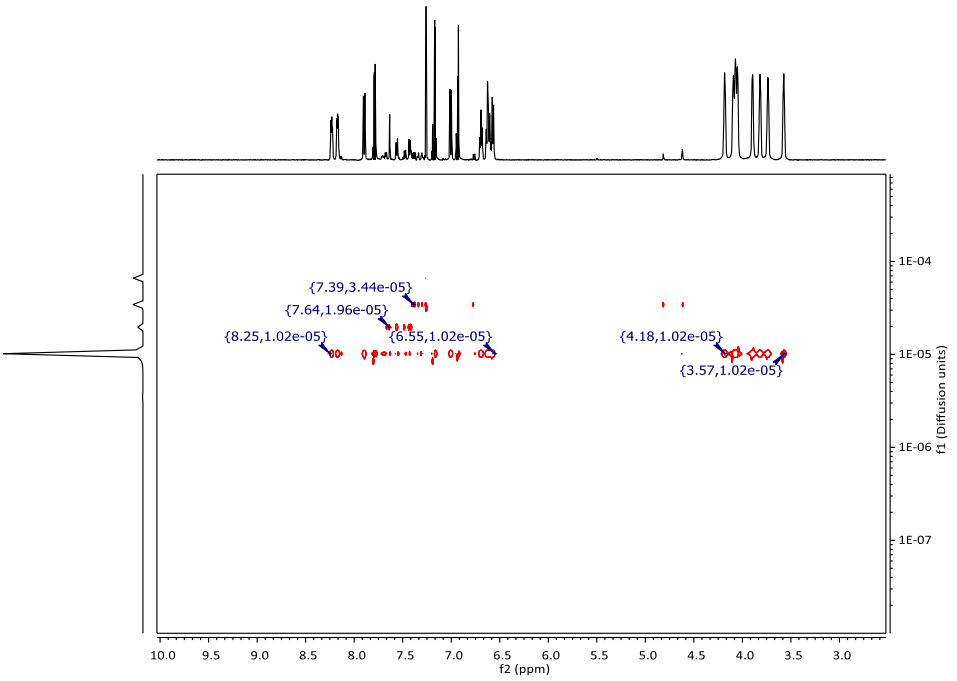

A piece of evidence that cannot be overlooked is the ^{19}F NMR figure **4.33** below which clearly shows two distinct peaks. Gehrig Et al. and others have shown that minor fluctuations can mean the difference between a compound being encapsulated within a complex as opposed to being free in solution in terms of interpreting ^{19}F spectra.

Figure 4.33 – ^{19}F spectra of the AQ-18-C-6 crown ether complexed with the triflate anion in CDCl3 at 298 K

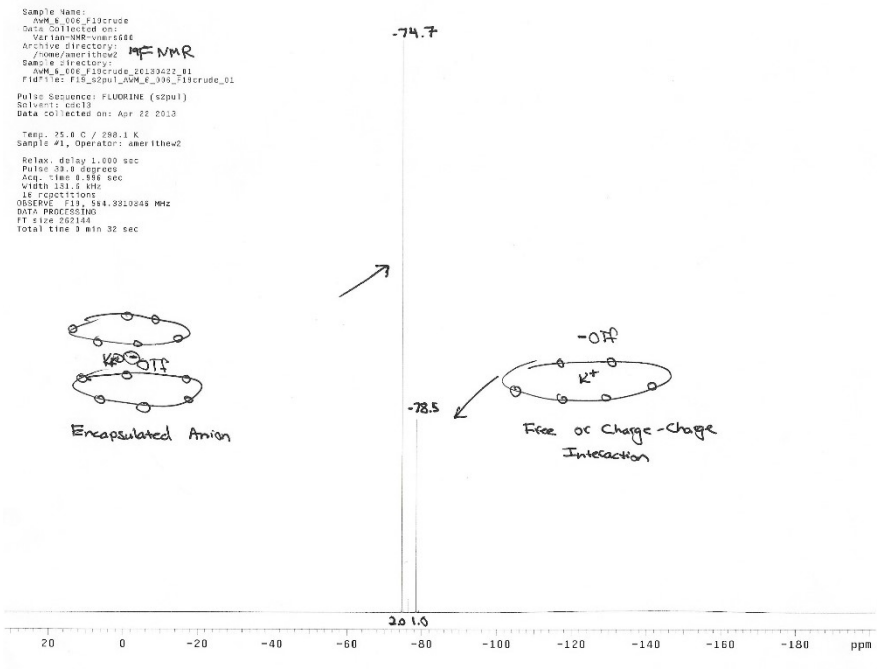

Figure 4.34– 2D DOSY spectra recorded for the 24 h equilibrium complex of the (4-Cl)TPB anion diffusing with the rest of the supramolecular peaks.

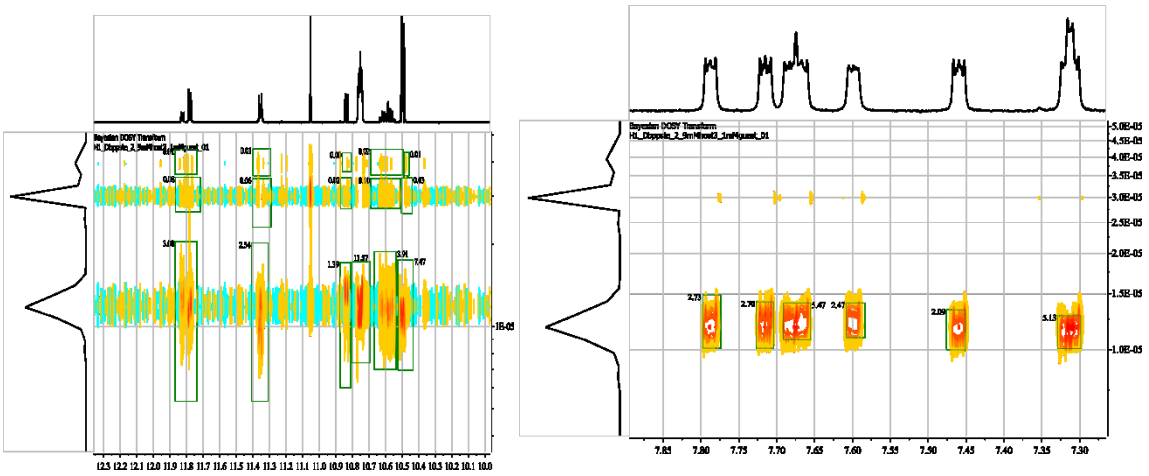

Pre-equilibrium complexes or encounter complexes have been demonstrated in the Literature before by Hirose Et al. who devised the equation (Hirose, 2009).

$$K_{obs} = \frac{k_1}{k_{-1}} = \Lambda \quad \textbf{4.11}$$

This equation states that the overall rate constant is the product of the forward rate constants divided by the rate of the backward reaction, which is also equal to the equilibrium constant as k_1/k_{-1} is the definition of the equilibrium process for the first association event. Examining the same experimental parameters as in the previous example, a spectra of a 1.07 Eq. /1.00 Eq. guest stoichiometry was observed to immediately bind the ligand K^+ when K(4-Cl)TPB was added to the NMR tube creating a resulting homogeneous mixture. The homogeneity of the diffusing species and the immediate chemical shifts further strengthens our hypothesis of faster diffusion of ions as a function of increasing solvent polarity.

Most often one finds in the literature the aforementioned salt used in artificial membranes during electrochemical cell testing as a “neutral ion carrier” that helps to perform the reverse effect and mediate ion exchange while maintaining charge neutrality to prevent polarization of the membrane. In this case (figure **4.35**) we see that the crown ether is actually solubilizing the K^+(4-chloro)TTPB.

Figure 4.35 – 2D DOSY Spectra at t= 3 m showing ithe presence of the solvent-seperated ion pair when the instantaneous titration is performed in pure $CDCl_3$

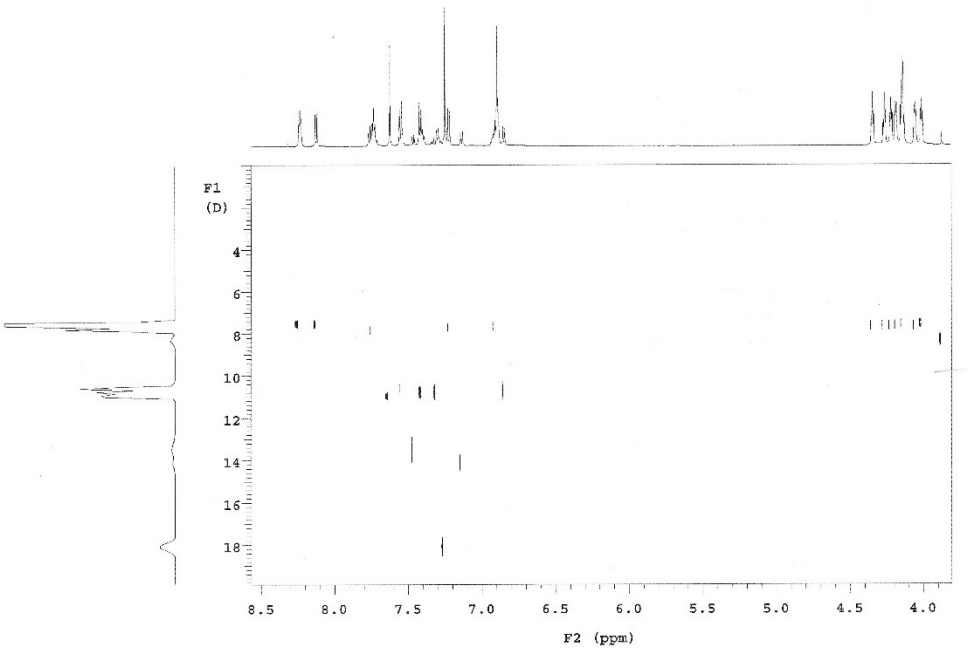

The same sample after 72 h. at ambient temperature with no stirring produced the spectra observed in figure **4.36**, with all the diffusion traces corresponding now to the 1:1 complex spectra along with 0.1 Eq. of leftover excess free ion pairs diffusing at a faster rate than the complex. This phenomena is unique because the entire self-assembly process of ion-pair

formation, complexation and equilibrium and excess salt can all be monitored as a function of time.

Figure 4.36 – The now homogenous equilibrium complex shown in fig. 4.37 but 72 h. after addition of the K^+

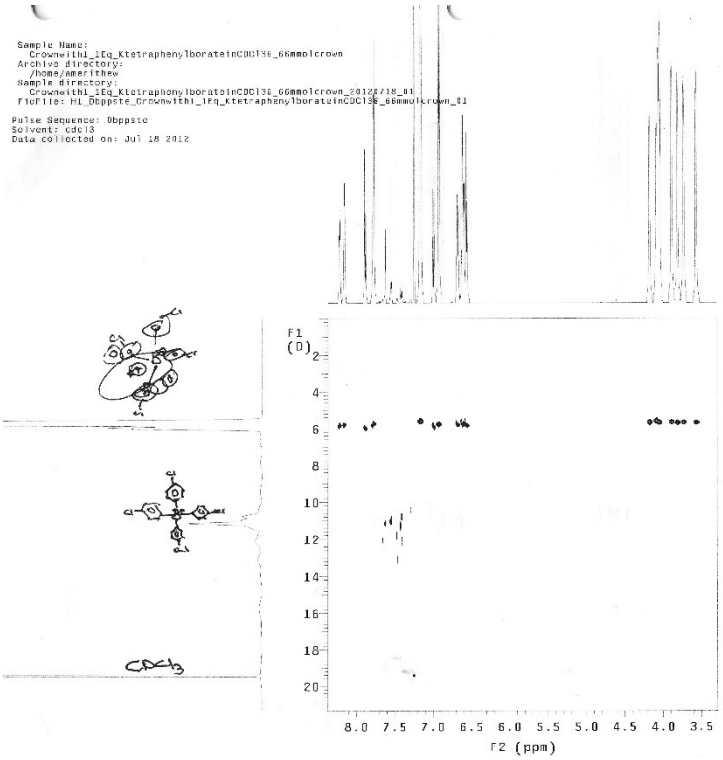

Figure 4.37 – Table of diffusion constants obtained for titration results of AQ-18-C-6 with K(4-Cl)TPB in 3:1 $CDCl_3$:THF

Stoichiometry	G/H Ratio	Time to Eq.**	$D_{free(salt)}$ X 10^{-5}	$D_{bound\ (AQ\text{-}18\text{-}C\text{-}6)}$ X 10^{-5}
0	0	0	0.85	1.42
1:1	0.11	72 h.	N/O	1.48
1:1	0.33	72 h.	N/O	1.53
1:1	0.66	72 h.	N/O	1.58
1:1	0.88	72 h.	N/O	1.61
1:1	1.00	76 h.	N/O	1.63
1:1	1.50	76 h.	1.1	1.63
1:1	2.00	76 h.	0.89	1.62

*N/O = Not observed
** The difference in time is due to spectrophotometer time required to collect data sets from each diffusion experiment

Figure 4.38 – Plot of the binary diffusion coefficient as a function of the ratio of guest to host with units of $cm^2 \bullet sec^{-1}$. The free salt (red squares) and co-complex (blue diamonds) diffusion coefficients are plotted as a function of increasing G/H ratio.

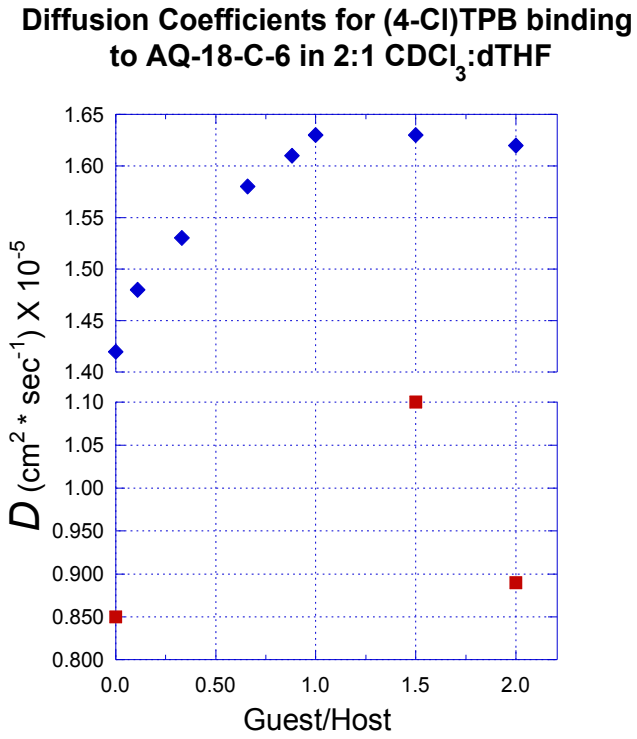

***For 0.0 to 1.0 Eq. K^+, there existed only a binary diffusion coefficient only. Diffusion traces for the excess guest could only be made out at greater than 1.0 Eq. K^+**

In figure **4.38**, a large increase in the value of DHG is observed between 0.11 and 0.88 equivalents of added K^+ that could be considered linear. Where a decrease in the value of DHG should be expected due to the doubling of molecular weight, the value of DHG actually increases through the entire titration (Cameron, 2001). In diffusion, anions travel much faster than cations and the complex diffusion could be governed by the large anion's contribution to the M.W. The maximum rate of change occurs at around X=0.5 equivalents of K^+ added, supporting the formation of a strong 1:1 complex (Chang, 2004). Through the

titration, a 1:1 stoichiometry is confirmed as the cross peaks return for the separate anion species, signifying an excess amount of reagent added. The excess 8 protons at a ratio of 1.5:1 and 16 protons at a ratio of 2:1 are observed in the 2D plane.

Figure 4.39– 2D DOSY integration along the 2D plane showing that the majority species is the 1:1 complex with the (4-Cl)TPB salts.

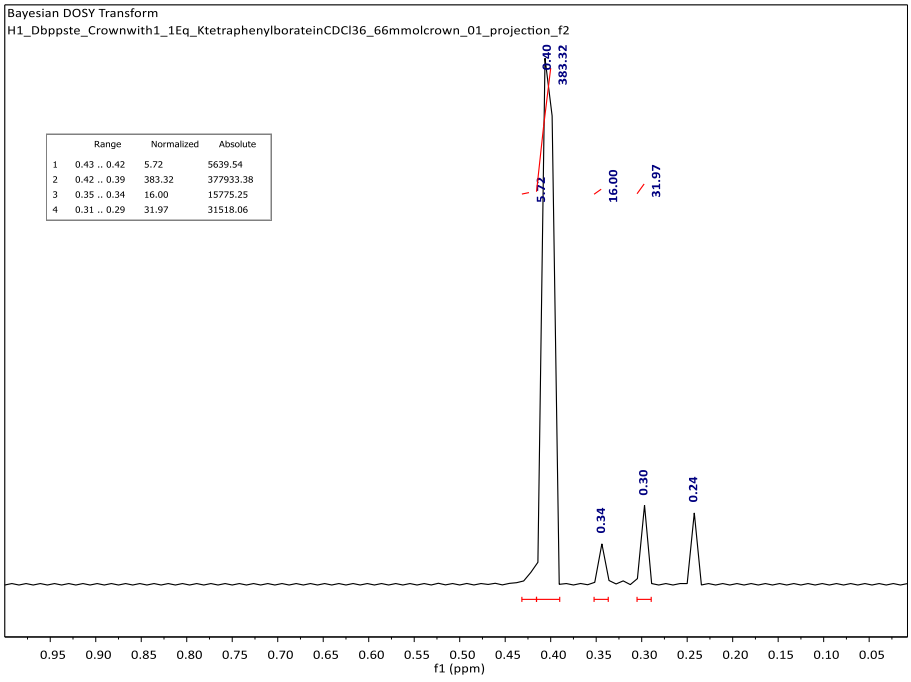

Although not much literature exists for ionic species or their respective behaviors in diffusion NMR, some studies support the speeding up of an ionic complex upon binding. As discussed before, the diffusion coefficient of the TPB anion is assumed because the salt is not soluble in chloroform. This effectively means that at [Host] =0, the salt does not have an effective diffusion coefficients because it is by definition not in solution. By creating a carrier-salt complex, diffusion becomes facilitative by the crown ether and should be

governed by the faster moving particle in the complex, the anion. In effect, a ditopic receptor is created that hosts both the cation and anion as will be discussed in the context of molecular modeling results in Chapter 6 (Gargiulli, 2009).

2D Competition Experiments with Co-Hosts 18-C-6, AQ-18-C-6

As discussed in Chapter 2, the primary effect of diffusion and the implications on reactive-flux can drastically alter membrane property and speed processes that in the past have proven to be the most rate limiting. A series of NMR experiments was set up to analyze the binding of AQ-18-C-6 with equimolar amounts of 18-Crown-6 was chosen as an internal reference as it is by far the most studied and well characterized crown ether. Physical properties have been recorded and stability constants measured in a variety of organic solvents using differing salts and multiple different characterization techniques such as ion-selective electrodes, electrochemical measurements, calorimetry, fluorescence, extraction and UV/Vis; all which of produce different values of the binding constant for the same crown. Like properties such as the diffusion constant, can also show different behaviors, even complete selectivity reversal behavior from liquid behavior when transitioning to the solid state (Yajima, 2010).

Basic 2D DOSY Methodology:

In this series of experiments, 18-C-6 ether along with AQ-18-C-6 ether are loaded into an NMR tube at the same concentration (ex. 5mM each = 10 mM total crown concentration) along with the guest salt at the same concentration as the crown ethers (5 mM). This effectively sets up is a competition between a well-known ionophore with a known binding

constant to aid in standardizing the unknown compound relative to 18-C-6. The diffusion constant of the equilibrating system is measured at each 24 h interval and recorded along with the 2D integration along the free/complexed diffusion lines. The relative K value between the 18-C-6 and AQ-18-C-6 is calculated as the ratio of the complexed diffusion integrals relative to the number protons present in the uncomplexed molecular integrals; normalized to the total uncomplexed carrier proton concentration.

Different surface tensions at interfaces in concentrated gradients causes convective instability due to Marangoni convection.

The type of the hydrodynamic instability is governed by the alkali metal expressed via its stability constants for the complex formed. More stable complexes trigger a higher precipitation, thereby favoring a Raleigh−Taylor instability. Complexes with a lower stability constant induce Marangoni cells which show disorder at the interface. Depending on the confinement of the experiment cell, the fluid motion can also follow a back-and-forth movement.

As shown in figure are the recorded values for the aforementioned procedure using triflate salts of both Na^+ and K^+ in isolated experiments. In the recording of the diffusion-constant measurements from the competitive experiments, the diffusion constant of the AQ-18-C-6 changes markedly while the diffusion constant of the 18-C-6 complex exhibits hardly any change at all in the presence of K^+ or Na^+ triflate in d_6DMSO. The integrals over time also begin to favor K^+ and the complex begins to speed up with increasing integration.

Figure 4.40 – 2D DOSY of equimolar AQ-18-C-6, 18-C-6 and K(4-Cl)TPB (5mM)

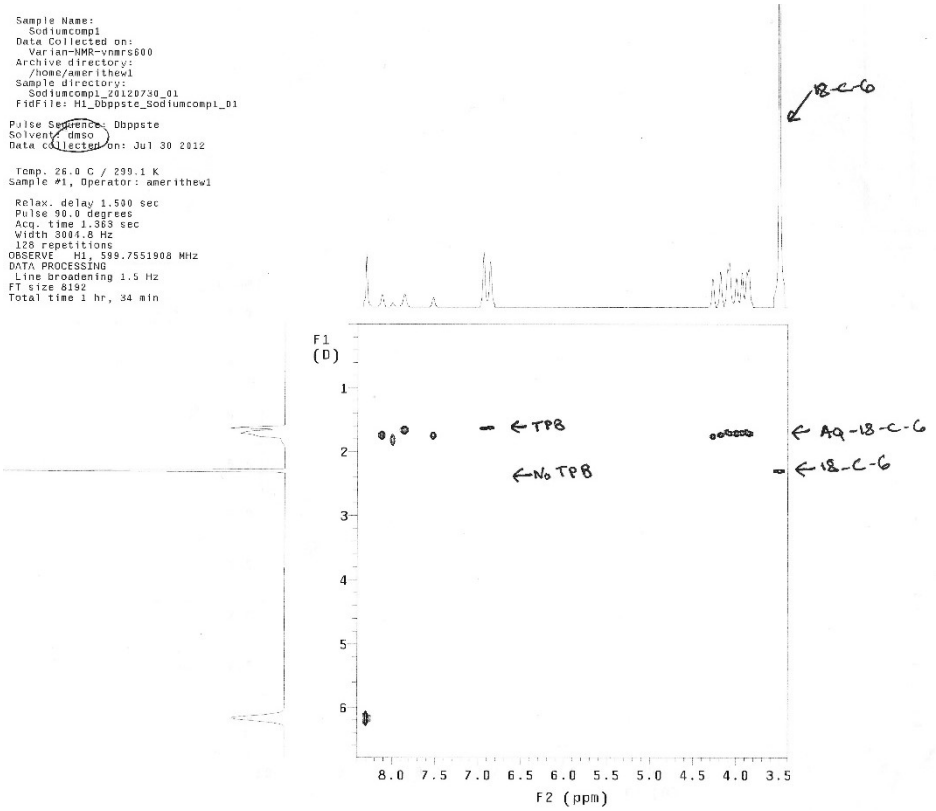

Potassium 4-Chlorotetraphenylborate

In the experiment where K(4-Cl)TPB is used as the K^+ source, *all* recordable traces correspond to strict formation of a 1:1 structure with the diffusion line running along the AQ-18-C-6 diffusion line, indicating with $\leq 10^5$ M^{-1}(limit of detection) certainty value that none of the standard 18-C-6 is bound to the large tetraphenylborate in any stable complexing mode.

The spectra for these experiments could be clearly deciphered. The ensuing experimental methodology could be used to qualitatively describe molecular recognition events and to calculate general affinity ratios for unknown complexes by using the integration ratios against a standardized complex (18-C-6).

Utilizing 2D DOSY spectroscopy, spectra were recorded immediately (≈3min), followed by acquisition of the same complex after allowing the NMR tube to equilibrate in a desiccator under Argon for 72 h. 3.48E-07 and 3.42 E-06 for the borate salt

Mass Spectroscopy Studies

Gas-phase affinities are generally used as qualitative markers of complex stoichiometry. In addition, much can be learned about the stability and structure of the complex in the solution phase (Frański, 2010). Taking into account the mixed-ligand effect from the source ion ($Na^{+)}$, we took extra precaution by preconditioning the Electrospray Ionization (ESI) with pure acetonitrile for 1 h. This proved effective for removing Na^+ and Cs^+ from the detector and spray lines. Competing in the gas phase and assuming M/Z counts per second (CPS) ratios correspond to the quantitative amounts of 1:1 and 2:1 stoichiometric K^+ and Na^+ structures, one can deduce the relative selectivity and stability of the complex.

ESI-MS is the preferred method for samples that are volatile enough to become vaporized under high vacuum in the gas phase once bound to a cation. The stability of the solution structure of the complex in the organic phase can be assessed by performing dilutions prior to sample injections, varying the solvent polarity to determine the lipophilicity of the complex and lastly, running competition experiments with known standards as mentioned before.

General procedure for Mass Spec Analysis

To confirm the predominant stoichiometry of the 1:1 mole ratio studied utilizing Job's Method, crystals of the AQ-18-C-6 complex stoichiometric ratio (7 mg) were recovered by slow evaporation of the solvent over three days and washed 3X(1mL) cold, dry $CHCl_3$.

The crystals were then dried under high vacuum for 48 h. to remove all potential solvent. The highly chromogenic bright yellow $K^+ \cdot H_2$ complex dissolved readily in methylene chloride, a solvent that which the uncomplexed crown ether has very little to no solubility. This allowed for ease of obtaining high-resolution ESI-MS due to the high volatility of this particular solvent. The flight efficiency of the sample was calibrated and the results tabulated and interpreted by high resolution Mass Spec Integration counts per second (CPS) versus the control matrix ion, Na^+ which was checked and found to have the same flight efficiency as the K^+ sample.

Figure 4.41 – Table of calculated affinities of cooperative versus uncooperative self-assembly equilibrium processes analyzed by ESI-MS$^+$ (Frański, 2010)

Stoichiometry G/H by Mass	Concentration (μM)	*K_2+K_3/K_1 (α)
1:1 L_1:K(OTf)	8.0 μM	3.28
2:1 L_1:K(OTf)	0.8 μM	8.17
3:1 L_1:K(OTf)	80 nM	0.14

***Calculated by integration of counts per second (CPS) of the absolute ion count**

****ESI-MS was recorded on a Waters Micromass QTOF II. Parameters: Capillary: 2.00 kV, cone: 2.0 V, coil volt 2.00 V, source T: 80˚C, desolv T: 100˚C, flow 10μL/min. Data was processed with MassLinks V 4.1.**

Figure 4.42 - Spectra 1 of 3 – Mass spectrometer analysis of Crown 1:2 complex in CH2Cl2 at 8 μM.

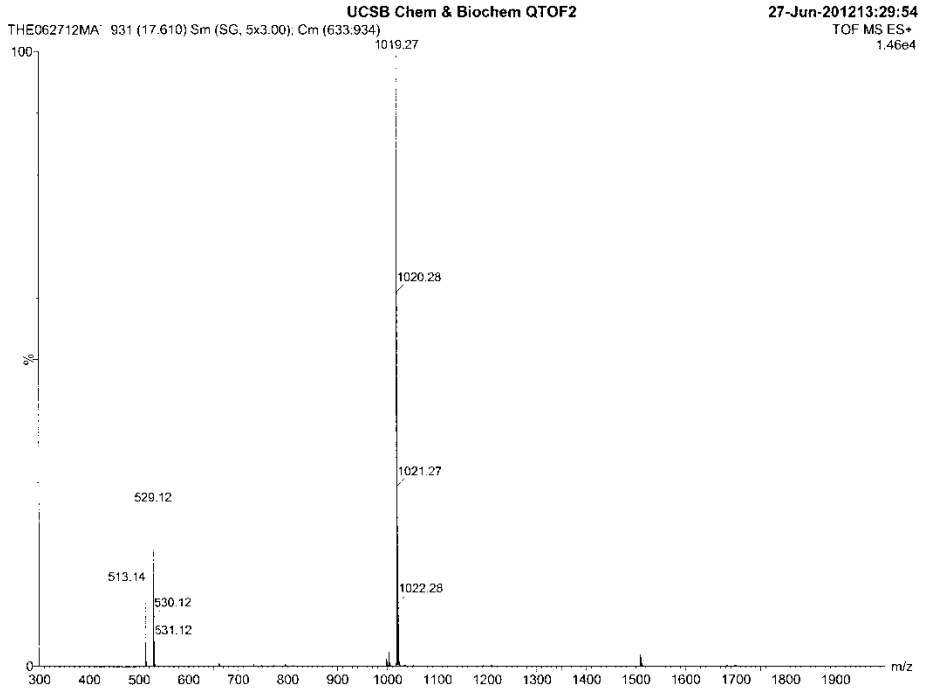

Figure 4.43 - Spectra 2 of 3 – Mass spectrometer analysis of Crown 1:2 complex in CH_2Cl_2 at 0.8 μM

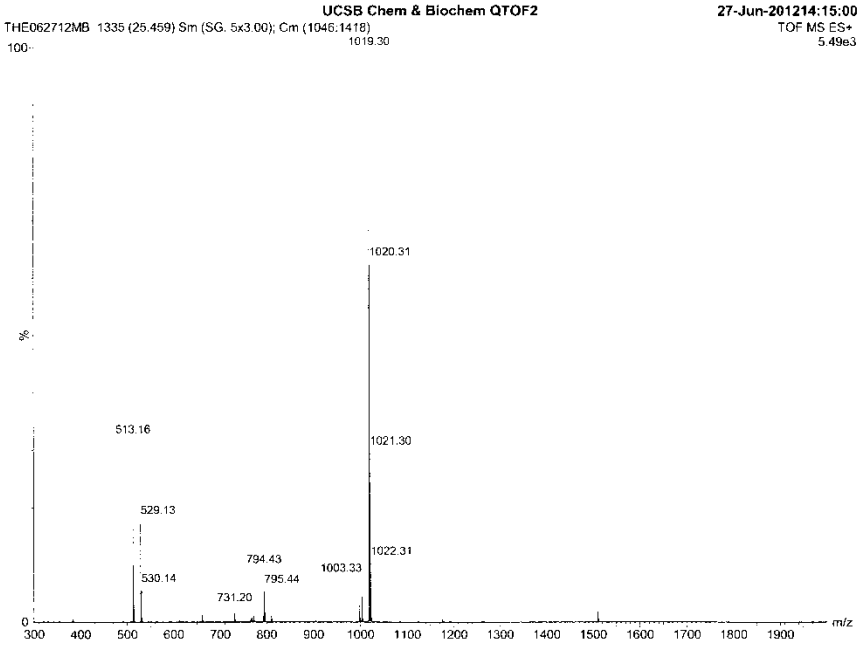

Figure 4.44 - Spectra 3 of 3 – Mass spectrometer analysis of Crown 1:2 complex in CH_2Cl_2 at 8 nM

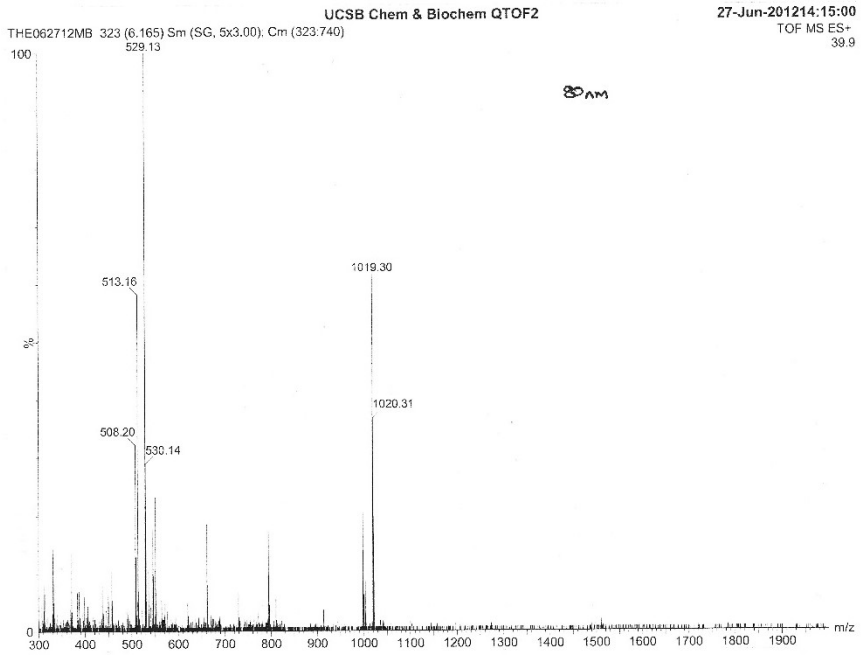

Shown in the following three sets of spectra are the existence of at least three equilibrium states in CH_2Cl_2; a 1:1, 2:1 and a scarce amount of 3:1 complex observed at higher sample concentrations (8 μM). Access to these equilibrium states has been shown in groundbreaking work to function as NAND logic gates (a NAND gate is one that produces a "false" response only when all inputs are true) which can be controlled by different inputs; in our case by K^+ salts with different size anions (Kim, 2013).

Electrochemistry

The cyclic voltammetry (CV) measurements conducted with 5 mM AQ-18-C-6 in anhydrous Dimethylformamide show three distinct redox processes occurring at -0.54 V, -1.30 V and -1.46 V as measured as a function of the half wave potential versus standard ferrocene. Upon the addition of potassium hexafluorophosphate, the first reduction of the crown shifted to -0.27 V and the second reduction increased to -1.36 with no tertiary processes observed, most likely a result of 2:1 and *I* max -18.6 μA.

Figure 4.45 – Current/voltage of uncomplexed Host Crown AN-B-18-C-6 in anhydrous DMF acquired at a scan rate of 10 mV/sec with 100 mM tetrabutylammonium sulphate (TBAS) supporting electrolyte.

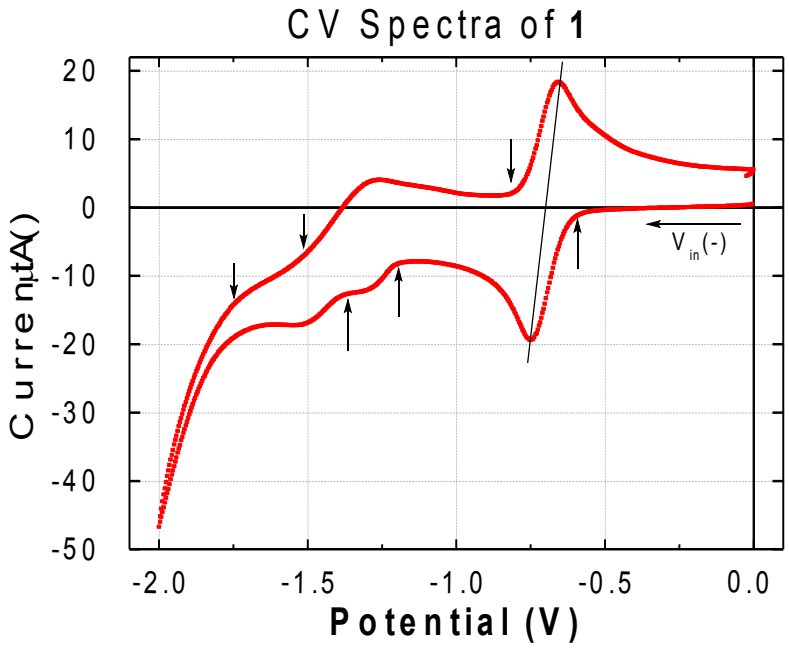

Figure 4.46 – Tabulated Reduction/Oxidation wave location from figure **4.34** above.

E_{RED}	E_{OX}	$E_{1/2}$
-0.59	-0.81	-0.70
-1.21	-1.51	-1.36
-1.40	-1.76	-1.58

Although the pH was not controlled in this experiment, Batchelor-McAuley did a number of pH dependent studies which showed that a 0.3 mM HCl solution was needed to observe a fully reversible oxidation/reduction peak and found that an increase in pH shifted the redox peaks to a more negative potential (Batchelor-McAuley, 2011). Although acid was not used in our experiment, one can clearly see three distinct reduction peaks corresponding

to the semiquinone along with reduction to the monoprotonated quinol form. The peak trace duration was 20 scans with 3 prescans and was highly reproducible. Refer to figure **4.46** for the peak data and figure **4.45** for the C/V diagram.

Figure 4.47 - Determination of the Equilibrium Constant for the 2:1 system utilizing triflate salts and 1:1 system using the tetraphenylborate salts.

Host/Guest Ratio	Method	Log K_1	Log K_2
1:1	**Computational**	**2.45**	
1:1	**Computational**	**3.13**	
1:1	**^{1}H NMR**	**2.11**	
2:1	**^{1}H NMR**	**3.28**	
	ESI-MS	**3.28**	**8.17**
1:1	**DOSY**	**7.14**	

Absorbance Spectroscopy

Figure 4.48 – Graph of the absorbance of the found complex at 303 nm as a function of K^+ concentration

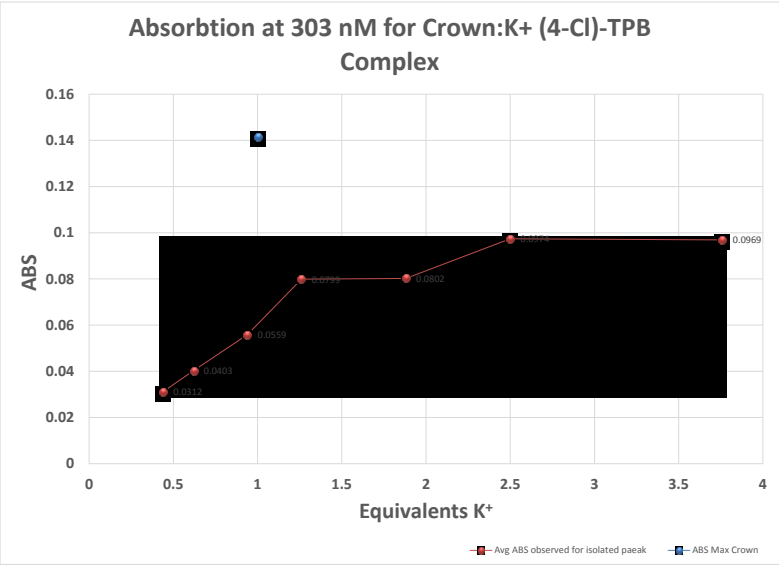

Shown in figure **4.48** above, the absorbance band at 303 nm was monitored as a function of guest concentration showing the maximum as a blue dot corresponding to the standard response at that wavelength. The plot rises steeply and then levels out at 0.08 ABS units with non-specific absorption attributed to excess K (4-Cl)TPB present in the solution. This would suggest that the complex is 1:1 in stoichiometry as the molecular weights of the crown and borate are within 4 g/mol of each other and their extinction coefficients are also comparatively similar (See supporting for extinction coefficient standard curve)

Figure 4.49 – Absorbance of the newly formed complex corrected for excess salt to give the new pure spectra of the complex. The absorbance at 303 nm was followed and deciphered to correspond to the newly formed complex.

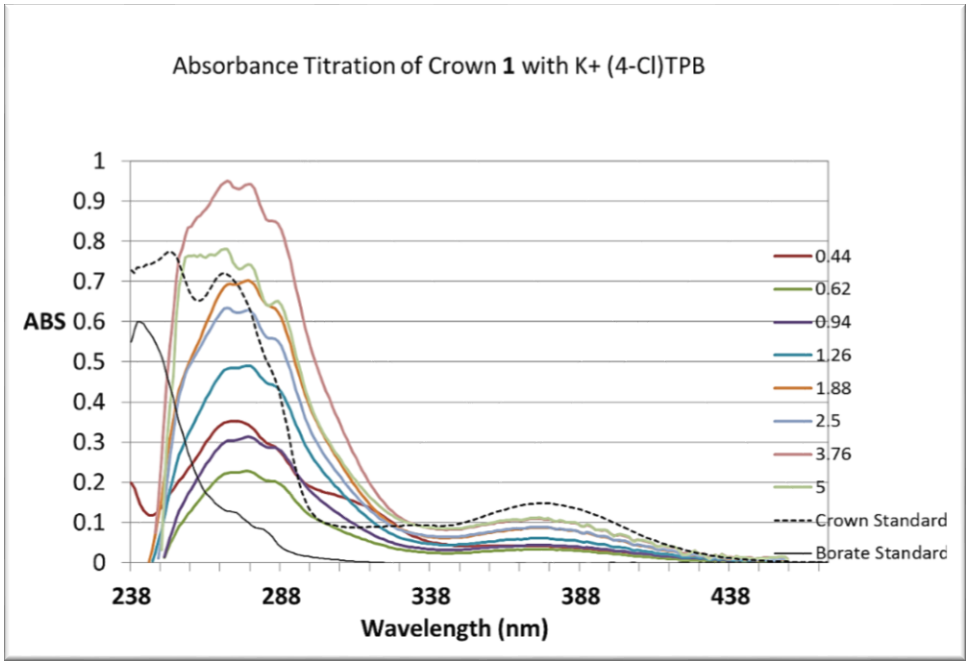

Figure **4.49** above shows the change in the absorbance (with the background due to salt subtracted) and is also modeled on the next page as a 3D mesh graph for clarity. What is observed is a higher value of the extinction coefficient of the newly formed complex which may be a result of charge-transfer complex formation (Conners, 1987). Charge-transfer complexes tend to photo bleach the spectra, which may account for the initial drop in absorbance through the addition of 1 Eq. of the K(4-ClTPB) salt as shown more clearly in figure **4.50**.

Figure 4.50 – 3D absorbance spectra with the relative peak shifts from the standard indicated by the colored arrows. The standard borate and AQ-18-C-6 are not included in this mesh plot for clarity.

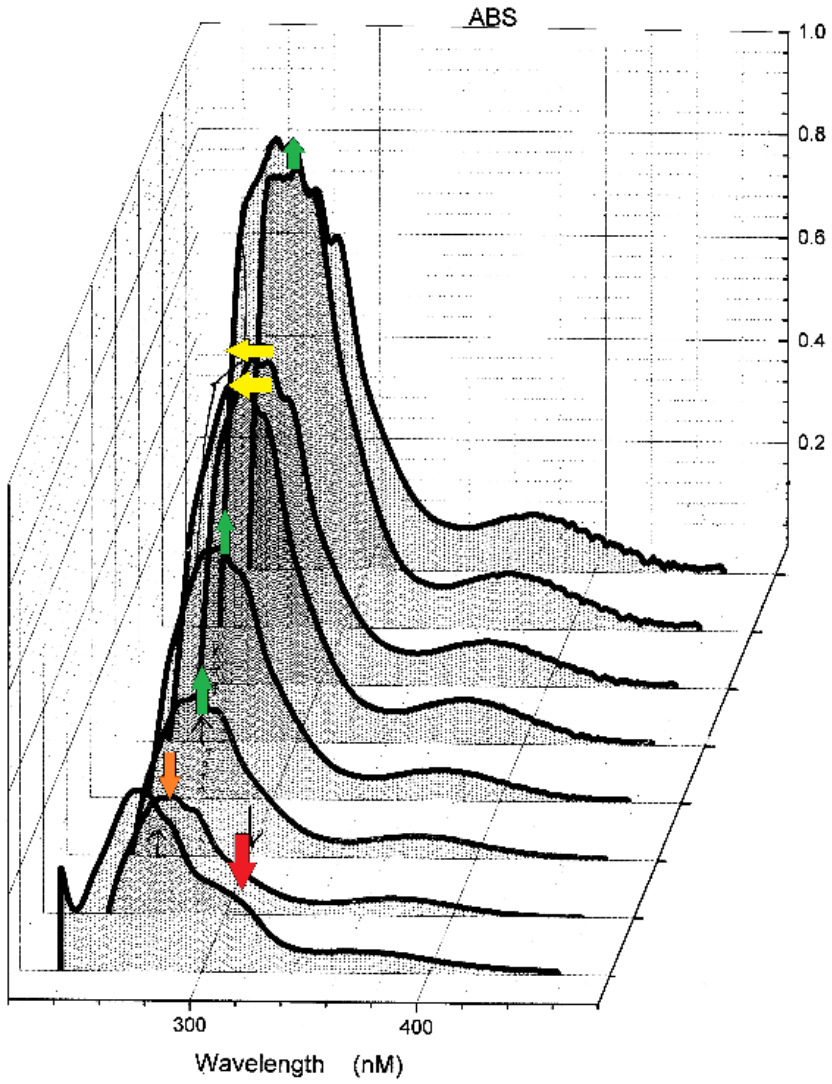

When fit to a global regression model (figure **4.51**) using the least squares method as before for the calculation of the binding constants for the ^{1}H NMR titration data, the binding constant was found to be $K_1 = 48 \cdot 10^3\ M^{-1}$ and $K_2 = 21 \cdot 10^3\ M^{-1}$. We observe now that $K_1 > K_2$, reinforcing the hypothesis of differential self-assembly due to anion size.

Figure 4.51 – Least squares fit of data from figures **4.47, 4.48**

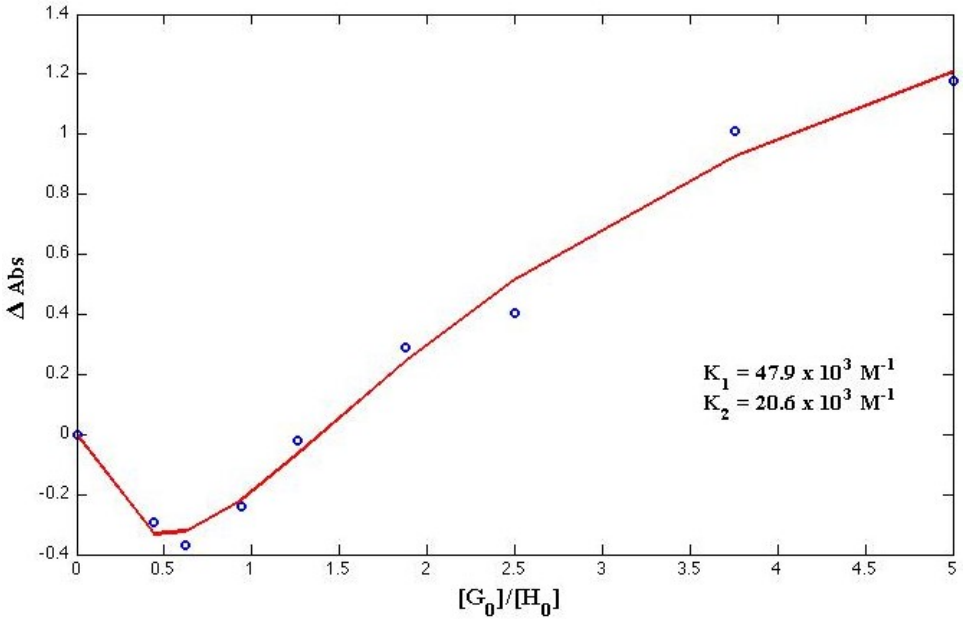

Upon substitution of the two hydroxyl groups in the 1,2-dihydroxyquinone framework, a large blue shift in the absorbance maximum is observed. The absorption maximum as measured for 1,2-dihydroxyquinone in methanol is 431.6 nm and when substituted blue shifts to a lower wavelength of 249.0 nm (Cysewski, 2012). Baram Et al. observed reversible charging of aromatic building blocks in photo functional supramolecular fibers that was postulated to be a result of Π-anion back bonding which could be the case with our anthraquinone (Baram, 2008).

XPS Spectroscopy of Alumina nanopores, functionalized SiO2 substrates

One of the most prolific methods of surface analysis of thin films, functionalized materials including organic and inorganic coatings, dyes, metals, etc. can be analyzed by a technique called X-Ray photoelectron spectroscopy (XPS). Each bond has a characteristic

binding energy and when excited by X-ray radiation, promotes electrons to the excited state where their resonance peaks are detected and composition analyzed. Another benefit of this method is that with use of the Thickogram, one can calculate the thickness of their respective samples very accurately. (Cumpson, 2000).

Figure 4.52 – Top 10 nm XPS spectra of functionalized substrate elemental composition showing an overall increase in organic material deposited.

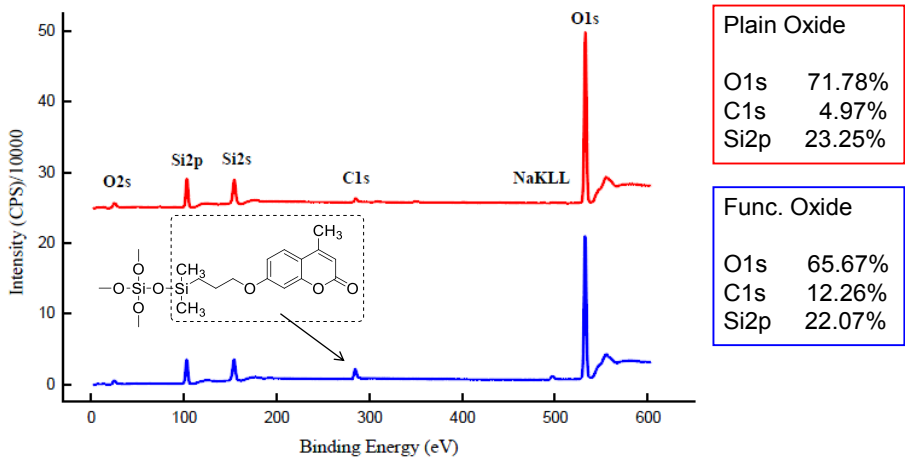

The main detail to look for in an XPS spectrum are the percent compositions that each element makes up and to compare these numbers with a control sample such as the plain oxide used in figure **4.52**. The main elements are silicon and oxygen in an inorganic framework of pure SiO2 lattice. The C1S peak in the control sample arises from thin films of grease that were not removed after the detailed cleaning process or from inherent organic contaminants that have gained access to the structure.

The difference between the control oxide elemental composition and the functionalized oxide are +7.29% C1s, -1.18 Si2p and -6.15 O1s, exactly as we would expect for our test

molecule shown in figure **4.53** below. The carbon content is increasing due to organic carbon framework of the molecule, oxygen dropping because the monolayer is not packed as densely with oxygen as it would be in a cubic lattice of SiO_2 and silicon showing a slight decrease for the same aforementioned reason.

Figure 4.53 – Detailed expansion of C1s region of the functionalized substrate

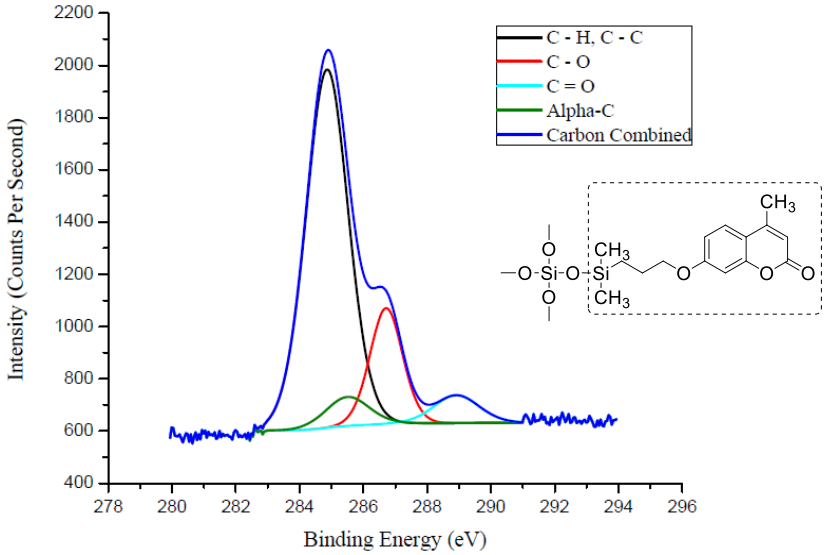

Figure 4.54 – IR spectra of functionalized quartz substrate

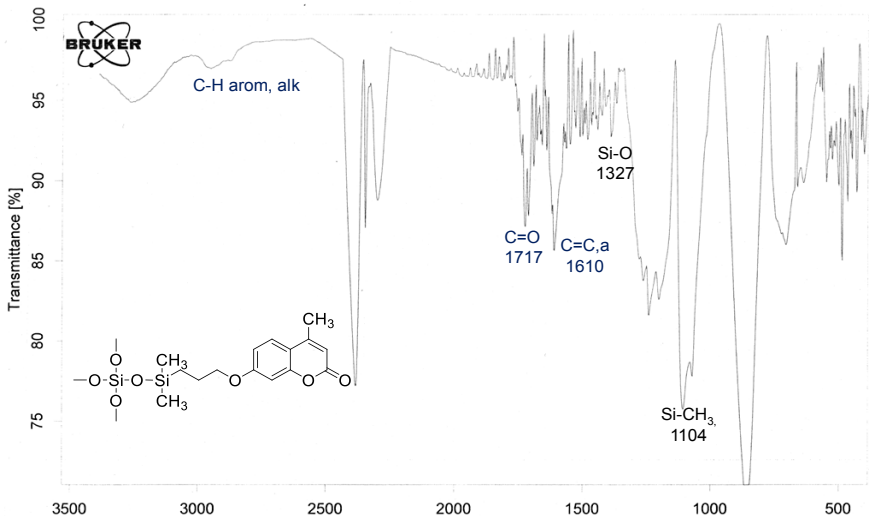

The functionalization procedure was followed with slight modification (see experimental) and was carried out successfully with the homemade 4-methylcoumarin mono-ethoxy silane with the confirmed XPS spectra showing which demonstrated monolayer formation in accordance with the Thickogram of 1.42 Å (Cumpson, 2000).

In figures **4.52** and **4.53**, the overall increase in carbon content versus the control cleaned slide are shown. The quality of the SiO_2 substrate and whether sodium borosilicate glass or pure quartz crystal is used determines the baseline for comparison of substrate functionalization. Whereas quartz has minor amounts of intrinsic defects, borosilicate glass is rich in the minerals Na^+, $Ca2^+$ and Cl^-, contributing to a low melting point and higher amounts of defects during the etch process due to "pitting" of regions where the concentration of these ions is high.

Molecular Vapor Deposition of APTES, CPTES

In the case that our molecules using the homogeneous method discussed earlier failed while trying to functionalize the 3D porous array; we would use the approach in which the substrates is first functionalized with non-sterically hindering reactive nucleophiles or electrophiles and later post functionalize the substrates with the appropriate coupling partner. Using the method of Dorvel Et al., the depositions were performed in an MVD machine at UCSB nanofabrication facility. Since both of these were volatile substrates, the gas phase transport should be high and the resulting XPS spectra showed even coatings with the desired molecular dimensions according to Thickogram measurements of the N1S peak before and after post-functionalization. The functionalization within the pore was assumed to be validated as the N1S peak was more intense than reported for non-porous, flat substrate materials.

The significance of these functionalization method and provides a novel use for the aforementioned methodology. Further, it achieved another goal in that a monolayer of thickness 1.42 A was calculated using the Thickogram (Cumpson, 2000) from the XPS which was to be essential to ensuring a uniform pore coating of a single layer in thickness with a controllable tether length of perhaps, alkyl type-spacers.

Kinetics

Figure 4.55 – Simple one-step complexation and resulting electrostatic potential map showing almost complete encapsulation of the target ion.

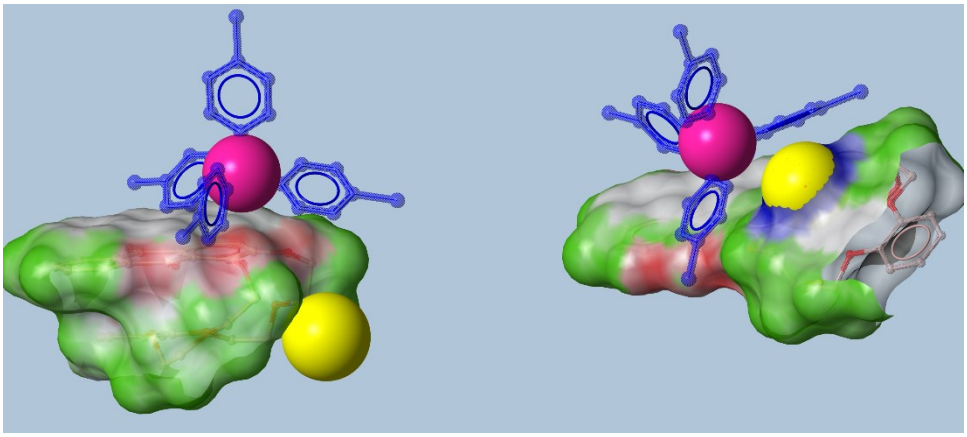

The kinetics of K^+ ion uptake with the (4-Cl)TPB anion that is most consistent with the COSY, HSQC, HMBC, NOESY and DOSY data presented thus far is shown in figure **4.55** above and consists of: 1) Breaking of the face-to-face intramolecular Π-stacking by formation of new face to edge Π-stack with the borate 2.) Unfolding to the planar confirmation while the TPB anion strengthens its interaction with the Π-system as the unfolding proceeds and exposes more aromatic surface topology for the TPB anion to interact with.

In order to better understand the kinetics of this system, varying amounts of K^+ (4-Cl)TTPB dissolved in pure THF were added at once in a single, microliter portion to a cuvette containing 25 μM Host complex and the signal immediately recorded. and monitored for initial rate constants. The first linear section of each abs/time trace was extracted and slope calculated and plotted in figure **4.56** below. The formation of the 1:1

H/G complex at 302 nm was monitored for kinetic analyses, corresponding to the isobestic point where the complex forms.

Figure 4.56 – Absorbance kinetic plot of [K^+] vs. initial rate constants for the K(4-Cl)TPB/AQ-18-C-6 system

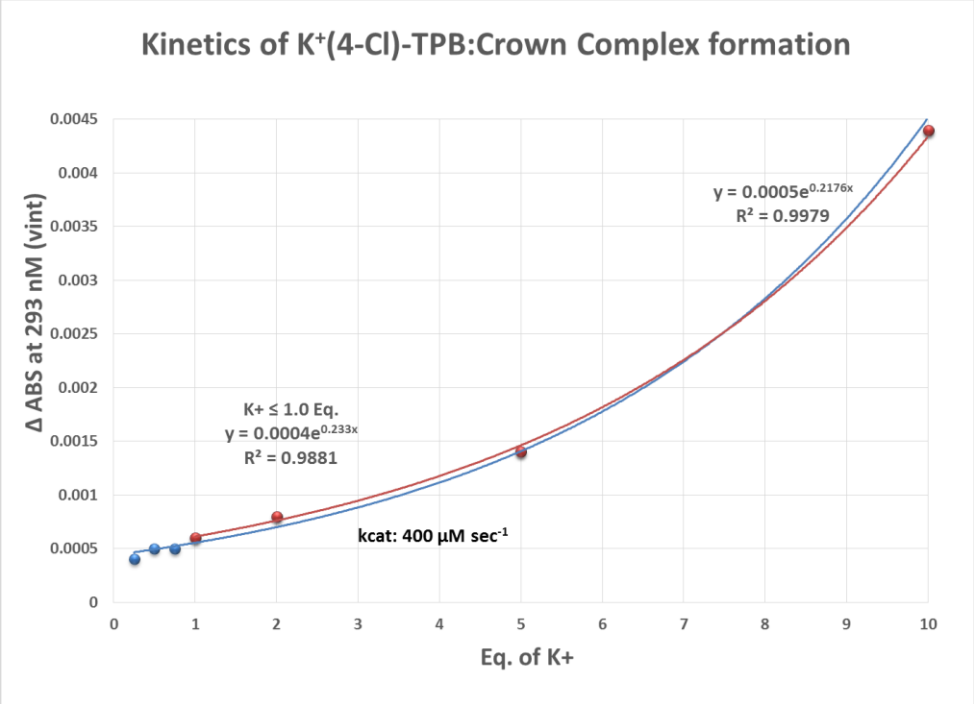

The first point of attention is the linearity of the points through two equivalents of the borate salt, shifting to a concave up graph which would indicate positive co-opertivity (Fielding, 2000), (Connors, 1987). Between zero and two equivalents of salt, the initial rate depends slightly on the amount of salt because therre exists a non-zero slope traversing these points. As you move through five equivalents up to ten, the graph rises sharply due to the excess overlap of the absorbance specturm of the excess borate titrated and the formed complex, increasing the initial absorbtion upon spiking the solution with the solution of

K^+(4-Cl)TPB. This was avoided as much as possible by deducing the complex spectrum by subtration of contributions from free salt and using the molar extinction coefficient (see Supporting Information for more information) Using this method, an isobestetic point was found at 302 nm.

Characterization of Alumina Nanoporous Membranes and Matrix Material

Characterization of Thin Films

The thin films deposited on the nanopore arrays were profiled using Dektak profilometry (see supporting for depth profiles) to test the surface roughness and thickness along a narrow scratch path. This provided information about the relative average thickness of the thin films above the plane of the pore, their shrink volume after curing, as well as their average thickness along the plane perpendicular to the pore axis.

Also these membranes were subjected to a number of mechanical tests which were of overall importance. Ideally, the goal was to have a flexible material that would hydrate upon exposure to water, selectively pulling out K^+ ions by supramolecular ion capture utilizing 18-C-6 cross-linked copolymer hydrogels polymerized by radical polymerization. Also of importance due to the biological aspect of the device was that the gel transition, T_{gel}, remain above 40˚C to avoid any potential melting.

Single Nanopores

Single nanopores were drilled by E-beam lithography by the author's co-workers at the nanofabrication facility at UCSB. The pores were anywhere from 5-10 nm (smaller pores if desired were filled in by atomic layer deposition (ALD)) in diameter and were used in

chapter **5** for transport experiments in the context of phospholipid bilayers for interpretable results.

This section aims to examine the resulting anodized alumina nanoporous membranes before and after the anodization processing step. The critical dimensions, periodicity, and density will be examined. Also discussed will be the characteristics of the thin films and their physical properties such as degree of swelling, Dektak profiling, as well as the consequence of defects on electrochemical pore sensitivity will be discussed. Characterization of the resulting nanopores in terms of their morphology, size, pore density as well as post-functionalization with the filler PEO matrix material synthesized in Chapter III.

Figure 4.57 – A silicon wafer freshly coated by E-beam vaporization of aluminum. The highly blue color of the Si wafer has disappeared and a mirrored finish of Al(s) has been deposited.

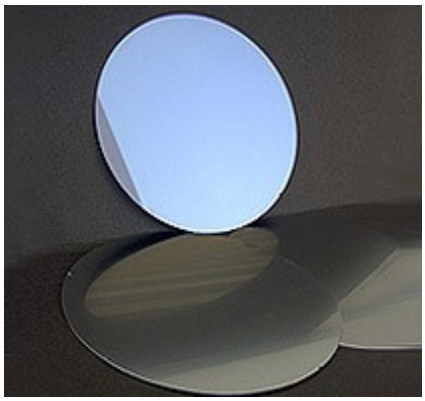

The deposition of aluminum can be performed by many different methods including sputtering, thermal evaporation and E-beam deposition, with the latter being the preferred

method of choice for simplicity of processing and maintenance of sample purity. The highly polished aluminum-coated Si wafer shown in figure **4.57** is an example of an ideal E-beam deposition of aluminum for our process.

After the deposition, the anodization process is carried out with the best results eliciting from the use of 6% H2SO4 at 1˚C for 1.5 h. with a working voltage of 10 V and I_{max} of 100 mA.

Figure 4.58 - A diced chip with a nanoporous array formed from the anodization of Aluminum to form alumina (Al_2O_3) embedded with nanopores.

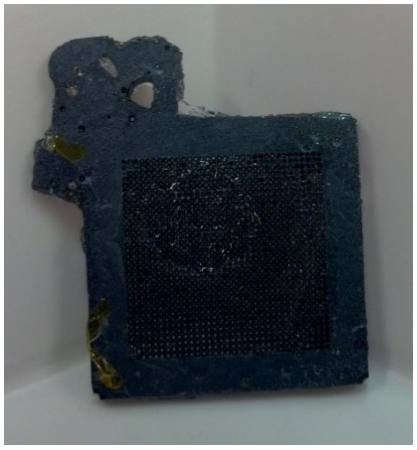

Comparing this method against using phosphoric (Wolfrum, 2006) or oxalic acids (Sulka, 2009), this method proved to produce the smallest pores (8-15 nm random) but also formed the most chaotic metallurgic characteristics with pore spacing characterized as random instead of the ideal ordered domains we were looking for. Upon backside etching to open the pores with phosphoric acid in a custom-fabricated chip holder, the anodized pores tensile strength went down markedly due to the loss of Si (s) from the supporting wafer. This made

for very delicate handling of the chips and many were found to have cracked due to the stress of the backside opening and loss of material upon etching. This really was not that big of an issue as only a small cross-section of the alumina chip would be used in the testing.

Figure 4.59 – XPS Spectra of APTES functionalized alumina nanoporous membranes

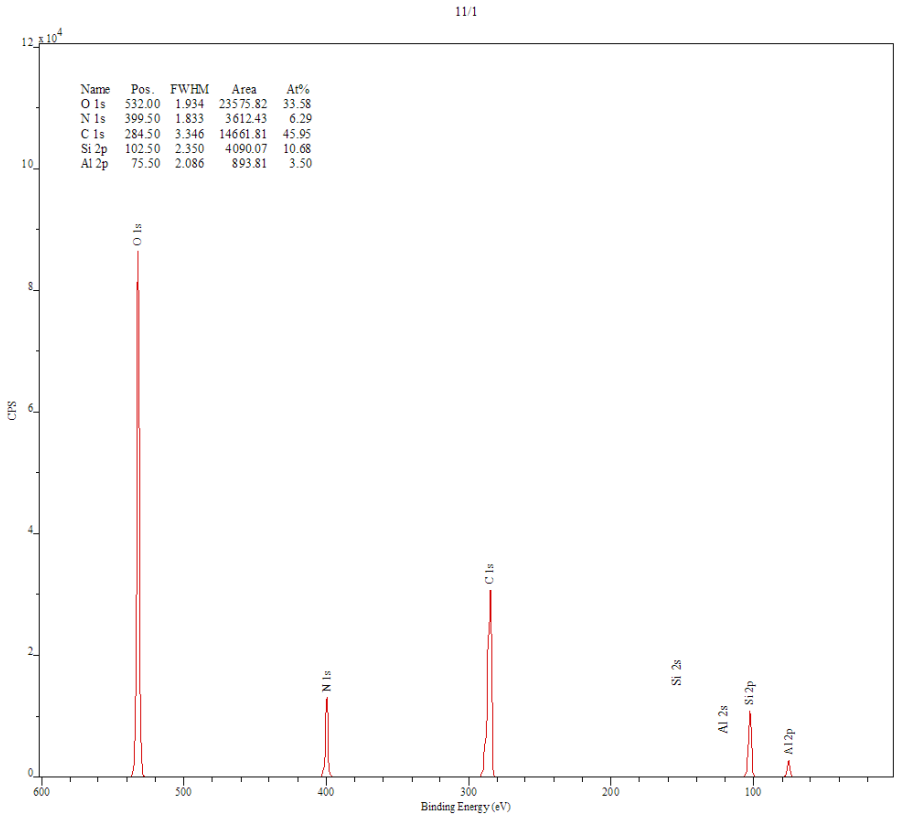

Figure 4.60 – XPS spectra of Spin-Coated nanoporous array with PEDOT:PSS semiconductor.

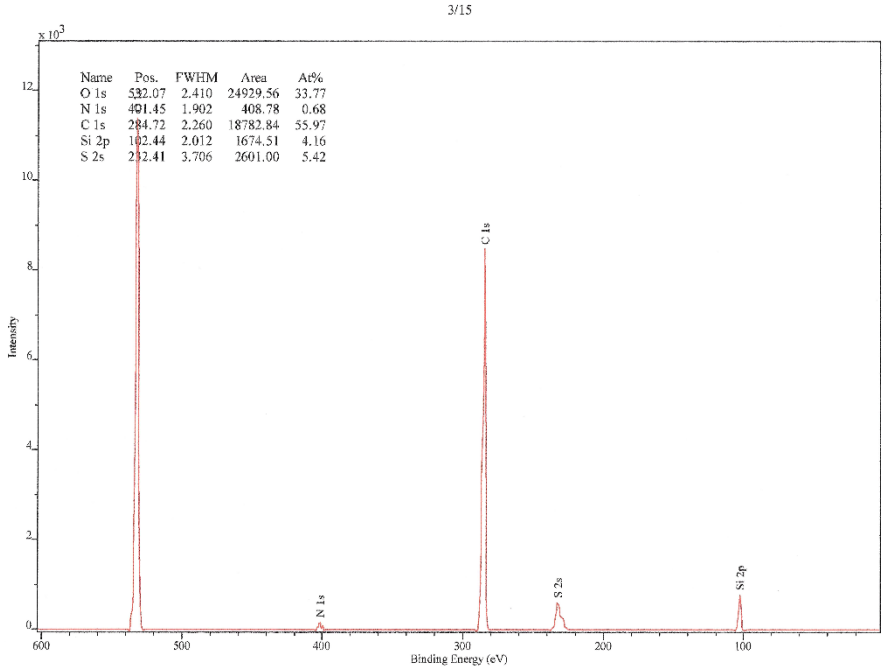

Figure 4.61 – XPS (C1S) Spectra of cyanoacrylate functionalized alumina nanoporous membrane

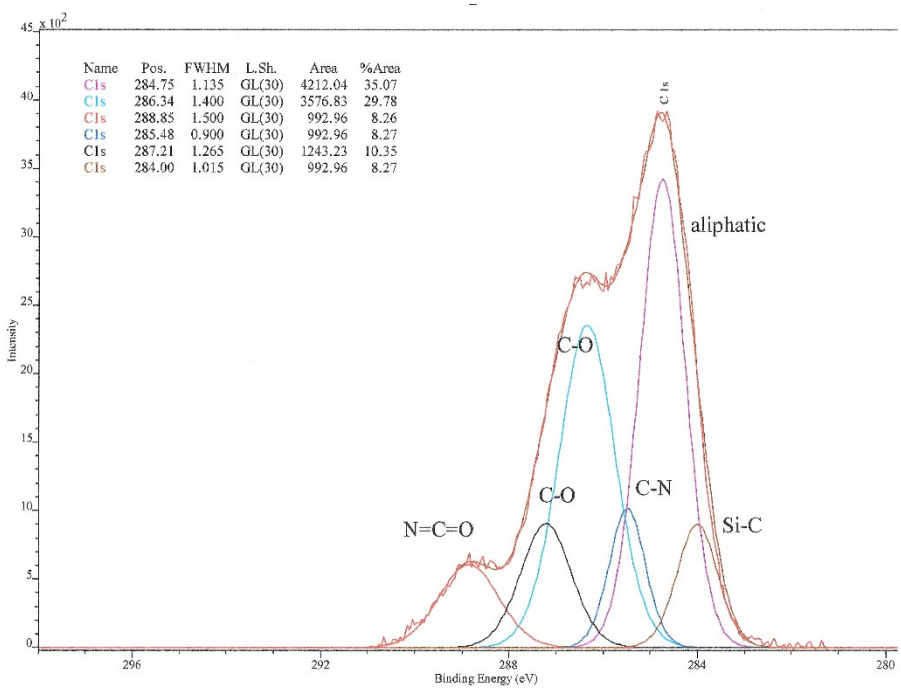

Figure 4.62 – Electron microscopy image of the nanoporous membrane showing pore sizes to be around 90-100 nm in diameter.

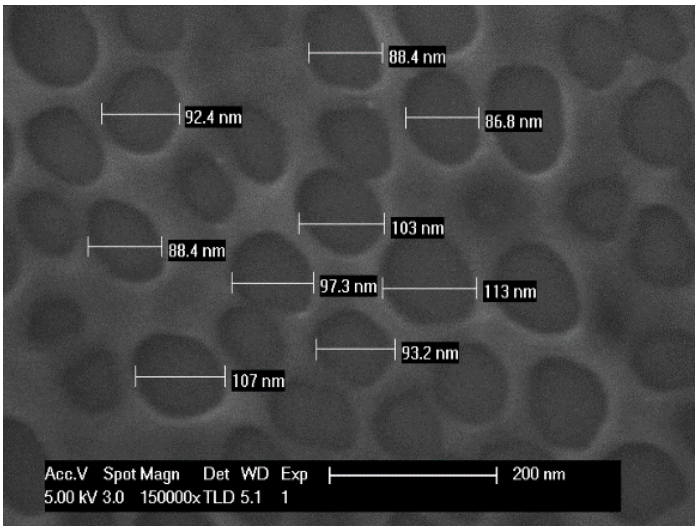

Figures 4.63 – Cut away profile of AAO nanopore showing the conical etching along with a crack through the membrane layer

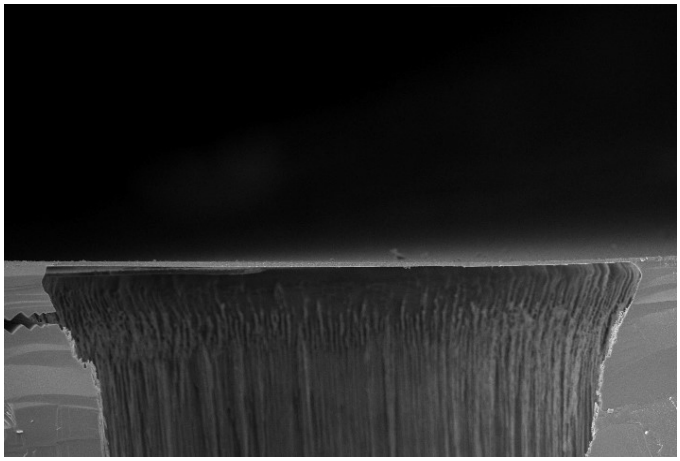

Figure 4.64 - The surface roughness and grain boundaries are clearly visible.

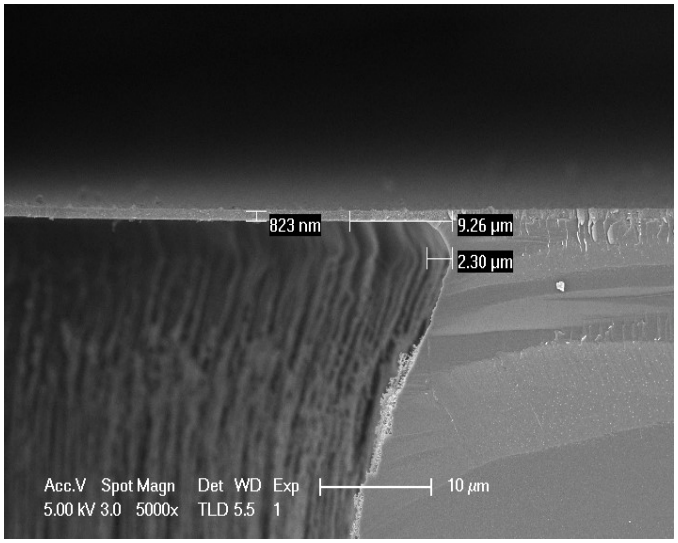

Figure 4.65 – Single nanopore filled with the material described in the experimental section of this manuscript. The filler consists of 25-30 PEO units terminated with triethoxysilane end groups. The cross linking agent is a photo acid generator which produces a smooth glass hydrogel membrane that fills the pore and the window down into the pore.

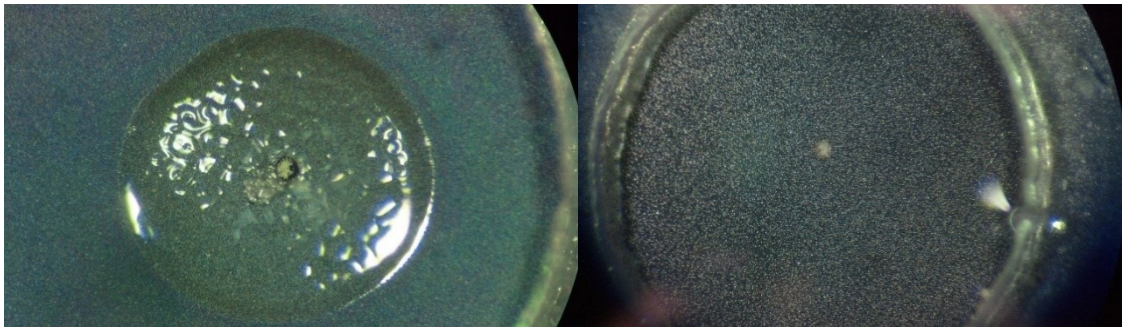

Chapter V - Molecular Modeling of Complexes and Biological Transduction cascades

Objective

This chapter will present the results of the computational simulations that guided the design of the AQ-18-C-6 ether by examining the monomeric precursors and their properties. These results helped elucidate the physical properties that led to a hypothesized positive co-operative binding affinity by the anthraquinone crown ether in the case of K^+ by an allosteric transition from the unbound state.

First, we will examine the structures of the neutral triflate complexes of HQ-18-C-5 to aid in the explanation of the unusual NMR shifts. NMR and Job's plots presented in Chapter **IV**. Next, the semiquinone radical anion as well as the fully reduced hydroquinone diradical are modeled and results compared energetically to the neutral structures. Lastly, the condition where one of the phenols has been deprotonated is compared to the radical ion case to observe any new behaviors and test our hypothesis that radical ion-pairing will increase the K_D of the complex.

Additionally, a model for the self-assembly of synthesized and to be synthesized polymer strands of the synthesized end-blocked 2-propyl-1,8-dihydroxyanthraquinonedimethyl/methyl silyl ether copolymer, the 3-propylbenyl-1,2-anthaquinonedimethyl/methylsilyl crown ether copolymer. Versions of these were also examined with a hypothetical "A" block of polyoxazoline comprising 100% of the "B" block chain length in order to visualize how this assembly would aggregate and self-assemble *in-silico*.

Molecular transport was modeled in rigorous simulations involving a 30 Å model bilayer under a -0.50 V electrochemical bias at 37°C to elucidate the behavior of our complex in a model lipid membrane under aqueous physiological conditions to mimic our potassium pump.

Empiracally, ultra-thin membranes constructed of phospholipid POPC were utilized in ultra-small nanopores to examine transport of K^+ by the mobile crown ether receptor across a span of 30-40 nM. Lastly, ABA polymer was used in a likewise manner in examining the kinetics of self-assembly of the bilayer. Membrane fusion experiments with the formed ABA membrane (d=10-12 nM) were conducted and results presented herein.

Computational Modeling of Host - Receptor Interactions

Molecular modeling is the visualization of macromolecular mechanics that predicts a lowest energy model using imposed physical constraints of chemistry. One of the most extensive areas explored by this idea is the modeling of ion channels (Garofoli, 2003), (Noskov, 2007), (Shrivastava, 2002) and their gating mechanisms (Bernèche, 2005), (Durell, 1998). The field began studying artificial ion channels through nanopores as early as a decade ago (Peter, 2005). While the idea is nothing new of utilizing modeling for the purpose of predicting reaction trajectories, quantum calculations of the reduction of quinones (Wass, 2006) supramolecular assembly processes (Zhou, 2011), predicting NMR spectra from structure, etc.; within the last decade, the computational community is becoming more recognized for its contribution to chemistry with the Nobel Prize in Chemistry awarded in the field of computational chemistry for the first time this past year.

This award acknowledged the significance of the science of computational chemistry by awarding Karplus and colleagues whom which were responsible for development of the underlying physics of the models as well as the basis sets used in the simulations.

These advances in computational computing led to more plausible hypothesis as far as how transport occurs in real biological systems. For instance, in figure **5.1** shown below, transport of a proton and a potassium ion are coupled together through active transport across the membrane in the H^+/K^+ symporter. This is used in the cells of the stomach to generate H^+ ions to make for an acidic environment. The process produces no energy and in fact is coupled to ATP hydrolyses, which uses energy. The energy cost then makes up for itself by generating a proton gradient producing chemical potential energy which provides the means to regulate further ion influx or efflux from the cell.

Figure 5.1 – Transport by "hopping mechanism" in the H+/K+ symporter.

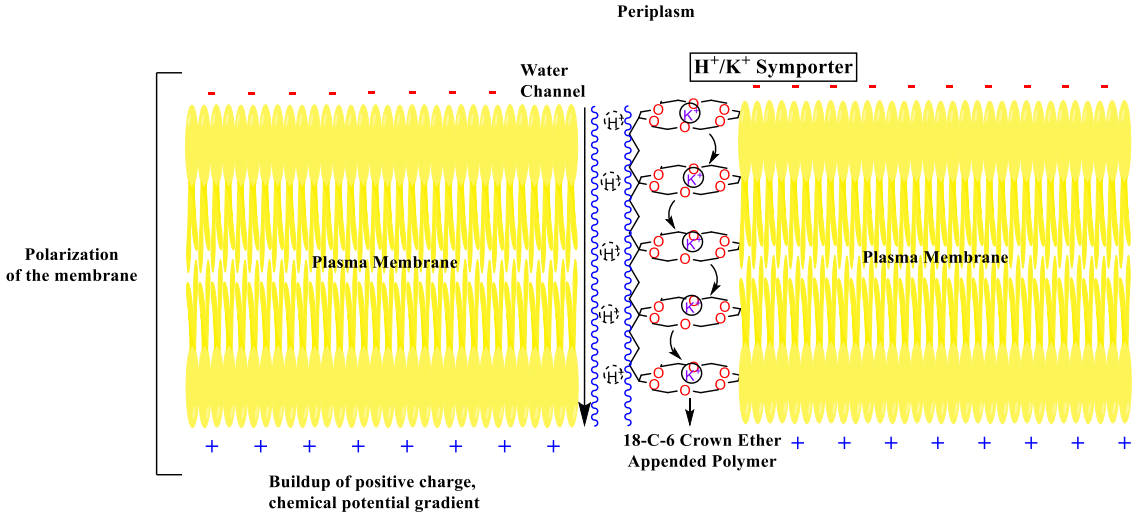

Practical Aspects of Computational Chemistry

In the biological context, devices developed and optimized at ambient laboratory cannot be extrapolated to real biological systems as the increase in temperature decrease in thermodynamic selectivity. As our objective is to design a system that is amenable to various polymeric systems as previously described. Systems that work well at room temperature are not representative of the conditions in the body. It should be understood that transport experiments carried out at 25°C will not give the same result as a transport experiment carried out at 37°C due to the increase in diffusion of all reacting species as a function of increasing *T*.

One area that we can learn much from in terms of self-assembly at varied temperatures is through computational chemistry. One can minimize the energy of a co-complex at a specific temperature and overlay the least energetic conformers to see how the tertiary structure assembles with increased heat at the press of a button.

The error of carrying out such an experiment becomes much higher when you must control the temperature. The computational method only adds preliminary results that convince or refute the scientist to investigate the property empirically. If one chooses to do the experiment first and is not biased toward the data generated from the experiment, computational chemistry can help back theories of what type of phenomenon is actually occurring.

Experimental Methodology

The Monte Carlo Method has been one of the most widely used methods in multi-variable problems where multiple degrees of freedom are available to a particular solution (Stroganov, 2008). It has also found widespread use in predicting tertiary polymer structures (Darling, 2007), ion transport through nanopores (Peter, 2005), the supramolecular assembly of pie-conjugated systems (Hoeben, 2005), drug discovery (Jorgensen, 2004) and in multi-step binding processes (Tochtrop, 2002). Monte Carlo Energy Minimization was used to fix and globally minimize both K^+ and Na^+ interaction with the crown ethers both with and without their respective anions. The aim of doing so was to be able to compare the structures and see what role, if any, the anion had on the self-assembly of the crown supramolecular structures as was performed in the case of the 1,4-benzoquinone crown examined earlier.

Modeling of individual Complexes

With the advent of modern supercomputers with upgraded processors and visual effects, it has become possible to model chemical systems from home desktop computers. Recent computational chemistry has been considered to be one of the most important tools across all fields of chemistry, as is CAD design in engineering and architecture.

Perhaps the most complicated model used in our system was the simulation of ion flux through a lipid bilayer, completed using ICM Molsoft LLC Software package. Due to the ordering of the membrane, self-assembly process and monitoring the flux of ions through the defined special coordinates simultaneously, multi-processor computer resources were utilized to speed up the simulation.

Main objectives:

1. Analyze the Pseudo BQ-18-C-5 uncomplexed and complexed with Na^+ and K^+
2. Analyze the AQ-18-C-6 in it's lowest energy state unbound and provide insight into the mechanism triggering the allosteric shift upon binding of K^+ but not Na^+
3. Analyze Tosylated "B" block redox-active anthraquinone polymer brush for secondary structure characteristics
4. Analyze a hypothetical polymer system comprising siloxanes with pendant AQ-18-C-6 side chains for self-assembly properties and π-stacking.
5. Model the AQ-18-C-6 complex using the biological simulation program ICM molecular to elucidate the transport mechanism though lipid bilayers.

Modeling of the complex in its reduced form without anion

The energies obtained from the 1,4-HQ-18-C-5 crown are much more negative than that of the benzoquinone form. The total energy of the complex (figure **5.6)** is -2.9 kcal/mol for Na^+ and -3.2 kcal/mol for K^+ and even lower for the 2:1 (figure **5.7**) structure observed with K^+. The case of K^+ when modeled had lower energetic conformers of the series; proving to elicit less ring strain while effectively forming a Π-cation interaction. In Chapter **IV**, the NMR and UV-Vis titration of both of these complexes was presented and showed almost an entire parts per million (PPM) shift of the phenolic protons by ^1H NMR indicating strong shielding and deshielding of the hydroquinone protons.

Models obtained without the presence of the anion using MM2 minimization followed by optimization with the CONFLEX interface.

Figures 5.2 – Top left – K+ bound slightly above the plane drawn in by charge-charge interactions with the phenoxides form of the 1,4-hydroquinone **Figure 5.3 –** Top Right – same but out of the plane of the ring when protonated. **Figure 5.4** bottom left – Na+ sits much better within the ring when deprotonated and **Figure 5.5 –** bottom right – sodium bound to the phenoxide or protonated form forms a stable salt/neutral crown complex in the case of sodium.

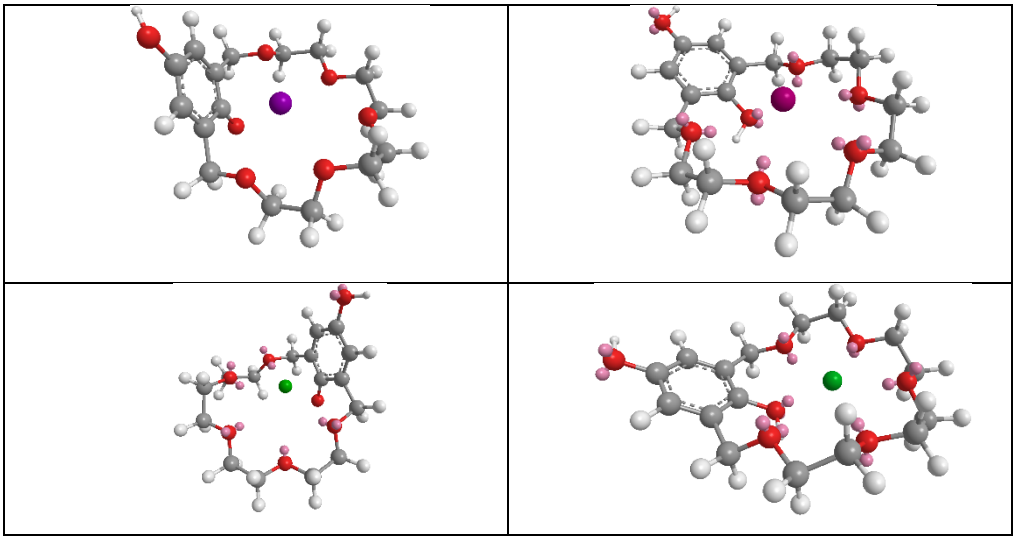

pKa exploitation in dihydroquinones

The pKa_1 of 1,4-hydroquinone ranges between 9-11 and is elevated by 2 pKa units for the loss of the second proton to form the di-anion species (Song, 2011). Thus, under physiological conditions at a pH of 7.4, we would not expect the hydroquinone functionality to exist in its anionic form. Furthermore, sources of alkalinity in the body are scarce as most

disease states are associated with an acidic environment due to increase in metabolic processes which release protons into solution, increasing the pH.

Modeling of the complexes in their radical and di-radical anion states

The BQ-18-C-5 was modeled after undergoing a single electron transfer to the radical anion form (1˙,4-SQ-18-C-5) where 1˙ represents the position of the radical. Comparatively, there is a large change in energy when compared with the hydroquinone forms (figure **5.11**) and this is especially prominent for the Na^+ case. Upon the second reduction, there is only a small increase in binding affinity of the receptor. This would tend to suggest that it is sufficient for the quinone to undergo a one electron reduction in conferring increased binding affinity instead of the much more unfavorable two-electron transfer.

Figure 5.6 - Table of binding energies of complexes showing selectivity for Na^+ over K^+ in each category.

Complex	Binding Energy (kJ/mol) – K+	Log Keq	Binding Energy (kJ/mol) – Na+	Log Keq
1,4-BQ-18-C-5	-1.3	1.69	-3.7	4.45
1,4-HQ-18-C-5	-3.2	3.64	-2.9	3.22
(2:1) 1,4-HQ-18-C-5	-4.3	5.67	N/A	N/A
1˙,4-SQ-18-C-5	-3.9	4.83	-5.6	9.59
1˙,4˙-HQ-18-C-5	-4.0	5.03	-5.8	10.4

Figure 5.7 – Space filling model of K+ inside the cavity of the 1,4-18-C-5 with the intraannular phenol deprotonated. Appreciable Π-cation interactions as well as charge dipole interactions dominate the binding interaction.

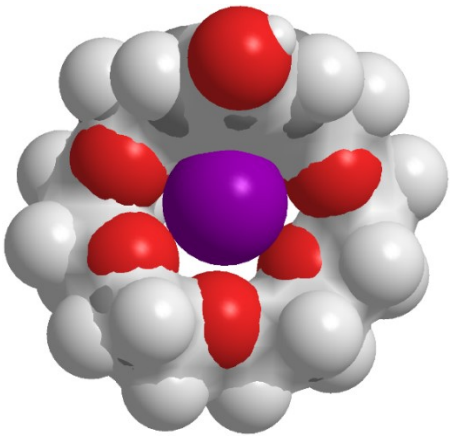

The former results modeled without the presence of the anion gives entirely different results due to the charge density increase on the cation in the simulation. There is no negative charge field to partially shield the positive formal charge of the cation. The most energetically favorable situation arises when the cation binds to the electron-rich crown ether cavity and that is the result observed in figures **5.2 – 5.6** above for 1,4-HQ-18-C-6.

Figure 5.8 – The lowest energy conformers without the presence of the anion is shown as a 2:1 complex in the case of K^+ and **figure 5.9** -1:1 complexation in the case of Na^+

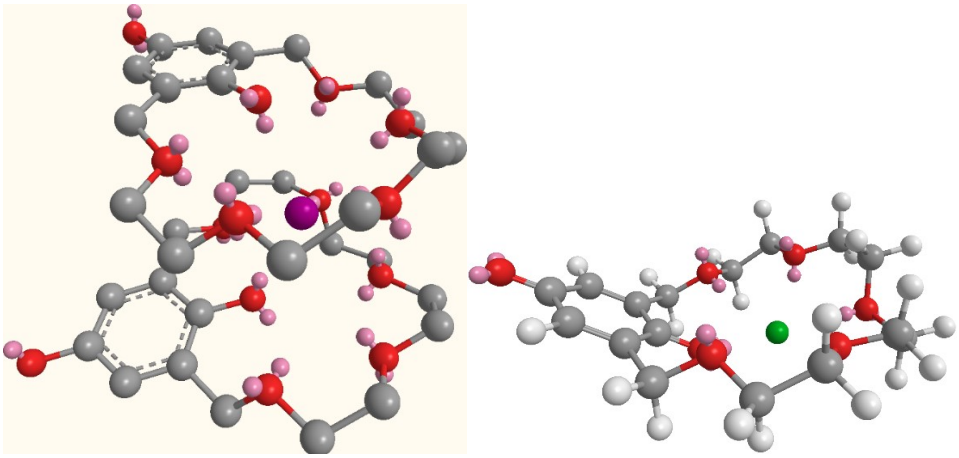

In addition to this stabilization is an appreciable π-cation interaction that further shields charge from the solvent giving an increase stability of this type of carrier, highlighted in figure **5.7**. In figures **5.8** and **5.9** are models of the lowest energetic conformers of both the sodium and potassium compounds modeled as their 2:1 and 1:1 complexes. The potassium complex prefers a staggered 2:1 sandwich conformation with the protons of the phenolic oxygen pointed away and the potassium atom hovering between both planes of the complex (figure **5.8**).

Figure 5.10 – Results from a simulation with 1:1 stoichiometry in the presence of an anion for the case of K^+.

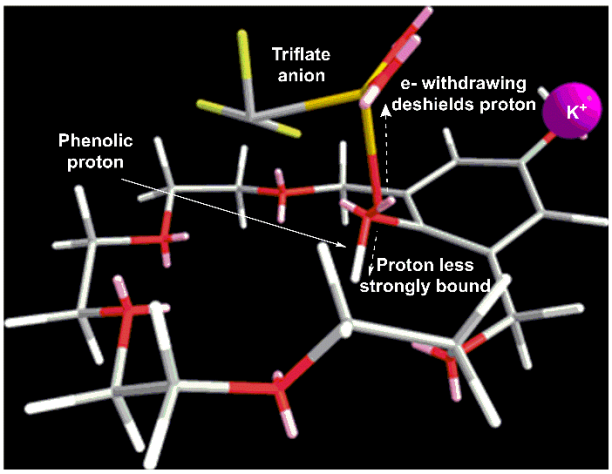

When the anion is included in the simulation, it is observed to play a pivotal role with the lone pair phenoxide anion and anion radicals as shown in figure **5.9** above. This may help to explain the NMR titration results for these compounds, and the large downfield and upfield shifts of the bound proton in each case. Refer to figure **5.9** for a physical description of the phenomenon.

1:1 and 2:1 potassium and sodium triflate complexes with AQ-18-C-6

The anthraquinone crown differed markedly in its 3D structure from the benzoquinone crown ether we just examined. In its uncomplexed form, the crown is folded over on itself to form a strong intramolecular face to face π-interaction between the electron rich diethoxybenzene ring and the electron-poor anthraquinone central ring. The bond distances are 3.43 Å and 3.26 Å, respectively.

Figure 5.11 – MMF94 minimized structure of the anthraquinone crown. The crown makes a very tight intramolecular face to face Π-bond between the electron rich diethoxy benzene group and the electron poor central anthraquinone ring.

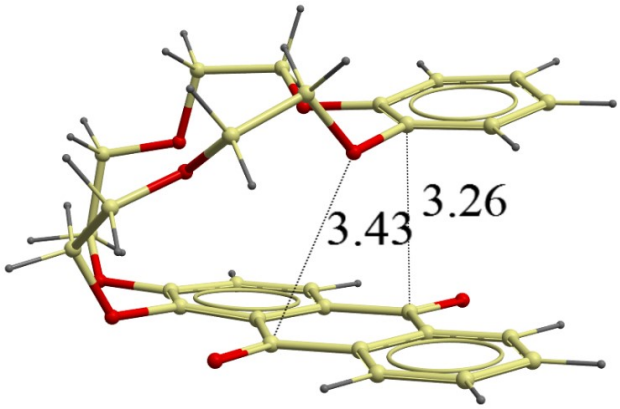

The computational studies carried out on the crown anthraquinone consists of the following simulations and models:

- Model the unbound structure to find the least energetic conformer.
- Simulate the minimization in the presence of K^+/Na^+.
- Repeat the simulations with anion present to examine the influence on supramolecular assembly.
- Model AQ-18-C-6 incorporated into an "ABA" triblock copolymer and examine self-aggregation effects and the formation of bis-crown complexes.
- Design and execute a Monte Carlo simulation of ion permeation with mobile ion carriers through a 30 Å model bio membrane with mobile AQ-18-C-6.

In the modeling of the uncomplexed structure shown in figure **5.12** above we can see that there is a propensity to fold over on itself to form an intramolecular Π network. This is

further promoted by the unfavorable overlap of the lone pairs of the ether oxygen at position 1 with the carbonyl oxygen lone pairs.

Figure 5.12 – Overlay of the positions of the bound sodium and potassium cations in the presence of no anions. The sodium (blue outline) structure is rather contorted whereas the potassium structure is spread out flat, maintaining the expected geometry of a di-benzo type crown.

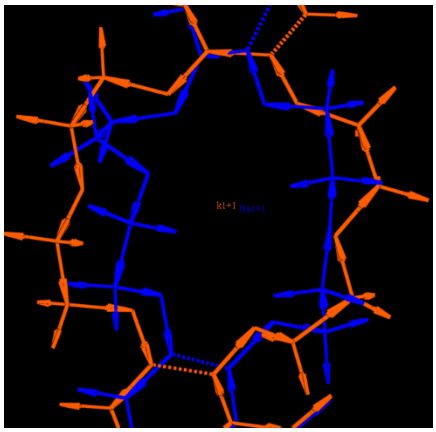

Modeling with Triflate Salts

Molecular modeling of our parent crown quinone was performed to understand the physical properties governing the selectivity for K^+ in the assembly of the complex. With knowledge from chapter **IV** which deduced the stoichiometry of the complex to be 2:1 for small anions in the case of K^+, we concentrated on this model for the majority of our computational studies.

Figures 5.13 (left) – Figure of the 2:1 complex in its most stable form without the anion present and **figure 5.14 -** (right) with the anion present.

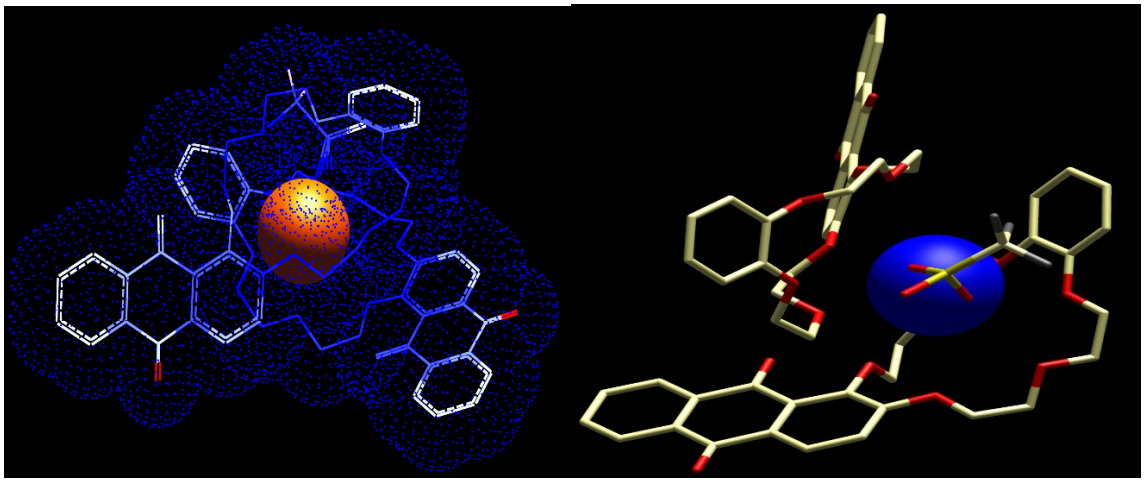

Figure 5.15– Prominent mode of complexation with Triflate salts**.**

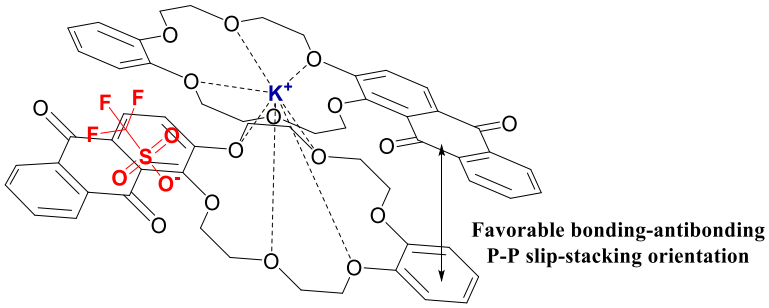

When modeled without the anion present initially; as shown in figure **5.13** above, the comparative overlay of the minimized structures shows the relative positions of Na^+ and K^+ within the ring cavity. Although K^+ does not fit entirely within the plain of the ring, it binds much lower than in the case of the 1,4-benzoquinone examined earlier and more importantly occupies a 4-point coordination with all but two of the six crown ether oxygen's. The propensity for the crown to dimerize to the bis complex once the ligand has bound is further

potentiated by the formation of a 2-fold semi-symmetrical octahedral array, the preferred coordination for K^+ in solution figure **5.14**. In the case of sodium, the coordination is two-fold and contorted, twisting the ring which appears to be too large for Na+ to make these contacts as can be seen in figure **5.13**. No 2:1 structure was observed computationally for Na+ with or without the anion present.

Modeling with 4-Cl-tetraphenylborate salts (4-ClTPB)

After many iterations, it became clear that a 1:1 structure dominated in this particular case due to the stability of the initial complex formed (-16.4 kcal/mol) and the steric hindrance the TPB anion imposed as seated above the entire receptor. The 4-ClTPB anion is tetrahedral in nature and quite lipophilic, contributing to its popular use as a neutral cation exchanger in lipid membrane experiments. The molecule itself has been shown to lower the barrier of activation for the rate limiting step in lipid membranes that is the solubilizing metal cations by ion-exchange mechanisms. The boron in the 4-ClTPB anion is essentially neutral, having an effective charge of -0.11 Hartree when electron delocalization is taken into account. This low charge density allows the anion to separate into a solvent-separated ion pair which can repair with other common cations making it an effective ion-exchange catalysts without altering the native electrochemistry of the membrane or system under study.

When the parent crown was modeled with the lipophilic neutral anion exchanger K(4-Cl)TPB, a new mode of binding became prominent and novel interactions including π-stacking interactions along with charge-charge and cation-dipole forces became the critical interactions. The complex shows a face on edge pi-stacking distance of 3.49 Å, in agreement

with other similar complexes which report face to face Π-stacking values of 3.32 Å (Hirose, 2007), (Langton, 2014).

The complex was modeled first as a 1:1 complex and then as a 2:1 complex since that was the predominant mode of binding with the triflate salts. Triflate salts do not have an extended π-system that can interact with the anthraquinone moiety that the 4-ClTPB anion possesses, therefore this mode of binding was quite different from the experiments handled with triflates.

On the other hand, Na^+ with a much higher charge density does not undergo exchange as K^+ does. When Na^+ was subjected to the same computational binding experiment it failed to bind to the crown ether oxygen as the stronger borate-sodium ionic bond failed to separate. The energy gained by the π-stacking of the borate with the sodium still bound to the TPB anion was not strong enough in magnitude to hold the complex together when modeled either with or without solvent.

Figure 5.16 – Close up of one of one of the phenyls of the $(4\text{-Cl})TPB^-$ anion (Cl green) forming a strong face on edge Π-stacking interaction with the anthraquinone ring.

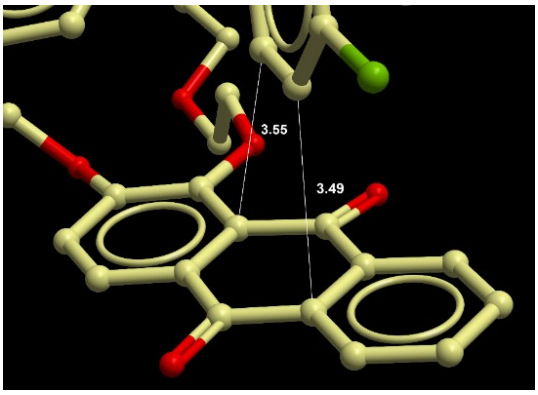

In figure **5.16** above is a close up of the face-on-edge interaction and the relative centroid atom positions including orbital overlap effects. The propensity to form a strong interaction between electron-rich diethoxybenzene and electron poor 9,10- anthraquinones is energetically favorable in minimizing the global free energy of the system. High-energy electrons have the tendency to try to occupy lower energy levels when available. This can be influenced by the relative permittivity of the medium, steric interactions and relative acidity of different functionality as described by hard/soft acid base theory.

Figure 5.17 – One-step complexation and resulting electrostatic potential map showing almost complete encapsulation of the target ion.

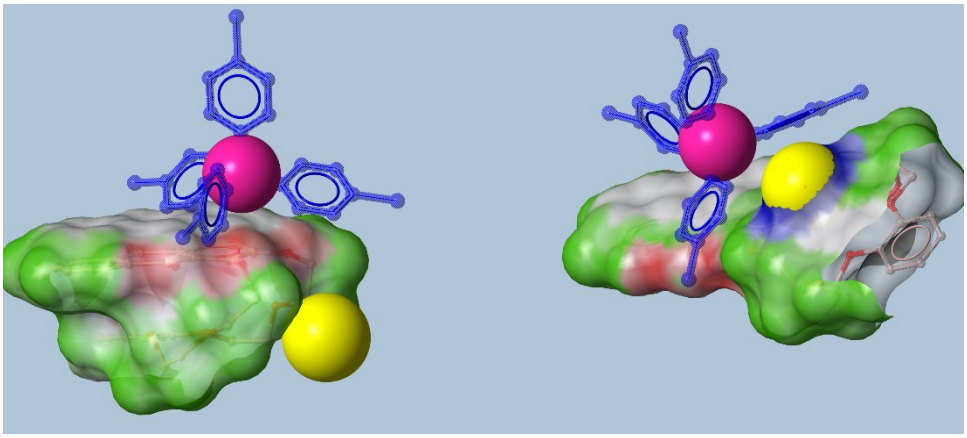

The significance of this interaction is manifested in the figure **5.17** above; modeling a two-step process of activation followed by complexation. In the model, derived computationally, the TPB anion disassociates with K^+. The anion immediately forms contacts with the electron-poor anthraquinone ring system of AQ-18-C-6. This causes a conformational change by breaking the intramolecular π-stacking network, replacing it with

the formation of an intermolecular π-stacking network. By this mechanism it is postulated that the crown ether becomes "unhinged", causing it to flip the crown ether oxygen ring up level with the plane of the anthraquinone subunit. Most of the charge is then encapsulated by charge-charge interactions along with ion-dipole, Van der Waals interactions and dispersion forces (figure **5.18**).

Figure 5.18 - Space-filling model showing the proximity of labeled atoms and the tight formation of the π-stack (Orange aromatic carbons). The K+ atom (purple) is lodged in the molecular cavity, separated from the TPB anion.

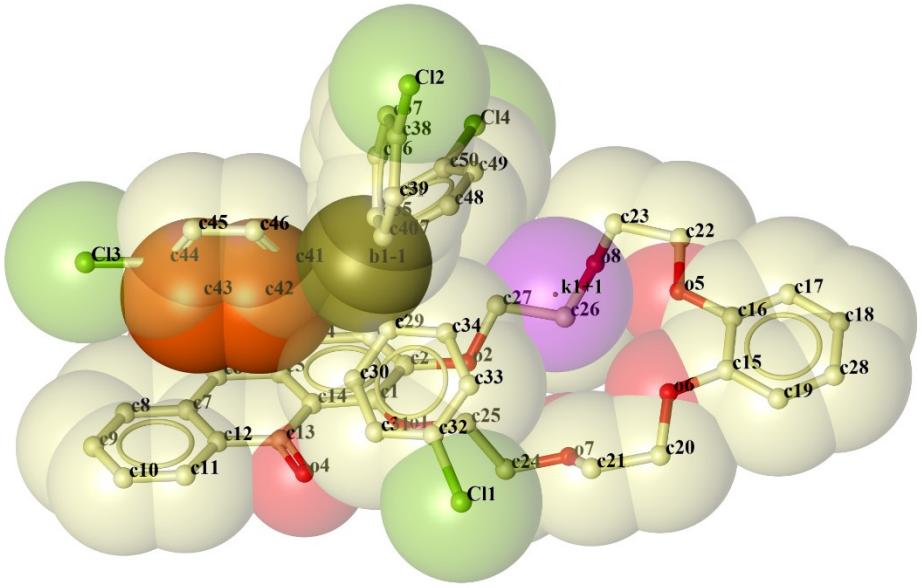

Procedure for Multi-variable Simulations

Formal charges were assigned and the structure minimized with a total of *N* components (anion, cation, ligand X *N, N* = 1(1:1 complex, N = 2 2:1 COMPLEXES) modeled as 1:1 stoichiometry. Calculations were performed at a constant temperature of 298 K with s step

size of 0.5 and frame size of 20-25. Table S shows the relative gas phase energies of the complexes and the calculated equilibrium constants, K_1 and K_2 along with the calculated selectivity coefficient. MM2 dynamic simulations were carried out utilizing CHEM 3D and Monte Carlo method using ICM Molecular Modeling Browser Pro.

Self-assembling "B" block with pendant anthraquinone subunits.

Siloxane polymers are used in everyday products such as shampoos and demonstrate remarkable biocompatibility. Siloxanes have been used in scar repair gels in such products such as Scar away® along with inorganic supporting materials such as SiO_2 to aid in reducing scaring.

Figure 5.19 – Actual Polymer formed from the hydrosilyation reaction of the Claisen-rearranged quinone.

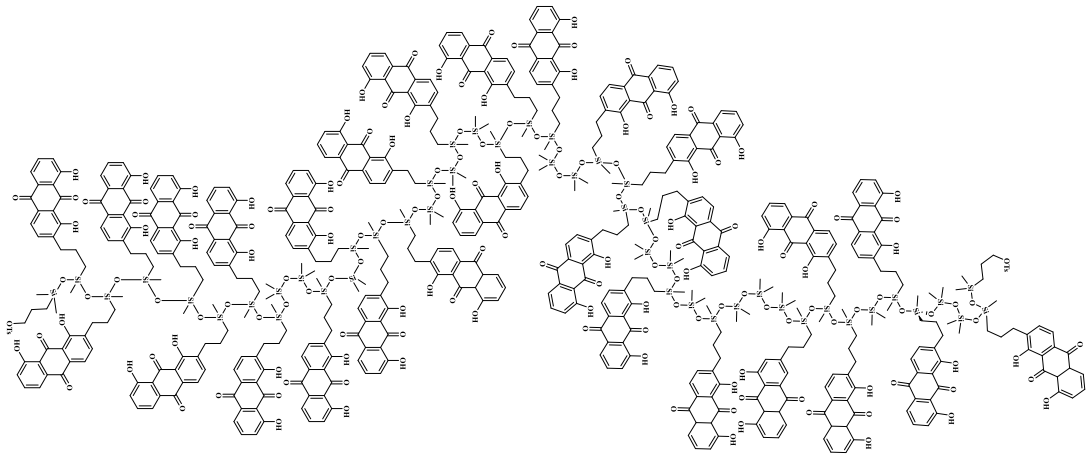

Figure 5.20 – 3D packing arrangement (can be viewed with R/B 3D glasses) of the anthraquinone "brush" with numerous π-stacking and intramolecular H-bonding interactions. The polymer is a gel with a T_{glass} of 40°C.

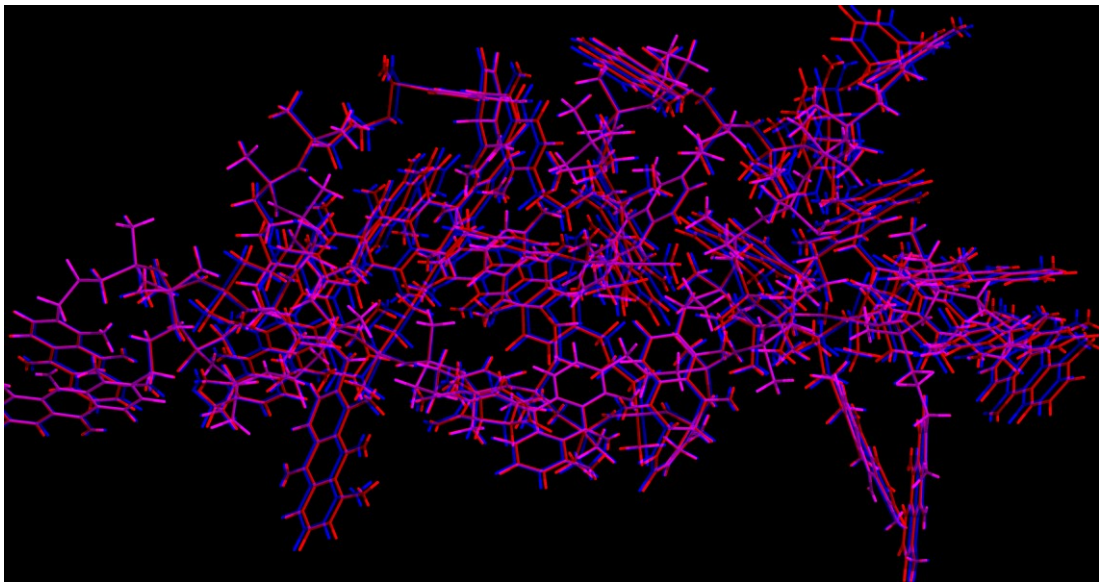

To mimic the crown ethers at approximately a 36% loading by polymer weight of the DNA interchelating polymer derived from the hydrosilylation of 2-allyl-1,8-dihydroxyanthraquinone(figures **5.21** and **5.22**); the structure was first built in ChemBioOffice v. 13 using Chemdraw and converted to the minimized conformer utilizing an unlimited amount of iterations to refine the bond angles, distances and close contacts. The minimized structures were then subjected to MMF94 simulation to observe the effects of the siloxane backbone and Π-systems behaved with one of two types of groups R=Me, Me (PDMS/PDHMS), R=Ph, R=Me (PMPS/PHPS). The intermolecular π-stacking observed in the 2:1 complex and the 1:1 complex with the TTPB anion would be a predominant self-assembly force in a polymeric system.

The results of the simulation state otherwise. The structure in figure **5.22** below shows an unorganized network of subunits trying to make any interaction possible including hydrogen and salt bonds as the pH was controlled at pH 7.4, the physiological pH of human blood. The reason this occurs looks to be the restricted radius of gyration about the propyl linker suggesting a much longer saturated hydrocarbon linker may be necessary to observe a higher degree of freedom and resulting translational flux.

Figure 5.21 – MMF94 minimization of Crown-Phenylsiloxane "B" block result after 72 hrs. convergence predicts a bi-phasic structure with the crown ether occupying a hydrophilic face and phenyl-substituted siloxane groups pointed down to form a hydrophobic face.

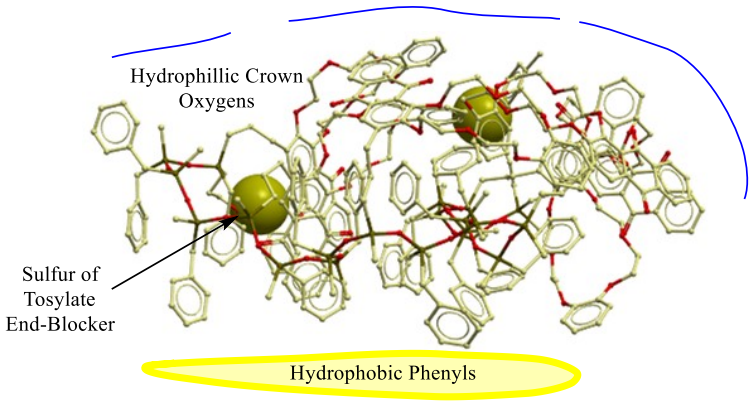

With the Phenyl-methyl-Crown "B" block a large degree of Π-stacking was observed between the phenyl rings of the polymer, the anthraquinone subunits of the crown ethers and the phenyl-anthraquinone interactions. The excess phenyl rings lie below the plane as shown in figure **5.21** above, forming a hydrophobic bubble while the more hydrophilic ether oxygen's are perched upward to avoid this hydrophobic effect.

Modeling of "ABA" triblock copolymer

The same preparation of polymers were made with six anthraquinone subunits but in this simulation, a polyoxazoline strand comprising the "A" block was extended 23 atoms (1/2 the length of the "B" block) giving 46 atoms of peptide total for each strand and approximately the same overall length as the "B" block.

Figure 5.22 – Close up of the packing of crown ethers in the "B" block of the ABA triblock copolymer system where block length B = 2 X A.

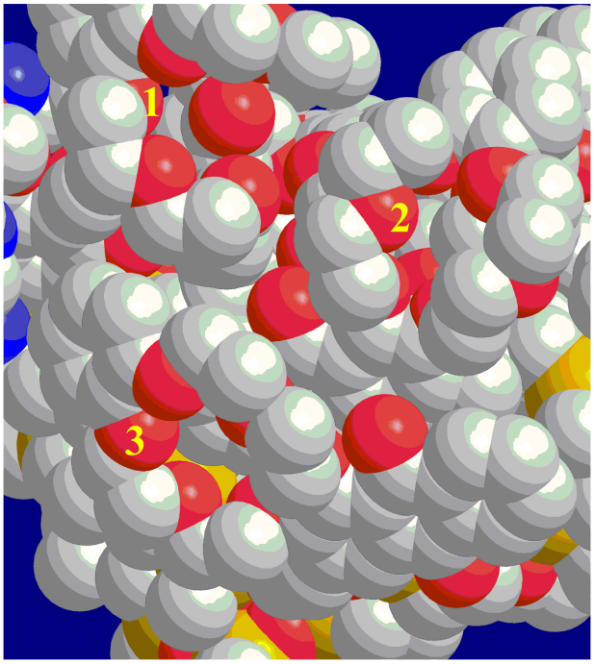

Three strands of ABA where the total length of the A block (hydrophilic) is approximately the same as the B block. A second preparation of polymer was prepared and built with 46 atoms of the peptide polyoxazoline flanking each end of the "B" block. A total of three strands were built and placed within diffusional proximity to one another so they would converge quickly for the lengthy simulation. Figure **5.24** shows the detail.

Figure 5.23 – Three strands of ABA triblock copolymer with pendant anthraquinone crown ethers (pointed out in green) aggregating near the center PDMS block. Blue = N, Red = O, Yellow = Si.

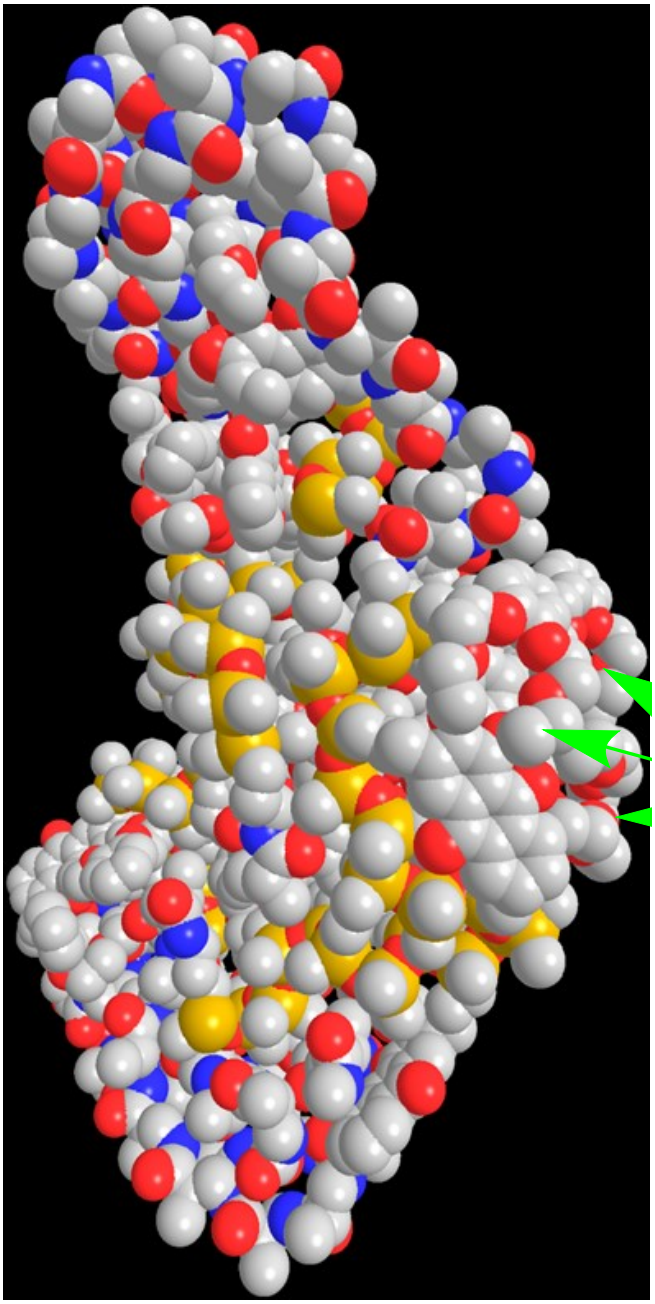

Figure 5.24 – Intramolecular face to face Π-stacking along the siloxane backbone of a single strand of ABA polymer (Highlighted white hashed box).

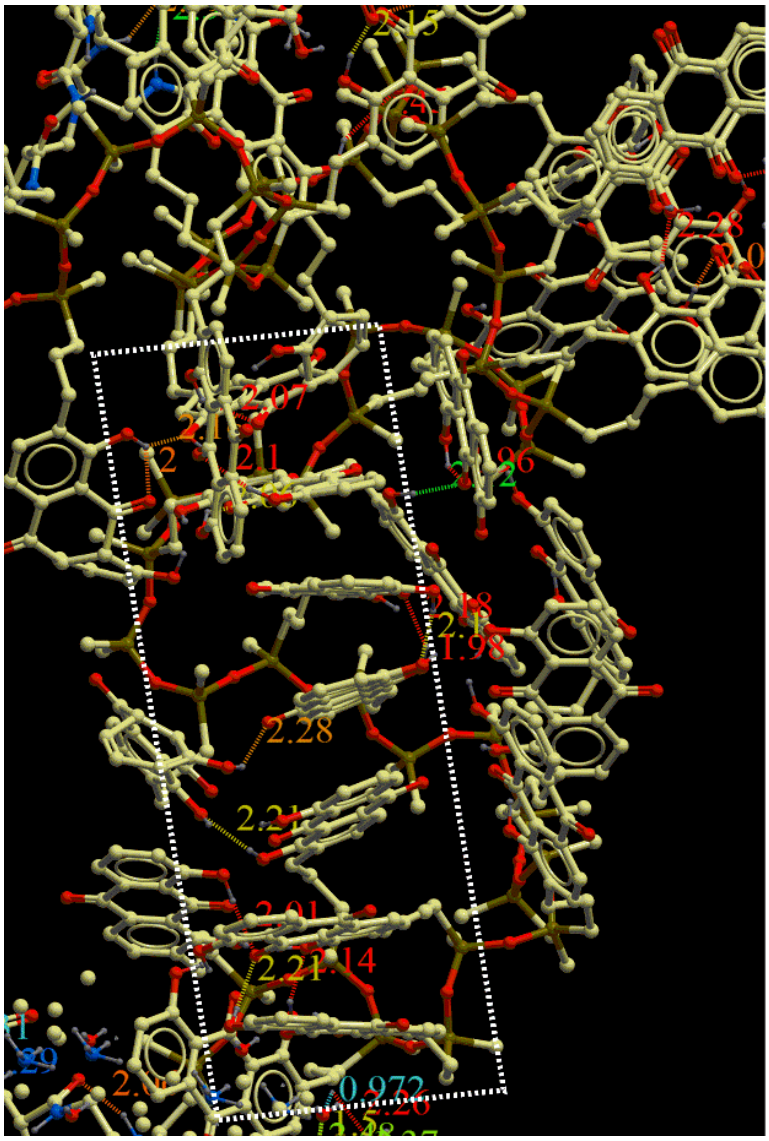

Concluding the studies with computational polymeric simulations it is quite clear that the siloxane backbone imparts a native curvature to the polymer structure; both in the case of the individual strand and multiple strands. One reason for this may be the β-silyl hyper

conjugation effect where an empty p-orbital of the silicon overlaps with the lone pair of the silyl ether. This section examined each of the building blocks individually as the polymer was built up from the "B" block, assembled into an ABA triblock with a short peptide, long peptide and finally concluded with multiple-strand interaction analysis.

Transport Properties

Computer Assisted Design (CAD) and molecular modeling have become an essential tool across the sciences, with recognition of a Nobel Prize awarded to Karplus and colleagues for their role in developing the fundamental conception of these computer programs. 2013 was the first year the Nobel has been awarded in the field of computational modeling.

In this study, many trials were performed of each type of simulation and programs were used to cross-verify each other to see if the same result could be repeated.

Simulation of Anthraquinone crown ether translocation

In order to mimic the cellular membrane environment, ICM Molsoft Browser Pro was utilized and the dielectrics of the hydrophilic portion of the membrane was modeled as having a log (P) (water/octanol scale) and hydrophobic portions of the membrane were defined as $\log_P(2)$ for the hydrophobic region accordingly. Water channels or other computationally demanding effects were ignored through the membrane region. A GRID map was set up to mimic the local concentration of Na^+, K^+ and Ca^{2+}, all present to a great extent in the extracellular fluid. The ions were placed on one side of the trans reservoir and

contained inside the purple grid box that defines the xyz-plane to be examined. Molecular mechanics simulations were then carried out with the ionophore AQ-18-C-6 free to diffuse along set boundaries, extending 8 Å into the aqueous environment to mimic the ion capture processes. The counter ion, in this case used was a triflate in accordance with our actual membrane studies.

To summarize the three day simulation, we can see that K^+ ions are in fact selectively transported while no appreciable amounts of Ca^{2+} or Na^+ is permitted to leak through the channel. The crown ether **1** tends to stack on itself as determined in other independent experiments determined from Job's method of continuous variation and mass spectral data. This is in contrast to an ion-capture event followed by a longitudinal diffusion to the *trans* side of the membrane. In this method, the extreme stability gained by the effects of π-stack and the hopping transport due to diffusion and Brownian motion are suggested to be the dominant mechanism. Without an applied potential the neutral form of the anthraquinone moiety is able to bind selectively K^+ over Na^+, $Ca2^+$ in a defined aqueous environment.

Figure 5.25 - Capped-clipped membrane model for transport across a computationally simulated lipid bilayer of 30Å, comprised of two hydrophilic regions (teal) representing the receiving and feed boundaries sandwiching the hydrophobic (gray regions)

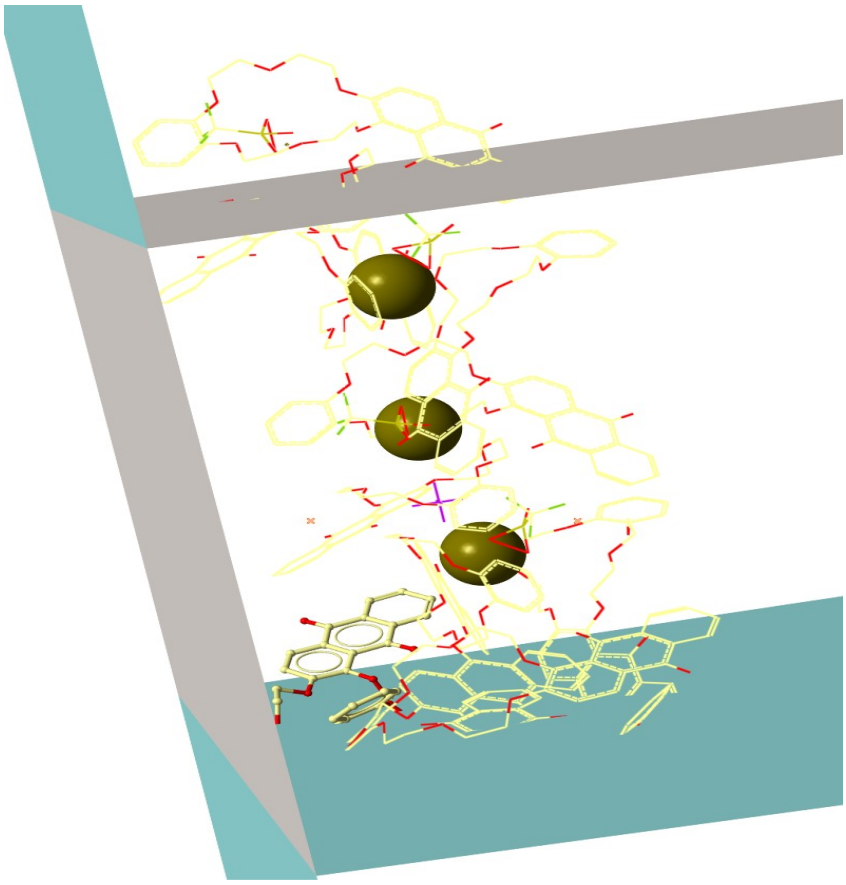

Monomeric Crown Transport Properties

To help summarize the section, we first examined the HQ-18-C-5 in terms of self-assembly properties and the effects of modeling the complex with or without the anion present. Also examined were the conditions where the crown phenolic proton is deprotonated or in the semiquinone radical form, both putting formal negative charges on the quinone. The result for both cases was alkali metal salt formation which lowered the

overall energy of both the K^+ and Na^+ structures, with the Na^+ being significantly lower in energy. Due to its charge density being higher than that of K^+, forming a stronger radical ion-cation pair. Also found was the preference for a 2:1 structure in the case of K^+, whereas a 1:1 complexation was favored for the Na^+ structure.

The same analysis was carried out for our AQ-18-C-6 molecule and the same 2:1 complexation was observed with or without the anion present (figures **5.14** and **5.15**) in the potassium case using triflate salts. Sodium showed no appreciable binding, this more than likely is a result of the lack of coordination preference. Where the K^+ was found to be complexed in a tetrahedral array in the 1:1 complex, rapidly interconverting to the 2:1 complex to complete the favored octahedral coordination.

In the case of computational simulations with (4-Cl)TPB salts, the dominating force was the establishment of two face on edge Π-interactions and the steric bulk of the anion blocking any other higher order structure from forming.

Polymeric Assemblies

For models of the synthesized pendant 2-propenyl-1,8-dihydroxyanthraquinone "B" block, a disordered structure that resembled a polymer brush formed. This could have arisen from the uneven distribution of hydrogen bond donors (2) and acceptors (1) having opposing charge interactions. A similar situation arose when six AQ-18-C-6 pendant side chains were modeled (figure **5.21**) attached to the "B" block. In this case a self-assembled bilayer of hydrophilic crown oxygen are found atop hydrophobic phenyl present on the chain in lieu of methyl. The polymer segments are single stranded and thus have maximum entropy, that is,

there is no "A" block to encompass or compress the monomeric subunits allowing for many degrees of freedom.

Examining the extended ABA assemblies (Isaacman, 2012), in figures **5.24-5.26** a more conformationally restricted structure takes shape due to the fact it cannot rotate about amide bonds as they have 40% π-character in conjugation with the carbonyl. This leads to further close packing and ordering of the "B" block domains. Clustering the crown ethers with other crown ethers as well as the creation of large face to face π-stacking networks exemplified in figure **5.26**.

Nanopore Transport Experiments utilizing POPC, ABA triblock copolymer (PMOXA-PDMS-PMOXA)

In our transport experiment, the anion was sure to be included to examine its fate in the transport process. Transport of Valinomycin with Picrate Anion is essential. Taking away the anion and replacing it with chloride leads to no transport at all (Hamilton, JACS).

Electrophysiological Characterization

As this was our first time we characterized transport through free standing membranes with mobile ionophores; testing of the transport matrices themselves in terms of stability (short and long term), thickness, kinetics of self-assembly and membrane resistance under a constant -50 mV potential was necessary.

The function of purified channels or channels in native membrane vesicles can be studied under voltage clamp conditions following their incorporation into an artificial membrane. For simplicity, these approaches can be divided into two themes: planar phospholipid bilayers and patch-clamped liposomes.

Figure 5.26 – Experimental setup for addition of solution of carrier in CHCl3 by micropipette to formed POPC bilayer/ABA triblock copolymer.

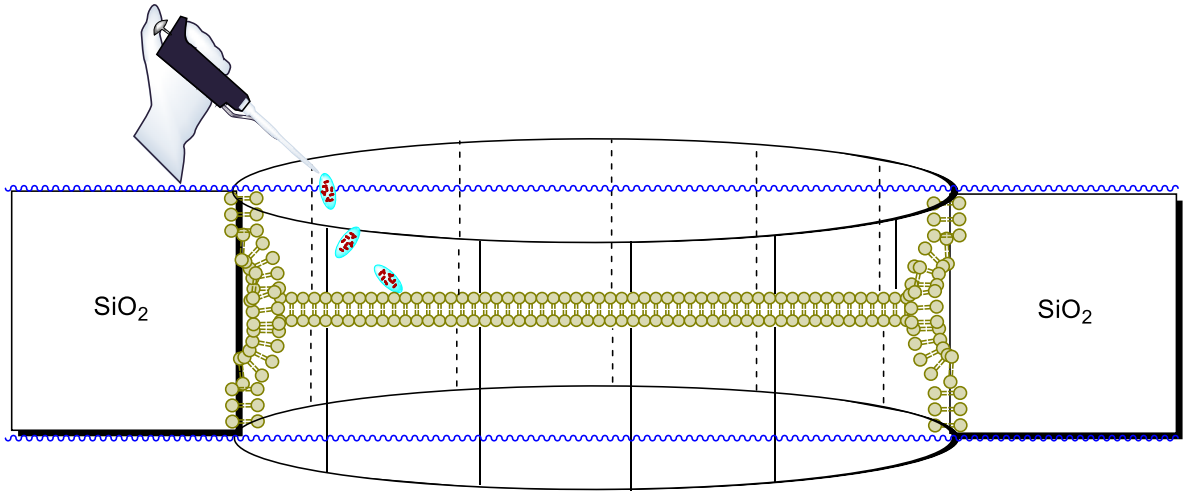

Phospholipid bilayers can be formed using two approaches:

- **Planar Phospholipid Bilayers** - In this technique, ion channels are incorporated into a membrane formed on a hole in a partition that separates two fluid-filled chambers. The material from which the partition is made, its orientation (vertical or horizontal), the size of the hole, and the method of its manufacture can vary as well as the method used to form the phospholipid bilayer and the composition of the bilayer. For instance, pre-cleaning of the nanoporous inorganic membrane with detergent, baking and final clean with piranha solution prior to formation of the bilayer leads to a 3x

fold increase in lateral diffusion of the membrane with high propensity for the formation of water domains or channels (Seu, 2007).

- **Painted bilayers-** Individual or mixtures of pure phospholipids are dispersed in the nonpolar solvent. n-decane (phospholipids are mixed in chloroform, dried with a stream of N_2, and suspended in n-decane at 20–50 mM). For a stable bilayer to form, the area surrounding the hole in the partition must be primed with a small volume of the n-decane phospholipid dispersion. Once the priming dispersion has dried the chambers on either side of the partition can be filled with an appropriate electrolyte solution and the bilayer can be formed. This is done by drawing a small quantity of phospholipid dispersion across the hole using some sort of implement; for example, a small plastic or glass rod, a pipette tip, or a small paintbrush with most bristles removed. Using this method the hole joining the two chambers is occluded with a thick layer of phospholipid.

Whether we model, characterize or hypothesize what a transporter may do in solution, the transport phenomena observed experimentally ultimately is the true test of device functionality. Transport phenomena may be measured by a variety of different methods including U-tube experiments, black lipid membrane transport, lipid bilayer insertion and translocation experiments, diffusion cells, chromatographic by electrophoresis. Naumann Et al. demonstrated the transport kinetics of Valinomycin in terms of a circuit using simulations and experiments to rationalize the complex (Naumann, 2003).

The aforementioned methods have all proved to be very time-consuming and only somewhat reproducible. Often times, bulk liquid membrane studies can take up to 72 hours to complete until equilibrium is reached. Conducting a transport experiment for three days requires the refilling of reservoirs due to evaporation of water and organic solvent along with other parameters that one must take into account when running experiments of this duration.

One of the goals of this thesis was to develop a method for testing transport that was practical on the laboratory time scale. By conducting our experiments through nanoporous membranes that are microns in thickness with a transport layer nanometers in thickness. The length and scaling of the experiment is greatly reduced to mere seconds in lieu of hours. As well as saving time this also greatly improving reproducibility and validity of results. Obtaining the transport results faster allowed for the screening of more potential receptors for their complexation ability.

To complement the findings to ultimately show selectivity for K^+ in aqueous solution, a series of tests were performed to verify transporter ability under electrochemical bias.

In a pre-drilled single nanopore with a diameter of 10 nm inset inside a10 mm X 10 mm wafer of SiO_2, free standing membranes were constructed from POPC. The membranes were on the order of nanometers (36-42 nm reproducibility) in thickness and were cast unloaded or loaded with carrier.

The same method was utilized with ABA triblock copolymer prepared by co-scientist Michael Isaacman (Isaacman, 2012). The ABA blocks were unfunctionalized in this case and had poldispersity indices ranging from 2.3-3.1. They formed self-assembling membranes, but not without much difficulty.

Procedure for free standing membranes without carrier 1

Single nanopores prepared by Ashfaque Uddin/Sukru Yemenhi via electron-beam lithography (EBL) were painted with POPC in anhydrous decane or chloroform. Chloroform was preferable due to the relative volatility whereas n-decane was advantageous for this preparation due to the high solubility of the POPC in this organic solvent. The POPC concentration was fifty percent by volume in a solution of $CHCl_3$. Approximately 100 μL of this stock solution was used to prepare the membrane as the drop was placed over the nanopore, which was outlined in gold etchant with a larger feature size for easy locating. The membranes were evaporated in a fume cupboard until a nanometer thick film developed (ca. time 1-2 h.).

Procedure for free standing membranes with carrier 1

Single nanopores courtesy of the former were painted with a solution of the composition shown in figure **5.28**. To ensure complete solubility, plenty of solvent (relative to the substrate) was used with the solvent being n-decane or chloroform respectively. The stock solutions were generally 100 μM.

All ABA formed membranes were first characterized in real time (figures **5.27-5.32**) to observe the kinetics of the ABA bilayer formation process and examine such properties such as background current leak and capacitance buildup across the membrane. We went through rigorous current/voltage testing to ensure reliability of the data.

Figure 5.27 – Instantaneous I/V plot for Crown Ether 1 in POPC membranes as a function of time

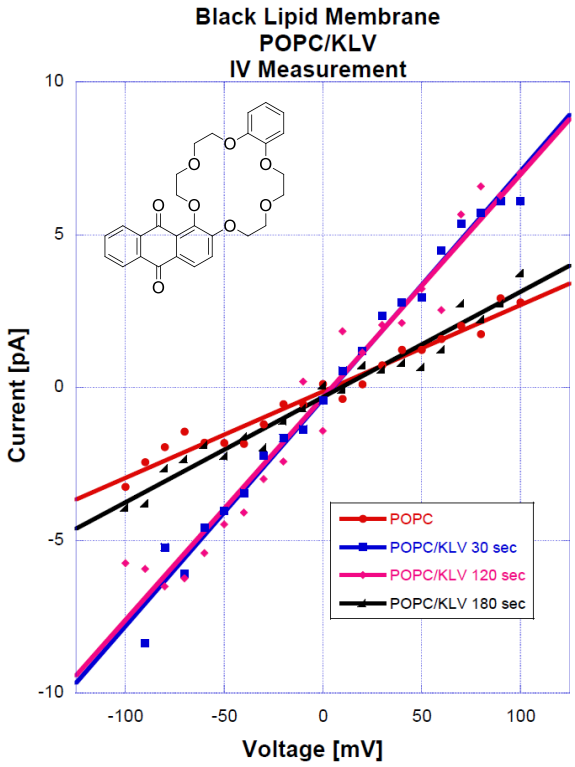

From figure **5.31**, one can see that the entire fusion and transport event for this bulk experiment plateaus at t = 30 sec and is stable for a total duration of 2 min before transport equilibria is attained when the carrier is directly inserted into the membrane.

Figure 5.28 - I/V sweep after formation of ABA bilayer shows slight increase in current across the membrane over time. The mustard color trace is initial trace one, fading to light yellow.

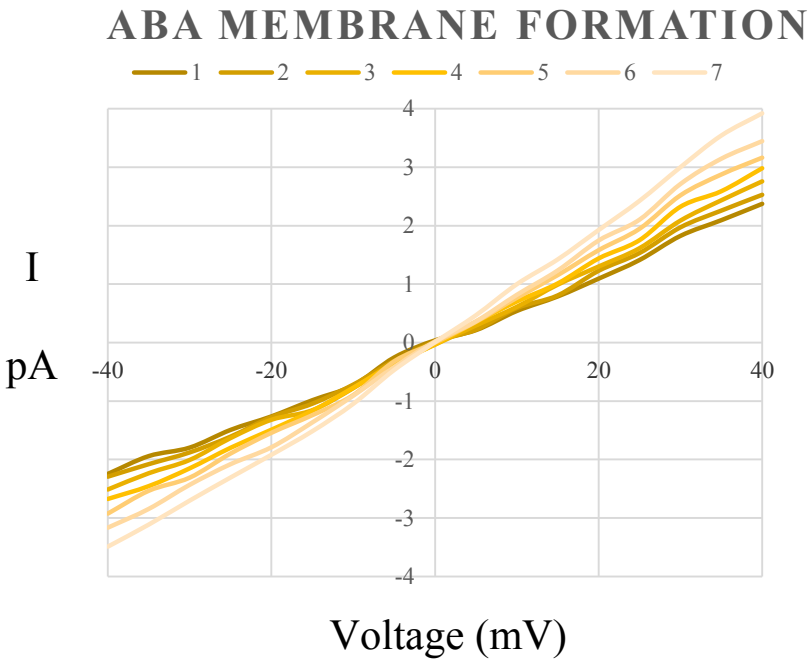

Figure 5.29 – Capacitance across the ABA membrane as a function of time

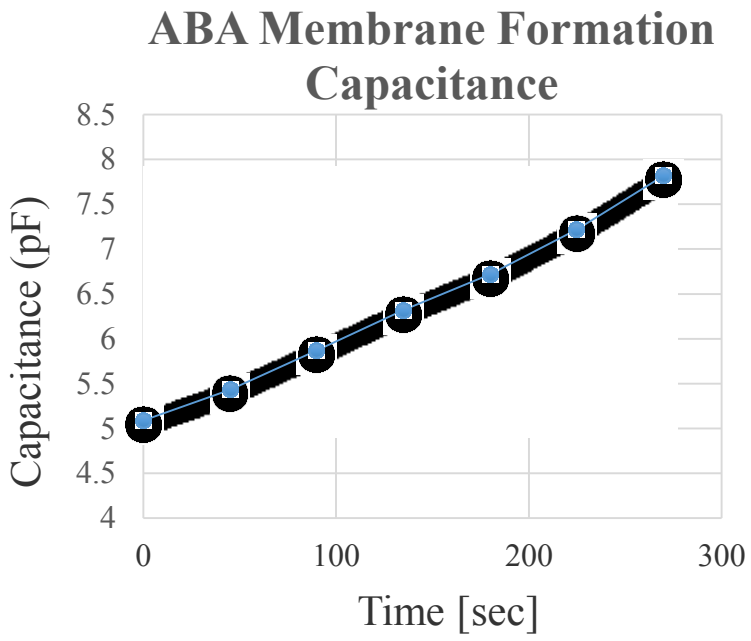

Figure 5.30 – ABA kinetics of stable bilayer formation shows ≈ 6 m. to self-assemble under an applied potential of -50 mV. t = 0-10 m.

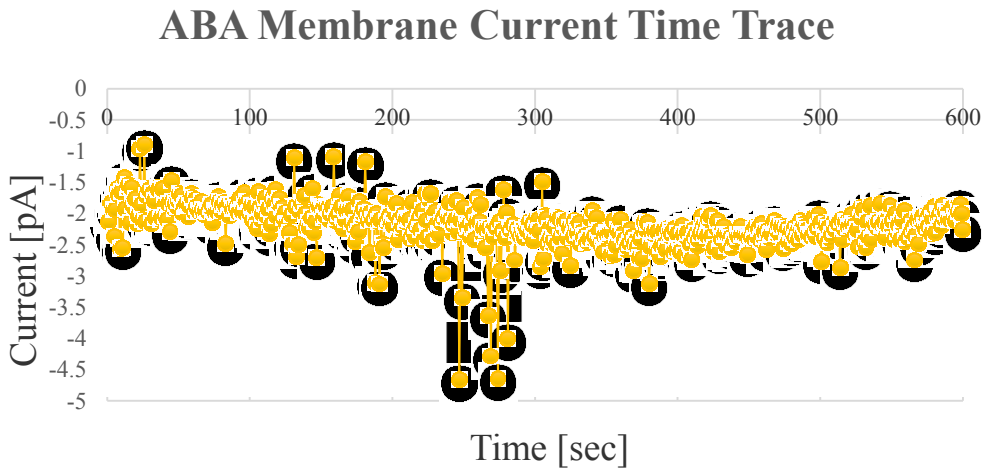

Figure 5.31 – ABA bilayer stability test current time trace for the last 55 minutes from above figure. t = 10 – 55 m.

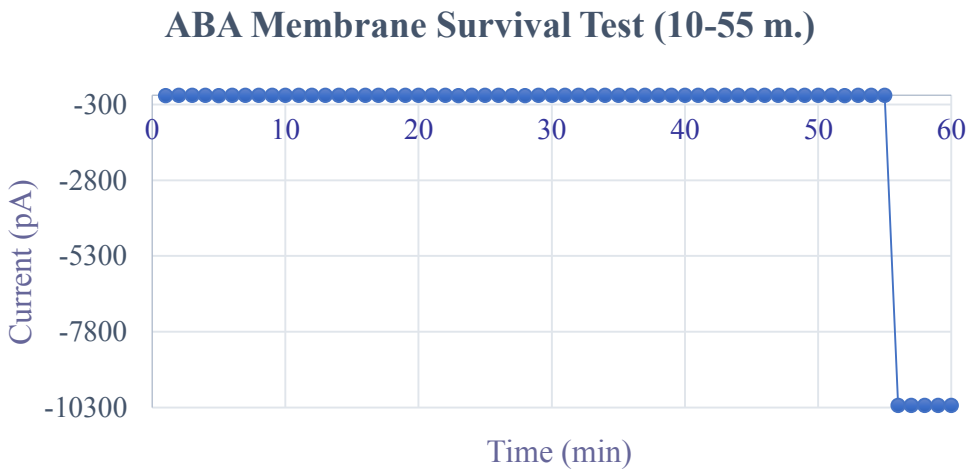

Pre-transport Studies

Figure **5.32** shows the average results from 3 independent trials for each entry. If a membrane broke prematurely or the data point was bad, the data point was thrown out. The standard deviation of peaks observed are calculated from the deviations of the three runs for most cases.

Figure 5.32 – Experimental results from free bilayer standing materials containing crown ether 1.

Membrane Composition	**Δ*I* *(pA)***	**SD***	**Notes**
PMOXA-PDMS-PMOXA	201	32	Carrier injected at 2.5 wt. % in $CHCl_3$
PMOXA-PDMS-PMOXA	329	34	Carrier injected at 5.0 wt. % in $CHCl_3$
PMOXA-PDMS-PMOXA, 1% wt. carrier	87	23	Stable membrane formed from $CHCl_3$
PMOXA-PDMS-PMOXA, 5% wt. carrier	439	29	Stable membrane formed from $CHCl_3$
POPC	89	14	Carrier dissolved in chloroform
POPC	323	27	Carrier dissolved in decane
POPC, 1% wt. carrier	110	13	POPC stable films formed from $CHCl_3$
POPC, 5% wt. carrier	634	18	Almost 5X change in flux across membrane compared to 1% loading by wt.

***Results calculated from three independent trials**

Figure 5.33 – Addition of AQ-18-C-6 produces fast K^+ spikes across ABA triblock membranes. Aliquots of 32 nM AQ-18-C-6 in $CHCl_3$ to the cis chamber (green arrow) produce stable current spike events through the membrane.

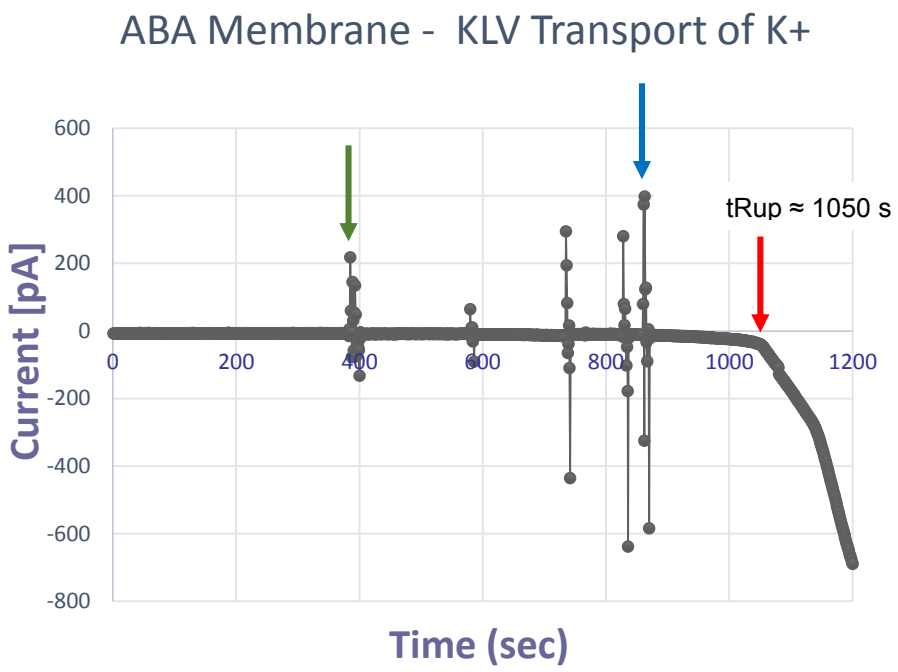

As shown in the table above, the most reliable transport data was recorded with membranes formed from POPC, although both ABA and POPC membranes did show transport behavior. As one can see from the CV vs. time plots, each of the injection-membrane fusion transport experiments happens in just seconds as recorded by potentiostat. With a sensitive potentiostat, it was possible to accurately record the peak currents and to do so in just a few seconds rather than days with the classical U-tube or bulk liquid membrane experiments. With this procedure, one can now judge whether they have an actively transporting molecule in real time.

From the linearity of the spikes in the plot, one can also see that fusion of the bulk liquid with carrier near the periphery of the membrane happens very quickly or that the solvent plays some sort of detergent effect, causing leakage of the electrolyte and current to pass through the membrane. The latter may be an effect of Marangoni convection, where different surface tensions at the interface lead to convective instability as new complexes form while others dissociate apart from one another (Cai, 2008). Precipitation of the co-complex due to the formation of a strong interaction at the interface could also elicit a convective instability which would be more characteristic of Raleigh-Taylor instability (Sczech, 2008). During experimental trials, we observed this phenomenon when the concentration of the carrier dissolved in $CHCl_3$ was too high upon addition of the aliquots to the formed membranes. Aggregation at the membrane interface was consistently a problem due to the scaling of the experiment. Several iterations of titrations were needed to attain the appropriate amount of carrier as well as its molarity in the $CHCl_3$ solution. This type of instability could manifest itself with weak complexes with low K_{eq} leading to formation of Marangoni cells which show pulsating character at the interface due to their amphiphilic nature (Cai, 2008). The latter explanation is not as likely since the standard deviations (table **5.28**) recorded are relatively small between the trials and the K_{eq} value rather high for this complex. The more appropriate mechanism of action is fusion with the membrane, with the solubilized ion diffusing with the carrier across the membrane. There was no unexplainable observations during these trials and were all highly reproducible.

To assess the qualitative kinetics of bilayer formation within the pore a prepared membrane comprising a resulting 10-12 nm film of ABA triblock copolymer was painted onto a 10 nM pore diameter nanopore in a solution of 50:50 EtOH:H2O. A stream of N_2 was

blown perpendicular to the plane of the pore to aid in drying and formation of the membrane in nanometer dimensions. After 1 hr., the pore was determined to have dried as there was no excess residue on the sides of the chip. The pore was immersed in a 1.0 M solution of KCl and the C/V diagrams figures **5.33** and **5.34** showing the variation in the current across the membranes were recorded, with the membrane lasting for a total of 55 minutes under the -50 mV potential.

ABA Copolymer Transport Studies

Before the studies with the carrier AQ-18-C-6 were executed, it was imperative that we start by utilizing classic transport experiments to observe the behavior of the carrier in its free state to assess the relative efficacy of translocation and carrier transport without imposing the restricted movement of surface-bound ionophores. Translational movement of ionophores bound to a polymer backbone, for instance, imposes additional constraints that can only be predicted computationally or examined physically by electron microscopy if the conditions permit clear imaging. For reference, the transport behavior is summarized in table **5.28** for all experiments carried out in this thesis.

With reference to figure **5.28** above, upon addition of a 32 nM aliquot of AQ-18-C-6 in $CHCl_3$ an initial peak spiking to just over 200 mV is noticed with the membrane resistance returning to the initial value. As more 32 nM aliquots are added in sequence, the peaks grow larger and larger as well as asymmetric about the y-axis, reflecting the effect of osmotic imbalance and disturbed electrochemical neutrality due to the capacitance buildup on the membrane as more and more carrier is added. The membrane proved to be very stable up to

a concentration of 128 nM carrier in chloroform, only to rupture after the fifth (160 nM) aliquot was added. This rupture occurs well after the addition of the final aliquot, which indicates an inherent lag-time/threshold of activation before the triggering of the disassembly process.

Figure 5.34 - Summary of Electrochemical Results obtained utilizing PMOXA-PDMS-PMOXA self-assembling bilayer

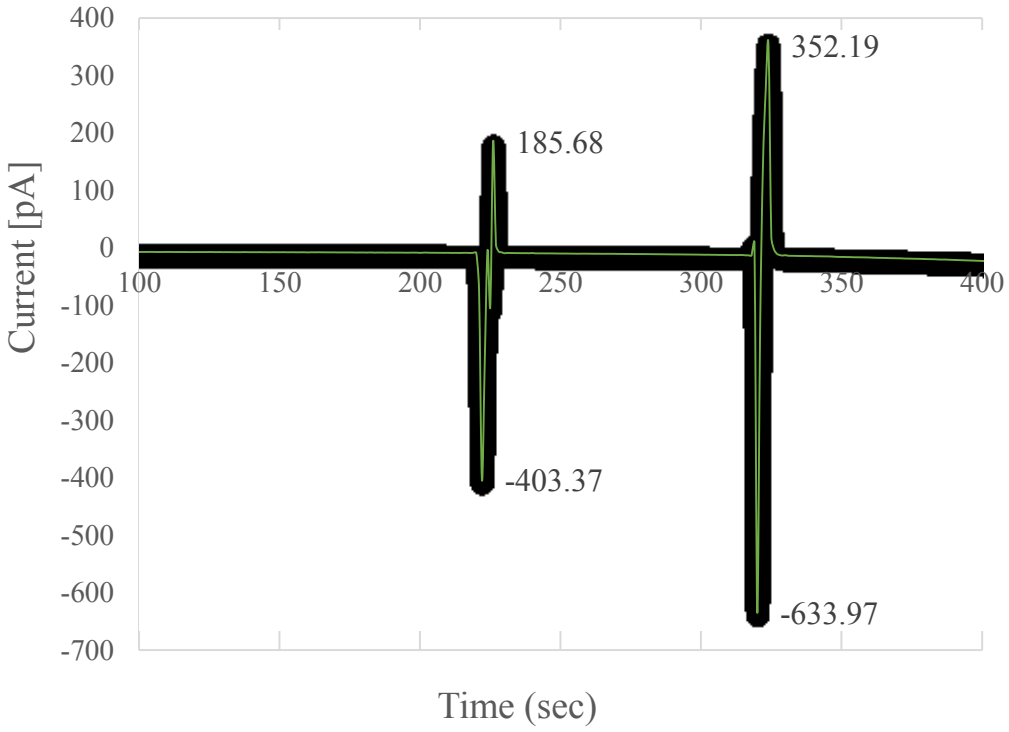

When the carrier is added to the membrane suspension after the initial formation of the POPC or ABA membrane (figure **5.31**), the time duration is on the order of 4 seconds for the initial events and cause current spikes up to 634 pA. Examining the graph closely, the

membrane resistance begins to decrease after the second addition of the ionophore quite rapidly, leaking to almost -14 pA at 400 seconds.

To summarize this chapter, we fit the HQ-18-C-6 to the best model under neutral, semiquinone radical, hydroquinone diradical as well as the intraannular phenol as deprotonated sets of conditions. Radical ion pairing within the ring did increase the binding affinity quite significantly and the deprotonated anion form almost as well as the radical more the result of charge rather than structural changes.

Utilizing large computational resources, we effectively modeled polymeric systems which were synthesized in this work, or were modeled as prototypes for future work and presented the results herein.

Utilizing ultra-thin “nanomembranes” comprised of POPC or ABA triblock copolymer, the self-assembly and ion translocation events were effectively shown by current-voltage diagrams we effectively carried out selective ion translocation experiments by measuring the increase in current across nM dimension

Chapter VI - Conclusion and Future Work

Objective

- Gather the characterization results from the computational design, synthesis, device fabrication and transport studies and devise potential routes and mechanism of action of the novel anthraquinone-based crown ether.
- Propose further synthetic methodology based on our "parent template" crown ether with more complex architectures incorporating proton-exchanging carboxylic acids
- Realize the significance in process improvement of synthetic methodology of the Claisen Rearrangement of mono-allyl quinones developed in Chapter **3** in comparison to the most recent published procedure in *JACS*.
- Suggest novel uses for the hydrosilyated polymers containing 1,8-dihydroxyanthraquinone subunits tethered at the 2-position to PDMS/PMS copolymer for use as ion-exchange membranes, ssDNA and nucleotide detection, as well as hydrophilic nature imparted by phenolic protons on what is normally a very hydrophobic "B" block.

The dissertation has presented a communal problem being defined as deterioration of the retina and proposed a biomimetic strategy using selective K^+ ionic gradients under redox control to generate and action potential. This action potential would normally be elicited through the perception and signal transduction of light produced by different wavelengths. The goal was to assemble a "prosthetic on a chip" that will hopefully restore a useful level of vision in patients who have suffered from macular degeneration. In this thesis, we

described a novel approach to the fabrication of this prosthetic utilizing ionic gradients of K^+ to elicit and action potential.

The main conclusion we can draw is that while the latter could not be functionalized further after learning of the relatively weak selectivity factor (6X) to (7X) between the K^+ and Na^+ titration, the new synthesis presented in the second scheme was indeed much more scripted and behavior predicted as each hypothesized model supported the rationale behind the existence of a 2:1 Crown Ether complex.

A more interesting fact discovered during both our ^1H NMR titration and combinations of COSY, NOESY, HMBC, HMQC analysis on a Bruker 800 MHz NMR was the complete inversion of a crown ether peak with a 1:1 stoichiometry. Without this resolution coupled with the use of a cryoprobe; data collection and determination of the 1:1 stoichiometry of the structure would never have been correctly deduced. Job Plots were reproducibly constructed for K^+ and Na^+ and the Na^+ always had an equilibrium maximum Keq <1, favoring a 1:1 structure that shows significant strain by H,H-COSY when using triflate salts. The K^+ always had preference for the 2:1 "sandwich-type" stoichiometry. Using the triflate but showed a differential mode of 1:1 self-assembly when the large aromatic and lipophilic (4-Cl)TPB anion was introduced into the system.

Although sometimes a 2:1 structure is present for 18-C-6 complexes, it is usually only prevalent for atoms with larger atomic radii such as Rb^+ and Cs^+. Sandwich complexes are sometimes observed for 15-C-5/K^+ complexes as K^+ is too large to completely fit within the plane of the ring. The one commonality between the two above situations is the fact that each cation seems to form a sandwich when much of its non-polar surface is exposed and slightly sits above the pane of the ring as in our case. To compensate for this, if there is an

excess of free Host in solution, it is favorable for that Host to couple with the 1:1 complex cooperatively to completely shield the charge in the low dielectric medium.

In another case where the anion is about the same size as the Host and it too is lipophilic in nature, a 1:1 structure is formed and does not progress on to the 1:2 structure as a consequence of the hydrophobic "shielding" effect requirement being met by the neutral ion pair in addition to very strong face on edge pi-pi interaction, modeled to be 3.51 Å (Char code 212B) approaching the theoretical limit this interaction can attain before the VDW repulsive term dominates.

NMR new insights

There have been many reported titrations, Job Plot's along with myriads of COSY and NOESY data presented in the literature. Although the converse is true for 2D DOSY diffusion data of charged molecular complexes. It is possible that DOSY is a very time consuming endeavor and often times planning a good study takes much NMR time and expense. The value of the data attained depending on the relative R^2 value however can be very enticing. In this study we used DOSY to confirm the stoichiometry of both of our complexes and to see how the behavior of the complexes interacting with each other over time changed with NMR peak shifts along with 2D diffusion traces and 2D plane integration to deduce the 2:1 Host:Guest complex with triflate salts.

Much fundamental work to the understanding of engineering effective devices like the final device shown in figure **6.1** was accomplished, albeit ongoing work has been passed off to this authors colleagues for further development.

Figure 6.1 – Final stack blueprint of the pre-selective hydrogel layer atop PEDOT electrodes sandwiching a nanoporous membrane of Al2O3 contains a novel redox-active crown ether as developed in this work. The pump is shown in its active state with the resulting action potential traveling down the dendrites toward the axon where it will be perceived by the brain.

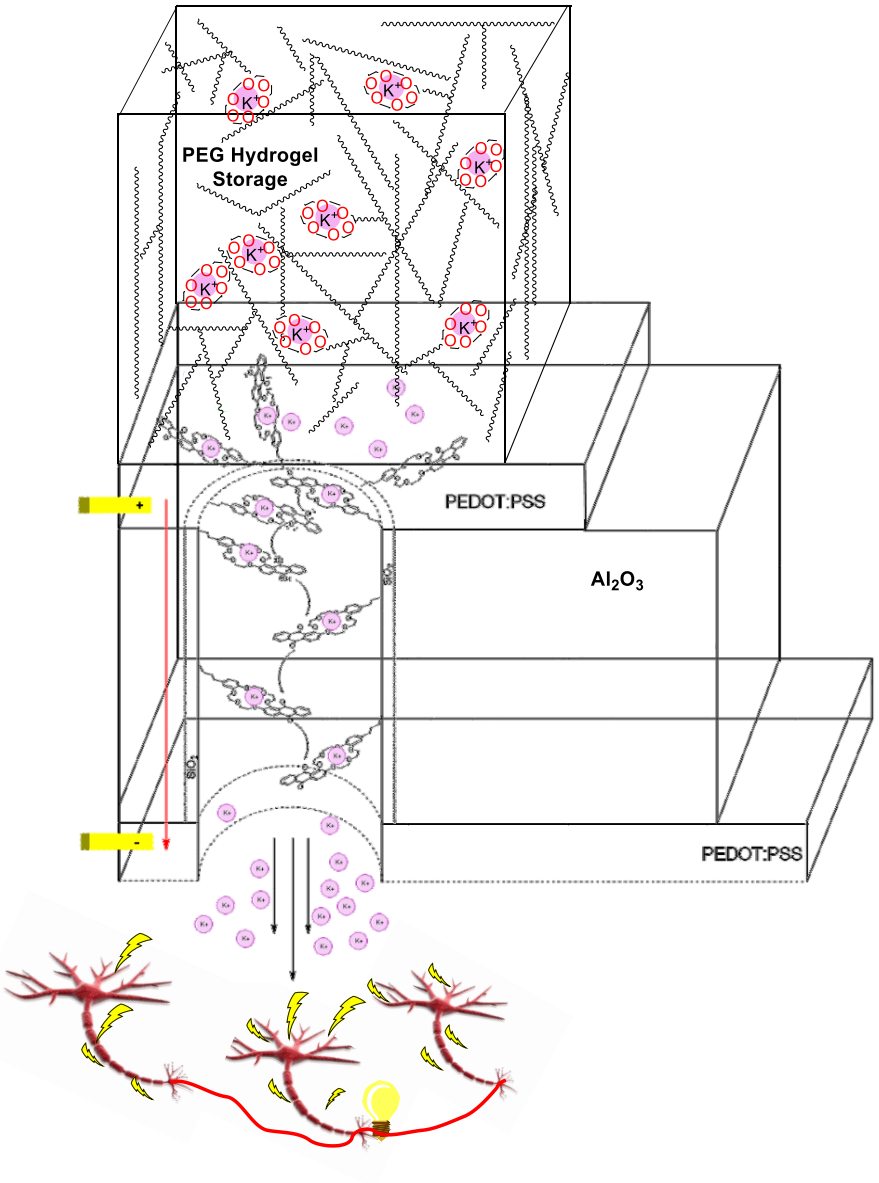

Figure 6.2 – Reaction kinetics of this 2:1 Substrate: Ligand Complex formation.

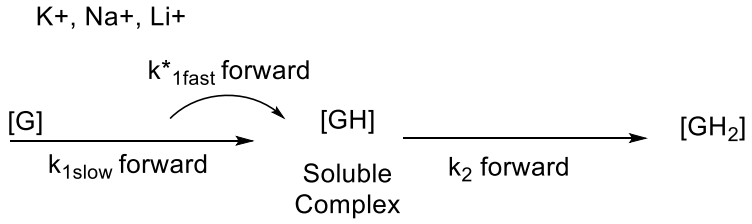

List of accomplishments toward overall device fabrication:

1. Showed a differential self-assemly of a novel redox-active crown ether based upon the counter-anion to potassium used in a particular complexation experiment.
2. Showed that the rate limiting step for ion uptake by AQ-18-C-6 as in Figure **6.2** involves the allosteric shift and the establishment of π-stacking interactions leading to an increase in K_{sp} of the salt
3. The rate of ion uptake is not instantaneous in non-homogenous systems such as mixtures of (4-Cl)TPB/AQ-18-C-6. By 2D DOSY NMR presented in Chapter **IV**, the mechanism of ion pair disassociation followed by capture by the crown ether is the predominant
4. Showed that the carrier AQ-18-C-6 is superior in its ability to capture potassium salts with *aromatic* anions versus the traditional 18-C-6 ether by a 2D DOSY competition experiment.
5. Using Job's Method of Continuous Variation, we were able to deduce the stoichiometry of both the BQ-18-C-5 and AQ-18-C-6 as 2:1 Host / Guest which was

then verified further by competitive ion bombardment experiments using Na^+ as the positive ion source.

6. With a selectivity factor of 7x over that of sodium as shown by Mass Spec, we can comfortably conclude that the crown will selectively complex K^+ in the blood over the much higher concentrated Na^+.
7. Several novel polymers with T_{gel} around 40°C containing 1,4-hydroquinone and 1,8-dihydroxyanthraquinone were synthesized and modeled computationally and could have potential novel uses as proton exchange membranes and DNA interchelators due to the low pKa of the 1,8-dihydroxyanthraquinone and extended π-system.
8. 2D DOSY experiments provide insight into the equilibrium of ion-pairs and molecular complexes and can give detailed structural integrations in the 2D plane as well as the 1D plane to deduce the relative number of diffusing species and the amount of each present.
9. ^{19}F spectra and accompanying DOSY show that bis-complexes such as the one formed between AQ-18-C-6 / K(OTf) tend to diffuse with their anions while 1:1 strucutres diffuse with the bulk solution unless another force such as intermolecular π-stacking is available to keep the anion proximal to the site of the crown.
10. Novel ionophoric matrix material to fill voids in the nanoporous membranes and maintain structural integrity of the brittle anondized alumina were developed.
11. Covalent functionalization of the alumina membrane using the small molecule nucleophile APTES and electrophile CPTES was achieved by MVD deposition method, leading to high grafting densities as shown in the XPS spectra (supporting information).

12. Computational simulations using the Monte Carlo method of a model biomembrane biased at -0.5 V with the developed crown ether embedded inside showed transport behavior through the combination of electrodiffusion and Brownian motion.
13. Although binding enhancement by redox processes were not attempted due to time constraints, the threshold for redox activation of the crown transporter was determined to be -0.57 V and completely reversible eliminating the concerns of overheating of the retina environment and device failure due to overoxidized carriers molecules.

Future Work

Carboxylic acid containing ionophores

Self-assembly is just part of the grand scheme of what can be done with modern-day supramolecular chemistry. As we discussed before, selective binding is the key objective of this study but it can be extended into a new area of functional materials that respond under an applied electrical potential termed supramolecular machines. Supramolecular machines are different than static supramolecular assemblies in that they actually use an input of work to provide a secondary transition or catalytic behavior.

Figure 6.3 – Hypothetical 24-C-8 derivative showing that there is just too much room in the cavity for an appreciable koff rate.

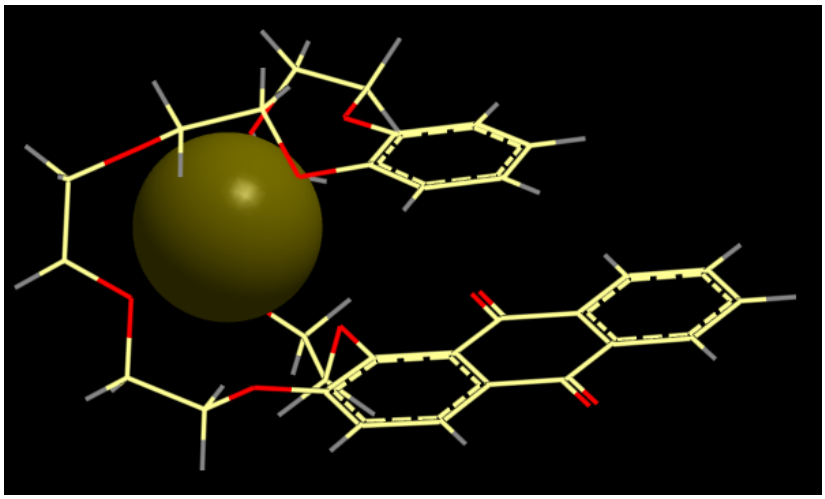

Computational Improvements included modeling of the following complexes

- Synthesis of a 24-C-8 molecule shown in figure **6.3** above.
- Synthesis of a crown carboxylic ether containing crown for symport in building the potential energy gradient.
- Incoorporrate a leading crown alkyl tether with the (Z)-alkene orientaiton to promote transport through carboxylic acid salt ion pairing/ H+ exchanges.
- Replacement of the benzene subunit of the crown with chirl cyclohexane derivatives to generate 4 enantiomers that would posses different affinities toward cation binding.

1. Polymeric/Monomeric Substrates for ion and DNA interaction

- Hydrosilyation of the completed crown ether derived from Eugenol into the backbone of a OTs-PDMS-PDHMS-PDMS-OTs.

- Interfacing the DNA interchelators synthesized in Chapter III to the inner portion of the inorgnic porous substrate.

Figure 6.4 - Extension of the crown structure to a 24-C-8 molecule shows that any type of extension of the ethylene units is unfavorable and lead to a net decrease in affinity for forming a separate ion pair as shown by the cation K^+ with Cl^- as the counterion.

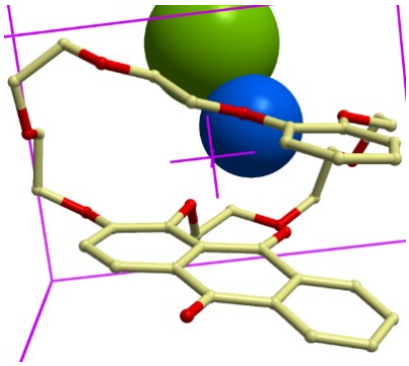

Figure 6.5 - Substitution of a trans-cyclohexane enables the ethlene bridge O1 to adopt the proper ethylene configuration of 120° nearest the quinone. Top - 2 D structure Bottom - Energy minimized structure (MMF94).

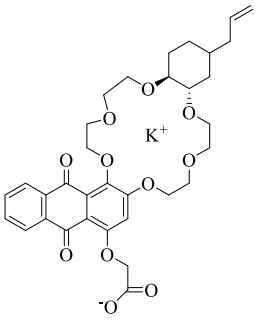

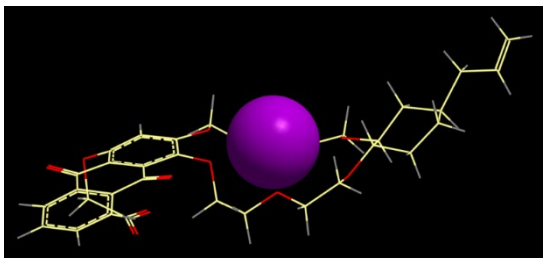

Figure 6.6 – Extending just one arm of the ether contorts the structure, leading to no formation of any K^+ complex.

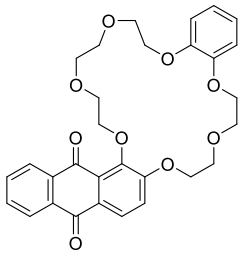

Acyclic-Phenol containing ionophores

Although not a direct intention of this study some byproducts were recycled in the form of acyclic crown ethers. That is to say, the Anthraquinone subunit was substituted at the 2-hydroxy-position in many cases and was found stripped of the tosylate end group after acid-based workup. These acyclic ionophores suffer from lack of preorganization but can form very strong complexes given enough time.

Figure 6.7 – Synthtic routes toward higher level archetectures and useful reactions developed during this work.

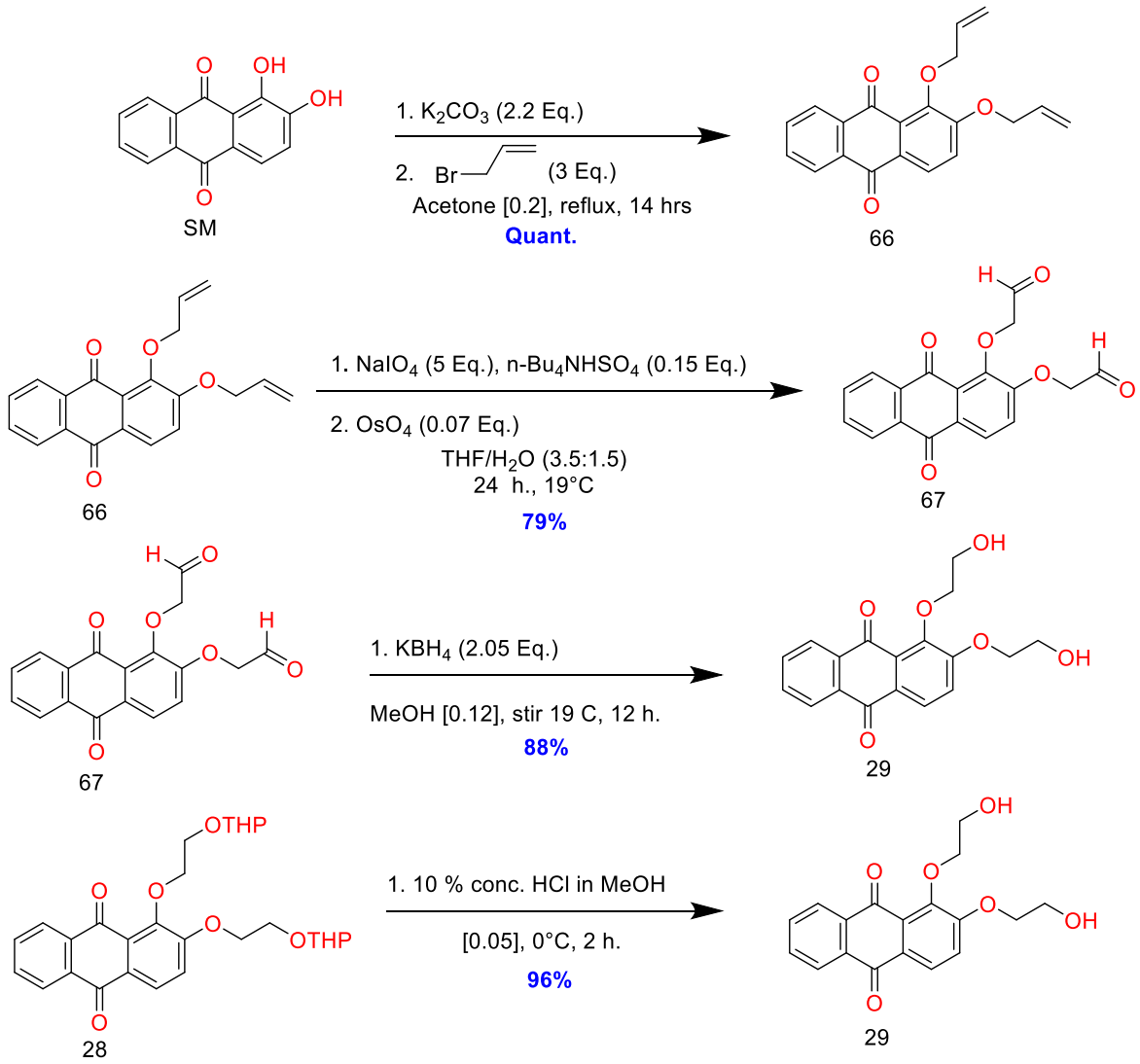

Several new key reactions and intermediates were developed in this work that were not exploited during the synthesis of crown ether presented herein.

The first method involves developing a facile way to access a variety of derivitives by converting then 1,2-dihydroxyanthraquinone starting material to the bisallylated

compound **66** followed by subsequent oxidative cleavage of the double bonds to aldehydes to give **67** in moderate yield. Careful reduction of **67** using potassium borohydride gave good yields of the diol **29** after recrystallization.

Two redox systems were examined computationally, synthetically and the theory of transporting K+ selectively discussed of these molecules examined under redox control. ; a previously reported system with 1,4-benzoquinone/quinol-18-C-5 in which characterization such as Job's method of Titration, 1 HNMR titration of the 1,4-benzoquiol form of the crown, complementing the previous extraction coefficients obtained by Sugihara Et al.

Depicted in figure **6.11** is the prototype to a new type of transporter derived from the parent compound 1,2,7-trihydroxyanthraquinone and the envisioned synthesis of such transporter is shown in Scheme **6.10**. The synthesis begins with the relatively low yielding cyclization of the 1,2-diol in a cyclic orthoester type dehydrative cyclization which was achieved in this study in 56-64% yield on a small scale. The second step would involve concentration of installing the nonyl (*Z*) chain using the Sonogashira method with the protected triflate and methyl ester chain terminated at the alkyne. Regioselective Lindlar-catalyzed reduction gives the (Z)-methyl ester. Next the quinone would be deprotected and cyclized with the respective ditosylated catechol-containing partner to give the protected ester macrocycle and finally after deprotection with NaOH and heat, the free (Z)-oriented acid is obtained.

Figure 6.8 – The first reactin to install the long chain olefin in the scheme below fails in acetone

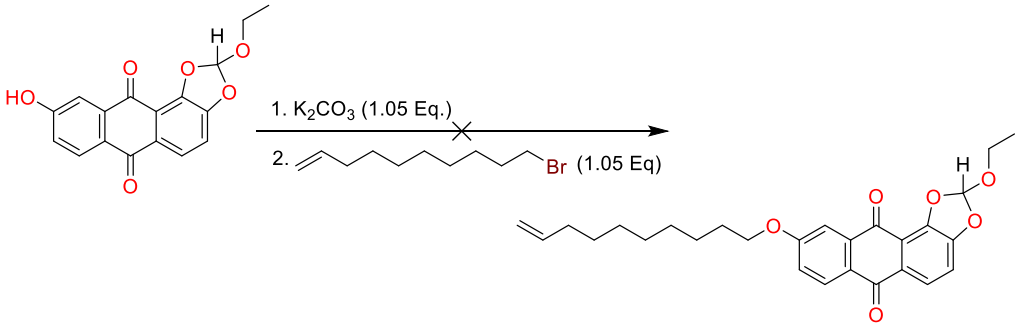

Figure 6.9 – Hypothetical "B" block with appended propyl tethers

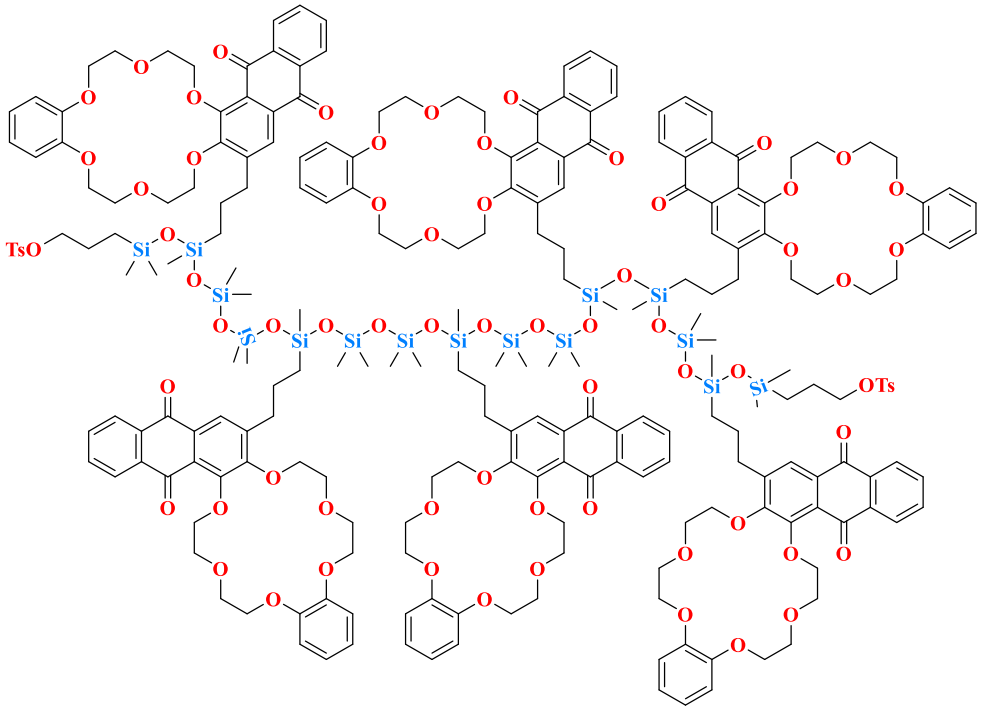

Figure 6.10 - Proposed synthesis of the carbocyclic acid from 1,2,7-trihydroxyanthaquinone.

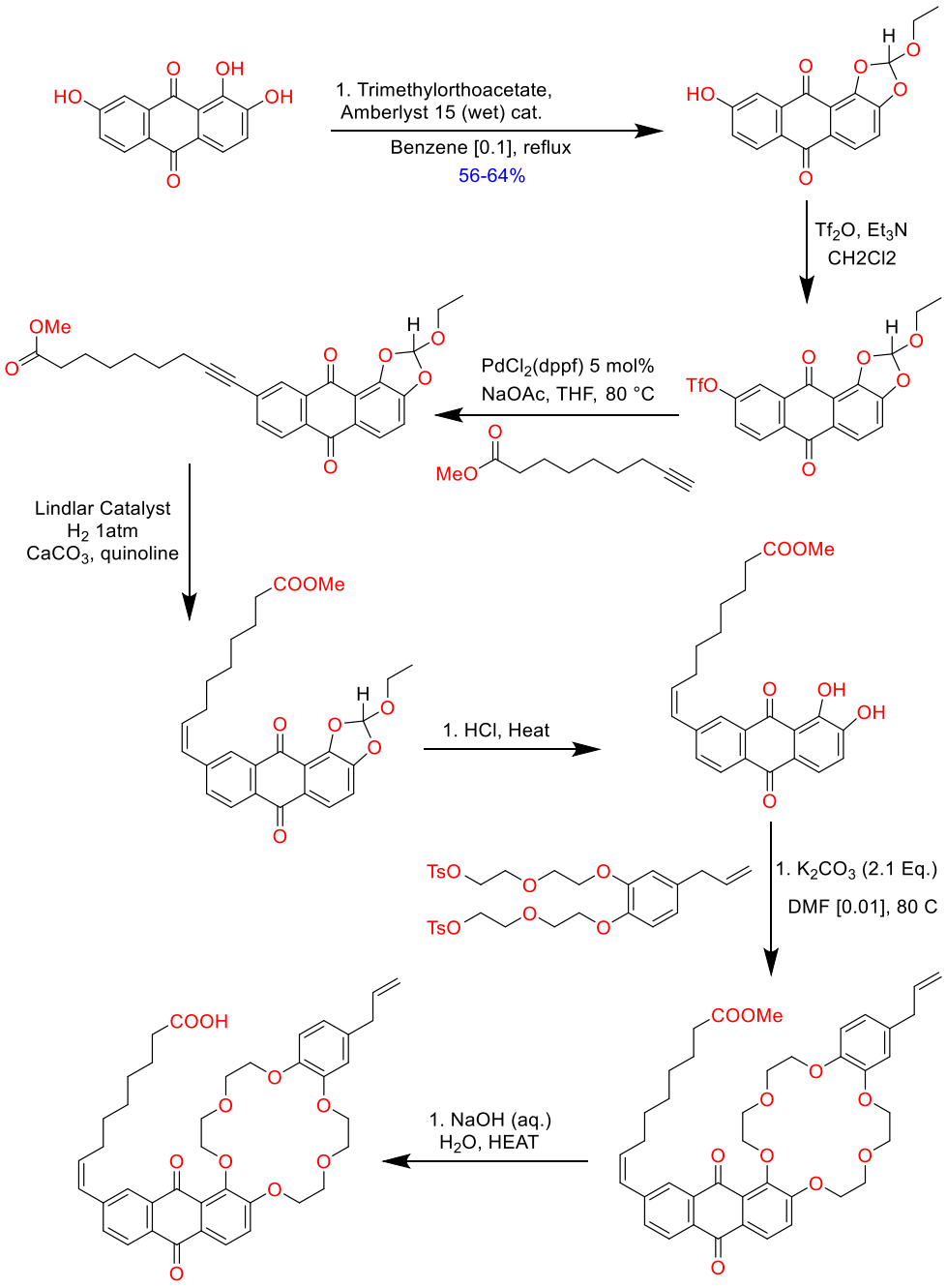

In this computation, we can examine the dynamic nature of the role of the intra-annular phenolic protons and the stabilization of the negative charge upon cation binding in both Acetonitrile and DMSO, both polar-aprotic solvents.

Figure 6.11 – (E)- 1,2,7-trihydroxyanthraquinone derivative with a nonyl - H+/counterion designed to increase the koff rate by "pulling" the cation out of the pocket and translocating it to the next acid in the chain. Shown below is the MMF94 simulation of the process with the critical bond having the (E) rather than (Z) orientation.

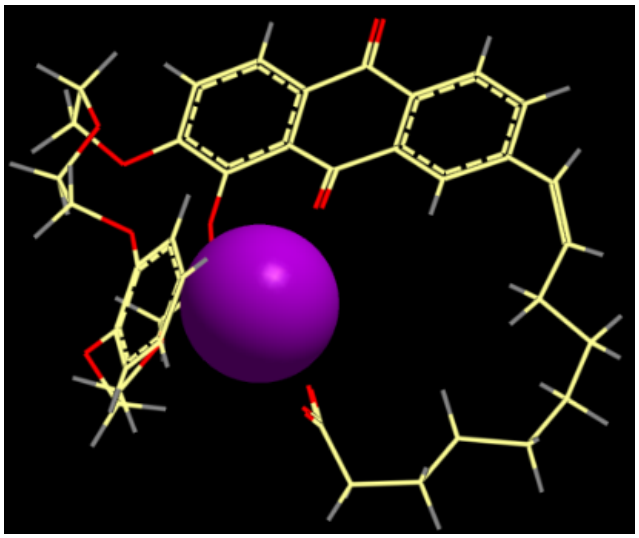

DNA interchelators

A variety of mono and dihydroxy anthraquinones underwent smooth regioselective allylation presumably due to their phenolic pKa differences and chelation-effect of the carbonyl-oxygen. The resulting mono-allylated derivatives underwent a smooth rearrangement to the corresponding ortho-substituted of dihydroxyanthraquinone derivatives. Upon heating in the melt under an inert atmosphere, solid allyloxyanthraquione

derivatives underwent a facile, quantitative and regioselective thermally induced 1-3,-ClaisenRearrangement yielding terminal substituted alkenel functional handles that has proven can further be carried on to derivatives such as phenaldehydes, phenol acetic-acids and precursors to doxorubicin-type drugs. This two-step green process flow hinges on the selective monoalkylations of di-phenolic anthracenediones utilizing group I alkali metal carbonates to give what is usually always a bright orange, low melting point solid. The second stage takes place with no reactants at all, just the solid monoallylether in the case of the anthraquinones, and neat oils in the case of the allyloxy-substituted benzenes.

Figure 6.12 – Table summarizing the alkylation and resulting Claisen Rearrangement of Anthraquinones discussed in this thesis.

Substrate	Alkylation Yield	MP °C of Allyloxyanthraquione Derivative	Rearrangement Temp	Time (hr.) to 100% conversion	Final Yield
1-allyloxy-8-hydroxy-9,10-anthracenedione	95%	135 C	180	12	**Quant. 2-propenyl-1,8-dihydroxy-9,10-anthracenedione**
2-allyloxy-1-hydroxy-9,10-anthracenedione	96%	145 C	180	24	**96% 3-propenyl-1,2-dihydroxy-9,10-anthracenedione**
1-allyloxy-4-methoxybenzene	**>99 %**	**N/A (l. @ 25 C)**	**180**	**12**	

The Claisen rearrangement is a convenient method for the introduction of terminal alkenyl subunits for further functionalization including epoxidation, cleavage by OsO4/NaIO4 to the aldehyde and hydrosilylation as well as many coupling reactions such as

the Suzuki and reaction with Grubbs catalysts. Most often the Claisen rearrangement of allyloxy-phenolic ethers is carried out under acidic catalysis AcOH/Ag^+ and in the case of liquid compounds the rearrangement is carried out thermally under solvent-free conditions. To the best of our knowledge, quantitative, regioselective Claisen rearrangements of solid high M.P. anthraquinone derivatives has yet to be reported. We herein report the facile rearrangement of solid allyoxyanthraquinones in the melt in sealed tubes to give the ortho-directed propeneyl group in excellent to quantitative yield as a new solid derivative.

Claisen Rearrangement of Anthraquinone derivatives.

Anthraquinones are known interchelators due to their extended electron rich π-systems interacting with DNA base pairs through this very route. Although this project is not the focus of this thesis, it did contribute to our understanding of which reactions would work using intermediates as precursors to test reactions on. One example discussed was the hydrosilyation of olefins containing different types of quinone functional groups. The surprising result we obtained prompted us to investigate 1,4-benzoquinones as these substrates did not hydrosilyate well, while their precursor compounds 1-hydroxy-4anisole's readily underwent hydrosilyation. Anthraquinones, as rigid as their stiff ring systems are compared to flexible hydrosiloxane, underwent facile hydrosilyation using Karstedt's catalysts in toluene. Thus, it was deduced that the 1,4-diene system in conjugation with the hyper conjugation of the quinone contributes to catalyst poisoning under standard reaction conditions.

Carrier Transport Mechanism

For the thin layer experiments using POPC and ABA triblock copolymer, both were found to assemble into nanometer-thick films that were stable for several hours after drying. Experiments conducted showed that carrier molecule AQ-18-C-6, when first embedded into the membrane before the start of electro diffusion showed s much smaller standard deviation compared with runs where a mixture of crown was injected adjacent to the membrane in close proximity as expected.

In a set of carefully controlled diffusion competition experiments described earlier in Chapter III, the qualitative effect of a Macromolecular encounter complex was observed for the first time when 1.0 Eq. of the solid (4-chloro)-TTPPB^{-}K^{+} salt (Tested for K_{sp} in $CDCl_3$, deter. Solubility<0.2 mg/mL) complex was added to a solution of 0.5 mL 7 mM DB-AQ-18C6. At first observation, the K+ salt underwent complete dissolution in the low dielectric medium in the presence of the crown within 3 min (repeated 3X) (S.E. +/- 7 s) and 2D DOSY One-shot sequence recorded immediately. The spectra revealed 3 separate measures of D that could be resolved, the free anion TTPB, the HOST-Guest complex and the free Host. After 24hrs at static equilibrium under Argon, the structure was again analyzed by the previous method. The spectra revealed a single major diffusive peak with trace amounts of the TTPB anion, perhaps solubilized by the common ion effect and overall increase in pi-character of the solution under study.

Perhaps a more interesting result is the same concentration of Host as above but also added to the solution is >99.9% 18-C-6 at a concentration of 7mM, with the concentration of K+(4-Chloro-TTPPB) being increased to 14 mM in the test solution. After 24hrs under convective stirring (magnetic stir bar) the solution was analyzed by 2D DOSY in dDMSO

and the peak corresponding to the 18-C-6 was practically un-shifted from its initial position and did not show any peaks along the 2D plane whereas the two peaks corresponding to the two types of aromatics of the TPB were observed to diffuse tightly along the averaged diffusion peak corresponding to the Host [AQ-18-C-6: K+TTPB$^-$] complex. This further validates the hypothesis that the π-stacking interactions in the intramolecular complex are lower in energy than the ion-solvent pair separation energy. $_d$DMSO is known to be extremely competitive for ion pairs in general and especially for K^+ as it can align itself in an octahedral coordination mode. Often in the literature K_{eq} is reported in such high polarity solvents such as dDMSO and the resulting equilibrium constant of the complex analyzed is usually weaker than other common solvents.

In this case of Crown Ether **1**, the formed complex is overall lower in energy than the uncomplexed **1** with contributions of around 5-6 kcal/mol for the face on edge π-stacking.

Figure 6.13 – ssDNA make its way through a polymer "brush" of echangable protons forming ammonium salts, phosphonium salts and hydrogen bond formation to slow DNA through different types of sensor platforms for use in DNA sequencing.

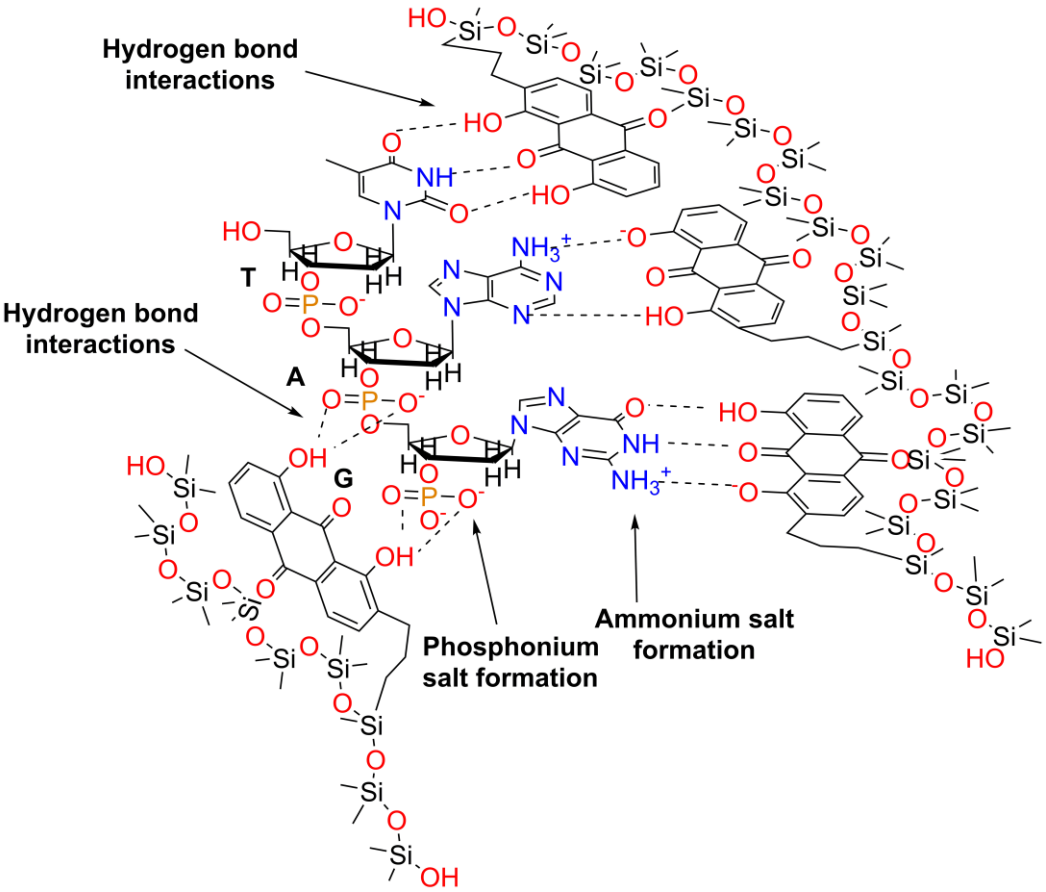

Electrochemically Controlled H-bonding Polymeric Materials for DNA capture

Today's day and age has attracted much attention to the sequencing of the human genome. Companies are battling for the latest on-chip detection of individual DNA base pairs and ssDNA. The latter has proven thus far the most robust and is prone to the least amount of errors in reading the DNA sequence, just as DNA polymerase reads the template strand from a ssDNA molecule in order to generate a new complementary strand. Sequencing individual base pairs relies on the theory that either an enzyme or molecular machine will severe the phosphodiester bond linkage and the resulting nucleotide will enter the sequencer as it is cleaved. This is not always been the case though as some nucleotides are not captured sequentially, leading to major errors in the reading of the nucleotide sequence.

As the term sequencer was used, we should spend some time to introduce the concept concerned in this thesis and that involves DNA sequencing through an on-chip-nanopore that is anywhere from 3-5 nm in diameter. As different size DNA passes through the pore, the current increases with a characteristic signature for each base pair; ideally in a stepwise manner. The major drawbacks are that nucleotides are very close in size and nanopore heights range from nanometer to micron size. This effectively reduces the residence time each nucleotide spends in the pore. The dwell time is on the order of microseconds to milliseconds as the negatively charged DNA is being pulled by electrodiffusion by a positive charge. All of these drawbacks often leave scientist wondering if a DNA translocation event has actually occurred because the resulting current change across the pore is very small and the CV step curve in turn – very noisy.

Many approaches are currently being undertaken to slow DNA down and increase the residence time in the pore. Most of these efforts involve functionalizing the pores with organic molecules, creating polymer "brushes" and even binding DNA base pairs themselves to the pore to make specific complementary base pairing schemes such as G-C and A-T.

In this thesis, the concentration was not so much on the DNA base pairs themselves, but the class of molecules we were in fact using were known DNA interchelators. Danthron, Alizarin Red , Purpurin all possessing a very rich tricyclic π-electron systems and are found in some studies to be beneficial to your health, sometimes harmful as they both potentially cause or effectively treat cancer. The mechanism by which these molecules produce there effect is by lodging (or interchelating) themselves between base pairs by π-stacking and not so much by hydrogen bonding as one may think.

With the materials already in hand, we decided to synthesize a variety of DNA base pair interchelators. These included derivatives from tri, di and mono hydroxyquinones with different substitution patterns. Brief analysis by our post-doc Ellie Corrigliano in solution gave Zetasizer measurements that pointed toward decreased zeta potential and hence decreased mobility; suggesting that the dsDNA had become more rigid and charges possibly masked by hydrogen bonding of the phenolic protons to the negatively charged phosphate backbone of DNA. The materials were characterized spectroscopically but characterization by functionalizing the pore was not successfully carried out. The synthesis of these molecules is presented in the following scheme and preparation of the materials in the experimental section.

Successful Contribution to the Green Chemistry Community

1. A process for the selective monoallylation of Alizarin is described.
2. A process for Claisen Rearrangement of the allyl group in the melt (thermal Claisen Rearrangement quantitative, regioselective, 1 (Z)-stereoisomer by 1 HNMR and 13 C NMR).

As our University strives to keep green, an approach to Claisen Rearrangements was developed that improves upon the state of the art for the molecules 1, 2-dihydroxyanthraquinone and 1,8-Dihydroxyanthraquinone. The use of heat to first melt the orange ally ether, holding the ether under rapidly stirred molten conditions for 18 under sealed vial conditions lead to quantitative yield of the ortho 3-allyl substituted Anthraquinones. These Anthraquinones in addition to the simple 2-allyl-1,4benzoquinone synthesized as in Chapter II were used as monomers and subsequently hydrosilyated under Karstedt's Pt. catalyst conditions in Toluene at 60 °C for 48 hrs. The properties of these new polymers were very much desirable over the Anthraquinones themselves ($CHCl_3$, Biphasic solvents) as they were soluble in almost all the different solvents tried, especially the aromatic and halogenated solvents. Perhaps for use with other acceptor-type molecules, a conducting proton-exchange membrane could be synthesized.

As we serendipitously discovered the value of this rearrangement and improved solubility of the new PDMS-AQ copolymer, we envisioned it to serve as an interesting low MP highly porous gel matrix that could swell to quite possibly accommodate 10X its weight in water due the hydrophobic/hydrophilic properties of the redox active, pH sensitive hydrogel-like material with a high degree of swelling and diffusivity for ions passing through it. Depending on the applied voltage, we could also potentially control whether the

cations would stay bound within the hydrogel layer under electrochemical reduction by metal-ion pairing, or be shunted along by breaking this ion-pairing interaction by electrochemical oxidation.

Finally, many other anthraquinone monomers were prepared as well as neutral crown ethers for storage of the intended cations. Some of these were acyclic versions of the Anthraquinones that had not cyclized as discussed earlier at the one position and others were protected acyclics intended to be utilized in a half and half cyclization with stronger nucleophiles such as the alkoxide of monoethylene-extended (via the extended alizarin bis-diol) and decreased reaction times. Procedures for the preparation of these derivatives can be found in the appendices along with the corresponding ^{1}H NMR spectra.

References

A. Gomaa, E. The Microscopic Free Energies of Solvation for K+ in Mixed Methanol (MeOH)-Dimethylformamide (DMFA) Solvents at 298.15 K. *Int. J. Theor. Math. Phys.* **2012**, *2*, 1–4.

Aberg, C.; Wennerström, H.; Sparr, E. Transport Processes in Responding Lipid Membranes: A Possible Mechanism for the pH Gradient in the Stratum Corneum. *Langmuir* **2008**, *24*, 8061–8070.

Ai, Y.; Liu, J.; Zhang, B.; Qian, S. Field Effect Regulation of DNA Translocation through a Nanopore. *Anal. Chem.* **2010**, *82*, 8217–8225.

Alam, A.; Takaguchi, Y.; Ito, H.; Yoshida, T.; Tsuboi, S. Multi-Functionalization of Gallic Acid towards Improved Synthesis of A- and B-DDB. *Tetrahedron* **2005**, *61*, 1909–1918.

Albano, E. V. Kinetic Scaling Behavior of the Two-Species Annihilation Reaction with Input. *J. Phys. Chem. C* **2011**, *115*, 24267–24273.

Albert, J. N. L.; Epps III, T. H. Self-Assembly of Block Copolymer Thin Films. *Mater. Today* **2010**, *13*, 24–33.

Al-Ibrahim, M. Flexible Large Area Polymer Solar Cells Based on poly(3-Hexylthiophene)/fullerene. *Sol. Energy Mater. Sol. Cells* **2004**, *85*, 13–20.

Allen, C.; Eisenberg, a; Mrsic, J.; Maysinger, D. PCL-B-PEO Micelles as a Delivery Vehicle for FK506: Assessment of a Functional Recovery of Crushed Peripheral Nerve. *Drug Deliv.* **2000**, *7*, 139–145.

Alvarado, E. Two-Dimensional Experiments with Vnmrj 2.2. **2011**, 1–13.

Ammer, J.; Sailer, C. F.; Riedle, E.; Mayr, H. Photolytic Generation of Benzhydryl Cations and Radicals from Quaternary Phosphonium Salts: How Highly Reactive Carbocations Survive Their First Nanoseconds. *J. Am. Chem. Soc.* **2012**, *134*, 11481–11494.

Anézo, C.; de Vries, A. H.; Höltje, H.-D.; Tieleman, D. P.; Marrink, S.-J. Methodological Issues in Lipid Bilayer Simulations. *J. Phys. Chem. B* **2003**, *107*, 9424–9433.

Ariga, K.; Mori, T.; Ishihara, S.; Kawakami, K.; Hill, J. P. Bridging the Di Ff Erence to the Billionth-of-a-Meter Length Scale : How to Operate Nanoscopic Machines and Nanomaterials by Using Macroscopic Actions. *Chem. Mater.* **2014**, *26*, 519–532.

Armstrong, C. NEUROSCIENCE: The Vision of the Pore. *Science (80-.).* **1998**, *280*, 56–57.

Aronica, C.; Guérin, J.; Chauvin, J.; Robert, V.; Lemercier, G. Optical Properties of a Donor–acceptor-Substituted “hemi-Cruciform” Catechol Derivative. *J. Photochem. Photobiol. A Chem.* **2010**, *211*, 147–151.

Atwood, J. L.; Barbour, L. J.; Jerga, A.; Schottel, B. L. Guest Transport in a Nonporous Organic Solid via Dynamic van Der Waals Cooperativity. *Science* **2002**, *298*, 1000–1002.

Babu, S. S.; Praveen, V. K.; Ajayaghosh, A. Functional Π-Gelators and Their Applications. *Chem. Rev.* **2014**, *114*, 1973–2129.

Banerjee, T.; Suresh, M.; Ghosh, H. N.; Das, A. Competitive Binding of Ba2+and Sr2+ to 18-Crown-6 in a Receptor with a 1-Methoxyanthraquinone Analogue as the Other Binding Site. *Eur. J. Inorg. Chem.* **2011**, *2011*, 4680–4690.

Baram, J.; Shirman, E.; Ben-Shitrit, N.; Ustinov, A.; Weissman, H.; Pinkas, I.; Wolf, S. G.; Rybtchinski, B. Control over Self-Assembly through Reversible Charging of the Aromatic Building Blocks in Photofunctional Supramolecular Fibers. *J. Am. Chem. Soc.* **2008**, *130*, 14966–14967.

Barbara, S. Guide to Formatting and Filing Theses and Dissertations. **2013**.

Barbero, C.; Miras, M. C.; Calvo, E. J.; Kötz, R.; Haas, O. A Probe Beam Deflection Study of Ion Exchange at Poly(vinylferrocene) Films in Aqueous and Nonaqueous Electrolytes. *Langmuir* **2002**, *18*, 2756–2764.

Basak, S. C.; Harriss, D. K. Comparative Study of Lipophilicity Uersus Topological Molecular Descriptors in Biological Correlations. *J. Pharm. Sci.* **1984**, *73*, 429–436.

Batchelor-mcauley, C.; Kozub, B. R.; Menshykau, D.; Compton, R. G. Voltammetric Responses of Surface-Bound and Solution-Phase Anthraquinone Moieties in the Presence of Unbuffered Aqueous Media. *J. Phys. Chem. C* **2011**, *115*, 714–718.

Beer, P. D.; Crowe, D. B.; Ogden, M.; Drewc, M. G. B.; Box, P. O.; Birmingham, B.; Rg, R.; Division, I.-C. I. P.; Park, A.; Sk, M. Ammo N I U M R Edox- Responsive Receptors Conta I N I Ng Multiple Ferrocene and Quinone Redox-Active Centres Attached to Di- and Tri-Aza Crown Ether Macrocyclest. *Dalt. Trans* **1993**, *90*, 2107.

Bell, T; Guzzo, F. Models for Planar Polyazamacrocyclic Ligands for Alkali Metal Ions. *JACs* **1984**, *106*, 6111–6112.

Benniston, A. C.; Harriman, A.; Li, P. Bidirectional Electron Transfer in Molecular Tetrads. *J. Am. Chem. Soc.* **2010**, *132*, 26–27.

Bernèche, S.; Roux, B. A Gate in the Selectivity Filter of Potassium Channels. *Structure* **2005**, *13*, 591–600.

Bertin, A.; Schlaad, H. Mild and Versatile (Bio-)Functionalization of Glass Surfaces via Thiol−Ene Photochemistry. *Chem. Mater.* **2009**, *21*, 5698–5700.

Bhattacharyya, a; Goswami, a. Effect of Cation Driven Loading of Dibenzo-18-Crown-6 in Nafion-117 Membrane on the Diffusion and Transport Behavior of Alkali Metal Ions. *J. Phys. Chem. B* **2009**, *113*, 12958–12963.

Binauld, S.; Hawker, C. J.; Fleury, E.; Drockenmuller, E. A Modular Approach to Functionalized and Expanded Crown Ether Based Macrocycles Using Click Chemistry. *Angew. Chemie* **2009**, *121*, 6782–6786.

Blackham, K. a. Introduction. *J. Neurointerv. Surg.* **2013**, *5*, 276.

Bliucvw, P. Molecular Recognition of Alkali-Ions by Crown- Ether-Functionalized Poly(alkylthiophenes)**. **1993**.

Bo, T.; Sladi, A. N.; Zlatovi, M.; Novakovi, I.; Trifunovi, A. N. A.; Ga, M. J. Regioselectivity of Conjugate Additions to Monoalkyl-1,4-Benzoquinones. *J. Serb. Chem. Soc.* **2002**, *67*, 547–551.

Botana, A.; Aguilar, J. A.; Nilsson, M.; Morris, G. A. J-Modulation Effects in DOSY Experiments and Their Suppression: The Oneshot45 Experiment. *J. Magn. Reson.* **2011**, *208*, 270–278.

Botana, A.; Howe, P. W. A.; Caër, V.; Morris, G. A.; Nilsson, M. High Resolution 13C DOSY: The DEPTSE Experiment. *J. Magn. Reson.* **2011**, *211*, 25–29.

Bourson, J.; Valeur, B. Ion-Responsive Fluorescent Compounds. 2. Cation-Steered Intramolecular Charge Transfer in a Crowned Merocyanine. *J. Phys. Chem.* **1989**, *93*, 3871–3876.

Breslow, R. International Symposium on Bioorganic Chemistry. In *Annals of the New York Academy of Sciences*; Breslow, R., Ed.; The New York Academy of Sciences: New York, 1986; Vol. 471.

Bringmann, G.; Menche, D.; Peters, K.; Peters, E.; Brun, R.; Bezabih, M.; Abegaz, B. M. Atropo-Enantioselective Total Synthesis of Knipholone and Related Antiplasmodial Phenylanthraquinones †. *Synthesis (Stuttg).* **2002**, *82*, 5595–5610.

Brown, T. L.; Oliver, J. P.; Weiss, E.; Hencken, G.; Rhine, W.; Stucky, G.; Zerger, R. P.; Stucky, G. D.; Ilsley, W. H.; Albright, M. J.; Anderson, T. J.; Glick, M. D.; Rundle, R. E.; Peterson, W.; Hogan, R.; Scherr, P. A.; Ferrier, L.; Ring, M. A.; Ritter, D. M.; Gaines, D. F.; Tabereaux, A.; Grimes, R. N.; Schaaf, T. F.; Butler, W.; Sadurski, E. A.; Glick, D.; Sayre, D.; Schmonsees, W.; Long, R. E. A. A, A. **1980**.

Brzoska, J. B.; Azouz, I. Ben; Rondelez, F. Silanization of Solid Substrates: A Step Toward Reproducibility. *Langmuir* **1994**, *10*, 4367–4373.

Bu, M.; Stadler, C.; Lambert, C.; Beck, M. Heterocyclic Quinones as Core Units for Redox Switches : UV – Vis / NIR , FTIR Spectroelectrochemistry and DFT Calculations on the Vibrational and Electronic Structure of the Radical Anions. *J. Electroanal. Chem.* **2000**, *484*, 24–32.

Burger, U. 108. The Acetolysis of. *Helv. Chim. Acta* **1980**, *63*, 1016–1033.

Bushweller, J. H.; Bartlett, P. A. Sulfoxide Analogues of Dihydro- and Tetrahydroprephenate as Inhibitors. *J. Org. Chem.* **1989**, *54*, 2404–2409.

Cai, Y.; Zhang Newby, B. Marangoni Flow-Induced Self-Assembly of Hexagonal and Stripelike Nanoparticle Patterns. *JACS* **2008**, *130*, 6076–6077.

Caicedo, H. M.; Dempere, L. A.; Vermerris, W. Template-Mediated Synthesis and Bio-Functionalization of Flexible Lignin-Based Nanotubes and Nanowires. *Nanotechnology* **2012**, *23*, 1–12.

Cameron, K. S.; Fielding, L. NMR Diffusion Spectroscopy as a Measure of Host-Guest Complex Association Constants and as a Probe of Complex Size. *J. Org. Chem.* **2001**, *66*, 6891–6895.

Cantrill, S. J.; Fyfe, M. C. T.; Heiss, A. M.; Stoddart, J. F.; White, A. J. P.; Williams, D. J. Tribenzo[27]crown-9: A New Ring for Dibenzylammonium Rods. *Org. Lett.* **2000**, *2*, 61–64.

Carreiio, M. C.; Ruano, J. L. G.; Toledo, M. A.; Urbano, A. N-Bromosuccinimide in Acetonitrile: A Mild and Regiospecific Nuclear Brominating Reagent for Methoxybenzenes and Naphthalenes. *J. Org. Chem.* **1995**, *60*, 5328–5331.

Casnati, A.; Pochini, A.; Ungaro, R.; Bocchi, C.; Ugozzoli, F.; Egberink, R. J. M.; Struijk, H.; Lugtenberg, R.; Jong, F. De; Reinhoudt, D. N. 1 , 3-AZternate Calix [4] Arenecrown-5 Conformers : New Synthetic Ionophores with Better K + / Na + Selectivity than Valinomycin. *Chem. Eur. J.* **1996**, *2*, 436–445.

Cernigliaro, G. J.; Blum, M. S.; Crewe, M.; Brand, M.; Utawanit, T.; Carpino, L. A.; Terry, P. H.; Thette, S. D.; Rundberg, G. S.; Press, A.; Diamanti, J.; Bingham, R.;

Wuest, H.; Jacob, I. J . Org. Chem., Vol. 41, No. 22, 1976 3627. *J. Org. Chem.* **1976**, *41*, 3627–3629.

Chan, Y.-T.; Li, X.; Yu, J.; Carri, G. A.; Moorefield, C. N.; Newkome, G. R.; Wesdemiotis, C. Design, Synthesis, and Traveling Wave Ion Mobility Mass Spectrometry Characterization of iron(II)- and ruthenium(II)-Terpyridine Metallomacrocycles. *J. Am. Chem. Soc.* **2011**, *133*, 11967–11976.

Chang, P.; Chen, C.-F. Antineoplastic Anthraquinones, II [1]. Design and Synthesis of 1,2-Heteroannelated Anthraquinones [2]. *J. Heterocycl. Chem.* **1996**, *33*, 367.

Chapin, J. C.; Kvasnica, M.; Purse, B. W. Molecular Encapsulation in Pyrogallolarene Hexamers Under Nonequilibrium Conditions. *J. Am. Chem. Soc.* **2012**, 120831122321007.

Chapman, B. E.; Kuchel, P. W. Diffusion-Ordered (DOSY) NMR of Solute Exchange Across the Human Erythrocyte Membrane : Including an Application of Post- Widder Laplace Inversion. In *Diffusion Fundamentals*; 2007; Vol. 4, pp. 8.1–8.15.

Chaudhury, S.; Bhattacharya, A.; Agarwal, C.; Goswami, a. Temperature Dependence of Ion and Water Diffusion in Crown Ether Loaded Nafion Matrix. *J. Phys. Chem. B* **2011**, *115*, 9395–9400.

Chehimi, M. M.; Djouani, F. XPS Studies of Multiphase Polymer Systems. *Polymer (Guildf).* **2011**.

Chifotides, H. T.; Giles, I. D.; Dunbar, K. R. Supramolecular Architectures with Π-Acidic 3,6-Bis(2-Pyridyl)-1,2,4,5- Tetrazine Cavities: Role of Anion−π Interactions in the Remarkable Stability of Fe(II) Metallacycles in Solution. *J. Am. Chem. Soc.* **2013**, *135*, 3039–3055.

Cho, E.-B.; Kim, D.; Jaroniec, M. Monodisperse Particles of Bifunctional Periodic Mesoporous Organosilica. *J. Phys. Chem. C* **2008**, *112*, 4897–4902.

Choi, C. M.; Kim, H. J.; Lee, J. H.; Shin, W. J.; Yoon, T. O. Supporting Information Ultraviolet Photodepletion Spectroscopy of Dibenzo-18-Crown-6- Ether Complexes with Alkali Metal Cations. 3–5.

Choi, C. M.; Kim, H. J.; Lee, J. H.; Shin, W. J.; Yoon, T. O.; Kim, N. J.; Heo, J. Ultraviolet Photodepletion Spectroscopy of Dibenzo-18-Crown-6-Ether Complexes with Alkali Metal Cations. *J. Phys. Chem. A* **2009**, *113*, 8343–8350.

Choi, C. M.; Lee, J. H.; Choi, Y. H.; Kim, H. J.; Kim, N. J.; Heo, J. Ultraviolet Photodepletion Spectroscopy of Dibenzo-18-Crown-6-Ether Complexes with Alkaline Earth Metal Divalent Cations. *J. Phys. Chem. A* **2010**, *114*, 11167–11174.

Choi, S. Q.; Jang, S. G.; Pascall, A. J.; Dimitriou, M. D.; Kang, T.; Hawker, C. J.; Squires, T. M. Synthesis of Multifunctional Micrometer-Sized Particles with Magnetic, Amphiphilic, and Anisotropic Properties. *Adv. Mater. Deerf. Beach Fla* **2011**, *23*, 2348–2352.

Chun, K.; Kim, T. H.; Lee, O.; Hirose, K.; Chung, T. D.; Chung, D. S.; Kim, H. Supporting Information Structure-Selective Recognition by Voltammetry : Enantiomeric Determination of Amines Using Azophenolic Crowns in Aprotic Solvent. 1–10.

Clavier, G. M.; Brugger, J.; Bouas-laurent, H.; Pozzo, J. 2 , 3-Di- N - Alkoxyanthraquinones as Gelators of Organic Solvents. *J. Chem. Soc., Perkin Trans. 2* **1998**, *2*, 2527–2534.

Cohen, Y.; Avram, L.; Frish, L. Diffusion NMR Spectroscopy in Supramolecular and Combinatorial Chemistry: An Old Parameter--New Insights. *Angew. Chem. Int. Ed. Engl.* **2005**, *44*, 520–554.

Combs, G. F. *The Vitamins: Fundamental Aspects in Nutrition and Health*; Elsevier Academic Press: Burlington, 2008.

Cooper, G. J. T.; Kitson, P. J.; Winter, R.; Zagnoni, M.; Long, D.-L.; Cronin, L. Modular Redox-Active Inorganic Chemical Cells: iCHELLs. *Angew. Chem. Int. Ed. Engl.* **2011**, *50*, 10373–10376.

Corry, B.; Hool, L. 7 Calcium Channels. *Channels* **1958**, 241–299.

Cousinié, S.; Gressier, M.; Alphonse, P.; Menu, M. Silica-Based Nanohybrids Containing Dipyridine , Urethan , or Urea Derivatives. *Structure* **2007**, 6492–6503.

Cumpson, P. J. The Thickogram : A Method for Easy Film Thickness Measurement in XPS. *Surf. Interface Anal.* **2000**, *29*, 403–406.

Cussler, E. L. *Diffusion: Mass Transfer in Fluid Systems*; Third.; Cambridge University Press: New York, 2009; pp. 1–631.

Cysewski, P.; Jeli, T. Accuracy of Color Prediction of Anthraquinone Dyes in Methanol Solution Estimated from First Principle Quantum Chemistry Computations. *J Mol Model* **2012**.

Dagnelie, G.; Keane, P.; Narla, V.; Yang, L.; Weiland, J.; Humayun, M. Real and Virtual Mobility Performance in Simulated Prosthetic Vision. *J. Neural Eng.* **2007**, *4*, S92–101.

Dalvit, C. *Fluorine NMR Spectroscopy for Biochemical Screening in Drug Discovery*; pp. 315–226.

Dannhauser, T. J.; Nango, M.; Oku, N.; Anzai, K.; Loach, P. A. Poly(ethy1enimine)-Linked. **1992**, 5865–5871.

Darling, S. B. Directing the Self-Assembly of Block Copolymers. *Prog. Polym. Sci.* **2007**, *32*, 1152–1204.

Davis, S. Organization of Methoxysilane Molecules on Iron. *Int. J. Adhes. Adhes.* **1996**, *16*, 5–15.

de Jong, L. a a; Uges, D. R. a; Franke, J. P.; Bischoff, R. Receptor-Ligand Binding Assays: Technologies and Applications. *J. Chromatogr. B. Analyt. Technol. Biomed. Life Sci.* **2005**, *829*, 1–25.

Dekeyser, C. M.; Buron, C. C.; Mc Evoy, K.; Dupont-Gillain, C. C.; Marchand-Brynaert, J.; Jonas, a M.; Rouxhet, P. G. Oligo(ethylene Glycol) Monolayers by Silanization of Silicon Wafers: Real Nature and Stability. *J. Colloid Interface Sci.* **2008**, *324*, 118–126.

Delgado, M.; Gustowski, D. A.; Yoo, H. K.; Gatto, V. J.; Gokel, G. W.; Echegoyen, L. Contrasting One- and Two-Cation Binding Behavior in. *JACs* **1988**, *110*, 119–124.

Delgado, M.; Wolf, R. E.; Hartman, J. R.; McCafferty, G.; Yagbasan, R.; Rawle, S. C.; Watkin, D. J.; Cooper, S. R. Redox-Active Crown Ethers. Electrochemical and Electron Paramagnetic Resonance Studies on Alkali Metal Complexes of Quinone Crown Ethers. *J. Am. Chem. Soc.* **1992**, *114*, 8983–8991.

Dergunov, S. a; Pinkhassik, E. Synergistic Co-Entrapment and Triggered Release in Hollow Nanocapsules with Uniform Nanopores. *J. Am. Chem. Soc.* **2011**, *133*, 19656–19659.

Dhananjeyan, M. R.; Milev, Y. P.; Kron, M. A.; Nair, M. G. Synthesis and Activity of Substituted Anthraquinones against a Human Filarial Parasite , Brugia Malayi. *J. Med. Chem.* **2005**, *48*, 2822–2830.

Diehl, B. P RINCIPLES IN NMR S PECTROSCOPY. In.

Ding, S.; Gao, C.; Gu, L.-Q. Capturing Single Molecules of Immunoglobulin and Ricin with an Aptamer-Encoded Glass Nanopore. *Anal. Chem.* **2009**, *81*, 6649–6655.

Dondoni, A. The Emergence of Thiol-Ene Coupling as a Click Process for Materials and Bioorganic Chemistry. *Angew. Chem. Int. Ed. Engl.* **2008**, *47*, 8995–8997.

Dorvel, B.; Reddy, B.; Block, I.; Mathias, P.; Clare, S. E.; Cunningham, B.; Bergstrom, D. E.; Bashir, R. Vapor-Phase Deposition of Monofunctional Alkoxysilanes for Sub-Nanometer-Level Biointerfacing on Silicon Oxide Surfaces. *Adv. Funct. Mater.* **2010**, *20*, 87–95.

Duncan, W. R.; Prezhdo, O. V. Electronic Structure and Spectra of Catechol and Alizarin in the Gas Phase and Attached to Titanium. *J. Phys. Chem. B* **2005**, *109*, 365–373.

DURELL, S. .; GUY, H. . Structural Model of the Outer Vestibule and Selectivity Filter of the Shaker Voltage-Gated K+ Channel. *Neuropharmacology* **1996**, *35*, 761–773.

Duval, S.; Floquet, S.; Simonnet-Jégat, C.; Marrot, J.; Biboum, R. N.; Keita, B.; Nadjo, L.; Haouas, M.; Taulelle, F.; Cadot, E. Capture of the [Mo3S4]4+ Cluster within a {Mo18} Macrocycle Yielding a Supramolecular Assembly Stabilized by a Dynamic H-Bond Network. *J. Am. Chem. Soc.* **2010**, *132*, 2069–2077.

Duveau, D. Y.; Arce, P. M.; Schoenfeld, R. A.; Raghav, N.; Cortopassi, G. A.; Hecht, S. M. Synthesis and Characterization of mitoQ and Idebenone Analogues as Mediators of Oxygen Consumption in Mitochondria. *Bioorg. Med. Chem.* **2010**, *18*, 6429–6441.

Edition, I.; Federation, R. Cyclization of 1 Hydroxy 2 (oxoalkynyl)anthraquinones. *Russ. Chem. Bull.* **2004**, *53*, 2798–2804.

Emanuel MAKRLiK, laroslava H. ;; KYRS, M. OF ALKALI METAL CATIONS WITH DIBENZO-18-CROWN-6 (C) (D). *Collect. Czechoslov. Chem. Commun.* **1984**, *49*, 39–44.

Erk, C; Erbay, E. Novel Macrocycles . Part 6 . Synthesis , Structures and Cation Binding from Optical Spectroscopy of. *J. Incl. Phenom. Macrocycl. Chem.* **2000**, *36*, 229–241.

Erk, Ç.; Faculty, S. Cation Recognition with Fluorophore Crown Ethers 1. *Ind. Eng. Chem. Res.* **2000**, *39*, 3582–3588.

Evans, N. H.; Beer, P. D. A Ferrocene Functionalized Rotaxane Host System Capable of the Electrochemical Recognition of Chloride. *Org. Biomol. Chem.* **2011**, *9*, 92–100.

Evan-Salem, T.; Frish, L.; van Leeuwen, F. W. B.; Reinhoudt, D. N.; Verboom, W.; Kaucher, M. S.; Davis, J. T.; Cohen, Y. Self-Assembled Ionophores from Isoguanosine: Diffusion NMR Spectroscopy Clarifies Cation's and Anion's Influence on Supramolecular Structure. *Chemistry* **2007**, *13*, 1969–1977.

Fabriciova, G.; García-Ramos, J. .; Miskovsky, P.; Sanchez-Cortes, S. Adsorption and Acidic Behavior of Anthraquinone Drugs Quinizarin and Danthron on Ag Nanoparticles Studied by Raman Spectroscopy. *Vib. Spectrosc.* **2004**, *34*, 273–281.

Feliz, M.; García, J.; Aragón, E.; Pons, M. Fast 2D NMR Ligand Screening Using Hadamard Spectroscopy. *J. Am. Chem. Soc.* **2006**, *128*, 7146–7147.

Fielding, L. Determination of Association Constants (Ka) from Solution NMR Data. *Tetrahedron* **2000**, *56*, 6151–6170.

Finazzo, C.; Doorslaer, S. Van; Schweiger, A. Solvent Effects of cobalt(II) Phthalocyanine in Sulfuric Acid: A Continuous Wave and Pulse EPR Study. *J. Porphyr. Phthalocyanines* **2003**, *07*, 89–96.

Firnkes, M.; Pedone, D.; Knezevic, J.; Döblinger, M.; Rant, U. Electrically Facilitated Translocations of Proteins through Silicon Nitride Nanopores: Conjoint and Competitive Action of Diffusion, Electrophoresis, and Electroosmosis. *Nano Lett.* **2010**, *10*, 2162–2167.

Firouzabadi, H.; Iranpoor, N.; Jafarpour, M. A Simple , Efficient , and Highly Selective Method for the Iodination of Alcohols Using ZrCl 4 / NaI. *Tetrahedron Lett.* **2004**, *45*, 7451–7454.

Fleming, I.; Ghosh, S. K. A Total Synthesis of Nonactin. *J. Chem. Soc. Chem. Commun.* **1994**, 2287.

Fleming, V.; Wade, W. E. A Review of Laxative Therapies for Treatment of Chronic Constipation in Older Adults. *Am. J. Geriatr. Pharmacother.* **2010**, *8*, 514–550.

Foerster, O. Beitrage Zur Pathophysiologie Der Sehbahn Und Der Sehsphare. *J. fur Psychol. und Neurol.* **1929**, *39*, 463–485.

Fomba, K. W.; Galvosas, P.; Roland, U.; Kärger, J.; Kopinke, F.-D. New Option for Characterizing the Mobility of Organic Compounds in Humic Acids. *Environ. Sci. Technol.* **2009**, *43*, 8264–8269.

Fonari, M. S.; Ganin, E. V.; Basok, S. S.; Lyssenko, K. a.; Zaworotko, M. J.; Kravtsov, V. C. Structural Study of Salicylic Acid Salts of a Series of Azacycles and Azacrown Ethers †. *Cryst. Growth Des.* **2010**, *10*, 5210–5220.

Frański, R.; Gierczyk, B. ESI-MS Detection of Very Weak Pi-Stacking Interactions in the Mixed-Ligand Sandwich Complexes Formed by Substituted Benzo-Crown Ethers and Metal Cations. *J. Am. Soc. Mass Spectrom.* **2010**, *21*, 545–549.

Freeman, R.; Kupce, E. Fast Multidimensional NMR by Hadamard Spectroscopy. *eMagRes* **2008**, 1–11.

Frensdorff, H. K. Stability Constants of Cyclic Polyether Complexes with Univalent Cations. *JACs* **1971**, *93*, 600–606.

Gan, Q.; Yang, L.; Guo, P.; Yang, J.; Duan, Z. 2,5,11,14-Tetra-Oxa-8-Aza-Dispiro-[13.4.0]nona-Deca-15,17,19-Triene. *Acta Crystallogr. Sect. E. Struct. Rep. Online* **2010**, *66*, o1128.

Ganin, E. V.; Basok, S. S.; Yavolovskii, A. a.; Botoshansky, M. M.; Fonari, M. S. From Chains to Ladders in Co-Crystals with 2,3-Thiophene-15-Crown-5, 2,3-Naphtho-15-Crown-5, and Bis-(18-Crown-6)-Stilbene Constructed by Weak Hydrogen Bonding. *CrystEngComm* **2011**, *13*, 674.

Gao, C.-Y.; Zhao, L.; Wang, M.-X. Designed Synthesis of Metal Cluster-Centered Pseudo-Rotaxane Supramolecular Architectures. *J. Am. Chem. Soc.* **2011**, *133*, 8448–8451.

Gargiulli, C.; Gattuso, G.; Liotta, C.; Notti, A.; Parisi, M. F.; Pisagatti, I.; Pappalardo, S.; Organica, C.; Chimiche, S. Calix [5] Arene-Based Heteroditopic Receptor for 2-Phenylethylamine Hydrochloride Host-Guest Interaction of a Charged Species with a Neutral. *J. Org. Chem.* **2009**, *74*, 4350–4353.

Garofoli, S.; Jordan, P. C. Modeling Permeation Energetics in the KcsA Potassium Channel. *Biophys. J.* **2003**, *84*, 2814–2830.

Garza, J.; Vargas, R.; Gonza, I.; Gonza, F. J. Theoretical and Electrochemical Study of the Quinone-Benzoic Acid Adduct Linked by Hydrogen Bonds. *J. Phys. Chem. A.* **2003**, *107*, 11161–11168.

Gehrig, P.; Morf, W. E.; Welti, M.; Simon, W. 23. Catalysis of Ion Transfer by Tetraphenylborates in Neutral Carrier-Based Ion-Selective Electrodes. *Helv. Chim. Acta* **1990**, *73*, 203–212.

George, S. C. Manufacturing of Multiphase Polymeric Systems. *Polymer (Guildf).*

Gerig, J. T. (UCSB). Fluorine NMR. **2001**, 1–35.

Gevorgyan, V.; Rubin, M.; Benson, S.; Liu, J.; Yamamoto, Y. A Novel B(C(6)F(5))(3)-Catalyzed Reduction of Alcohols and Cleavage of Aryl and Alkyl Ethers with Hydrosilanes. *J. Org. Chem.* **2000**, *65*, 6179–6186.

Gholivand, M. B.; Kashanian, S.; Peyman, H.; Roshanfekr, H. DNA-Binding Study of Anthraquinone Derivatives Using Chemometrics Methods. *Eur. J. Med. Chem.* **2011**, *46*, 2630–2638.

Ghosh, B. D.; Lott, K. F.; Ritchie, J. E. Conductivity Dependence of PEG Content in an Anhydrous Proton Conducting Sol - Gel Electrolyte. *Chem. Mater* **2005**, *17*, 661–669.

Giorgetti, A.; Carloni, P. Molecular Modeling of Ion Channels: Structural Predictions. *Curr. Opin. Chem. Biol.* **2003**, *7*, 150–156.

Giribabu, L.; Kumar, C. V.; Reddy, P. Y. Porphyrin-Rhodanine Dyads for Dye Sensitized Solar Cells. *J. Porphyr. Phthalocyanines* **2006**, *10*, 1007–1016.

Gokel, G. W.; Leevy, W. M.; Weber, M. E. Crown Ethers: Sensors for Ions and Molecular Scaffolds for Materials and Biological Models. *Chem. Rev.* **2004**, *104*, 2723–2750.

Gong, H.-Y.; Rambo, B. M.; Lynch, V. M.; Keller, K. M.; Sessler, J. L. "Texas-Sized" Molecular Boxes: Building Blocks for the Construction of Anion-Induced Supramolecular Species via Self-Assembly. *J. Am. Chem. Soc.* **2013**, *135*, 6330–6337.

Grabow, W. W.; Zakrevsky, P.; Afonin, K. a; Chworos, A.; Shapiro, B. a; Jaeger, L. Self-Assembling RNA Nanorings Based on RNAI/II Inverse Kissing Complexes. *Nano Lett.* **2011**, *11*, 878–887.

Graf, N.; Yeğen, E.; Lippitz, A.; Treu, D.; Wirth, T.; Unger, W. E. S. Optimization of Cleaning and Amino- Silanization Protocols for Si Wafers to Be Used as Platforms for Biochip Microarrays by Surface Analysis (XPS, ToF-SIMS and NEXAFS Spectroscopy). *Surf. Interface Anal.* **2008**, *40*, 180–183.

Gu, F.; Zhang, L.; Teply, B. a; Mann, N.; Wang, A.; Radovic-Moreno, A. F.; Langer, R.; Farokhzad, O. C. Precise Engineering of Targeted Nanoparticles by Using Self-Assembled Biointegrated Block Copolymers. *Proc. Natl. Acad. Sci. U. S. A.* **2008**, *105*, 2586–2591.

Guerrero-Martínez, A.; Palafox, M. a.; Tardajos, G. Unexpected Binding Mode of Gemini Surfactants and Γ-Cyclodextrin: DOSY as a Tool for the Study of Complexation. *Chem. Phys. Lett.* **2006**, *432*, 486–490.

Guo, J.-B.; Xiang, J.-F.; Chen, C.-F. Synthesis of A Bis-Macrotricyclic Host and Its Complexation with Secondary Ammonium Salts: An Acid-Base Switchable Molecular Handcuff. *European J. Org. Chem.* **2010**, *2010*, 5056–5062.

Haines, D. E.; O'Hanlon, D. C.; Manna, J.; Jones, M. K.; Shaner, S. E.; Sun, J.; Hopkins, M. D. Oxidation-Potential Tuning of Tungsten-Alkylidyne Complexes over a 2 V Range. *Inorg. Chem.* **2013**, *52*, 9650–9658.

Hamilton, J. A.; Sabesan, M. N.; Steinrauf, L. K. Crystal Structure of Valinomycin Potassium Picrate : Anion Effects on Valinomycin Cation Complexes. *JACs* **1981**, *103*, 5880–5885.

Han, Y.; Mayer, D.; Offenhausser, a; Ingebrandt, S. Surface Activation of Thin Silicon Oxides by Wet Cleaning and Silanization. *Thin Solid Films* **2006**, *510*, 175–180.

Hankins, M. G.; Hayashita, T.; Kasprzyk, S. P.; Bartsch, R. A. Immobilization of Crown Ether Carboxylic Acids on Silica Gel and Their Use in Column Concentration of Alkali Metal Cations from Dilute Aqueous Solutions Are Immobilized on Silica Gel and Utilized for Column. *Anal. Chem.* **1996**, *68*, 2811–2817.

Harris, Daniel, C. *Quantitative Chemical Analysis*; Fiorillo, J., Ed.; Seventh.; W. H. Freeman and Company: China Lake, 2007; pp. 1–644.

Harth, E. M.; Hecht, S.; Helms, B.; Malmstrom, E. E.; Fre, J. M. J.; Hawker, C. J. The Effect of Macromolecular Architecture in Nanomaterials : A Comparison of Site Isolation in Porphyrin Core Dendrimers and Their Isomeric Linear Analogues. *JACS* **2002**, *124*, 3926–3938.

Haynes, D. H.; Pressman, B. C.; Kowalskys, A. A Nuclear Magnetic Resonance Study of "Na+ Complexing by Ionophores. *1Biochemistry* **971**, *10*, 852–860.

Heginbotham, L.; Lu, Z.; Abramson, T.; MacKinnon, R. Mutations in the K+ Channel Signature Sequence. *Biophys. J.* **1994**, *66*, 1061–1067.

Heinze, K.; Lang, H. Ferrocene - Beauty and Function. *Organomettalics* **2013**, *32*, 5623–5625.

Henderson, D. a; Collier, P. N.; Pavé, G.; Rzepa, P.; White, A. J. P.; Burrows, J. N.; Barrett, A. G. M. Studies on the Total Synthesis of Lactonamycin: Construction of Model ABCD Ring Systems. *J. Org. Chem.* **2006**, *71*, 2434–2444.

Hernandez-Perez, A. C.; Collins, S. K. A Visible-Light-Mediated Synthesis of Carbazoles. *Angew. Chem. Int. Ed. Engl.* **2013**, *52*, 12696–12700.

Heydari, A.; Khalilzadeh, M. A.; Lakouraj, M. M.; Zamenian, B.; Khaksar, S. Amberlyst-15 as a Heterogeneous Reusable Catalyst for the Synthesis of a -Hydroxy Phosphonates in Water. *SYNLETT* **2007**, 2347–2350.

Hirose, K.; Nakamura, Y.; Tobe, Y. Remarkable Effects of Chirality on Deslipping Reactions of Diastereomeric Rotaxanes and Relevant Mechanism Involving Pre-Equilibrium. *Org. Lett.* **2009**, *11*, 145–147.

Hirose, K.; Nishihara, K.; Harada, N.; Nakamura, Y.; Masuda, D.; Araki, M.; Tobe, Y. Highly Selective and High-Yielding Rotaxane Synthesis via Aminolysis of Prerotaxanes Consisting of a Ring Component and a Stopper Unit. *Org. Lett.* **2007**, *9*, 2969–2972.

Hirose, K.; Goshima, Y.; Wakebe, Y. T.; Naemura, K. First Step of Our Supramolecular Method Using (R)-Valinol as Example. First Step of Our Supramolecular Method Using (S)-Valinol as Example. 6. Spreadsheets for Evaluation of Δ. 1–30.

Ho, M.-L.; Hsieh, J.-M.; Lai, C.-W. C.-H. C.; Peng, H.-C.; Kang, C.; Wu, I.-C.; Chen, Y.-C.; Chou, P.-T. 15-Crown-5 Functionalized Au Nanoparticles Synthesized via Single Molecule Exchange on Silica Nanoparticles: Its Application to Probe 15-Crown-5/K + /15-Crown-5 “Sandwiches” as Linking Mechanisms. *J. Phys. Chem. C* **2009**, *113*, 1686–1693.

Hoeben, F. J. M.; Jonkheijm, P.; Meijer, E. W.; Schenning, A. P. H. J. About Supramolecular Assemblies of Pi-Conjugated Systems. *Chem. Rev.* **2005**, *105*, 1491–1546.

Hoffman, R. E.; Shabtai, E.; Rabinovitz, M.; Iyer, V. S.; Müllen, K.; Rai, A. K.; Bayrd, E.; Scott, L. T. Self-Diffusion Measurements of Polycyclic Aromatic Hydrocarbon Alkali Metal Salts. *J. Chem. Soc. Perkin Trans. 2* **1998**, 1659–1664.

Holland, D. P.; †; Struts, A. V.; ‡; Brown, M. F.; Thompson*, and D. H.; Thompson, D. H. Bolalipid Membrane Structure Revealed by Solid-State 2H NMR Spectroscopy. *JACs* **2008**, *130*, 4584–4585.

Hosseinzadeh, R.; Lasemi, Z. Selective Iodination of Alcohols with NaI / Amberlyst 15 in Acetonitrile. *SYNLETT* **2004**, *4*, 635–638.

Hu, B.-H.; Messersmith, P. B. Protection of 3,4-Dihydroxyphenylalanine (DOPA) for Fmoc Solid-Phase Peptide Synthesis. *Tetrahedron Lett.* **2000**, *41*, 5795–5798.

Hu, J.; Liu, S. Engineering Responsive Polymer Building Blocks with Host-Guest Molecular Recognition for Functional Applications. *Acc. Chem. Res.* **2014**, *ASAP*, NYA.

Humayun, M. S.; Weiland, J. D.; Fujii, G. Y.; Greenberg, R.; Williamson, R.; Little, J.; Mech, B.; Cimmarusti, V.; Van Boemel, G.; Dagnelie, G.; de Juan, E. Visual Perception in a Blind Subject with a Chronic Microelectronic Retinal Prosthesis. *Vision Res.* **2003**, *43*, 2573–2581.

Hutchinson, David W.; Thorton, D. M. The Synthesis of 1,1-Cyclopropanediylbis(phosphonic Acid). *Synthesis (Stuttg).* **1990**.

Ida, S.; Ouchi, M.; Sawamoto, M. Template-Assisted Selective Radical Addition toward Sequence-Regulated Polymerization: Lariat Capture of Target Monomer by Template Initiator. *J. Am. Chem. Soc.* **2010**, *132*, 14748–14750.

Insti-, N. Synthesis of Lipophilic 18-Crown-6 Diacids for the Membrane Transport of Alkaline-Earth Cations. *J. Org. Chem.* **1984**, *49*, 753–761.

Ions, P. SODIUM-POTASSIUM PUMP Medicine for the Heart. 2–3.

Isaacman, M. J.; Barron, K. a; Theogarajan, L. S. Clickable Amphiphilic Triblock Copolymers. *J. Polym. Sci. A. Polym. Chem.* **2012**, *50*, 2319–2329.

Isaksson, J.; Kjäll, P.; Nilsson, D.; Robinson, N. D.; Berggren, M.; Richter-Dahlfors, A. Electronic Control of Ca2+ Signalling in Neuronal Cells Using an Organic Electronic Ion Pump. *Nat. Mater.* **2007**, *6*, 673–679.

Izatt, R. M. . P. K. . B. J. S. Kinetic Data for Macrocycle Interaction with Cations and Anions. *Chem. Rev.* **1991**, *91*, 1721–2085.

Janigro, D.; Leaman, S. M.; Stanness, K. A. Dynamic in Vitro Modeling of the Blood – Brain Barrier : A Novel Tool for Studies of Drug Delivery to the Brain. *In Vitro* **1999**, *2*.

Jenks, W. P. *Advanced Org. Chem.*; 1985.

Ji, H.-F.; Dabestani, R.; Brown, G. M.; Hettich, R. L. Synthesis and Sensing Behavior of Cyanoanthracene Modified 1,3-Alternate calix[4]benzocrown-6: A New Class of Cs+ Selective Optical Sensors. *J. Chem. Soc. Perkin Trans. 2* **2001**, 585–591.

Jo, M.; Kosiorowska, M. A.; Wasiak, M. Effect of Temperature on the Process of Hydrophobic Hydration . Part II . Hydrophobic Hydration of 15-Crown-5 and 18-Crown-6 Ethers. *J. CHem. Eng. Data* **2010**, *55*, 5138–5143.

Jonkheijm, P.; Weinrich, D.; Köhn, M.; Engelkamp, H.; Christianen, P. C. M.; Kuhlmann, J.; Maan, J. C.; Nüsse, D.; Schroeder, H.; Wacker, R.; Breinbauer, R.; Niemeyer, C. M.; Waldmann, H. Photochemical Surface Patterning by the Thiol-Ene Reaction. *Angew. Chem. Int. Ed. Engl.* **2008**, *47*, 4421–4424.

Jorgensen, W. L. The Many Roles of Computation in Drug Discovery. *Science* **2004**, *303*, 1813–1818.

Jung, S.; Yi, H. Fabrication of Chitosan-Poly(ethylene Glycol) Hybrid Hydrogel Microparticles via Replica Molding and Its Application toward Facile Conjugation of Biomolecules. *Langmuir* **2012**, *28*, 17061–17070.

Kawai, H.; Nagamura, T.; Mori, T.; Yoshida, K. Picosecond Mechanism of Metal-Ion-Sensitive Fluorescence of Phenylimidazoanthraquinone with Azacrown. *J. Phys. Chem. A* **1999**, *103*, 660–664.

Kellogg, R.M. Rubidium and Cesium Carbonates. *Thieme* **2006**, 1497–1516.

Kempen, E.; Brodbelt, J. A Method for the Determination of Binding Constants by Electrospray Ionization Mass Spectrometry. *Anal. Chem.* **2000**, *72*, 5411–5416.

Khire, V. S.; Yi, Y.; Clark, N. a.; Bowman, C. N. Formation and Surface Modification of Nanopatterned Thiol-Ene Substrates Using Step and Flash Imprint Lithography. *Adv. Mater.* **2008**, *20*, 3308–3313.

Killops, K. L.; Campos, L. M.; Hawker, C. J. Robust, Efficient, and Orthogonal Synthesis of Dendrimers via Thiol-Ene "Click" Chemistry. *J. Am. Chem. Soc.* **2008**, *130*, 5062–5064.

Kim, D. S.; Lynch, V. M.; Park, J. S.; Sessler, J. L. Three Distinct Equilibrium States via Self-Assembly: Simple Access to a Supramolecular Ion-Controlled NAND Logic Gate. *J. Am. Chem. Soc.* **2013**, *135*, 14889–14894.

Kim, H.; Schall, O. F.; Fang, J.; Trafton, J. E.; Lu, T.; Atwood, J. L.; Gokel, G. W. DIRECT NUCLEOPHILIC AROMATIC SUBSTITUTION. *Jouranl Phys. Org. Chem.* **1992**, *5*, 482–495.

Kim, J. K.; Yang, S. Y.; Lee, Y.; Kim, Y. Functional Nanomaterials Based on Block Copolymer Self-Assembly. *Prog. Polym. Sci.* **2010**, *35*, 1325–1349.

Kim, S. K.; Sessler, J. L.; Gross, D. E.; Lee, C.-H.; Kim, J. S.; Lynch, V. M.; Delmau, L. H.; Hay, B. P. A calix[4]arene Strapped calix[4]pyrrole: An Ion-Pair Receptor Displaying Three Different Cesium Cation Recognition Modes. *J. Am. Chem. Soc.* **2010**, *132*, 5827–5836.

Kita, Y.; Arisawa, M.; Gyoten, M.; Nakajima, M.; Hamada, R.; Tohma, H.; Takada, T. Oxidative Intramolecular Phenolic Coupling Reaction Induced by a Hypervalent Iodine(III) Reagent: Leading to Galanthamine-Type Amaryllidaceae Alkaloids. *J. Org. Chem.* **1998**, *63*, 6625–6633.

Kitagawa, S.; Uemura, K. Dynamic Porous Properties of Coordination Polymers Inspired by Hydrogen Bonds. *Chem. Soc. Rev.* **2005**, *34*, 109–119.

Kitaori, K.; Furukawa, Y.; Yoshimoto, H. Integrated Chemical Process : Convenient Synthesis of Catalysis of CsF. *Adv. Synth. Catal.* **2001**, *343*, 95–101.

Klauke, S.; Goertz, M.; Rein, S.; Hoehl, D.; Thomas, U.; Eckhorn, R.; Bremmer, F.; Wachtler, T. Stimulation with a Wireless Intraocular Epiretinal Implant Elicits Visual Percepts in Blind Humans. *Invest. Ophthalmol. Vis. Sci.* **2011**, *52*, 449–455.

Kobayashi, S.; Sugiura, M.; Kitagawa, H.; Lam, W. W.-L. Rare-Earth Metal Triflates in Organic Synthesis. *Chem. Rev.* **2002**, *102*, 2227–2302.

Koizumi, M.; Dietrich-buchecker, C.; Sauvage, J. FULL PAPER A [2] Catenane Containing 1 , 1 J -Binaphthyl Units and 1 , 10-Phenanthroline Fragments : Synthesis and Intermolecular Energy Transfer Processes. *European J. Org. Chem.* **2004**, 770–775.

Kou, X.; Zhu, C.; Izattt, R. M. Novel Benzene-Bridged Macrobi- and Macrotricyclic Polyethers. *J. Org. Chem.* **1993**, *58*, 7694–7699.

Kowalewski, J. Mathematical Models in Cellular Biophysics Jacob Kowalewski Licentiate Thesis, KTH AlbaNova University Center, 2007, pp. 1–50.

Kuboniwa, H. A Coiled Synthetic Carboxylic Lonophore Capable of Encapsulating a Potassium Ion. *J. CHEM. SOC., CHEM. COMMUN* **1985**, 1468–1469.

Kuboniwa, H.; Yamaguchi, K.; Hirao, A.; Nakahama, S.; Yamazaki, N. Conformational Analysis of a Synthetic Carboxylic Ionophore in Solution by1H NMR Spectroscopy. *Magn. Reson. Chem.* **1986**, *24*, 961–964.

Kumar, S.; Hundal, G.; Bhalla, V.; Hundal, M. S.; Singh, H. The Synthesis and X-Ray Structure Analysis of an Unusual Bent Anthraquinone Based Coronand. *J. Chem. Res.* **1998**, 794–795.

Kyba, E. P.; Helgeson, R. C.; Madan, K.; Gokel, G. W.; Tarnowski, T. L.; Moore, I. S. S.; Cram, D. J. Host-Guest Complexation. 1. Concept and Illustrationla. *J. Am. Chem. Soc.* **1977**, *99*, 2564–2571. (67) Connors, K. A. *Binding Constants*; John Wiley & Sons, Ed.; First.; New York, Chichester, Brisbane, Toronto, Singapore, 1987; pp. 1–411.

Lai, R. Y.; Plaxco, K. W.; Heeger, A. J. Aptamer-Based Electrochemical Detection of Picomolar Platelet-Derived Growth Factor Directly in Blood Serum Variant of PDGF at 1 nM Directly in Undiluted , Unmodified. *Anal. Chem.* **2007**, *79*, 229–233.

Langton, M. J.; Beer, P. D. Rotaxane and Catenane Host Structures for Sensing Charged Guest Species. *Acc. Chem. Res.* **2014**, *ASAP*, A–E.

Larsen, B. a; Deria, P.; Holt, J. M.; Stanton, I. N.; Heben, M. J.; Therien, M. J.; Blackburn, J. L. Effect of Solvent Polarity and Electrophilicity on Quantum Yields and Solvatochromic Shifts of Single-Walled Carbon Nanotube Photoluminescence. *J. Am. Chem. Soc.* **2012**, *134*, 12485–12491.

Laslau, C.; Williams, D. E.; Wright, B. E.; Travas-Sejdic, J. Measuring the Ionic Flux of an Electrochemically Actuated Conducting Polymer Using Modified Scanning Ion Conductance Microscopy. *J. Am. Chem. Soc.* **2011**, *133*, 5748–5751.

Lee, A. E.; Grace, M. R.; Meyer, A. G.; Tuck, K. L. Fluorescent Zn2+ Chemosensors, Functional in Aqueous Solution under Environmentally Relevant Conditions. *Tetrahedron Lett.* **2010**, *51*, 1161–1165.

Lee, J. Y.; Lee, S. S. S. Y.; Park, S.; Kwon, J.; Sim, W. Unsymmetrical Calixcrowns Incorporating Hard and Soft Loops as a New Scaffold for Multinuclear Endo/exocyclic Complexation and Networking. *Inorg. Chem.* **2009**, *48*, 8934–8939.

Lehmann, M. W.; Evans, D. H. Mechanism of the Electrochemical Reduction of 3,5-Di- Tert -Butyl-1,2-Benzoquinone. Evidence for a Concerted Electron and Proton Transfer Reaction Involving a Hydrogen-Bonded Complex as Reactant †. *J. Phys. Chem. B* **2001**, *105*, 8877–8884.

Lehn. Supramolecular Chemistry—Scope and Perspectives Molecules, Supermolecules, and Molecular Devices(Nobel Lecture). *Angew. Chemie Int. Ed. English* **1988**, *27*, 89–112.

Lehn, J. M. Supramolecular Chemistry: Receptors, Catalysts, and Carriers. *Science (80-.).* **1985**, *227*, 849–856.

Lehn, J. Supramolecular Chemistry- Scope and Perspectives : Molecules-Supermolecules- Molecular Devices. *J. Incl. Phenom.* **1988**, *6*, 351–396.

Lemoine, D.; Jiang, R.; Taly, A.; Chataigneau, T.; Specht, A.; Grutter, T. Ligand-Gated Ion Channels: New Insights into Neurological Disorders and Ligand Recognition. *Chem. Rev.* **2012**.

Lickiss, P. D. The Synthesis and Structure of Organosilanols. *Adv. Inorg. Chem.* **1995**, *42*, 147–262.

Lien-Tsai, Y.; Cha'o-Kuang, C. The Solution of the Blasius Equation by the Differential Transformation Method. *Math. Comput. Model.* **1998**, *28*, 101–111.

Lin, W.; Yuan, L.; Cao, Z.; Feng, J.; Feng, Y. Fluorescence Enhancement of Coumarin–quinoline by Transition Metal Ions: Detection of Paramagnetic Ni2+ and Co2+. *Dye. Pigment.* **2009**, *83*, 14–20.

Liu, C.-H.; Chiu, L.-K.; Yeh, J.-Y.; Tsiang, R. C.-C. Making Organic-Inorganic Nanocomposites via Selective Dispersion of PS-Tethered SiO2 Particles in Polystyrene-Block-Polymethylmethacrylate Copolymer. *J. Nanomater.* **2012**, *2012*, 1–7.

Liu, F.; Helgeson, R. C.; Houk, K. N. Building on Cram ' S Legacy : Stimulated Gating in Hemicarcerands. *Acc. Chem. Res.* **2014**.

Liu, G. Chemical Processing of Assembled Block Copolymers. *Chem. Process.* **2011**.

Liu, H.; Zhang, Y.; Hu, J.; Li, C.; Liu, S. Multi-Responsive Supramolecular Double Hydrophilic Diblock Copolymer Driven by Host-Guest Inclusion Complexation between Î²-Cyclodextrin and Adamantyl Moieties. *Macromol. Chem. Phys.* **2009**, *210*, 2125–2137.

Liu, W.; Member, S.; Vichienchom, K.; Member, S.; Clements, M.; Demarco, S. C.; Hughes, C.; Mcgucken, E.; Humayun, M. S.; Juan, E. De; Weiland, J. D.; Greenberg, R. A Neuro-Stimulus Chip with Telemetry Unit for. *IEEE J. Solid State Circuits* **2000**, *35*, 1487–1497.

Long, S.; Tao, X.; Campbell, E.; MacKinnon, R. Atomic Structure of a Voltage-Dependent K+ Channel in a Lipid Membrane-like Environment. *Nature* **2007**, *450*.

Lu, J.; Wu, L.; Jiang, J.; Zhang, X. Helical Nanostructures of an Optically Active Metal-Free Porphyrin with Four Optically Active Binaphthyl Moieties: Effect of Metal-Ligand Coordination on the Morphology. *Eur. J. Inorg. Chem.* **2010**, *2010*, 4000–4008.

Mahoney, J. M.; Beatty, a M.; Smith, B. D. Selective Recognition of an Alkali Halide Contact Ion-Pair. *J. Am. Chem. Soc.* **2001**, *123*, 5847–5848.

Maisch, S.; Buckel, F.; Effenberger, F. Preparation of High Quality Electrical Insulator Self-Assembled Monolayers on Gold. Experimental Investigation of the Conduction Mechanism through Organic Thin Films. *J. Am. Chem. Soc.* **2005**, *127*, 17315–17322.

Marcus, R. A. Electron Transfer Theory and Its Inception. *Phys. Chem Chem. Phys.* **2012**, *14*, 13729–13730.

Marius, P.; de Planque, M. R. R.; Williamson, P. T. F. Probing the Interaction of Lipids with the Non-Annular Binding Sites of the Potassium Channel KcsA by Magic-Angle Spinning NMR. *Biochim. Biophys. Acta* **2012**, *1818*, 90–96.

Marsella, M. J.; Swager, T. M. Designing Conducting Polymer-Based Sensors: Selective Ionochromic Response in Crown Ether-Containing Polythiophenes. *J. Am. Chem. Soc.* **1993**, *115*, 12214–12215.

Martín-Hidalgo, M.; Camacho-Soto, K.; Gubala, V.; Rivera, J. M. Self-Assembled Cation Transporters Made from Lipophilic 8-Phenyl-2'-Deoxyguanosine Derivatives. *Supramol. Chem.* **2010**, *22*, 862–869.

Martino, R.; Gilard, V. F LUORINE -19 OR P HOSPHORUS -31 NMR S PECTROSCOPY : A P OWERFUL T ECHNIQUE FOR B IOFLUID M ETABOLIC S TUDIES AND P HARMACEUTICAL F ORMULATION A NALYSIS OF F LUORINATED OR P HOSPHORYLATED D RUGS.

Maruyama, K.; Sohmiya, H.; Tsukube, H. ONE-STEP SYNTHESIS AND ELECTROCHEMICALLY ENHANCED CATION-BINDING PROPERTIES OF NOVEL "QUINONOID CROWN ETHERS."*Tetrahedron Lett.* **1985**, *26*, 3583–3586.

Masia, M.; Rey, R. Reaction Rate Theory Approach to Thermodynamic State Dependence of Hydration Shell Exchange for Li + (Aq). *J. Phys. Chem. B* **2003**, *107*, 2651–2659.

Material, S.; This, C. C.; Society, T. R. Supporting Information for "Drastic Selectivity Reversal on Crown-Ether Based Ion-Sensing Membranes Made of Ordered Mesoporous Silica and Conventional Sol-Gel Derived One" Setsuko Yajima,. **2010**, *13*, 5–6.

Matsuo, T.; Morimoto, N. Visual Acuity and Perimacular Retinal Layers Detected by Optical Coherence Tomography in Patients with Retinitis Pigmentosa. *Br. J. Ophthalmol.* **2007**, *91*, 888–890.

Matthews, S. E.; Schmitt, P.; Felix, V.; Drew, M. G. B.; Beer, P. D. Calix[4]tubes: A New Class of Potassium-Selective Ionophore. *J. Am. Chem. Soc.* **2002**, *124*, 1341–1353.

Matthias Firnkes†, Daniel Pedone†, Jelena Knezevic†, Markus Döblinger‡, and U. R. Electrically Facilitated Translocations of Proteins through Silicon Nitride Nanopores: Conjoint and Competitive Action of Diffusion, Electrophoresis, and Electroosmosis.

Mcelvain, S. M. Redox-Switched Crown Ethers. Cyclic-Acyclic Interconversion Coupled with Redox between Dithiol and Disulfide Summary: *J. Org. Chem.* **1984**, *92*, 3440–3442.

McGuire, M. *Nutritional Sciences: From Fundamentals to Food*; Thomson/Wadsworth: Belmont, CA, 2007.

McOmie, J. F. W.; West, D. E. . 3,3'-Dihydroxybiphenyl. *Org. Syn.* **2002**, *5*, 412–413.

Megyes, T.; Jude, H.; Grósz, T.; Bakó, I.; Radnai, T.; Tárkányi, G.; Pálinkás, G.; Stang, P. J. X-Ray Diffraction and DOSY NMR Characterization of Self-Assembled Supramolecular Metallocyclic Species in Solution. *J. Am. Chem. Soc.* **2005**, *127*, 10731–10738.

Meillon, J.-C.; Voyer, N. A Synthetic Transmembrane Channel Active in Lipid Bilayers. *Angew. Chem. Int. Ed. Engl.* **1997**, *36*, 967–969.

Mishchenko, O. G.; Maslennikov, S. V.; Spirina, I. V.; Kurskii, Y. a.; Faerman, V. I.; Maslennikov, V. P. Photolytic Transformations of P-Quinones. *Russ. J. Gen. Chem.* **2008**, *78*, 1529–1532.

Mohammad Zadeh Kakhki, R.; Rounaghi, G. Competitive Bulk Liquid Membrane Transport of Heavy Metal Cations Using the 18-Crown-6 Ligand as an Ionophore. *J. Chem. Eng. Data* **2011**, *56*, 3169–3174.

Moore, S. J.; Fisher, M. G.; Yano, M.; Tong, C. C.; Gale, P. A. A Dual Host Approach to Transmembrane Transport of Salts. *Chem. Commun. (Camb).* **2011**, *47*, 689–691.

Moran, J.; Schreiber, E. C.; Engel, E. *Nuclear Methylation of Some Phenolic Compounds*; 1952; pp. 127–129.

Mouro, C.; Mutzenhardt, P.; Diter, B.; Canet, D. HR-DOSY Experiments with Radiofrequency Field Gradients (RFG) and Their Processing according to the HD Method. *Magn. Reson. Chem.* **2002**, *40*, S133–S138.

Mühlstein, L.; Riederer, M.; Platschek, B.; Bein, T. In Situ Functionalization of Mesoporous Silica within the Pores of Anodic Alumina Membranes. *J. Mater. Chem.* **2009**, *19*, 9195.

Mukherjee, S.; Bauri, A. K.; Bhattacharya, S. Photophysical Investigations and Binding Strength in Supramolecular Interaction of a Newly Designed Diporphyrin Tweezer with Fullerenes C60 and C70 in Solution. *Chem. Phys. Lett.* **2010**, *500*, 128–139.

Mutalib Md Jani, A.; Anglin, E. J.; McInnes, S. J. P.; Losic, D.; Shapter, J. G.; Voelcker, N. H. Nanoporous Anodic Aluminium Oxide Membranes with Layered Surface Chemistry. *Chem. Commun. (Camb).* **2009**, 3062–3064.

Nabeshima, T.; Nishida, D.; Saiki, T. Synthesis of Redox Active Large Macrocyclic Hosts and the Recognition of Secondary Ammonium Salts. *Tetrahedron* **2003**, *59*, 639–647.

Nakatsuji, Shinichi; Ohmori, Yuko; Iyoda, Masahiko; Nakashima, Kenchiro; Akiyama, S. Synthesis and Properties of Crown Compounds Containing Anthraquinone Nuclei. *Bull. Chem. Soc. Jpn.1* **1983**, *56*, 3185–3186.

Naumann, R.; Walz, D.; Schiller, S. M.; Knoll, W. Kinetics of v Alinomycin-Mediated K ’ Ion Transport through Tethered Bilayer Lipid Membranes. *J. Electroanal. Chem.* **2003**, *551*, 241–252.

Nelson, W. K. The Chemistry of the Triethylsilicyl Group. **1933**, *3*, 195–202.

Niedzwiecki, D. J.; Grazul, J.; Movileanu, L. Single-Molecule Observation of Protein Adsorption onto an Inorganic Surface. *J. Am. Chem. Soc.* **2010**, *132*, 10816–10822.

Normale, S.; Cavalieri, P. In Silico Study of Molecular-Engineered Nanodevices: A Lockable Light-Driven Motor in Dichloromethane Solution. *J. Phys. Chem. Lett.* **2013**, *4*, 3885–3890.

Noskov, S. Y.; Roux, B. Ion Selectivity in Potassium Channels. *Biophys. Chem.* **2006**, *124*, 279–291.

Orvig, C.; Board, E.; Edwards, P. G.; Hahn, F. E.; Champness, N. R.; Dempsey, J. L.; Winkler, J. R.; Gray, H. B.; Stephenson, A.; Ward, M. D. Hydrogenation of Arenes and N-Heteroaromatic Compounds over Ruthenium Nanoparticles on poly(4-Vinylpyridine): A Versatile Catalyst Operating by a Substrate-Dependent Dual Site Mechanism†. *Dalt. Trans* **2011**, *40*, 10621–10632.

Ouellet, M.; Voyer, N.; Auger, M. Membrane Interactions and Dynamics of a 21-Mer Cytotoxic Peptide: A Solid-State NMR Study. *Biochim. Biophys. Acta* **2010**, *1798*, 235–243.

Pallavicini, P.; Dacarro, G.; Galli, M.; Patrini, M. Spectroscopic Evaluation of Surface Functionalization Efficiency in the Preparation of Mercaptopropyltrimethoxysilane Self-Assembled Monolayers on Glass. *J. Colloid Interface Sci.* **2009**, *332*, 432–438.

Pantoja-Uceda, D.; Arolas, J. L.; García, P.; López-Hernández, E.; Padró, D.; Aviles, F. X.; Blanco, F. J. The NMR Structure and Dynamics of the Two-Domain Tick

Carboxypeptidase Inhibitor Reveal Flexibility in Its Free Form and Stiffness upon Binding to Human Carboxypeptidase B. *Biochemistry* **2008**, *47*, 7066–7078.

Park, C.; Yoon, J.; Thomas, E. L. Enabling Nanotechnology with Self Assembled Block Copolymer Patterns. *Polymer (Guildf).* **2003**, *44*, 6725–6760.

Park, H.; Lee, S. Determination of the Active Site Protonation State of Beta-Secretase from Molecular Dynamics Simulation and Docking Experiment: Implications for Structure-Based Inhibitor Design. *J. Am. Chem. Soc.* **2003**, *125*, 16416–16422.

Park, J.-W.; Park, Y. J.; Jun, C.-H. Post-Grafting of Silica Surfaces with Pre-Functionalized Organosilanes: New Synthetic Equivalents of Conventional Trialkoxysilanes. *Chem. Commun. (Camb).* **2011**, *47*, 4860–4871.

Park, Y.; Apodaca, D. C.; Pullen, J.; Advincula, R. C. Highly Sensitive and Selective "Turn-on" Calcium Cation Sensing from a Dendronic Terthiophene Tetraethylene Glycol (TEG) Molecule. *J. Phys. Chem. B* **2010**, *114*, 13084–13094.

Parlayan, S.; Başoğlu, A.; Ocak, M.; Alp, H.; Kantekin, H.; Ocak, Ü. Complexation of Metal Ions with the Novel Diazadithia Crown Ether Carrying Two Anthryl Pendants in Acetonitrile–tetrahydrofuran. *J. Incl. Phenom. Macrocycl. Chem.* **2009**, *67*, 133–140.

Patel, A.; Lindhorst, T. K. Multivalent Glycomimetics : Synthesis of Nonavalent Mannoside Clusters with Variation of Spacer Properties. *Carbohydr. Res.* **2006**, *341*, 1657–1668.

Patel, S.; Vuillard, L.; Cleasby, A.; Murray, C. W.; Yon, J. Apo and Inhibitor Complex Structures of BACE (beta-Secretase). *J. Mol. Biol.* **2004**, *343*, 407–416.

Pedersen, C. J. Cyclic Polyethers and Their Complexes with Metal Salts. *JACs* **1967**, *89*, 7017–7037.

Pedersen, C. J.; Frensdorff, H. K. Macrocyclic Polyethers and Their Complexes. *Angew. Chem. Int. Ed. Engl.* **1972**, *11*, 16–25.

Percec, V; Heck, G; Johansson, D; Tomazos, M; Kawasumi, P; Chu, P; Ungar, G. *MOLECULAR RECOGNITION DIRECTED SELF-ASSEMBLY OF SUPRAMOLECULAR LIQUID CRYSTALS*; Cleveland, 1994; pp. 1–62.

Peter, C.; Hummer, G. Ion Transport through Membrane-Spanning Nanopores Studied by Molecular Dynamics Simulations and Continuum Electrostatics Calculations. *Biophys. J.* **2005**, *89*, 2222–2234.

Peter, J.; Vogtle, F. Neue Chromoionophore. *Chem. Ber.* **1981**, *114*, 638–651.

Pinkhassik*, S. A. D. and E. Supporting Information Synergistic Co-Entrapment and Triggered Release in Hollow Nanocapsules with Uniform Nanopores. *Angew. Chemie Int. Ed. English* **2007**, *6*, 3–6.

Piyathaisere, D.; Margalet, C.; Shyu, J.; D'Anna, S.; Weiland, J. Heat Effects on the Retina. *Opthalmic Surgery, Lasers and Imaging* **2003**, *2*, 114–120.

Platonov, A. Y.; Evdokimov, A. N.; Kurzin, A. V.; Maiyorova, H. D. Solubility of Potassium Carbonate and Potassium Hydrocarbonate in Methanol. *J. Chem. Eng. Data* **2002**, *47*, 1175–1176.

Platschek, B.; Keilbach, A.; Bein, T. Mesoporous Structures Confined in Anodic Alumina Membranes. *Adv. Mater.* **2011**, *23*, 2395–2412.

Pliska, V. K. Substrate Binding to Enzymes, 2001, 1–10.

Pohlers, G.; Scaiano, J. C.; Sinta, R.; Brainard, R.; Pai, D. Mechanistic Studies of Photoacid Generation from Substituted 4,6-Bis(trichloromethyl)-1,3,5-Triazines. *Chem. Mater.* **1997**, *9*, 1353–1361.

Privett, B. J.; Shin, J. H.; Schoenfisch, M. H. Electrochemical Sensors. *Anal. Chem.* **2010**, *82*, 4723–4741.

Qazi, M. A.; Qureshi, I.; Memon, S. A Highly Copper Selective Chromogenic calix[4]arene Derivative. *New J. Chem.* **2010**, *34*, 2579.

Qiu, X.-L.; Li, G.; Wu, G.; Zhu, J.; Zhou, L.; Chen, P.-L.; Chamberlin, a R.; Lee, W.-H. Synthesis and Biological Evaluation of a Series of Novel Inhibitor of Nek2/Hec1 Analogues. *J. Med. Chem.* **2009**, *52*, 1757–1767.

Rahmen, M. A.; Kwon, N.-H.; Won, M.-S.; Hyun, M.-H.; Shim, Y.-B. Selective Binding of NH4 + by Redox-Active Crown Ethers: Application to a NH4 + Sensor. *Anal. Chem.* **2004**, *76*, 3660–3665.

Rajapakse, H. a; Nantermet, P. G.; Selnick, H. G.; Munshi, S.; McGaughey, G. B.; Lindsley, S. R.; Young, M. B.; Lai, M.-T.; Espeseth, A. S.; Shi, X.-P.; Colussi, D.; Pietrak, B.; Crouthamel, M.-C.; Tugusheva, K.; Huang, Q.; Xu, M.; Simon, A. J.; Kuo, L.; Hazuda, D. J.; Graham, S.; Vacca, J. P. Discovery of Oxadiazoyl Tertiary Carbinamine Inhibitors of Beta-Secretase (BACE-1). *J. Med. Chem.* **2006**, *49*, 7270–7273.

Ramadas, S.; Krupadanam, G. L. D. Enantioselective Acylation of 2-Hydroxymethyl-2 , 3-Dihydrobenzofurans Catalysed by Lipase from Pseudomonas Cepacia (Amano PS) and Total Stereoselective Synthesis of (−) - (R) -MEM-Protected Arthrographol. *Alcohol* **2000**, *11*, 3375–3393.

Rashatasakhon, P.; Jaiyu, A.; Rojanathanes, R.; Muangsin, N.; Chaichit, N.; Sukwattanasinitt, M. X-Ray Guided 1H NMR Analysis of Pinched Cone calix[4]arenes. *J. Mol. Struct.* **2010**, *963*, 22–26.

Raven; Johnson; Losos; Singer. *Biology*; Seventh.; McGrawHill: New York; p. 986,987.

Reed, M. I. Z. A. T.; Pawlak, K.; Bradshaw, J. S.; Technobgies, I. B. C. A.; Box, P. O. Thermodynamic and Kinetic Data for Macrocycle Interaction with Cations and Anions (5) L . F . Lindoy , ' Heavy Metal Chemistry of Mixed Donor Macrocyclic Ligands : Strategies for Obtaining. *Chem. Rev.* **1991**, *91*, 1721–2085.

Rizzo, J. F. Perceptual Efficacy of Electrical Stimulation of Human Retina with a Microelectrode Array during Short-Term Surgical Trials. *Invest. Ophthalmol. Vis. Sci.* **2003**, *44*, 5362–5369.

Roadshow, A.; Gmbh, A. T. DOSY 3.1 News and Additions in the Diffusion Software. **2011**.

Roush, W. R.; Madar, D. J. Towards the Synthesis of Streptovaricin Fully Elaborated Aromatic Precursors and Coupling D : Synthesis of with Ansa Chain Fragments. *Tetrahedron Lett.* **1993**, *34*, 1553–1556.

Roux-Fromy, M. On the Hill Plot of NMR Data for Titration of Protein Residues. *Biophys. Struct. Mech.* **1982**, *8*, 289–306.

Russell, T. P.; Thurn-Albrecht, T.; Tuominen, M.; Huang, E.; Hawker, C. J. Block Copolymers as Nanoscopic Templates. *Macromol. Symp.* **2000**, *159*, 77–88.

Saji, Tetsuo; Kinoshita, I. Electrochemical Ion Transport with Ferrocene Functionalized Crown Ether. *J. CHEM. SOC., CHEM. COMMUN* **1986**, 716–717.

Sakai, N.; Mareda, J.; Vauthey, E.; Matile, S. Core-Substituted Naphthalenediimides. *Chem. Commun. (Camb).* **2010**, *46*, 4225–4237.

Sakai, R.; Yonekawa, T.; Otsuka, I.; Kakuchi, R.; Satoh, T.; Kakuchi, T. Host – Guest Complexation-Triggered Chiroptical Change of Poly (Phenylacetylene) S Bearing Binaphthocrown Ether Moieties on the Main Chain. *J. Polym. Sci. Part A* **2010**, *48*, 1197–1206.

Salvador, J. a. R.; Ppinto, R. M. a.; Silvestre, S. M. Recent Advances of Bismuth(III) Salts in Organic Chemistry: Application to the Synthesis of Aliphatics, Alicyclics, Aromatics, Amino Acids and Peptides, Terpenes and Steroids of Pharmaceutical Interest. *Mini. Rev. Org. Chem.* **2009**, *6*, 241–274.

Sandor, P. High Resolution Diffusion-Ordered Spectroscopy (HR-DOSY), 2011, 1–8.

SANGAMESH G. KUMBAR, MICHELLE D. KOFRON, L. S. N.; LAURENCIN, C. T. Cell Behavior Toward Nanostructured Surfaces. In *Biomedical Nanostructures*; John Wiley & Sons, 2008; pp. 261–294.

Sasaki, Y.; Mukai, M.; Kawasaki, A.; Yasuhara, K.; Kikuchi, J. Switching of the Enzymatic Activity Synchronized with Signal Recognition by an Artificial DNA Receptor on a Liposomal Membrane. *Org. Biomol. Chem.* **2011**, *9*, 2397–2402.

Sassetti, C. M.; Boyd, D. H.; Rubin, E. J. Genes Required for Mycobacterial Growth Defined by High Density Mutagenesis. *Mol. Microbiol.* **2003**, *48*, 77–84.

Savić, R.; Eisenberg, A.; Maysinger, D. Block Copolymer Micelles as Delivery Vehicles of Hydrophobic Drugs: Micelle-Cell Interactions. *J. Drug Target.* **2006**, *14*, 343–355.

Savko, M.; Kaščáková, S.; Gbur, P.; Miškovský, P.; Uličný, J. Performance of Time Dependent Density Functional Theory on Excitations of Medium Sized Molecules – Test on Ionic Forms of Anthraquinone Dihydroxy Derivatives. *J. Mol. Struct. THEOCHEM* **2007**, *823*, 78–86.

Sawada, M.; Okumura, Y.; Shizuma, M.; Takai, Y.; Hidaka, Y.; Yamada, H.; Tanaka, T.; Kaneda, T.; Hirose, K.; Misumi, S.; Chem, A. N. A. Enantioselective Complexation of Carbohydrate or Crown Ether Hosts with Organic Ammonium Ion Guests Detected by FAB Mass Spectrometry. *JACS* **1993**, *115*, 7381–7388.

Schnaars, D. D.; Wu, G.; Hayton, T. W. Silylation of the Uranyl Ion Using B(C6F5)3-Activated Et3SiH. *Inorg. Chem.* **2011**, *50*, 9642–9649.

Schwartz, M. A.; Rose, B. F.; Holton, R. A.; Scott, S. W. Intramolecular Oxidative Coupling of Diphenolic, Monophenolic, and Nonphenolic Substrates. *JACs* **1977**, *99*, 2572–2576.

Scott, E. R.; White, H. S.; Phipps, J. B. Iontophoretic Transport through Porous Membranes Using Scanning Electrochemical Microscopy: Application to in Vitro Studies of Ion Fluxes through Skin. *Anal. Chem.* **1993**, *65*, 1537–1545.

Sczech, R.; Eckert, K.; Acker, M. M. Convective Instability in a Liquid-Liquid System due to Complexation with a Crown Ether. *J. Phys. Chem. A* **2008**, *112*, 7357–7364.

Selektor, S. L.; Shokurov, A. V.; Arslanov, V. V.; Gorbunova, Y. G.; Birin, K. P.; Raitman, O. a.; Morote, F.; Cohen-Bouhacina, T.; Grauby-Heywang, C.; Tsivadze, A.

Y. Orientation-Induced Redox Isomerism in Planar Supramolecular Systems. *J. Phys. Chem. C* **2014**, *118*, 4250–4258.

Sereda, G. a.; Akhvlediani, D. G. Methylation of 1,8-Dihydroxy-9,10-Anthraquinone with and without Use of Solvent-Free Technique☆. *Tetrahedron Lett.* **2003**, *44*, 9125–9126.

Seu, K. J.; Pandey, A. P.; Haque, F.; Proctor, E. a; Ribbe, A. E.; Hovis, J. S. Effect of Surface Treatment on Diffusion and Domain Formation in Supported Lipid Bilayers. *Biophys. J.* **2007**, *92*, 2445–2450.

Shabtai, E.; Hoffman, R. E.; Cheng, P.-C.; Bayrd, E.; Preda, D. V.; Scott, L. T.; Rabinovitz, M. Reduced Corannulenes: 1,8-Dicorannulenyloctane Anions, a Supramolecular Octaanion. *J. Chem. Soc. Perkin Trans. 2* **2000**, 129–133.

Shaikh, J.; Ankola, D. D.; Beniwal, V.; Singh, D.; Kumar, M. N. V. R. Nanoparticle Encapsulation Improves Oral Bioavailability of Curcumin by at Least 9-Fold When Compared to Curcumin Administered with Piperine as Absorption Enhancer. *Eur. J. Pharm. Sci.* **2009**, *37*, 223–230.

Sharghi, H.; Aghapour, G. Claisen Rearrangement of Allyloxyanthraquinones with Silver / Potassium Iodide in Acetic Acid as a New Attention in Recent Years due to Their Industrial Applica- We Examined the Title Reaction for the Use of Ag / KI and. *J. Org. Chem.* **2000**, *65*, 2813–2815.

Shealy, Y. F.; Krauth, C. a; Struck, R. F.; Montgomery, J. a. 2-Haloethylating Agents for Cancer Chemotherapy. 2-Haloethyl Sulfonates. *J. Med. Chem.* **1983**, *26*, 1168–1173.

Shieh, W.; Dell, S.; Repic, O. (DBU) for the Esterification of Carboxylic Acids with Dimethyl Carbonate. *Society* **2002**, 2188–2191.

Shih, J. S.; Popov, A. I. Potassium-39 NMR Studies of Potassium Salts in Various Solvents. *Inorg. Nucl. Chem. Lett.* **1977**, *13*, 105–110.

Shih, J. S.; Popov, A. I.; Lansing, E. (Received 3 January 1977). *INORG. NUCL. CHEM. Lett.* **1977**, *13*, 105–110.

Shimakoshi, H.; Maeda, D.; Hisaeda, Y. Supramolecular Assemblies of Crown-Substituted Dinickel and Dicobalt Complexes with Guest Cation Binding. *Supramol. Chem.* **2011**, *23*, 131–139.

Shrivastava, I. H.; Sansom, M. S. Simulations of Ion Permeation through a Potassium Channel: Molecular Dynamics of KcsA in a Phospholipid Bilayer. *Biophys. J.* **2000**, *78*, 557–570.

Shrivastava, I. H.; Peter Tieleman, D.; Biggin, P. C.; Sansom, M. S. P. K+ versus Na+ Ions in a K Channel Selectivity Filter: A Simulation Study. *Biophys. J.* **2002**, *83*, 633–645.

Shukla, M.; Dorai, K. Resolving Overlaps in Diffusion Encoded Spectra Using Band-Selective Pulses in a 3D BEST-DOSY Experiment. *J. Magn. Reson.* **2011**, *213*, 69–75.

Shvarev, A. Photoresponsive Ion-Selective Optical Sensor. *J. Am. Chem. Soc.* **2006**, *128*, 7138–7139.

Singh, U. S.; Scannell, R. T.; An, H.; Carter, B. J.; Hecht, S. M. DNA Cleavage by Di- and Trihydroxyalkylbenzenes. *JACs* **1995**, *117*, 12691–12699.

Singhana, B.; Jamison, A. C.; Hoang, J.; Lee, T. R. Self-Assembled Monolayer Films Derived from Tridentate Cyclohexyl Adsorbates with Alkyl Tailgroups of Increasing Chain Length. *Langmuir* **2013**, *29*, 14108–14116.

Soemo, A. R.; Wirth, M. J. Lipid Bilayer Blanketing versus Penetrating Silica Colloidal Crystals. *Langmuir* **2010**, *26*, 2196–2199.

Song, J.; Dai, L.; Ji, Y.; Xiao, F.; Bolink, H. J.; Cappelli, L.; Coronado, E.; Parham, A.; Vasylyev, M.; Neumann, R.; Han, M. R.; Hirayama, Y.; Hara, M.; Wang, Y.; Cao, G.; Moon, C.; Dalpian, G. M.; Zhang, Y.; Wei, S.; Li, J.; Tawarayama, H.; Utsuno, F.; Inoue, H.; Hosono, H.; Song, Y.; Modrow, H.; Henry, L. L.; Saw, C. K.; Doomes, E. E.; Palshin, V.; Hormes, J.; Kumar, C. S. S. R. Green Light-Emitting Solid-State Electrochemical Cell Obtained from a Homoleptic Iridium(III) Complex Containing Ionically Charged Ligands. *Chem. Mater* **2006**, *18*, 2778–2780.

Song, Y.; Buettner, G. R. Thermodynamic and Kinetic Considerations for the Reaction of Semiquinone Radicals to Form Superoxide and Hydrogen Peroxide. *Free Radic Biol Med.* **2011**, *49*, 919–962.

Song, Y.-A.; Melik, R.; Rabie, A. N.; Ibrahim, A. M. S.; Moses, D.; Tan, A.; Han, J.; Lin, S. J. Electrochemical Activation and Inhibition of Neuromuscular Systems through Modulation of Ion Concentrations with Ion-Selective Membranes. *Nat. Mater.* **2011**, *10*, 980–986.

Sousa, F.; Fernandes, P. A.; Joa, M. Protein – Ligand Docking : Current Status and Future. *Bioinformatics* **2006**, *26*, 15–26.

Spencer, P. S.; Palmer, V. S. Interrelationships of Undernutrition and Neurotoxicity: Food for Thought and Research Attention. *Neurotoxicology* **2012**.

Stang, P. J. Abiological Self-Assembly via Coordination: Formation of 2D Metallacycles and 3D Metallacages with Well-Defined Shapes and Sizes and Their Chemistry. *J. Am. Chem. Soc.* **2012**, *134*, 11829–11830.

Stein, J.; Lewis, L. N.; Smith, K. a.; Lettko, K. X. Mechanistic Studies of Platinum-Catalyzed Hydrosilylation. *J. Inorg. Organomet. Polym.* **1991**, *1*, 325–334.

Steinbeck, C. a; Chmelka, B. F. Rapid 1H[13C]-Resolved Diffusion and Spin-Relaxation Measurements by NMR Spectroscopy. *J. Am. Chem. Soc.* **2005**, *127*, 11624–11635.

STEINRAUF, L. K. Crystal Structures of Valinomycin with Potassium Tetrachloroaurate and Rubidium Tetrachloroaurate with Comparisons to Other Monovalent Cation Complexes. In *Proc. Int. Symp.Biomol. Struct Interactions, Suppl. J· Biosci.,*; 1985; pp. 293–306.

Stevenson, G. R.; Alegria, A. E. Equilibrium Studies by Electron Spin Resonance. VI. Benzoquinone Free Ion-Ion Pair Equilibrium. *J. Phys. Chem.* **1973**, *77*, 3100–3102.

Still, Clark, W.; Kahn, M.; Mitra, A. Rapid Chromatographic Technique for Preparative Seperations with Moderate Resolution. *J. Org. Chem.* **1978**, *43*, 2923–2925.

Stöver, H. D. H.; Robillard, M.; Detellier, C. Potassium-39 Nuclear Magnetic Resonance Study of the Complexation of Potassium Thiocyanate by Dibenzo-30-Crown-10 in Nitromethane. *Polyhedron* **1987**, *6*, 577–581.

Stranius, K.; Iashin, V.; Nikkonen, T.; Muuronen, M.; Helaja, J.; Tkachenko, N. Effect of Mutual Position of Electron Donor and Acceptor on Photoinduced Electron Transfer in Supramolecular Chlorophyll-Fullerene Dyads. *J. Phys. Chem. A* **2014**, *118*, 1420–1429.

Stroganov, O. V; Novikov, F. N.; Stroylov, V. S.; Kulkov, V.; Chilov, G. G. Lead Finder: An Approach to Improve Accuracy of Protein-Ligand Docking, Binding Energy Estimation, and Virtual Screening. *J. Chem. Inf. Model.* **2008**, *48*, 2371–2385.

Sugihara, K.; Kamiya, H.; Yamaguchi, M.; Kaneda, T.; Misumi, S. Synthetic Macrocyclic Ligands. III Synthesis of a Quinone-Hydroquinone Reox System Incorporated with Complexing Ability Toward Cations. *Tetrahedron Lett.* **1981**, *22*, 1619–1622.

Sulka, G. D.; Stępniowski, W. J. Structural Features of Self-Organized Nanopore Arrays Formed by Anodization of Aluminum in Oxalic Acid at Relatively High Temperatures. *Electrochim. Acta* **2009**, *54*, 3683–3691.

Sumner, N. J.; Spisak, S. N.; Filatov, A. S.; Rogachev, A. Y.; Zabula, A. V; Petrukhina, M. A. Double-Concave Binding of Bicorannulenyl Dianion: Cesium vs Lithium Salts. *Organomettalics* **2014**, *ASAP*, A–E.

Sun, J.; Stone, G. M.; Balsara, N. P.; Zuckermann, R. N. Structure–Conductivity Relationship for Peptoid-Based PEO–Mimetic Polymer Electrolytes. *Macromolecules* **2012**, *45*, 5151–5156.

Sun, L.; von Gersdorff, J.; Sobek, J.; Kurreck, H. Novel Biomimetic Models for Photosynthesis: Porphyrins Covalently Linked to Redox-Active Crown Ether Quinones. *Tetrahedron* **1995**, *51*, 3535–3548.

Sun, Z.; Kim, H. K. Growth of Ordered, Single-Domain, Alumina Nanopore Arrays with Holographically Patterned Aluminum Films. *Appl. Phys. Lett.* **2002**, *81*, 3458.

Surkau, G.; Böhm, K. J.; Müller, K.; Prinz, H. Synthesis, Antiproliferative Activity and Inhibition of Tubulin Polymerization by Anthracenone-Based Oxime Derivatives. *Eur. J. Med. Chem.* **2010**, *45*, 3354–3364.

Synthesis, O.; Click, T. Supporting Information. *Mater. Res.* 1–12.

Taft, R. W. Linear Steric Energy Relationships. *JACS* **1953**, *75*, 4538–4539.

Tagliazucchi, M.; Azzaroni, O.; Szleifer, I. Responsive Polymers End-Tethered in Solid-State Nanochannels: When Nanoconfinement Really Matters. *J. Am. Chem. Soc.* **2010**, *132*, 12404–12411.

Tagne Kuate, A. C.; Schürmann, M.; Schollmeyer, D.; Hiller, W.; Jurkschat, K. The First Examples of a Crown Ether Intramolecularly Encapsulating Mono- and Diorganotin Dications: Synthesis and Structures of [PhSnCH2([16]crown-5)][ClO4]2 and [HOSnCH2([16]crown-5)][Y]2 (Y=ClO4, CF3SO3). *Chemistry* **2010**, *16*, 8140–8146.

Tashiro, S.; Minoda, A.; Yamada, M.; Shionoya, M. One-Pot, Template Syntheses of a New Class of Metallomacrocycles with a Tetraoxime Cyclic Skeleton. *Inorg. Chem.* **2009**, *48*, 10093–10101.

Taylor, P.; Madje, B. R.; Shelke, K. F.; Sapkal, S. B.; Kakade, G. K.; Shingare, S. Green Chemistry Letters and Reviews An Efficient One-Pot Synthesis of Anthraquinone Derivatives Catalyzed by Alum in Aqueous Media. *Green Chem. Lett. Rev.* **2010**, *3*, 269–273.

Thangavel, A.; Elder, I. a; Sotiriou-Leventis, C.; Dawes, R.; Leventis, N. Breaking Aggregation and Driving the Keto-to-Gem-Diol Equilibrium of the N,N'-Dimethyl-

2,6-Diaza-9,10-Anthraquinonediium Dication to the Keto Form by Intercalation in cucurbit[7]uril. *J. Org. Chem.* **2013**, *78*, 8297–8304.

The Mendeley Support Team. Getting Started with Mendeley. *Mendeley Desktop*, 2011, 1–16.

Theil, A.; Hitce, J.; Retailleau, P.; Marinetti, A. A Synthetic Approach to Macrocyclic , Chiral Phosphane Derivatives with Crown-Ether-Like Structures. *European J. Org. Chem.* **2006**, *2006*, 154–161.

Thontasen, N.; Levita, G.; Malinowski, N.; Deng, Z.; Rauschenbach, S.; Kern, K. Grafting Crown Ether Alkali Host - Guest Complexes at Surfaces by Electrospray Ion Beam Deposition. *J. Phys. Chem. C* **2010**, *114*, 17768–17772.

Thordarson, P. Determining Association Constants from Titration Experiments in Supramolecular Chemistry. *Chem. Soc. Rev.* **2011**, *40*, 1305–1323.

Tian, B.; Liu, J.; Dvir, T.; Jin, L.; Tsui, J. H.; Qing, Q.; Suo, Z.; Langer, R.; Kohane, D. S.; Lieber, C. M.; Boston, H. Supplementary Information for Macroporous Nanowire Nanoelectronic Scaffolds for Synthetic Tissues. 1–27.

Tochtrop, G. P.; Richter, K.; Tang, C.; Toner, J. J.; Covey, D. F.; Cistola, D. P. Energetics by NMR: Site-Specific Binding in a Positively Cooperative System. *Proc. Natl. Acad. Sci. U. S. A.* **2002**, *99*, 1847–1852.

Toma, H. E. Supramolecular Nanotechnology : From Molecules to Devices. *Curr. Sci.* **2008**, *95*, 1202–1225.

Tominaga, M.; Masu, H.; Azumaya, I. Construction and Charge-Transfer Complexation of Adamantane-Based Macrocycles and a Cage with Aromatic Ring Moieties. *J. Org. Chem.* **2009**, *74*, 8754–8760.

Trammell, S. a; Seferos, D. S.; Moore, M.; Lowy, D. a; Bazan, G. C.; Kushmerick, J. G.; Lebedev, N. Rapid Proton-Coupled Electron-Transfer of Hydroquinone through Phenylenevinylene Bridges. *Langmuir* **2007**, *23*, 942–948.

Treat, N. D.; Mates, T. E.; Hawker, C. J.; Kramer, E. J.; Chabinyc, M. L. Temperature Dependence of the Di Ff Usion Coe Ffi Cient of PCBM in Poly(3-Hexylthiophene). *Macromolecules* **2013**, *41*, 1002–1007.

Trost, B. M.; Caldwell, G. The Di-T-Butylsiylene Protecting Group for Diols. *Tetrahedron Lett.* **1981**, *22*, 4999–5002.

Trivisiol, E.; Le Berre-Anton, V.; Leclaire, J.; Pratviel, G.; Caminade, A.-M.; Majoral, J.-P.; Franois, J. M.; Meunier, B. Dendrislides, Dendrichips: A Simple

Chemical Functionalization of Glass Slides with Phosphorus Dendrimers as an Effective Means for the Preparation of Biochips. *New J. Chem.* **2003**, *27*, 1713.

Tucker, J. W.; Stephenson, C. R. J. Shining Light on Photoredox Catalysis: Theory and Synthetic Applications. *J. Org. Chem.* **2012**, *77*, 1617–1622.

Tundo, P.; Selva, M. The Chemistry of Dimethyl Carbonate. *Acc. Chem. Res.* **2002**, *35*, 706–716.

Turner, R. T.; Hong, L.; Koelsch, G.; Ghosh, A. K.; Tang, J. Structural Locations and Functional Roles of New Subsites S 5 , S 6 , and S 7 in. *Society* **2005**, *2*, 105–112.

Ullman, A. M.; Sun, X.; Graham, D. J.; Lopez, N.; Nava, M.; De Las Cuevas, R.; Müller, P.; Rybak-Akimova, E. V; Cummins, C. C.; Nocera, D. G. Electron-Transfer Studies of a Peroxide Dianion. *Inorg. Chem.* **2014**, *53*, 5384–5391.

Umamaheswari, J.; Sangaranarayanan, M. V. Charge Transport through Chemically Modified Electrodes: A General Analysis for Ion Exchange and Covalently Attached Redox Polymers. *J. Phys. Chem. B* **1999**, *103*, 5687–5697.

Uysal, S.; Cuello, L. G.; Cortes, D. M.; Koide, S.; Kossiakoff, A. A.; Perozo, E. Mechanism of Activation Gating in the Full-Length KcsA K Þ Channel. *PNAS* **2011**, *108*, 11896–11899.

Valade, A.-G. A. A.; Harakat, D.; Guyot, J.; Laprévote, O.; Dugat, D.; I, R. N. Macrocyclic 14-Membered-Ring Diketal Dilactams: Spectroscopic Studies and Conformational Analysis of Their Complexes with Divalent Cations. *Eur. J. Inorg. Chem.* **2010**, *2010*, 3278–3289.

Valentini, M.; Rüegger, H.; Pregosin, P. S. Applications of Pulsed-Gradient Spin-Echo (PGSE) Diffusion Measurements in Organometallic Chemistry. *Helv. Chim. Acta* **2001**, *84*, 2833–2853.

Valeur, B.; Leray, I. Design Principles of Fluorescent Molecular Sensors for Cation Recognition. *Coor. Chem. Rev.* **2000**, *205*, 3–40.

Vany, P.; York, N. Ionic Conductivity and Diffusion at Infinite Dilution. *Monogr. Soc. Res. Child Dev.* **2012**, *77*, 81–86.

Vasile, E.; Dumitru, F.; Razvan, A.; Oprea, O.; Andronescu, C. NOVEL UREIDO-4 ' -AMINOBENZO-15-CROWN-5-ETHER PERIODIC. *Dig. J. Nanomater. Biostructures* **2013**, *8*, 433–444.

Vellaccio, F.; Phelan, J. M.; Trottier, R. L.; Napier, T. W.; Kemp, D. S. Catechol and Substituted Catechol-Derived Ortho Esters, Models for Protected Active Esters in Peptide Synthesis. *J. Org. Chem.* **1981**, *46*, 3087–3091.

Verebová, V.; Adamcik, J.; Danko, P.; Podhradský, D.; Miškovský, P.; Staničová, J. Anthraquinones Quinizarin and Danthron Unwind Negatively Supercoiled DNA and Lengthen Linear DNA. *Biochem. Biophys. Res. Commun.* **2014**, *444*, 50–55.

Wall, S. De; Barbour, L.; Gokel, G. Cation-Π Complexation of Potassium Cation with the Phenolic Sidechain of Tyrosine. *J. Am. ...* **1999**, *68*, 8405–8406.

Walschus, F. L. U. Immobilization of Oligonucleotides for Biochemical Sensing by Self-Assembled Monolayers : Thiol-Organic Bonding on Gold and Silanization on Silica Surfaces. *Anion Sens.* **2005**, 37–56.

Wang, J. *ANALYTICAL Electrochemistry*; John Wiley & Sons: Hoboken, 2000; Vol. 2.

Wang, Y.; Kakiuchi, T.; Yasui, Y.; Mirkin, M. V. Kinetics of Ion Transfer at the Ionic Liquid/water Nanointerface. *J. Am. Chem. Soc.* **2010**, *132*, 16945–16952.

Wass, J. R. T. J.; Ahlberg, E.; Panas, I.; Schiffrin, D. J. Quantum Chemical Modeling of the Reduction of Quinones. *J. Phys. Chem. A* **2006**, *110*, 2005–2020.

Watanabe, K.; Iwata, Y.; Adachi, S.; Nishikawa, T.; Yoshida, Y.; Kameda, S.; Ide, M.; Saikawa, Y.; Nakata, M. Synthetic Studies on Lactonamycins: Synthesis of the Model BCDEF Aglycon. *J. Org. Chem.* **2010**, *75*, 5573–5579.

Webber, P. R. A.; Cowley, A.; Beer, P. D. Calix [4] Semitube Diquinone : A Potassium Selective Redox-Active Ionophore. *Dalt. Trans* **2003**, 3922–3926.

Weiland, J. D.; Liu, W.; Humayun, M. S. Retinal Prosthesis. *Annu. Rev. Biomed. Eng.* **2005**, *7*, 361–401.

Weiss, T. F. *Cellular Biophysics*; First.; The MIT Press: London, 1996; pp. 1–692.

Whitesides, G. M. Whitesides' Group: Writing a Paper. *Adv. Mater.* **2004**, *16*, 1375–1377.

Wienk, M. M.; Stolwijk, T. B.; Sudholter, E. J. R.; Reinhoudt, D. N. Stabilization of Crown Ether Containing Supported Liquid Membranes. *J. Am. Chem. Soc.* **1990**, *112*, 797–801.

Witiak, D. T.; Kamat, T. P. L.; Allison, D. L.; Liebowitqt, S. M.; Glaser, R.; Holliday, J. E.; Moeschberger, M. L.; Schaller, J. P. Bis(bioreductive) Alkylating Agents:

Synthesis and Biological Activity in a Nude Mouse Human Carcinoma Model. *J. Med. Chem.* **1983**, *26*, 1679–1686.

Witiak, D. T.; Loper, T.; Ananthan, S.; Almerico, A. M.; Verhoef, V. L.; Filppi, J. A. Mono and Bis(bioreductive) Alkylating Agents: Synthesis and Antitumor Activities in a B16 Melanoma Model. *J. Med. Chem.* **1989**, *32*, 1636–1642.

Wolf, G. The Discovery of the Visual Function of Vitamin A. *J. Nutr.* **2001**, *131*, 1647–1650.

Wolf, R. E.; Cooper, S. R. Redox-Active Crown Ethers: Molecules Designed to Couple Ion Binding with. *JACs* **1984**, *106*, 4646–4647.

Wolfenden, R. Thermodynamic and Extrathermodynamic Requirements of Enzyme Catalysis. *Biophys. Chem.* **2003**, *105*, 559–572.

Wolfrum, B.; Mourzina, Y.; Sommerhage, F.; Offenhäusser, A. Suspended Nanoporous Membranes as Interfaces for Neuronal Biohybrid Systems. *Nano Lett.* **2006**, *6*, 453–457.

Wu, Y.; Cheng, G.; Katsov, K.; Sides, S. W.; Wang, J.; Tang, J.; Fredrickson, G. H.; Moskovits, M.; Stucky, G. D. Composite Mesostructures by Nano-Confinement. *Nat. Mater.* **2004**, *3*, 816–822.

Wu, Y.; Livneh, T.; Zhang, Y. X.; Cheng, G.; Wang, J.; Tang, J.; Moskovits, M.; Stucky, G. D. Templated Synthesis of Highly Ordered Mesostructured Nanowires and Nanowire Arrays. *Nano Lett.* **2004**, *4*, 2337–2342.

Xia, L.; Jia, Y.; Tong, S.; Wang, J.; Han, G. Interfacial Behavior of Phase Transfer Catalysis of the Reaction between Potassium Thiocyanate and P-Nitrobenzyl Bromide with Crown Ethers as Catalysts. *Kinet. Catal.* **2010**, *51*, 69–74.

Xie, Y.; Xue, J.; Wang, L.; Wang, X.; Jin, K.; Chen, L.; Wang, Y. Surface Modification of Single Track-Etched Nanopores with Surfactant CTAB. *Langmuir* **2009**, *25*, 8870–8874.

Xu, X.-D.; Yang, H.-B.; Zheng, Y.-R.; Ghosh, K.; Lyndon, M. M.; Muddiman, D. C.; Stang, P. J. Self-Assembly of Dendritic Tris(crown Ether) Hexagons and Their Complexation with Dibenzylammonium Cations. *J. Org. Chem.* **2010**, *75*, 7373–7380.

Yadav, J.; Reddy, B.; Swamy, T. Bi(OTf)3-Catalyzed Allylation of Quinones with Allyltrimethylsilane. *Tetrahedron Lett.* **2003**, *44*, 4861–4864.

Yajima, S.; Nakajima, T.; Higashi, M.; Kimura, K. Drastic Selectivity Reversal on Crown-Ether Based Ion-Sensing Membranes Made of Ordered Mesoporous Silica and Conventional Sol-Gel Derived One. *Chem. Commun. (Camb).* **2010**, *46*, 1914–1916.

Yamada, N. L. Kinetic Process of Formation and Reconstruction of Small Unilamellar Vesicles Consisting of Long- and Short-Chain Lipids. *Langmuir* **2012**, *28*, 17381–17388.

Yamaguchi, A.; Uejo, F.; Yoda, T.; Uchida, T.; Tanamura, Y.; Yamashita, T.; Teramae, N. Self-Assembly of a Silica-Surfactant Nanocomposite in a Porous Alumina Membrane. *Nat. Mater.* **2004**, *3*, 337–341.

Yamaguchi, A.; Yoda, T.; Suzuki, S.; Morita, K.; Teramae, N. Diffusivities of tris(2,2'-Bipyridyl)ruthenium inside Silica-Nanochannels Modified with Alkylsilanes. *Anal. Sci.* **2006**, *22*, 1501–1507.

Yamaguchi, K; Kuboniwa, H; Nagami, S; Bando, T; Hirao, A; Nakahama, S; Yamazaki, N. Studies on Synthetic Ionophores. X. Tansport Behavior of Na+ and K+ with an W-Hydroxy Carboxylic Acid Containing Octaether Linkages as a Synthetic Analog of Natural Carboxylic Acid Ionophores through an Organic Liquid Membrane. *Bull. Chem. Soc. Jpn.* **1995**, *68*, 315–321.

Yamaguchi, Y.; Matsubara, Y.; Ochi, T.; Wakamiya, T. Supporting Information. *Mercury 3*, 1–15.

Yamaguchi, Y.; Matsubara, Y.; Ochi, T.; Wakamiya, T.; Yoshida, Z.-I. How the Pi Conjugation Length Affects the Fluorescence Emission Efficiency. *J. Am. Chem. Soc.* **2008**, *130*, 13867–13869.

Yamaguchi, Y.; Tanaka, T.; Kobayashi, S.; Wakamiya, T.; Matsubara, Y.; Yoshida, Z.-I. Light-Emitting Efficiency Tuning of Rod-Shaped Pi Conjugated Systems by Donor and Acceptor Groups. *J. Am. Chem. Soc.* **2005**, *127*, 9332–9333.

Yang, N. *Encyclopedia of Toxicology*; Elsevier, 2014; pp. 1138–1140.

Yang, Y.-W.; Sun, Y.-L.; Song, N. Switchable Host-Guest Systems on Surfaces. *Acc. Chem. Res.* **2014**, *ASAP*.

Yapar, G.; Erk, Ç. The Synthesis of Dibenzo[3n]crown-N by Novel Methods and Their Cation Binding Studied by Fluorescence Spectroscopy. Part IV. *J. Incl. Phenom. Macrocycl. Chem.* **2002**, *42*, 145–150.

Yarkoni, O.; Donlon, L.; Frankel, D. Creating a Bio-Hybrid Signal Transduction Pathway : Opening a New Channel of Communication between Cells and Machines. *Bioinspir. Biomim.* **2012**, 1–7.

Zhang, C.; Ueno, K.; Yamazaki, A.; Yoshida, K.; Moon, H.; Mandai, T.; Umebayashi, Y.; Dokko, K.; Watanabe, M. Chelate E Ff Ects in Glyme / Lithium Bis (Tri Fl Uoromethanesulfonyl) Amide Solvate Ionic Liquids . I . Stability of Solvate Cations and Correlation with Electrolyte Properties. *J. Phys. Chem. B* **2014**, *118*, 5144–5153.

Zhang, M.; Luo, Y.; Zheng, B.; Xia, B.; Huang, F. Improved and Controlled Complexation of Paraquat Derivatives by the Formation of a Bis(m-Phenylene)-26-Crown-8-Based Lariat Ether. *European J. Org. Chem.* **2010**, *2010*, 5543–5547.

Zhang, N.; Samanta, S. R.; Rosen, B. M.; Percec, V. Single Electron Transfer in Radical Ion and Radical-Mediated Organic, Materials and Polymer Synthesis. *Chem. Rev.* **2014**, *ASAP*, NYA.

Zheng, W.; Wang, Z. G. Morphology of ABC Triblock Copolymers. *Macromolecules* **1995**, *28*, 7215–7223.

Zhou, G. Bin; Khan, I. M.; Smid, J. Solvent-Free Cation-Conducting Polysiloxane Electrolytes with Pendant Oligo(oxyethylene) and Sulfonate Groups. *Macromolecules* **1993**, *26*, 2202–2208.

Zhou, H.; Sun, Z.; Hoshi, T.; Kashiwagi, Y.; Anzai, J.-I.; Li, G. Electrochemical Studies of Danthron and the DNA-Danthron Interaction. *Biophys. Chem.* **2005**, *114*, 21–26.

Zhou, T.; Huang, D.; Caflisch, A. Is Quantum Mechanics Necessary for Predicting Binding Free Energy ? Belonging to Different Classes : The West Nile Virus NS3 Serine Protease (WNV PR), the Aspartic Protease of the Human Immunodeficiency Virus (HIV-1 PR), and the Human Cyclin-Dependent. *Energy* **2008**, 4280–4288.

Ziegler, F. E.; Belema, M. Chiral Aziridinyl Radicals : An Application to the Synthesis of the Core Nucleus of FR-900482 of an Aziridinyl Radical into a Functionalized Indole Nucleus . The Route Employs a Selective Polonovski. *J. Org. Chem.* **1997**, *62*, 1083–1094.

Zrenner, E. Will Retinal Implants Restore Vision? *Science* **2002**, *295*, 1022–1025.

Appendices

Experimental Procedures - Synthesis

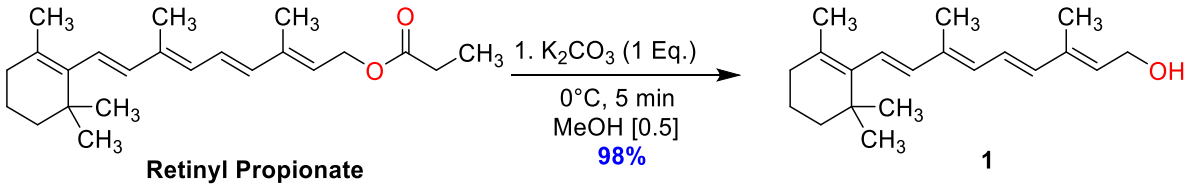

Synthesis of 1 - To a stirred solution of 0.34 g Retinyl propionate ester (1 mmol, 1.0 Eq.) in 2 mL anhydrous methanol at 0°C was added 0.14 g anhydrous potassium carbonate (1 mmol, 1.0 Eq.). The mixture was stirred vigorously for 5 min at 0°C, where by TLC 20% EtOAc:Hexanes the reaction was complete. The crude mixture was partitioned between 10mL diH_2O/10 mL hexanes and aqueous phase extracted an additional 2 X (5 mL) hexanes, organic layers combined, dried over Na_2SO_4 and filtered through a fritted glass funnel. The solvent was removed under reduced pressure to yield 1 (0.28 g, 98% yield) as a pure light yellow oil. ^{1}H NMR (600 MHz, Chloroform-d) δ 6.61 (m, 1H), 6.29 (d, 1H), 6.15 (d, 1H), 6.12 (m, 1H), 6.10 (m, 1H), 5.69 (t, 2H), 4.31(m, 2H), 2.01 (t, 2H), 1.90 (s, 6H), 1.71 (s, 3H), 1.61 (m, 2H), 1.46 (m, 2H), 1.00 (m, 6H, gem-CH_3)

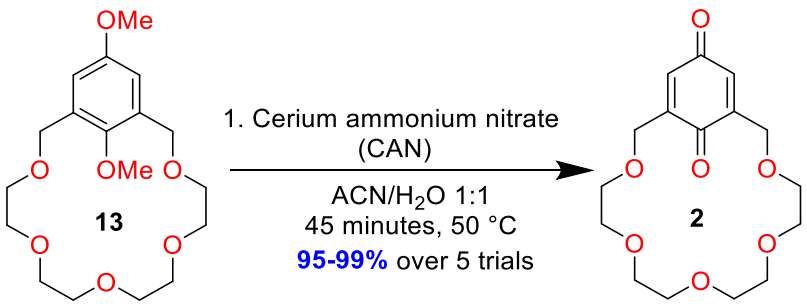

Synthesis of 2 - 1,4-Benzoquinone-2,6-18crown5. A solution of 5.00 g 13 (14.04 rnmol) in 60 mL acetonitrile and a solution of 19.45 ceric ammonium nitrate in 60 mL diH_2O were mixed and stirred for 45 minutes at 50°C. After cooling to room temperature, 200 mL dichloromethane and 100 mL diH20 was added to the mixture in a 1L seperatory funnel. The organic phase was separated, dried over anhydrous $MgSO_4$, and concentrated to yield a bright orange syrup. Column chromatography using EtOAc as eluent gave 4.4 g, 96% as solid yellow crystals. M.P. 76.5°C. ^{1}H NMR (600 MHz, Chloroform-d) δ 3.54 (m, 8H), 3.62 (m, 4H), 3.75 (m, 4H), 4.53 (s, 4H), 6.72 (s, 2H)

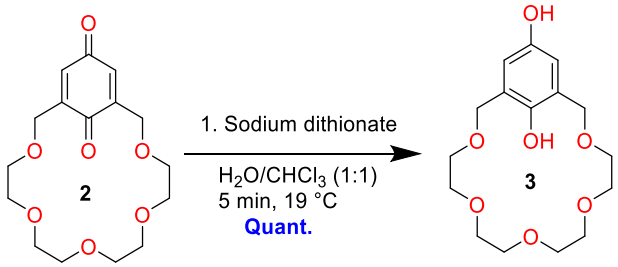

Synthesis of 3 – Method A) 0.7 g 1,4-benzoquinone-2,6,-18-crown-5 (2.2 mmoL, 1.0 Eq.) is added to a 250-mL separatory funnel containing 65 mL CHCl3 and 65 mL of a 5% w/w solution of sodium dithionate in diH20 at 19°C. The flask was shaken until no more orange color could be seen visually (ca time 3 m.) and allowed to stand for an additional 5 m to let the layers separate. The organic layer was dried over anhydrous Na2SO4, filtered and concentrated to yield 0.71 g, 100% of a white solid which was pure by 1H NMR.

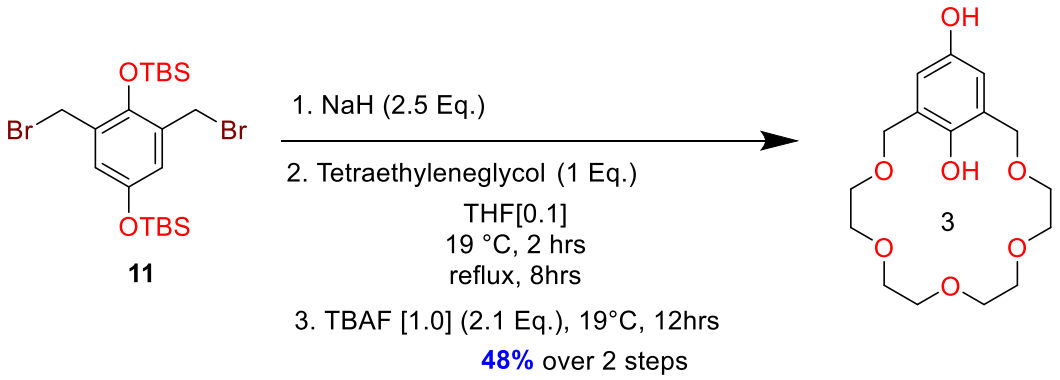

Method B) The same general procedure and scale was utilized as in the synthesis of **13, Method B** for preparing the sodium hydride and tetraethyleneglycol. When the cyclization had gone to completion by TLC (8 h.), 6.5 mL (6.5 mmoL, 2.1 Eq.) of a 1.0 M solution of tetrabutylammonium fluoride in THF was added at 19°C and the mixture stirred overnight for 12 h. where TLC indicated the reaction had gone to completion. The reaction was worked up by partitioning between 50 mL CH2Cl2/ 50 mL 0.1 M citric acid, organic layer dried over MgSO4, filtered and concentrated. Elution on SiO2 using 100% CH2Cl2 yielded 0.49 g of the hydroquinone crown ether, 48% yield.

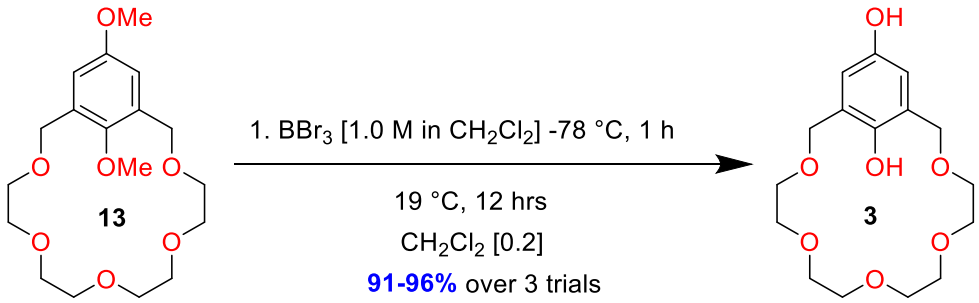

Method C) 0.1 g **13** (0.28 mmol, 1.0 Eq.) is added to a 5 mL pear shaped falsk with small Teflon stir bar and fitted with a reaction inlet joint and rubber septum. 0.84 mL anhydrous distilled dichloromethane is then added to the solid under Ar (g) and reaction flask cooled to -78°C in an acetone/dry ice bath. Next, 0.56 mL of a 1.0 M solution of BBr_3 (2.0 Eq., 0.56

mmoL) in CH_2Cl_2 is added SLOWLY over the course of 10 m and reaction stirred for 1 h at -78°C. The reaction is then removed from the ice bath and allowed to come to 19°C, where the mixture us stirred for an additional 12 h. The mixture is then cooled to 0°C in a water/ice bath and 50 mg (6 Eq., 63µL) anhydrous MeOH is added at once to quench the reaction. The reaction is stirred for 1 h at 0°C. A small amount of activated carbon (≈10-15mg) is then added and the mixture stirred at room temperature overnight for 12 h. The mixture is then taken up in a pipette and eluted through a separate pipette with a small plug of glass wool, celite 545 and a small amount of sand. The celite pad is washed 3 X (2mL) CH2Cl2 to yield 90 mg, 98% yield of the hydroquinone.

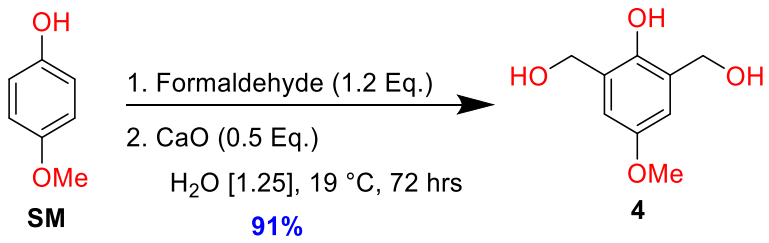

Synthesis of 4 - 62.0 g 4-methoxyphenol (0.5 mol, 1.0 Eq.) was added to a 3-neck 1000 mL round bottom flask equipped with a large stir bar. 400 mL diH2O was then added under an atmosphere of argon. Argon was also bubbled at a moderately vigorous rate as the solution was stirred for an additional 20 m. 97.4 mL of a 37 wt % solution of formaldehyde (1.2 mols, 2.1 Eq.) in H2O was added, followed by the immediate addition of 14.0 g calcium oxide (0.25 mol, 0.5 Eq.) in portions over 15 minutes via powder funnel (Ar atmosphere maintained). The mixture was stirred as vigoursly as possible at 1600 RPM at 19 ˚C until all solids dissolved (ca time = 45 m.) and the solution was a pale yellow color. The flask was then stored in a dark, undisturbed cabinet for 3 days where upon return, bright white crystals in a supertanant of deeper yellow solution deposited in a large mass. The crystals were

broken with ½" stir rod and stirring commenced as 40 mL anhy. glacial acetic acid was added in 10 mL portions and the solution slowly heated to approximately 80 ˚C until no more solids were present. 30 grams activated carbon was added and the mixture stirred for 2 h at 80 ˚C, then poured hot through a pad of fresh activated carbon/celite/sand/M fritted funnel into a vacuum flask where crystals began to crash out of solution immediately. The solution was allowed to cool to 19 ˚C, stand for an additional h and then placed in 4 ˚C fridge for an additional 2 h. The white crystals were filtered off in a course fritted funnel and washed 4X 200 mL di H2O and allowed to air dry. The crystals were then washed with 3X100 mL EtOAc, dried in a vacuum desiccator overnight to yield 91% as white granular crystals. 1H NMR

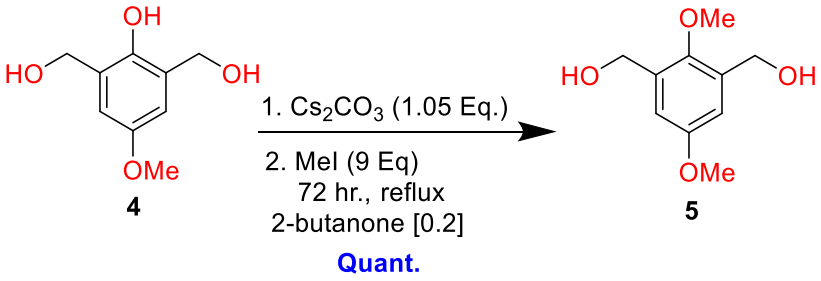

Synthesis of 5 - To a 50-mL round bottom flask is first added 1.84 g of triol **4** (10 mmol, 1 Eq.) followed by addition of 3.42 g solid Cs_2CO_3 (10.5 mmoL, 1.05 Eq.). The flask is put under inert atmosphere and 20 mL distilled 2-butanone added via syringe. The mixture is stirred vigorously and 4.26 g methyl iodide (3 Eq. 30 mmoL) added through the septum and mixture brought to reflux. Every 24 h. for a total of 3 repetitions, another 4.26 g methyl iodide is added after cooling the mixture to room temperature for a total of 9 Eq. methyl iodide. After 72 h, TLC shows completion of the reaction, the reaction is then cooled to room temperature and filtered through ½" pad of celite 545 topped with quartz wool to give

a clear solution. The celite pad was washed with an additional 2 X 20 mL 2-butanone and the mixture concentrated in vacuo to give 1.98 g of pure **5** (2,5-dimethoxy-1,3-phenylene) dimethanol, 100% yield.

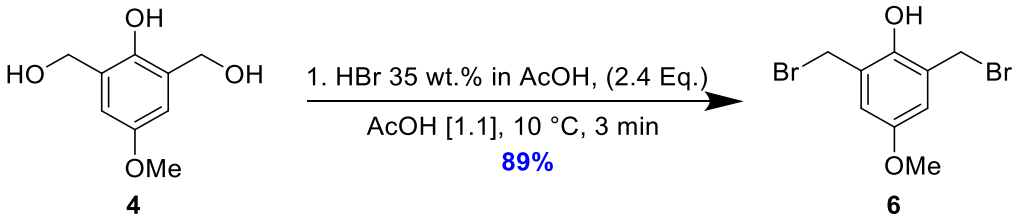

Synthesis of 6 - In a small 10 ml conical flask with triangular stirbar is first added 3.0 ml anhydrous acetic acid followed by 2.3 ml of a 35 wt.% solution of HBr in AcOH (1.07 g, 13.2 mmol) and flask cooled to 10-15°C under argon. Next, 1.00 g (5.4 mmol, 1.0 Eq.) crystalline (2-hydroxy-5-methoxy-1,3-phenylene)dimethanol is added via powder funnel and the solid completely dissolves. With rapid stirring, the product begins to crash out at t = 3 m. and at once solidifies the entire reaction mass with crystalline product. The flask is immediately dumped out with aid of a teflon scoopula onto a fine scintered glass filter funnel and vacuum applied to remove AcOH. The product is then washed 2 X 1 ml cold AcOH followed by 3 X 2 ml pentane and dreid in a scintillation vial under high vacuum overnight to yield 1.5 g of a yellowish solid, 89%. The product was purified by recrystallization from cyclohexane and melted at 113-114'.

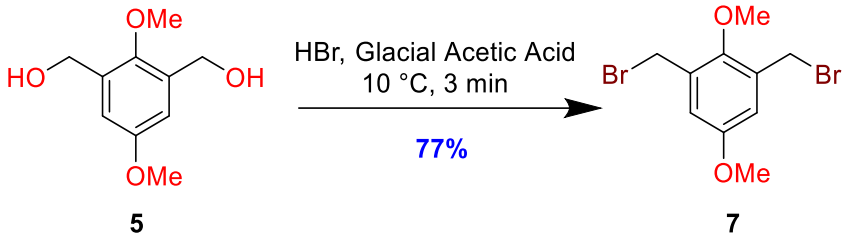

Synthesis of 7 – The same procedure for the preparation of **6** was followed from substrate **5** to give **7** to give a yield of 72%.

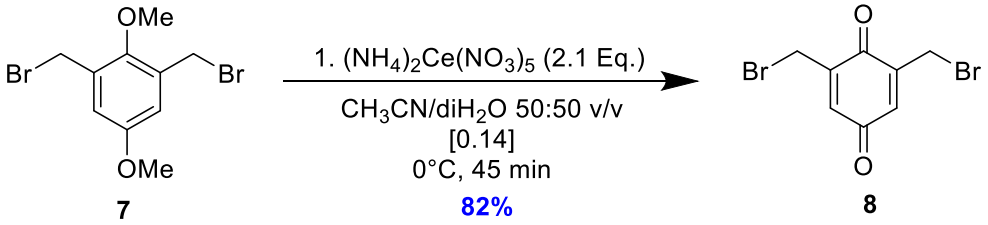

Synthesis of 8 – Method A) 0.5 g 2,6-bis(bromomethyl)-4-methoxyphenol (1.6 mmol, 1.0 Eq.) was added to a 15-ml RBF with teflon coated stir bar, stoppered under Argon and 6 ml acetonitrile added and stirring commenced. After complete dissolution, the reaction was cooled to 0°C, and a solution of ceric ammonium nitrate (1.86 g, 3.4 mmol, 2.1 Eq.) in 6 ml diH_2O (prepared in a 10 ml Flacon tube) was taken up via 10-ml syringe and added to the solution of phenol. TLC's at 15 and 45 min in 20% EtOAc:Hex confirmed the formation of a single non-polar spot Rf: 0.40 whereas the starting material resided at Rf: 0.32. The mixture was then poured into 6 ml H_2O/ 25 ml CH_2Cl_2 and aqueous layer extracted an additional 2 X 10 ml CH_2Cl_2, organic layers combined and dried over anhy. $MgSO_4$, filtered and concentrated to yield a crude brown solid. Immediate column chromatography over silica gel using 3:2 CH_2Cl_2/Hexanes afforded 77% of pure product in the first row of fractions. The product was stored in the -20°C freezer, covered in foil. 'H NMR ($CDCl_3$,) 6 4.28 (s, 4 H, CH2Br), 6.91 (s, 2 H, =CH).

Method B) Starting from 1,3-bis(bromomethyl)-2,5-dimethoxybenzene (**7**) the same procedure was followed and yielded 82% of **8.**

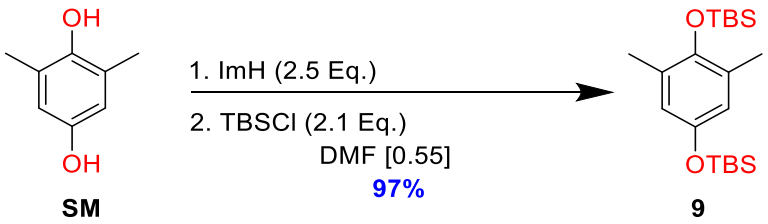

Synthesis of 9 - In a 50 ml pear bottom flask, 6.0 g dry imidazole (vacuum desiccator) (90 mmoL, 2.5 Eq.) is added and the flask is stoppered. The imidazole is solvated in 20 ml anhydrous DMF and stirring is started. 5.00 g (36 mmol, 2.1 Eq.) 2,6-dimethyl-1,4-hydroquinone is added to this mixture via powder funnel, followed by dropwise addition of a solution of 11.45 g *tert*-butyldimethylsilylchloride (76 mmoL, 2.1 Eq.) in 10 mL DMF over 5 min. The mixture is stirrred for 10 min at 19 °C and then elevated to 40 °C for an additional 14 hrs to ensure complete protection of the hindered phenol. The mixture is then poured directly into a 500 ml separatory funnel containing 75 mL hexane/75 ml $NaHCO_3$ and aqueous phase extracted 2 X 50 ml hexane, organic layers combined, dried over anhy Na2SO4, filtered and concentrated to yield a clear oil. The crude mixture is subjected to column chromatography, 2% EtOAc/Hexanes to give 12.9 g of a clear oil.

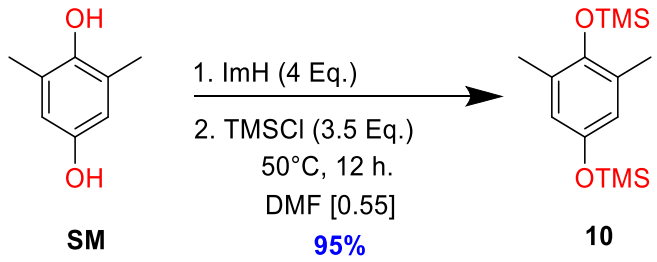

Synthesis of 10 – The procedure is analogous to the preparation of **9**, with exception of the amount of equivalents of the volatile silyl chloride and imidazole used (indicated in reaction scheme). Yield, 95% on a 5 g scale.

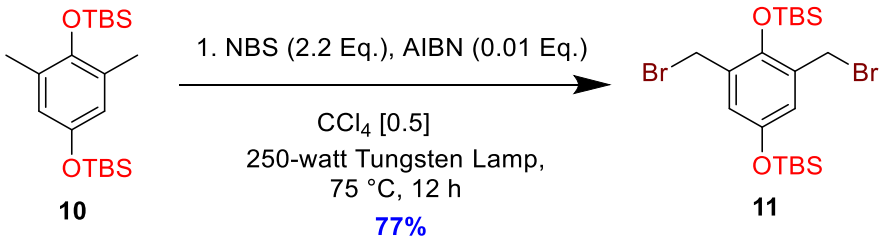

Synthesis of 11 - 2.0 g (5.5 mmol, 1.0 Eq.) of the disilyether of 1,4-hydroquinone was added to a 50 mL Schlenk flask along with Teflon-coated stirbar. The flask was evacuated, filled with nitrogen and 5 mL CCl4 was added via syringe. The stopper was removed and 2.14 g (12 mmol, 2.2 Eq.) N-bromosuccinamide was added in one portion via powder funnel, followed immediately by 90 mg Azobisazobutyrlnitrile (AIBN) (0.55 mmol, 0.01Eq.) The flask was washed down with the remaining 6 mL CCl4 and stirring started cautiously. The reation is heated to 75 C and irradiated with a 250-watt tungsten lamp for 12 h. TLC shows evolution of mono-bromo, di-bromo products at 12 hrs TLC indicates about 80% converstion to the di-brominated product along with mono and unbromonated trace spots. The reaction is cooled to 19 C and washed by adding 30 mL CH2Cl2 and washing the organic layer 3 X 20 mL diH2O. The organic layers are dried with MgSO4 and filtered through a fritted glass funnel, concentrated to yield a crude light brown oil. The oil was columned on silica (10% EtOAc:90 % hexane) to yield 2.22 g, 77% of a clear oil.

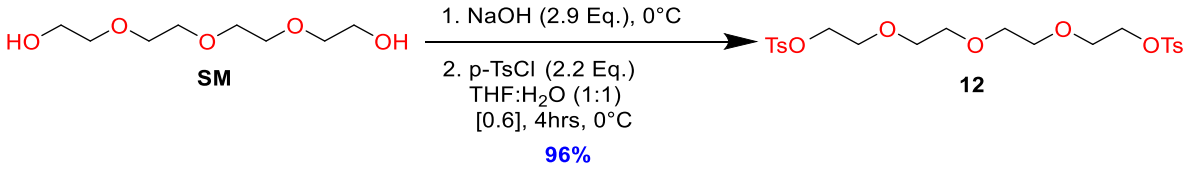

Synthesis of 12 - General Tosylation Procedure: To a solution of diol (5.0 g, 18 mmoL, 1 Eq.) in 15 mL NaOH (2.9 Eq based on NaOH M.W.)/5 mL THF is added (2.2 Eq., 39 mmol) p-toluenesulfonylchloride dissolved in 10 mL THF over 1 hr, maintaining the reaction mixture at 0 C under vigorously stirred conditions. The reaction is stirred vigorously until no starting material is present (t=4hrs) by TLC 80:20 Hexanes: EtOAc and the solution evaporated at ambient temperature under high vacuum to remove the THF. The mixture is then back-extracted into 100 mL H2O/ 100 mL CH2Cl2, extracting the water layer 2X50 mL additional CH2Cl2 and finally washed gently with 100 mL sat. NaCl solution. The organic layer is separated, dried over anhy. Na2SO4 and concentrated to give the di-tosylated derivative in essentially quantative yield, 4.14 g, >99% yield.

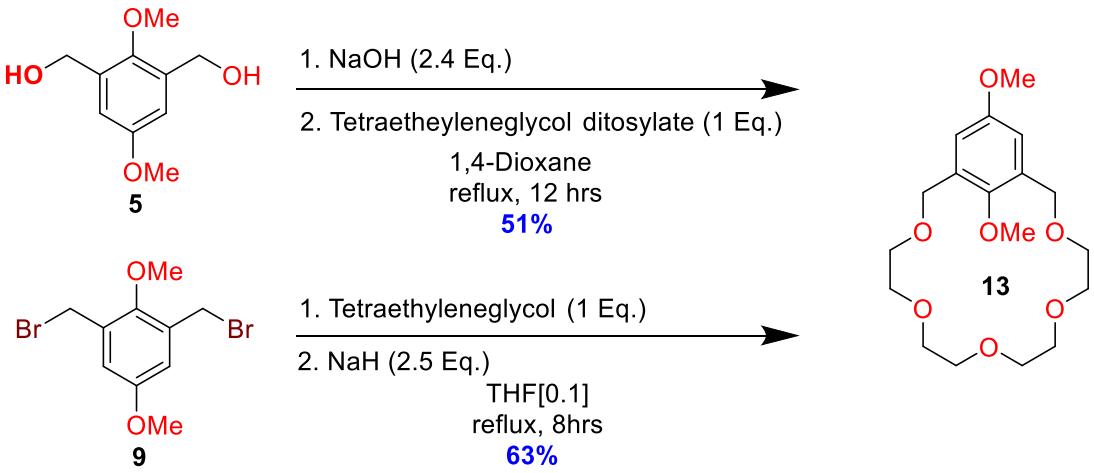

Synthesis of 13 - Method A) To a 1 L RBF with large Teflon stir bar was added 8.6 g (2-hydroxy-5-methoxy-1,3-phenylene)dimethanol (1.0 Eq., 46.7 mmoL) followed by cannula transfer of 400 mL freshly distilled 1,4-dioxane (from Na/benzophenone). Next, 14.5 g (0.36 mol, 7.8 Eq.) finely ground freshly prepared sodium hydroxide was added to the stirred solution via powder funnel and the solution stirred for 5 minutes at 19°C. In a separate 100 mL pear shaped flask, 23.5 g tertraethyleneglycolditosylate **12** (46.7 mmol, 1.0 Eq.) was

dissolved in 70 mL dioxane and transferred via cannula at once to the 1 L reaction flask. The flask was heated to reflux for 12 hrs, cooled to room temperature, filtered to remove any solids and concentrated to yield a crude white solid/oil mixture. The mixture was taken up in dichloromethane (100 mL) and washed with 100 mL diH_2O, dried over anhy. MgSO4, filtered and concentrated to yield 19 g crude crown mixture. The mixture was then columned on silica gel 2% MeOH/CH_2Cl_2 to give 8.49 g **13** as pure white crystals, 51% yield.

Method B) To a flame-dried 100 mL RBF flask is added a 0.31 g sodium hydride (60% w/w in mineral oil) (2.5 Eq., 7.7 mmoL) and the solid washed with hexanes 3 X 5 mL. The flask is evacuated and put under Ar(g) and a solution of 0.6 g anhydrous Tetraethyleneglycol (1.0 Eq., 3.1 mmoL) in 10 mL THF is slowly added drop wise to the neat sodium hydride with rapid stirring at 0°C and allowed to come to 19°C after 10 m. at 0°C. 1.0 g of the dibromide **9** (1.0 eq., 3.1 mmoL) is dissolved in 20 mL THF and added at once to the rapidly stirring mixture. The mixture is refluxed for 8 h, being worked up and purified as in method A above to yield 0.69 g of a white crystalline solid, 63% yield.

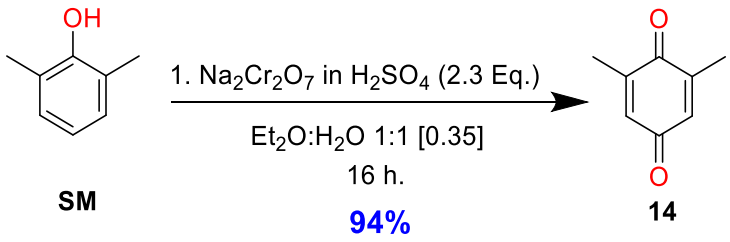

Synthesis of 14 -To a stirred solution at 19 °C containing 2.00 g (16.36 mmol) of 2,6-dimethylphenol (31) in 20mL of diethyl ether was added dropwise a solution containing 11.0 g (36.9 mmol) of sodium dichromate-dihydrate and 7 mL of sulfuric acid in 20 mL of water (Jones reagent). The reaction mixture was stirred at 19 °C for 16 h, and was then poured into 150 mL of water. The product was extracted using three 150-mL portions of

ether. The combined organic layer was washed with 150mL of water, then with 150mL of brine, and was then dried ($MgSO_4$) and concentrated under reduced pressure to afford 2,6-dimethyl-p-benzoquinone (14) as a yellow solid; yield 2.10 g (94%); mp: 65–66 °C; silica gel TLC 0.60 (5:1 hexanes/ethyl acetate); 1H NMR (600 MHz, CDCl3) δ 2.05 (s, 6H) and 6.55 (s, 2H)

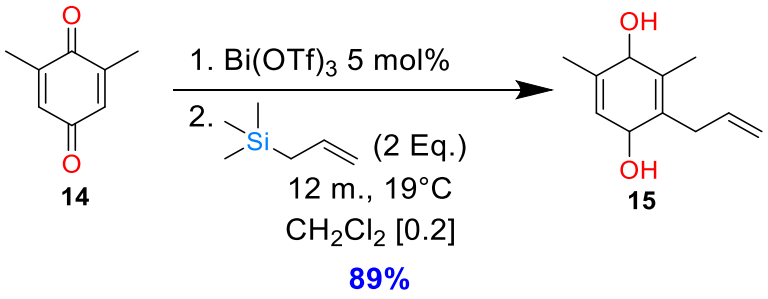

Synthesis of 15 - A mixture of 0.27 g 2,6-dimethyl-1,4benzoquinone (**14**) (1 Eq., 2 mmol), 33 mg $Bi(OTf)_3$ (0.025 Eq., 0.05 mmol) and 0.46 g allyltrimethylsilane (2 Eq.,4 mmol, 0.64mL) in dichloromethane (10 mL) was stirred at room temperature for 12 m. After completion of the reaction as indicated by TLC, the reaction mixture was quenched with water (15 mL) and extracted with dichloromethane (2×10 mL). Evaporation of the solvent followed by purification on silica gel using 5% ethyl acetate-hexanes afforded 0.32 g, 89% yield of the pure allyl derivative. ^1H NMR ($CDCl_3$) ?: 3.30 (d, 2H, J=6.5 Hz), 4.35 (brs, 1H), 4.40 (brs, 1H), 5.09 (dd, 2H, J=1.7, 17.3 Hz), 5.95–6.0 (ddt, 1H, J=6.5, 10.2, 17.3 Hz), 6.57–6.75 (m,3H).

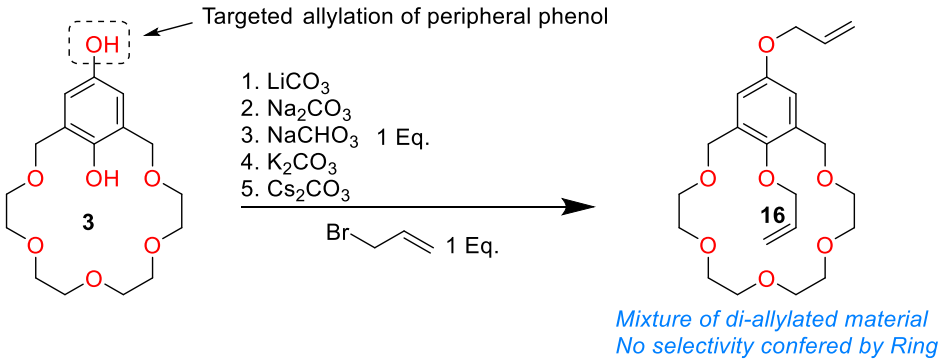

Synthesis of 16 – General Procedure: 1 Eq. of the above carbonate salts was added to a 0.2 M solution of 3 in anhydrous DMF at room temperature and the reaction was stirred for 1 h. at room temperature. 1.0 Eq. freshly distilled allyl bromide was then added and the mixture stirred until no more progress was seen by TLC. Crude ^{1}H NMR were taken to determine the ratio of intraannular to peripheral substitution See **S-16**. The ratio of products was nearly almost 50:50 and both products had an Rf value of 0.6 using 10% MeOH/CH_2Cl_2 which made the solid white product impossible to separate by chromatography.

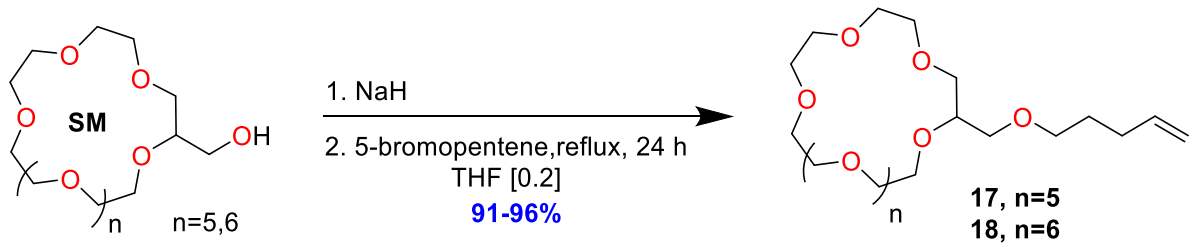

Synthesis of 17 - To a flame-dried 50 mL RBF flask is added a 0.12 g sodium hydride (60% w/w in mineral oil) (1.5 Eq., 3 mmoL) and the solid washed with hexanes 3 X 2 mL. The flask is evacuated and put under Ar(g) and a solution of 0.5 g anhydrous 2-hydroxymethyl-15-crown-5 (1.0 Eq., 2.0 mmoL) in 10 mL THF is slowly added drop wise to the neat sodium hydride with rapid stirring at 0°C and allowed to come to 19°C after 10 m. at 0°C.

0.36 g of 5-bromopentene (1.2 Eq., 2.4 mmoL, 0.28 mL) is then added and the reaction mixture brought to a gentle reflux for 24 h. The mixture is then hydrolyzed by the addition of 0.12 mL diH20, 0.24 mL of 2M NaOH and finally 0.24 mL diH2O. 50 mg activated carbon, anhy Na2SO4 are added to the mixture and stirred for 2 h. The reaction is then filtered through a plug of celite 545 with additional Na_2SO_4 atop the pad and washed thouroughly 3 X 5 mL anhy THF. The crude mixture is concentrated in vacuo to yield a yellowish oil that upon purification using 15% EtOAc:Hexanes on SiO_2 furnished 0.58 g of a clear, viscous oil, 91% yield.

Synthesis of 18 – The procedure was followed as outlined in 17. Yield, 96% of a clear viscous oil.

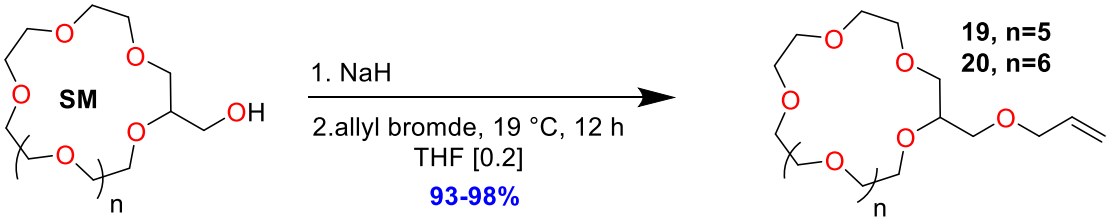

Synthesis of 19 and 20 – Procedure was followed as in **17** above but required no heating and only 12 h. to go to completion. Elution on SiO_2 using a slightly more polar mobile phase of 5% MeOH:CH2Cl2 furnished

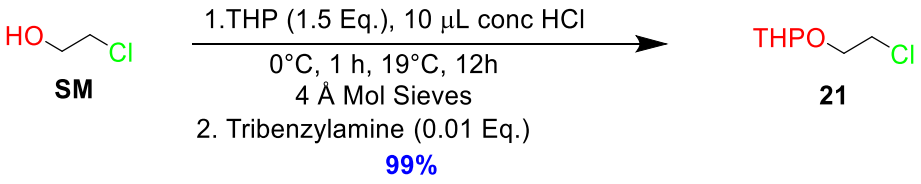

Synthesis of 21 – To a chilled solution at 0°C of 16.1 mL distilled 2-chloroethanol (from Drierite) (1.0 Eq., 19.4 g, 0.16 mol) and 21.9 mL (1.0 Eq., 20.3 g, 0.16 mol) freshly distilled dihydropyran (from Na) in a 250 mL RBF is added 1 drop concentrated hydrochloric acid and the mixture stirred for 1 h. at 0°C followed by 12 h at 19°C. After the reaction went to completion, 0.46 g tribenylamine (0.01 Eq. 1.6 mmoL) is added and the mixture is fractionally distilled at 1-2 torr, 39°C with one bulk fraction coming after the forrun of unreacted dihydropyran to yield 26.18 g, 99% of a clear oil.

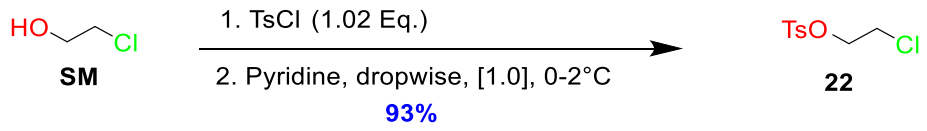

Synthesis of 22 - A solution of 15 g of 2-chloroethanol (1.0 Eq. 0.19 mol) in 130 mL of dry pyridine was cooled to 0°C, and a solution of 36.2 g (1.02 Eq. 0.19 mol) of tosyl chloride in 60 mL of dry pyridine was added with stirring at a rate so that the temperature of the reaction mixture never exceeded 2°C (ca. time 2 h.). The mixture was then placed in the refrigerator for 18 h. After 18 h at 4°C, the reaction mixture was poured over crushed ice, and the resulting aqueous solution was extracted with CH_2C1_2. The organic layer was washed (0°C) with 6 N HCI solution, with brine, dried, and evaporated at 25°C to give a viscous oil which was chromatographed on silica gel (2% MeOH in CH2C12) to give 41.5 g, 93% yield of the tosylate as a low viscosity clear oil.

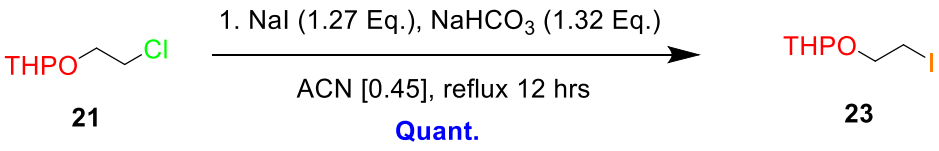

Synthesis of 23 – Method A) To a suspension of NaHCO3 and NaI in anhydrous distilled acetonitrile is added via syringe dissolved in acetonitrile compound **21** and the mixture

brought to reflux under Ar (g) and covered in aluminum foil to avoid exposure to ambient light (fast discoloration occurs). The THP ether was distilled under reduced pressure (0.1-1 torr, 49-65°C) fractions B and C were carried onto the next step.

Method B) General Procedure for THP protection of primary alcohols: A 250-mL 2-neck RBF containing (0.1 Eq, 5.8 mmol) pyridinium-p-toluenesulfonate is charged with 24 mL anhydrous dichloromethane and 10 g (58 mmol, 1 Eq.) 2-iodoethanol is added at once. The flask is cooled in an acetone/crushed ice bath at -10 C and freshly distilled tetrhydropyran (1.5 Eq.) is added over 30 minutes via syringe pump.with vigourous stirring. The mixture is stirred for an additional 15 minutes on ice and temperature brought to ambient for an additional 2 hours. The stirbar was removed and mixture extracted in a seperatory funnnel containing sat. NaCHO3 (50mL)/CH2Cl2 (50ml), 3X, organic layers combined and finally washed 1 X 50 mL sodium thiosulfate, followed by 50 mL of sat. NaCl soln. The organic layer was dried over anhy. Na2SO4, filtered and concentrated to give the title compound in nearly quantitative yield. The crude mixture was subject to distillation under high vacuum through a jacketed distillation head (water cooled) and collected in a flask sitting in a dry ice/Acetone bath. The yield after distillation was nearly quantitative (14.8 g, 99%).

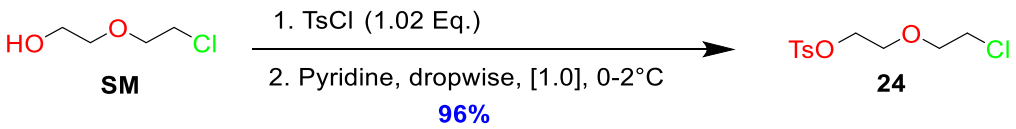

Synthesis of 24 – Refer to the procedure in synthesis **22.** Slightly viscous clear oil.

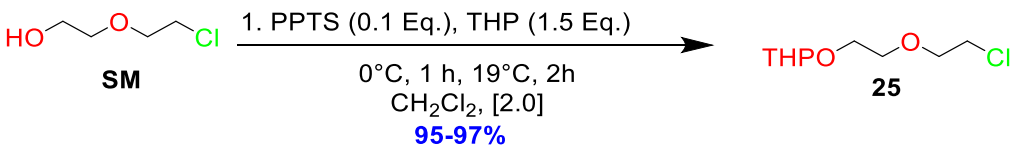

Synthesis of 25 – Refer to the general procedure for THP protection of primary alcohols. (**Synthesis 23, Method B**)

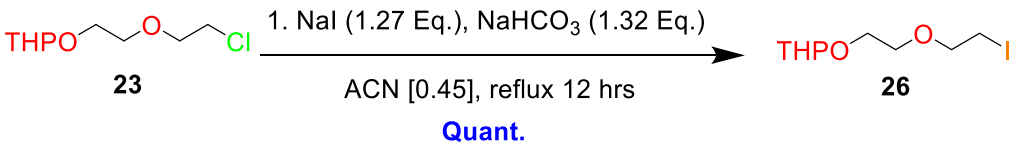

Synthesis of 26 – Refer to Synthesis **23**, Method **A.** Yield, quantitative**.** Gives a non-viscous clear oil when freshly distilled, discoloration occurs upon prolonged exposure to light or air. All THP ethers containing iodide halogen functionality were stored in a -20°C freezer under Ar(g). No decomposition was noticed under these conditions.

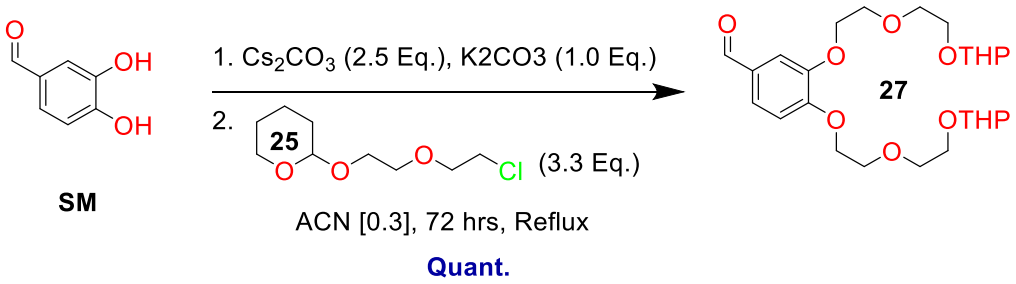

Synthesis of 27 – To a stirred suspension of 10.0 g (1.0 Eq., 72.4 mmoL) 3,4-dihydroxybenzaldehyde, 58.6 g cesium carbonate (2.5 Eq. 0.18 mol) and 10 g potassium carbonate (1.0 Eq., 72.4 mmoL) in 240 mL anhydrous acetonitrile is added 50.0 g (3.3 Eq., 0.24 mol) 2-(2-(2-chloroethoxy)ethoxy)tetrahydro-2H-pyran 21 under inert atmosphere. The mixture is brought to reflux under rapidly stirred conditions for a duration of 72 h., cooled to 19°C, filtered through a 50mm sintered glass funnel containing ½" anhy. Na_2SO_4, topped with quartz wool, and concentrated to yield a crude non-viscous reddish oil**.** The mixture was pure by ^{1}H NMR giving a yield of 35.0 g, 100%.

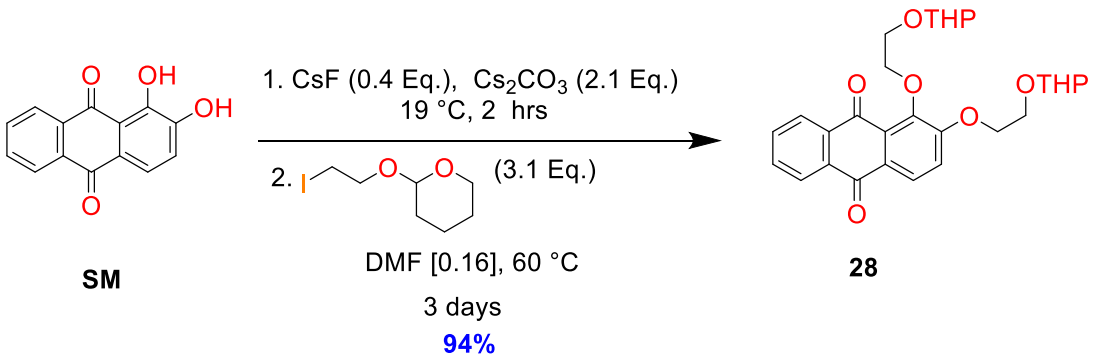

Synthesis of 28 – 1.0 g 1,2-dihydroxyanthraquinone (1.0 Eq., 4.2 mmol), 0.25 g cesium fluoride (0.4 Eq., 1.7 mmol) and 2.9 g cesium carbonate (2.1 Eq., 8.7 mmol) are dissolved in 26 mL anhydrous DMF and the mixture is stirred for 2 h. at 19°C. Next, 3.3 g 2-(2-iodoethoxy)tetrahydro-2H-pyran (3.1 Eq., 12.9 mmol) is added via syringe and the reaction vessel is covered in aluminum foil and the temperature is raised to 60°C monitoring the reaction by TLC 3:1 Hexanes/EtOAc for 3 days where the reaction was observed to go to completion. The mixture was cooled to 19°C, filtered through a 25mm sintered glass funnel and filter cake washed 3 X (10 mL) DMF. The flow through was distilled to remove the DMF and excess 2-(2-iodoethoxy)tetrahydro-2H-pyran, drying additionally under ultra-high vacuum at 50°C overnight. The solid mixture was then taken up in 50 mL dichloromethane, washed with 50 mL diH2O, followed by 50 mL sat. sodium thiosulfate and the organic layer dried over anhydrous $MgSO_{4,\ filtered,}$ concentrated to yield 1.94g, 94% yield pure **28** as a yellow solid.

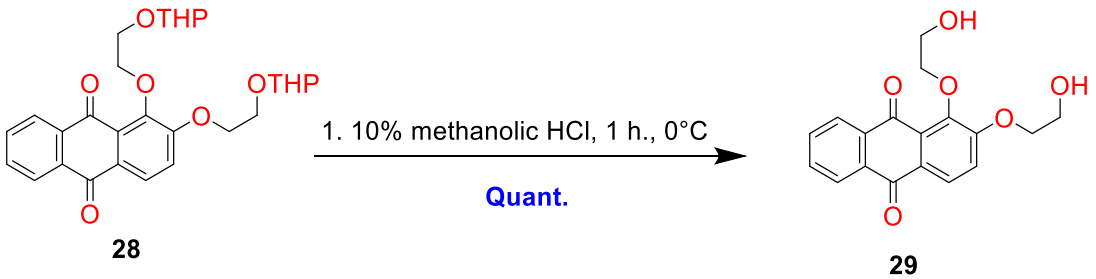

Synthesis of 29 -

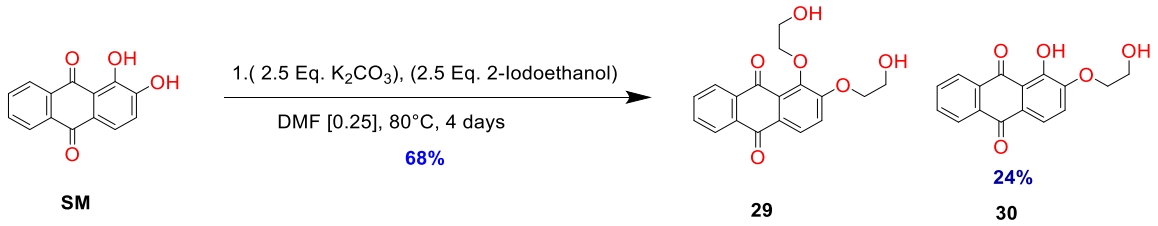

Synthesis of 30

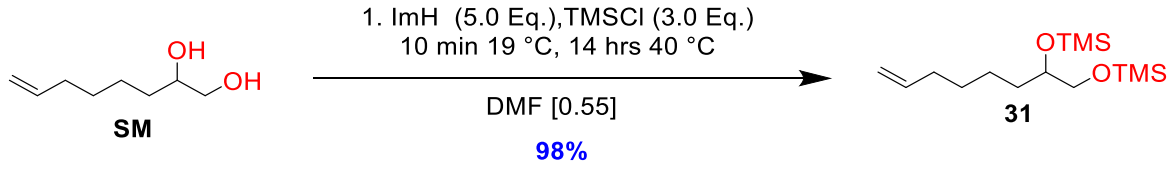

Synthesis of 31 – See procedure S-9

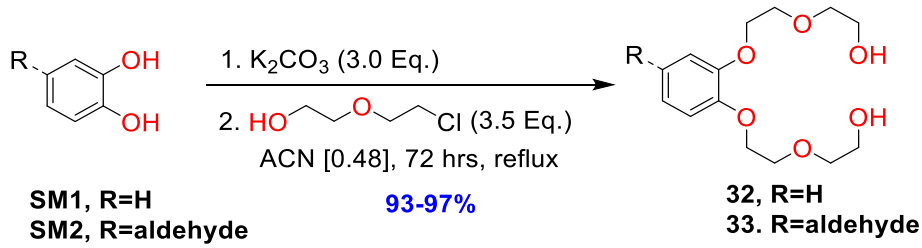

Synthesis of 32 and 33 - General Williamson Ether Synthesis Conditions:

To a 300 mL suspension of 3,4-dihydroxybenzaldehyde (10 g, 91 mmoL) and potassium carbonate (3.5 Eq. 320 mmoL) (powdered) in anhy. acetonitrile in a 2-neck 500 mL round bottom flask with jacketed reflux condenser is added 3.3 Eq. freshly distilled ( ) 2-(2-chloro)ethoxyethanol. The mixture is refluxed for 72 hours under argon until no starting material appears by TLC. The mixture is then filtered to remove salts, concentrated and 100 mL distilled water added. The aqueous solution is extracted with EtOAc (3X100mL), dried over anhy Na_2SO_4, filtered and concentrated to give a yellow oil which was purified by column (50:50 Hex/EtOAc) to give the clear pure diol, 93-97% yield.

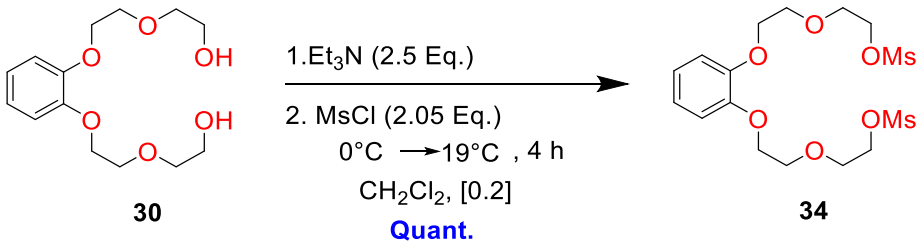

Synthesis of 34 To a stirred suspension of 1.0g of 2,2'-(((1,2-phenylenebis(oxy))bis(ethane-2,1-diyl))bis(oxy))diethanol (3.49 mmol, 1 Eq.) in a 50mL schlenck tube in 17.45mL of dichloromethane 1.02mL of triethylamine (7.33 mmol, 2.1 Eq.). With extreme caution, 0.568mL of methanesulfonylchloride (7.33 mmol, 2.1 Eq.) was added drop wise to the mixture over the course of twelve minutes at 0°C, and then stirred for an hour until room temperature was reached. Once the reaction was at room temperature it was stirred for an additional twelve hours. The mixture was filtered through a small plug column of silica gel. The solvent was removed under reduced pressure to yield 2 (1.429g, 93% yield) as a clear oil. The degree of isotope labeling was determined by 1H NMR (> 99%): ^{1}H NMR (600 MHz, Chloroform-d) δ 7.03 – 6.78 (m, 1H), 4.42 – 4.39 (m, 1H), 4.17 – 4.14 (m, 1H), 3.92 – 3.87 (m, 1H), 3.87 – 3.83 (m, 1H), 3.09 – 3.03 (m, 3H); ^{13}C NMR (151 MHz, Chloroform-d) δ 148.67 , 121.73 , 114.43 , 76.79 , 69.90 , 69.40 , 69.21 , 68.63 , 37.69 , 29.68; HRMS (ESI^{+}) calculated for $C_{16}H_{26}O_{10}S_2Na$ (M+Na) 465.09; found 465.0840.

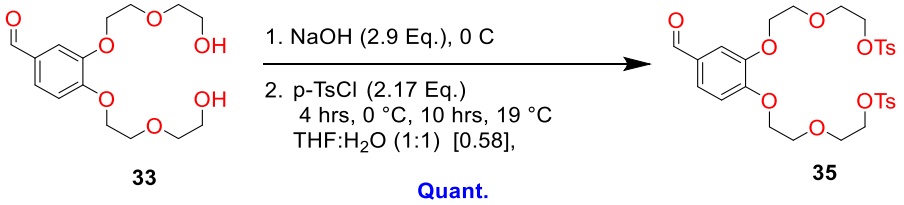

Synthesis of 35 - General Tosylation Procedure:

To a solution of diol (5.0 g, 18 mmoL, 1 Eq.) in 15 mL NaOH (2.9 Eq based on NaOH M.W.)/5 mL THF is added (2.2 Eq., 39 mmol) p-toluenesulfonylchloride dissolved in 10 mL THF over 1 hr, mainaing the reaction mixture at 0 C under vigourously stirred conditions. The reaction is stirred vigoursly until no starting material is present (t=4hrs) by TLC 80:20 Hexanes:EtOAc and the solution evaporated at ambient temperature under high vacuum to remove the THF. The mixture is then back-extracted into 100 mL H2O/ 100 mL CH2Cl2, extracting the water layer 2X50 mL additional CH2Cl2 and finally washed gently with 100 mL sat. NaCl solution. The organic layer is seperated, dried over anhy. Na2SO4 and concentrated to give the di-tosylated derivative in essentially quantative yield, 4.14 g, >99% yield.

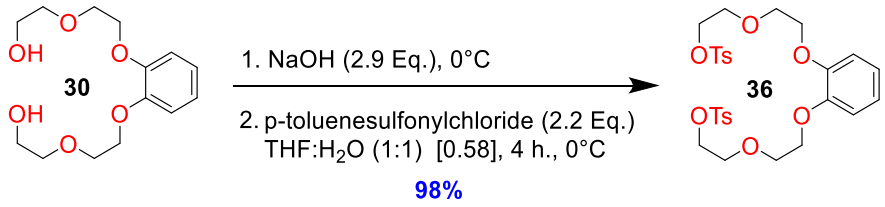

Synthesis of 36 – See general Tosylation procedure for synthesis of **36. Clear, viscous oil, 98% yield.**

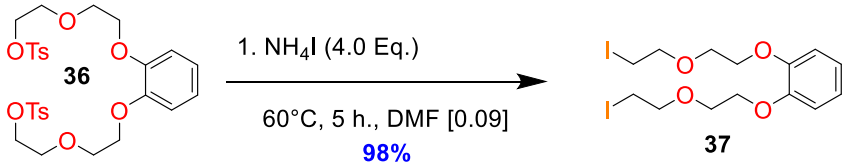

Synthesis of 37 - To 4 Eq. (64 mmoL) of anhydrous ammonium iodide in 150 mL anhy. DMF [0.09], was added the bisphenylenedioxoditosylate compound glycol derivative dissolved in 30 mL anhy DMF via syringe at once at ambient temperature. The mixture was stirred vigoursly for 10 min at ambient, and temperature slowly raised to 60 C using a

heating block. The mixture was stirred for a total of 5 hours at 60 C and concentrated in vacuo to remove excess DMF. The mixture was taken up in equal volume hexane/1M HCl (200 mL tota), extracting additionally 2 X 50 mL hexane to give the pure iodide, 7.6 g, 95% yield.

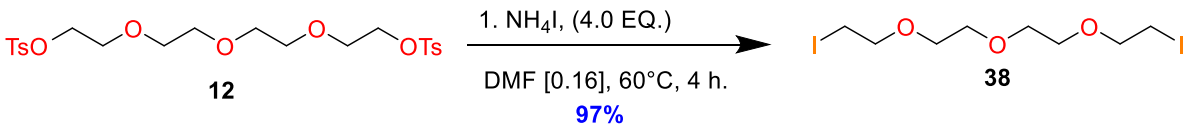

Synthesis of 38 – Procedure **S37** was used to transform the bis-tosylate PEGDT into the diiodide in 97% yield. The substance was a clear fluid oil.

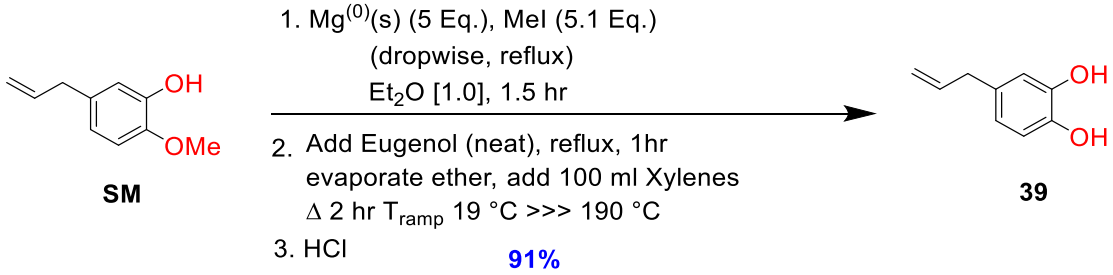

Synthesis of 39

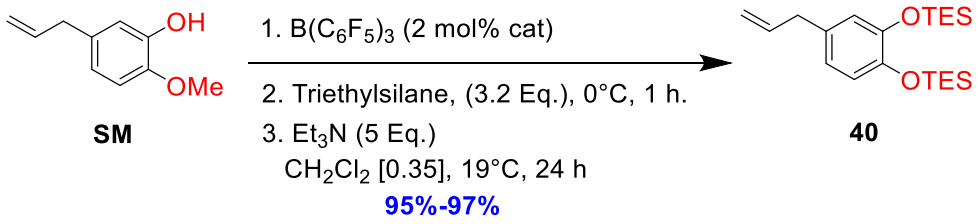

Synthesis of 40 – 70 mg Tris(pentafluorophenyl)borane (0.02 Eq., 0.14 mmol) along with 1.0 g 5-allyl-2-methoxyphenol (1 Eq., 6.8 mmol) were added to a 2-neck 50-mL RBF with reflux condenser containing 17 mL anhydrous distilled dichloromethane and the mixture was cooled to 0°C. 2.5 g freshly distilled triethylsilane (3.2 Eq., 21.7 mmol) was added dropwise at first until bubbling was noticed in the reaction mixture, the addition was slowed to give a constant, controlled bubbling (ca. add. time 1h @ 0°C) and under careful supervision, the reaction was gradually warmed to 19°C by adding no more ice to the wet ice bath and finally ice bath removed and mixture stirred at 19°C for 24 h. to ensure complete hydrosilylation of the alcohol/ether functionality. At t=24 h., 3.44 g triethylamine (5.0 Eq., 34 mmol) is added along with 100 mg of activated carbon, and the mixture stirred for an additional 24 h. The entire reaction mixture is then poured through a tall 25 mm diameter sintered glass funnel containing the following layers from the bottom up: Brockman Grade I alumina (1 inch), activated carbon (1/8”), celite 545 (2 inch), quartz wool and sand (1 inch) giving 2.48 g, 97% yield of a clear, non-viscous oil.

Method A)

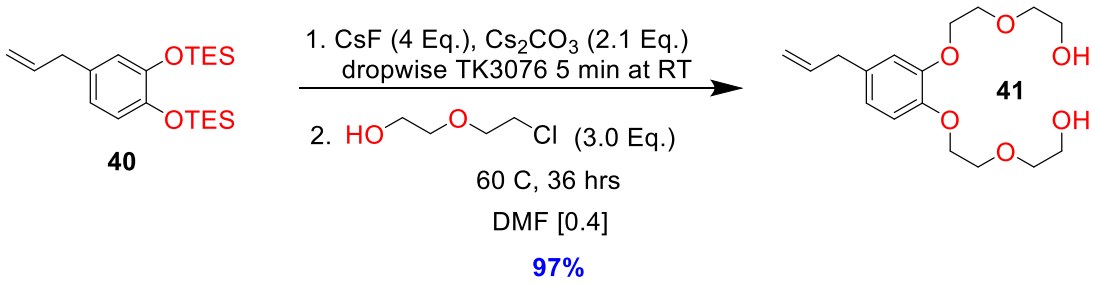

Method B)

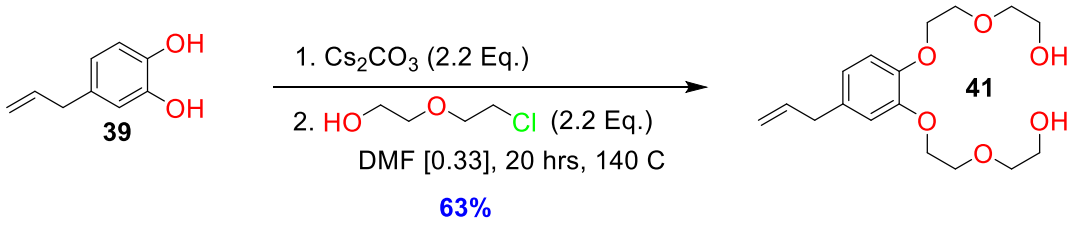

Synthesis of 41 – Method A) To a degassed suspension of 4.8 g (4 Eq., 31.7 mmol) CsF and 5.4 g Cs_2CO_3 (2.1 Eq., 16.6 mmoL) in 24 mL anhydrous freshly distilled DMF contained under inert Ar (g) atmosphere (Crucial to reaction success) is added neat 3.0 g (1.0 Eq., 7.9 mmoL) of the bis-TES protected Eugenol **37** followed immediately by addition of 3.0 g (3.0 Eq., 23.8 mmol) freshly distilled 2-(chloroethoxy)ethanol and the reaction is covered in aluminum foil and slowly brought to a temperature of 50°C where by hour 36 TLC analysis (via needle/capillary) indicates complete conversion of the starting material to the di-alkylated product. The mixture is filtered through a CLEAN sintered glass funnel to remove initial salts, washing with 3 X (5mL) fresh DMF. The flow-through is distilled under reduced pressure and inert atmosphere to remove excess DMF. The crude oil is dissolved in 50 mL CH_2Cl_2/ 50 mL diH_2O and allowed to separate. The organic layer is collected and dried over anhy. $MgSO_4$, filtered and concentrated to yield 2.5 g, 97% of a pure clear viscous oil.

Method B) - To a 2-neck 50-mL RBF with reflux condenser is added 1.5 g (10.1 mmol, 1 Eq.) 4-allylbenzene-1,2-diol followed by 3X vac/purge cycles of Ar(g). 20 mL anhydrous DMF is added through the septum and stopper briefly removed as 7.2 g Cs_2CO_3 (2.2 Eq., 22.2 mmoL) is added in one portion via powder funnel under positive Ar(g) pressure, rinsing down the sides with the reserved 10 ml DMF, replacing the septum stopper. After 10 minutes of vigourous stirring, 2.8 g (2.2 Eq., 22.2 mmoL, 2.33 mL) 2-(chloroethoxy)ethanol

is added dropwise via syringe and the stopper is replaced with a greased glass plug. The temperature is increased to a gentle reflux and the mixture begins to darken to a yellowish color. Reflux is continued until at T=20 h, TLC (90:10) CH2Cl2:MeOH Rf: 0.43 (di-alkylated product) indicates no starting material remains. The mixture is cooled to room temperature and filtered to remove solids. The solids are washed with 2 X (5 ml) DMF and concentrated to a minimal volume. The resulting oil is columned on Silica gel previously deactivated and dried with 10% Et_3N in CH_2Cl_2 using a 90:10 mixture of CH_2Cl_2:MeOH to elute the pure product in the third row 2.1 g, 63% yield.

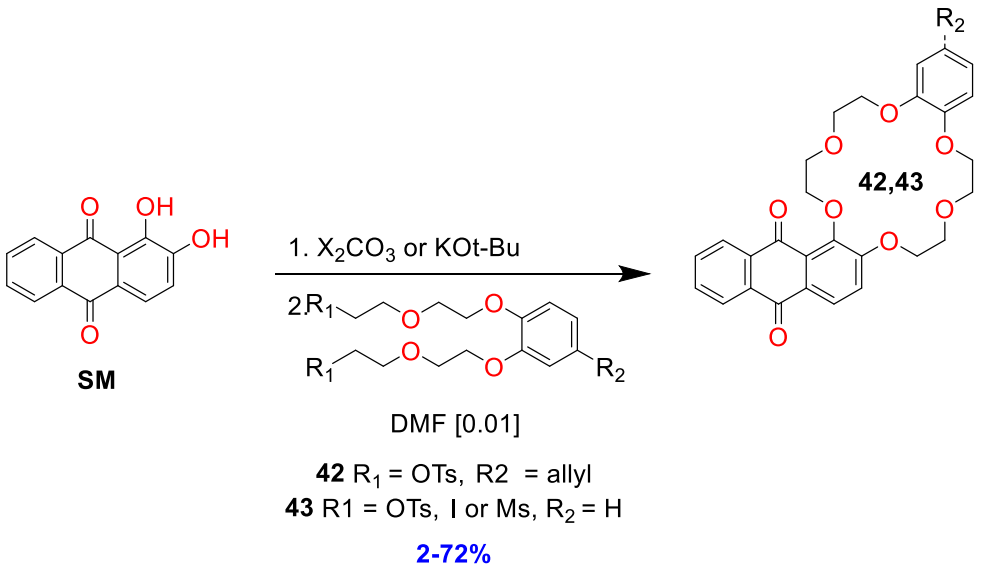

Synthesis of 42 and 43 –

To a three-neck, 1000mL, flask containing 700mL of anhydrous dimethylformamide and a medium teflon-coated, egg-shaped stir bar is added 1.68g of 1,2-dihydroxy-9,10-anthracenedione (7.0 mmol, 1.0 Eq.). The solid is dissolved and 6.84 g of anhydrous cesium carbonate (21.0mmol, 1.0 Eq.) is added in one portion via powder funnel. Finally, 9.4mL

(140mmol, 20.0 Eq.) of freshly distilled 2-chloroethanol is added via syringe through the rubber septum at once. The reaction is then heated in an oil bath at 110°C for eighteen hours. The reaction was then further heated at 130°C for an additional eight hours. After eight hours at 130°C, the reaction was lowered to 120°C overnight for an additional ten hours. At the forty-six hour mark, no progress could be seen, an additional 2.28g of cesium carbonate (7.0mmol, 1.0 Eq.) for a total of 4 Eq., as well as 11.25g of 2-chloroethanol (140mmol, 20 Eq.) for a total of 40 Eq. while the temperature was kept at a constant 120°C. At the seventy-two hour mark the temperature was increased to 165°C with vigorous stirring for an additional eighteen hours. The reaction was then filtered through a medium sintered glass, fritted funnel into a 2L round bottom flask, and condensed under reduced pressure to yield a mustard colored semi-solid. The solid paste was extracted with three portions of boiling 9:1 ethyl acetate (EtOAC), 200p ethanol (EtOH). The remaining paste was dissolved in 50:50 pyridine, EtOH, about 100mL, and 25mL of EtOAC was added to aid the dissolution of the crude paste. Both the EtOAC, EtOH and the pyridine, EtOH, and EtOAC solutions were treated with anhydrous sodium sulfate (Na_2SO_4) and activated carbon, just below their boiling points. They were then filtered through celite and Na_2SO_4 in a fritted funnel and concentrated down under reduced pressure to yield .606g, 45% yield of a light yellow solid. Spectral Info (Compound **43**) The degree of isotope labeling was determined by 1H NMR (> 99%): ^{1}H NMR (800 MHz, Chloroform-d) δ 8.27 – 8.23 (m, 2H), 8.14 (d, *J* = 8.5 Hz, 1H), 7.75 (td, *J* = 7.2, 1.7 Hz, 2H), 7.24 (d, *J* = 8.7 Hz, 1H), 6.95 – 6.90 (m, 4H), 4.36 (t, *J* = 4.8 Hz, 2H), 4.28 (t, *J* = 5.2 Hz, 2H), 4.25 – 4.23 (m, 2H), 4.21 (dd, *J* = 5.1, 3.2 Hz, 2H), 4.16 (q, *J* = 5.2 Hz, 4H), 4.08 – 4.07 (m, 2H), 4.03 (t, *J* = 4.6 Hz, 2H); ^{13}C NMR (201 MHz, Chloroform-d) δ 182.66 , 182.37 , 158.37 , 149.23 , 148.69 (d, *J* = 3.1 Hz), 135.12 , 133.81 ,

133.45 , 132.97 , 127.39 , 127.15 (d, J = 9.5 Hz), 126.65 , 125.16 , 121.81 , 121.27 , 116.80 , 114.70 , 113.77 , 73.09 , 70.79 , 70.29 , 69.85 , 69.72 , 69.51 , 69.16 , 68.43 , 29.69; HRMS (ESI $^{+}$) calculated for $C_{28}H_{26}O_8$ Na (M+Na) 513.15; found 513.1505.

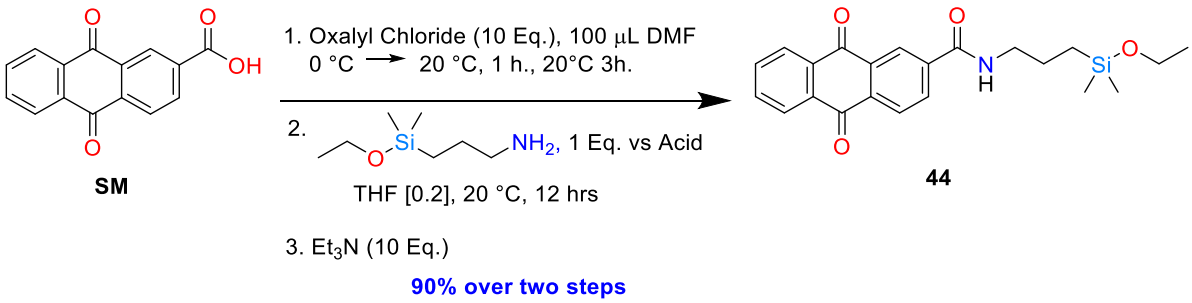

Synthesis of 44- (Step 1 of 2) - 1.0 g 9,10-dioxo-9,10-dihydroanthracene-2-carboxylic acid (1 Eq., 4 mmoL) is added to a 50-mL pear-shaped flask with stirbar and the mixture is solvated in 20 mL anhydrous CH2Cl2 and cooled to 0°C. Next, 5.08 g oxalyl chloride is added and the suspension is stirred rapidly (does not dissolve) followed by catalytic distilled DMF (100µL). The heterogeneous mixture is stirred for 1 h. at 0°C and then gradually warmed to 19°C, where the mixture bubbled rapidly with evolution of CO2 gas becomeming homogenous and clear. After stirring for an additional 3 h. at 19°C, the stir bar is removed via oven-dried stirbar remover and the mixture distilled under slight vacuum to remove the solvent and excess oxalyl chloride and finally dried under high-vacuum overnight at 50°C to furnish a tan solid. The compound was used without further purification. An NMR was taken to confirm all carboxylic acid peaks had disappeared and compared with standard spectra (SDBS). 1.05 g of dried, 98% of pure material was obtained and used immediately in the next step.

Step 2 of 2: 1.05 g (1 Eq. 3.9 mmol) of the acid chloride was dissolved in 20 mL of a 50:50 mixture of THF:PhMe at 0°C and 0.56 g 3-aminopropyldimethylethoxysilane (1.0 Eq., 3.9 mmol) was added in one shot followed by the addition of 3.95 g triethylamine (10 Eq., 39 mmoL) and the reaction allowed to come to room temperature.

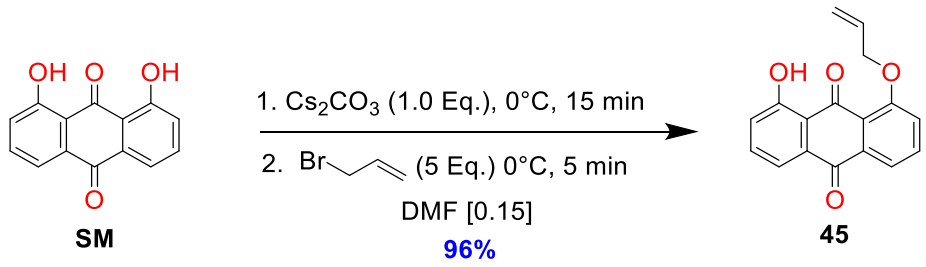

Synthesis of 45 1.0 g (1.0 Eq., 4.2 mmol) recrystallized, dry 2,3-dihydroxyanthracene-9,10-dione is dissolved in 28 mL anhydrous DMF and 0.53 g (1.5 Eq., 6.2 mmol) sodium bicarbonate is added via powder funnel. The mixture is stirred for 30 m. at 19°C and 2.5 g freshly distilled allyl bromide is added to the mixture. The mixture is brought to a temperature of 50°C and stirred at this temperature for 48 h.. 8.1 g solid anhydrous citric acid (10 Eq., 42 mmol) is added to the cooled mixture, stirred for 20 minutes, and the mixture is poured into a 500 mL beaker containing 350 mL diH_2O cooled to 0°C in a wet ice bath. The product immediately crashed out as a bright orange solid, refrigerated for an additional 4 hrs, filtered, washed 4 X (100mL) diH2O and dried under vacuum in a desiccator over Drierite for 48 hrs to give 1.07 g, 91% yield of the pure monoallylether as a bright orange solid.

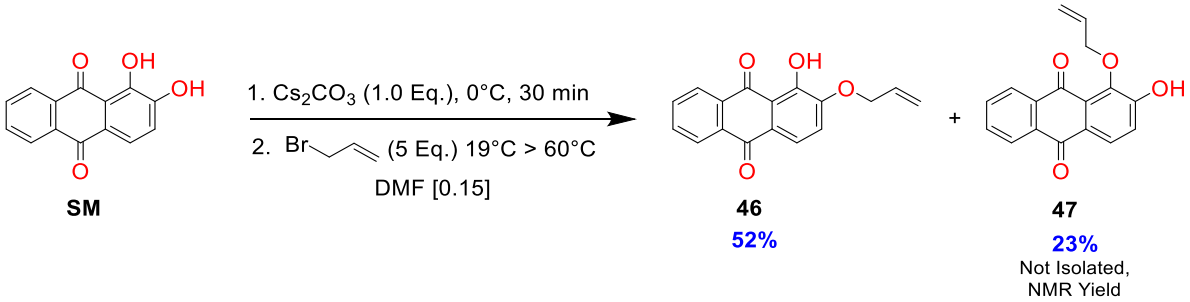

Synthesis of 46 and S47 – See procedure **48** below. The

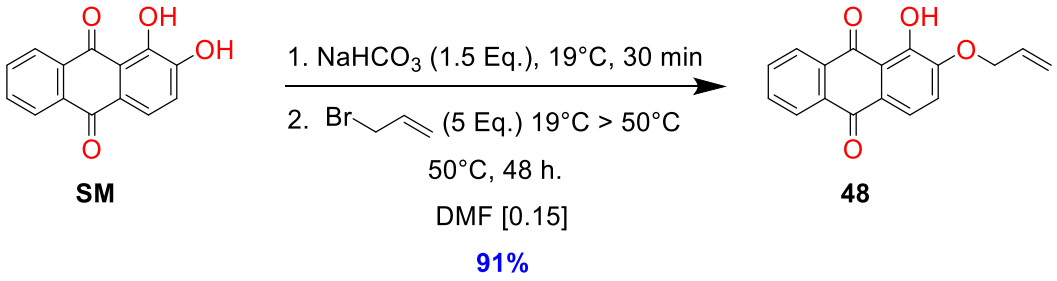

Synthesis of 48 – 1.0 g (1.0 Eq., 4.2 mmol) recrystallized, dry 2,3-dihydroxyanthracene-9,10-dione is dissolved in 28 mL anhydrous DMF and 0.53 g (1.5 Eq., 6.2 mmol) sodium bicarbonate is added via powder funnel. The mixture is stirred for 30 m. at 19°C and 2.5 g freshly distilled allyl bromide is added to the mixture. The mixture is brought to a temperature of 50°C and stirred at this temperature for 48 h.. 8.1 g solid anhydrous citric acid (10 Eq., 42 mmol) is added to the cooled mixture, stirred for 20 minutes, and the mixture is poured into a 500 mL beaker containing 350 mL diH_2O cooled to 0°C in a wet ice bath. The product immediately crashed out as a bright orange solid, refrigerated for an additional 4 hrs, filtered, washed 4 X (100mL) diH2O and dried under vacuum in a desiccator over Drierite for 48 hrs to give 1.07 g, 91% yield of the pure monoallylether as a bright orange solid.

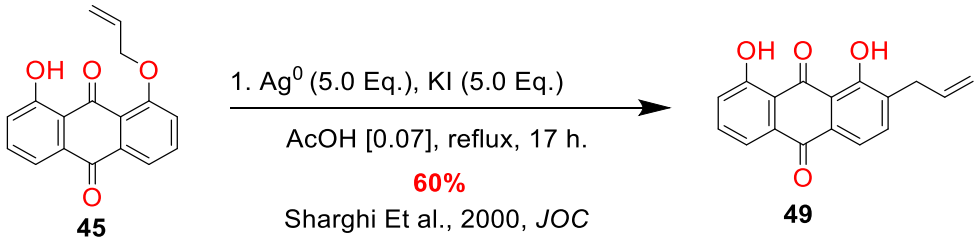

Synthesis of 49 – 1.0 g 1-allyoxy-8-hydroxy-9,10-anthracenedione (1 Eq. 3.6 mmoL) is dissolved in 45 mL glacial acetic acid and 2.95 g potassium iodide (5.0 Eq., 18 mmol) followed by 1.92 g of silver powder (5.0 Eq., 18 mmol) and the reaction brought to reflux for 17 h. where no more product formation was indicated by TLC. The mixture is then filtered hot (100°C) through a sintered glass funnel and the solids are washed with 20 mL hot glacial acetic acid. The recovery flask is distilled under reduced pressure to remove any glacial acetic acid remaining in the crude mixture. The crude solid is chromatographed on SiO_2 2-5%MeOH:$CHCl_3$ to give 0.6 g, 60% of the rearranged product 46.

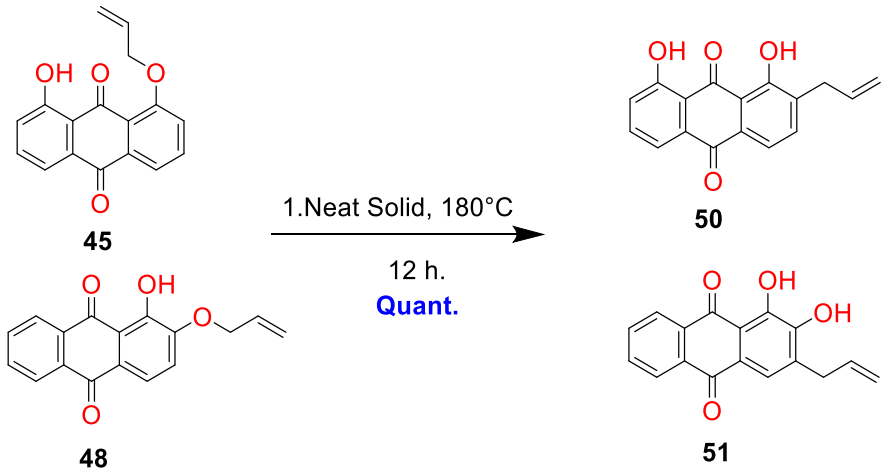

Synthesis of 50 and 51 – To a 50 mL low profile cylindrical pressure vessel with large egg-shaped stir bar (3/4”) is added 5.0 g (1.0 Eq., 17.8 mmol) of the respective monoallylether

40 or **45**. The flask is purged with Ar (g), sealed tightly and the bright orange substrate is heated in the dark slowly to 180°C, with melting occurring at T≈130°C. The melt is stirred at 180°C for 12 h., cooled to 19°C and solidified to give 5.0 g, 100% of the rearranged 2 and 3-substituted propenyl dihydroxyanthraquinones **50** and **51**.

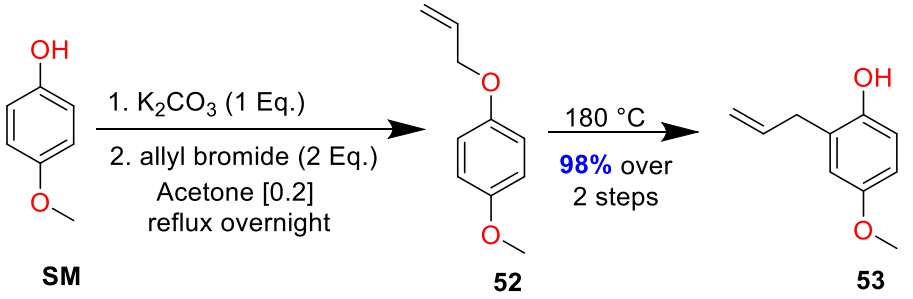

Synthesis of 52 and 53 – See procedure **S64** for the preparation of **52, 99% yield.**

Preperation of 53 - 5.00 g of the crude pure **52** was added to a 15 mL round bottom flask with stir bar and reaction inlet with septum. The flask was evacuated/ backfilled with Ar(g) for a total of 3 times. The mixture is then heated to 180˚C on a heating bock with rapid stirring and at t=12 hrs, complete conversion to the rearranged phenol **53** was complete by TLC (10% EtOAc:hexanes) to give 4.95 g of 53, 99% yield.

.

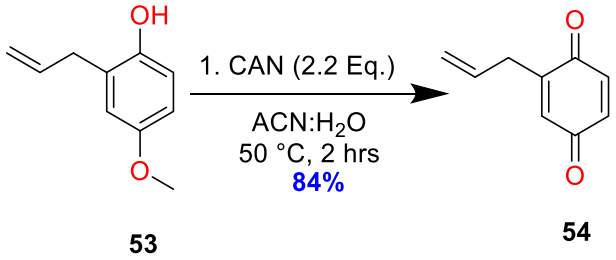

Synthesis of 54 – See procedure **S-2**. Red/orange oil.

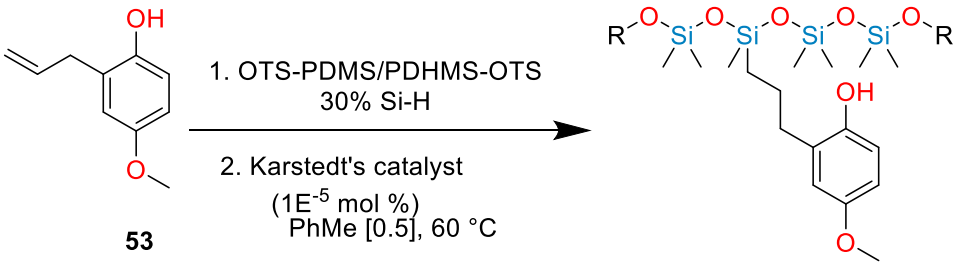

Synthesis of 55 – See procedure S-64 for hydrosilyation procedure. Purification on SiO2 using 2-5% EtOAc:Hexanes gradient elution to give 55 as a bright reddish-orange oil in quatitative yield.

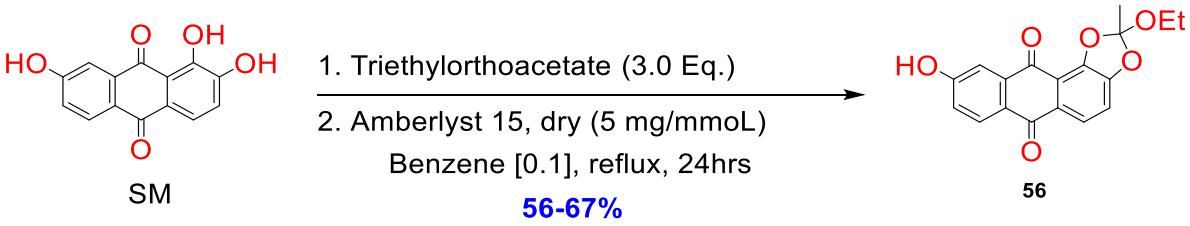

Synthesis of 56 - To a 100 mL 2 neck flask equipped with a Dean-Staark trap and reflux condenser is added 1.54 g 1,2,7-trihydroxy-9,10-anthracene (1.0 Eq., 6 mmol) dione, 30 mg Amberlyst 15 (dry) ion exchange resin, 2.9 g triethylorthoacetate (3.0 Eq., 18 mmol, 3.3 mL) and 60 mL distilled benzene. The heterogeneous mixture is brought to reflux for a duration of 24 h. and cooled to room temperature. The heterogenous mixture is filtered through a sintered glass funnel, rinsed with 25 mL EtOAc, dried and was identified as 0.62 g of recovered starting material. The flow-though is added to a 250-mL separatory funnel, washed with 50 mL sat. $NaCHO_3$, dried over anhy. Na2SO4, filtered and concentrated. The crude protected alcohol is columned on SiO2 10% EtOAc:PhMe to give 1.3 g, 67% of the orthoesther as a yellow solid.

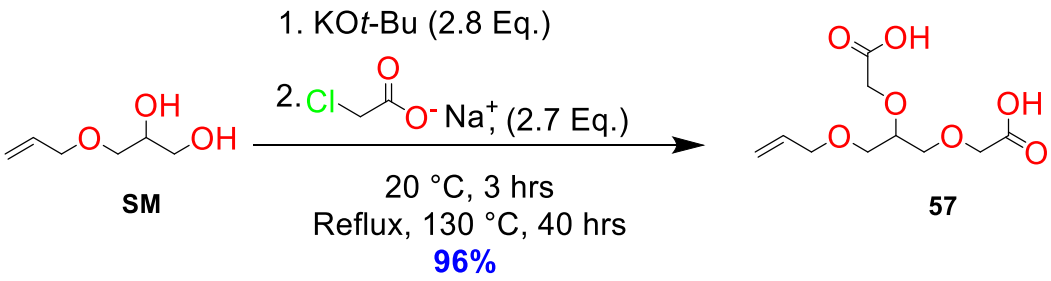

Synthesis of 57 – To a 500 mL 2 neck round bottom flask equipped with a ¾ inch Teflon coated stir bar and water jacketed reflux condenser is first added stir bar is added potassium tert-butoxide (31.3 g, 0.28 mol, 2.8 Eq.) followed by 2-choroaceticacid sodium salt (31.3 g, 0.27 mols, 2.7 Eq) to a stirred solution of 300 mL anhydrous t-butanol. The mixture is stirred vigoursely for 5 minutes at 19 C and 3-allyoxy-1,2-propane diol (13.2 g, 0.1 mol, 1.0 Eq.) is added in one portion to the rapidly stirred mixture. The mixture is heated to reflux for 40 hours where a check by TLC indicated all spots had disappeared and a polar spot RF:0.06 90:10 CH2Cl2:MeOH was observed using KMNO4 dip. The mixture was cooled, filtered, rinsed with 50 ml EtOAc and extracted 3 X 100 mL EtOAc from 100 mL 1 M HCl. The organic layers were combined, washed with 100 mL sat NaCl soln. and dried over anhydrous sodium sulfate, filtered and concentrated to yield a viscous brown oil which was distilled slowly to remove the light fraction (b.p. 135-145, 0.8-2.0 torr) which was discarded leaving the pure acid in the distillation flask. Yield:

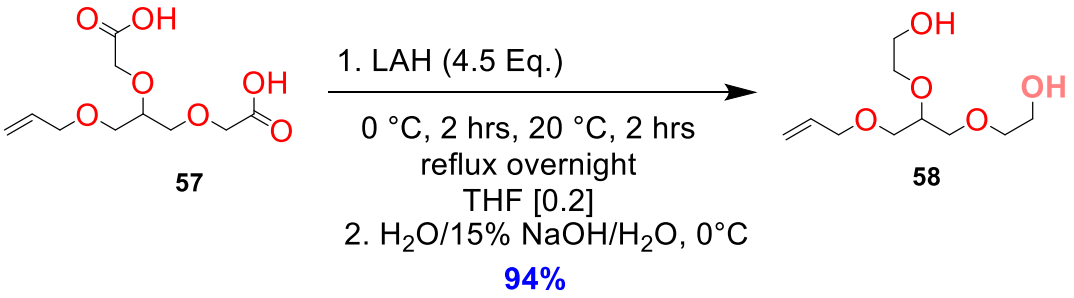

Synthesis of 58 – To a suspension of lithium aluminum hydride (6.1 g, 0.16 mol, 4 Eq) in 260 mL THF at 0 C was added the di-carboxylic acid (10 g, 40 mmol, 1.0 Eq.) dissolved in 50 mL anhy. THF over 15 mminutes. The reaction was allowed to stir for 1 hour at 0 C, ice bath removed and stirred at 19 C for 3 hours and finally refluxed overnight for an additional 12 hrs, cooled to 0 C and quenched with the following procedure: first added was 6.12 mL diH2O, 6.12 mL 15% NaOH, 18.3 mL diH20 until all evolution of H2(g) ceased. The mixture is then cautiously warmed to room temperature after 1 hour of stirring and additions of quenchers and filtered through a 2" pad of anhydrous sodium sulfate padded with cotton to afford the pure diol in quantitative yield.

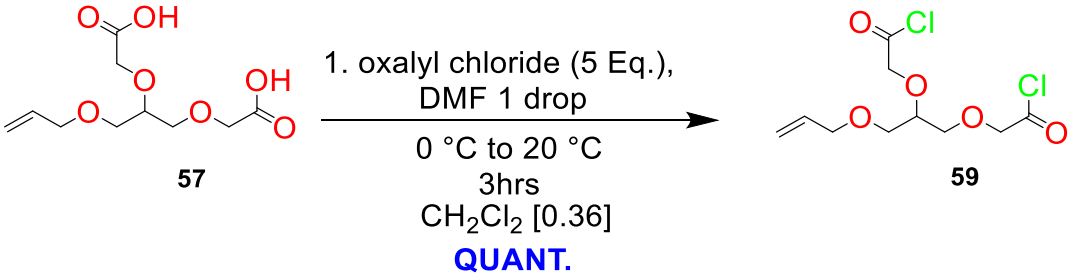

Synthesis of 59 – In a 25 mL pear-shaped RBF with teflon-coated stirbar is added 1.0 g (4 mmol, 1.0 Eq.) of bis-acid **54** in 11 mL freshly distilled CH_2Cl_2 followed by 2.5 g oxalyl chloride (5 Eq., 20 mmol, 1.7 mL) and the mixture is cooled to 0°C in a wet ice bath. After 5 m. of stirring, 1 drop (10 µL, cat) dimethylformamide is added and the mixture brought to

20°C and stirred for an additional 3 h. to ensure completion of the reaction. The solvent is removed under reduced pressure and the crude bis-acid chloride is dried under high vacuum overnight to yield 1.15 g, 100%.

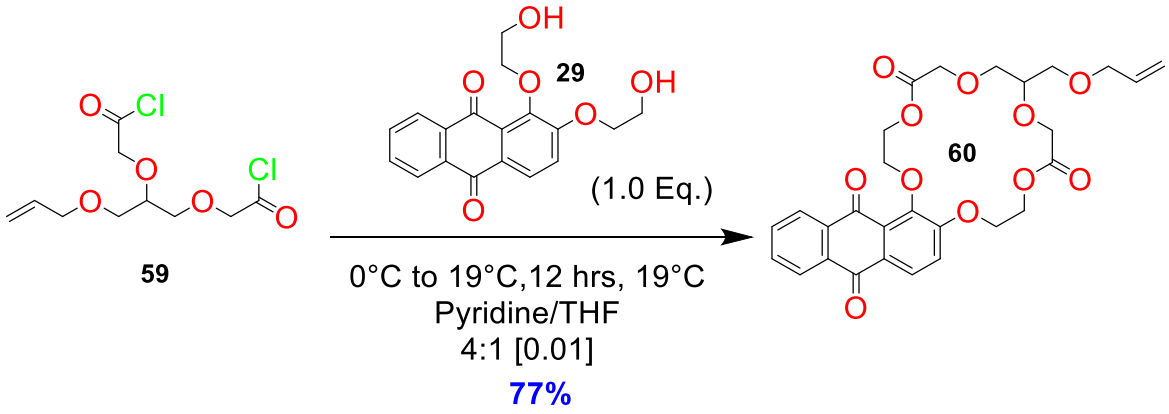

Synthesis of 60 – To a 250 mL round bottom flask containing 0.33 g (1.0 Eq., 1 mmol) of the bis-anthracene diol dissolved in 80 mL anhy pyridine/20 mL anhy THF at 0°C is added at once, 0.29 g (1.0 Eq., 1 mmol) of bis-acid chloride 56 via syringe and the mixture is permitted to come to 19°C and stirred for 12 h total. The mixture is concentrated to dryness and chromatographed on SiO2 10-20 % gradient EtOAc:Hexanes to give 0.42 g, 77% of the bis-macrocyclic ester **57**.

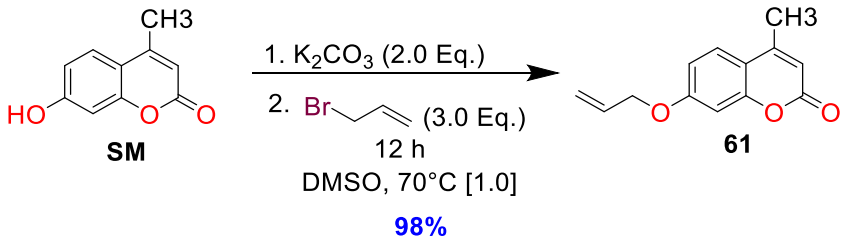

Synthesis of 61 - To a flame-dired 2-neck 500 mL RBF is added 5.0 g of recrystallized (from ABS. EtOH) 4-methylumbeliferone (28.4 mmoL, 1.0 Eq.) The flask is evacuated and side inlet opened briefly to allow for the adddtion of 4.7 g anhy. potassium carbonate. (34 mmoL, 1.2 Eq.) followed by addition of 30 mL anhydrous DMSO. The mixture is stirred for

20 m at 19°C and temperature raised to 80°C for 12 hrs where TLC shows complete conversion to the monoallylether. The mixture is cooled, diluted with 170 mL diH20 and placed in the refrigerator for 4 h to induce crystallization. The precipitate was filtered and washed 5 X (50 mL) ice cold diH20, dried under high vacuum in a desiccator to yield 6.02 g of a white solid, 98%.

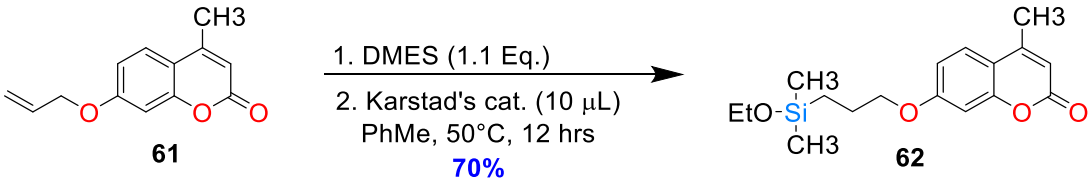

Synthesis of 62 – To a desiccator dried 15 mL cylindrical high pressure flask is added a small teflon-coated stirbar and topped with a rubber septum. 0.5 g (2.3 mmol, 1.0 Eq.) 7-(allyloxy)-4-methyl-2H-chromen-2-one is then added followed by 5 mL anhydrous freshly distilled toluene. With a long microliter syringe, 2 µL Karstedt's catalysts is added under argon followed by dropwise addition of 0.27 g (1.1 Eq., 2.5 mmol) dimethylethoxysilane. The mixture becomes clear after 5 m. at 19°C, and the mixture is slowly heated to 50°C and stirred overnight for an additional 12 h. where is was determined by NMR that the reaction had gone to 75% conversion. Activated charcoal ≈50 mg was added to the stirred suspension along with 0.1 mL triethylamine and the mixture stirred for an additional 24 hrs at room temperature before being filtered through a 0.5" inch pad of Celite 545, concentrated in vacuo to yield a golden oil which was determined to be 70% by mass of the desired product along with remaining unreacted monomer. The mixture was used without

further purification since only the functionalized monomers would react in a manner consistent with SiO2 grafting. M/Z 320.13 ca. 320.14.

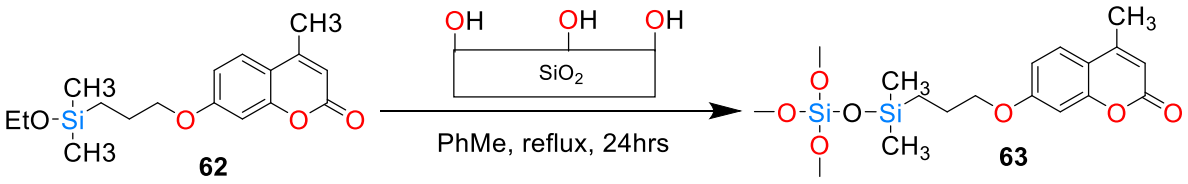

Synthesis of 63 – See corresponding chapter for detailed description. The product on quartz substrate was characterized by IR spectroscopy as well as XPS with spectra given as **S-57**.

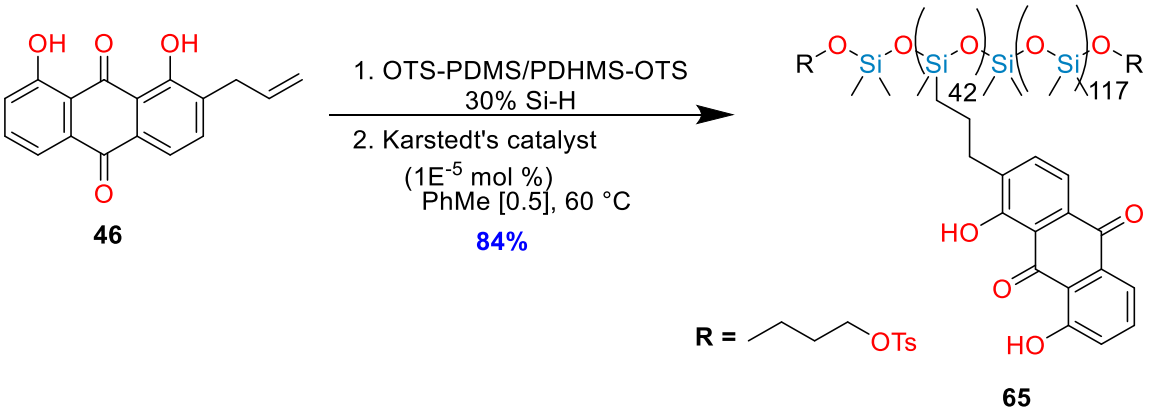

Synthesis of 64 - To a 50-mL round bottom flask with Teflon stir bar is first added 1.00 g (# mmoL, 1.0 Eq. M.W.) hydrosiloxane copolymer (30% Si-H side chain density) followed by the addition of # g (45 Eq., mmol) 2-allyl-1,8-dihydroxy-9,10-anthracenedione. Next, 30 mL freshly distilled toluene is added to the mixture and the

reaction is stirred for 30 m until homogenous. 10 µL Karstedts catalyst (2.5 % Pt in Xylenes) (cat.) is added under an argon matrix and the mixture is heated slowly to 60°C and stirred for 36 h. at this temperature. At t=36hrs, NMR analysis of the crude mixture showed no olefin protons and no residual Si-H peak, indicating 100% incorporation of the calculated monomer. The mixture was cooled to 19°C, transferred to a 250-mL separatory funnel and portioned between 100 mL 0.1M citric acid/ 70 mL toluene, organic layer separated, dried over Na2SO4, filtered and concentrated to yield the crude mixture as a dark red semi-solid syrup. The mixture was carefully transferred to a soxhlett extraction apparatus filled with diethyl ether and the crude mixture was extracted for 24 h. to give the pure polymer g, 84% yield. . ^{1}H NMR (600 MHz, Chloroform-d) δ 3.54 (m, 8H), 3.62 (m, 4H), 3.75 (m, 4H), 4.53 (s, 4H), 6.72 (s, 2H)

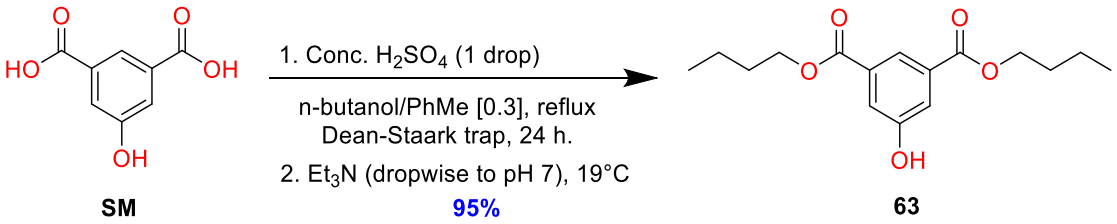

SM **63**

Synthesis of 63 – To a 500 mL RBF with large egg-shaped Teflon stir bar is added 10.0 g 5-hydroxyisophthalic acid (55 mmol, 1.0 Eq.) followed by the addition of 90 mL anhydrous n-butanol / 180 mL anhydrous PhMe. The Dean-Staark trap was prefilled with distilled toluene. Next, under a positive pressure atmosphere of Ar(g), 1 drop (approx. 20 µL) concentrated H2SO4 is added and the RBF sealed with vacuum-greased joints secured with keck-clamps. The mixture is heated to reflux with the fume hood down until the azeotrope reaches the water-cooled reflux condenser, and the solvent begins to drop into the Dean-Staark trap. After the reflux is stabilized, the reaction is stirred at reflux for 24 h. to ensure

complete esterification of the acid groups. The reaction is then briefly cooled to 50˚C, triethylamine is then added until litmus paper indicates yellow (pH 7.0) (approx. 5 drops or 0.1 mL) and the mixture is stirred and brought to reflux once again. The Dean-Staark trap is then opened and solvent allowed to escape until the mixture begins to turn cloudy. 30 mL of hot distilled toluene is then added to resolubilize the mixture at reflux. With a heat-protection glove the refluxing mixture is allowed to cool slightly and the grease is removed along with the stirbar and Dean-Staark trap. The hot mixture (appox 100˚C) is poured through a hot fritted glass funnel containing 1 inch of anhydrous sodium sulfate and allowed to cool to room temperature. As the solution cooled, crystallization gradually began and eventually one could no longer see the mother liquor. The crystals were cooled further in the refrigerator for 4 h. at 4˚C, filtered, rinsed with cold toluene and dried under high vacuum to yield 15.35 g of the pure bis-esther **63,** 95% yield**.**

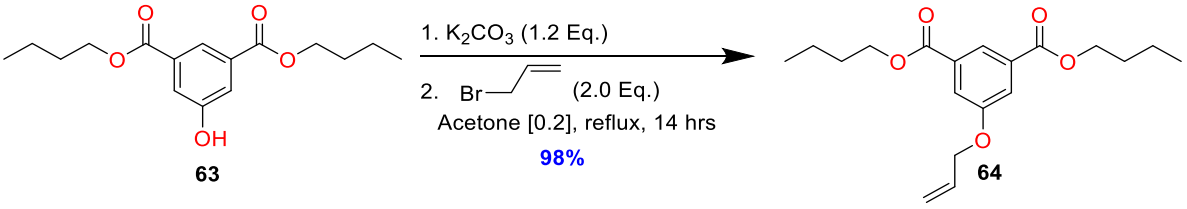

Synthesis of 64 – To a suspension of 15.0 g of the phenol 63 (1.0 Eq. 51 mmol) and 8.4 g anhy. potassium carbonate (1.2 Eq., 61 mmol) in 250 mL acetone is added with stirring, 8.94 mL (12.34 g) distilled allyl bromide (2.0 Eq. 0.1 moles) and the mixture is brought to reflux for 14 h. where by TLC (5% EtOAc: Hexanes) all starting material had been consumed. The mixture was cooled, filtered and concentrated to yield 16.7 g, 98% yield of a clear, non-viscous oil which was pure by NMR.

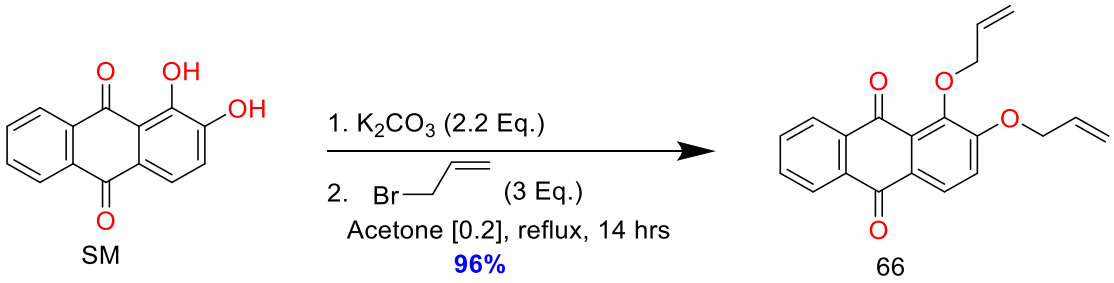

Synthesis of 66 – To a suspension of 1.0 g (4.1 mmol, 1 Eq.) Alizarin, 1.57 g anhydrous potassium carbonate (9.2 mmol, 2.2 Eq.) in 20 mL anhydrous acetone is added 1.45 g distilled allyl bromide (12.3 mmol, 1mL, 3 Eq.) via syringe and the bright red reaction is brought to reflux for 14 h., where the color changed from red to yellow upon completion, another 20 mL of acetone is added and the mixture is filtered hot through a fritted glass funnel and washed with 20 mL hot acetone. The mixture was concentrated until a slightly hazy appearance appeared. 10 mL acetone was added to bring the mixture to clear and the mixture was allowed to cool slowly on a hot plate that had just been turned offwith aluminum foil. After 10 h. cooling to ambient, crystallization had occurred and the mixture was filtered and washed with 20 mL cold acetone, dried under high vacuum overnight to give 1.26 g of a bright yellow solid, 96% yield.

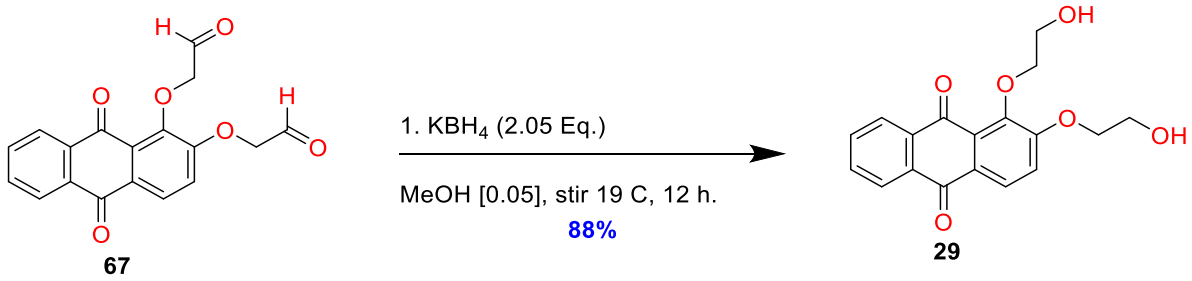

S67 - To a mixture of 0.65 g of the bis-aldehyde anthraquinone (2 mmol, 1 Eq.), in a solution of 13 mL methanol was added in two portions 0.22 g potassium borohydride (4.1 mmol, 2.05 Eq.) (contained in a small vial) and the solution began to bubble slightly. The reaction was stirred for 12 h. at 19°C, whereby TLC indicated the formation of a much more polar product. The reaction was cooled to 0°C and 15 mL 2N HCl was added. The reaction was permitted to stir for an additional hr at 19°C, stir bar removed (rinsed with MeOH (2 mL) and mixture allowed to stand in the refrigerator for 4 h. Yellow hair-like fibers deposited throughout the flask and were immediately filtered off and washed 3 X (5mL 2N HCl) in a sintered glass funnel, followed by 3 X (5mL diH2O) to give 0.66 g of the diol in **88%** crystallized yield.

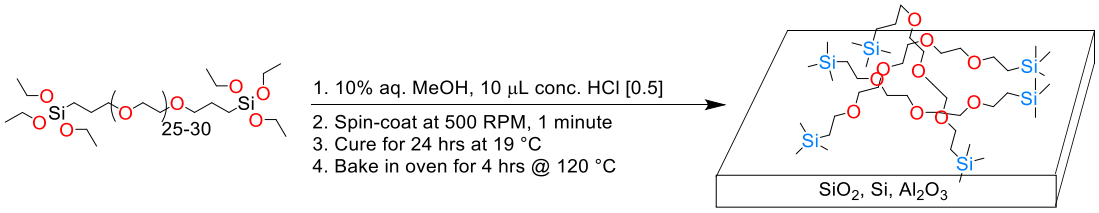

In a 5-mL vial with teflon screw cap is added 100 mg solid 1,2-bis(triethoxysilyl)polyethyleneglycol (25-30 EO units per strand) followed by 2 mL of a 10 % aqueous solution of methanol. 10 mL concentrated HCl (aq.) is added and the mixture vortexed on a mini-vortexer for 1 minutes until the solution became clear. 200 mL of the prepared solution is deposited @ 500 RPM for 1 m on a cleaned, moistened substrate with contact angle <15° from the plane. The films are air dried at 19 °C for 24 hours and finally baked at 120°C for a duration of 4 h. A clear, semi-flexible layer was formed after the final cure.

Microfabrication

Anodization of Aluminum (s) to form Alumina (Al_2O_3)

The process of Alumina anodization begins with the addition of dielectric layers to prevent current path before etching to the silicon. The silicon substrates used were approximately 300 microns in thickness and the dielectric used was SiO_2 (deposited from TEOS) with a nominal thickness of 10-20 nm of SiO2 grown in 1 hr. E-beam deposition of metallic aluminum produced a layer of aluminum that was approximately 1.52 microns in thickness. The edge boundaries were masked off so as not to anodize the sides or back edge of the wafer. Copper tape was connected to the aluminum layer on the topside of the wafer to form the anode(positive electrode) and a glassy carbon electrode served as the source electrode, both suspended in a 1 L beaker containing 6% H_2SO_4 at the same level so the electrodes were aligned parallel to one another. The solution is allowed to cool to 1°C for 10 minutes with light stirring of a stir bar. The anodization begins rapidly once the initial DC current and voltage are switched on at 100 mA, 10 V, for 1.5 h which produced the smallest pores of any method being 8-15 nm average diameter. The ordering of the pores was regular under these controlled conditions.

Electrochemistry

The CV spectra of the crown Anthraquinone AQ-18-C-6 was taken in acetonitrile using tetrabutyl ammoniumhexafluorophosphate [0.1] with a Pt-working disk electrode, Ag reference electrode and Pt counter-electrode. The resulting onsets of reduction were at -0.54 EV, 1.21 EV and -1.39 EV, respectively. Ferrocene was used as the internal standard giving

a standard reduction potential for the first wave as 1.3 EV. The procedure was repeated 3 times with differing scan rates of 60, 100 and 200 scans/min and no differences were seen in the CV spectra with reference to onset of reduction or oxidation.

Membrane Studies –

Figure S? – ABA triblock copolymer films were the least robust, giving a new trace corresponding to decreased resistance for each scan represented in the diagram. After 5 minutes of cycling through this equilibrium process, the copolymer became stable and current fixed.

END SYNTHESIS

^{1}H NMR Spectra

Figure S1 - **^{1}H NMR spectra of all (*E*)-retinol in $CDCl_3$ at 298 K**

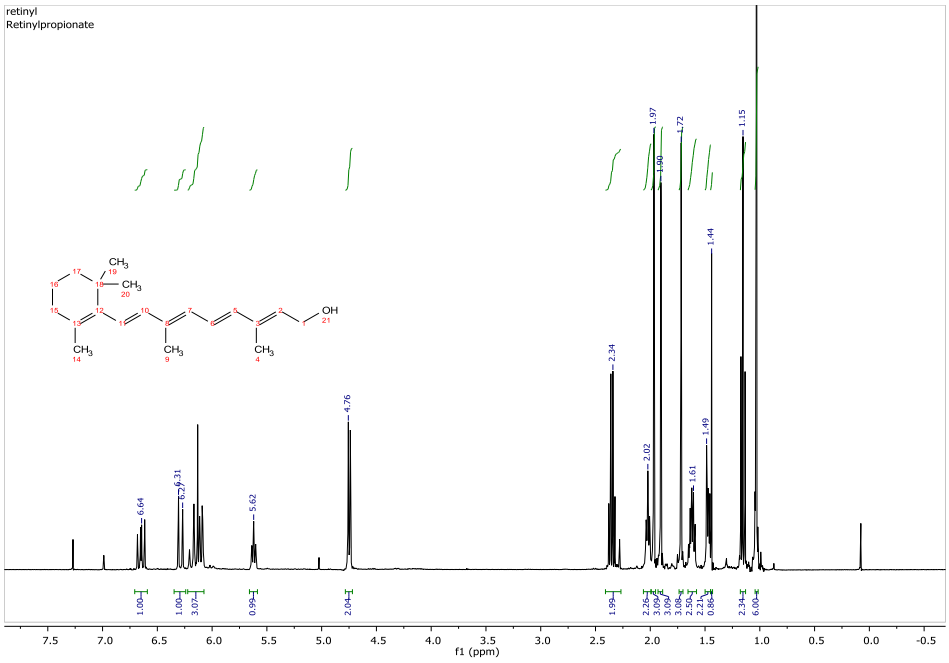

Figure S2 – ^{1}H NMR spectra BQ-18-C-6 in $CDCl_3$ at 298 K.

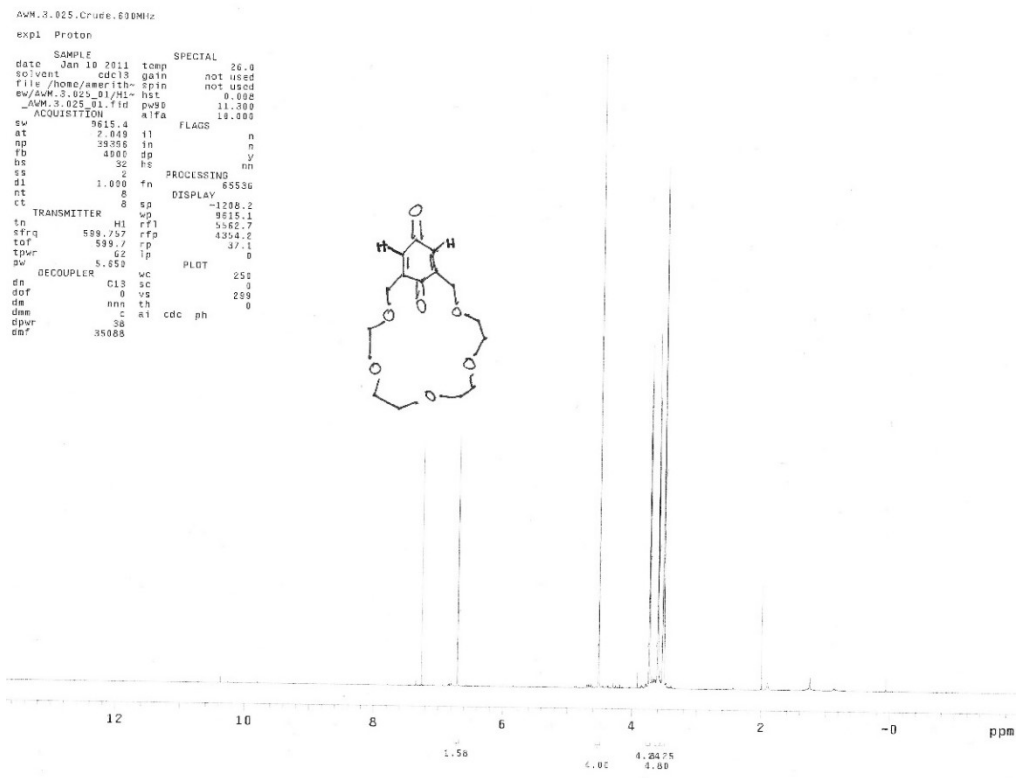

Figure S3 – ^{1}H NMR spectra of 2-allyl-3,5-dimethylbenzene-1,4-diol

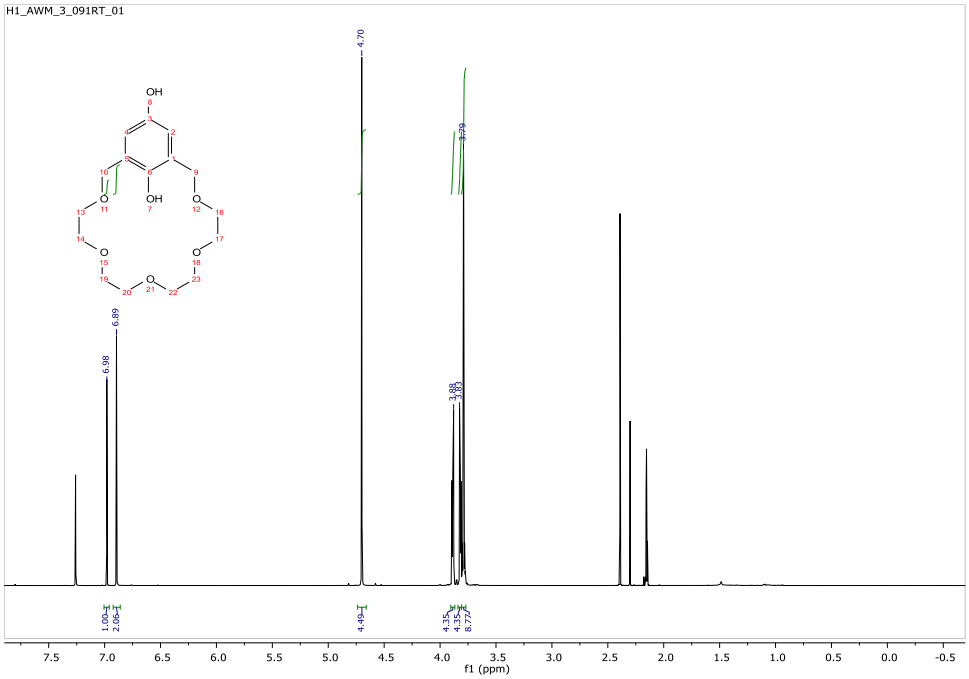

Figure S4 – ^{1}H NMR spectra of 2-allyl-3,5-dimethylbenzene-1,4-diol

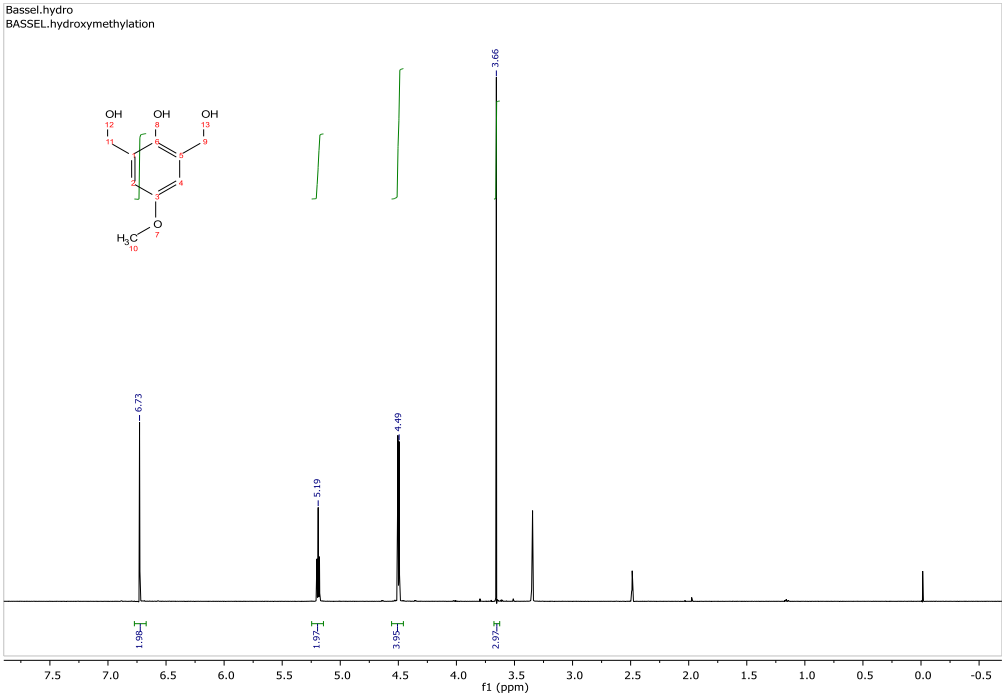

Figure S5 – ^{1}H NMR spectra of 2-allyl-3,5-dimethylbenzene-1,4-diol

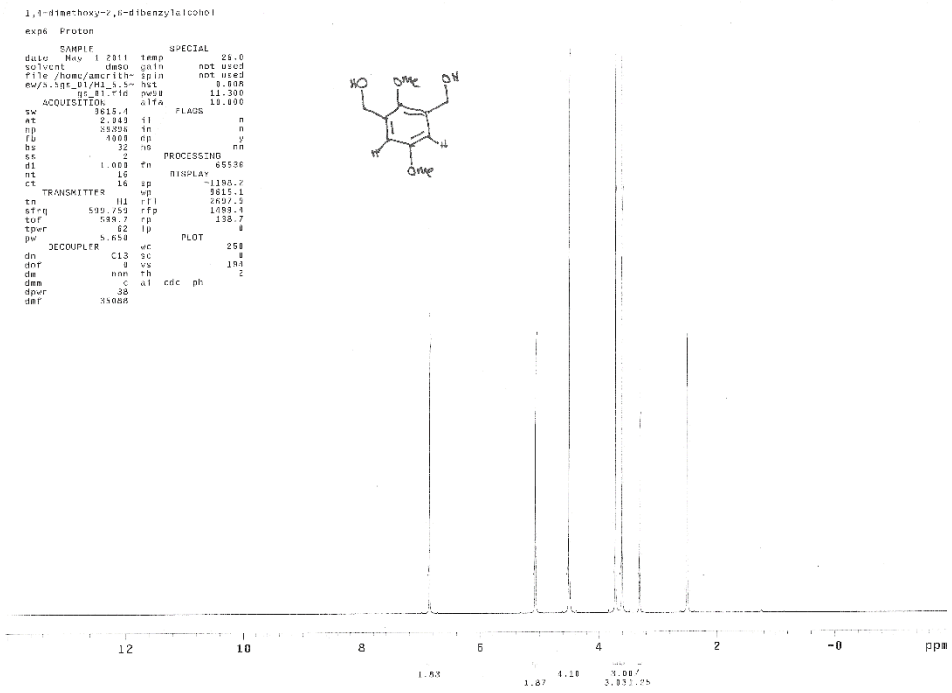

Figure S7 – ^{1}H NMR bis-2,5-dibromomethyl-1,4-dimethoxyanisole at 298 K

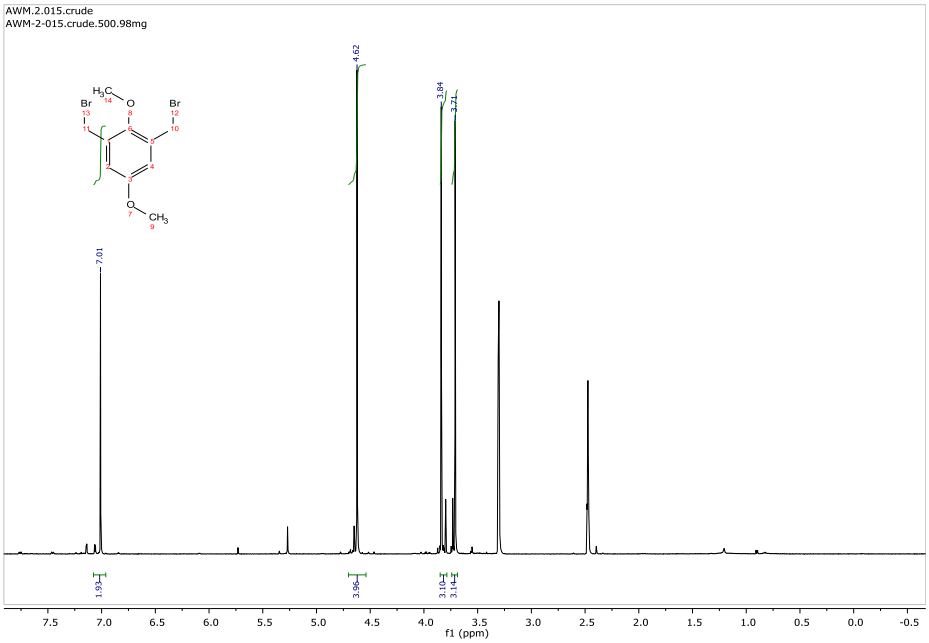

Figure S9 – TBS protected 2,5-dimethyl-1,4bis-tert-butoxydimethylsilane

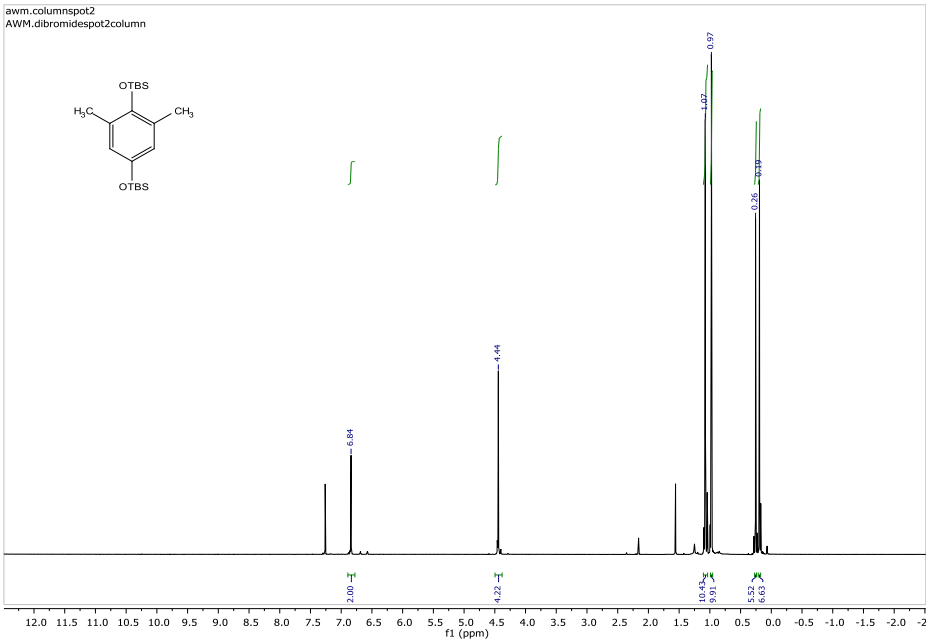

Figure S10 – 1,4-trimethoxysilyl-2,5-dimethyldehydroquinone

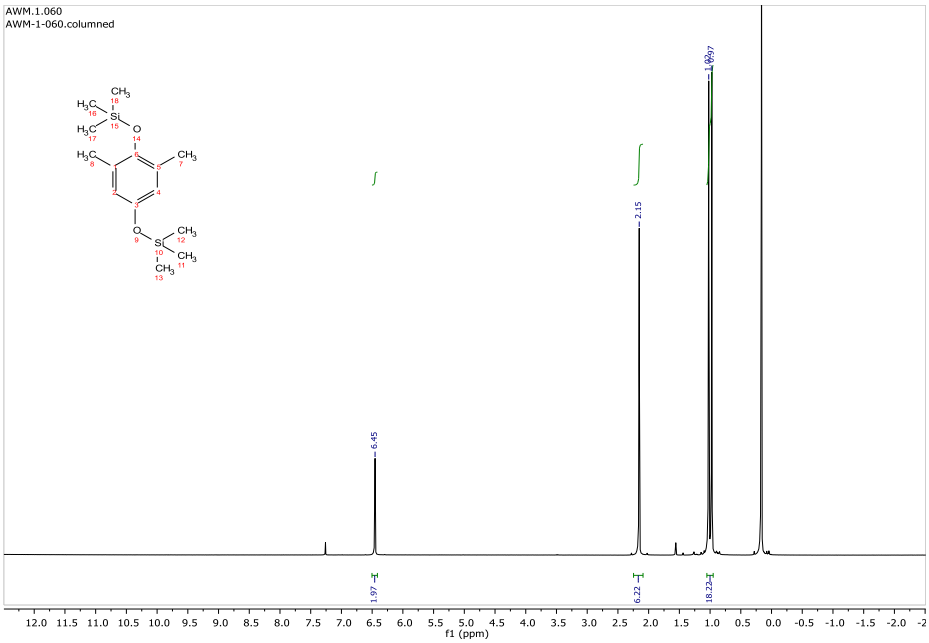

Figure S11 – ^{1}H NMR bis-2,5-dibromomethyl-1,4-dimethoxyanisole at 298 K

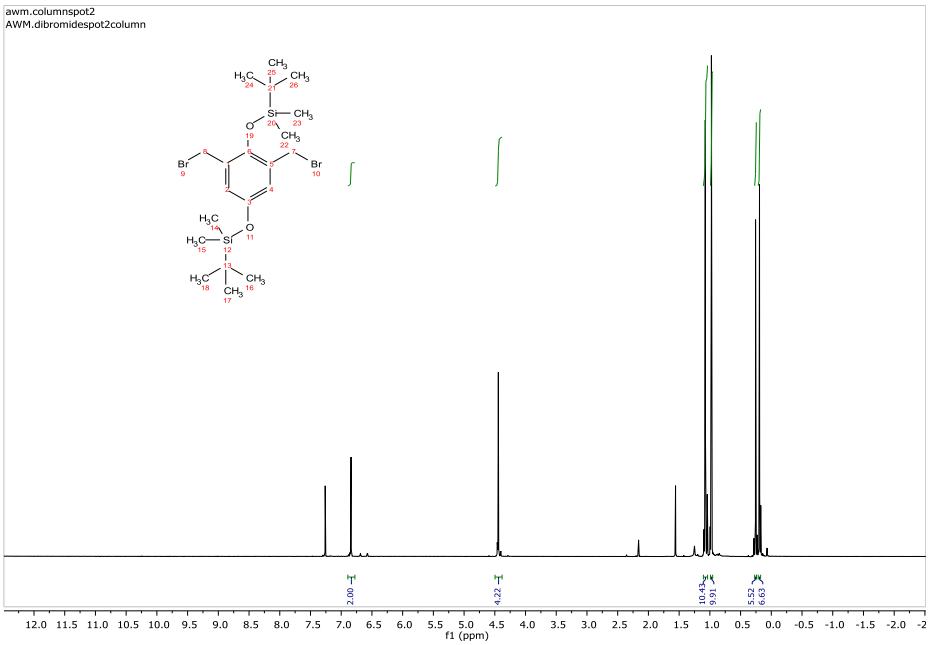

Figure S12 – ^{1}H NMR spectra of tetraethyleneglycolditosylate in $CDCl_3$ at 298 K

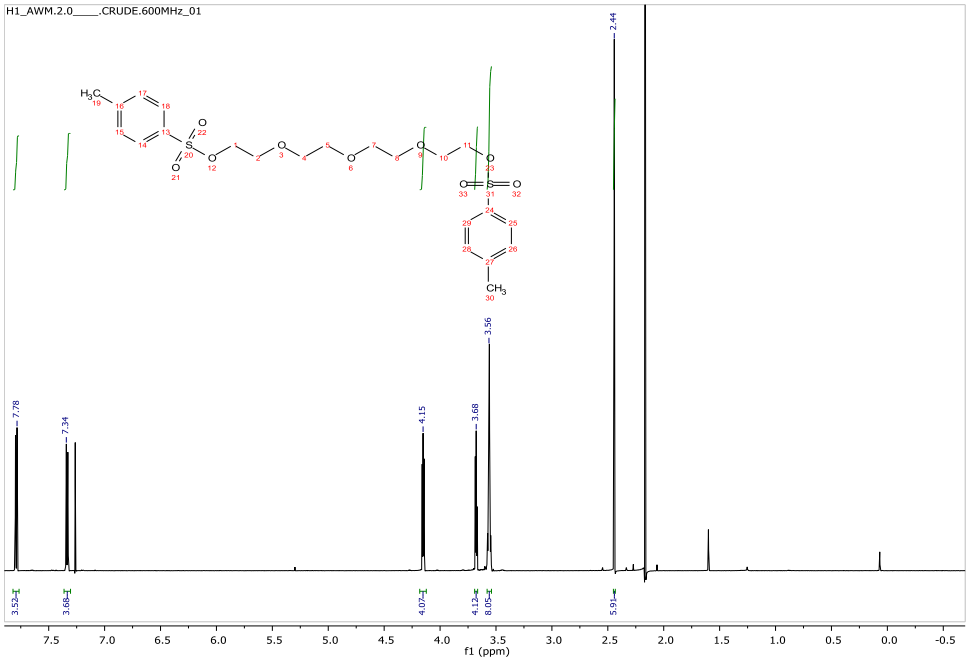

Figure S13 – ^{1}H NMR spectra of 1,4-dimethoxy-18-crown-5 in $CDCl_3$

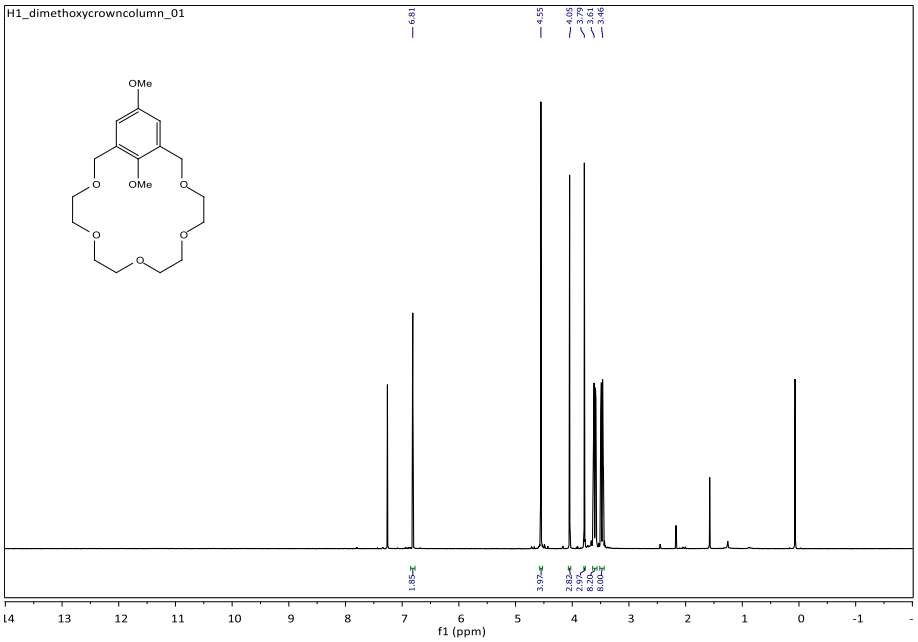

Figure S14 - ^{1}H NMR spectra of 2,5-dimethylbenzoquinone in CDCl3 at 298 K

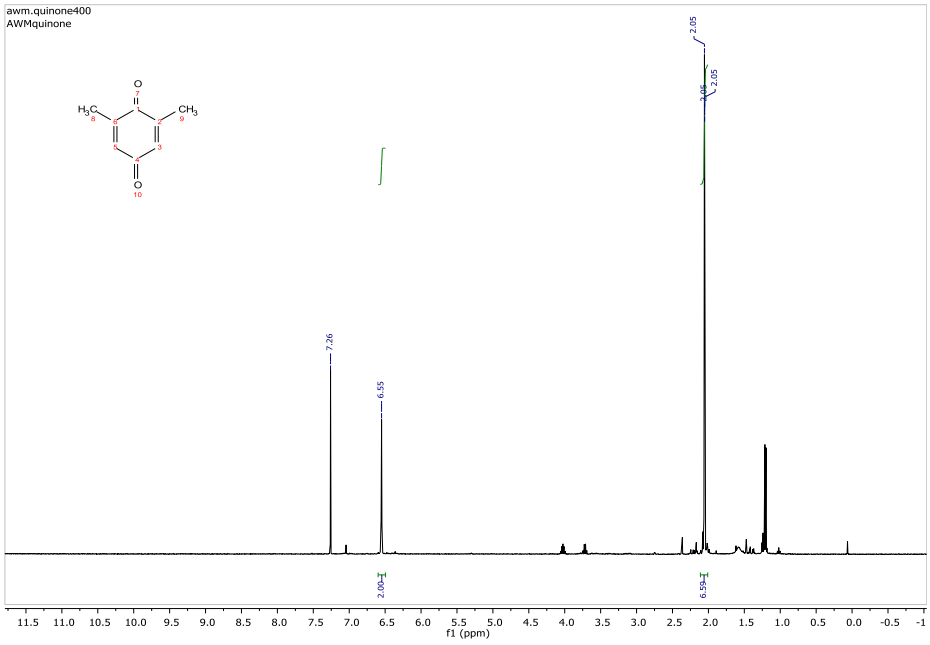

Figure S15 – ^{1}H NMR spectra of 2-allyl-3,5-dimethylbenzene-1,4-diol in CDCl3 at 298 K

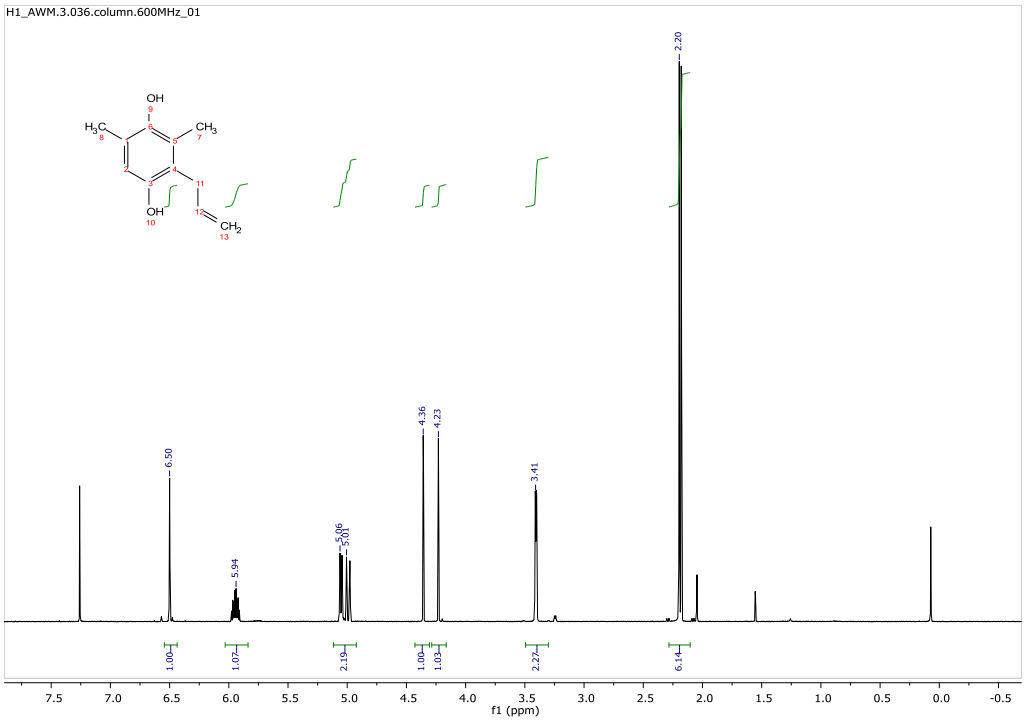

Figure S16A – 1,4 – dialllyl-2-5-demthyphenylene-18-C-5 in CDCl3 at 298 K

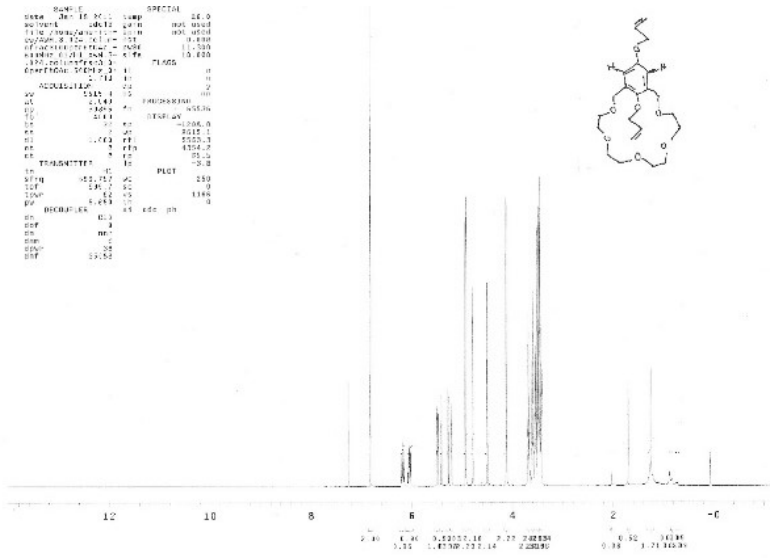

Figure S16B – Mixture of regioisomers 1.5:0 intraannular:peripheral in $CDCl_3$ at 298 K

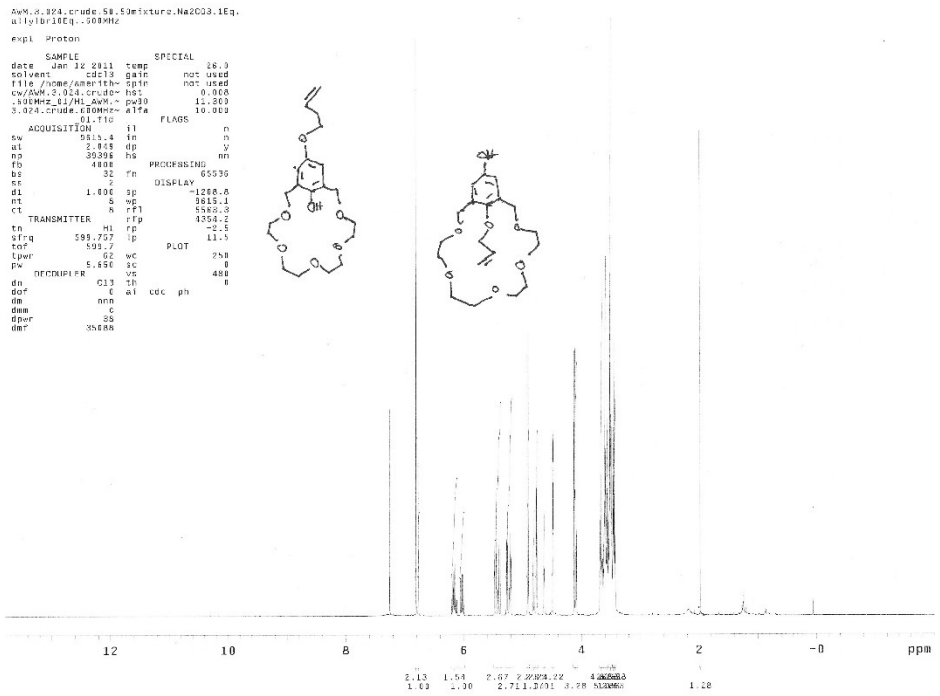

Figure S17 – ^{1}H NMR spectra of 2-pentenyl-2methoxy-15-C-5 in CDCl3 at 298K

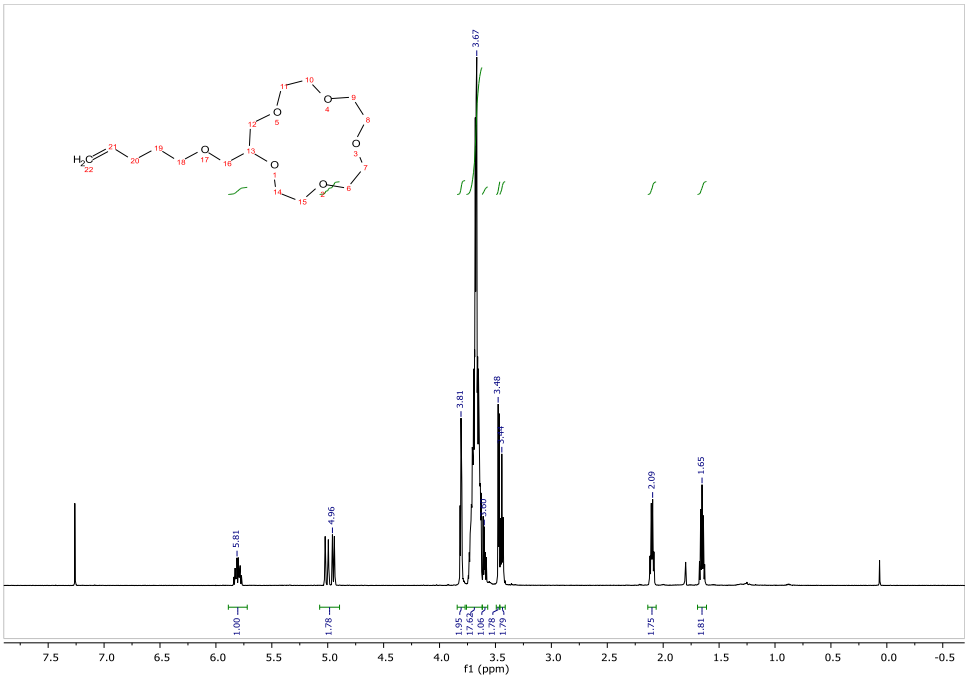

Figure S18– ^{1}H NMR spectra of pentenyl extended 2-hydroxymethyl 18-C-6

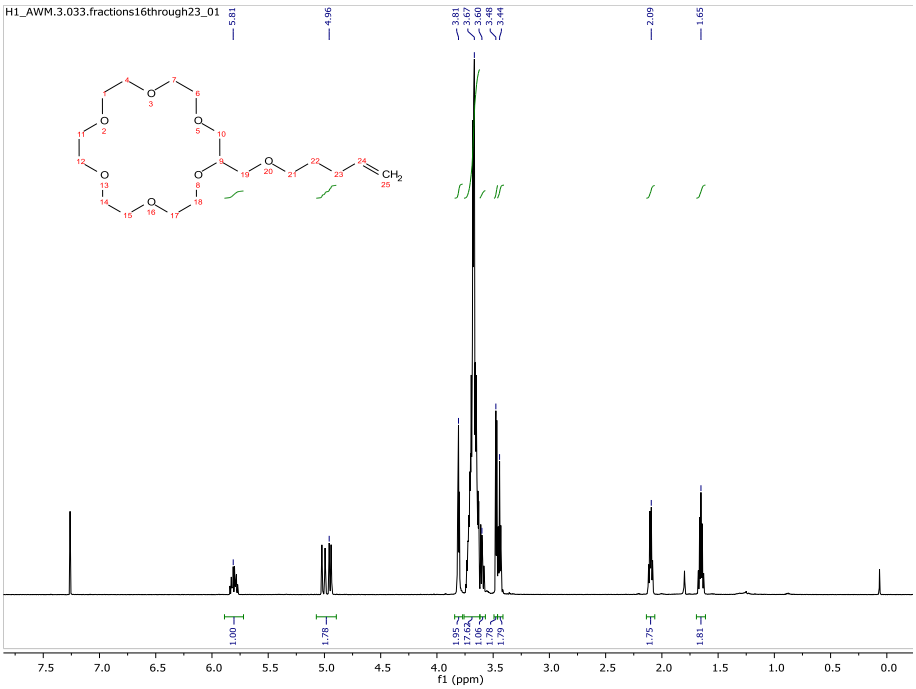

Figure S19 – ^{1}H NMR spectra of 2-allyl-3,5-dimethylbenzene-1,4-diol

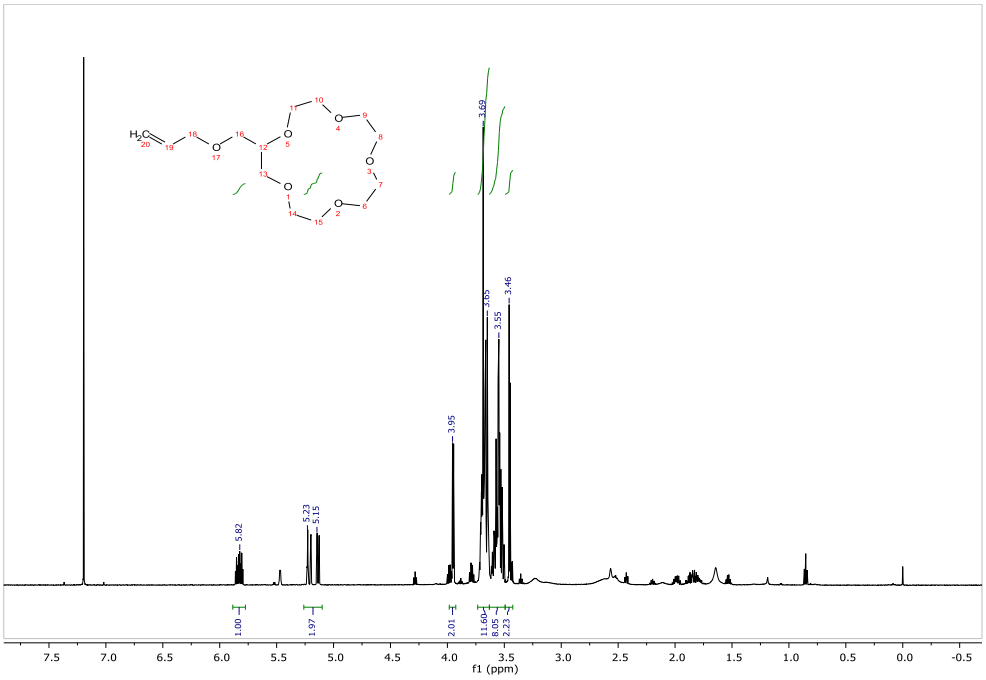

Figure S20 – ^{1}H NMR spectra of 2-allyl-ethoxymethyl-18-C-6 in CDCl3 at 298K

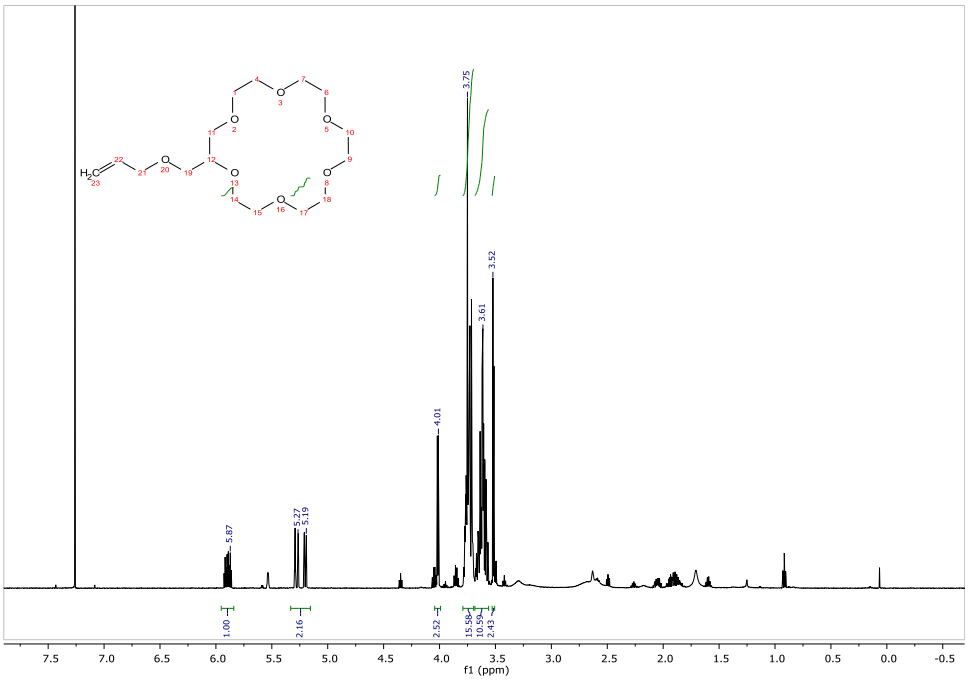

S22 – Tosylated 2-chloroethanol in CDCl3 at 298 K

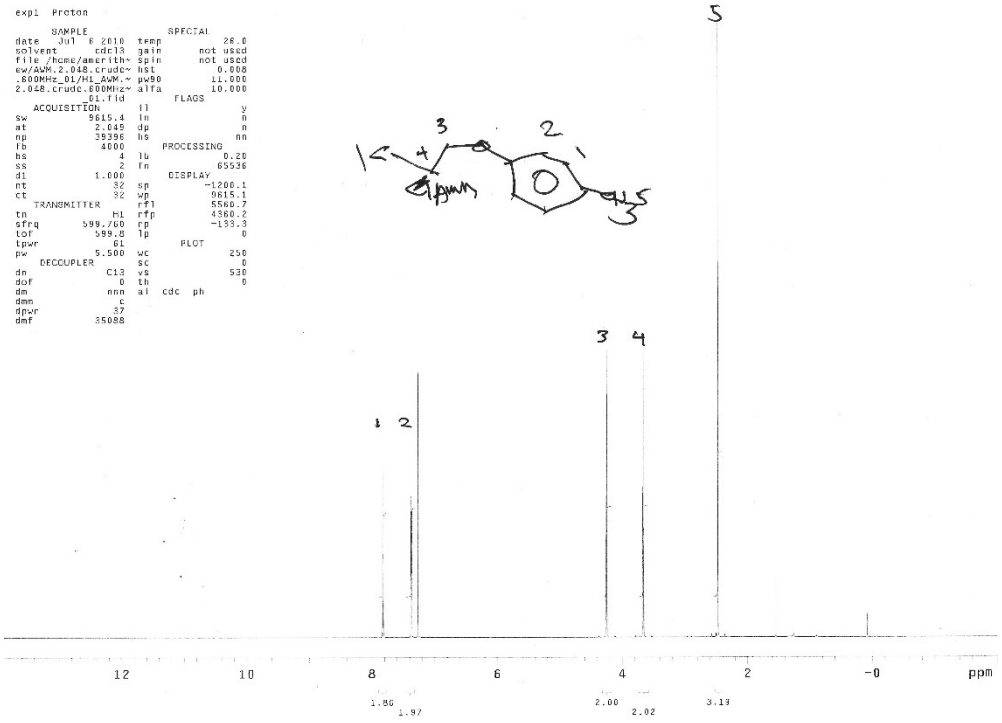

S23 – 2-iodoethanoltetrahydropyranal ether in CDCl3 at 298 K.

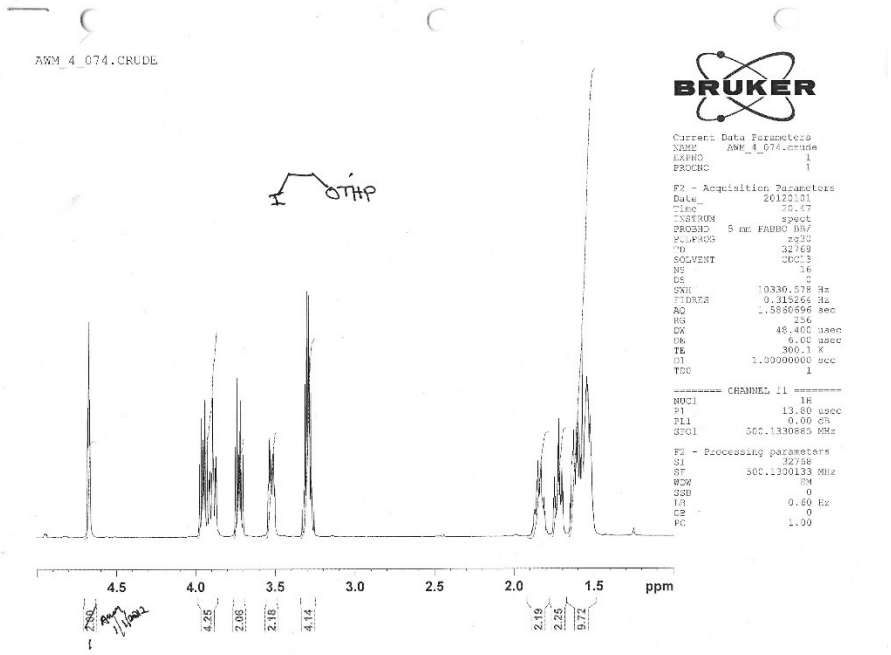

S25 – THP-protected 2-(chloroethoxy)ethanol

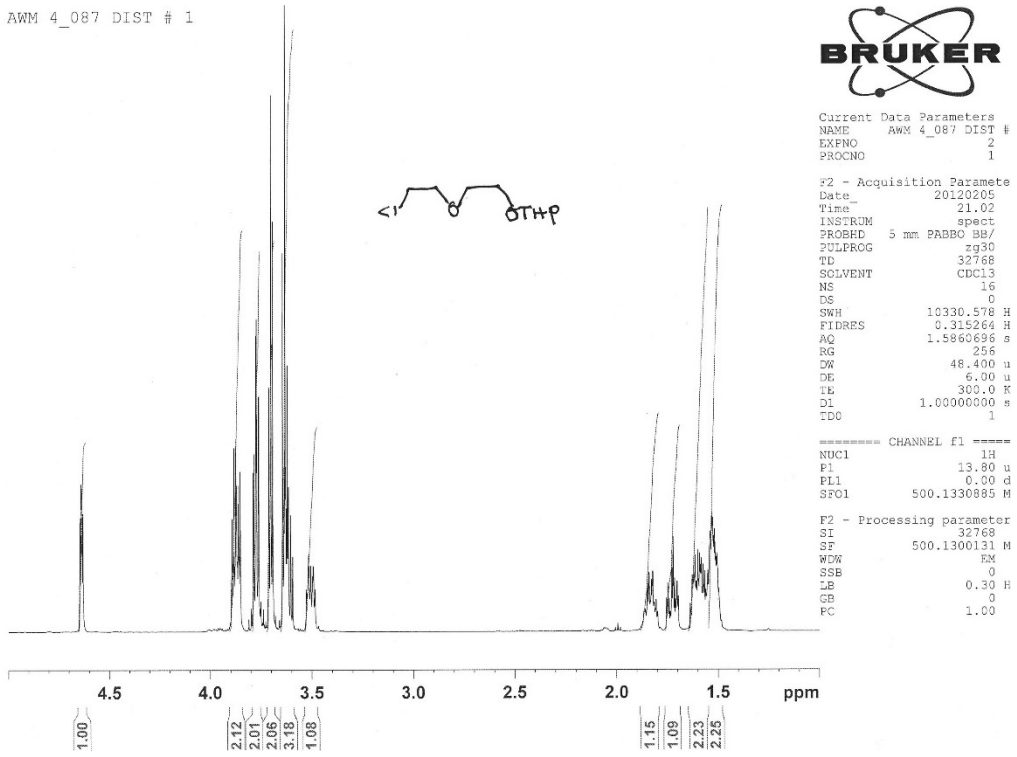

S26 – THP protected iodo(ethoxy)ethanol in $CDCl_3$ at 298 K

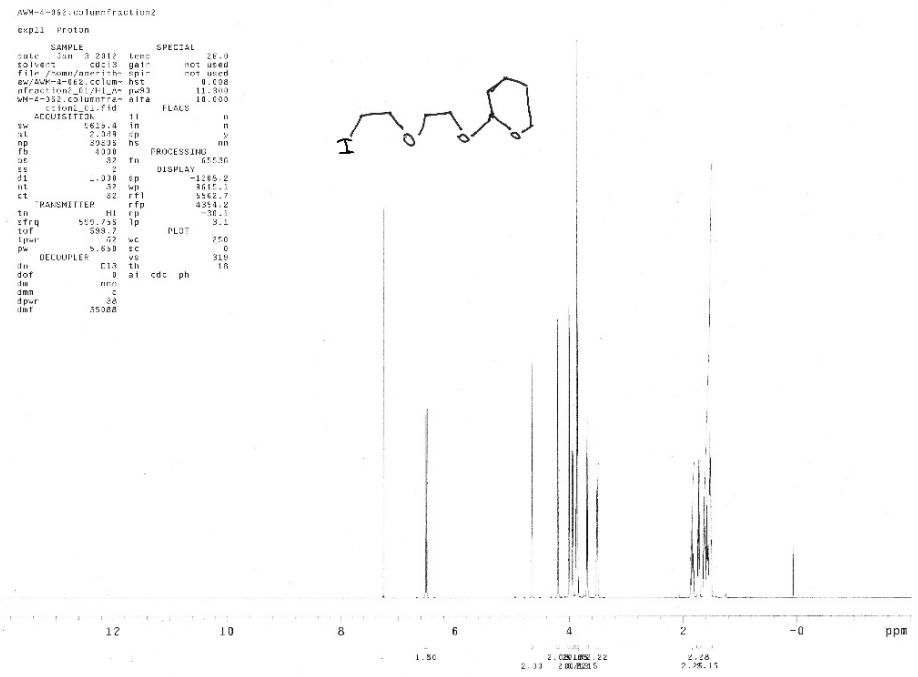

S27 – Bis-THP protected PEG extended benzyaldehyde in CDCl3 at 298 K

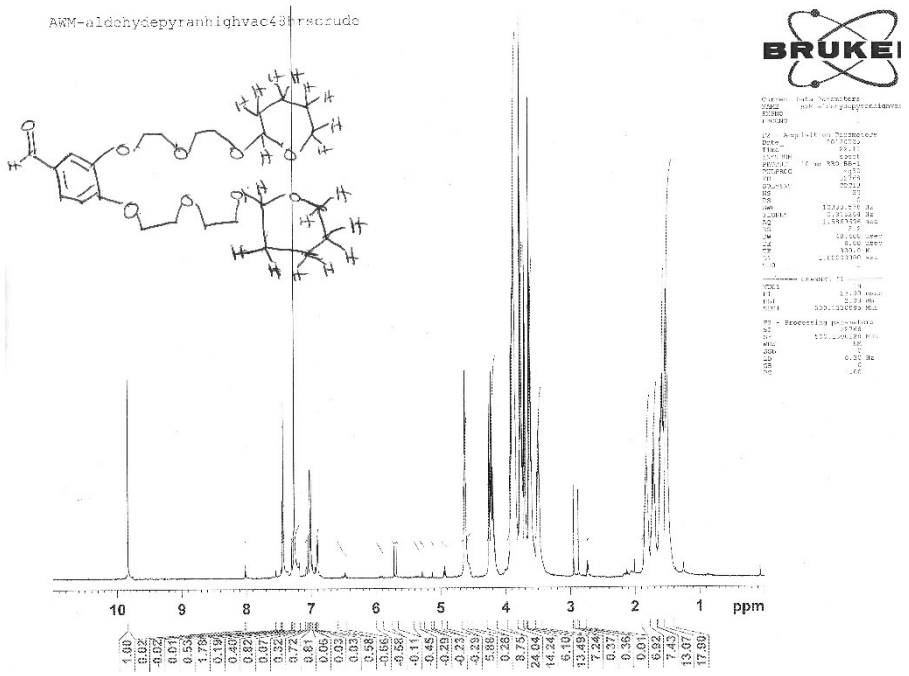

S28 – Bis-THP extended ethylene glycols of Alizarin in CDCl3 at 298 K

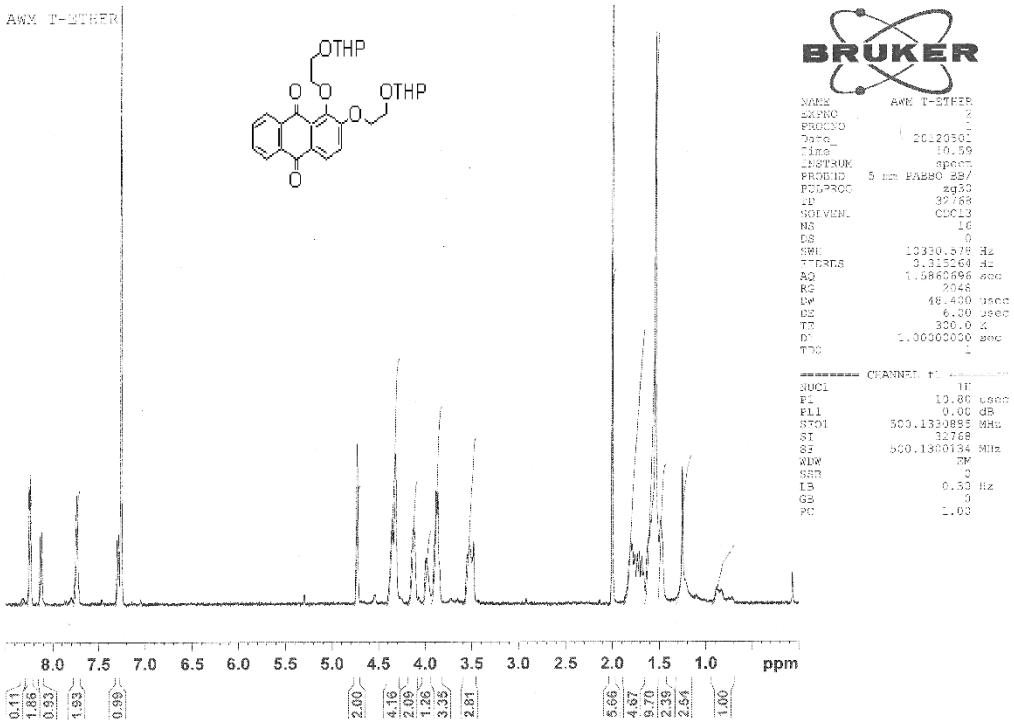

S29 – ^{1}H NMR (600 MHz, Chloroform-d) of 2,2'-(((1,2- phenylenebis(oxy)) bis(ethane-2,1-diyl))bis(oxy))diethanol in $CDCl_3$ at 298 K

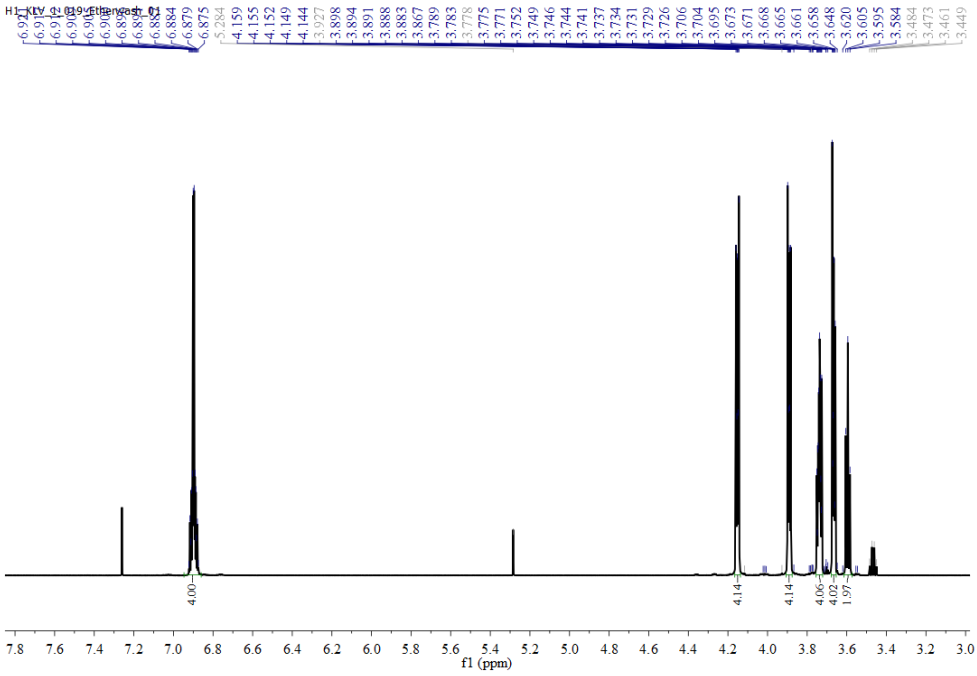

S30 – 1-hydroxy-2-ethoxyethyleneglycolanthraquinone in CDCl3 at 298 K

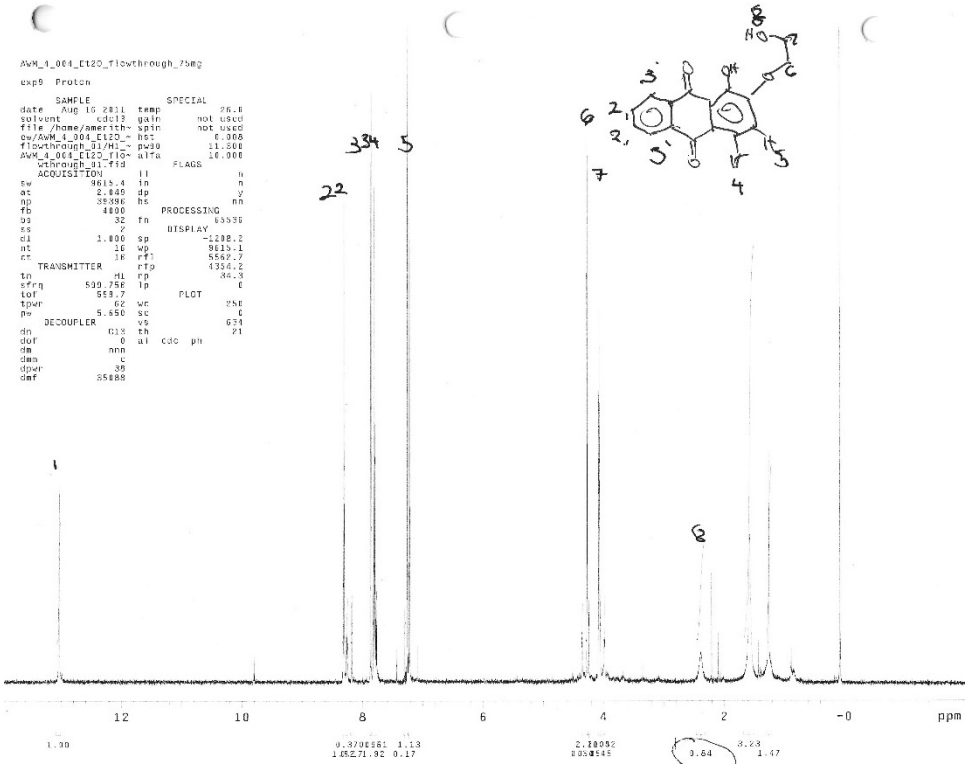

S31-bis-TMS protected 7-octene-bis-1,2-triethoxysilane in $CDCl_3$ at 298 K

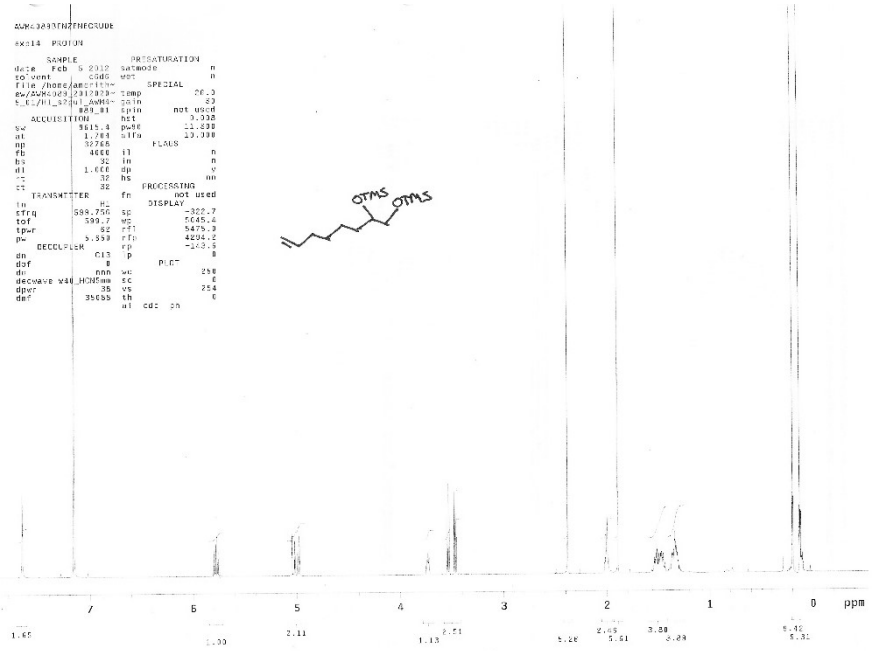

S33 – Extended benzyaldehyde ethoxyethanol extended bis-diol in $CDCl_3$ at 298 K

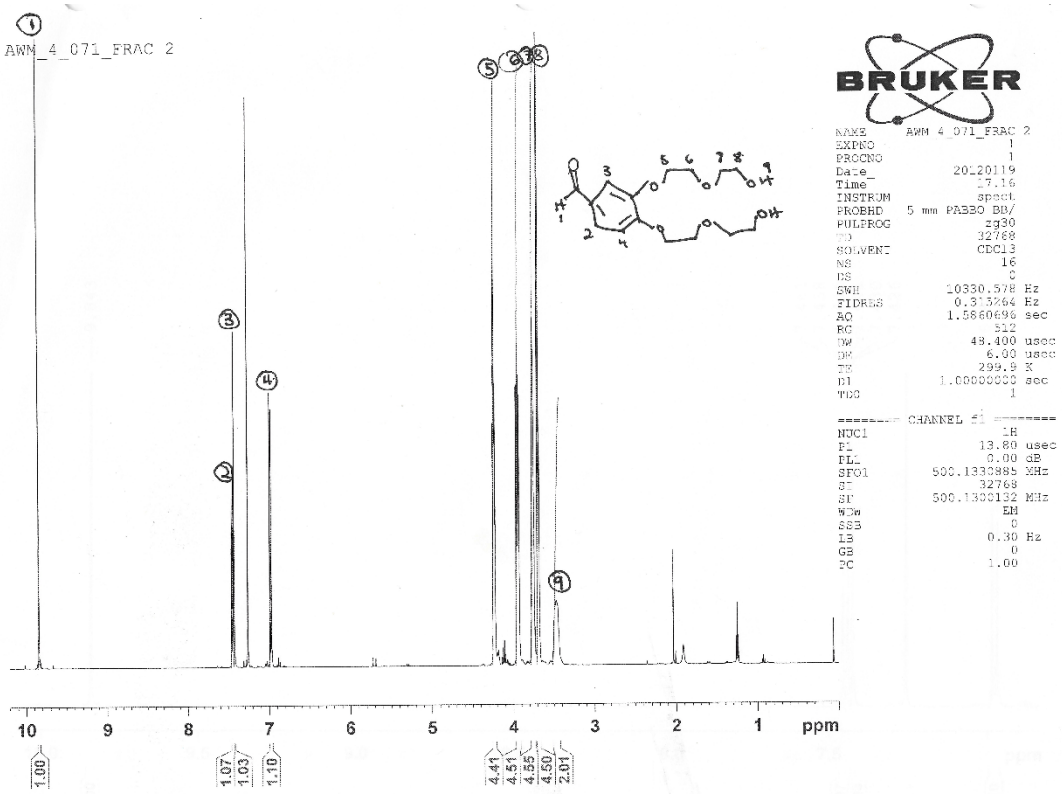

S34A – bis dimeyslate in $CDCl_3$ at 298 K

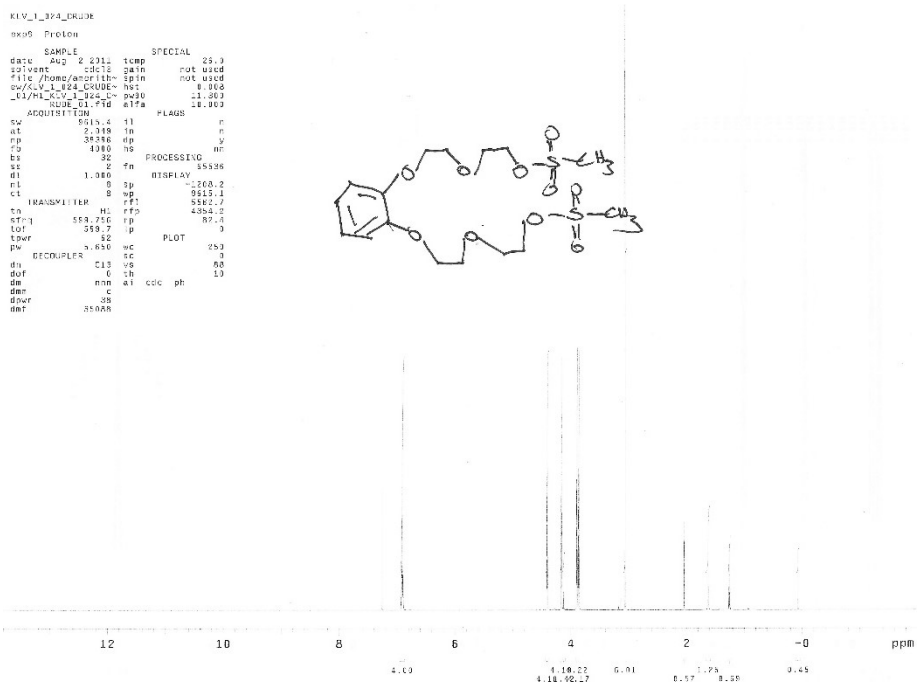

S34B - – ^{13}C NMR Spectra of dimesylate of extended catechol in $CDCl_3$ at 298 K

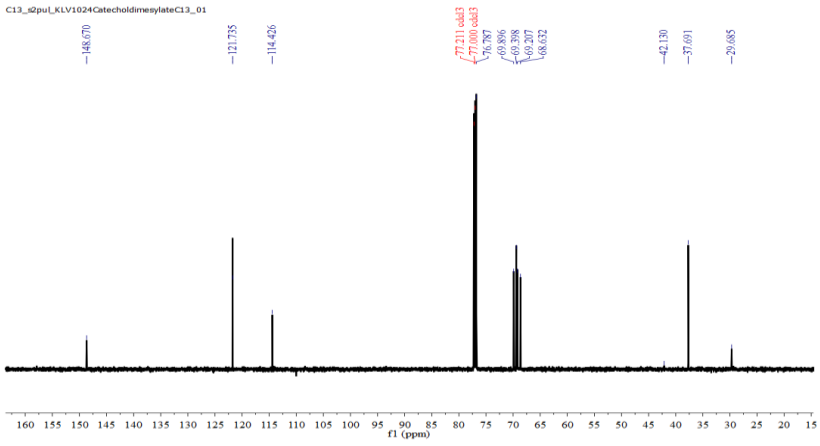

S35- Tosylated benzyaldehyde glycol in $CDCl_3$ at 298 K

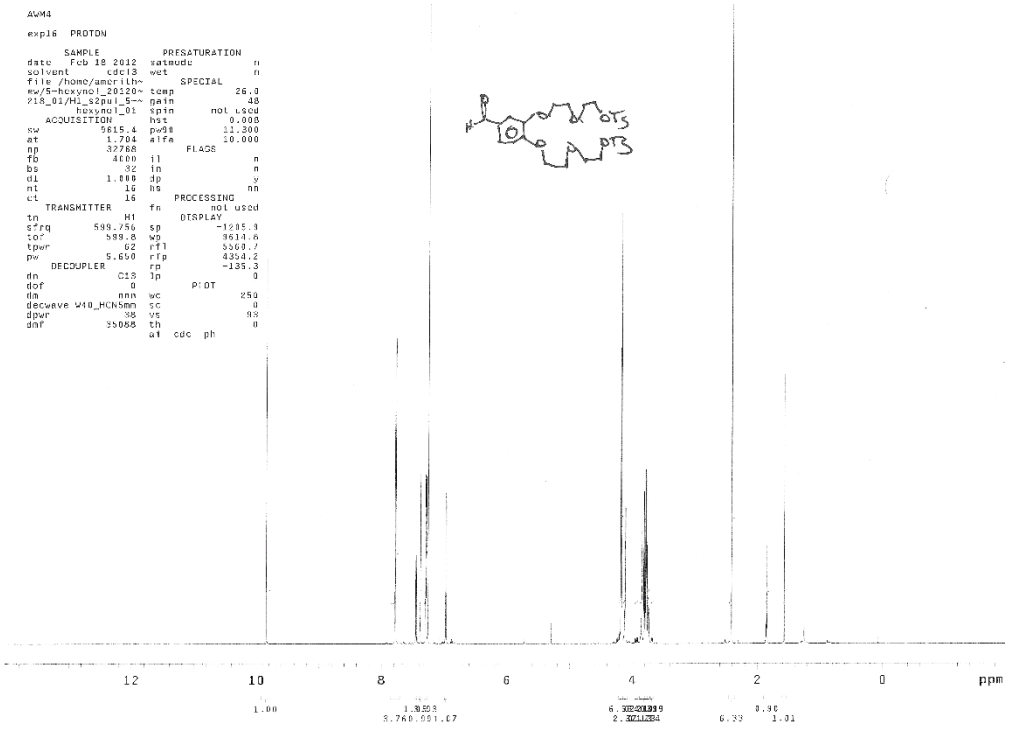

S37 – bisdiiodoethoxyethyleneglycol in $CDCl_3$ at 298 K

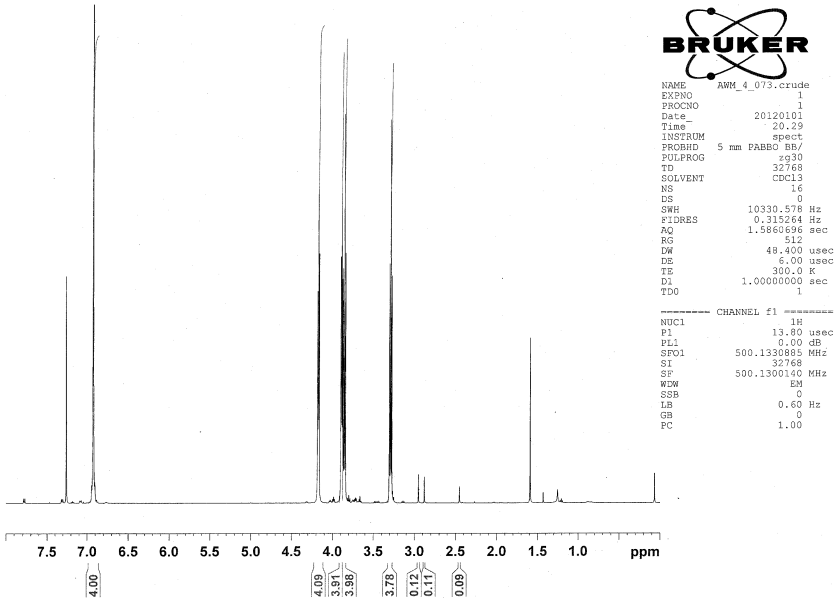

S39 - 3-allyl-1,2-dihydroxybenzene in $CDCl_3$ at 298 K

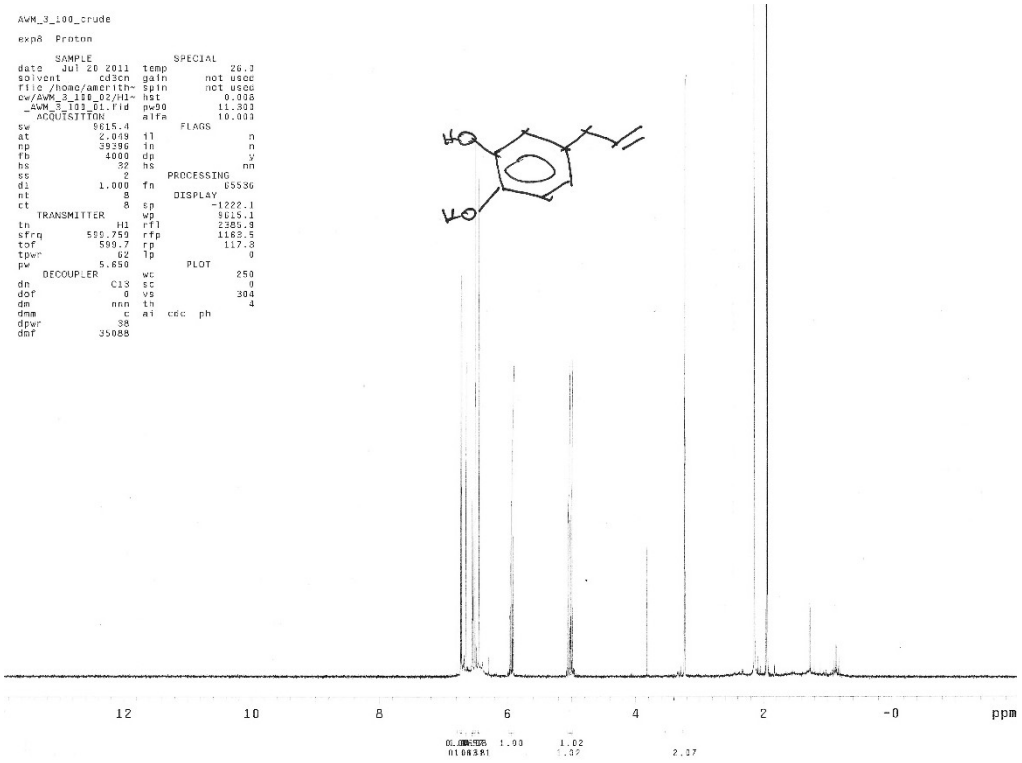

S40 – 1H NMR Spectra of 4-allyl-1,2-bis-triethoxysilylbenzene in CDCl3 at 298

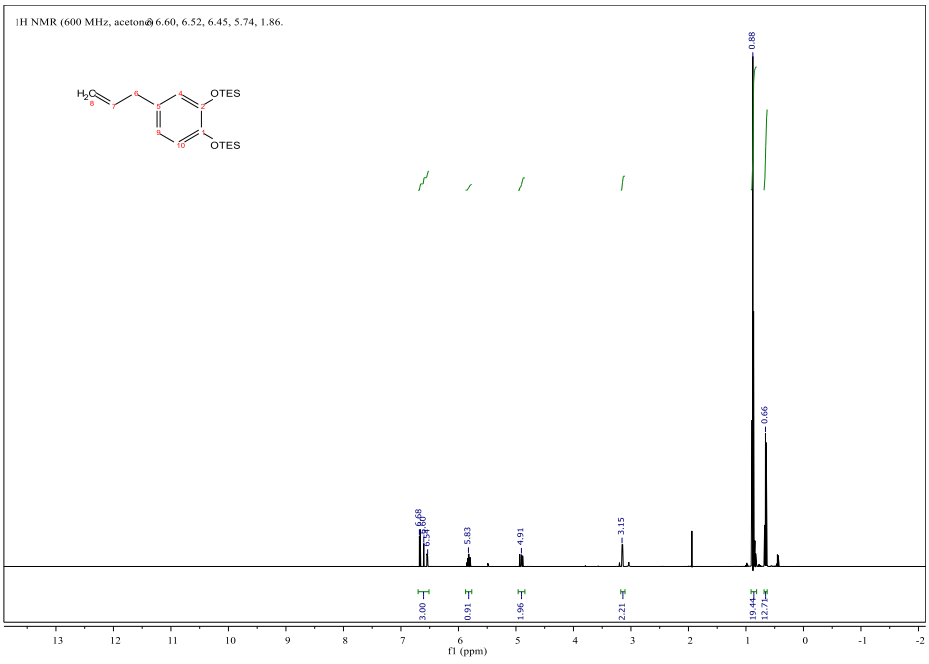

S41 – 1H NMR of Eugenol-derived ethoxyethanol extended aromatic glycol

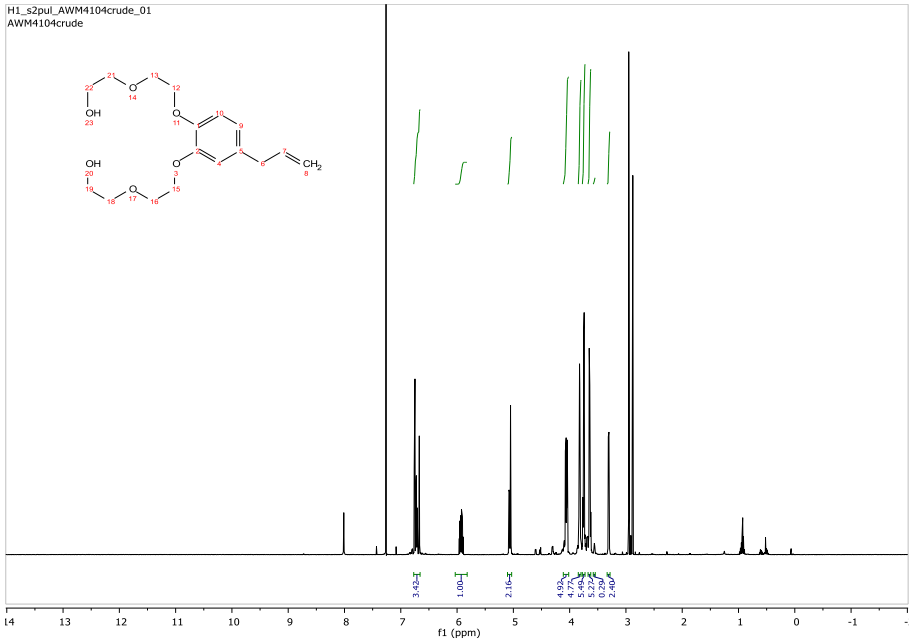

S44A –(800 MHz) ^{1}H NMR of AQ-18-C-6 in $CDCl_3$ at 298K

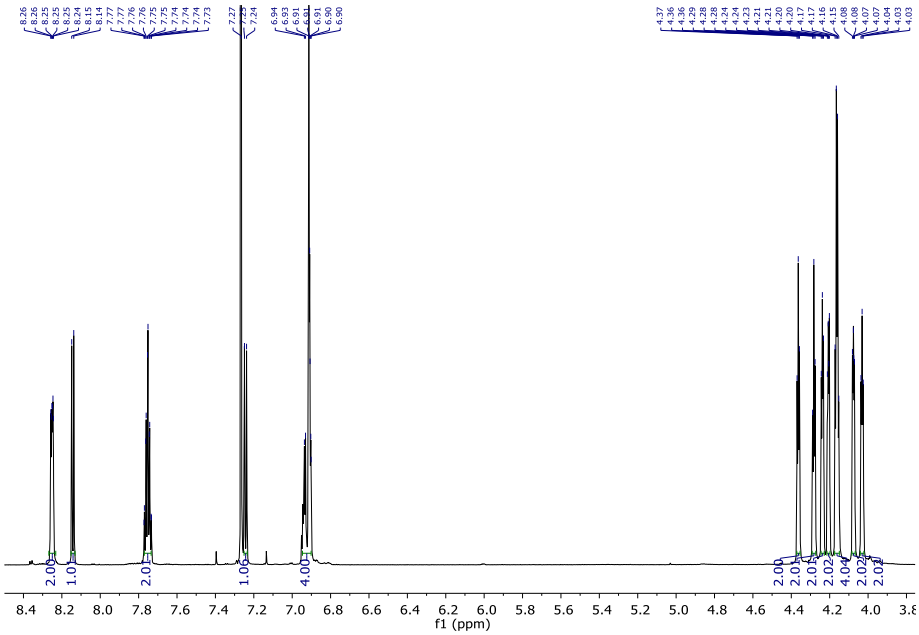

S44B - ^{13}C NMR (800 MHz) of uncomplexed AQ-18-C-6 crown ether in $CDCl_3$ at 298 K

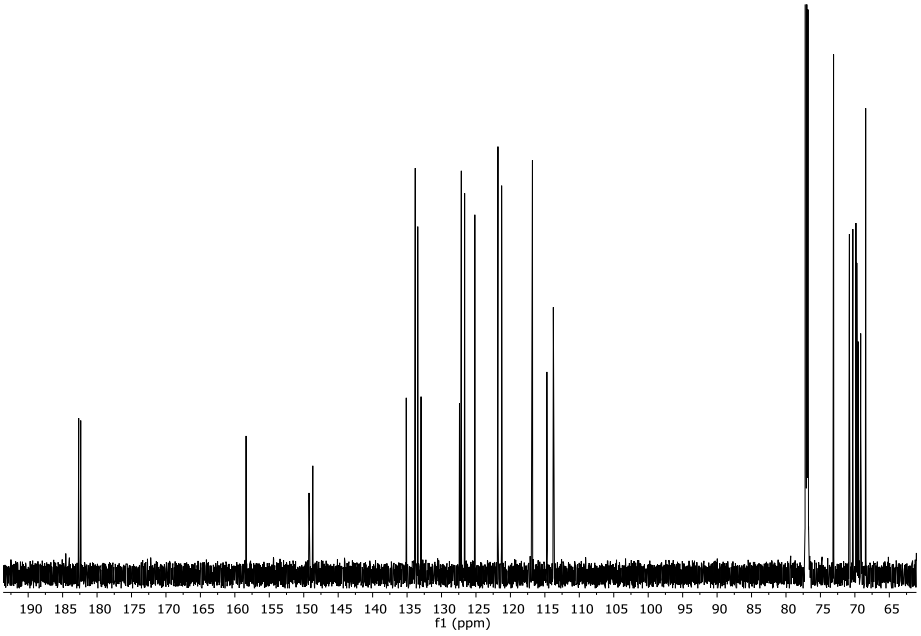

S42C - ^{13}C NMR (800 MHz) of AQ-18-C-6 • $K^+(^-OTf)$ complex (5mM) in $CDCl_3$ at 298 K

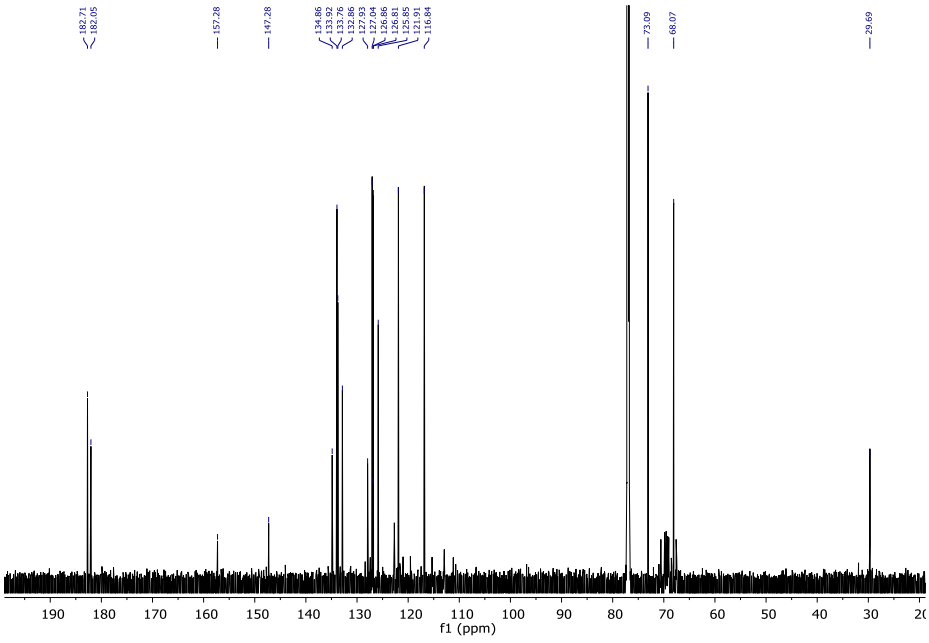

Figure S42D – (800 MHz) 2D HMBC spectrum of AQ-18-C-6 in $CDCl_3$ at 298.15K

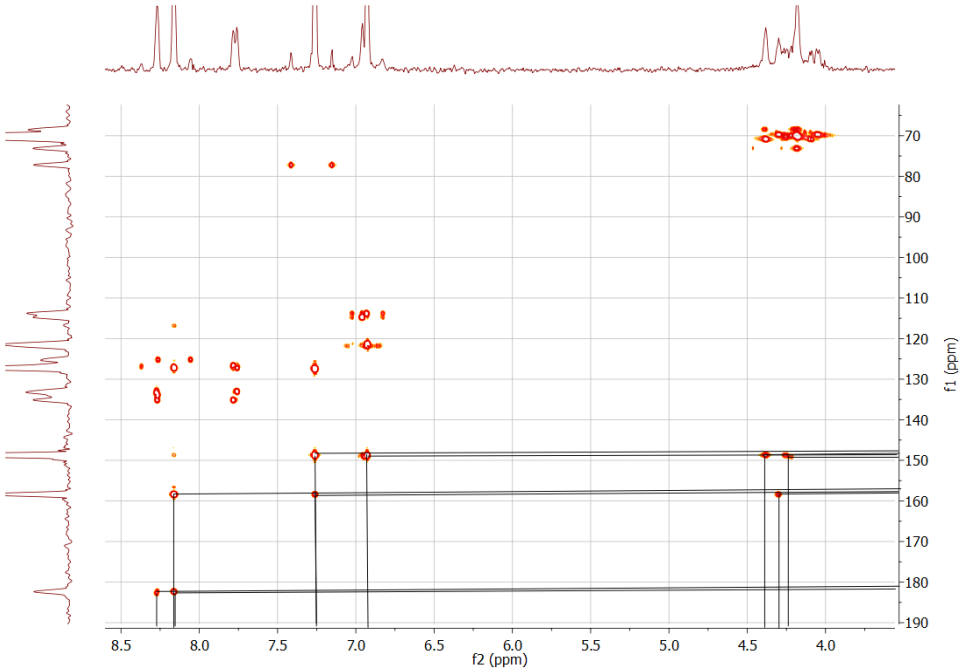

Spectra S42E - 2D HSQC Standard spectrum of AQ-18-C-6 in $CDCl_3$ at 298.15K (800 MHz)

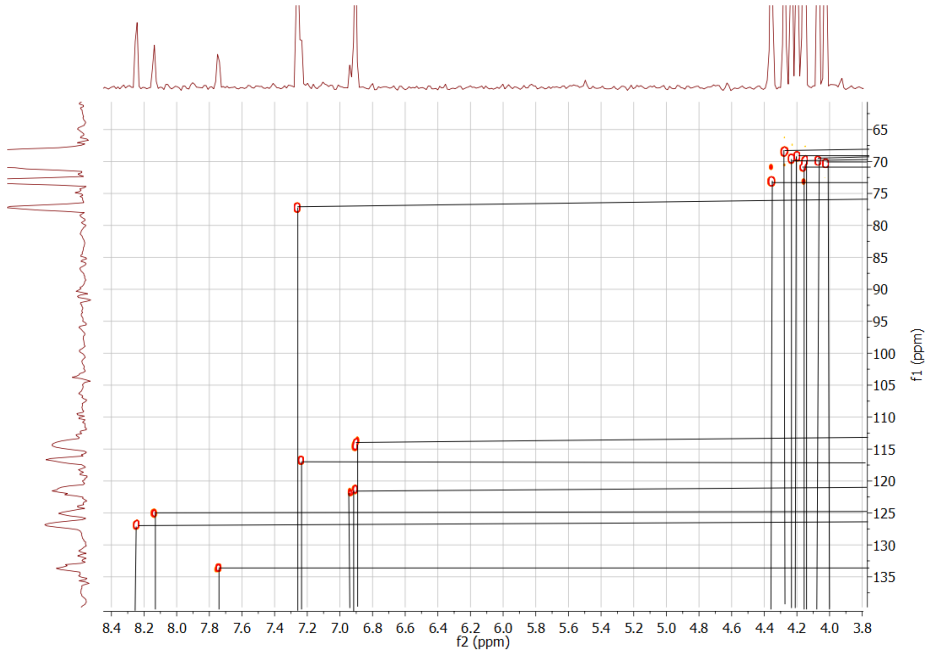

Spectra S42F - (800 MHz) 2D HMBC spectrum of AQ-18-C-6 • K(OTf) in $CDCl_3$ at 298.15K

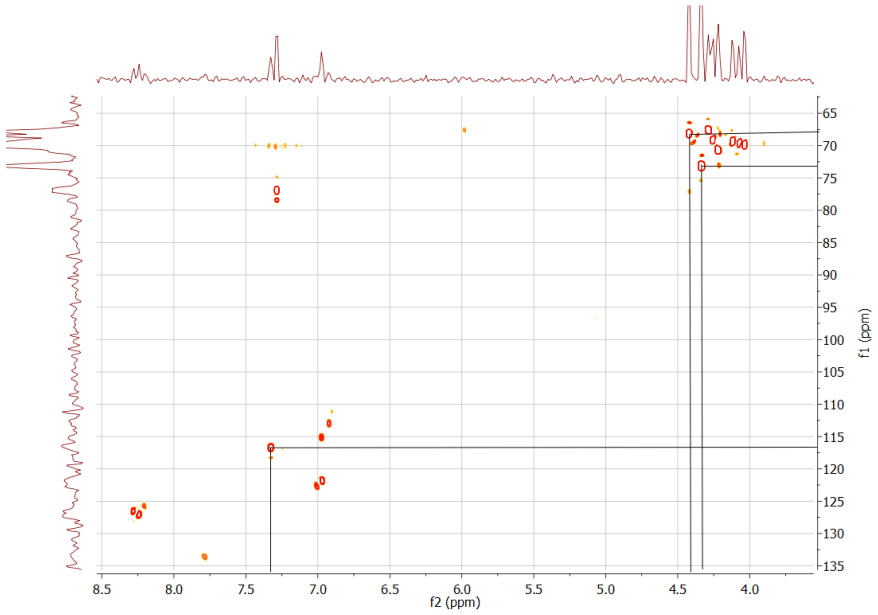

Figure S43 – 3-allylappended AQ-18-C-6 in CDCl3 at 298 K

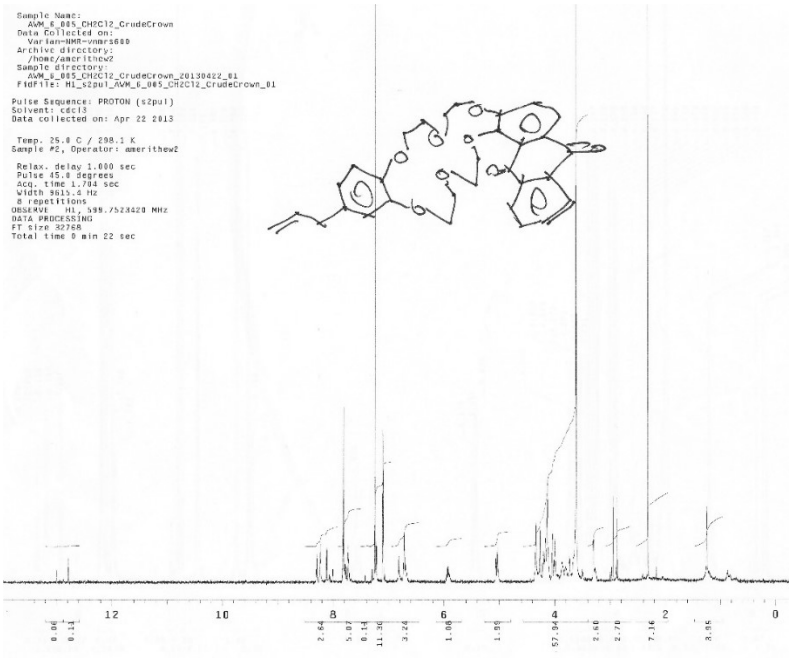

Figure S 44A – ^{1}H NMR of 9,10-dioxo-9,10-dihydroanthracene-2-carbonyl chloride in CDCl3 at 298 K

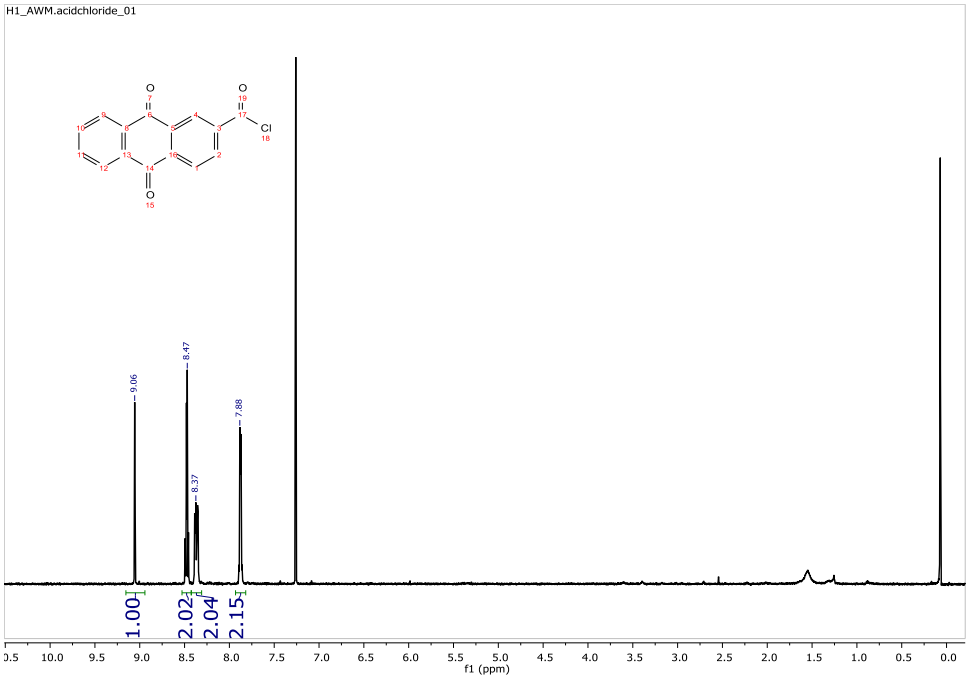

Figure S44B – ^{1}H NMR spectra of 4-hydroxy-2-propenylanisole i in $CDCl_3$ at 298 K

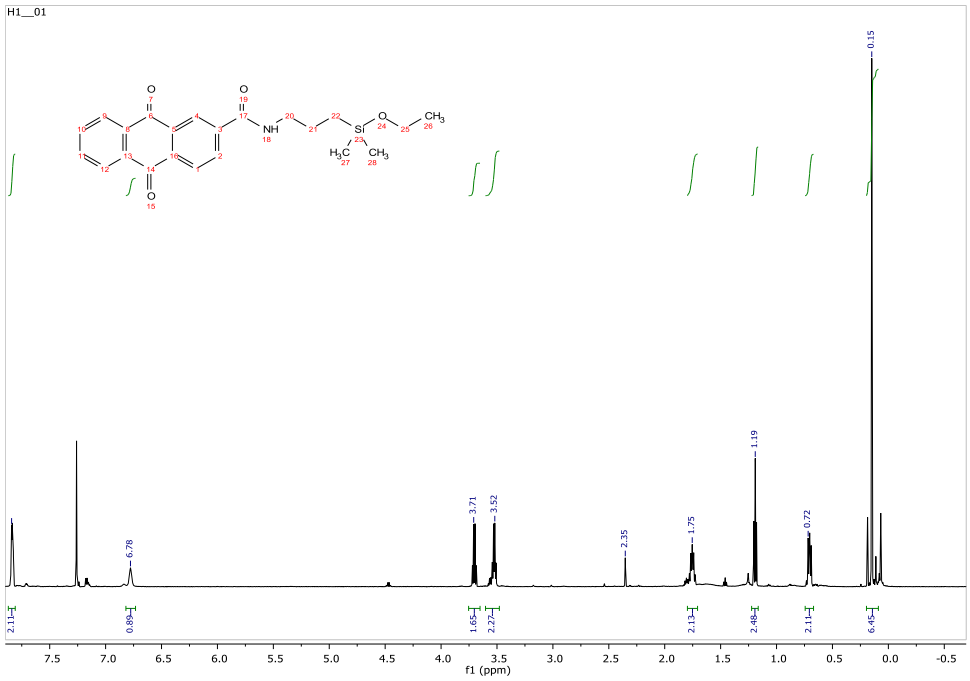

Figure S 45 – 1H NMR Spectra of 1-allyloxy-8-hydroxy-9,10-anthraquinone in CDCl3 at 298 K.

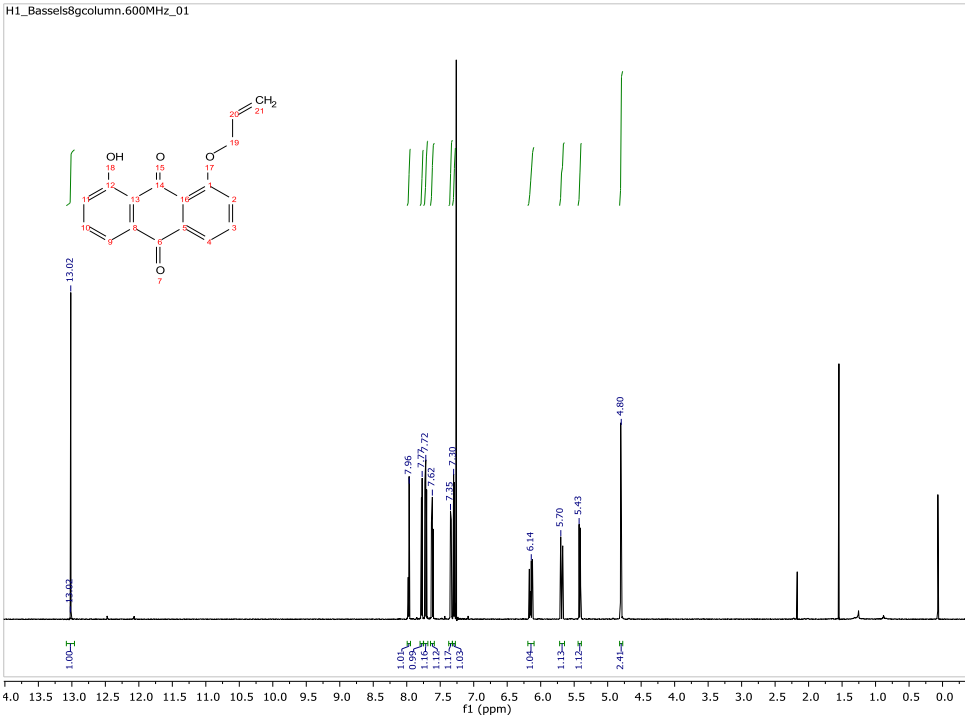

Figure S46 - ^{1}H NMR spectra of 2-allyl-3,5-dimethylbenzene-1,4-diol in $CDCl_3$ at 298 K

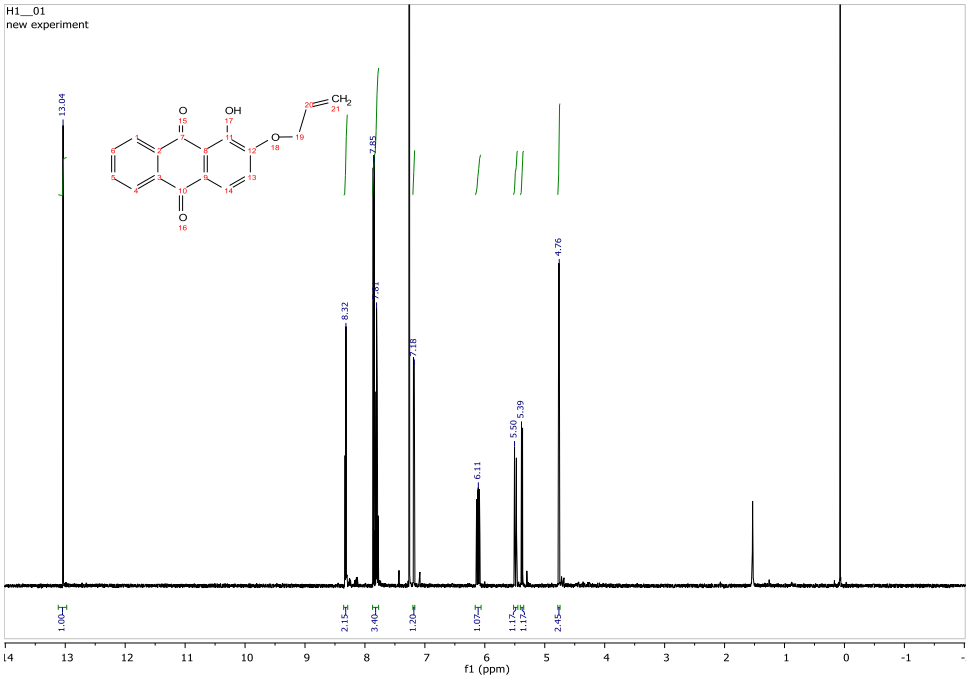

Figure S53 – ^{1}H NMR spectra of 4-hydroxy-2-propenylanisole in $CDCl_3$ at 298 K

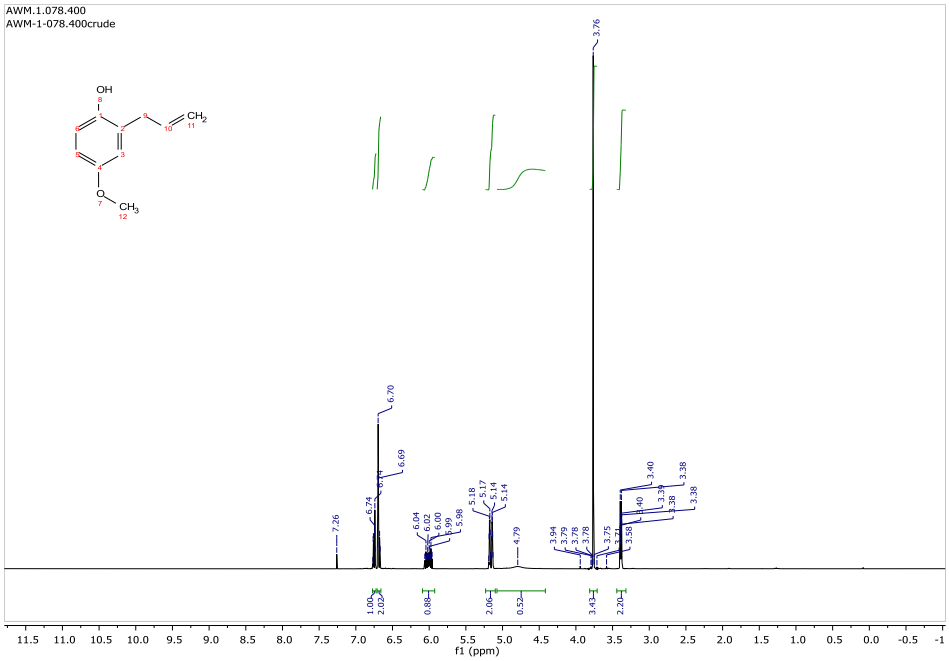

Figure S59 –Extended bis-acid chlorides in $CDCl_3$ at 298 K

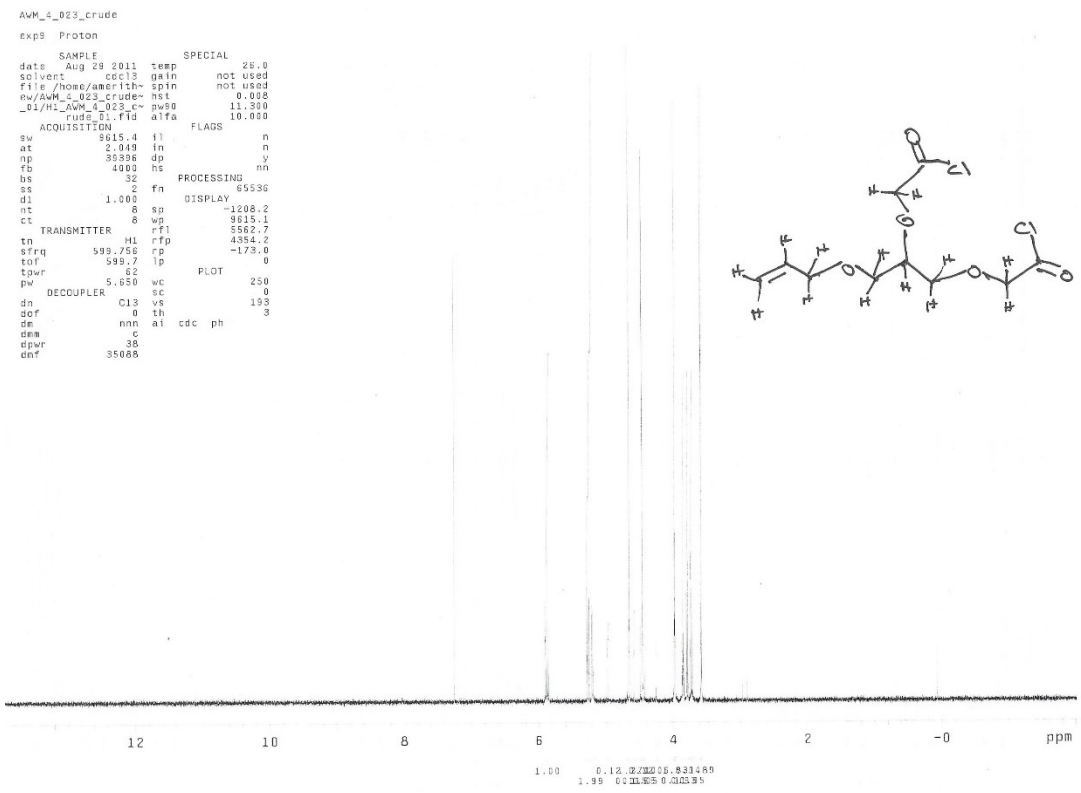

Figure S51 – 4-propenyl-2,3-dihydroxy-9,10-anthraquinone in $CDCl_3$ at 298 K

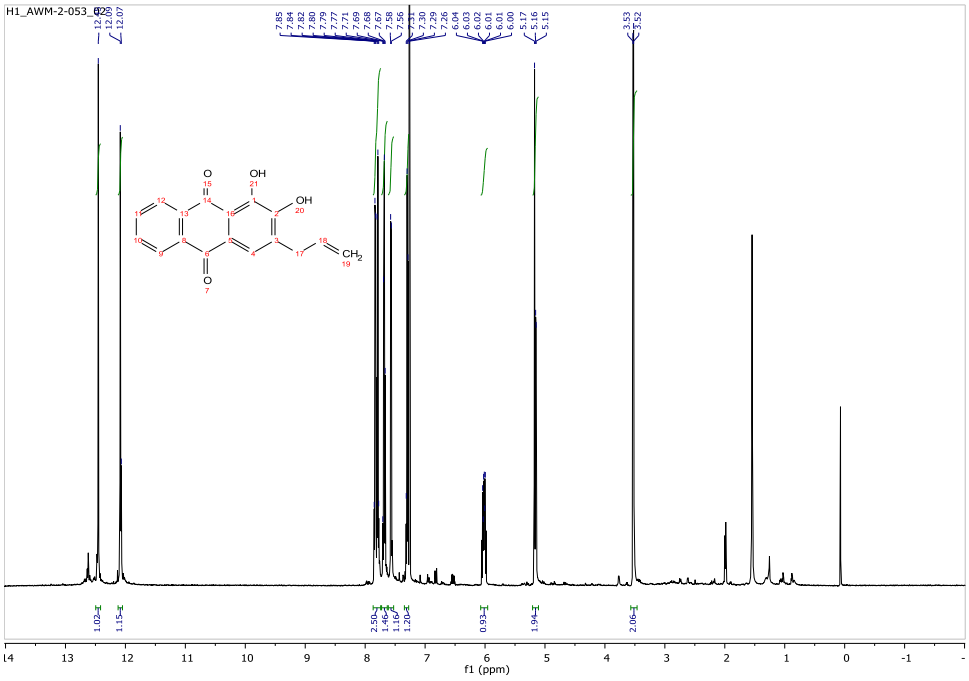

Figure S52 - ^{1}H NMR spectra of 1-(allyloxy)-4-methoxybenzene in $CDCl_3$ at 298 K

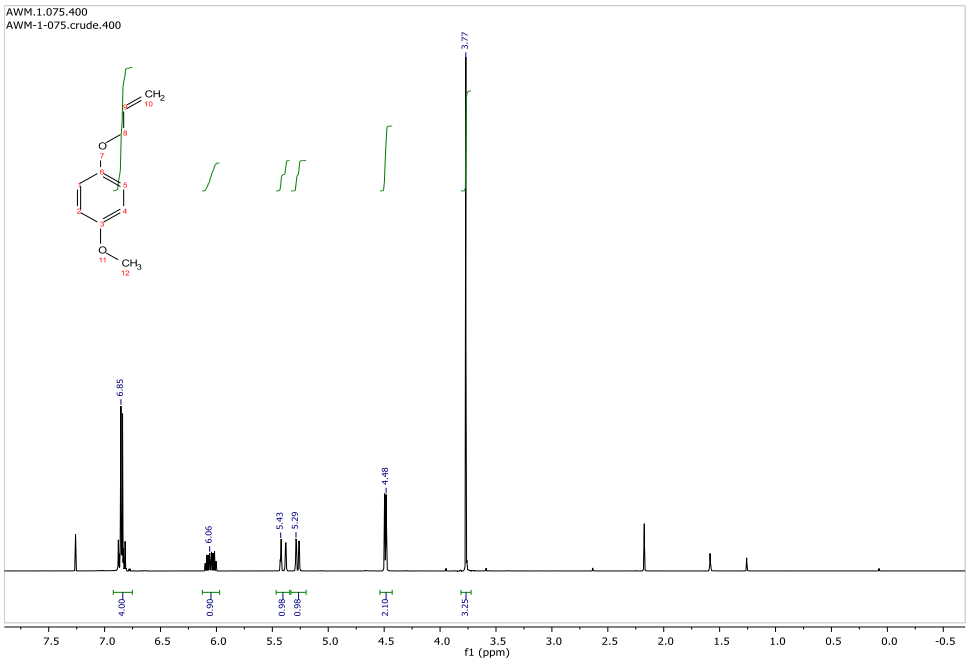

Figure S53– 1H NMR of 2-(allyl)-4-methoxyphenol in $CDCl_3$ at 298 K

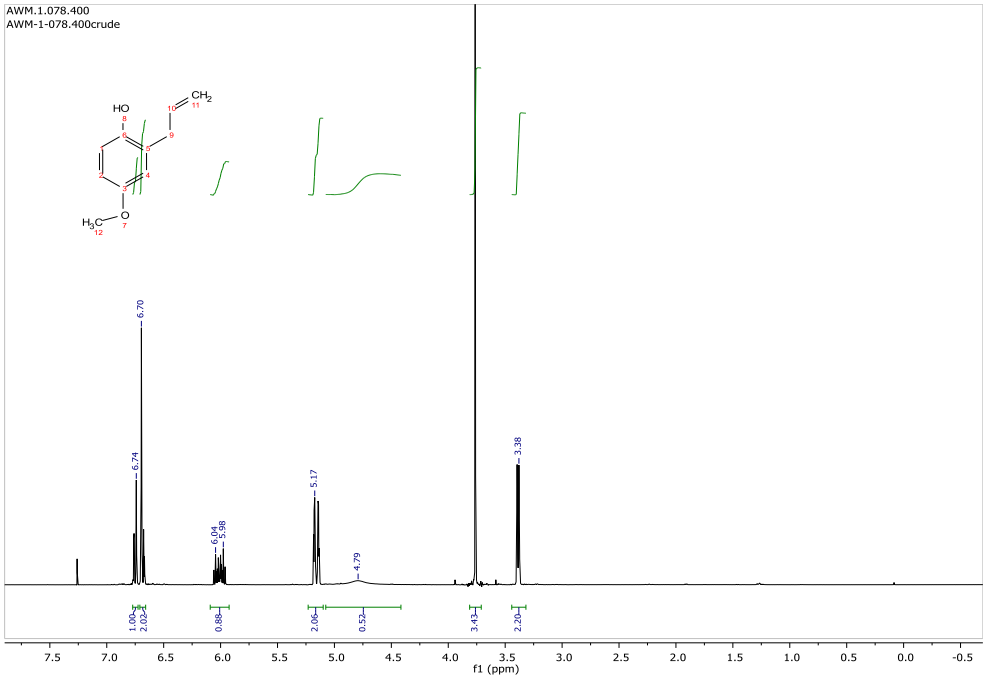

Figure S54 – 2-propenyl-1,4-benzoquinone in $CDCl_3$ at 298 K

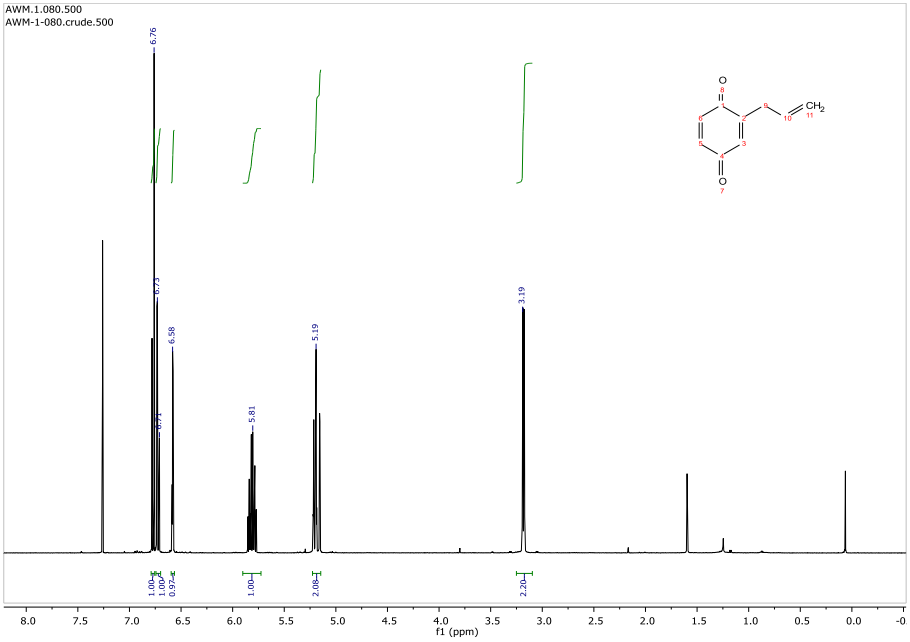

Figure S55 – functionalized "B" block with pendant 1-hydroxy-2-propyl-4-methoxybenzene side chains at loading(fractional).

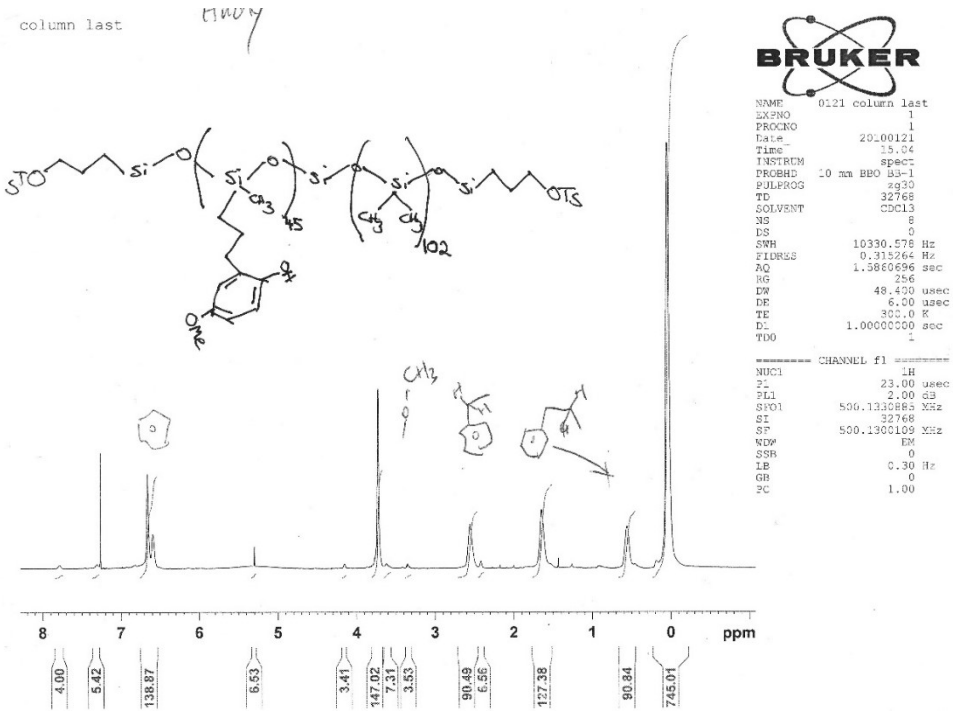

Figure S57 – 1H NMR of bis-dicarboxylic acid olefin **57** in CDCl3 at 298 K

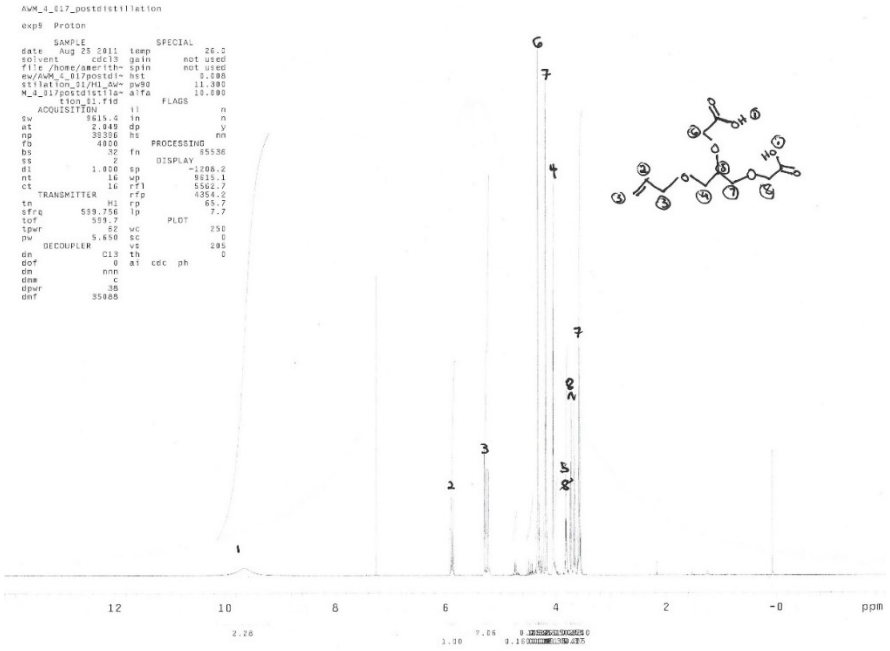

S58 - 2,2'-((3-(allyloxy)propane-1,2-diyl)bis(oxy))bis(ethan-1-ol) in $CDCl_3$ at 298 K

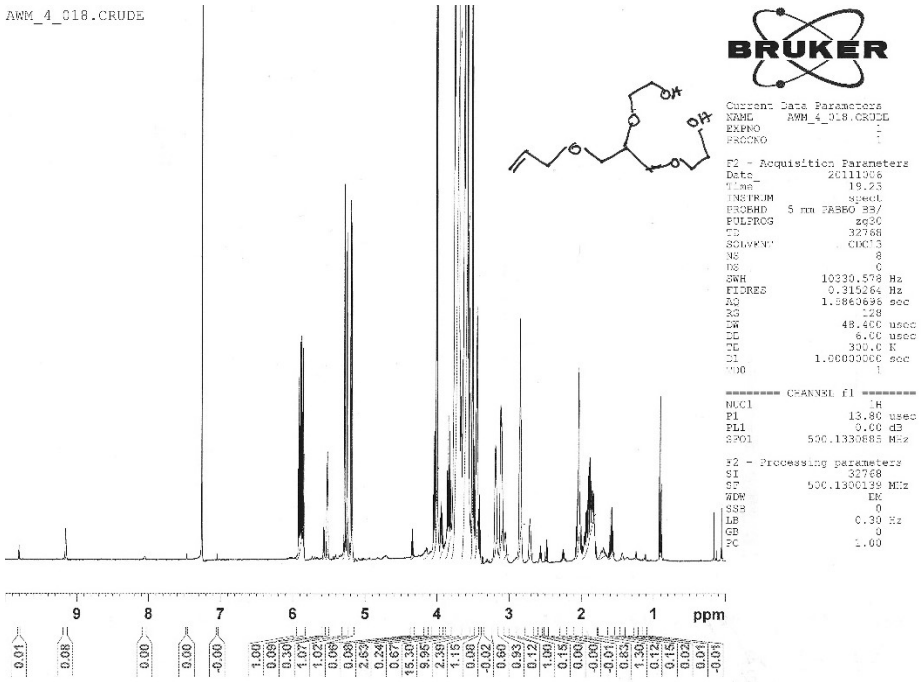

Figure S62 – 1H NMR of coumarin mono-ethoxy dimethyl silane in $CDCl_3$ at 298 K

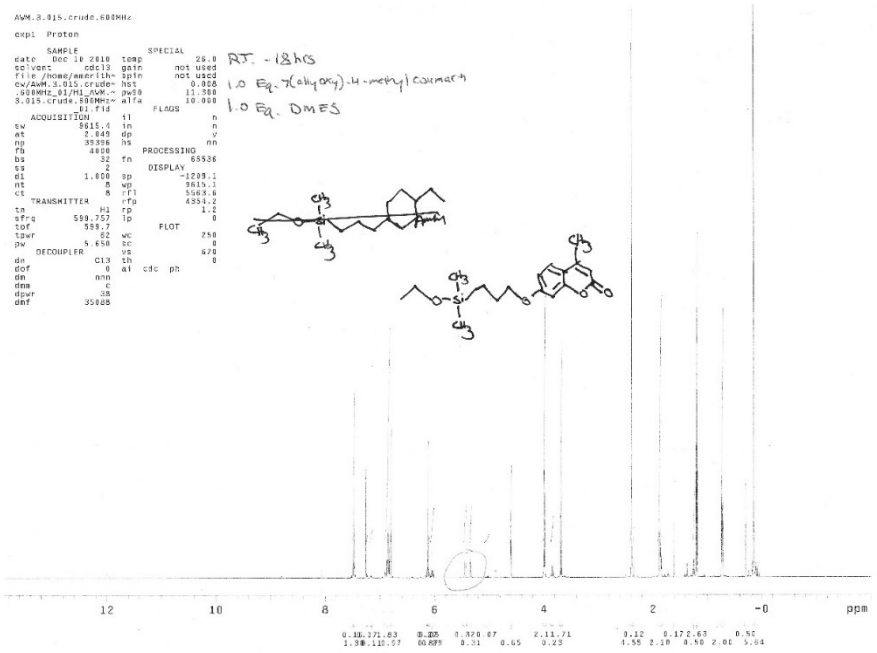

Figure S29 – 1 H NMR Spectra of bisethyloxyaldehyde anthraquinone in $CDCl_3$ at 298 K.

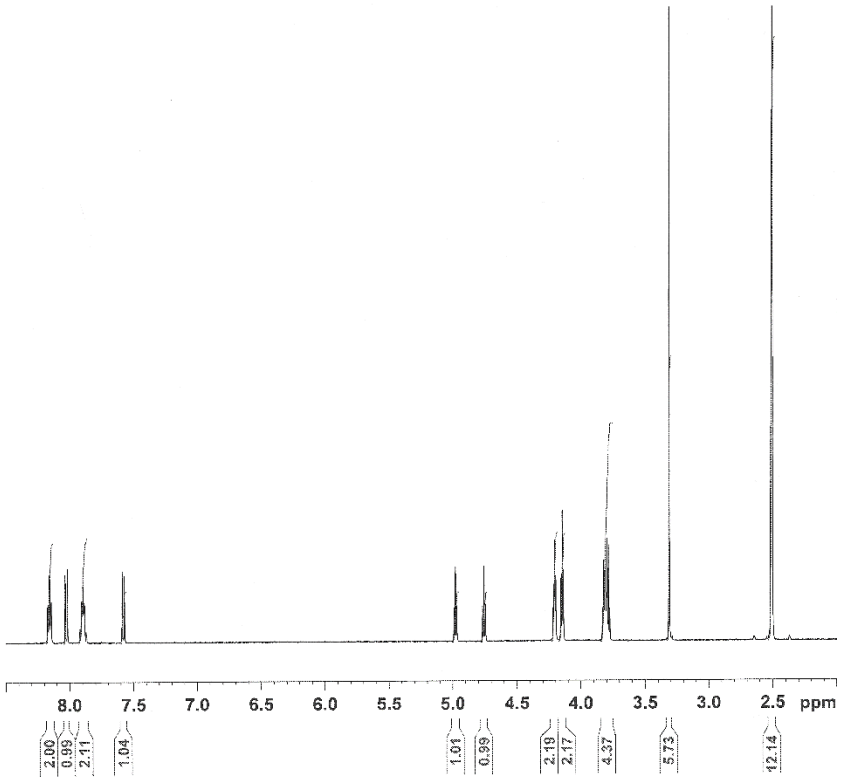

Figure S60 – ^{1}H NMR spectra of allylated crown esther 60 in $CDCl_3$ at 298 K.

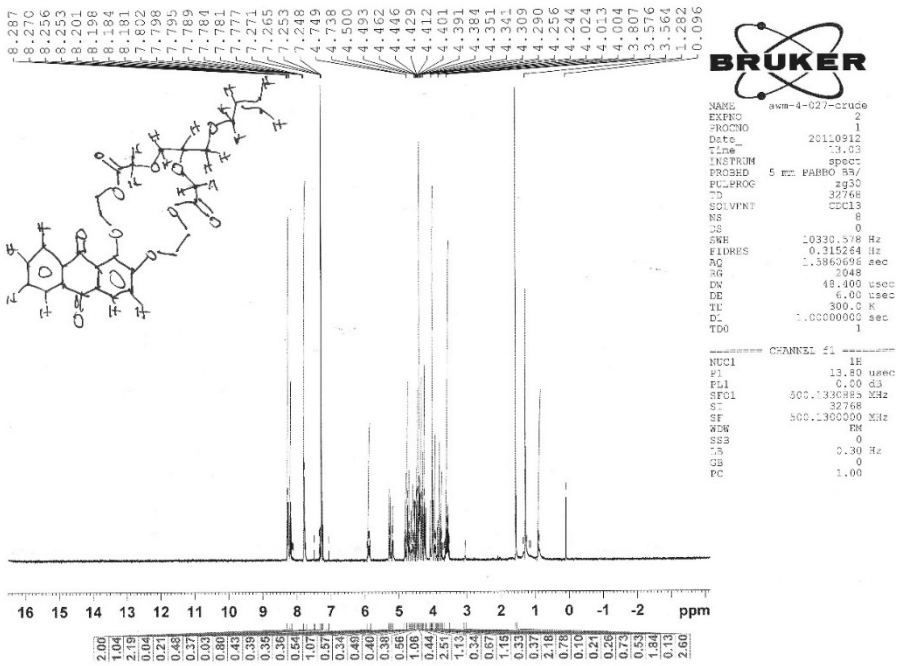

Figure S62 – Dmiethylethoxysilane monomer in $CDCl_3$ at 298 K

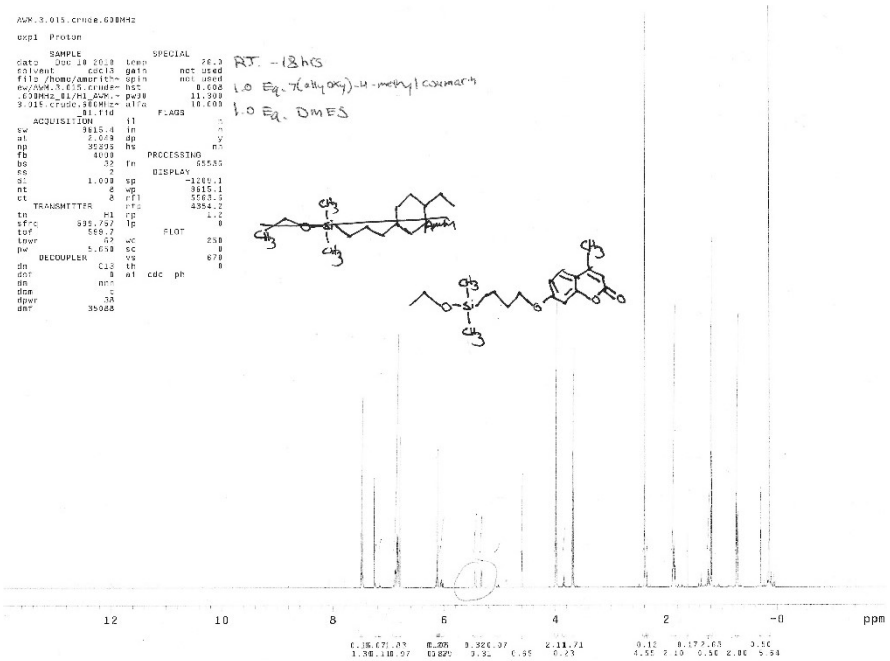

Figure S64 – Purifyied “B” block capped with Tosylate end-blockers with 2-propenyl-1,8-dihydroxyanthraquinone pendant side chains in $CDCl_3$ at 298 K

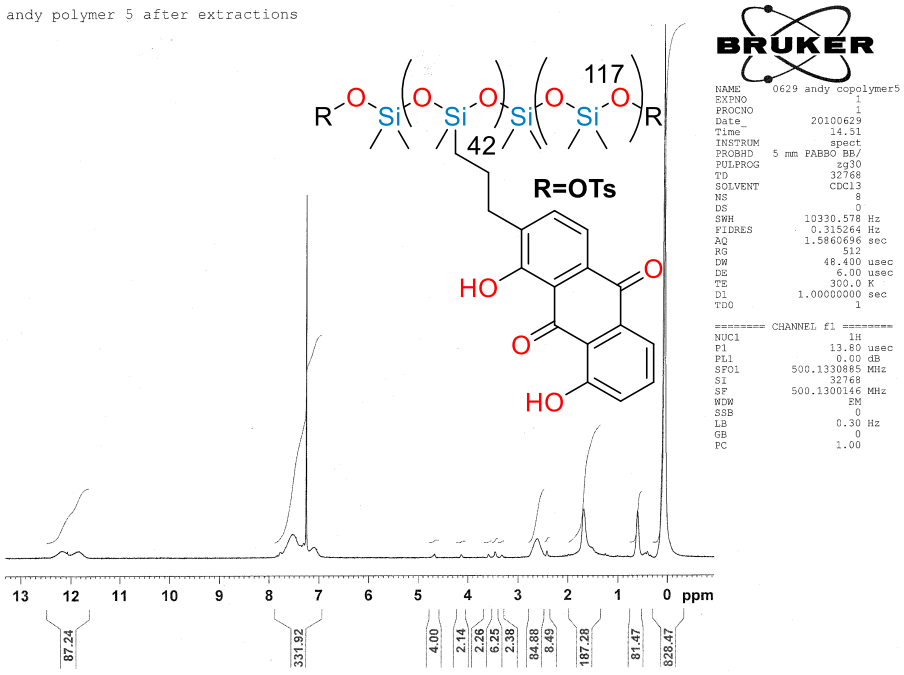

Figure S64 – 3,5-Dibutylbenzoateallayoxybenzene in CDCl3 at298 K.

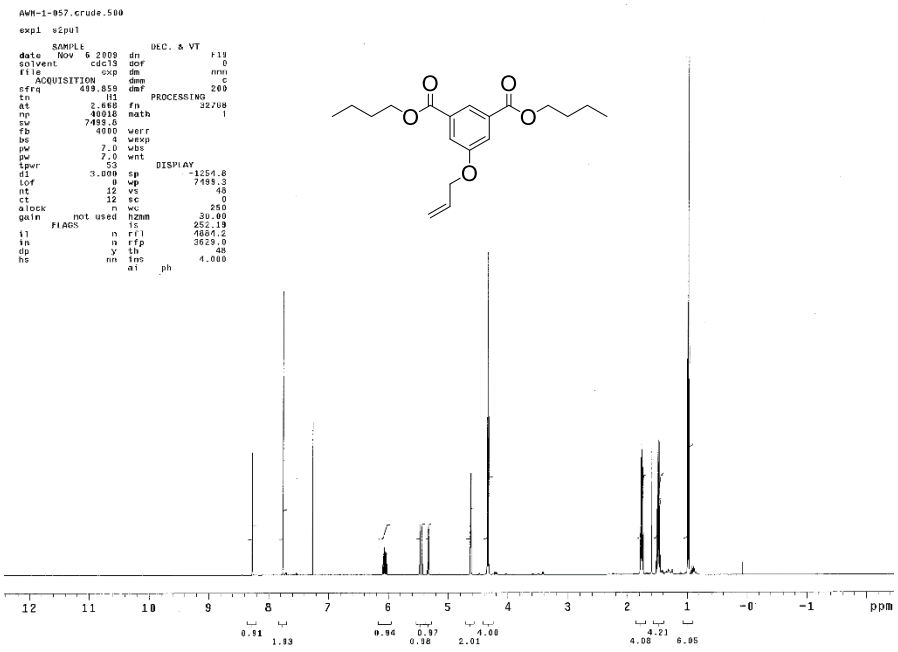

Figure S67 – ^{1}H NMR of 2,2'-((9,10-dioxo-9,10-dihydroanthracene-1,2-diyl)bis(oxy))diacetaldehyde in in $CDCl_3$ at 298 K

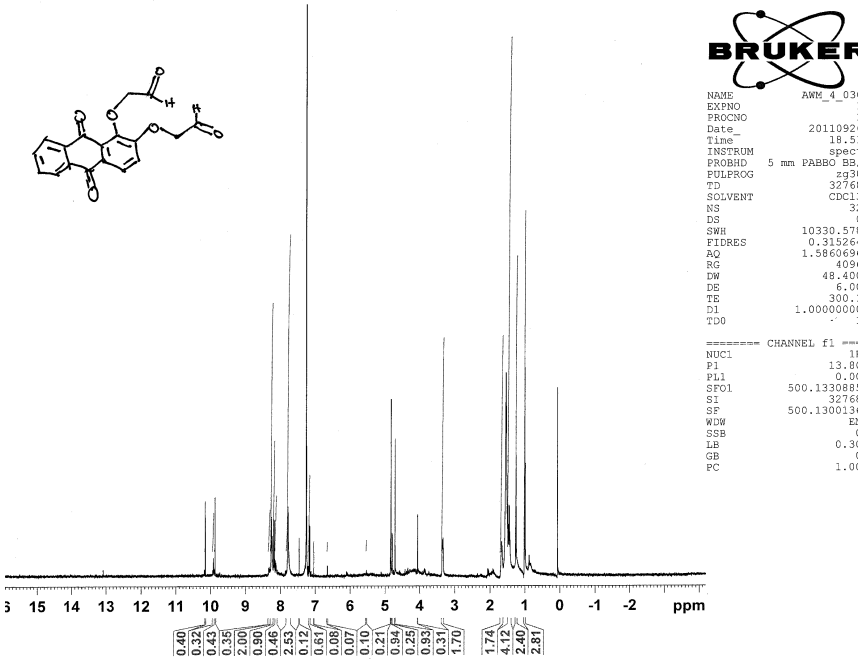

Figure S68 – 2D DOSY of the AQ-18-C-6 • (4-Cl)TPB complex diffusing as a single entity

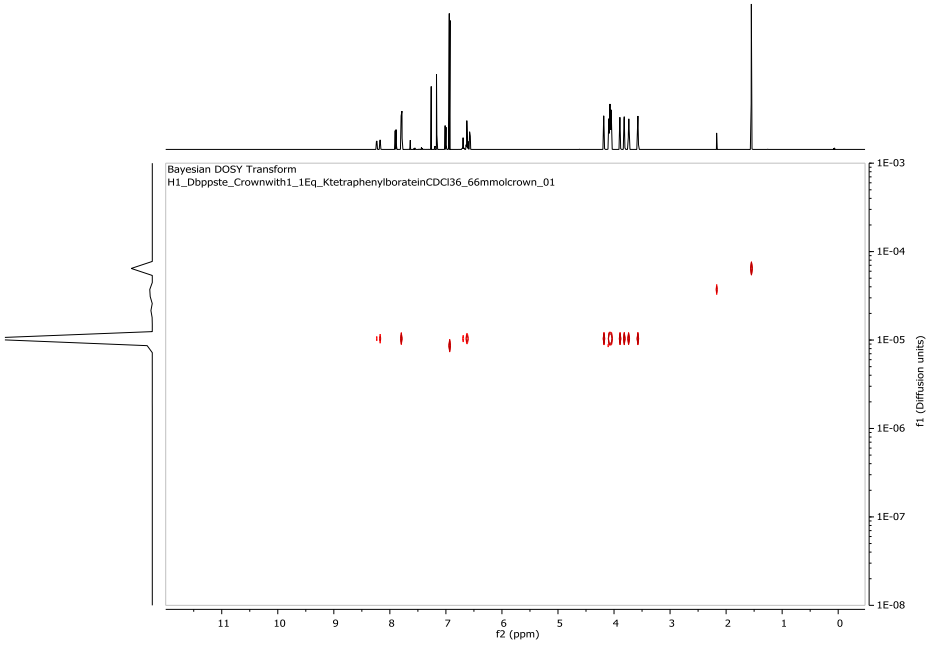

Figure S69 – 2D DOSY standard for DOSY titration of K+(4-Cl)TPB in 3:1 v/v CdCl3:d6THF

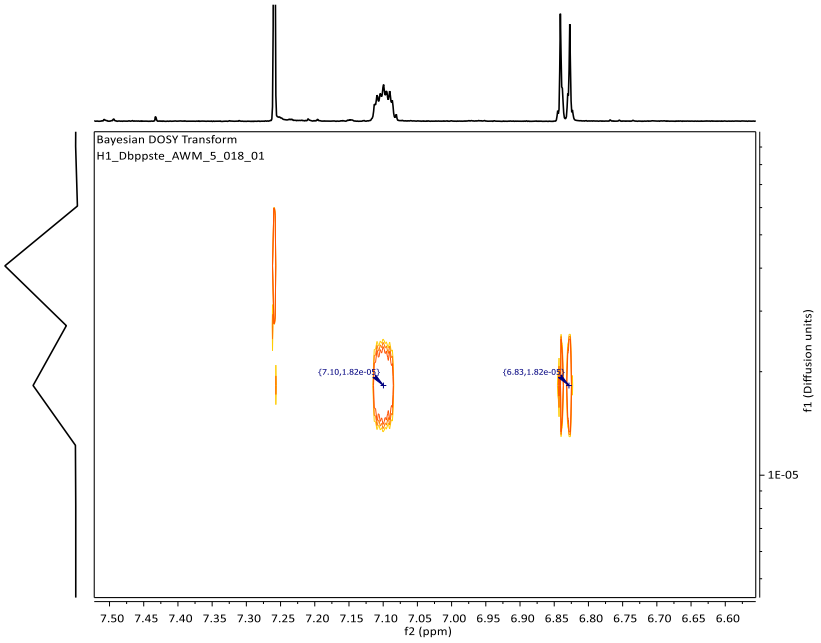

.

Figure S70 – 18-C-6 diffusion standard (10mM) in dDMSO at 298 K.

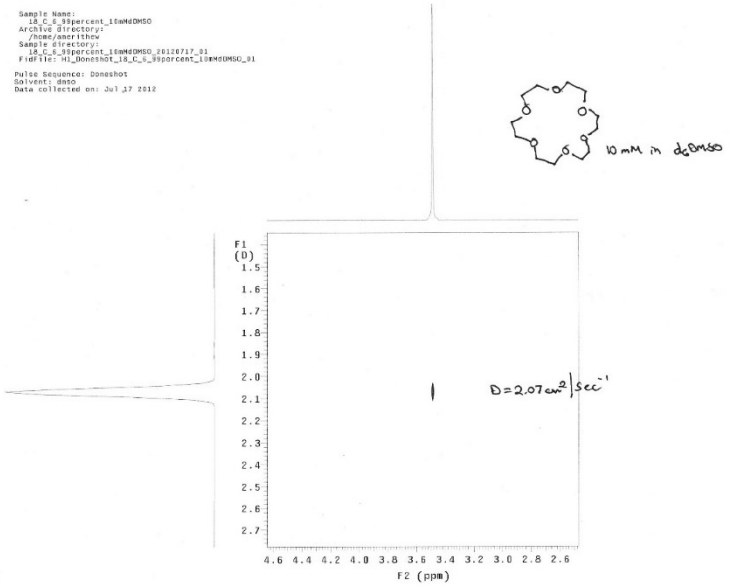

Figure S71 – 2D DOSY Spectra of AQ-18-C-6 complexed with K(4-ClTPB) in dDMSO at 298 K.

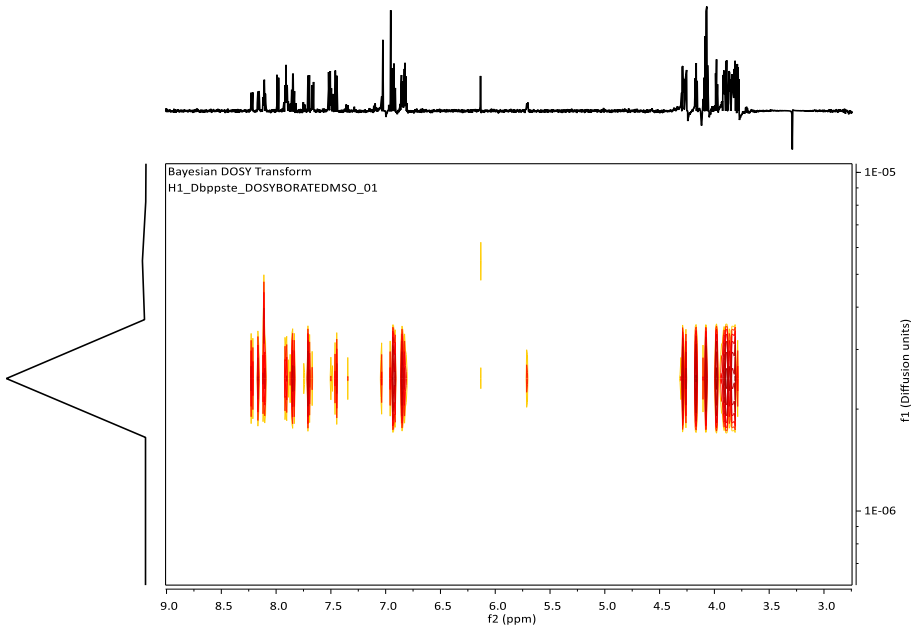

Figure S72 – Integration of the 2D plane shows a selectivity factor of log K 7.13 for the 1:1 complex over all species present in the mixture

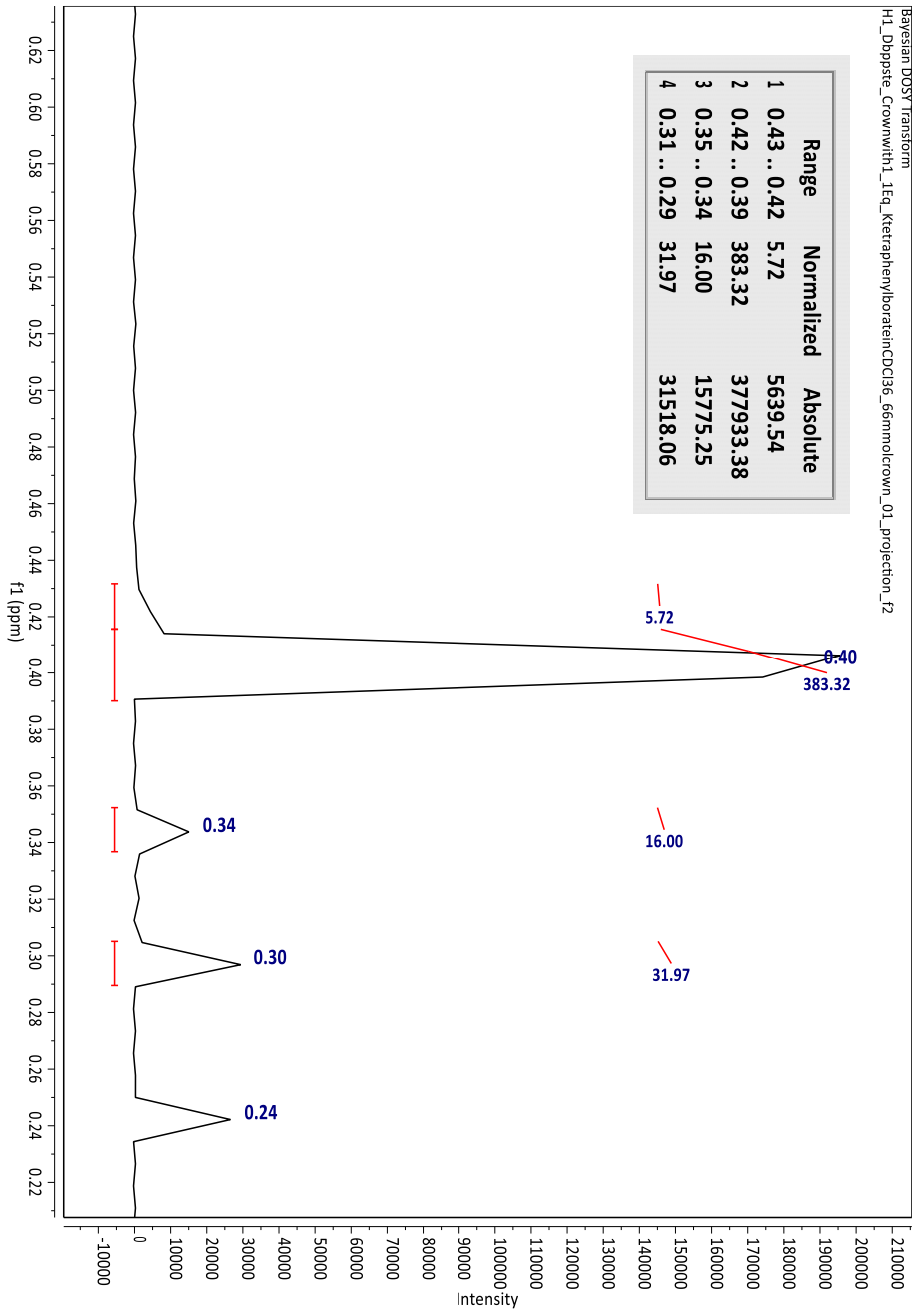

Figure S73 – 19F NMR of the JOB Plot Point G (1:1) mole ratio AQ-18-C-6 to K(OTf) showing 2:1 complexation

Figure S74 – 1H NMR Spectra of extended allyl-catechol bisditosylate leaving group in CDCl3 at 298 K.

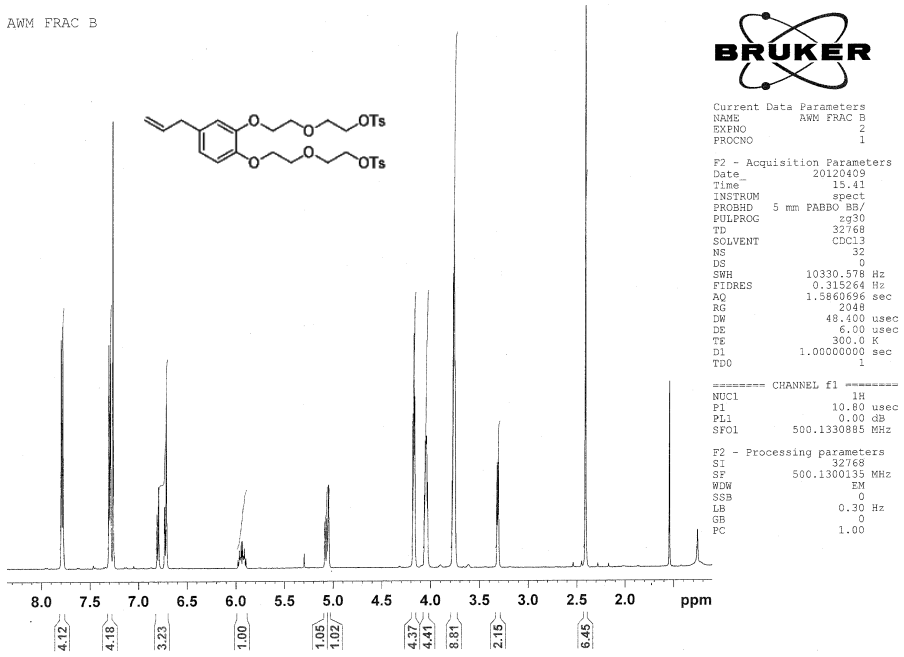

Figure S75 – [1]H NMR spectra of K+(4-Cl0TPB) complex in CDCl3 at 298 K, 72 h. post addition.

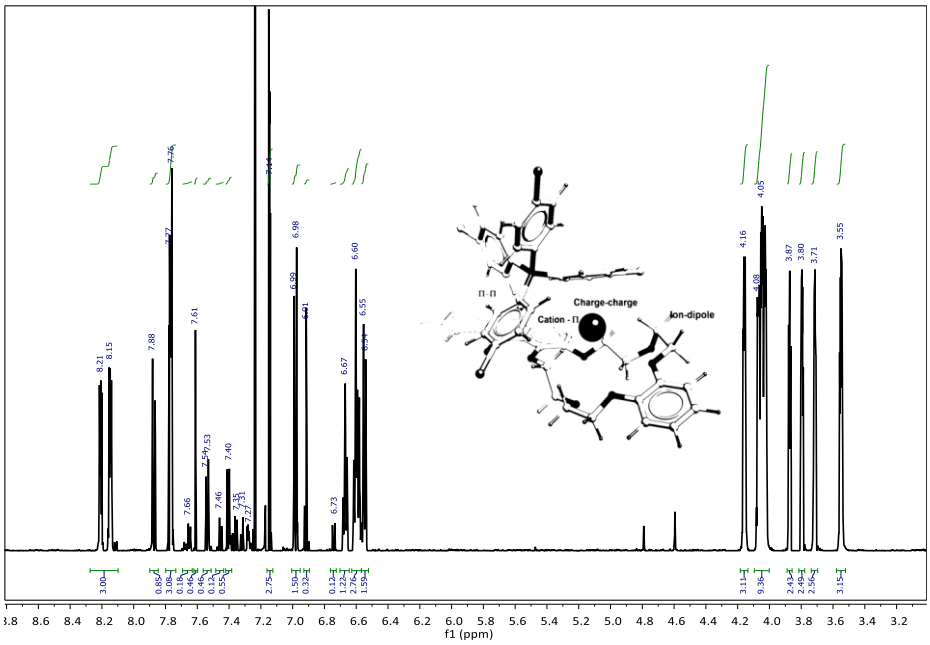

Figure S76 – Stacked 1H NMR plot of the standard (top spectra) and cold temperature (bottom spectra) NMR taken at 233 K (-40˚C)

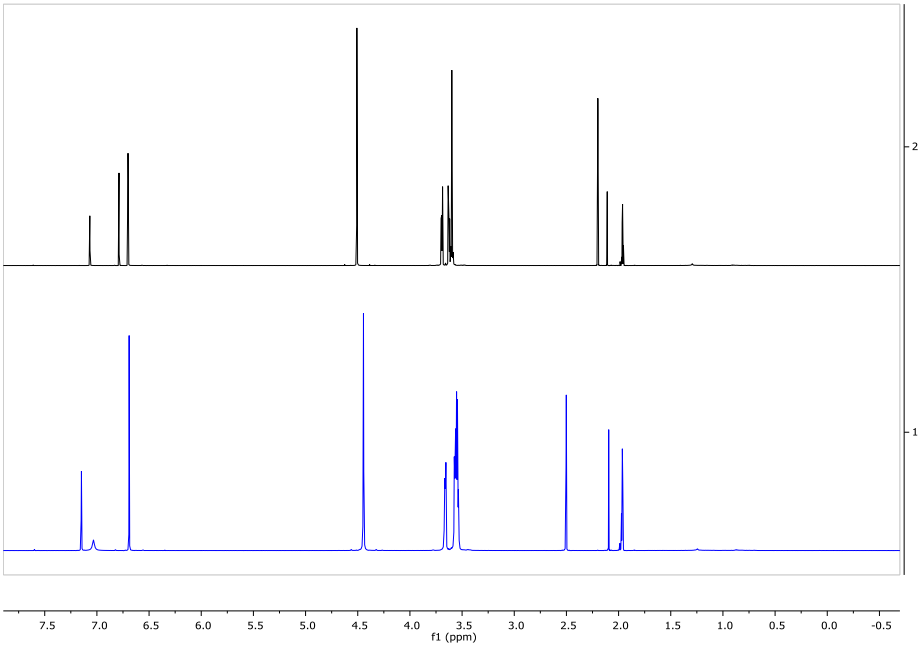

Figure S77– IR spectra of the uncomplexed crown ether AQ-18-C-6 (taken from $CDCl_3$) on NaCl salt plate

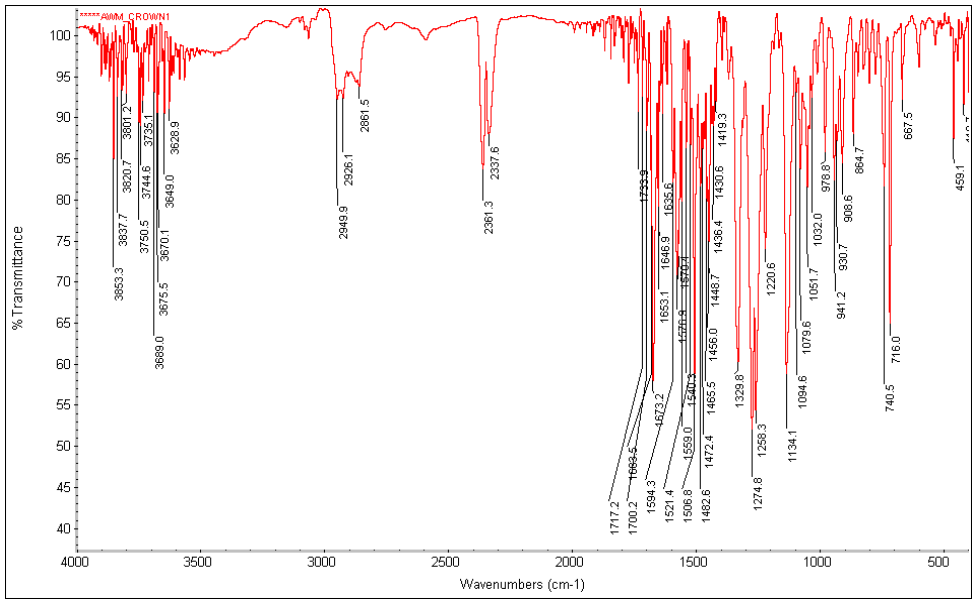

Figure 78 – IR spectra of the complexed crown ether (1:1 stoichiometry) AQ-18-C-6 • K(OTf) compelx (taken from $CDCl_3$) on NaCl salt plate

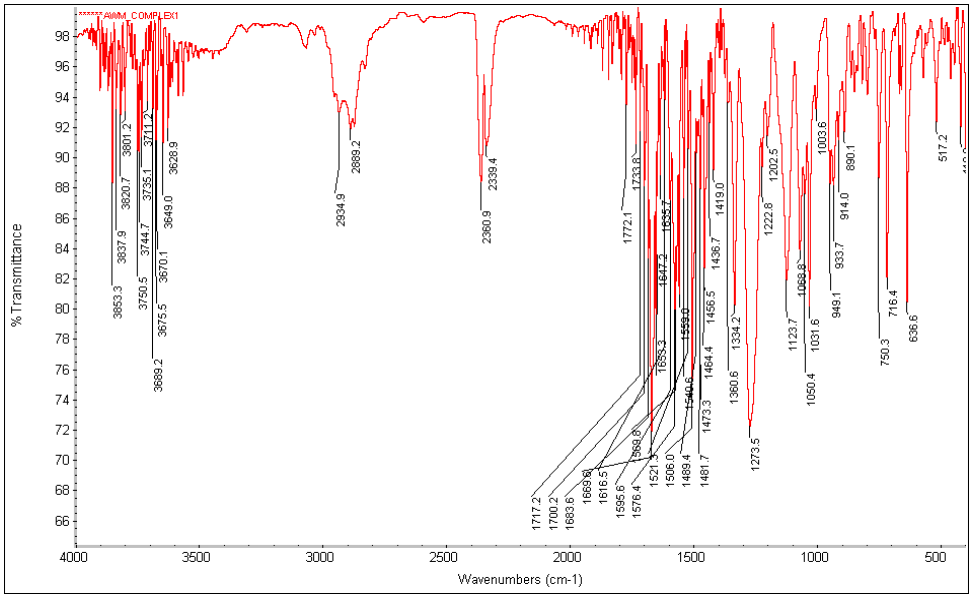

Figure S79 – Standard Molar Extinction Coefficient for the Anthraquinone Crown Ether

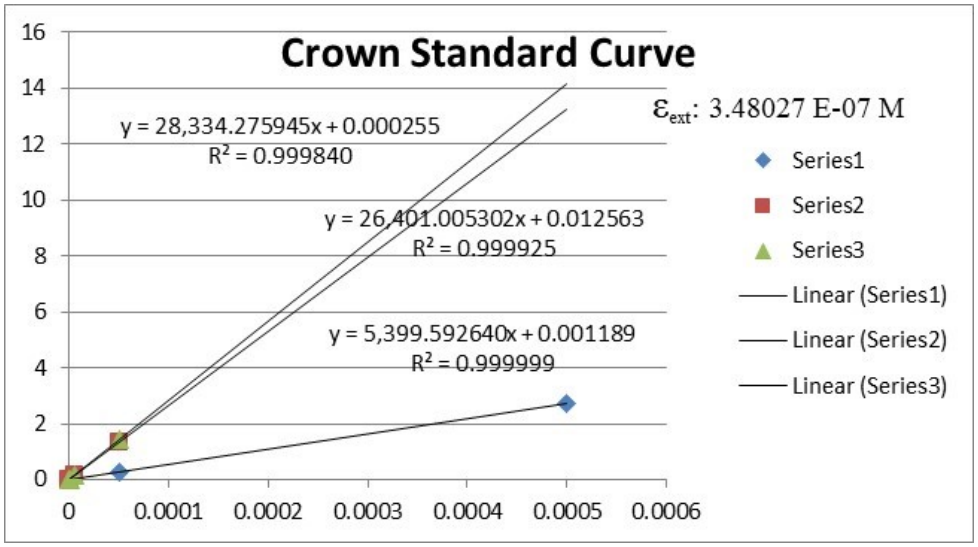

Figure S80 – Standard Molar Extinction Coefficient for K(4-Cl)TPB in 3:1 $CHCl_3$:THF

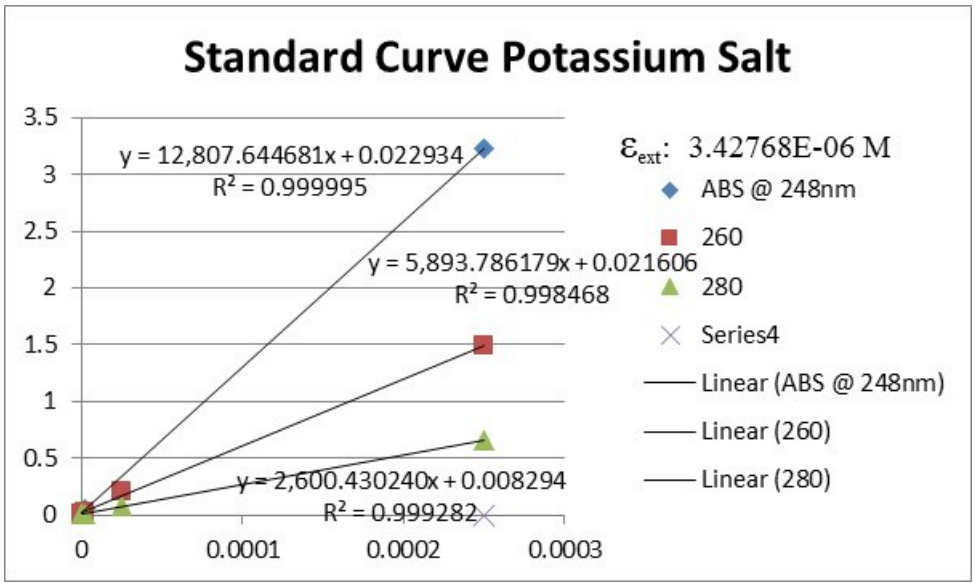

Figure S81 – Spin-coat images of the different formulations from Table **3.44** in the text. Pictures are of the intact film (left side) and track-etched DekTak profilometry photos on the right labeled with letters corresponding to the sample

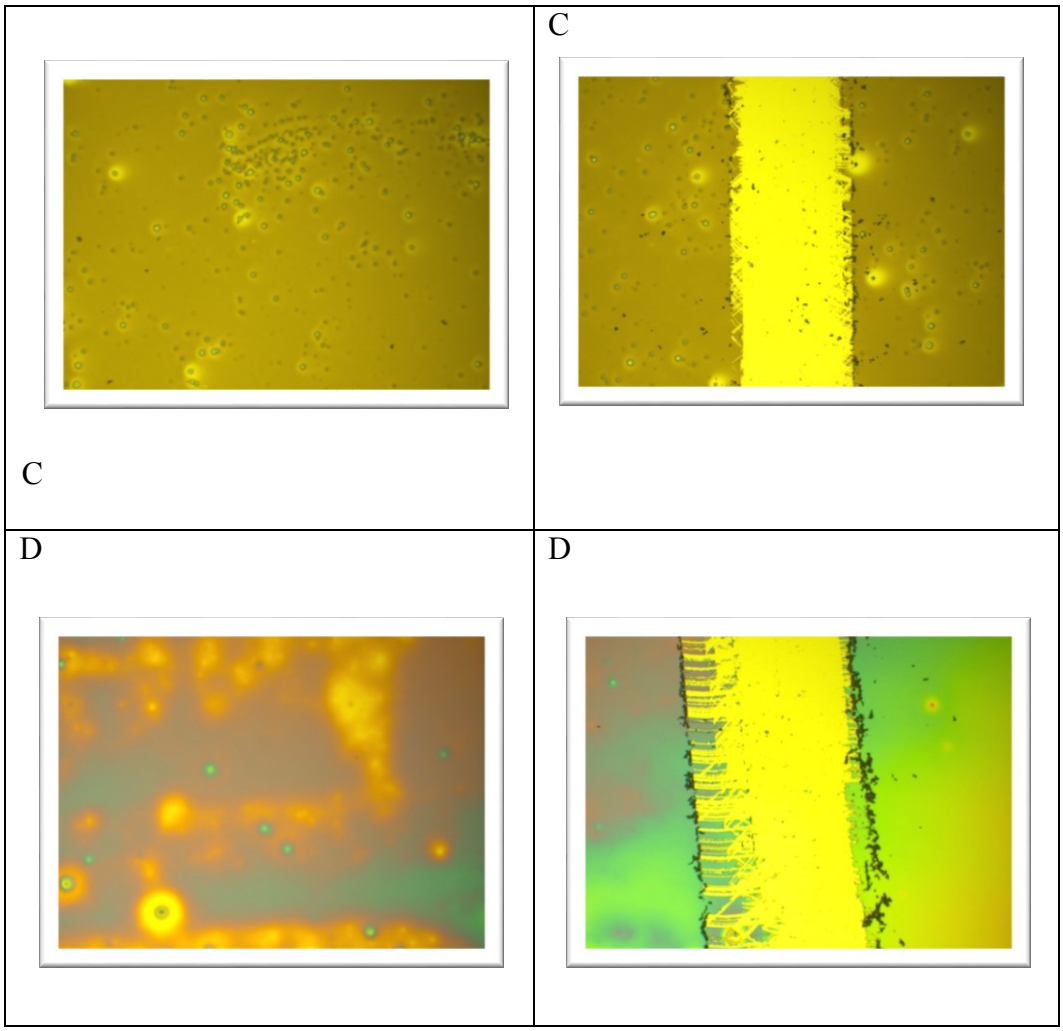

E 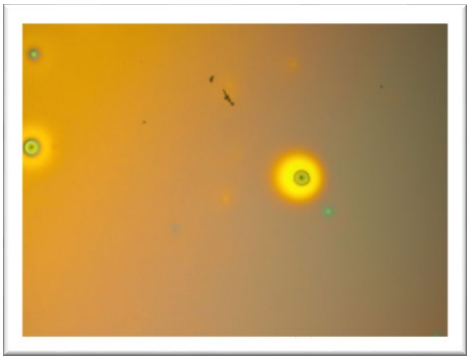	E 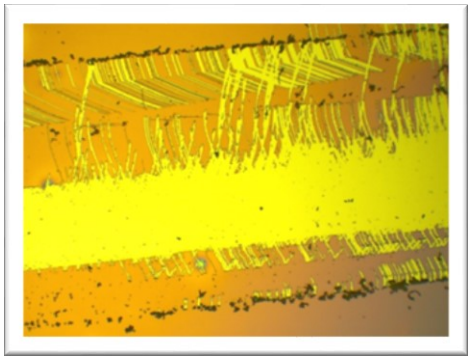
F 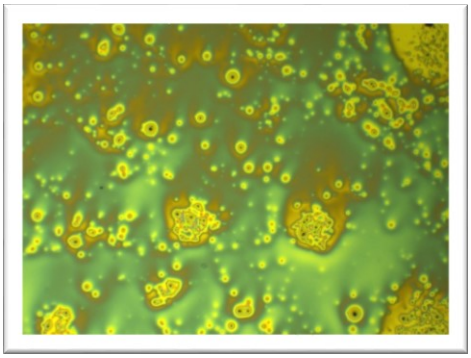	F 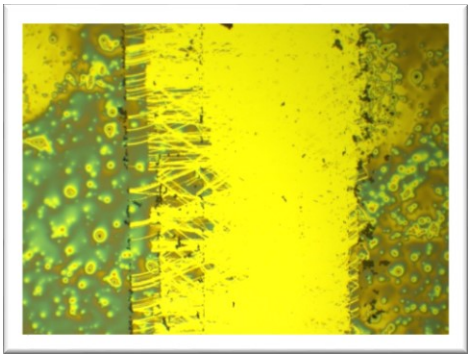
G 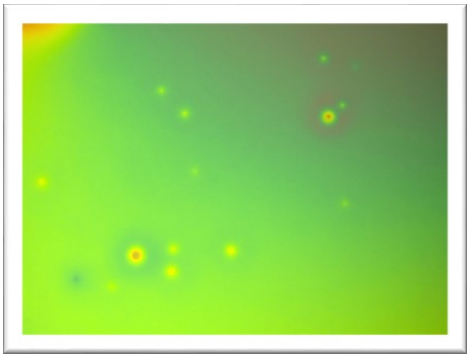	G 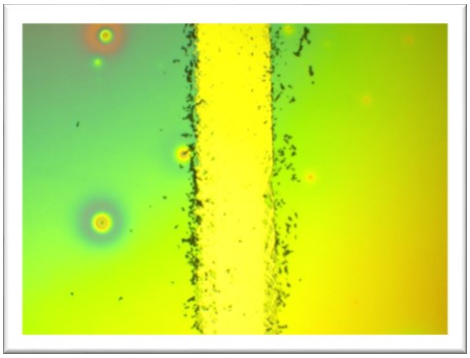

H 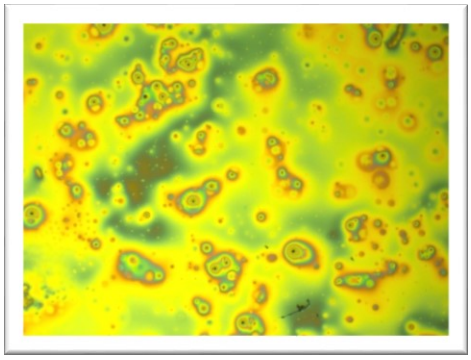	H 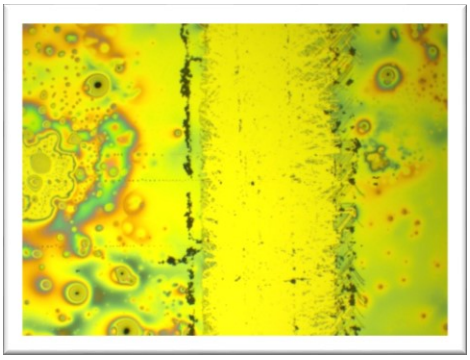
I 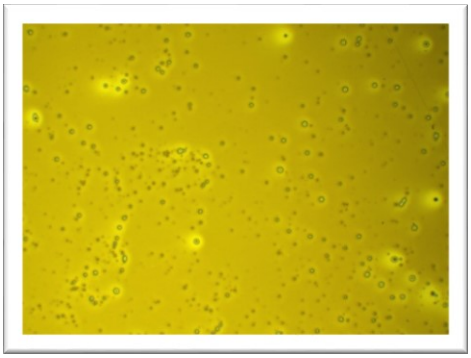	I 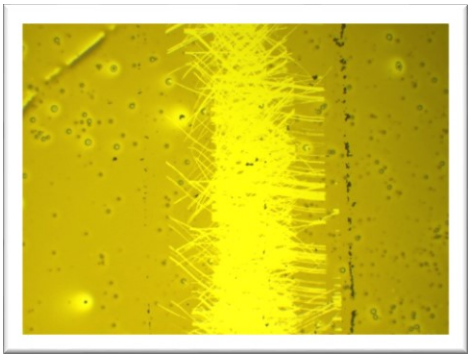
J 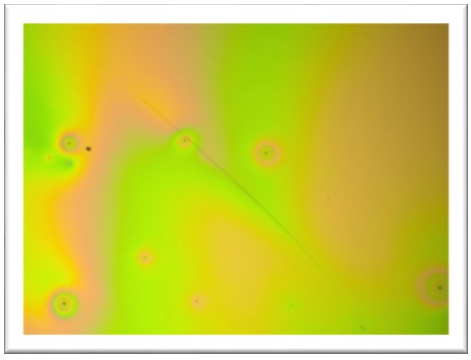	J 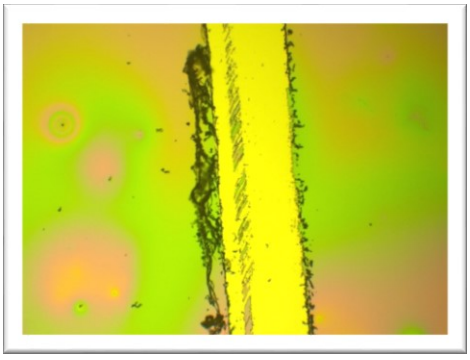

Figure S82– Depth profile of film spun @ 5K for 1 min with 0.5% Benzoyl Peroxide with pure tetraethyleneglycoldiacrylate

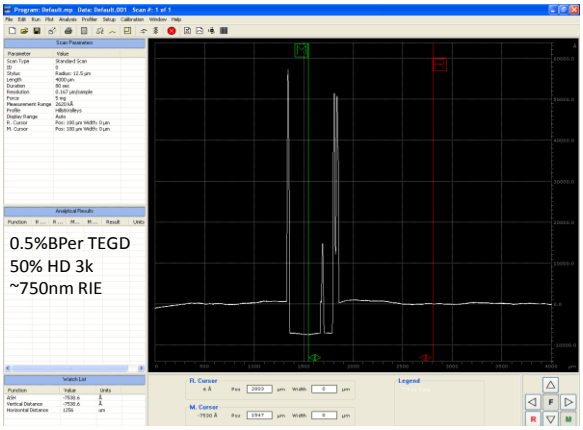

Figure S83– Depth profile of film spun @ 5K for 1 min with 0.5% Benzoyl Peroxide with pure tetraethyleneglycoldiacrylate

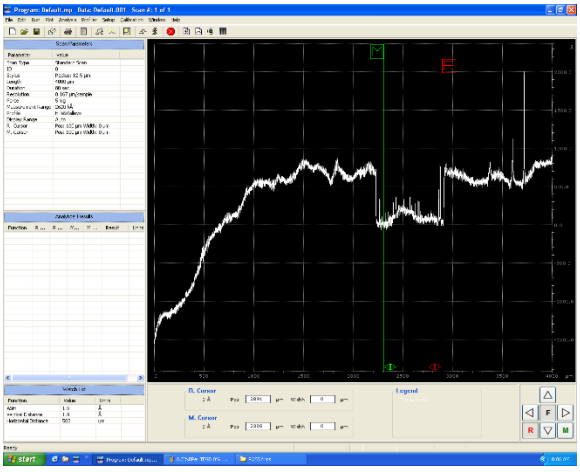

Figure S84 - DekTak profile of a 50-70 nm film spun at 5K with 0.5% Benzoyl Peroxide initiator

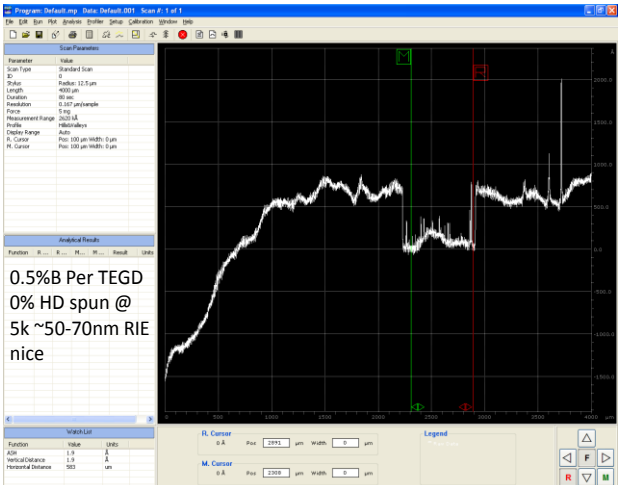

Figure S85 - XPS spectra of the Oxygen Peak from the functionalized alumina membrane with APTES

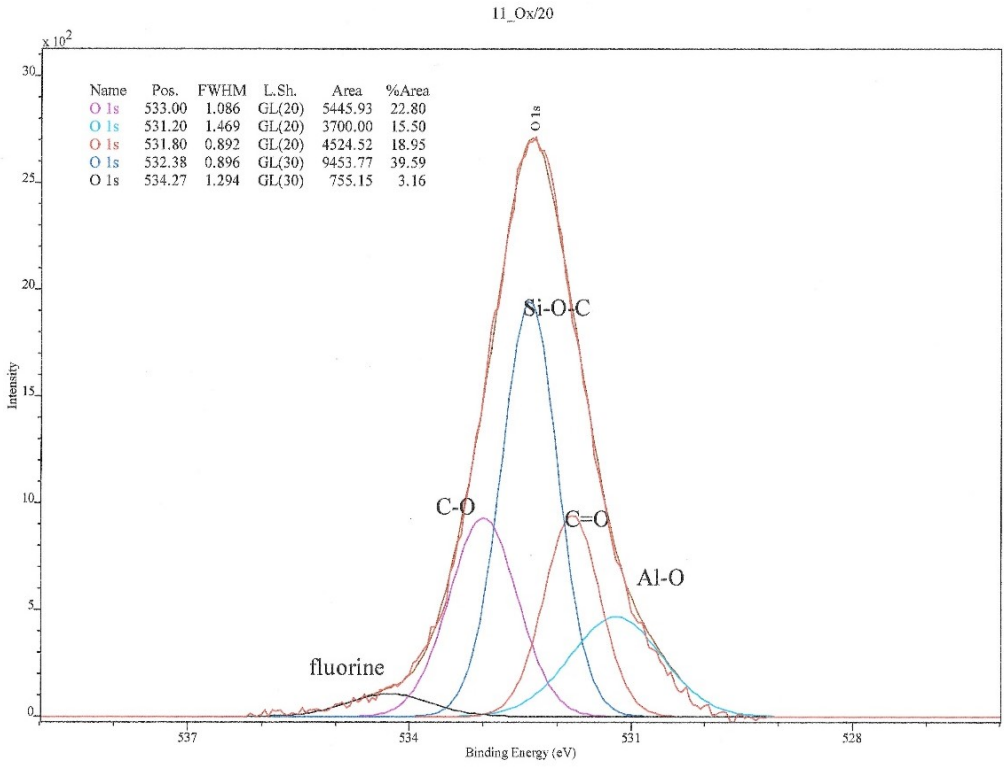

Figure S86- XPS spectra for the functionalized alumina membrane with APTES

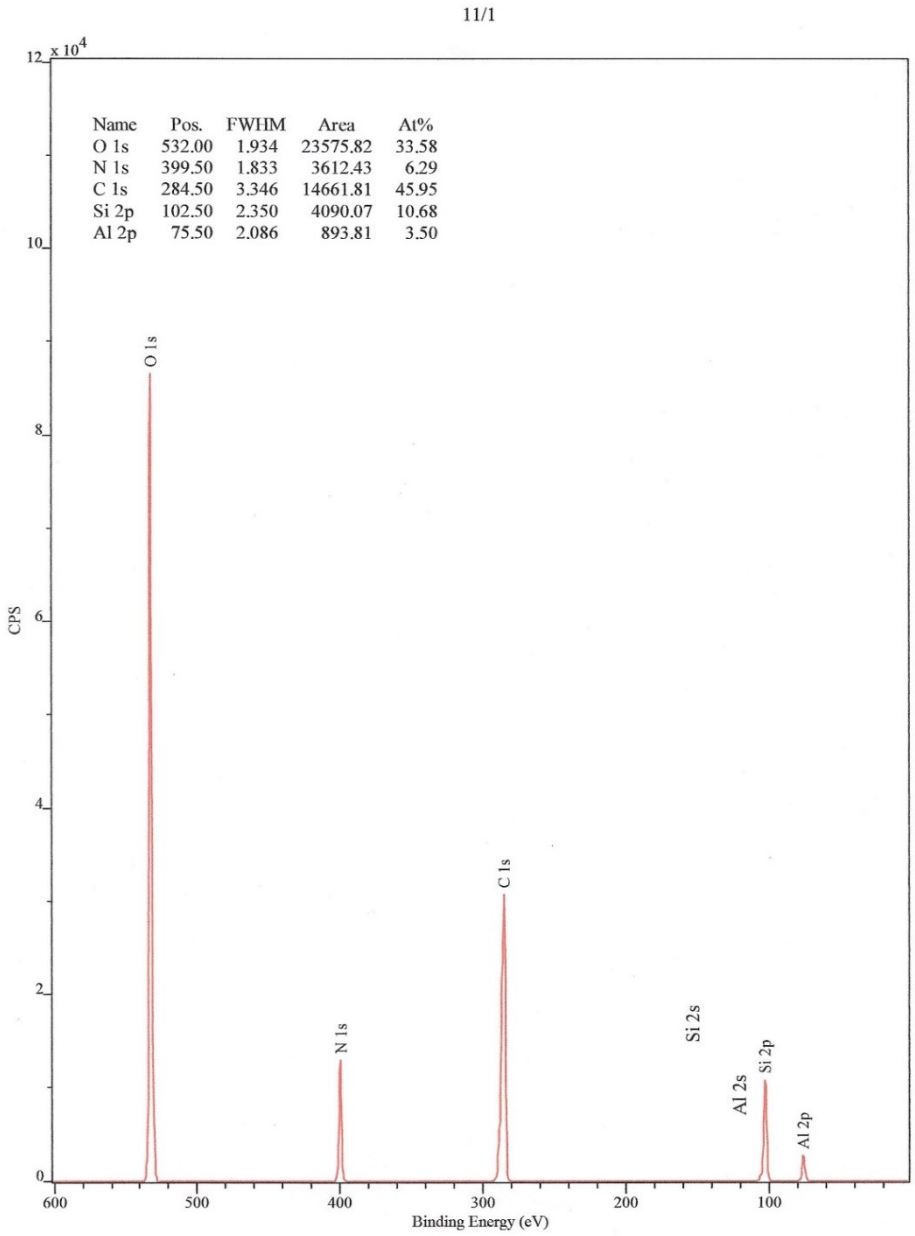

S87 – C1S Spectra of the PEDOT:PSS coated nanopore arrays functionalized with APTES. Multiple signals are present due to the PEDOT:PSS polymer, APTES carbon chain

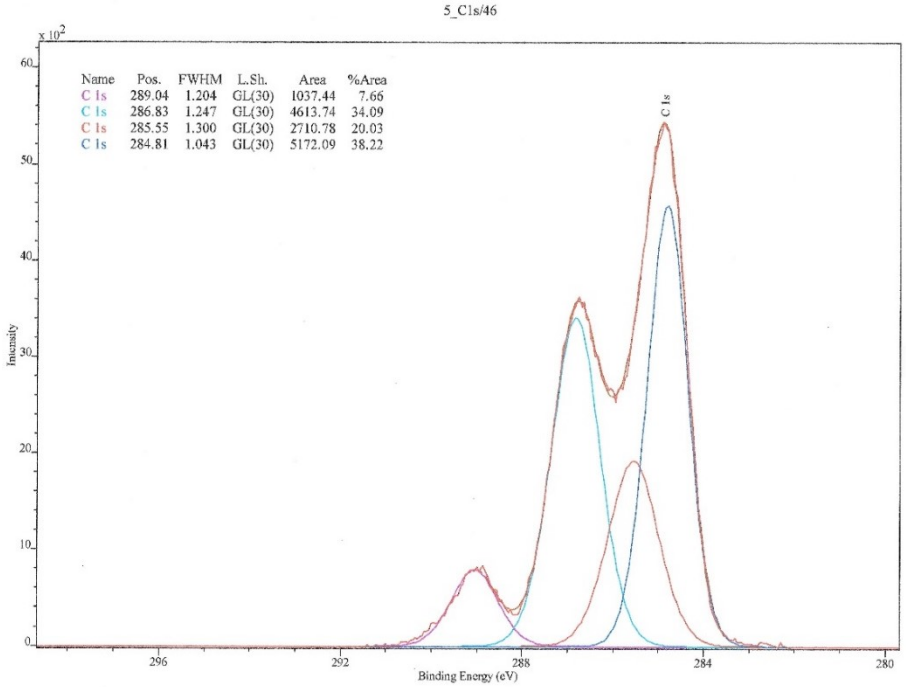

S88 – C1S Spectra of the nanopore arrays functionalized with ICPTES

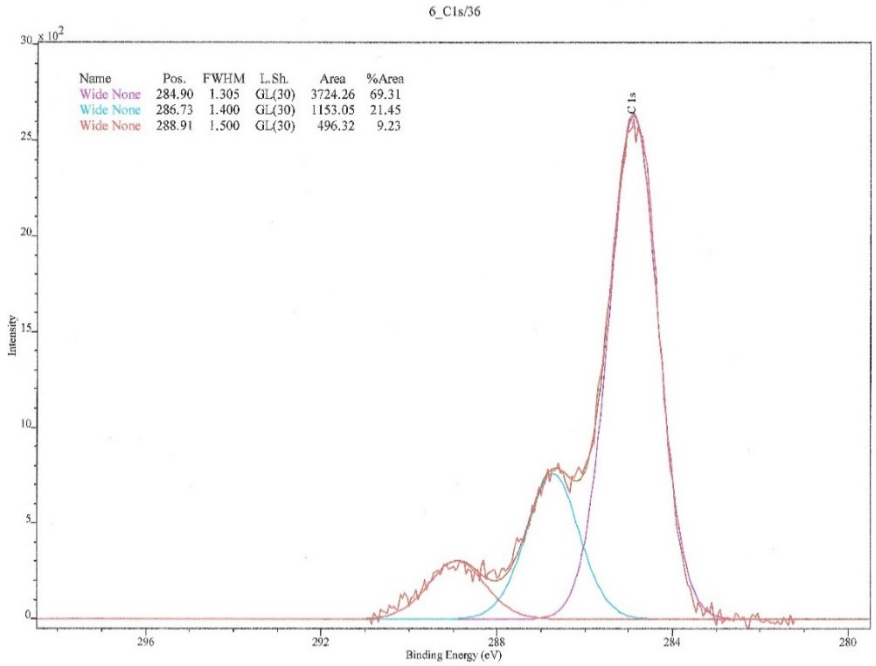

S89 – N1S XPS peak showing the distribution of protonated amines to nuetral amines for the functionalized alumina nanopore with APTES.

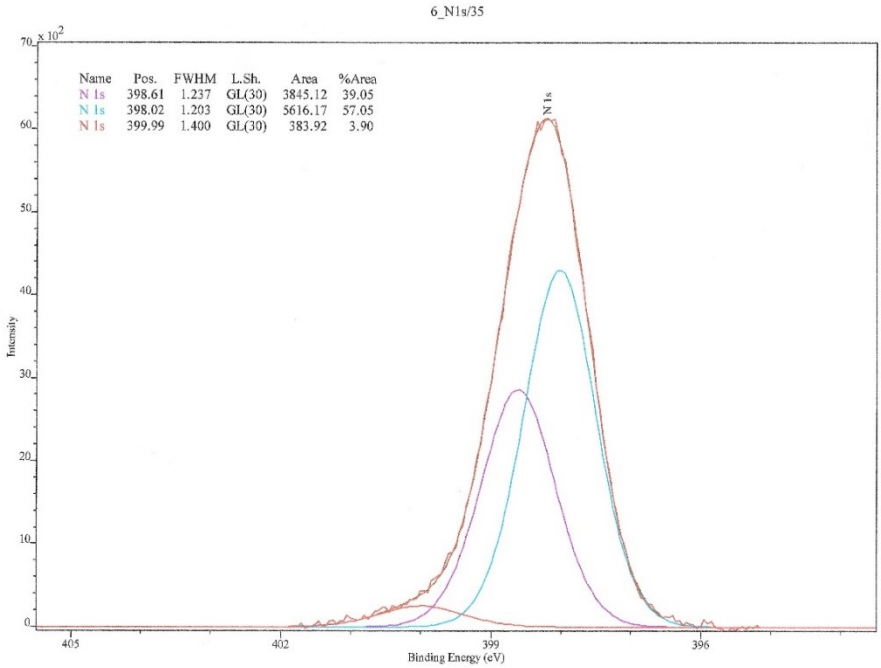

S90 – XPS close up of oxygen present as Al2O3 and O-Si-O oxygens

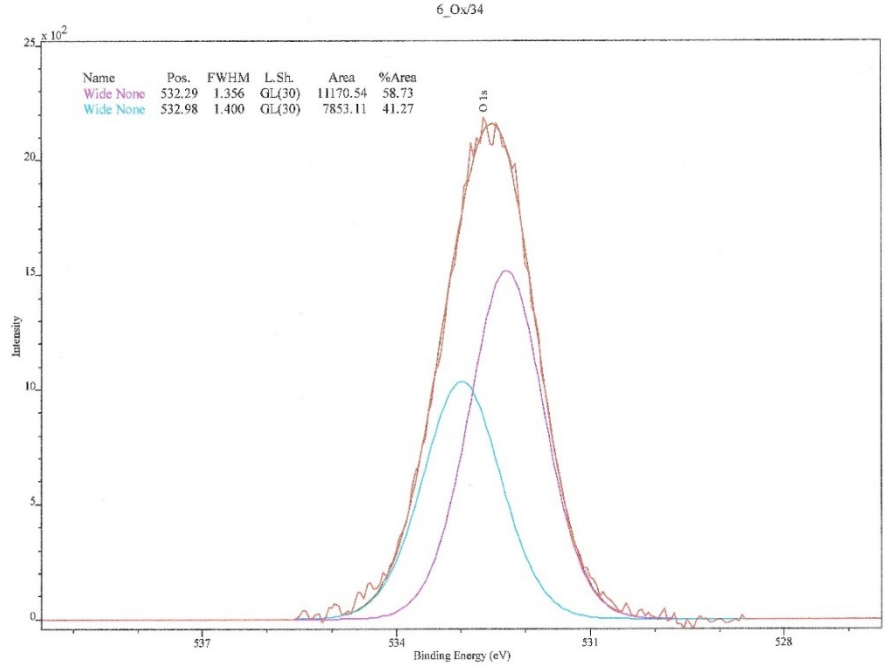

S91 – XPS spectra of PEDOT:PSS spin coated alumina nanoporous membrane

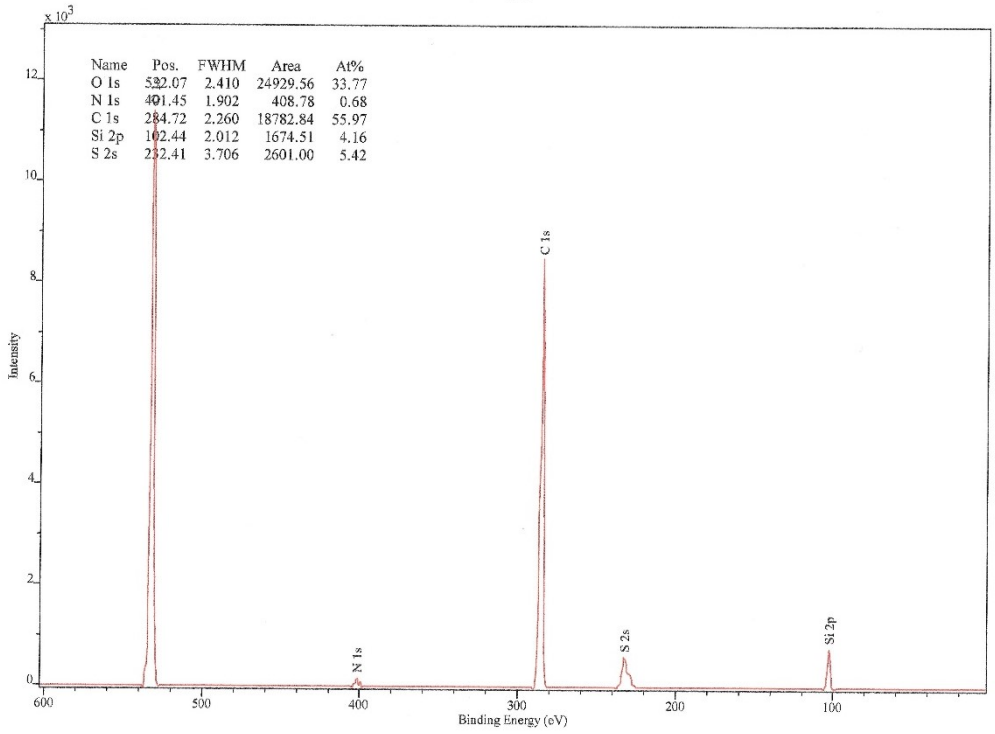

S92 – C1S Spectra of the IPTES coated nanopore arrays. Interprutted by Dr. Tom Mates

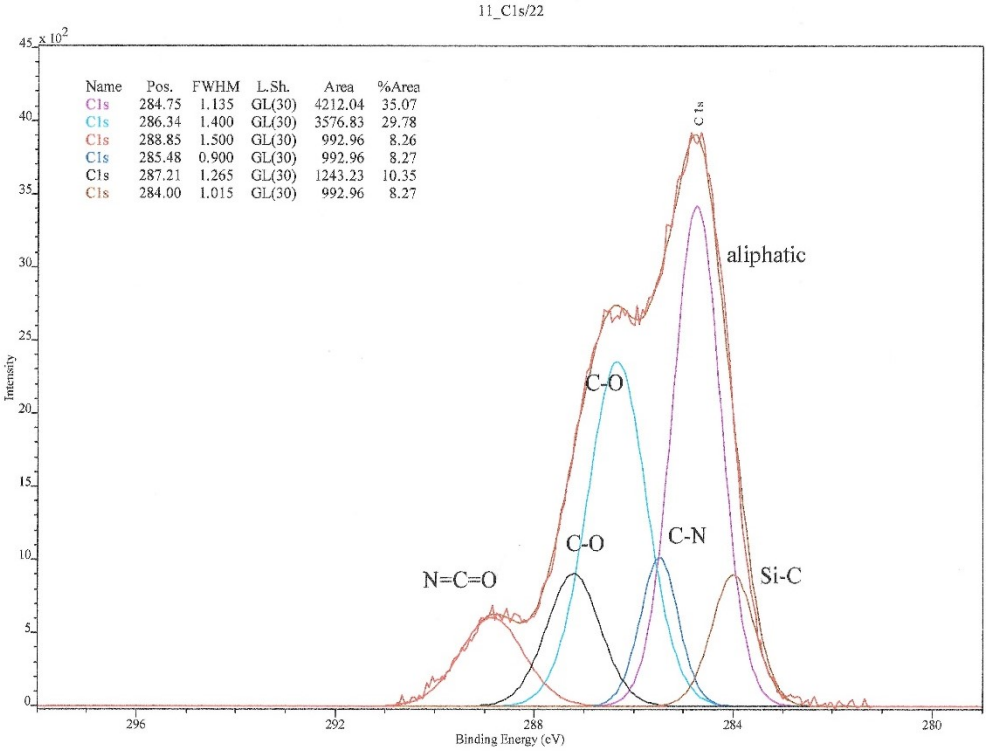

Figure S93 – Custom Teflon chamber used during transport experiments as outlined in Chapter 5.